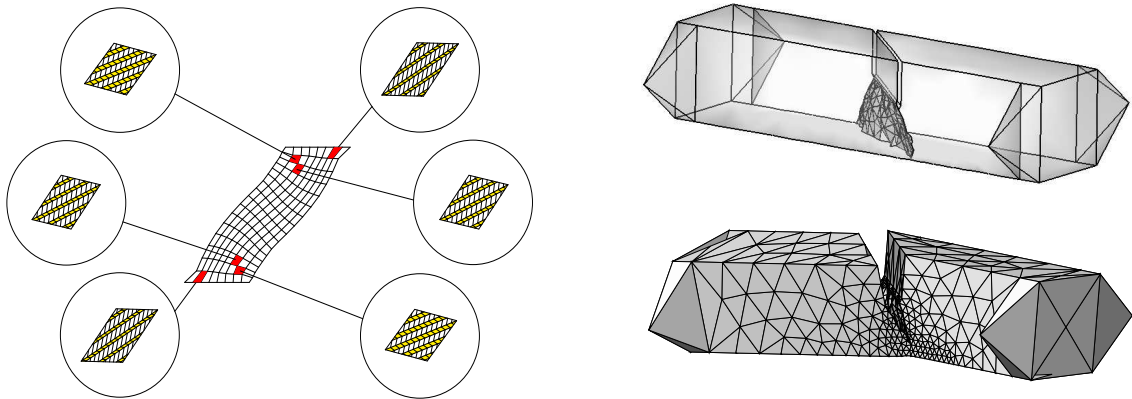


# Aspects of Energy Minimization in Solid Mechanics: Evolution of Inelastic Microstructures and Crack Propagation

Ercan Gürses



$$I(\varphi_{n+1}^*, \mathcal{I}_{n+1}^*; \Gamma_{n+1}^*) = \min_{\varphi_{n+1}, \mathcal{I}_{n+1}; \Gamma_{n+1}} \int_{\mathcal{B}_{\Gamma_{n+1}}} W(\nabla \varphi_{n+1}, \mathcal{I}_{n+1}; \Gamma_{n+1}) dV$$

Bericht Nr.: I-19 (2007)  
Institut für Mechanik (Bauwesen), Lehrstuhl I  
Professor Dr.-Ing. C. Miehe  
Stuttgart 2007









# **Aspects of Energy Minimization in Solid Mechanics: Evolution of Inelastic Microstructures and Crack Propagation**

Von der Fakultät Bau- und Umweltingenieurwissenschaften  
der Universität Stuttgart zur Erlangung der Würde  
eines Doktor-Ingenieurs (Dr.-Ing.)  
genehmigte Abhandlung

vorgelegt von

**Ercan Gürses**

aus Ankara (Türkei)

Hauptreferat : Prof. Dr.-Ing. C. Miehe

Koreferat : Prof. Dr. rer. nat. K. Hackl

Tag der mündlichen Prüfung: 13. Juli 2007

Institut für Mechanik (Bauwesen) der Universität Stuttgart

2007

**Herausgeber:**

Prof. Dr.-Ing. habil. C. Miehe

**Organisation und Verwaltung:**

Institut für Mechanik (Bauwesen)

Lehrstuhl I

Universität Stuttgart

Pfaffenwaldring 7

70550 Stuttgart

Tel.: ++49(0)711/685-66378

Fax: ++49(0)711/685-66347

© Ercan Gürses  
Institut für Mechanik (Bauwesen)  
Lehrstuhl I  
Universität Stuttgart  
Pfaffenwaldring 7  
70550 Stuttgart  
Tel.: ++49(0)711/685-69259  
Fax: ++49(0)711/685-66347

Alle Rechte, insbesondere das der Übersetzung in fremde Sprachen, vorbehalten. Ohne Genehmigung des Autors ist es nicht gestattet, dieses Heft ganz oder teilweise auf fotomechanischem Wege (Fotokopie, Mikrokopie) zu vervielfältigen.

ISBN 3-937859-07-1 (D 93 Stuttgart)

## Abstract

This work deals with theoretical energy minimization principles and the development of associated computational tools for the description of microstructure evolution and fracture in solid mechanics. The thesis consists of two parts: (i) The description of inelastic deformation microstructures and their evolution in non-convex unstable solids and (ii) the development of a variational framework for configurational-force-driven brittle fracture based on energy minimization principles.

In the first part, a general framework is developed for the treatment of material instabilities and microstructure developments in inelastic solids. Material instabilities and microstructure developments are interpreted as the outcome of non(quasi)-convex variational problems which often suffer from the lack of solutions in the classical sense. The proposed framework is based on a mathematical relaxation theory which is associated with the replacement of non-quasiconvex potentials with their generalized convex envelopes. Furthermore, deformation microstructures and their evolution are studied for three different constitutive material responses: the symmetry-breaking martensitic phase transformations, the single-slip crystal plasticity and the isotropic damage mechanics. For this purpose specific numerical relaxation algorithms are proposed for each constitutive response. The performance of numerical relaxation schemes is presented by several representative examples.

In the second part, a variational formulation of quasistatic brittle fracture in elastic solids is outlined and a finite-element-based computational framework is proposed for the two- and three-dimensional crack propagation. The starting point is a variational setting that recasts a monotonic quasistatic fracture process into a sequence of incremental energy minimization problems. The proposed numerical implementation exploits this variational structure. It introduces discretized crack patterns with configurational-force-driven incremental crack segment and crack surface releases. These releases of crack segments and surfaces constitute a sequence of positive definite subproblems with successively decreasing overall stiffness, providing an extremely robust algorithmic setting in the postcritical range. The formulation is embedded into an accompanying  $r$ -adaptive crack-pattern adjustment procedure with configurational-force-based indicators in conjunction with crack front constraints. The performance of the proposed algorithm is demonstrated by means of several two- and three-dimensional crack propagation examples and comparisons with experiments.

## Zusammenfassung

Die Arbeit befaßt sich mit Theorie und Numerik der Entwicklung von Mikrostrukturen und Bruch in der Festkörpermechanik. Sie besteht aus zwei Teilen: (i) Beschreibung von inelastischen Deformationsmikrostrukturen und ihrer Evolution in nichtkonvexen instabilen Körpern und (ii) Entwicklung einer Variationsformulierung für konfigurationskraftgetriebenen spröden Bruch basierend auf Energieminimierungsprinzipien.

Im ersten Teil wird eine allgemeine Struktur für die Behandlung von materiellen Instabilitäten und Mikrostrukturentwicklungen in inelastischen Körpern entwickelt. Materielle Instabilitäten und Mikrostrukturentwicklungen werden als Resultate nicht-(quasi)-konvexer Variationsprobleme gedeutet, für die häufig keine klassischen Lösungen existieren. Die vorgeschlagene Methodik basiert auf einer mathematischen Relaxierungstheorie, bei der die nicht-(quasi)-konvexen Potentiale durch ihre generalisierten konvexen Hüllen ersetzt werden. Außerdem werden Deformationsmikrostrukturen und ihre Entwicklung für drei unterschiedliche Klassen von Materialverhalten analysiert: symmetriebrechende martensitische Phasenumwandlungen, Kristallplastizität und isotrope Bruchmechanik. Zu diesem Zweck werden spezifische numerische Relaxierungsalgorithmen für jede der erwähnten Klassen von Materialverhalten vorgeschlagen. Die Leistungsfähigkeit der numerischen Relaxierungsmethoden wird durch einige repräsentative Beispiele dargestellt.

Im zweiten Teil wird eine Variationsformulierung für quasistatischen spröden Bruch in elastischen Körpern behandelt und ein auf der Methode der Finiten Elemente basierender Ansatz für die zwei- und dreidimensionale Rißausbreitung vorgeschlagen. Ausgangspunkt ist eine Variationsstruktur, die einen monotonen quasistatischen Bruchprozeß als eine Folge inkrementeller Energieminimierungsprobleme darstellt. Die vorgeschlagene numerische Implementierung nutzt diese Variationsstruktur aus. Auf diese Weise werden diskrete Rißmuster durch die konfigurationskraftgetriebene Ausbreitung von Rißsegmenten und Rißoberflächen erzeugt. Das Entstehen von Rißsegmenten und -oberflächen stellt eine Folge positiv definiter Teilprobleme mit sukzessiv abnehmender Gesamtsteifigkeit dar, was zu einem extrem robusten Algorithmus im postkritischen Bereich führt. Die Formulierung ist außerdem in ein r-adaptives Verfahren zur Anpassung des Rißmusters mit konfigurationskraftbasierten Indikatoren und Zwangsbedingungen durch die Rißfront eingebettet. Die Leistungsfähigkeit des vorgeschlagenen Algorithmus wird anhand einiger zwei- und dreidimensionaler Rißausbreitungsbeispiele und dem Vergleich mit Experimenten demonstriert.

## Preface

Although there is a single name on the cover of this thesis, it would not be accomplished in its current form without the help of many individuals. Being aware of the danger that exists by naming the people who contributed in one way or another to this dissertation, I may have unintentionally overlooked some other contributors. For this reason I apologize in advance.

The work presented in this thesis was carried out between the years 2002 and 2007 while I was a co-worker at the Institute of Applied Mechanics, Chair I at the University of Stuttgart. The financial support provided by Deutsche Forschungsgemeinschaft (DFG) under grant SFB404/C11 “Mathematische Modelle zur Plastizität bei finiten Deformationen” is gratefully acknowledged.

First of all, I would like to express my deep appreciation for Professor Christian Miehe for his willingness to take me into his research group and unconditional warm welcome to all foreign co-workers. During my five-years occupation in his institute he was extremely supportive and showed great confidence in me. This dissertation could not have been written without him who not only gave me impassioned and intensive guidance but also encouraged and challenged me throughout my academic program. I would also like to thank Professor Klaus Hackl for his interest in my work and for his acceptance to become co-referee for my thesis. Furthermore, I want to express my earnest gratitude to Professor Erman Tekkaya for motivating and supporting me to continue my graduate studies in Germany.

My most sincere thanks go to my roommate and a special friend Serdar Göktepe whom I know for twelve years. In addition to our long-standing close friendship I had many very helpful and fruitful scientific discussions which undoubtedly helped me to a great extent to improve my knowledge on theoretical and computational mechanics.

I am thankful to my work colleagues for the pleasant atmosphere and working conditions at the Institute of Applied Mechanics. In this respect I want to thank specially Joel Mendez for his very cordial and generous friendship and Manuel Birkle for his helps and contribution to chapter 10 as an outcome of our graceful cooperation.

My sincere gratitude goes to two former colleagues Dr. Matthias Lambrecht and Dr. Nikolas Apel for their warm friendship and help with many private and scientific issues. During my master thesis I had the opportunity and the chance to work with Dr. Matthias Lambrecht which was a true great pleasure. Chapters 5 and 6 of the thesis are mainly based on the outcome of intensive cooperation with him.

I am also very grateful to Alp Karakaya, Serkan Nohut and Bařaran Özmen whom I supervised during their master theses. Their work and many interesting scientific discussions with them contributed directly or indirectly to the thesis. In particular the direct contributions by Bařaran Özmen to chapter 4 and indirect contributions by Alp Karakaya to chapter 9 are gratefully acknowledged.

I would like to acknowledge and extend my heartfelt thanks to three very special friends Özgür Akan, Volkan Demir and Nezh Sömen to whom I am indebted for reasons best known to themselves.

Finally, I would like to express my eternal gratitude to my parents, Sülün and Deniz Gürses for their everlasting love and support, for their good care over long years and for helping me to become the person I am today. This includes also my brother Eren Gürses, my sister-in-law Elif Gürses and my nephew, very recent addition to our extended family, Derin Gürses.

Stuttgart, August 2007

Ercan Gürses

## Contents

<b>1. Introduction</b> . . . . .	<b>1</b>
1.1. Motivation and State of the Art . . . . .	1
1.1.1. Description of Microstructures based on Energy Relaxation . . . . .	1
1.1.2. Configurational Force Driven Brittle Fracture . . . . .	4
1.2. Outline of the Thesis . . . . .	7
<b>2. Mathematical Preliminaries and Notions of Convexity</b> . . . . .	<b>9</b>
2.1. Mathematical Preliminaries . . . . .	9
2.2. Existence of Global Minimizers . . . . .	12
2.3. Convex Sets . . . . .	13
2.4. Convex Functions . . . . .	14
2.5. Convexity and Weak Convexity Notions of Free Energy Function . . . . .	15
2.5.1. Convexity of Free Energy Function . . . . .	15
2.5.2. Polyconvexity . . . . .	17
2.5.3. Quasiconvexity . . . . .	19
2.5.4. Rank-One Convexity . . . . .	20
2.6. Lack of Convexity and Non-Existence of Minimizers . . . . .	21
<b>3. Variational Formulation of Inelasticity and Relaxation Theory</b> . . . . .	<b>23</b>
3.1. Incremental Variational Formulation of Inelastic Materials . . . . .	23
3.1.1. Internal Variable Formulation of Inelastic Materials . . . . .	23
3.1.2. Local Incremental Minimization for Standard Dissipative Solids . . . . .	24
3.1.3. Dissipation Functions for Single-Surface Models of Inelasticity . . . . .	26
3.1.4. Global Incremental Minimization for Standard Dissipative Solids . . . . .	27
3.2. Existence and Stability of Incremental Solutions . . . . .	28
3.2.1. Check of Rank-One Convexity for the Incremental Stress Potential . . . . .	29
3.2.2. Global Formulation for Two-Dimensional Problems . . . . .	30
3.2.3. Algorithmic Implementation for Two-Dimensional Problems . . . . .	31
3.3. Relaxation of a Non-Convex Constitutive Response . . . . .	32
3.3.1. Quasiconvexified Relaxed Incremental Variational Problem . . . . .	32
3.3.2. Rank-One-Convexified Relaxed Incremental Variational Problem . . . . .	34
3.3.3. First-Order Rank-One-Convexified Incremental Variational Problem . . . . .	35
<b>4. Application of Relaxation Theory to Phase Transformations</b> . . . . .	<b>39</b>
4.1. The Model Problem: Martensitic Phase Transformations . . . . .	39
4.1.1. Transformation Matrices and Energy Storage . . . . .	39
4.1.2. Energy Wells . . . . .	41
4.1.3. The Geometrically Linear Theory . . . . .	42
4.1.4. Relaxation of Two-Well Potentials . . . . .	43
4.1.5. Relaxation of Three-Well Potentials . . . . .	47

4.2.	Numerical Examples of Relaxation in Phase Transformations . . . . .	49
4.2.1.	Simple Tension Test . . . . .	49
4.2.2.	Microstructure Development in a Homogeneous Test . . . . .	51
4.2.3.	Biaxial Tension Test of a Perforated Plate . . . . .	53
<b>5.</b>	<b>Application of Relaxation Theory to Single-Slip Plasticity . . . . .</b>	<b>57</b>
5.1.	The Canonical Model-Problem: Multiplicative Single-Slip Plasticity . . . . .	57
5.1.1.	Energy Storage Function and Stress Response . . . . .	57
5.1.2.	Dissipation Function and Evolution of Internal Variables . . . . .	58
5.1.3.	Algorithmic Approximation of the Incremental Work Function . . . . .	59
5.1.4.	Algorithmic Setting of the Constitutive Minimization Problem . . . . .	61
5.1.5.	Stress Update and Elastic-Plastic Moduli for Plastic Loading . . . . .	62
5.1.6.	Relaxation of Non-Convex Multiplicative Single-Slip Plasticity . . . . .	63
5.2.	Numerical Examples of Relaxations in Single-Slip Plasticity . . . . .	65
5.2.1.	Microstructure Development in a Homogeneous Tension Test . . . . .	68
5.2.2.	Microstructure Development in a Homogeneous Shear Test . . . . .	69
5.2.3.	Relaxation of an Inhomogeneous Elastoplastic Strip in Tension . . . . .	71
5.2.4.	Relaxation of an Inhomogeneous Elastoplastic Strip in Shear . . . . .	74
<b>6.</b>	<b>Application of Relaxation Theory to Damage Mechanics . . . . .</b>	<b>77</b>
6.1.	The Model Problem: Isotropic Damage Mechanics . . . . .	77
6.1.1.	One-Dimensional Damage Model . . . . .	77
6.1.2.	Two-Dimensional Isochoric Damage Model . . . . .	82
6.1.3.	Extension of Relaxation Algorithm to Three-Dimensional Analysis . . . . .	85
6.1.4.	Visualization and Interpretation of Isotropic Microstructures . . . . .	86
6.2.	Numerical Examples of Relaxations in Damage Mechanics . . . . .	86
6.2.1.	Volume Preserving Cyclic Loading Test . . . . .	87
6.2.2.	Tension Test of a Perforated Plate in Two-Dimensional Framework . . . . .	89
6.2.3.	Tension Test of a Perforated Plate in Three-Dimensional Framework . . . . .	90
<b>7.</b>	<b>Theories of Brittle Fracture . . . . .</b>	<b>93</b>
7.1.	Stress Concentrations in Solids . . . . .	93
7.1.1.	Stress Trajectories . . . . .	93
7.1.2.	Infinite Plate with Circular Hole under Tension . . . . .	93
7.1.3.	Infinite Plate with Elliptical Hole under Tension . . . . .	97
7.2.	Stress Intensity Factors Approach to Fracture . . . . .	100
7.3.	Energetic Approach to Fracture . . . . .	102
7.3.1.	Griffith Theory . . . . .	103
7.3.2.	Energy Release Rate . . . . .	106
7.3.3.	Equivalence of Energy Release Rate and Stress Intensity Factor . . . . .	107
7.3.4.	$J$ -Integral . . . . .	109
7.3.5.	Relationship Between $J$ -Integral and Energy Release Rate . . . . .	111



7.4.	Atomistic Approach to Fracture . . . . .	113
7.5.	Crack Tip Plasticity and Cohesive Fracture Theories . . . . .	115
<b>8.</b>	<b>Configurational Forces in Brittle Fracture Mechanics . . . . .</b>	<b>121</b>
8.1.	Concept of Configurational Forces . . . . .	121
8.2.	Alternative Derivations of Energy Momentum Tensor . . . . .	121
8.2.1.	Eshelby's Thought Experiment . . . . .	121
8.2.2.	Formal Derivation from a Lagrangian Density . . . . .	122
8.2.3.	Projection of Balance Laws onto Material Manifold . . . . .	124
8.2.4.	Derivation from the Noether's Theorem . . . . .	125
8.2.5.	Derivation from Invariance Requirements . . . . .	126
8.3.	Configurational-Force-Driven Brittle Crack Propagation . . . . .	130
8.3.1.	Basic Geometry of a Solid with a Crack . . . . .	131
8.3.2.	Global Elastic Response of a Solid with Cracks . . . . .	134
8.3.3.	Crack Evolution Obtained by Maximum Dissipation . . . . .	136
8.4.	Restriction to Geometrically Linear Theory . . . . .	137
<b>9.</b>	<b>Staggered Algorithm for Brittle Crack Propagation . . . . .</b>	<b>141</b>
9.1.	Spatial Discretization of the Solid with a Crack . . . . .	141
9.2.	Global Response of the Spatially Discretized Solid . . . . .	141
9.3.	Time Discretization of the Crack Evolution Problem . . . . .	143
9.4.	Staggered Algorithm for Incremental Energy Minimization . . . . .	145
9.5.	Discretization in Geometrically Linear Theory . . . . .	146
9.6.	Algorithmic Treatment of Two-Dimensional Crack Propagation . . . . .	147
9.6.1.	Data Structures for Crack Release with Node Doubling . . . . .	147
9.6.2.	Data Update due to Segment Release and Node Doubling . . . . .	149
9.7.	Algorithmic Treatment of Three-Dimensional Crack Propagation . . . . .	152
9.7.1.	Data Structures for 3-D Crack Release with Node Doubling . . . . .	152
9.7.2.	Data Update due to Facet Release and Node Doubling . . . . .	154
<b>10.</b>	<b>Representative Numerical Examples . . . . .</b>	<b>159</b>
10.1.	Two-Dimensional Crack Propagation Examples . . . . .	159
10.1.1.	Single Edge Notched Tensile Test I . . . . .	159
10.1.2.	Single Edge Notched Tensile Test II . . . . .	162
10.1.3.	Symmetric Three Point Bending Test . . . . .	164
10.1.4.	Asymmetric Three Point Bending Test . . . . .	166
10.1.5.	Brazilian Splitting Test . . . . .	168
10.1.6.	Tensile Test with Two Notches and Holes . . . . .	168
10.1.7.	Square Notched Specimen under Simple Shear . . . . .	169
10.1.8.	Comparison of Different Crack Criteria . . . . .	172
10.2.	Three-Dimensional Crack Propagation Examples . . . . .	174
10.2.1.	Simple Tension Test . . . . .	174

---

10.2.2. Asymmetric Bending of Notched Specimens . . . . .	176
10.2.3. Torsion Test of Notched Prismatic Beam . . . . .	178
10.2.4. Bending of Notched Beams with Holes . . . . .	180
<b>11. Summary and Outlook . . . . .</b>	<b>183</b>
11.1. Description of Microstructures based on Energy Relaxation . . . . .	183
11.2. Configurational Force Driven Brittle Fracture . . . . .	184
<b>A. Derivatives for Convexification of Single-Slip Plasticity . . . . .</b>	<b>187</b>
<b>B. Derivatives for Convexification in Damage Mechanics . . . . .</b>	<b>188</b>
<b>C. Basics of Complex Functions . . . . .</b>	<b>189</b>
<b>D. The Linear Elastic Crack Tip Fields . . . . .</b>	<b>191</b>
D.1. The Anti-Plane Shear Problem - Mode III Cracking . . . . .	191
D.2. Mode I Cracking . . . . .	194
D.3. Mode II Cracking . . . . .	198
<b>E. Closed Form Solutions of Stress Intensity Factors . . . . .</b>	<b>198</b>

## 1. Introduction

Variational minimization and maximization principles have been successfully employed in the study of many problems from several branches of sciences. These include, for example, the principle of minimum potential energy in elasticity theory, the Hamiltonian principles in classical field theories, applications of the free discontinuity problem to fracture mechanics, signal and image reconstruction and the Fermat's principle in optics. In recent years, the activity of research on variational minimization principles, particularly in the areas theoretical, applied and computational mechanics and applied mathematics has been increased. It is the aim of this contribution to develop theoretical and computational approaches for the description of some aspects of solid mechanics based on energy minimization principles. More precisely, the goals of this work are: (i) *Description of inelastic deformation microstructures and their evolution in non-convex unstable solids* and (ii) *development of a variational framework for configurational-force-driven brittle fracture based on energy minimization principles.*

### 1.1. Motivation and State of the Art

**1.1.1. Description of Microstructures based on Energy Relaxation.** Microstructures that are observed in nature often show complex patterns with length scales much smaller than characteristic macroscopic dimensions of the problem considered. It is possible mathematically to describe these microstructures by *non-convex variational problems*. Furthermore, it has been shown that non-existence of minimizers in these variational problems are closely related to *fine scale oscillatory infimizing sequences* which are interpreted as *microstructures*. In particular, there is a strong parallelism between the microstructures that develop in martensitic phase transformations and fine scale oscillatory infimizing sequences of energy functionals describing phase transforming elastic crystals, see BALL & JAMES [14, 15], CHU & JAMES [44], JAMES & HANE [107], BHATTACHARYA [22] among others.

The boundary value problems of non-linear elasticity can be formulated as variational minimization problems, i.e. find the deformation map  $\varphi : \mathcal{B} \subset \mathcal{R}^n \rightarrow \mathcal{R}^m$  such that,

$$\inf_{\varphi \in \mathcal{W}^{1,p}(\mathcal{B})} \left\{ I(\varphi) = \int_{\mathcal{B}} \psi(\nabla \varphi) dV \mid \varphi = \bar{\varphi} \text{ on } \partial \mathcal{B} \right\} \quad (1.1)$$

where  $\psi$  denotes the energy storage function. The existence of solutions for this problem demands the *sequential weak lower semicontinuity* of the functional  $I$  which is ensured provided that the energy storage function  $\psi$  possesses particular weak convexity and growth conditions. For vector valued variational problems the crucial weak convexity notion is the *quasiconvexity* (MORREY [157]) which is indeed equivalent to the sequential weak lower semicontinuity of the energy functional under suitable growth assumptions. Other important notions which provide lower and upper bounds for quasiconvexity are the *polyconvexity* (BALL [12]) and the *rank-one convexity*.

Non-convex variational problems which often suffer from the lack of solutions in the classical sense can be treated by the *relaxation theory*, see DACOROGNA [51]. That is the replacement of the non-quasiconvex storage function  $\psi$  by its quasiconvex envelope

$$\psi_Q(\nabla \varphi) = \inf_{\mathbf{w} \in \mathcal{W}_0^{1,p}(D)} \frac{1}{|D|} \int_D \psi(\nabla \varphi + \nabla \mathbf{w}) dV \quad (1.2)$$

in (1.1). In contrast to the original problem, the relaxed functional  $I_Q$  is well posed and has a minimizer. Moreover, minimums of the relaxed problem  $I_Q$  are exactly the weak limits of infimizing sequences for the original functional  $I$ , i.e.  $\min I_Q(\varphi) = \inf I(\varphi)$ . Unfortunately,  $\psi_Q$  is defined through an integral minimization problem without a local characterization and there is no general methodology known for the determination of this envelope. However, there are some exceptional cases in which the quasiconvex envelope is obtained analytically, see KOHN [116] and PIPKIN [184] for double-well energies and DESIMONE & DOLZMANN [57, 58] for nematic elastomers. Moreover, there exist upper and lower bounds of quasiconvex envelopes which can be employed to design numerical schemes for the computation of suitable approximations, see BHATTACHARYA & DOLZMANN [23], BARTELS ET AL. [19] and DOLZMANN [60]. The canonical bounds are the so-called polyconvex and rank-one convex envelopes. In particular, the computation of rank-one convex hulls have been extensively studied, e.g. ARANDA & PERDREGAL [7] and DOLZMANN [59], since the rank-one convexification describes intrinsically laminate type microstructures (PEDREGAL [179]) that are observed in many materials.

The *martensitic phase transformation* in crystalline solids is one of the most successful application areas of the relaxation theory, see MÜLLER [163], BHATTACHARYA [22], DOLZMANN [60] and CARSTENSEN [38]. The martensitic solids exhibit abrupt changes in their crystalline structure if they are cooled down below or heated up above a critical temperature. The high and low temperature phases are often denoted as the austenite and the martensite, respectively. The austenite has a greater symmetry than the martensite and this gives rise to symmetry-related variants of the martensite during a transformation. The material response of this kind can be described by *multi-well* energy storage functions

$$\psi(\mathbf{F}) = \min_{i=0\dots N} \{\psi_i(\mathbf{F})\} \quad \text{with} \quad \psi_i(\mathbf{F}) = \begin{cases} = 0 & \text{if } \mathbf{F} = \mathbf{Q}U_i \\ > 0 & \text{otherwise} \end{cases} \quad (1.3)$$

which are clearly non-convex. These energies yield multiple stress-free states and lead to fine scale mixture of martensite variants during a phase transformation. In recent years, simulation of martensitic microstructures based on different relaxation approaches have been performed by LUSKIN [128], GOVINDJEE & MIEHE [80], CARSTENSEN [38], GOVINDJEE, MIELKE & HALL [81], DOLZMANN [60], AUBRY, FAGO & ORTIZ [11], BARTELS ET AL. [19], KRUŽÍK, MIELKE & ROUBÍČEK [120], GOVINDJEE, HACKL & HEINEN [79] among others. Furthermore, there are applications of the relaxation theory beyond the analysis of crystalline microstructures in martensitic transformations. DESIMONE & DOLZMANN [57, 58] and CONTI, DESIMONE & DOLZMANN [47] have studied nematic elastomers which undergo a nematic to isotropic phase transformation.

The relaxation theory can be applied to *inelastic materials* similar to the elastic constitutive response of martensitic phase transformations if a *variational formulation of inelasticity* is constructed. However, this is only possible in an incremental sense within discrete time steps. The set up of a general incremental variational formulation of inelasticity has been developed in the recent works MIEHE [142] and MIEHE, SCHOTTE & LAMBRECHT [149] which are conceptually in line with the papers ORTIZ & REPETTO [175], ORTIZ & STAINIER [177] and CARSTENSEN, HACKL & MIELKE [40]. The key idea can be described as follows, for further details see aforementioned works. The general internal variable formulation of inelasticity for *generalized standard media* is governed by two scalar functions: the *energy storage function*  $\psi$  and the *dissipation function*  $\phi$ . The general set

up of this generic type of material model can be related to the works BIOT [24], ZIEGLER & WEHRLI [218], GERMAIN [78], HALPHEN & NGUYEN [92], see also the recent treatments by MAUGIN [132] and NGUYEN [167]. It covers a broad spectrum of constitutive models in viscoelasticity, plasticity and damage mechanics. For this class of materials we consider a variational formulation

$$W(\mathbf{F}_{n+1}) = \inf_{\mathcal{I}} \int_{t_n}^{t_{n+1}} [\dot{\psi} + \phi] dt \quad \text{with} \quad \mathcal{I}(t_n) = \mathcal{I}_n \quad (1.4)$$

where a quasi-hyperelastic stress potential at discrete time steps is obtained from a local *minimization problem of the constitutive response* with respect to internal variables  $\mathcal{I}$ . The underlying basic approach is the determination of a path of internal variables in a finite increment of time that minimizes a generalized incremental work expression.

The incremental variational formulation outlined above gives the opportunity to analyze inelastic microstructures and define the stability of the incremental inelastic response in terms of terminologies used in elasticity theory, see for instance DACOROGNA [51], CIARLET [45], MARSDEN & HUGHES [130] and ŠILHAVÝ [200]. Here, the incremental potential obtained from the *incremental energy minimization principle* (1.4) for standard dissipative solids plays a crucial role. The inelastic solid is considered to be *stable* if this potential is *quasiconvex*. On the other hand, the lack of quasiconvexity gives rise to the formation of microstructures. This formulation extends rate-type energetic definitions of material stability by PETRYK [181, 182] in terms of velocity fields to a finite-step-sized setting in terms of absolute placement fields. However, as noted already, quasiconvexity is a global integral condition which is hard to verify in practice. More manageable condition is the slightly weaker rank-one convexity notion that is considered to be a close approximation of quasiconvexity. The incremental potential  $W$  is said to be *rank-one convex* if

$$W(\xi \mathbf{F}_1 + (1 - \xi) \mathbf{F}_2) \leq \xi W(\mathbf{F}_1) + (1 - \xi) W(\mathbf{F}_2) \quad \text{for} \quad \mathbf{F}_2 - \mathbf{F}_1 = \mathbf{m} \otimes \mathbf{N} \quad (1.5)$$

holds for every  $0 \leq \xi \leq 1$ ,  $\mathbf{m}, \mathbf{N} \in \mathcal{R}^3$  and  $\mathbf{F}_1, \mathbf{F}_2 \in \mathcal{R}_+^{3 \times 3}$ . As already pointed out in MIEHE & LAMBRECHT [147, 146] classical conditions of material stability of elastic-plastic solids outlined in HILL [100] and RICE [191] are consistent with the infinitesimal form of the rank-one convexity, i.e. the strong ellipticity or Legendre-Hadamard condition. In the context of inelasticity, relaxation methods have been recently started to be studied. A relaxation algorithm based on rank-one convexification and sequential lamination has been developed by ORTIZ & REPETTO [175] and ORTIZ, REPETTO & STAINIER [176] and applied for the modeling of dislocation structures in single crystal plasticity. On the basis experimental observations, they employed strong assumptions with respect to the form and type microstructure, e.g. constant volume fraction of phases. MIEHE & LAMBRECHT [147, 146] have investigated small and large strain phenomenological strain softening plasticity models by using relaxation theory with substantial restrictions on possible microstructures. Furthermore, a one-dimensional softening plasticity model have been studied in LAMBRECHT, MIEHE & DETTMAR [122]. CARSTENSEN, HACKL & MIELKE [40] analyzed the relaxation of single slip multiplicative plasticity which became later a canonical model problem, see for example HACKL & HOPPE [91], MIEHE, LAMBRECHT & GÜRSSES [148], BARTELS ET AL. [19], CONTI & ORTIZ [48] and CONTI & THEIL [49]. Note that strain softening and slip plasticity models have different origins of non-convexity. The former has a non-monotonic stress function governed by non-convex

incremental potentials while in the latter one non-convexity raises due to geometrical constraints imposed by the slip system. Another softening mechanism in constitutive material models is due to damage which provides an alternative area of application for relaxation, see FRANCFORT & MARIGO [71] and GÜRSES & MIEHE [86].

**1.1.2. Configurational Force Driven Brittle Fracture.** Fracture is one of the main failure mechanisms of engineering materials and structural components. The assessment of fracture through theoretical and computational models is not only a challenging task in mechanics but also of great importance from the engineering point of view. Theoretical foundations of the classical theory of brittle fracture can be traced back to the seminal works of GRIFFITH [84, 85], where a framework based on energetic considerations were employed for equilibrium crack problems. Griffith proposed that solids have a *surface energy* which must be compensated for a given crack to propagate. Then the critical load level for a given crack is found by the *principle of minimum potential energy* of elasticity with an extension that takes into account the *surface energy* of the solid. Although Griffith was the first to relate the strength of materials to the crack size quantitatively, fracture mechanics is accepted mainly as an engineering discipline after Irwin's contributions, IRWIN [103, 104, 105]. Instead of considering the energy of the whole system with a given crack, IRWIN [104, 105] examined the stress field in the neighborhood of the crack tip and introduced the celebrated concept of *stress intensity factors*  $K$  as functions of the crack geometry and the loading. Based on the works of Irwin, it has been shown that the stress field in a linear elastic cracked solid can be expressed as

$$\sigma_{ij} = \left( \frac{K}{\sqrt{2\pi r}} \right) f_{ij}(\theta) + \sum_{n=0}^{\infty} A_n r^{n/2} g_{ij}^n(\theta) \quad (1.6)$$

in terms of functions  $f_{ij}(\theta)$  and  $g_{ij}(\theta)$  in a polar coordinate system  $r - \theta$  attached to the crack tip. The second term on the right hand side represents the higher order (non-singular) contributions to the solution which depend on the geometry of the problem. Note that the solution given above contains for any particular configuration a leading term depending on  $1/\sqrt{r}$  which approaches to infinity as  $r \rightarrow 0$ , while the other term vanishes. Irwin also related the *stress intensity factors*  $K$  to the *energy release rate* of Griffith. An alternative approach to elastic brittle fracture originated in the work of BARENBLATT [16], which accounts for the cohesive forces at the crack tip. In the theory of Barenblatt, possible fracture surfaces ahead of a crack are allowed to separate with a resistance due to atomic cohesive forces. As a consequence of these forces, the singularity at the crack tip disappears and stresses become bounded. Later, RICE [189] introduced the path independent  $J$ -integral describing the energy flux into the crack tip for two-dimensional crack problems, see also CHEREPANOV [42], who proposed independently the same path independent integral. The vectorial  $J$ -integral in the large strain framework is defined by

$$\mathbf{J} = \int_{\Gamma} [ \psi(\mathbf{F}) \mathbf{1} - \mathbf{F}^T \partial_{\mathbf{F}} \psi(\mathbf{F}) ] \mathbf{N} \, dS, \quad (1.7)$$

where  $\Gamma$  is an arbitrary curve that surrounds the crack tip with an outward normal  $\mathbf{N}$ . A precedent in a different application was established by ESHELBY [66]. Eshelby introduced the Maxwell-elasticity tensor  $\Sigma$  (later called the energy momentum tensor, ESHELBY [68])

$$\Sigma = \psi(\mathbf{F}) \mathbf{1} - \mathbf{F}^T \mathbf{P} \quad \text{with} \quad \mathbf{P} = \partial_{\mathbf{F}} \psi(\mathbf{F}) \quad (1.8)$$



in order to characterize forces acting on dislocations and defects which are often referred to as *configurational* or *material forces*. Its normal component, when integrated over a closed surface, is identical to the path independent  $J$ -integral. We refer in this context to the review articles by COTTEREL [50] and ERDOGAN [64], which provide an overview on the history and the current status of the fracture mechanics or the books by KANNINEN & POPELAR [111] and ANDERSON [6] for comprehensive treatments of the topic. Later, STUMPF & LE [207] and MAUGIN & TRIMARCO [135] developed *local variational formulations* for the evolution problem of brittle fracture based on material *configurational forces* acting on crack tip singularities in the sense of ESHELBY [66, 68, 69] and RICE [189]. We refer to MAUGIN [133], GURTIN [88] and KIENZLER & HERRMANN [113] for a treatment of configurational forces in a broader context. GURTIN & PODIO-GUIDUGLI [89, 90] employed *configurational forces* for crack propagation in a non-variational framework, where configurational forces are considered as primitive objects with their own balance equation.

Engineering numerical treatments of discrete fracture based on *cohesive zone* constitutive formulations in the sense of BARENBLATT [16] and DUGDALE [61] started with the work of HILLERBORG, MODEER & PETERSSON [98] and have been dramatically increased in recent years. In this context, a broad spectrum of alternative finite element based computational strategies for the *modeling of discontinuities* were developed in the last two decades. We refer to the *interface element formulations* of NEEDLEMAN [166] for void nucleation and interfacial debonding and XU & NEEDLEMAN [216], CAMACHO & ORTIZ [37] for two-dimensional dynamic fracture and fragmentation. ORTIZ & PANDOLFI [174] extended these formulations to three dimensional setting where triangular interface elements are embedded into a quadratic tetrahedral mesh for the modeling of dynamic cohesive fracture. Later PANDOLFI & ORTIZ [178] further developed their approach to incorporate an adaptive insertion of the interface elements when they are required. Furthermore, *element enrichment strategies* were proposed in the context of enhanced-assumed strain finite element design (EAS) of strong discontinuities by SIMÓ, OLIVER & ARMERO [202], OLIVER [171]. See also JIRASEK [109] and MOSLER [158] for a comparative study and a review of strong discontinuity approaches. The third category of approaches is concerned with *nodal enrichment strategies*, usually denoted as *extended finite element (XFEM)* or *partition of unity finite element (PUFEM) methods*. This approach was developed first for two-dimensional linear elastic fracture mechanics by BELYTSCHKO & BLACK [20] and MOËS, DOLBOW & BELYTSCHKO [154] and is based on the partition of unity concept of MELENK & BABUŠKA [139]. Later, a three-dimensional model for non-planar crack propagation has been developed by MOËS, GRAVOUIL & BELYTSCHKO [155] and GRAVOUIL, MOËS & BELYTSCHKO [82] based on XFEM together with level sets. In addition to linear elastic fracture mechanics applications, XFEM was also employed for cohesive crack modeling by WELLS & SLUYS [212], MOËS & BELYTSCHKO [153] in two dimensions and recently by GASSER & HOLZAPFEL [75] and AREIAS & BELYTSCHKO [8] in three dimensions. In the very recent work of OLIVER, HUESPE & SANCHEZ [172], the *element* and the *nodal enrichment* strategies are compared in detail with regard to their accuracy, robustness and computational costs both in two and three dimensions. Similar to XFEM formulations, a cohesive segments method has been developed by REMMERS, DE BORST & NEEDLEMAN [187], where the discontinuity is modeled by unconnected piecewise linear segments. The method also exploits the partition of unity property of the shape functions. As a fourth basic concept, *discontinuous Galerkin formulations* based on Nitsche's method were proposed by HANSBO & HANSBO [93] for the simulation of the

discontinuities in a general framework not restricted to crack modeling. Following this concept, a mixed discontinuous Galerkin interface-element-type method was developed by MERGHEIM, KUHL & STEINMANN [140]. We refer to the review articles by KARIHALOO & XIAO [112] for the modeling of cracks in finite element context without remeshing and DE BORST, REMMERS & NEEDLEMAN [55] for cohesive zone models in FEM. In all above mentioned methods the underlying mesh structure remains more or less unchanged. In contrast, various types of *remeshing techniques* have been developed for the modeling of a crack propagation, see BITTENCOURT ET AL. [25] and BOUCHARD ET AL. [27]. The very recent works of MEDIAVILLA, PEERLINGS & GEERS [137, 136] combine continuum damage models with discrete crack modeling based on adaptive remeshing and propose a new continuous-discontinuous approach for ductile fracture simulations.

Computational implementations of *brittle fracture propagation* based on the Griffith-type criterion are rare in the literature. Fracture formulations based on a minimization of the energy (alternatively a maximization of dissipation) is thermodynamically motivated and related to *configurational forces*, see MAUGIN & TRIMARCO [135], GURTIN & PODIO-GUIDUGLI [89] and MIEHE & GÜRSES [143]. The computation of the configurational forces in the context of finite element discretizations goes back to the work of BRAUN [33], where these forces were employed as an indicator for the discretization error in a physically homogeneous body. FE-computation of configurational forces  $\mathbf{g}_I$  for elastic solids having defects like cracks, dislocations or phase boundaries have been outlined by STEINMANN, ACKERMANN & BARTH [206], DENZER, BARTH & STEINMANN [56], MUELLER, KOLLING & GROSS [161] and HEINTZ, LARSSON, HANSBO & RUNESSON [96] and has an analogous structure to the standard nodal force vector  $\mathbf{f}_I$ , i.e.

$$\mathbf{f}_I := - \mathbf{A} \int_{\mathcal{B}^e} \mathbf{B}_I^T \mathbf{P} \, dV \quad \text{and} \quad \mathbf{g}_I := - \mathbf{A} \int_{\mathcal{B}^e} \mathbf{B}_I^T \boldsymbol{\Sigma} \, dV . \quad (1.9)$$

An attempt towards the implementation of configurational-force-driven *fracture propagation* was first performed by MUELLER & MAUGIN [162], where the crack direction is related to the nodal configurational force at the crack tip obtained from the finite element computation, see also KOLLING & MUELLER [118] for an application to dynamic fracture. Recently, alternative configurational-force-driven elastic fracture implementations appeared in LARSSON & FAGERSTRÖM [124] and FAGERSTRÖM & LARSSON [70] for XFEM-based and HEINTZ [95] for discontinuous-Galerkin-based methods. MIEHE & GÜRSES [143, 144] and MIEHE, GÜRSES & BIRKLE [145] proposed an approach to brittle fracture propagation based on node doubling, interface release and alignment algorithms which are adaptively controlled by configurational forces. It is based on the exploitation of a global dissipation postulate and yields the crack propagation  $\dot{\mathbf{a}}_I$  in the same direction of the configurational force  $\mathbf{g}_I$

$$\mathcal{D} = \sum_{I \in \partial\Gamma} \mathbf{g}_I \cdot \dot{\mathbf{a}}_I \geq 0 \quad \implies \quad \dot{\mathbf{a}}_I = \dot{\gamma} \frac{\mathbf{g}_I}{|\mathbf{g}_I|} \quad (1.10)$$

locally at crack front nodes  $I \in \partial\Gamma$ . The dissipation  $\mathcal{D}$  is obtained from the inner product of the material forces  $\mathbf{g}_I$  acting on crack tip nodes and the material velocity  $\dot{\mathbf{a}}_I$  of the node  $I$  in the material structural configuration.

The classical Griffith-type theory of brittle fracture is restricted to problems where an initial crack is present. In other words, it cannot predict the *crack initiation* in a body



free of defects. This restriction of the classical Griffith theory of brittle fracture can be overcome by incremental *global* variational formulations as suggested by FRANCFORT & MARIGO [72] and BULIGA [36]. The aspect of *global energy minimization* is considered as one of the important theoretical impacts on fracture mechanics in recent years. An initial attempt towards the computational implementation of global minimization as a *regularized global minimization problem* was proposed by FRANCFORT & MARIGO [72], BOURDIN, FRANCFORT & MARIGO [30] similar to finite element formulations of image segmentation, see also BOURDIN [28] and BOURDIN & CHAMBOLLE [29] based on a minimization of the Mumford-Shah functional (MUMFORD & SHAH [165]). These global variational problems are governed by functionals involving volume and surface energies and appear in a variety of areas in applied sciences. They are denoted as *free discontinuity problems* and their numerical approximation as outlined for example in BRAIDES [31] is often performed with the help of the *theory of  $\Gamma$ -convergence*, see DAL MASO [53], BRAIDES [32], and *special functions of bounded variations* (SBV), see AMBROSIO, FUSCO & PALLARA [5].

## 1.2. Outline of the Thesis

**Chapter 2** outlines the mathematical preliminaries and fundamental principles which are needed for further developments. Therein, function spaces, strong and weak convergence of sequences, convexity and weak convexity notions – polyconvexity, quasiconvexity and rank-one convexity – are discussed. Furthermore, the existence theorems in non-linear elasticity theory and their relation to the convexity properties of energy storage functions are provided.

In **Chapter 3** we briefly describe the incremental variational formulation of inelastic materials and extend the results of non-linear elasticity provided in Chapter 2 to incremental response of inelastic materials. The main focus is then put on the relaxation theory for non-convex incremental variational problems of inelasticity. In particular, relaxation methods based on approximations of quasiconvex envelopes by rank-one convex envelopes are discussed.

We give a short review on the martensitic phase transformations in **Chapter 4**. It includes the concepts of transformation matrices, symmetry breaking variants, energy wells and compatibility conditions. In addition, the relaxation theory outlined in Chapter 3 is applied to the simple double- and three-well problems which show some fundamental features of the phase transformations. We demonstrate also the evolution of microstructures in terms of first- and second-order laminates.

**Chapter 5** is concerned with the constitutive modeling of single-slip plasticity which can be considered as the limit case of the multi-slip crystal plasticity with infinite latent hardening. A semi-analytical computational relaxation algorithm is proposed based on the first-order rank-one relaxation. Consequently, this leads to the solution of the non-convex minimization problem of relaxation for boundary value problems within a reasonable time. The results of the relaxation algorithm are presented by several numerical examples which include the visualization of microstructures and their evolution.

In **Chapter 6** as a model problem the damage mechanics is treated. First, we start with a scalar one-dimensional model and develop a relaxation algorithm. In two-dimensional setting, an isotropic damage model is considered that affects only the isochoric part of the constitutive response. We then propose a computational relaxation scheme based on isotropic microstructures contrary to previous applications with laminate-type

microstructures. This relaxation procedure is shown to be equivalent to the first-order rank-one convexification. Finally, we extend the formulation to three dimensional setting and present some numerical examples.

**Chapter 7** contains a brief overview about brittle fracture theories. We present some of the well-known approaches in the literature. These cover the stress intensity factors of Irwin, the energetic approach and the energy release rate of Griffith and the  $J$ -integral of Rice. The relations among different theories are provided as well. Further information of more technical nature such as the derivation of the singular stress fields and the closed form solutions of stress intensity factors are provided in Appendices D and E. In addition, the atomistic treatments and the cohesive theories of brittle fracture are shortly discussed.

The configurational forces are addressed in **Chapter 8** with a particular focus on their application to fracture mechanics. Starting with the Eshelby's thought experiment alternative derivations of the energy momentum tensor are outlined. These cover approaches based on a Lagrangian density, a projection of balance laws onto material manifold, the Noether's theorem and particular invariance requirements. Furthermore, we develop a thermodynamically consistent variational framework for quasi-static crack propagation in elastic solids and show that both the elastic equilibrium response as well as the local crack evolution follow in a natural format by exploitation of a global Clausius-Planck inequality in the sense of Coleman's method. Consequently, the crack propagation direction is identified by the material configurational force which maximizes the local dissipation at the crack front.

In **Chapter 9** a staggered computational algorithm for quasi-static crack propagation is developed. The variational formulation outlined in Chapter 8 is realized numerically by a spatial discretization with standard three-noded constant strain triangles and four-noded linear tetrahedral finite elements in two and three dimensions, respectively. Therefore, the constitutive setting of crack propagation in the space-discretized finite element context is naturally related to discrete nodes of a typical finite element mesh. In a consistent way with the node-based setting, the discretization of the evolving crack discontinuity is performed by the doubling of critical nodes and interfaces between finite elements. The crucial step for the success of this procedure is its embedding into an r-adaptive crack-segments and facets reorientation procedure based on configurational-force-based indicators in conjunction with crack front constraints. Here, successive crack releases appear in discrete steps associated with the given space discretization. These are performed by a staggered loading-release algorithm of energy minimization at frozen crack state followed by the successive crack releases at frozen deformation. This constitutes a sequence of positive definite discrete subproblems with successively decreasing overall stiffness, providing a very robust algorithmic setting in the postcritical range.

We demonstrate in **Chapter 10** the predictive capabilities of the proposed formulation of brittle crack propagation by means of representative numerical simulations and comparisons with experiments from the literature. These cover a broad spectrum of two- and three-dimensional examples such as simple tension, symmetric and asymmetric bending, Brazilian splitting, shear and torsion tests. Moreover, studies with respect to the accuracy of the numerical computation of configurational forces are performed and comparisons with other crack propagation criteria are presented.

## 2. Mathematical Preliminaries and Notions of Convexity

In this chapter we briefly review important mathematical concepts and definitions which are required for the subsequent treatments. These include some vector and function spaces, weak convergence of sequences and different convexity notions. These play important roles in existence theorems of variational problems and will be utilized in the development of relaxation methods in Chapter 3. For more detailed discussions or in depth mathematical studies, readers are referred to ROCKAFELLAR [193], DACOROGNA [51, 52], REDDY [186] and KREYSZIG [119]. See also CIARLET [45], MARSDEN & HUGHES [130], ŠILHAVÝ [200] and PEDREGAL [180] for mathematical treatments of non-linear elasticity.

### 2.1. Mathematical Preliminaries

An abstract space is a set of elements which can be numbers, matrices, sequences or functions satisfying certain axioms. By choosing different sets of axioms one obtains various types of abstract spaces. The most important ones for our considerations are *vector spaces*. A vector space  $X$  is a set which has vector addition and scalar multiplication operations. Furthermore, the set has to be closed under addition and scalar multiplication, and these operations have to satisfy following axioms for all  $\mathbf{u}, \mathbf{v}, \mathbf{w} \in X$  and  $\alpha, \beta \in \mathcal{R}$

$$\begin{array}{ll}
 \mathbf{u} + \mathbf{v} = \mathbf{v} + \mathbf{u} & \mathbf{u} + (\mathbf{v} + \mathbf{w}) = (\mathbf{u} + \mathbf{v}) + \mathbf{w} \\
 \mathbf{u} + \mathbf{0} = \mathbf{u} & \mathbf{u} + (-\mathbf{u}) = \mathbf{0} \\
 \alpha(\beta\mathbf{u}) = (\alpha\beta)\mathbf{u} & 1\mathbf{u} = \mathbf{u} \\
 \alpha(\mathbf{u} + \mathbf{v}) = \alpha\mathbf{u} + \alpha\mathbf{v} & (\alpha + \beta)\mathbf{u} = \alpha\mathbf{u} + \beta\mathbf{u}
 \end{array} \tag{2.1}$$

where  $\mathbf{0}, -\mathbf{u} \in X$  are the zero element and the additive inverse of  $\mathbf{u}$ , respectively. For example, the real line  $\mathcal{R}$  and the set  $\mathcal{R}^n$  of  $n$ -tuples are vector spaces. In addition, by endowing a vector space  $X$  with a norm  $\|\cdot\|$ , an inner product  $\langle \cdot, \cdot \rangle$  or a metric  $d(\cdot, \cdot)$  one obtains *normed*, *inner product* and *metric spaces*. Definitions of norm, inner product and metric on a vector space  $X$  are not unique, however, they need to fulfill some axioms, see for example REDDY [186] and KREYSZIG [119]. For instance, let  $\mathbf{u}, \mathbf{v} \in \mathcal{R}^n$  then the length (Euclidean norm) of  $\mathbf{u}$  defines a norm, the scalar product  $\mathbf{u} \cdot \mathbf{v}$  specifies an inner product and the distance between  $\mathbf{u}$  and  $\mathbf{v}$  is a metric. It is common to generate a metric  $d(\mathbf{u}, \mathbf{v})$  by using a norm, i.e.  $d(\mathbf{u}, \mathbf{v}) = \|\mathbf{u} - \mathbf{v}\|$ , and a norm by inner product, i.e.  $\|\mathbf{u}\| = \langle \mathbf{u}, \mathbf{u} \rangle^{1/2}$ . Hence, inner product spaces are normed spaces and normed spaces are metric spaces as well. Complete normed spaces (complete in the metric defined by the norm) and complete inner product spaces (complete in the metric defined by the inner product) are known to be *Banach* and *Hilbert* spaces, respectively. While a Hilbert space is always a Banach space, the converse does not necessarily hold. For further details and notion of completeness see for instance KREYSZIG [119] and REDDY [186].

As a next step some function spaces will be defined. Sets  $\mathcal{C}^m(\mathcal{B})$  with integer  $m \geq 0$  and  $\mathcal{L}^p(\mathcal{B})$  with  $1 \leq p < \infty$  denote  $m$ -times continuously differentiable and  $p$ -integrable functions on  $\mathcal{B}$ , respectively. The  $\mathcal{L}^p$  norm of a function  $f : \mathcal{B} \rightarrow \mathcal{R}$  is defined as

$$\boxed{\|f\|_{\mathcal{L}^p(\mathcal{B})} = \left[ \int_{\mathcal{B}} |f(\mathbf{x})|^p dx \right]^{1/p} \quad \text{for } 1 \leq p < \infty .} \tag{2.2}$$

A function  $f : \mathcal{B} \rightarrow \mathcal{R}$  is said to be in  $\mathcal{L}^p(\mathcal{B})$  provided that the corresponding norm is bounded, i.e.  $\|f(\mathbf{x})\|_{\mathcal{L}^p(\mathcal{B})} < \infty$ . If  $\mathbf{f} : \mathcal{B} \rightarrow \mathcal{R}^n$ ,  $\mathbf{f} = (f_1, \dots, f_n)$  is a vector valued function and  $f_i \in \mathcal{L}^p(\mathcal{B})$  (or  $f_i \in \mathcal{C}^m(\mathcal{B})$ ) for every  $i = 1, \dots, n$  then we write  $\mathbf{f} \in \mathcal{L}^p(\mathcal{B})$  (or  $\mathbf{f} \in \mathcal{C}^m(\mathcal{B})$ ). The standard choice of an inner product of two functions  $f : \mathcal{B} \rightarrow \mathcal{R}$  and  $g : \mathcal{B} \rightarrow \mathcal{R}$  in  $\mathcal{L}^2(\mathcal{B})$  is given by

$$\langle f, g \rangle_{\mathcal{L}^2(\mathcal{B})} = \int_{\mathcal{B}} f(\mathbf{x})g(\mathbf{x})d\mathbf{x} . \quad (2.3)$$

The spaces  $\mathcal{C}^m(\mathcal{B})$  and  $\mathcal{L}^p(\mathcal{B})$  characterize the differentiability and integrability of functions, respectively. According to their order of differentiability and integrability following relations  $\mathcal{C}^m(\mathcal{B}) \subset \mathcal{C}^n(\mathcal{B})$  and  $\mathcal{L}^p(\mathcal{B}) \subset \mathcal{L}^q(\mathcal{B})$  hold for  $m \geq n$  and  $p \geq q$ . The latter is valid provided that  $\mathcal{B}$  is bounded. The *Sobolev space*  $\mathcal{W}^{s,p}(\mathcal{B})$  with integer  $s \geq 0$  and  $1 \leq p < \infty$  is defined by

$$\mathcal{W}^{s,p}(\mathcal{B}) = \{f \in \mathcal{L}^p(\mathcal{B}) \mid \nabla^\alpha f \in \mathcal{L}^p(\mathcal{B})\} \quad \text{for } \alpha = 1 \dots s , \quad (2.4)$$

where  $\nabla^\alpha f$  denotes the  $\alpha^{th}$  order weak partial derivative of  $f$ . If a function  $f \in \mathcal{C}^1(\mathcal{B})$  then notions of the weak derivative and the usual one coincide. The Sobolev spaces specify not only the order of integrability of function  $f$  itself but derivatives  $\nabla^\alpha f$  as well. A norm associated with  $\mathcal{W}^{s,p}(\mathcal{B})$  reads

$$\|f\|_{\mathcal{W}^{s,p}(\mathcal{B})} = \left[ \sum_{\alpha=0}^s \|\nabla^\alpha f\|_{\mathcal{L}^p(\mathcal{B})}^p \right]^{1/p} \quad \text{for } 1 \leq p < \infty . \quad (2.5)$$

A function  $f : \mathcal{B} \rightarrow \mathcal{R}$  is then said to be in  $\mathcal{W}^{s,p}(\mathcal{B})$  if  $\|f(\mathbf{x})\|_{\mathcal{W}^{s,p}(\mathcal{B})} < \infty$ . In the case of vector valued functions, i.e.  $\mathbf{f} : \mathcal{B} \rightarrow \mathcal{R}^n$ ,  $\mathbf{f} = (f_1, \dots, f_n)$  is said to be in  $\mathcal{W}^{s,p}(\mathcal{B})$  if  $f_i \in \mathcal{W}^{s,p}(\mathcal{B})$  for every  $i = 1, \dots, n$ . The Sobolev spaces are related among each other such that  $\mathcal{W}^{s,p}(\mathcal{B}) \subset \mathcal{W}^{t,q}(\mathcal{B})$  for  $s \geq t$  and  $p \geq q$ . The case  $p = \infty$  in both  $\mathcal{L}^p$  and  $\mathcal{W}^{s,p}$  spaces is allowed provided that the corresponding definitions (2.2) and (2.5) are modified as follows

$$\begin{aligned} \|f\|_{\mathcal{L}^\infty(\mathcal{B})} &= \inf \{ \alpha \mid |f| \leq \alpha \text{ a.e. in } \mathcal{B} \} \\ \|f\|_{\mathcal{W}^{s,\infty}(\mathcal{B})} &= \max_{0 \leq \alpha \leq s} \{ \|\nabla^\alpha f\|_{\mathcal{L}^\infty(\mathcal{B})} \} . \end{aligned} \quad (2.6)$$

Note that the function spaces  $\mathcal{C}^m(\mathcal{B})$ ,  $\mathcal{L}^p(\mathcal{B})$  and  $\mathcal{W}^{s,p}(\mathcal{B})$  are vector spaces.

The existence theory that will be outlined in the next section requires the notions of convergence and weak convergence. Therefore, they are addressed now. Let  $X$  be a normed vector space. A scalar or vectorial sequence  $\varphi_n \in X$  is said to be (*strongly*) *convergent* if there exists a  $\varphi \in X$  such that

$$\lim_{n \rightarrow \infty} \|\varphi_n - \varphi\| = 0 . \quad (2.7)$$

This is written either  $\lim_{n \rightarrow \infty} \varphi_n = \varphi$  or in short  $\varphi_n \rightarrow \varphi$  and reads as  $\varphi$  is the (strong) limit of  $\varphi_n$ . Note that the strong convergence in a finite dimensional vector space  $X = \mathcal{R}^n$  requires the convergence of each component of  $n$ -tuple. A generalization of the convergence condition (2.7) is required particularly for function spaces. To this end, the notion

of weak convergence has been introduced. A sequence  $\varphi_n$  in a normed vector space  $X$  *weakly converges* to  $\varphi$  if

$$\boxed{\lim_{n \rightarrow \infty} l(\varphi_n) \rightarrow l(\varphi) \quad \text{for all } l \in X^* ,} \tag{2.8}$$

where  $X^*$  and  $l : X \rightarrow \mathcal{R}$  stand for the dual space of  $X$  and a bounded linear functional, respectively. Weak convergence of a sequence  $\varphi_n$  is denoted by  $\varphi_n \rightharpoonup \varphi$  where  $\varphi$  is the weak limit of  $\varphi_n$ . The weak convergence  $\varphi_n \rightharpoonup \varphi$  in  $\mathcal{L}^p(\mathcal{B})$  for  $1 \leq p < \infty$  is of particular interest and reads

$$\int_{\mathcal{B}} \varphi_n \xi dx \rightarrow \int_{\mathcal{B}} \varphi \xi dx \quad \text{for all } \xi \in \mathcal{L}^q(\mathcal{B}) \tag{2.9}$$

where  $\mathcal{L}^q(\mathcal{B})$  is the dual space of  $\mathcal{L}^p(\mathcal{B})$  satisfying  $1/p+1/q = 1$ . For instance, in  $\mathcal{L}^p([0, 2\pi])$  with  $1 \leq p < \infty$  the sequences  $\varphi_n = \cos(nx)$  and  $\varphi_n = \sin(nx)$  converge weakly to 0 but not strongly, i.e.  $\varphi_n \rightharpoonup 0$  and  $\varphi_n \not\rightarrow 0$ . In the case of  $p = \infty$  the definition of weak convergence is formally the same as (2.9). However, one talks about weak \* convergence, i.e.  $\varphi_n \overset{*}{\rightharpoonup} \varphi$ , if (2.9) holds for all  $\xi \in \mathcal{L}^1(\mathcal{B})$ . Necessity of this differentiation is due to fact that the dual of  $\mathcal{L}^\infty(\mathcal{B})$  is strictly larger than  $\mathcal{L}^1(\mathcal{B})$ , see for example DACOROGNA [52] pp.17-18. In Sobolev spaces  $\mathcal{W}^{1,p}(\mathcal{B})$ , which is of particular importance in non-linear elasticity, the weak convergence of  $\varphi_n$  requires that both  $\varphi_n$  and  $\nabla \varphi_n$  converge weakly in  $\mathcal{L}^p(\mathcal{B})$ . Note that strong convergence implies weak convergence with the same limit but the converse is not true in general. However, for finite dimensional normed spaces, i.e.  $X = \mathcal{R}^n$ , weak convergence implies strong convergence. In order to clarify further the concept of weak convergence we consider an example.

**Example:** (MARSDEN & HUGHES [130] p.380) A sequence  $\varphi_n \in \mathcal{L}^2(\mathcal{B})$  with  $\mathcal{B} = [0, 1]$  is given by

$$\varphi_n(x) = \begin{cases} u_1 & \text{if } x \in [(i-1)/n, i\xi/n] \\ u_2 & \text{if } x \in [i\xi/n, i/n] \end{cases} \quad \text{for } i = 1 \dots n \tag{2.10}$$

where  $\xi \in [0, 1]$  and  $u_1, u_2 \in \mathcal{R}$ . First three elements of the sequence  $\varphi_n$  are plotted in Figure 2.1 for the case  $\xi = 0.5$ . Even though the sequence  $\varphi_n$  is not strongly convergent, it converges weakly. The weak limit of  $\varphi_n$  is  $\xi u_1 + (1 - \xi)u_2$ , i.e.  $\varphi_n \rightharpoonup \xi u_1 + (1 - \xi)u_2$ .

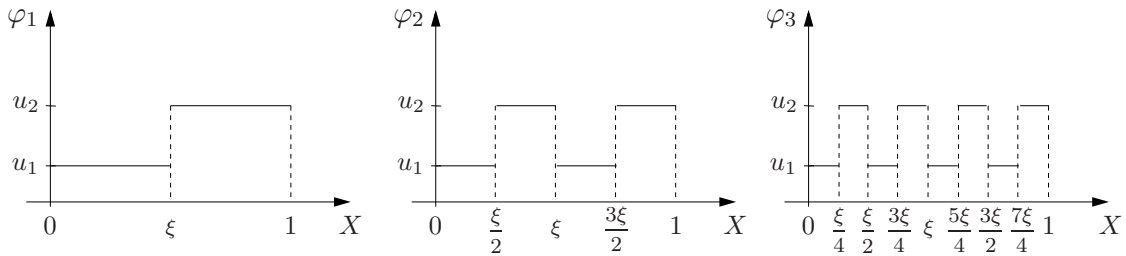


**Figure 2.1:** An example of weakly convergent but strongly non-convergent sequence. The sequence  $\varphi_n$  weakly converges to  $\xi u_1 + (1 - \xi)u_2$ .

## 2.2. Existence of Global Minimizers

In the subsequent treatments we will be interested in minimization problems of functionals which in a general setting can be recast into the form

$$\inf_{\mathbf{u} \in X} \left\{ I(\mathbf{u}) = \int_{\mathcal{B}} f(\mathbf{x}, \mathbf{u}, \nabla \mathbf{u}) dx \mid \mathbf{u} = \bar{\mathbf{u}} \text{ on } \partial \mathcal{B} \right\}. \quad (2.11)$$

Particularly, the minimization problem (2.11) can be reformulated for the boundary value problems of non-linear elasticity as follows. Find the deformation map

$$\varphi_t : \begin{cases} \mathcal{B} \rightarrow \mathcal{S} \subset \mathcal{R}^3 \\ \mathbf{X} \mapsto \mathbf{x} = \varphi_t(\mathbf{X}) \end{cases} \quad (2.12)$$

such that the energy functional  $I(\varphi)$  is minimized, i.e.

$$\boxed{\inf_{\varphi \in \mathcal{W}^{1,p}(\mathcal{B})} \left\{ I(\varphi) = \int_{\mathcal{B}} \psi(\nabla \varphi) dV \mid \varphi = \bar{\varphi} \text{ on } \partial \mathcal{B} \right\}} \quad (2.13)$$

where  $\psi$  denotes the energy storage function. Non-empty, open and bounded set  $\mathcal{B}$  denotes the reference configuration of the body. It is often assumed that the deformation map belongs to the Sobolev space  $\mathcal{W}^{1,p}(\mathcal{B})$  so that the deformation gradient  $\mathbf{F} = \nabla \varphi$  is well defined for  $\mathbf{X} \in \mathcal{B}$ . In (2.13) we consider for simplicity no external energy contribution and only the displacement boundary conditions on the boundary  $\partial \mathcal{B}$  of the body.

As pointed out by BALL [13] and CIARLET [45] the existence of equilibrium solutions of the non-linear boundary value problems can be proven by different ways. The first one does not consider the minimization problem (2.13) and applies the implicit function theorem directly to the strong form, i.e. equilibrium equations together with boundary conditions. This approach will not be discussed here and a detailed treatment can be found for example in CIARLET [45] chapter 6. The second route, frequently referred to as the classic method, is based on finding solutions  $\varphi^*$  of  $\delta I(\varphi) = 0$  and further analyzing higher order variations of  $I(\varphi)$  to determine whether  $\varphi^*$  is a minimum, maximum or just a stationary point. The first variation of the functional  $\delta I(\varphi) = 0$  yields the so-called *Euler-Lagrange* equations. For further details of the classic method see for instance LANZOS [123] and DACOROGNA [52]. The last approach makes use of the *direct methods of calculus of variations* and will be outlined briefly. The starting point is, similar to the preceding method, the minimization of the energy functional  $I(\varphi)$  defined in (2.13). There exists at least a solution of the minimization problem (2.13) if the functional  $I$  is

- (i) *sequentially weakly lower semicontinuous (swlsc)*, i.e.

$$\boxed{\liminf_{n \rightarrow \infty} I(\varphi_n) \geq I(\varphi) \quad \text{for all } \varphi_n \rightharpoonup \varphi \text{ in } \mathcal{W}^{1,p}(\mathcal{B})} \quad (2.14)$$

- (ii) *coercive* over  $\mathcal{W}^{1,p}(\mathcal{B})$ , i.e. for some  $c_0 \in \mathcal{R}_+$  and  $c_1 \in \mathcal{R}$

$$\boxed{I(\varphi) \geq c_0 \|\varphi\|_{\mathcal{W}^{1,p}(\mathcal{B})} + c_1 \quad \text{for all } \varphi \in \mathcal{W}^{1,p}(\mathcal{B})} \quad (2.15)$$



see for example DACOROGNA [51] p.48. Note that the minimization (2.13) is defined in an *infinite dimensional space*. This brings opposite to finite dimensional problems the necessity of weak convergence notions. In case of finite dimensional minimization problems, i.e. for  $I : X \subset \mathcal{R}^n \rightarrow \mathcal{R}$  find  $\inf_{\varphi \in X} \{I(\varphi)\}$ , the *swlsc* is replaced by the *lower semicontinuity*

$$\liminf_{n \rightarrow \infty} I(\varphi_n) \geq I(\varphi) \quad \text{for all } \varphi_n \rightarrow \varphi . \quad (2.16)$$

Note that the lower semicontinuity condition (2.16) requires, contrary to (2.14), the strong convergence of sequences. The condition (2.14) is in general hard to verify directly. However, the *swlsc* of  $I$  can be guaranteed if the function  $\psi$  in (2.13) satisfies some convexity conditions. In the case of *scalar problems*, i.e.  $\varphi : \mathcal{B} \subset \mathcal{R} \rightarrow \mathcal{R}$  and  $\psi : \mathcal{R} \rightarrow \mathcal{R}$ , the *convexity* of  $\psi$  is a necessary condition for the *swlsc* of  $I$ . In vectorial problems, e.g.  $\varphi : \mathcal{B} \subset \mathcal{R}^3 \rightarrow \mathcal{R}^3$  and  $\psi : \mathcal{R}_+^{3 \times 3} \rightarrow \mathcal{R}$ , convexity is a sufficient condition, however it is far from being a necessary condition, see DACOROGNA [51] p.97. The relevant generalization for vectorial problems is the *quasiconvexity* condition introduced by MORREY [157]. Following the approach based on direct methods of calculus of variations, the minimization problem (2.13) is solved in three steps:

- (i) Show that the functional  $I$  is bounded below and then select a minimizing sequence  $\varphi_n$ , i.e. there exists  $\alpha \in \mathcal{R}$  such that

$$\alpha = \inf_{\varphi \in \mathcal{W}^{1,p}} I(\varphi) \quad \text{and} \quad I(\varphi_n) \rightarrow \alpha \quad \text{as } n \rightarrow \infty ,$$

- (ii) Find a subsequence  $\varphi_{n_k}$  of  $\varphi_n$  that converges weakly, i.e.

$$\varphi_{n_k} \rightharpoonup \varphi^* \quad \text{as } k \rightarrow \infty ,$$

- (iii) Show that  $I(\varphi)$  is sequentially weakly lower semicontinuous, see (2.14)

for further details see DACOROGNA [52] chapter 3, JOST & LI-JOST [110] chapter 4 and MARSDEN & HUGHES [130] p.377.

Since the existence of minimizers of the functional  $I$  is closely related to the *convexity* or *weak convexity* conditions of the free energy function  $\psi$  in what follows various convexity notions and related topics will be addressed.

### 2.3. Convex Sets

We consider a finite-dimensional real vector space  $X = \mathcal{R}^n$  equipped with a scalar (inner) product  $\langle \cdot, \cdot \rangle$  and a norm operator  $\|\cdot\| = \langle \cdot, \cdot \rangle^{1/2}$ .  $U$  denotes a subset of  $\mathcal{R}^n$  and elements  $\mathbf{u} \in \mathcal{R}^n$  are called as vectors. A *closed line segment*  $[\mathbf{u}, \mathbf{v}]$  in  $\mathcal{R}^n$  is defined by the set

$$[\mathbf{u}, \mathbf{v}] = \{ \mathbf{w} \mid \mathbf{w} = \xi \mathbf{u} + (1 - \xi) \mathbf{v} \} \quad \text{with } \xi \in [0, 1] \quad \text{and} \quad \mathbf{u}, \mathbf{v} \in \mathcal{R}^n . \quad (2.17)$$

A subset  $U$  of  $\mathcal{R}^n$  is said to be convex if any closed line segment

$$[\mathbf{u}, \mathbf{v}] \in U \quad \text{for every } \mathbf{u}, \mathbf{v} \in U . \quad (2.18)$$

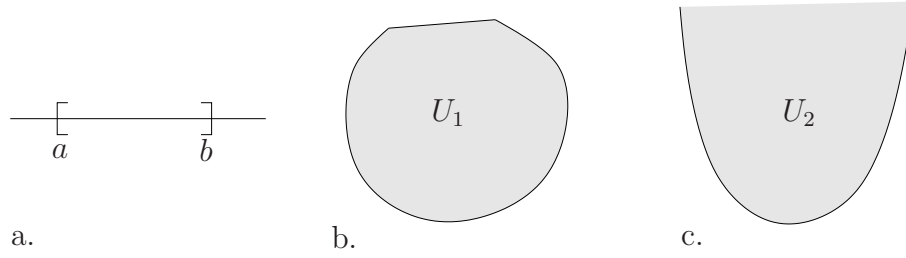


**Figure 2.2:** Examples of convex sets. a.) A closed interval  $[a, b] \in \mathcal{R}$  as a convex set. b.) A bounded convex set  $U_1 \subset \mathcal{R}^n$ . c.) An unbounded convex set  $U_2 \subset \mathcal{R}^n$ .

From (2.18) it is clear that in one dimension  $X = \mathcal{R}$  any interval generates a convex set. *Hyperplanes* in any dimension  $\mathcal{R}^n$

$$H(\mathbf{v}, \alpha) = \{\mathbf{u} \in \mathcal{R}^n \mid \langle \mathbf{u}, \mathbf{v} \rangle = \alpha\} \quad (2.19)$$

are other examples of convex sets. Furthermore, it is possible to convexify non-convex sets. The resulting set after the convexification of  $U \subset \mathcal{R}^n$  is the smallest convex set that contains  $U$ . This set is denoted as

$$\text{con}(U) = \left\{ \sum_{i=1}^p \xi_i \mathbf{u}_i \mid \mathbf{u}_i \in U, \xi_i \geq 0, \sum_{i=1}^p \xi_i = 1, p \geq 1 \text{ and arbitrary} \right\} \quad (2.20)$$

and called as the *convex hull* of  $U$ . For instance, a closed line segment  $[\mathbf{u}, \mathbf{v}]$  is a convex hull of two distinct points  $\mathbf{u}$  and  $\mathbf{v}$ . In Figures 2.2 and 2.3 some convex sets and convex hulls of a non-convex sets are visualized.

## 2.4. Convex Functions

Let  $U \subset \mathcal{R}^n$  be a non-empty convex set. A function  $f : U \in \mathcal{R}^n \rightarrow \bar{\mathcal{R}} := \mathcal{R} \cup \{+\infty\}$  is called *convex* if

$$f(\xi \mathbf{u} + (1 - \xi) \mathbf{v}) \leq \xi f(\mathbf{u}) + (1 - \xi) f(\mathbf{v}) \quad \forall \quad \xi \in [0, 1] \quad \text{and} \quad \mathbf{u}, \mathbf{v} \in U. \quad (2.21)$$

$f$  is referred to as *strictly convex* when (2.21) holds for  $\mathbf{u} \neq \mathbf{v}$  strictly. The *epigraph* of a function  $f : U \in \mathcal{R}^n \rightarrow \bar{\mathcal{R}}$  is defined as the set of points lying on or above its graph

$$\text{epi } f = \{(\mathbf{u}, \alpha) \in U \times \mathcal{R} \mid f(\mathbf{u}) \leq \alpha\} \subset \mathcal{R}^{n+1}. \quad (2.22)$$

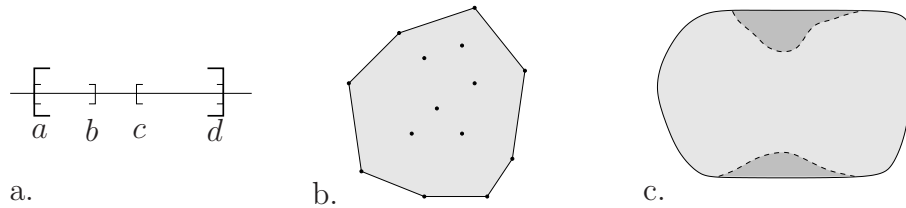


**Figure 2.3:** Examples of non-convex set and convex hulls. a.) Union of two closed intervals  $U = [a, b] \cup [c, d]$  is not convex, and  $\text{con}(U) = [a, d]$ . b.) A set of points  $\bullet$  is not convex and its convex hull is shown by the grey area. c.) A non-convex set is shown with the dashed line and its convex hull with the solid line.



As noted by ROCKAFELLAR [193] a function  $f : U \in \mathcal{R}^n \rightarrow \bar{\mathcal{R}}$  is convex if and only if its epigraph  $\text{epi } f \subset U \times \bar{\mathcal{R}}$  is a convex set. In Figures 2.4a and 2.4b convex and non-convex scalar functions  $f : [a, b] \in \mathcal{R} \rightarrow \bar{\mathcal{R}}$  and their epigraphs are visualized. It is possible to extend the condition (2.21) for functions that are not necessarily defined on convex sets, see CIARLET [45] p.167 and ŠILHAVÝ [200] p.257. A function  $\tilde{f} : U \in \mathcal{R}^n \rightarrow \bar{\mathcal{R}}$  is convex if there exists according to (2.21) a convex function  $f : \text{con}(U) \rightarrow \bar{\mathcal{R}}$  such that  $\tilde{f}(\mathbf{u}) = f(\mathbf{u})$  for all  $\mathbf{u} \in U$ .

Before starting with the discussion of convexity properties of stored energy functions we give the definitions of subgradient and subdifferential of functions. Let  $f : U \in \mathcal{R}^n \rightarrow \bar{\mathcal{R}}$  and  $\mathbf{u} \in U$ .  $\boldsymbol{\lambda} \in \mathcal{R}^n$  is said to be a *subgradient* of  $f$  at  $\mathbf{u}$  if the following holds

$$f(\mathbf{v}) \geq f(\mathbf{u}) + \boldsymbol{\lambda} \cdot (\mathbf{v} - \mathbf{u}) \quad (2.23)$$

for every  $\mathbf{v} \in U$ . The set of all subgradients of  $f$  at  $\mathbf{u}$  is called as the *subdifferential* of  $f$  at  $\mathbf{u}$  and often denoted by  $\partial f(\mathbf{u})$ . To illustrate, consider the scalar convex function  $f(u) = |u|$ . The subdifferential of  $f$  at  $u = 0$  is then the closed interval  $[-1, 1]$ . For the cases  $u < 0$  and  $u > 0$  the subdifferential coincides with the usual derivative and takes the values  $-1$  and  $1$ , respectively.

## 2.5. Convexity and Weak Convexity Notions of Free Energy Function

In the sequel, we concentrate on different convexity notions of free energy functions that are assumed to be given in terms of the deformation gradient  $\mathbf{F}$ .

**2.5.1. Convexity of Free Energy Function.** The free energy function  $\psi : \mathcal{R}_+^{3 \times 3} \rightarrow \bar{\mathcal{R}}$  is said to be *convex* if for every  $\xi \in [0, 1]$  the following condition holds,

$$\boxed{\psi(\xi \mathbf{F}_1 + (1 - \xi) \mathbf{F}_2) \leq \xi \psi(\mathbf{F}_1) + (1 - \xi) \psi(\mathbf{F}_2) \quad \forall \quad \mathbf{F}_1, \mathbf{F}_2 \in \mathcal{R}_+^{3 \times 3},} \quad (2.24)$$

where  $\mathcal{R}_+^{3 \times 3}$  stands for the set of all second order tensors with positive determinant. Note that the set  $\mathcal{R}_+^{3 \times 3}$  is not convex and its convex hull constitutes the set of all second order tensors, i.e.  $\text{con}(\mathcal{R}_+^{3 \times 3}) = \mathcal{R}^{3 \times 3}$ . The proof can be found in CIARLET [45] p.162. Observe that the convexity condition (2.24) does not require any differentiability of the free energy  $\psi$ . Provided that  $\psi : \mathcal{R}_+^{3 \times 3} \rightarrow \bar{\mathcal{R}}$  is differentiable, (2.24) can be reformulated

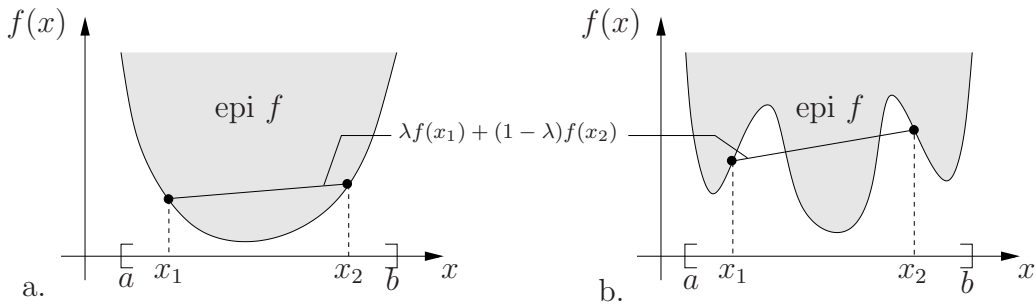


**Figure 2.4:** Examples of convex and non-convex functions. a.) A convex function  $f : [a, b] \in \mathcal{R} \rightarrow \bar{\mathcal{R}}$  with a convex epigraph. b.) A non-convex function  $f : [a, b] \in \mathcal{R} \rightarrow \bar{\mathcal{R}}$  with a non-convex epigraph.

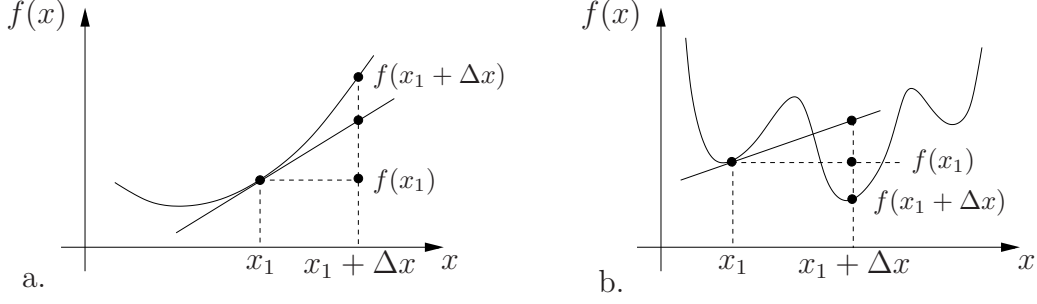


**Figure 2.5:** Examples of convex and non-convex differentiable functions. a.) The convex function  $f : [a, b] \in \mathcal{R} \rightarrow \mathcal{R}$  is everywhere above its tangent plane. b.) The non-convex function  $f : [a, b] \in \mathcal{R} \rightarrow \mathcal{R}$  is not everywhere above its tangent plane.

with substitutions  $\Delta \mathbf{F} = \mathbf{F}_1 - \mathbf{F}_2$  and  $\mathbf{F} = \mathbf{F}_2$  as follows,

$$\frac{\psi(\mathbf{F} + \xi \Delta \mathbf{F}) - \psi(\mathbf{F})}{\xi} \leq \psi(\mathbf{F} + \Delta \mathbf{F}) - \psi(\mathbf{F}) \quad \text{for } \xi > 0. \quad (2.25)$$

Taking the limit  $\xi \rightarrow 0$  yields the definition of directional derivative

$$\frac{d}{d\xi} [\psi(\mathbf{F} + \xi \Delta \mathbf{F})]_{\xi=0} \leq \psi(\mathbf{F} + \Delta \mathbf{F}) - \psi(\mathbf{F}). \quad (2.26)$$

Computation of this derivative at  $\xi = 0$  gives an alternative definition of convexity. A differentiable free energy function  $\psi : \mathcal{R}_+^{3 \times 3} \rightarrow \bar{\mathcal{R}}$  is said to be *convex* if

$$\boxed{\psi(\mathbf{F}) + \mathbf{P}(\mathbf{F}) : \Delta \mathbf{F} \leq \psi(\mathbf{F} + \Delta \mathbf{F}) \quad \forall \quad \mathbf{F}, (\mathbf{F} + \Delta \mathbf{F}) \in \mathcal{R}_+^{3 \times 3},} \quad (2.27)$$

where  $\mathbf{P} = \partial_{\mathbf{F}} \psi(\mathbf{F})$  is the first Piola-Kirchhoff stress tensor. The condition (2.27) is illustrated in Figures 2.5a and 2.5b for convex and non-convex scalar functions, respectively. From equation (2.27) one can also write

$$\begin{aligned} \psi(\mathbf{F}_2) + \mathbf{P}(\mathbf{F}_2) : (\mathbf{F}_1 - \mathbf{F}_2) &\leq \psi(\mathbf{F}_1) \\ \psi(\mathbf{F}_1) + \mathbf{P}(\mathbf{F}_1) : (\mathbf{F}_2 - \mathbf{F}_1) &\leq \psi(\mathbf{F}_2) \end{aligned} \quad (2.28)$$

Summing up two equations given above provides another definition of convexity for differentiable functions

$$\boxed{[\mathbf{P}(\mathbf{F}_1) - \mathbf{P}(\mathbf{F}_2)] : (\mathbf{F}_1 - \mathbf{F}_2) \geq 0 \quad \forall \quad \mathbf{F}_1, \mathbf{F}_2 \in \mathcal{R}_+^{3 \times 3}.} \quad (2.29)$$

For twice differentiable free energy functions  $\psi$ , division of (2.29) twice by  $\xi > 0$  after the following substitutions  $\mathbf{F}_1 = \mathbf{F} + \xi \Delta \mathbf{F}$  and  $\mathbf{F}_2 = \mathbf{F}$  yields in the limit  $\xi \rightarrow 0$  the definition of directional derivative

$$\frac{d}{d\xi} [\mathbf{P}(\mathbf{F} + \xi \Delta \mathbf{F})]_{\xi=0} : \Delta \mathbf{F} \geq 0. \quad (2.30)$$

Evaluation of the derivative at  $\xi = 0$  results in another alternative convexity condition. A twice differentiable free energy function  $\psi : \mathcal{R}_+^{3 \times 3} \rightarrow \bar{\mathcal{R}}$  is said to be *convex* if

$$\boxed{(\mathbf{F}_2 - \mathbf{F}_1) : \mathbb{C}(\mathbf{F}_1) : (\mathbf{F}_2 - \mathbf{F}_1) \geq 0 \quad \forall \quad \mathbf{F}_1, \mathbf{F}_2 \in \mathcal{R}_+^{3 \times 3},} \quad (2.31)$$

where  $\mathbb{C}(\mathbf{F}_1) = \partial_{\mathbf{F}\mathbf{F}}^2 \psi(\mathbf{F}_1)$  denotes the usual tensor of elastic moduli. If the free energy function of a hyperelastic solid satisfies any of the convexity conditions (2.24), (2.27), (2.29) or (2.31) together with some coercivity, continuity and measurability requirements then there exist at least a function which minimizes the associated minimization problem (2.13), see CIARLET [45] p.355 for the proof. On the other hand, as outlined for example in MARSDEN & HUGHES [130], the convexity restriction on the free energy  $\psi$  is too strong and physically unacceptable due to the following reasons:

- (i) HILL [99] pointed out that strict convexity of the free energy implies *uniqueness of solutions* and therefore precludes global buckling of solids under consideration.
- (ii) COLEMAN & NOLL [46] observed that convexity of the free energy function is incompatible with material frame invariance.
- (iii) As remarked by BALL [12] convexity of the free energy precludes the physical limit condition

$$\psi(\mathbf{F}) \rightarrow \infty \quad \text{as} \quad \det \mathbf{F} \rightarrow 0^+ . \quad (2.32)$$

**Incompatibility of convexity with material frame indifference.** The principle of material frame indifference states that  $\psi(\mathbf{F}) = \psi(\mathbf{Q}\mathbf{F})$  for all  $\mathbf{Q} \in \mathcal{SO}(3)$ . Consider for example two deformation gradients

$$\mathbf{F}_1 = \mathbf{1} = \begin{bmatrix} 1 & 0 & 0 \\ 0 & 1 & 0 \\ 0 & 0 & 1 \end{bmatrix} \quad \text{and} \quad \mathbf{F}_2 = \mathbf{Q} = \begin{bmatrix} 0 & 1 & 0 \\ -1 & 0 & 0 \\ 0 & 0 & 1 \end{bmatrix} . \quad (2.33)$$

$\mathbf{F}_1$  and  $\mathbf{F}_2$  correspond to the identity tensor and a clockwise 90° rotation around the third axis, respectively. If  $\psi$  is convex, then according to (2.24) the following condition has to hold

$$\psi(\bar{\mathbf{F}}) \leq \frac{1}{2}(\psi(\mathbf{F}_1) + \psi(\mathbf{F}_2)) \quad \text{with} \quad \bar{\mathbf{F}} = \frac{1}{2}(\mathbf{F}_1 + \mathbf{F}_2) = \begin{bmatrix} 0.5 & 0.5 & 0 \\ -0.5 & 0.5 & 0 \\ 0 & 0 & 1 \end{bmatrix} \quad (2.34)$$

where  $\xi = \frac{1}{2}$  is chosen. Note that  $\psi(\mathbf{F}_1) = 0$  since  $\mathbf{F}_1 = \mathbf{1}$  represents the undeformed state and  $\psi(\mathbf{F}_2) = 0$  due to principle of material frame indifference, i.e.  $\psi(\mathbf{Q}\mathbf{F}_1) = \psi(\mathbf{F}_1)$  and  $\mathbf{F}_2 = \mathbf{Q}\mathbf{F}_1$ . Therefore, the right hand side of the above inequality is zero. On the other hand,  $\bar{\mathbf{F}}$  describes a clockwise rotation of 45° around third axis superimposed to a volumetric deformation with  $\det[\bar{\mathbf{F}}] = 0.5$ . Consequently, as a physical requirement  $\psi(\bar{\mathbf{F}})$  has to be greater than zero. This leads to a contradiction with the convexity condition which was pointed out first in COLEMAN & NOLL [46], see also TRUESDELL & NOLL [209] p.163. For further details and discussion of the other physical conflict ( $\psi(\mathbf{F}) \rightarrow \infty$  as  $\det \mathbf{F} \rightarrow 0^+$ ) see CIARLET [45] and SCHRÖDER [197].

**2.5.2. Polyconvexity.** Due to previously mentioned drawbacks of the convexity criterion, a weaker requirement, namely the polyconvexity of the free energy was introduced by BALL [12]. A function  $\psi : \mathcal{R}_+^{3 \times 3} \rightarrow \bar{\mathcal{R}}$  is called *polyconvex* if there exists a convex function  $\bar{\psi} : \mathcal{R}_+^{3 \times 3} \times \mathcal{R}_+^{3 \times 3} \times \mathcal{R}_+ \rightarrow \bar{\mathcal{R}}$  such that

$$\psi(\mathbf{F}) = \bar{\psi}(\mathbf{F}, \text{cof } \mathbf{F}, \det \mathbf{F}) \quad (2.35)$$

where  $\text{cof } \mathbf{F}$  stands for the cofactor defined by  $\text{cof } \mathbf{F} = (\det \mathbf{F})\mathbf{F}^{-T}$ . In other words,  $\psi(\mathbf{F})$  is said to be polyconvex if  $\bar{\psi}(\mathbf{F}, \text{cof } \mathbf{F}, \det \mathbf{F})$  is convex with respect to  $\mathbf{F}$ ,  $\text{cof } \mathbf{F}$  and  $\det \mathbf{F}$ . In contrast to the convexity, the polyconvexity condition does not conflict with any physical requirement, nevertheless it still guarantees together with some growth conditions the existence of minimizing deformations. Following BALL [12], later MÜLLER, QI & YAN [164] provided an existence theorem. It states that there exists a global minimizer of (2.13) if  $\psi$  is polyconvex and satisfies the growth condition

$$\psi(\mathbf{F}) \geq c_0(\|\mathbf{F}\|^2 + \|\text{cof } \mathbf{F}\|^{3/2}) - c_1 \quad \forall \quad \mathbf{F} \in \mathcal{R}_+^{3 \times 3} \quad (2.36)$$

for some constants  $c_0 \in \mathcal{R}_+$  and  $c_1 \in \mathcal{R}$ . Note that if a function is convex then it is also polyconvex. Next some concrete functions are examined to clarify the difference between the notions of convexity and polyconvexity.

**Example:** (CIARLET [45] p.176) The function  $\psi(\mathbf{F}) = \|\text{cof } \mathbf{F}\|^2$  is polyconvex but not convex. In order to see that consider the following deformation gradients  $\mathbf{F}_1$  and  $\mathbf{F}_2$

$$\mathbf{F}_1 = \begin{bmatrix} 2 & 0 & 0 \\ 0 & 1 & 1 \\ 0 & 0 & 1 \end{bmatrix} \quad \text{and} \quad \mathbf{F}_2 = \begin{bmatrix} 1 & 0 & 0 \\ 0 & 2 & 0 \\ 0 & 0 & 1 \end{bmatrix} \quad (2.37)$$

and compute

$$\xi\psi(\mathbf{F}_1) + (1 - \xi)\psi(\mathbf{F}_2) = 9 \quad \text{and} \quad \psi(\xi\mathbf{F}_1 + (1 - \xi)\mathbf{F}_2) = \xi^4 - 2\xi^3 - \xi^2 + 2\xi + 9. \quad (2.38)$$

Insertion of the above results into the convexity condition (2.24) renders the following inequality

$$\xi^4 - 2\xi^3 - \xi^2 + 2\xi \leq 0 \quad (2.39)$$

which is not satisfied for all  $0 \leq \xi \leq 1$ . Thus, the convexity condition is not fulfilled. On the other hand,  $\psi(\mathbf{F}) = \bar{\psi}(\text{cof } \mathbf{F}) = \|\text{cof } \mathbf{F}\|^2$  is a polyconvex function. The function  $\bar{\psi}(\mathbf{H}) = \|\mathbf{H}\|^2$  is a convex function according to (2.31), i.e.

$$(\mathbf{H}_2 - \mathbf{H}_1) : \partial_{\mathbf{H}\mathbf{H}}^2 \bar{\psi}(\mathbf{H}_1) : (\mathbf{H}_2 - \mathbf{H}_1) = \|\mathbf{H}_2 - \mathbf{H}_1\|^2 \geq 0 \quad (2.40)$$

confirming that  $\psi(\mathbf{F}) = \|\text{cof } \mathbf{F}\|^2$  is a polyconvex function.

**Example:** (CIARLET [45] p.176) The function  $\psi(\mathbf{F}) = \det \mathbf{F}$  is polyconvex but not convex. In order to prove this we consider the deformation gradients given in (2.37) and compute

$$\xi\psi(\mathbf{F}_1) + (1 - \xi)\psi(\mathbf{F}_2) = 2 \quad \text{and} \quad \psi(\xi\mathbf{F}_1 + (1 - \xi)\mathbf{F}_2) = -\xi^2 + \xi + 2. \quad (2.41)$$

Insertion of (2.41) into the convexity condition (2.24) leads to the inequality  $-\xi^2 + \xi \leq 0$  which is not satisfied for  $0 \leq \xi \leq 1$ . But  $\psi(\mathbf{F}) = \bar{\psi}(\det \mathbf{F}) = \det \mathbf{F}$  is a polyconvex function since  $\psi(\delta) = \delta$  is a convex function of  $\delta$ .

**Example:** The last example is concerned with the polyconvexity of compressible *Neo-Hookean Material*

$$\psi(\mathbf{F}) = \frac{\mu}{2}[\|\mathbf{F}\|^2 - 3] + \frac{\mu^2}{\lambda}[(\det \mathbf{F})^{-\frac{\lambda}{\eta}} - 1]. \quad (2.42)$$

The polyconvexity of (2.42) can be shown by proving that  $\bar{\psi}(\mathbf{F}, \det \mathbf{F}) = \psi(\mathbf{F})$  is convex with respect to  $\mathbf{F}$  and  $\det \mathbf{F}$ . Since  $\det \mathbf{F}$  is a scalar, the convexity with respect to  $\det \mathbf{F}$  requires the second derivative

$$\frac{\partial^2 \bar{\psi}}{\partial (\det \mathbf{F})^2} = (\lambda + \mu)(\det \mathbf{F})^{-\frac{\lambda+2\mu}{\mu}} \geq 0 \quad (2.43)$$

to be positive and it is satisfied for all  $\det \mathbf{F} > 0$  and material parameters  $\lambda, \mu > 0$ . Hence, the free energy function is convex with respect to  $\det \mathbf{F}$ . Convexity with respect to  $\mathbf{F}$  is fulfilled as well while

$$(\mathbf{F}_2 - \mathbf{F}_1) : \frac{\partial^2 \bar{\psi}}{\partial \mathbf{F}^2} : (\mathbf{F}_2 - \mathbf{F}_1) = \|\mathbf{F}_2 - \mathbf{F}_1\|^2 \geq 0 \quad (2.44)$$

where  $\partial_{\mathbf{F}\mathbf{F}}^2 \bar{\psi} = \mathbb{I}$ . Consequently, the Neo-Hookean free energy given in (2.42) is polyconvex.

Ogden- and Mooney-Rivlin-type models also satisfy the polyconvexity condition. On the other hand, free energy functions of St.Venant-Kirchhoff-type and models based on Hencky tensor are known to be non-polyconvex, see CIARLET [45]. Apart from above mentioned works, which are concerned with isotropic hyperelastic models, SCHRÖDER & NEFF [198] have recently proposed the construction of polyconvex free energy functions based on invariant formulations for transversally isotropic elastic solids.

**2.5.3. Quasiconvexity.** The concept of quasiconvexity, introduced by MORREY [157], is a more general and weaker condition than polyconvexity. Polyconvexity of a function implies quasiconvexity as well. The quasiconvexity of the free energy  $\psi$  augmented with some additional growth conditions ensures the *sequential weak lower semicontinuity* (*swlsc*) of the corresponding functional  $I(\varphi)$  in (2.13). Furthermore, as already pointed out, the existence of solutions of the minimization problem is guaranteed if the energy functional  $I(\varphi)$  is *swlsc*. As noted in ŠILHAVÝ [200] p.387, the quasiconvexity of  $\psi$  is a *necessary*, and under technical hypotheses also *sufficient*, condition for the *swlsc* of the functional  $I(\varphi)$ . More precisely, as pointed out in BALL [13], according to the results of MORREY [157] and ACERBI & FUSCO [1], the minimization problem (2.13) attains a global minimum if  $\psi(\mathbf{F})$  is quasiconvex and fulfills the growth condition

$$c_1 \|\mathbf{F}\|^p - c_0 \leq \psi(\mathbf{F}) \leq c_2 (\|\mathbf{F}\|^p + 1) \quad \forall \quad \mathbf{F} \in \mathcal{R}_+^{3 \times 3} \quad (2.45)$$

for some constants  $p > 1$ ,  $c_0 \in \mathcal{R}$  and  $c_1, c_2 \in \mathcal{R}_+$ . Note that the growth condition (2.45) is not consistent with (2.32). A free energy  $\psi : \mathcal{R}_+^{3 \times 3} \rightarrow \mathcal{R}$  is said to be *quasiconvex* if the following inequality

$$\boxed{\frac{1}{\text{vol}(\mathcal{D})} \int_{\mathcal{D}} \psi(\mathbf{F} + \nabla \mathbf{w}) dV \geq \psi(\mathbf{F})} \quad (2.46)$$

holds for every bounded open set  $\mathcal{D} \in \mathcal{B}$  and  $\mathbf{w} \in \mathcal{R}^3$  with  $\mathbf{w} = \mathbf{0}$  on the boundary  $\partial \mathcal{D}$ .  $\mathcal{D}$  stands for a part of the body  $\mathcal{B}$  and  $\text{vol}(\mathcal{D})$  is the corresponding volume of that part. This condition states that for all possible fluctuations  $\mathbf{w}$  in  $\mathcal{D}$  with  $\mathbf{w} = \mathbf{0}$  on  $\partial \mathcal{D}$ , the homogeneous deformation given by  $\mathbf{F}$  provides a minimizer of the total stored energy in  $\mathcal{D}$ . In other words, the inequality (2.46), when considered for a fixed domain  $\mathcal{D}$ , describes the principle of minimum potential energy for the reference body  $\mathcal{D}$  under homogeneous

displacement boundary conditions. Although the definition of quasiconvexity seems to be dependent on a chosen domain  $\mathcal{D}$ , in fact it is not. If the condition (2.46) holds for a domain  $\mathcal{D}$  then it holds for every such domain, see DACOROGNA [51] p.101 for the proof. Note that quasiconvexity is not a pointwise condition on the stored energy function and is difficult to verify in practice. Even though quasiconvexity is a mathematically natural hypothesis for the existence of solutions, non-quasiconvex energy storage functions are of high interest since they can model materials that undergo phase transformations or broadly speaking microstructure formations.

**2.5.4. Rank-One Convexity.** Rank-one convexity is a more general condition than quasiconvexity. Thus, the quasiconvexity of  $\psi(\mathbf{F})$  implies rank-one convexity. A free energy  $\psi : \mathcal{R}_+^{3 \times 3} \rightarrow \mathcal{R}$  function is said to be *rank-one convex* if for every  $0 \leq \xi \leq 1$

$$\boxed{\psi(\xi \mathbf{F}_1 + (1 - \xi) \mathbf{F}_2) \leq \xi \psi(\mathbf{F}_1) + (1 - \xi) \psi(\mathbf{F}_2) \quad \text{for } \mathbf{F}_2 - \mathbf{F}_1 = \mathbf{m} \otimes \mathbf{N}} \quad (2.47)$$

holds where  $\mathbf{m}, \mathbf{N} \in \mathcal{R}^3$  and  $\mathbf{F}_1, \mathbf{F}_2 \in \mathcal{R}_+^{3 \times 3}$ . In other words,  $\psi(\mathbf{F})$  is rank-one convex provided that it is convex along rank-one lines. The condition (2.47) reads equivalently as follows, if

$$\tilde{\psi}(\xi) = \psi(\mathbf{F} + \xi \mathbf{m} \otimes \mathbf{N}) \quad (2.48)$$

is convex in  $\xi$  for all  $\mathbf{F} \in \mathcal{R}_+^{3 \times 3}$  and  $\mathbf{m}, \mathbf{N} \in \mathcal{R}^3$  then  $\psi : \mathcal{R}_+^{3 \times 3} \rightarrow \mathcal{R}$  is rank-one convex. Similar to alternative derivations of convexity (2.24-2.31), rank-one convexity can also be formulated in different ways. For twice differentiable functions, following the same steps with additional condition  $\mathbf{F}_2 - \mathbf{F}_1 = \mathbf{m} \otimes \mathbf{N}$  one obtains analogous to (2.31)

$$\boxed{(\mathbf{m} \otimes \mathbf{N}) : \mathbb{C}(\mathbf{F}_1) : (\mathbf{m} \otimes \mathbf{N}) \geq 0 \quad \forall \mathbf{F}_1 \in \mathcal{R}_+^{3 \times 3} \quad \text{and} \quad \mathbf{m}, \mathbf{N} \in \mathcal{R}^3,} \quad (2.49)$$

where  $\mathbb{C}(\mathbf{F}_1) = \partial_{\mathbf{F}\mathbf{F}}^2 \psi(\mathbf{F}_1)$ . The inequality (2.49) is also referred to as the *Legendre-Hadamard* or the *ellipticity* condition. If (2.49) holds strictly for non-zero vectors  $\mathbf{m}, \mathbf{N} \in \mathcal{R}^3$  then it is called as the *strong Legendre-Hadamard* or the *strong ellipticity* condition. In geometrically linear elasticity theory the strong ellipticity is a necessary and sufficient condition for the existence traveling waves having real wave speeds, see MARSDEN & HUGHES [130] p.240.

Four convexity notions discussed so far are related for arbitrary finite valued vectorial problems, e.g.  $\psi : \mathcal{R}_+^{3 \times 3} \rightarrow \mathcal{R}$ , as follows:

$$\boxed{\text{convexity} \Rightarrow \text{polyconvexity} \Rightarrow \text{quasiconvexity} \Rightarrow \text{rank-one convexity} .} \quad (2.50)$$

The inverse relations are not valid in general. However, for scalar functions  $\psi : \mathcal{R} \rightarrow \mathcal{R}$  all four notions are equivalent. Note that if the function is quadratic then polyconvexity, quasiconvexity and rank-one convexity coincide for  $n = 2$  and quasiconvexity and rank-one convexity coincide even for higher dimensions ( $n \geq 3$ ), see DACOROGNA [51] p.126. Before the consideration of non-existence of minimizers, we close the discussion of different convexity notions with an example.

**Example:** (ALIBERT & DACOROGNA [4]) Let  $f : \mathcal{R}^{2 \times 2} \rightarrow \mathcal{R}$  be defined as

$$f(\mathbf{F}) = \|\mathbf{F}\|^2 (\|\mathbf{F}\|^2 - 2\gamma \det \mathbf{F}) \quad (2.51)$$

where  $\gamma \in \mathcal{R}$  and  $\mathbf{F} \in \mathcal{R}^{2 \times 2}$ . Then there exist  $\epsilon > 0$  such that

$$\begin{aligned} f \text{ is convex} &\Leftrightarrow |\gamma| \leq \frac{2}{3}\sqrt{2} & f \text{ is polyconvex} &\Leftrightarrow |\gamma| \leq 1 \\ f \text{ is quasiconvex} &\Leftrightarrow |\gamma| \leq 1 + \epsilon & f \text{ is rank-one convex} &\Leftrightarrow |\gamma| \leq \frac{2}{\sqrt{3}}. \end{aligned} \quad (2.52)$$

In the above example as noted by ALIBERT & DACOROGNA [4] it is not known whether  $1 + \epsilon = 2/\sqrt{3}$  is possible or not.

## 2.6. Lack of Convexity and Non-Existence of Minimizers

In the sequel, we demonstrate in simple one-dimensional setting how non-convex storage functions lead to non-existence of solutions of the minimization problem (2.13). Consider a bar of unit length  $\mathcal{B} = (0, 1)$  under a simple longitudinal deformation with homogeneous boundary conditions  $\varphi(0) = \varphi(1) = 0$ . We denote the scalar deformation gradient by  $F = d\varphi/dX$ . The energy density is given as

$$\psi(F) = (F^2 - 1)^2. \quad (2.53)$$

Besides, the total energy functional is assumed to be

$$I(\varphi) = \int_0^1 [\psi(F) + \varphi^2] dX = \int_0^1 [(F^2 - 1)^2 + \varphi^2] dX. \quad (2.54)$$

An attempt to minimize the total energy  $I(\varphi)$  over all possible continuous deformations  $\varphi$  automatically leads to a fine scale mixtures between the two deformation gradients  $F = 1$  and  $F = -1$ . Since both contributions to the energy functional ( $\psi(F)$  and  $\varphi^2$ ) are non-negative the smallest possible value of  $I(\varphi)$  is zero, i.e.  $\inf\{I(\varphi)\} = 0$ . In order to reach a zero energy level the deformation has to satisfy simultaneously two conditions (i)  $F = \pm 1$  and (ii)  $\varphi = 0$ . However, if  $\varphi = 0$  almost everywhere, then the deformation gradient  $F$  becomes zero and this leads to  $I(\varphi) > 0$ . On the other hand, if we set  $F = \pm 1$  a.e. then  $\varphi \neq 0$  which yields  $I(\varphi) > 0$ . Therefore, we conclude that both requirements (i) and (ii) can not be fulfilled at the same time. However, a sequence of continuous deformations,  $\varphi_n$  for  $n = 1, \dots, \infty$ , can be used to make the energy closer to zero by increasing  $n$ . In order to construct such a sequence, we start with

$$\varphi_1(X) = \begin{cases} X & \text{if } 0 < X < 1/2 \\ 1 - X & \text{if } 1/2 \leq X < 1 \end{cases} \quad (2.55)$$

as seen in Figure 2.6. Therefore, the total energy in (2.54) becomes

$$I(\varphi_1) = \int_0^{1/2} X^2 dX + \int_{1/2}^1 (1 - X)^2 dX = \frac{1}{12}. \quad (2.56)$$

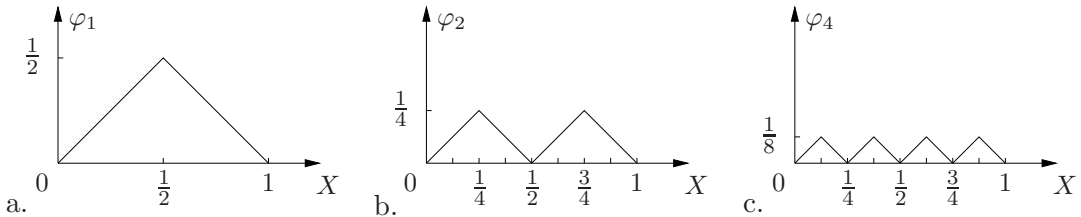


**Figure 2.6:** A minimizing sequence  $\varphi_n$  of deformations for a.)  $n = 1$  and  $I(\varphi_1) = 1/12$ , b.)  $n = 2$  and  $I(\varphi_2) = 1/48$ , c.)  $n = 4$  and  $I(\varphi_4) = 1/196$ . The total energy for a member of the sequence is  $I(\varphi_n) = 1/12n^2$ . So the minimizing sequence yields  $I(\varphi_n) \rightarrow 0$  as  $n \rightarrow \infty$ .



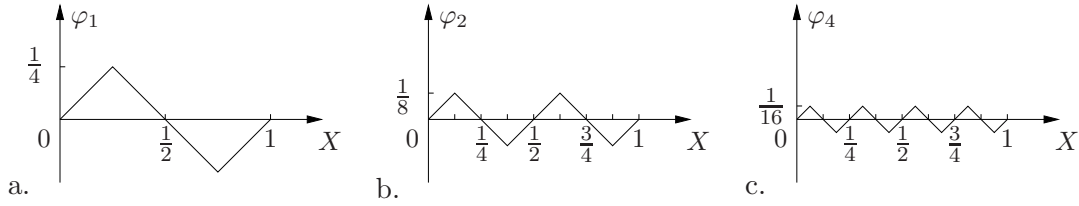


**Figure 2.7:** A minimizing sequence  $\varphi_n$  of deformations alternative to the one in Figure 2.6 for a.)  $n = 1$ , b.)  $n = 2$  and c.)  $n = 4$ . The sequence yields  $I(\varphi_n) \rightarrow 0$  as  $n \rightarrow \infty$ .

The energy can be made smaller if we consider other elements of the sequence  $\varphi_n$  with  $n > 1$ , see Figure 2.6. Therefore, for any integer  $n$  let  $\varphi_n$  be the deformation given by

$$\varphi_n = \begin{cases} X & \text{if } 0 < X < 1/2n \\ 1/n - X & \text{if } 1/2n \leq X < 2/2n \end{cases} \quad (2.57)$$

and its periodical extension to the interval  $(0, 1)$ . Note that this minimizing sequence is not unique, see for example MÜLLER [163] and Figure 2.7 for another construction. The total energy for the  $n^{\text{th}}$  member of the sequence is  $1/12n^2$ , i.e.  $I(\varphi_n) = 1/12n^2$ . Consequently, as  $n \rightarrow \infty$  the energy  $I(\varphi_n) \rightarrow 0$ . On the other hand, although  $\varphi = 0$  is not a minimizer, the minimizing sequence converges to zero as  $n \rightarrow \infty$ . In other words, energy of the limit of deformation sequences is greater than the limit of energy

$$I(\lim_{n \rightarrow \infty} \varphi_n) > \lim_{n \rightarrow \infty} I(\varphi_n) \quad (2.58)$$

which violates the *weak lower semicontinuity of the functional I*. As a consequence, we say that due to non-convex stored energy function (2.53) this minimization problem has no solution in the classical sense and generates fine scale alternating gradients. These oscillating gradients are often referred to as *fine scale microstructures*. In the minimization problem (2.54), contrary to the original one (2.13), there is an additional term  $\varphi^2$  in the energy functional  $I(\varphi)$ . This is required in order to get this interesting behavior in simple one dimensional problem. A detailed investigation of this problem for different boundary conditions with and without lower order term  $\varphi^2$  can be found in CARSTENSEN [38, 39]. It has been shown there depending on the boundary conditions non-convex variational problems may have *infinitely many, unique* or *no solution*. Another interesting one-dimensional example stems from the optimization of an elastic two phase composite beam. As a consequence of non-convex cost function the optimal composite beam also shows an infinitely fine oscillatory mixture of two constituents, see CHERKAEV [43] for further details. Note that in higher dimensions without any need of an extra term a similar oscillatory behavior of minimizing sequences is attainable, see for example BHATTACHARYA [22] pp.89-92.



### 3. Variational Formulation of Inelasticity and Relaxation Theory

In this chapter the key ingredients of the constitutive variational formulation for standard dissipative materials proposed in MIEHE [142] and MIEHE, SCHOTTE & LAMBRECHT [149] are briefly summarized. Furthermore, the existence results of non-linear elasticity based on weak convexity properties of energy storage functions (given in Section 2.2) are extended to the incremental response of inelasticity. Finally, the relaxation theory is outlined and an algorithmic relaxation method based on a rank-one convexification is addressed.

#### 3.1. Incremental Variational Formulation of Inelastic Materials

**3.1.1. Internal Variable Formulation of Inelastic Materials.** Let  $\varphi : \mathcal{B} \times \mathcal{R}_+ \rightarrow \mathcal{R}^3$  denote the non-linear deformation map of an inelastic continuum  $\mathcal{B} \subset \mathcal{R}^3$  at a material point  $\mathbf{X} \in \mathcal{B}$  and time  $t \in \mathcal{R}_+$ , see Figure 3.1. We denote the deformation gradient in a standard way as  $\mathbf{F} = \nabla\varphi$  with  $J = \det[\mathbf{F}] > 0$ . Focusing on purely mechanical problems, the stress response of the material is physically constrained by the so-called Clausius-Planck inequality for the dissipation of the material

$$\mathcal{D} = \mathbf{P} : \dot{\mathbf{F}} - \dot{\psi} \geq 0 \quad , \quad (3.1)$$

where  $\mathbf{P}$  denotes the first Piola-Kirchhoff stress tensor.  $\psi$  is an *energy storage function* that is assumed to depend on the deformation  $\mathbf{F}$  and a generalized vector  $\mathcal{I} \in \mathcal{G}$  of internal variables. It describes an energy storage mechanism in a deforming solid material.  $\mathcal{G}$  indicates a vector space  $\mathcal{R}^n$  of  $n$  scalar functions of internal variables which may be constrained to a manifold, e.g. the Lie group  $SL(3)$  of unimodular tensors in isochoric finite inelasticity. The storage function must satisfy the principle of material frame invariance, i.e.  $\psi(\mathbf{Q}\mathbf{F}, \mathcal{I}) = \psi(\mathbf{F}, \mathcal{I})$  for all  $\mathbf{Q} \in \mathcal{SO}(3)$ . Furthermore, as a physical constraint it is assumed to be normalized to a zero energy level and a stress free state at the reference configuration, i.e.  $\psi(\mathbf{1}, \mathcal{I}_0) = 0$  and  $\partial_{\mathbf{F}}\psi(\mathbf{1}, \mathcal{I}_0) = \mathbf{0}$ . Insertion of the free energy  $\psi(\mathbf{F}, \mathcal{I})$  into (3.1) yields, by a standard argument often denoted as Coleman's method, the constitutive equation for the stresses

$$\mathbf{P} = \partial_{\mathbf{F}}\psi(\mathbf{F}, \mathcal{I}) \quad (3.2)$$

and the reduced dissipation inequality

$$\mathcal{D} = \mathcal{F} \cdot \dot{\mathcal{I}} \geq 0 \quad \text{with} \quad \mathcal{F} := -\partial_{\mathcal{I}}\psi(\mathbf{F}, \mathcal{I}) \quad , \quad (3.3)$$

where  $\mathcal{F} \in \mathcal{R}^n$  is a generalized vector of internal forces conjugate to the variables  $\mathcal{I}$ . The model of finite inelasticity needs to be supplemented by constitutive equations which determine the evolution of the internal variables  $\mathcal{I}$  in time. A broad spectrum of inelastic solids is covered by the so-called *standard dissipative media*, where the evolution  $\dot{\mathcal{I}}$  of the internal variables on  $\mathcal{G}$  is governed by a scalar *dissipation function*  $\phi(\dot{\mathcal{I}}, \mathcal{I})$  depending on the flux  $\dot{\mathcal{I}}$  of the internal variables and the internal variables  $\mathcal{I}$  themselves. Time-dependent viscoelastic response can be described by smooth dissipation functions. However, plasticity and dry friction are (partially) time-independent or non-viscous irreversible processes, governed by non-smooth dissipation functions. Rate-independent dissipation functions are positively homogeneous of degree one with respect to the flux  $\dot{\mathcal{I}}$ , i.e.  $\phi(\epsilon\dot{\mathcal{I}}, \mathcal{I}) = \epsilon\phi(\dot{\mathcal{I}}, \mathcal{I})$  for all  $\epsilon \in \mathcal{R}_+$ . Such a function has a cone-like graph and

is not differentiable at the point  $\dot{\mathcal{I}} = \mathbf{0}$ . As a consequence, it needs a generalization of the differential operator of smooth functions to the notion of a *subdifferential operator*  $\partial$  of non-smooth convex functions as in (2.23), see MOREAU [156], HALPHEN & NGUYEN [92], NGUYEN [167] and references therein. The set

$$\mathcal{E} = \partial_{\dot{\mathcal{I}}}\phi(\mathbf{0}, \mathcal{I}) = \{ \mathcal{F} \mid \mathcal{F} \cdot \dot{\mathcal{I}} \leq \phi(\dot{\mathcal{I}}, \mathcal{I}) \text{ for all } \dot{\mathcal{I}} \} \quad (3.4)$$

is a convex domain of admissible forces, often denoted as the elastic domain of the forces. The element  $\mathcal{F} \in \mathcal{E}$  of the subdifferential is a *subgradient* of the non-smooth function  $\phi$  at  $\dot{\mathcal{I}} = \mathbf{0}$ , see (2.23). In terminologies of convex non-smooth analysis, the dissipation function  $\phi$  is then the support function of the convex set  $\mathcal{E}$ . The dissipation function governs the evolution of  $\mathcal{I}$  in time by the constitutive differential equation

$$\mathbf{0} \in \partial_{\mathcal{I}}\psi(\mathbf{F}, \mathcal{I}) + \partial_{\dot{\mathcal{I}}}\phi(\dot{\mathcal{I}}, \mathcal{I}) \quad \text{with} \quad \mathcal{I}(0) = \mathcal{I}_0 \quad (3.5)$$

often referred to as Biot's equation of standard dissipative systems, see BIOT [24], ZIEGLER & WEHRLI [218], GERMAIN [78], HALPHEN & NGUYEN [92], NGUYEN [167]. The two constitutive equations (3.2) and (3.5) determine the stress response of a smooth normal-dissipative material in a deformation-driven process where  $\mathbf{F}$  is prescribed.

Based on the definition (3.3)<sub>2</sub> of the internal forces  $\mathcal{F}$ , one introduces a dual dissipation function  $\phi^*$  by the Legendre-Fenchel transformation, see for example ROCKAFELLAR [193],

$$\phi^*(\mathcal{F}, \mathcal{I}) = \sup_{\dot{\mathcal{I}}} \{ \mathcal{F} \cdot \dot{\mathcal{I}} - \phi(\dot{\mathcal{I}}, \mathcal{I}) \} \quad (3.6)$$

depending on the forces  $\mathcal{F}$  and the internal variables  $\mathcal{I}$ . The definitions (3.3)<sub>2</sub> and (3.6) induce the two alternative representations

$$\mathcal{F} \in \partial_{\dot{\mathcal{I}}}\phi(\dot{\mathcal{I}}, \mathcal{I}) \quad \text{and} \quad \dot{\mathcal{I}} \in \partial_{\mathcal{F}}\phi^*(\mathcal{F}, \mathcal{I}) \quad (3.7)$$

of Biot's equation (3.5)<sub>1</sub>. The reduced dissipation inequality (3.3)<sub>1</sub> then takes the form

$$\mathcal{D} = \partial_{\dot{\mathcal{I}}}\phi(\dot{\mathcal{I}}, \mathcal{I}) \cdot \dot{\mathcal{I}} \geq 0 . \quad (3.8)$$

This inequality serves as a fundamental, physically-based constraint on the dissipation function  $\phi$ . It is a priori satisfied by assuming  $\phi$  *convex* with respect to the first argument, i.e. the flux  $\dot{\mathcal{I}}$ , and prescribing the properties  $\phi(\mathbf{0}, \mathcal{I}) = 0$  and  $\phi(\dot{\mathcal{I}}, \mathcal{I}) \geq 0$ . Positively homogeneous of degree one dissipation functions in rate-independent theories have the property  $\partial_{\dot{\mathcal{I}}}\phi(\dot{\mathcal{I}}, \mathcal{I}) \cdot \dot{\mathcal{I}} = \phi(\dot{\mathcal{I}}, \mathcal{I})$  due to  $\phi(\epsilon\dot{\mathcal{I}}, \mathcal{I}) = \epsilon\phi(\dot{\mathcal{I}}, \mathcal{I})$  for all  $\epsilon \in \mathcal{R}_+$ . Therefore, equation (3.8) yields  $\mathcal{D} = \phi(\dot{\mathcal{I}}, \mathcal{I}) \geq 0$  which states that the evaluation of the dissipation function yields the dissipation for the case of a rate-independent response.

**3.1.2. Local Incremental Minimization for Standard Dissipative Solids.** We now proceed with the construction of an integrated version of the constitutive equations giving a consistent approximation of the continuous differential equation (3.5) in a finite time increment  $[t_n, t_{n+1}] \in \mathcal{R}_+$ . Here, a key point is the definition of an *incremental stress potential function*  $W$  depending on the deformation  $\mathbf{F}_{n+1} = \mathbf{F}(t_{n+1})$  at time  $t_{n+1}$  that determines the stresses at  $t_{n+1}$  by the quasi-hyperelastic function evaluation

$$\mathbf{P}_{n+1} = \partial_{\mathbf{F}}W(\mathbf{F}_{n+1}) . \quad (3.9)$$

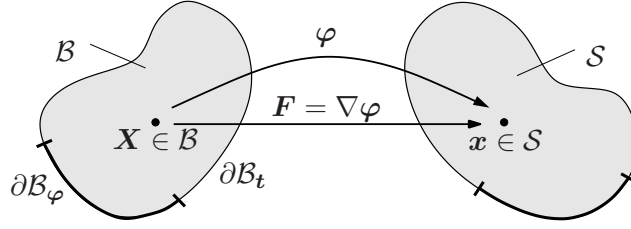


**Figure 3.1:** Deformation of a solid. The deformation map  $\varphi_t : \mathbf{X} \mapsto \mathbf{x}$  is defined on  $\mathcal{B}$  and maps initial points  $\mathbf{X} \in \mathcal{B}$  to current ones  $\mathbf{x} \in \mathcal{S}$ . The boundary  $\partial\mathcal{B}$  decomposes into a part where the deformation is prescribed and a part where the tractions are given, i.e.  $\partial\mathcal{B} = \partial\mathcal{B}_\varphi \cup \partial\mathcal{B}_t$  and  $\partial\mathcal{B}_\varphi \cap \partial\mathcal{B}_t = \emptyset$ .

Clearly, this function must cover characteristics of the storage function  $\psi$  and the dissipation function  $\phi$  introduced above. To this end, the variational problem

$$W(\mathbf{F}_{n+1}) = \inf_{\mathcal{I} \in \mathcal{G}} \left\{ \int_{t_n}^{t_{n+1}} [\dot{\psi} + \phi] dt \right\} \quad \text{with} \quad \mathcal{I}(t_n) = \mathcal{I}_n \quad (3.10)$$

is considered for standard dissipative materials proposed in MIEHE [142] and MIEHE, SCHOTTE & LAMBRECHT [149]. For prescribed deformation, this problem defines the incremental stress potential function  $W$  as a minimum of the generalized work

$$\mathcal{W}(\mathbf{F}_{n+1}, \mathcal{I}_{n+1}) = \int_{t_n}^{t_{n+1}} [\dot{\psi} + \phi] dt \quad (3.11)$$

done on the material in the time increment  $[t_n, t_{n+1}]$  under consideration. Starting with the given initial condition  $\mathcal{I}(t_n) = \mathcal{I}_n$ , the minimum problem defines an optimal path of the internal variables  $\mathcal{I}(t)$  for  $t \in [t_n, t_{n+1}]$ , including the right boundary value  $\mathcal{I}_{n+1} = \mathcal{I}(t_{n+1})$ . We refer to MARTIN [131] and the recent works of ORTIZ & REPETTO [175], ORTIZ & STAINIER [177], CARSTENSEN, HACKL & MIELKE [40] and MIELKE [150, 151, 152] for discussions of extremum paths and energetic formulations in linear and non-linear plasticity.

The two equations (3.9) and (3.10) provide an approximate variational counterpart of the continuous setting (3.2) and (3.5) of the constitutive equations in the discrete time step  $[t_n, t_{n+1}]$  under consideration. The consistency of the finite-step-sized variational formulation (3.10) with the continuous evolution problem for the limit  $[t_n, t_{n+1}] \rightarrow dt$ , when the finite increment becomes infinitely small, has already been shown in MIEHE, SCHOTTE & LAMBRECHT [149]. Here an alternative argumentation is demonstrated, see also MIEHE, LAMBRECHT & GÜRSES [148]. Observe that the variational principle (3.10) can be recast into

$$\tilde{W}(\Delta\mathbf{F}_{n+1}) = \inf_{\Delta\mathcal{I}} \left\{ \int_{t_n}^{t_{n+1}} [\dot{\psi} + \phi] dt \right\} \quad \text{with} \quad \Delta\mathcal{I}(t_n) = \mathbf{0}, \quad (3.12)$$

where the current deformation and internal variables were expressed by  $\mathbf{F}_{n+1} = \mathbf{F}_n + \Delta\mathbf{F}_{n+1}$  and  $\mathcal{I}(t) = \mathcal{I}_n + \Delta\mathcal{I}(t)$  for  $t \in [t_n, t_{n+1}]$ . We then obtain for the limit  $[t_n, t_{n+1}] \rightarrow dt$  the incremental variational problem

$$\tilde{W}(d\mathbf{F}) = \inf_{d\mathcal{I}} \left\{ [\dot{\psi} + \phi] dt \right\} \quad (3.13)$$

at infinitesimally small steps. Setting  $[\dot{\psi} + \phi]dt = \partial_{\mathbf{F}}\psi(\mathbf{F}, \mathcal{I}) : d\mathbf{F} + \partial_{\mathcal{I}}\psi(\mathbf{F}, \mathcal{I}) : d\mathcal{I} + \phi(d\mathcal{I}/dt, \mathcal{I})dt$ , we obtain at once Biot's equation (3.5) as the associated Euler equation. This shows the consistency of the variational formulation (3.10) with the continuous evolution problem. When (3.10) is applied to problems in plasticity, it defines for the finite-step-sized incremental problem of the flow theory of plasticity a minimization path as used in the deformation theory of plasticity, see MARTIN [131] for more details. This provides a consistent symmetry-preserving basis for time-discrete numerical formulations of finite plasticity. Note that a further derivative of (3.9) with respect to  $\mathbf{F}$  yields the tangent moduli

$$\mathbb{C}_{n+1} = \partial_{\mathbf{F}\mathbf{F}}^2 W(\mathbf{F}_{n+1}) \quad (3.14)$$

at time  $t = t_{n+1}$ .

**3.1.3. Dissipation Functions for Single-Surface Models of Inelasticity.** An elastic domain of the internal forces is a key feature of rate-independent models of elasto-plasticity and damage. In classical treatments of these models, the convex elastic domain  $\mathcal{E}$  defined in (3.4) is directly described in the constitutive modeling. To this end, consider a function  $f(\mathcal{F}, \mathcal{I})$  depending on the internal forces  $\mathcal{F}$  and the internal variables  $\mathcal{I}$ . The level surface  $f(\mathcal{F}, \mathcal{I}) = c(\mathcal{I})$  with the *threshold function*  $c(\mathcal{I})$  is assumed to describe the boundary  $\partial\mathcal{E}$  of the convex domain  $\mathcal{E}$ . Then

$$\mathcal{E} = \{ \mathcal{F} \mid f(\mathcal{F}, \mathcal{I}) \leq c(\mathcal{I}) \} \quad (3.15)$$

is called the elastic domain of the internal forces. We denote  $f$  as the *level set function*. The function is assumed to be (i) convex with respect to the forces  $f(\theta\mathcal{F}_2 + (1-\theta)\mathcal{F}_1, \mathcal{I}) \leq \theta f(\mathcal{F}_2, \mathcal{I}) + (1-\theta)f(\mathcal{F}_1, \mathcal{I})$  for all  $\{\mathcal{F}_1, \mathcal{F}_2\} \in \mathcal{E}$  and  $\theta \in [0, 1]$ , (ii) positively homogeneous of degree one

$$f(\theta\mathcal{F}, \mathcal{I}) = \theta f(\mathcal{F}, \mathcal{I}) \quad \text{for } \theta > 0 \quad (3.16)$$

and (iii) zero at the origin  $f(\mathbf{0}, \mathcal{I}) = 0$ . The level set function  $f$  and the threshold function  $c$  together define a *flow criterion function*  $\chi(\mathcal{F}, \mathcal{I}) = f(\mathcal{F}, \mathcal{I}) - c(\mathcal{I})$ , a standard terminology of rate-independent plasticity. Representations of the functions  $f$  and  $c$  for specific materials are obtained from combined hardening and caloric experiments. For a known elastic domain (3.15), i.e. known functions  $f$  and  $c$ , the dissipation function  $\phi$  for a rate-independent model of inelasticity may be defined by a generalization of the classical *principle of maximum dissipation* of plasticity theory. It defines the dissipation function by the constrained maximum problem

$$\phi(\dot{\mathcal{I}}, \mathcal{I}) = \sup_{\mathcal{F} \in \mathcal{E}} \{ \mathcal{F} \cdot \dot{\mathcal{I}} \} . \quad (3.17)$$

The maximization problem (3.17) with the inequality constraint  $f(\mathcal{F}, \mathcal{I}) - c(\mathcal{I}) \leq 0$  can be solved by a Lagrange method

$$\phi(\dot{\mathcal{I}}, \mathcal{I}) = \sup_{\mathcal{F}, \dot{\gamma} \geq 0} \{ \mathcal{F} \cdot \dot{\mathcal{I}} - \dot{\gamma} [f(\mathcal{F}, \mathcal{I}) - c(\mathcal{I})] \} . \quad (3.18)$$

The associated Karush-Kuhn-Tucker equations determine the evolution of the internal variables along with the loading-unloading conditions

$$\dot{\mathcal{I}} = \dot{\gamma} \partial_{\mathcal{F}} f(\mathcal{F}, \mathcal{I}) \quad \wedge \quad \dot{\gamma} \geq 0 \quad \wedge \quad f \leq c \quad \wedge \quad \dot{\gamma}(f - c) = 0 . \quad (3.19)$$

Insertion of (3.19) into (3.3)<sub>1</sub> and exploiting the homogeneity (3.16) of the level set function gives the dissipation of the rate-independent formulation

$$\mathcal{D} = f(\mathcal{F}, \mathcal{I})\dot{\gamma} = c(\mathcal{I})\dot{\gamma} \geq 0. \quad (3.20)$$

Thus, the thermodynamical consistency of the rate-independent model is ensured by choosing a threshold function

$$c(\mathcal{I}) \geq 0 \quad (3.21)$$

with positive image. Insertion of (3.19) into (3.18) gives, after some algebraic manipulations, the simple representation of the dissipation function

$$\phi = c(\mathcal{I})\dot{\gamma} \quad (3.22)$$

with an image identical to the dissipation. Thus, as already mentioned, in the rate-independent inelasticity evaluation of the dissipation function yields the dissipation.

#### 3.1.4. Global Incremental Minimization for Standard Dissipative Solids.

The existence of the constitutive minimization problem (3.10) allows the introduction of an incremental minimization formulation of the boundary-value problem of finite inelasticity for standard dissipative solids. For this purpose, consider a functional of the current deformation field  $\varphi_{n+1}$  at the right boundary of the increment  $[t_n, t_{n+1}]$

$$I(\varphi_{n+1}) = \int_{\mathcal{B}} W(\mathbf{F}_{n+1}) dV - [\Pi_{ext}(\varphi_{n+1}) - \Pi_{ext}(\varphi_n)] \quad (3.23)$$

with the global load potential function

$$\Pi_{ext}(\varphi_{n+1}) = \int_{\mathcal{B}} \varphi_{n+1} \cdot \boldsymbol{\gamma} dV + \int_{\partial\mathcal{B}_t} \varphi_{n+1} \cdot \mathbf{t} dA \quad (3.24)$$

of dead body forces  $\boldsymbol{\gamma}(\mathbf{X}, t)$  in  $\mathcal{B}$  and surface tractions  $\mathbf{t}(\mathbf{X}, t)$  on  $\partial\mathcal{B}_t$ .  $W$  is the incremental stress potential function defined in (3.10). As outlined in MIEHE & LAMBRECHT [146, 147], the current deformation map of inelastic standard dissipative materials can then be determined by a *principle of minimum incremental energy for standard dissipative solids*

$$I(\varphi_{n+1}^*) = \inf_{\varphi_{n+1} \in \mathcal{W}^{1,p}(\mathcal{B})} \{I(\varphi_{n+1})\} \quad (3.25)$$

subject to the essential boundary condition  $\varphi_{n+1} = \bar{\varphi}(\mathbf{X}, t_{n+1})$  on  $\partial\mathcal{B}_\varphi$  associated with prescribed deformations  $\bar{\varphi}$  at  $\mathbf{X} \in \partial\mathcal{B}_\varphi$ . As usual, we consider a decomposition of the surface into a part where the deformation is prescribed and a part where the tractions are given, i.e.  $\partial\mathcal{B} = \partial\mathcal{B}_\varphi \cup \partial\mathcal{B}_t$  and  $\partial\mathcal{B}_\varphi \cap \partial\mathcal{B}_t = \emptyset$ . The minimization problem (3.25) governs the response of the inelastic solid in the finite increment  $[t_n, t_{n+1}]$  in a structure identical to the *principle of minimum potential energy* in finite elasticity. The discretization of the variational principle (3.25) can be performed in a straightforward manner by a displacement-type finite element method and is commented on for the relaxed problem in Section 3.3.3. The minimization problem (3.25) has formally the same structure as (2.13). However, (3.25) is valid for an incremental problem and solved at the right boundary of a time increment  $[t_n, t_{n+1}]$  while (2.13) is also applicable for processes continuous in time.

### 3.2. Existence and Stability of Incremental Solutions

As already pointed out in MIEHE & LAMBRECHT [146, 147] and MIEHE, LAMBRECHT & GÜRSES [148], a key advantage of the above outlined variational formulation is the opportunity to analyze the *incremental stability of inelastic solids* in terms of terminologies used in finite elasticity. In what follows we relate the material stability of standard dissipative solids to global *weak convexity properties of the incremental stress potential*. Recall that weak convexity notions discussed in Section 2.5.3, in particular the quasiconvexity, play a key role in the existence results of vectorial variational problems. As far as the stability of inelastic solids is concerned the subsequent treatments may be understood as consistent extensions of the energetic rate formulations proposed by PETRYK [181, 182] in terms of velocity fields to the finite-step-sized incremental setting in terms of absolute placement fields.

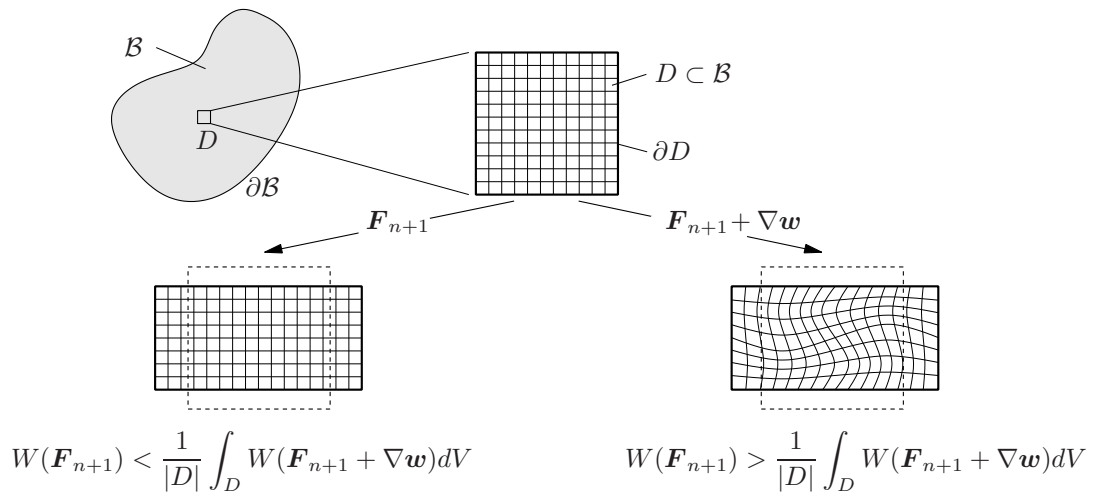


**Figure 3.2:** Interpretation of incremental energetic stability conditions of an inelastic material in terms of quasiconvexity. A given homogeneous deformation state  $\mathbf{F}_{n+1}$  of the material is stable if superimposed fine scale fluctuation patterns  $\nabla \mathbf{w}$  with support on the boundary  $\partial D$  increase the averaged incremental stress potential on  $D$ .

Extending results of the existence theory in finite elasticity summarized in Section 2.2 (see also BALL [12], CIARLET [45], DACOROGNA [51], MARSDEN & HUGHES [130] and ŠILHAVÝ [200]) to the incremental response of standard dissipative solids in a finite time step  $[t_n, t_{n+1}]$ , we consider the *sequentially weakly lower semicontinuity* (swlsc) of the functional (3.23) as the key property for the *existence of minimizers* of the variational problem (3.25). The internal part of the functional (3.23) is assumed to be sequentially weakly lower semicontinuous, if the incremental stress potential defined by the constitutive minimization problem (3.10) is quasiconvex and satisfies some growth conditions, see for example DACOROGNA [51] and ACERBI & FUSCO [1]. We regard the *quasiconvexity* of the incremental stress potential  $W$  as the fundamental criterion for the incremental material stability of the inelastic solid, see Figure 3.2 for an illustration. This weak convexity property was introduced by MORREY [157] and already discussed in Section 2.5.3.

As noted before in the context of non-linear elasticity, the well-motivated concept of quasiconvexity is based on a spatial integral condition which is hard to verify in practice. Recalling the relations of weak convexity conditions (2.50), we consider the slightly weaker rank-one convexity condition as a close approximation of the quasiconvexity and focus on



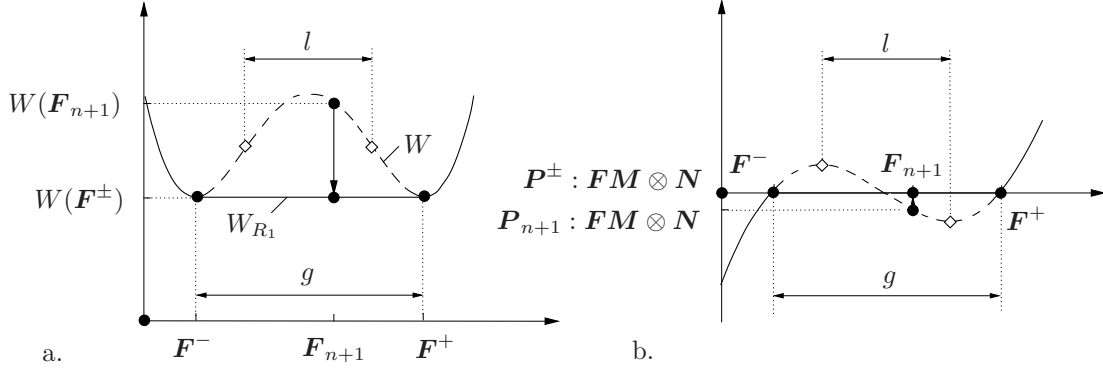


**Figure 3.3:** Qualitative representation of a non-convex incremental potential and its convexification.  $l$  and  $g$  characterize the ranges where the *local* and the *global* convexity criterion are not satisfied, respectively. a.) At  $\mathbf{F}_{n+1}$  the potential  $W$  is not rank-one convex (dashed line). As a consequence, the macroscopic deformation state  $\mathbf{F}_{n+1}$  is not stable and decomposes into micro-phases  $\mathbf{F}^{\pm}$  which determine the rank-one convex envelope (solid line). b.) The relaxed stress-strain relation characterizes a snap-through behavior between the two micro-phases  $\mathbf{F}^{\pm}$  due to the constant slope of the rank-one convex envelope.

the rank-one convexity as a practically usable criterion for material stability. In addition to its practical applicability, as noted by ŠILHAVÝ [200] p.278, “*the experience shows that the difference between global quasiconvexity and rank-one convexity is relatively small*”.

### 3.2.1. Check of Rank-One Convexity for the Incremental Stress Potential.

The notion of rank-one convexity is already discussed in Section 2.5.4 and in the framework of non-linear elasticity its necessary condition is given in (2.47). In the sequel, we consider the following equivalent reformulation of (2.47). The incremental stress potential  $W$  is said to be *rank-one convex* if the condition

$$W(\xi \mathbf{F}^+ + (1 - \xi) \mathbf{F}^-) \leq \inf_{\xi, \mathbf{F}^+, \mathbf{F}^-} \{ \xi W(\mathbf{F}^+) + (1 - \xi) W(\mathbf{F}^-) \} \quad (3.26)$$

holds for all *laminate deformations*  $\mathbf{F}^+$  and  $\mathbf{F}^-$  which satisfy the condition

$$\text{rank}[\mathbf{F}^+ - \mathbf{F}^-] \leq 1 \quad (3.27)$$

in terms of the volume fraction  $\xi \in [0, 1]$ . Condition (3.27) ensures the compatibility of the micro-phases ( $\pm$ ) along their interface. The rank-one convexity condition (3.26) rules out the development of local fine scale microstructures in the form of first-order laminates. Hence, the material is stable if the superimposed first-order laminate-type fluctuation field yields a higher energy level than the homogeneous deformation  $\mathbf{F}_{n+1}$ .

A qualitative picture of a non-convex, unstable incremental response is given in Figure 3.3. Observe carefully that (3.26) is a *global stability criterion* that needs the knowledge about the global range of instability between  $\mathbf{F}^-$  and  $\mathbf{F}^+$ . The material stability cannot be directly decided in terms of a given local deformation  $\mathbf{F}_{n+1}$ , but needs the rank-one convex hull construction governed by  $\mathbf{F}^-$  and  $\mathbf{F}^+$ . As shown in MIEHE & LAMBRECHT [146, 147] and LAMBRECHT [121] classical conditions of material stability of elastoplastic solids outlined in HILL [100] and RICE [191] are consistent with this local convexity condition, which are often motivated by the consideration of wave propagation in solids. The Hadamard condition (2.49) when computed for a single deformation state  $\mathbf{F}_{n+1}$  defines a material

instability in terms of a negative curvature of the stress potential  $W$  locally at  $\mathbf{F}_{n+1}$ . Note that the definition  $\mathbb{C} = \partial_{\mathbf{F}\mathbf{F}}^2 \psi(\mathbf{F})$  in (2.49) has to be replaced with  $\mathbb{C}_{n+1} = \partial_{\mathbf{F}\mathbf{F}}^2 W(\mathbf{F}_{n+1})$  in the context of incremental variational formulation of inelasticity. As shown in Figure 3.3, the associated range of instability is different from the one predicted by the global condition (3.26). In the sequel, we focus on the global stability condition (3.26), which is much harder to evaluate than its local counterpart (2.49). However, the effort needed for the check of (3.26) is already a part of the convexification analysis for the incremental energy relaxation discussed in the subsequent Section 3.3.

**3.2.2. Global Formulation for Two-Dimensional Problems.** In what follows the rank-one convexity condition (3.26) is rewritten for two-dimensional problems. To this end, we introduce the ansatz

$$\mathbf{F}^\pm = \mathbf{F}_{n+1} \mathbf{L}^\pm \quad \text{with} \quad \begin{cases} \mathbf{L}^+ = \mathbf{1} + (1 - \xi)d \mathbf{M} \otimes \mathbf{N} \\ \mathbf{L}^- = \mathbf{1} - \xi d \mathbf{M} \otimes \mathbf{N} \end{cases} \quad (3.28)$$

for the two deformation phases that satisfies the condition (3.27). It models a first-order laminate in terms of the two Lagrangian unit vectors  $\mathbf{M}$  and  $\mathbf{N}$ . For two-dimensional problems, these vectors can be parameterized by two angles  $\varphi$  and  $\chi$

$$\mathbf{M}(\varphi) = [\cos \varphi \ \sin \varphi]^T \quad \text{and} \quad \mathbf{N}(\chi) = [\cos \chi \ \sin \chi]^T. \quad (3.29)$$

The scalar  $d$  describes the intensity of the bifurcation on the micro-scale.  $\xi$  is the volume fraction of the phase (+) and can be understood as a probability measure in the sense of YOUNG [217]. Hence, deformations microstructures consisting of two phases (+) and (−) are characterized by *four micro-variables*

$$\mathbf{q} = [\xi, d, \varphi, \chi]^T \in \mathcal{Q} \quad (3.30)$$

for a two-dimensional description of the rank-one laminate. These are constrained to lie in the admissible domain

$$\mathcal{Q} = \{\mathbf{q} \mid 0 \leq \xi \leq 1, d \geq 0, 0 \leq \varphi \leq \pi, 0 \leq \chi \leq \pi\}. \quad (3.31)$$

With this notation at hand, we write the global rank-one convexity condition (3.26) for two-dimensional problems as the minimization problem

$$W(\mathbf{F}_{n+1}) \leq \inf_{\mathbf{q} \in \mathcal{Q}} \{\bar{W}^h(\mathbf{F}_{n+1}, \mathbf{q})\} \quad (3.32)$$

in terms of the function

$$\bar{W}^h(\mathbf{F}_{n+1}, \mathbf{q}) = \xi W(\mathbf{F}^+(\mathbf{F}_{n+1}, \mathbf{q})) + (1 - \xi)W(\mathbf{F}^-(\mathbf{F}_{n+1}, \mathbf{q})) \quad (3.33)$$

that represents the volume average of the potentials over the two deformation phases. Obviously, (3.32) holds as an equality if the micro-variables assume the values  $\xi = 0$ ,  $\xi = 1$  or  $d = 0$ . In these cases one or both micro-phases  $\mathbf{F}^\pm$  are identical to the macroscopic deformation  $\mathbf{F}_{n+1}$ . Figure 3.3a provides a visual demonstration of a non-convex incremental stress potential  $W(\mathbf{F}_{n+1})$  which is greater than the interpolation of the potentials  $W(\mathbf{F}^+)$  and  $W(\mathbf{F}^-)$  corresponding to the phases (+) and (−). As a consequence, the homogeneous deformation state is not stable and decomposes into the micro-deformations  $\mathbf{F}^\pm$  which minimize the function  $\bar{W}^h$  with respect to the variables  $\mathbf{q}$ .



**Box 3.1:** Overview: Minimization Principles for Standard Dissipative Solids

- (M) Constitutive Model.  $\mathbf{F} = \nabla\varphi$  at  $\mathbf{X} \in \mathcal{B}$  is the local deformation of the material and  $\mathcal{I} \in \mathcal{G}$  a generalized vector of internal variables. A normal-dissipative set of local material equations has the structure

$$\begin{aligned} \text{stresses} \quad & \mathbf{P} = \partial_{\mathbf{F}}\psi(\mathbf{F}, \mathcal{I}) \\ \text{evolution equation} \quad & \partial_{\mathcal{I}}\psi(\mathbf{F}, \mathcal{I}) + \partial_{\dot{\mathcal{I}}}\phi(\dot{\mathcal{I}}, \mathcal{I}) = 0, \quad \mathcal{I}(0) = \mathcal{I}_0 \end{aligned}$$

defined in terms of an energy storage function  $\psi$  and a dissipation function  $\phi$ .

- (C) Incremental Variational Formulation of Constitutive Model. In a finite time increment  $[t_n, t_{n+1}]$ , the *minimization problem of the constitutive response*

$$\begin{aligned} \text{stresses} \quad & \mathbf{P}_{n+1} = \partial_{\mathbf{F}}W(\mathbf{F}_{n+1}) \\ \text{stress potential} \quad & W(\mathbf{F}_{n+1}) = \inf_{\mathcal{I}} \int_{t_n}^{t_{n+1}} [\dot{\psi} + \phi] dt, \quad \mathcal{I}(t_n) = \mathcal{I}_n \end{aligned}$$

determines the current internal state  $\mathcal{I}_{n+1} \in \mathcal{G}$  and provides a potential for the stresses at time  $t_{n+1}$ .

- (S) Stability of Incremental Constitutive Response. In  $[t_n, t_{n+1}]$  the *material is locally stable if the incremental stress potential  $W$  is quasiconvex*

$$\text{stable response} \quad W(\mathbf{F}_{n+1}) \leq \inf_{\mathbf{w}} \left\{ \frac{1}{|D|} \int_D W(\mathbf{F}_{n+1} + \nabla\mathbf{w}) dV \right\}$$

for all possible fluctuations  $\mathbf{w}$  on the domain  $D$ .

- (R) Microstructure Development in Unstable Materials. For an unstable non-convex response, the *incremental minimization problem of quasiconvexification*

$$\begin{aligned} \text{macro-stresses} \quad & \bar{\mathbf{P}}_{n+1} = \partial_{\mathbf{F}}W_Q(\mathbf{F}_{n+1}) \\ \text{relaxation} \quad & W_Q(\mathbf{F}_{n+1}) = \inf_{\mathbf{w}} \left\{ \frac{1}{|D|} \int_D W(\mathbf{F}_{n+1} + \nabla\mathbf{w}) dV \right\} \end{aligned}$$

provides a relaxed quasiconvex hull  $W_Q$  of  $W$  and determines the current microstructure fluctuation field  $\mathbf{w}$ .

**3.2.3. Algorithmic Implementation for Two-Dimensional Problems.** In a typical incremental analysis of an inelastic solid, the accompanying check of incremental rank-one convexity in  $[t_n, t_{n+1}]$  needs the solution of the local minimization problem (3.32)

$$\inf_{\mathbf{q} \in \mathcal{Q}} \{\bar{W}^h(\mathbf{F}_{n+1}, \mathbf{q})\} \begin{cases} = W(\mathbf{F}_{n+1}) & : \text{ for rank-one convex } W \text{ at } \mathbf{F}_{n+1} \\ < W(\mathbf{F}_{n+1}) & : \text{ for not rank-one convex } W \text{ at } \mathbf{F}_{n+1} \end{cases} \quad (3.34)$$

for the four variables  $\mathbf{q}$  defined in (3.30). The necessary condition of the minimization problem

$$\partial_{\mathbf{q}}\bar{W}^h = \mathbf{0} \quad (3.35)$$

is a non-linear equation for the determination of the micro-variables  $\mathbf{q}$ . As the function  $\bar{W}^h$  is non-convex with respect to  $\mathbf{q}$ , a standard Newton iteration scheme for arbitrary initial values cannot be directly applied. In order to overcome the difficulty in finding the global minimum for the non-convex problem under consideration, the following elementary solution procedure is applied. In a first step, we discretize the admissible range of the micro-variables and filter out the minimum

$$\mathbf{q}_0 = \arg \left\{ \inf_{\mathbf{q}^h \in \mathcal{Q}} \{ \bar{W}^h(\mathbf{F}_{n+1}, \mathbf{q}^h) \} \right\} \quad \text{with} \quad \mathbf{q}^h = \left[ \frac{i}{n}, \frac{j}{n}, \frac{k}{n}\pi, \frac{l}{n}\pi \right]^T \quad (3.36)$$

on a given raster for  $n \in \mathcal{N}$  and  $\{i, j, k, l\} \in \{1 \dots n\}$ . Note that the admissible range for the variable  $d$  is unbounded. However, by conducting numerical studies the relevant range can be figured out.  $\mathbf{q}_0$  then serves as a starting value for subsequent Newton-Raphson updates

$$\mathbf{q} \Leftarrow \mathbf{q} - [\partial_{\mathbf{q}\mathbf{q}}^2 \bar{W}^h]^{-1} [\partial_{\mathbf{q}} \bar{W}^h] \quad \text{for} \quad \|\partial_{\mathbf{q}} \bar{W}^h(\mathbf{F}_{n+1}, \mathbf{q})\| > \text{tol} . \quad (3.37)$$

The derivatives of the function  $\bar{W}^h$  with respect to the micro-variables  $\mathbf{q}$  are summarized in the Appendix A. An alternative probabilistic solution strategy for the non-convex minimization problem can be found in BARTELS ET AL. [19]. The approach is based on the computation of the objective function (3.33) several (100 to 10000) times, construction of clusters from these sampling points and then identification of a best point from these clusters.

### 3.3. Relaxation of a Non-Convex Constitutive Response

As pointed out in the recent papers MIEHE & LAMBRECHT [146, 147] and MIEHE, LAMBRECHT & GÜRSERES [148] the incremental variational formulation for the constitutive response in Section 3.1 opens up the opportunity to resolve the developing microstructure in unstable standard dissipative solids by a relaxation of the associated non-convex incremental variational problem. If the above outlined material stability analysis detects a non-convex incremental stress potential  $W$ , an energy-minimizing *deformation microstructure* is assumed to develop as conceptually pointed out in Section 2.6. A *relaxation* is associated with a *quasiconvexification* of the non-convex function  $W$  by constructing its *quasiconvex envelope*  $W_Q$  as schematically indicated in Figure 3.3. Formally it replaces the variational problem (3.23) which may have no solution by the one (3.38) which has a solution. On the other hand, physically, quasiconvexity is the passage from a microscopic energy to a macroscopic energy that is obtained by an averaging over fine scale oscillations. This section develops a framework for a relaxation of standard dissipative solids based on a first-order rank-one convexification. A summary of the incremental variational formulation together with the stability of inelastic response and the relaxation of unstable materials is given in Box 3.1. For a detailed mathematical discussion on the relaxation theory readers are referred to DACOROGNA [51], MÜLLER [163] and CARSTENSEN [38].

**3.3.1. Quasiconvexified Relaxed Incremental Variational Problem.** If material instabilities are detected at a point  $\mathbf{X} \in \mathcal{B}$  of the solid by a failure of conditions (3.26) or (3.32), we face with the incremental potential  $W$  that is not rank-one convex in some region of the inelastic solid. If the incremental potential function  $W$  is not rank-one convex, the internal part of the functional (3.23) is assumed not to be sequentially weakly lower semicontinuous. Hence, the existence of solutions of (3.25) is not ensured. In other words, the minimum of the incremental boundary-value problem (3.25) is not attained.

Following DACOROGNA [51] and ACERBI & FUSCO [1] we consider the *relaxed energy functional*

$$I_Q(\boldsymbol{\varphi}_{n+1}) = \int_{\mathcal{B}} W_Q(\mathbf{F}_{n+1}) dV - [\Pi_{ext}(\boldsymbol{\varphi}_{n+1}) - \Pi_{ext}(\boldsymbol{\varphi}_n)] , \quad (3.38)$$

where the internal part of the relaxed energy functional is obtained by replacing the non-convex integrand  $W$  in (3.23) by its *quasiconvex envelope*  $W_Q$ . The current deformation field of the elastoplastic solid is then determined by the relaxed incremental variational principle

$$I_Q(\boldsymbol{\varphi}_{n+1}^*) = \inf_{\boldsymbol{\varphi}_{n+1} \in \mathcal{W}^{1,p}(\mathcal{B})} \{ I_Q(\boldsymbol{\varphi}_{n+1}) \} \quad (3.39)$$

that *minimizes the relaxed incremental potential energy*  $I_Q$  for the admissible deformation field. The quasiconvexified incremental stress potential  $W_Q$  is defined by the minimization problem

$$W_Q(\mathbf{F}_{n+1}) = \inf_{\mathbf{w} \in \mathcal{W}_0^{1,p}(\mathcal{B})} \left\{ \frac{1}{|D|} \int_D W(\mathbf{F}_{n+1} + \nabla \mathbf{w}) dV \right\} \quad (3.40)$$

with respect to the microscopic fluctuation field  $\mathbf{w}$  that constitutes the development of a deformation microstructure, subject to the boundary condition  $\mathbf{w} = \mathbf{0}$  on  $\partial D$  which provides a support on  $\partial D$ . The first and second derivatives of the relaxed potential  $W_Q$  function define relaxed stresses and tangent moduli

$$\bar{\mathbf{P}}_{n+1} = \partial_{\mathbf{F}} W_Q(\mathbf{F}_{n+1}) \quad \text{and} \quad \bar{\mathbb{C}}_{n+1} = \partial_{\mathbf{F}\mathbf{F}}^2 W_Q(\mathbf{F}_{n+1}) \quad (3.41)$$

in an analogous format to (3.9) and (3.14). The relaxed problem (3.39) is considered to be a *well-posed problem* as close as possible to the original unstable problem (3.25) which has no solution. The minimization problem (3.40) of quasiconvexification is similar to the minimization problem of homogenization of heterogeneous materials, see MIEHE [142] and MIEHE, SCHOTTE & LAMBRECHT [149]. It determines a micro-fluctuation field  $\mathbf{w}$  on an arbitrarily chosen domain  $D \subset \mathcal{R}^3$ . Although the relaxation is originally related with the construction of a *quasiconvex envelope*  $W_Q$ , it is often approximated by *convex*, *polyconvex* or *rank-one convex* envelopes due to difficulty in determining the quasiconvex hull. See for example, BARTELS ET AL. [19], ARANDA & PERDREGAL [7], DOLZMANN [59] and AUBRY, FAGO & ORTIZ [11] for different numerical polyconvexification and rank-one convexification algorithms. The convex ( $C$ ), polyconvex ( $P$ ), quasiconvex ( $Q$ ) and rank-one convex ( $R$ ) envelopes of  $W$  are formally given by

$$\begin{aligned} W_C &= \sup \{ \tilde{W} \leq W \mid \tilde{W} \text{ is convex} \} \\ W_P &= \sup \{ \tilde{W} \leq W \mid \tilde{W} \text{ is polyconvex} \} \\ W_Q &= \sup \{ \tilde{W} \leq W \mid \tilde{W} \text{ is quasiconvex} \} \\ W_R &= \sup \{ \tilde{W} \leq W \mid \tilde{W} \text{ is rank-one convex} \} . \end{aligned} \quad (3.42)$$

They are obviously related by

$$W_C \leq W_P \leq W_Q \leq W_R \quad (3.43)$$

as a consequence of (2.50) and (3.42). Rarely, in some applications quasiconvex envelopes  $W_Q$  can be determined analytically. One of the approaches for the computation of  $W_Q$  is as follows: (i) Find upper and lower bounds of  $W_Q$ , e.g. canonical choices would be  $W_P$  and  $W_R$ , and (ii) show that they coincide  $W_P = W_R$ . Consequently, it yields from (3.43) clearly that  $W_P = W_Q = W_R$ . In DESIMONE & DOLZMANN [57, 58] and DOLZMANN [60] such an analytical construction is developed for nematic elastomers. Having in mind the implications (3.43) and the experience that shows the difference between  $W_Q$  and  $W_R$  is in general small, in what follows we focus on a rank-one convexification as a practically manageable numerical relaxation method.

**3.3.2. Rank-One-Convexified Relaxed Incremental Variational Problem.** A failure of rank-one convexity conditions (3.26) or (3.32) indicates the instability of the homogeneous deformation state  $\mathbf{F}_{n+1}$  and the development of a pattern of first- and higher-order laminates. We consider the *relaxed energy functional*

$$I_R(\varphi_{n+1}) = \int_{\mathcal{B}} W_R(\mathbf{F}_{n+1}) dV - [\Pi_{ext}(\varphi_{n+1}) - \Pi_{ext}(\varphi_n)], \quad (3.44)$$

where the internal part of the relaxed energy functional is obtained by replacing the non-convex integrand  $W$  in (3.23) by its *rank-one-convex envelope*  $W_R$ , which is considered to be close to the quasiconvex envelope  $W_Q$ . The current deformation field of the elastoplastic solid is then determined by the relaxed incremental variational principle

$$I_R(\varphi_{n+1}^*) = \inf_{\varphi_{n+1} \in \mathcal{W}^{1,p}(\mathcal{B})} \{I_R(\varphi_{n+1})\} \quad (3.45)$$

that *minimizes the relaxed incremental potential energy*  $I_R$  for the admissible deformation field. The rank-one convexified function is defined by the minimization problem

$$W_R(\mathbf{F}_{n+1}) = \inf_{\xi_i, \mathbf{F}_i} \left\{ \sum_{i=1}^N \xi_i W(\mathbf{F}_i) \right\} \quad \text{with} \quad (\xi_i, \mathbf{F}_i) \in \{H \cap R_N\}. \quad (3.46)$$

Here,  $H$  denotes the set of all volume fractions  $\xi_i$  and phases  $\mathbf{F}_i$  for which the following two conditions hold: (i) The sum of the volume fractions equals one and the sum of the weighted phases  $\xi_i \mathbf{F}_i$  yields the homogeneous macro-deformation, i.e.

$$H = \{(\xi_i, \mathbf{F}_i) \mid \sum_{i=1}^N \xi_i = 1 \wedge \mathbf{F}_{n+1} = \sum_{i=1}^N \xi_i \mathbf{F}_i\}, \quad (3.47)$$

where  $N$  is the number of phases. The volume fractions  $\xi_i \in [0, 1]$  can be understood to play the role of a probability measure in the sense of YOUNG [217], see also MÜLLER [163] for further details. (ii) The fractions  $\xi_i$  and phases  $\mathbf{F}_i$  must be elements of the set  $R_N$ . For the development of one laminate ( $N = 2$ ) the set is defined as

$$R_2 = \{(\xi_i, \mathbf{F}_i) \mid \text{rank}[\mathbf{F}_1 - \mathbf{F}_2] \leq 1\} \quad \text{with} \quad i \in \{1, 2\}. \quad (3.48)$$

Elements of  $R_2$  have the property that the difference between the two phases gives a rank-one tensor. In case of a decay of the homogeneous state into three or more phases the set  $R_N$  has the non-trivial representation

$$R_N = \left\{ (\xi_i, \mathbf{F}_i) \left| \begin{array}{l} \text{rank}[\mathbf{F}_1 - \mathbf{F}_2] \leq 1 \\ \zeta_1 = \xi_1 + \xi_2, \quad \beta_1 = (\xi_1 \mathbf{F}_1 + \xi_2 \mathbf{F}_2) / \zeta_1 \\ \zeta_i = \xi_{i+1}, \quad \beta_i = \mathbf{F}_{i+1} \quad \forall \quad 2 \leq i \leq N-1 \end{array} \right. \right\}, \quad (3.49)$$

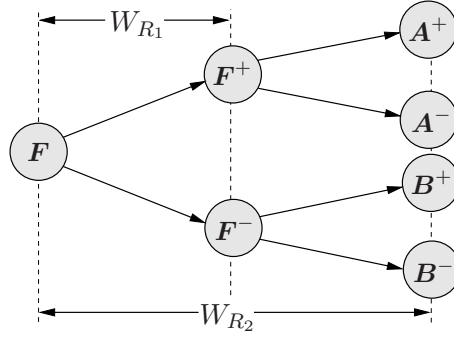


**Figure 3.4:** Rank-one convexification and development of sequential laminates. The rank-one convexification  $W_{R_k}(\mathbf{F}_{n+1})$  based on Kohn-Strang's recursion formula implies the development of a sequential laminate. Starting from the homogeneous deformation state  $\mathbf{F}_{n+1}$  any phase of level  $k-1$  decomposes into two phases (+) and (-) of level  $k$ . As a consequence, a typical binary tree structure emerges.

see DACOROGNA [51] p.114 for a detailed discussion. The rank-one convexification theorem (3.46) has the serious drawbacks that (i) one cannot a priori prescribe the  $N$  emerging phases and (ii) the set  $R_N$  is difficult to evaluate. KOHN & STRANG [117] proposed a very similar construction to (3.46) in order to characterize the rank-one convexification based on a recursion formula. Starting with

$$W_{R_0}(\mathbf{F}_{n+1}) = W(\mathbf{F}_{n+1}) , \quad (3.50)$$

one computes the functions

$$W_{R_k}(\mathbf{F}_{n+1}) = \inf_{\xi^+, \xi^-, \mathbf{F}^+, \mathbf{F}^-} \{ \xi^+ W_{R_{k-1}}(\mathbf{F}^+) + \xi^- W_{R_{k-1}}(\mathbf{F}^-) \} \quad \text{with } k \geq 1 \quad (3.51)$$

for the scales  $k = 1, 2, 3, \dots$ . After an infinite number of steps  $k \rightarrow \infty$  the exact rank-one convexified incremental stress potential

$$W_R(\mathbf{F}_{n+1}) = \lim_{k \rightarrow \infty} W_{R_k}(\mathbf{F}_{n+1}) \quad (3.52)$$

is obtained. The first and second derivatives of this convexified function then define relaxed stresses and tangent moduli

$$\bar{\mathbf{P}}_{n+1} = \partial_{\mathbf{F}} W_R(\mathbf{F}_{n+1}) \quad \text{and} \quad \bar{\mathbb{C}}_{n+1} = \partial_{\mathbf{F}\mathbf{F}}^2 W_R(\mathbf{F}_{n+1}) . \quad (3.53)$$

According to this approach any phase of order  $k-1$  decomposes into two phases (+) and (-) of order  $k$  which are elements of the sets  $H$  and  $R_2$ , and minimize the average of the corresponding incremental stress potentials. The developing micro-phases form a *sequential laminate*. For instance, Figure 3.3.2 shows a typical binary tree structure of a rank-2 laminate. The unstable macroscopic deformation state  $\mathbf{F}_{n+1}$  decomposes into two micro-phases  $\mathbf{F}^+$  and  $\mathbf{F}^-$  of micro-level 1 which again split into two pairs of micro-phases  $\mathbf{A}^+$ ,  $\mathbf{A}^-$  and  $\mathbf{B}^+$ ,  $\mathbf{B}^-$  of micro-level 2. The rank-one convexified potential  $W_{R_2}$  then consists of the volume average of the stress potentials  $W$  at the root of the tree.

### 3.3.3. First-Order Rank-One-Convexified Incremental Variational Problem.

**First-Order Rank-One-Convexification for 2-D Problems.** We approximate the exact rank-one convexification procedure outlined above by a *two-scale analysis* that

takes into account only the first micro-level. Hence, an unstable macro-deformation  $\mathbf{F}_{n+1}$  decomposes into the two phases  $\mathbf{F}^+$  and  $\mathbf{F}^-$  modeled by ansatz (3.28). Then the first-order rank-one convexification of the non-convex function  $W$  is obtained for two-dimensional problems by the minimization problem

$$W_{R_1}(\mathbf{F}_{n+1}) = \inf_{\mathbf{q} \in \mathcal{Q}} \{ \bar{W}^h(\mathbf{F}_{n+1}, \mathbf{q}) \} \quad (3.54)$$

for the function  $\bar{W}^h$  defined in (3.33) with respect to the micro-variables  $\mathbf{q}$  defined in (3.30). Note that the exploitation of this minimization problem is already needed for the check (3.32) of rank-one convexity. The solution procedure has already been outlined in Section 3.2.3.

A problem similar to (3.54) was solved in LAMBRECHT, MIEHE & DETTMAR [122] for a one-dimensional strain-softening elastic-plastic bar. A schematic visualization is given in Figure 3.3. It depicts the shape of a non-convex incremental potential  $W$ , its convexification  $W_R$  and the associated derivatives which define the stresses. Obviously, the stress potential  $W$  is not rank-one convex at the current deformation  $\mathbf{F}_{n+1}$ . As a consequence, the homogeneous deformation state is not stable and decomposes into the phases  $\mathbf{F}^+$  and  $\mathbf{F}^-$  depicted in Figures 3.3a and 3.3b. The solution of the minimization problem (3.54) yields solutions of  $\xi$ ,  $d$ ,  $\varphi$ ,  $\chi$ , which in the two-dimensional context determine two stable phases.

**Computation of Relaxed Stresses and Tangent Moduli.** The relaxed stresses and moduli are obtained by straightforward evaluation of derivatives (3.53) of the function (3.33). The first derivative of (3.54) with respect to the deformation  $\mathbf{F}_{n+1}$  at the solution point  $\mathbf{q}^*$  reads

$$\partial_{\mathbf{F}} W_{R_1} = \partial_{\mathbf{F}} \bar{W}^h + [\partial_{\mathbf{q}} \bar{W}^h][\partial_{\mathbf{F}} \mathbf{q}] . \quad (3.55)$$

Here, the last term vanishes due to the necessary condition (3.35) of the minimization problem. Thus we identify the macro-stresses

$$\bar{\mathbf{P}}_{n+1} = \partial_{\mathbf{F}} \bar{W}^h . \quad (3.56)$$

The second derivative reads

$$\partial_{\mathbf{F}\mathbf{F}}^2 W_{R_1} = \partial_{\mathbf{F}\mathbf{F}}^2 \bar{W}^h + [\partial_{\mathbf{F}\mathbf{q}}^2 \bar{W}^h][\partial_{\mathbf{F}} \mathbf{q}] . \quad (3.57)$$

Here, the sensitivity of the fluctuation with respect to the macro-deformation is obtained by taking the linearization of (3.35), yielding  $\partial_{\mathbf{F}} \mathbf{q} = -[\partial_{\mathbf{q}\mathbf{q}}^2 \bar{W}^h]^{-1}[\partial_{\mathbf{q}\mathbf{F}}^2 \bar{W}^h]$ . Insertion into (3.57) finally specifies the definition (3.53)<sub>2</sub> of the macro-moduli to

$$\bar{\mathbb{C}}_{n+1} = \partial_{\mathbf{F}\mathbf{F}}^2 \bar{W}^h - [\partial_{\mathbf{F}\mathbf{q}}^2 \bar{W}^h][\partial_{\mathbf{q}\mathbf{q}}^2 \bar{W}^h]^{-1}[\partial_{\mathbf{q}\mathbf{F}}^2 \bar{W}^h] . \quad (3.58)$$

Observe that the macro-moduli consist of the volume average of the micro-moduli and a softening part. The latter is the consequence of the flexibility of the rank-one laminate due to the phase decay. The algorithm of first-order rank-one convexification is summarized in Box 3.2. All derivatives of the function  $\bar{W}^h$  which are needed for the local Newton scheme (3.37) and the above stresses and moduli are summarized in the Appendix A.

**Box 3.2:** First-Order Rank-One Convexification of Incremental Response

1. Database  $\{\mathbf{F}_{n+1}, \mathcal{I}_n^+, \mathcal{I}_n^-\}$  and starting value  $\mathbf{q}_0 = \{\xi, d, \mathbf{N}, \mathbf{M}\}_0$  given.
2. Set micro-deformation phases

$$\mathbf{F}^\pm = \mathbf{F}_{n+1} \mathbf{L}^\pm \quad \text{with} \quad \begin{cases} \mathbf{L}^+ = \mathbf{1} & +(1-\xi)d\mathbf{M} \otimes \mathbf{N} \\ \mathbf{L}^- = \mathbf{1} & - \quad \quad \quad \xi d\mathbf{M} \otimes \mathbf{N} \end{cases}$$

3. Evaluate minimization function

$$\bar{W}^h(\mathbf{F}_{n+1}, \mathbf{q}) = \xi W(\mathbf{F}^+) + (1-\xi)W(\mathbf{F}^-)$$

and its derivatives  $\partial_{\mathbf{F}} \bar{W}^h$ ,  $\partial_{\mathbf{q}} \bar{W}^h$ ,  $\partial_{\mathbf{F}\mathbf{F}}^2 \bar{W}^h$ ,  $\partial_{\mathbf{q}\mathbf{q}}^2 \bar{W}^h$ ,  $\partial_{\mathbf{q}\mathbf{F}}^2 \bar{W}^h$  which are provided in Appendix A.

4. Convergence check: If  $(\|\partial_{\mathbf{q}} \bar{W}^h\| \leq \text{tol})$  go to 6.
5. Newton update of micro-variables

$$\mathbf{q} \Leftarrow \mathbf{q} - [\partial_{\mathbf{q}\mathbf{q}}^2 \bar{W}^h]^{-1} [\partial_{\mathbf{q}} \bar{W}^h]$$

6. Set relaxed macro-stresses and tangent macro-moduli

$$\bar{\mathbf{P}}_{n+1} = \partial_{\mathbf{F}} \bar{W}^h \quad \text{and} \quad \bar{\mathbb{C}}_{n+1} = \partial_{\mathbf{F}\mathbf{F}}^2 \bar{W}^h - [\partial_{\mathbf{F}\mathbf{q}}^2 \bar{W}^h] [\partial_{\mathbf{q}\mathbf{q}}^2 \bar{W}^h]^{-1} [\partial_{\mathbf{q}\mathbf{F}}^2 \bar{W}^h]$$

**Update of the Internal Variables.** As mentioned above, the convexification analysis can be considered as a two-scale homogenization analysis of two micro-phases (+) and (−) which develop due to an instability of the homogeneous deformation state. As a consequence, in each phase different internal variables  $\mathcal{I}^+$  and  $\mathcal{I}^-$  emerge. After the transition to the next time increment the constitutive response at the beginning of the new increment must coincide to that at the end of the previous increment. This statement induces the separate update of the internal variables for each phase

$$\mathcal{I}_n^+ \Leftarrow \mathcal{I}_{n+1}^+ \quad \text{and} \quad \mathcal{I}_n^- \Leftarrow \mathcal{I}_{n+1}^- . \quad (3.59)$$

As a consequence, the loss of rank-one convexity of the incremental stress potential marks the transition from a homogeneous one-phase analysis to a two-phase relaxation analysis. In the subsequent increments, the minimizing phases may further develop. However, a stable homogeneous state can be recovered if the volume fraction  $\xi$  becomes zero or one. Then only one phase remains, i.e.  $\mathbf{F}^- = \mathbf{F}_{n+1}$  or  $\mathbf{F}^+ = \mathbf{F}_{n+1}$ . Accordingly, we perform the update of the homogeneous internal variables

$$\mathcal{I}_n \Leftarrow \mathcal{I}_{n+1}^- \quad \text{if} \quad \xi = 0 \quad \text{or} \quad \mathcal{I}_n \Leftarrow \mathcal{I}_{n+1}^+ \quad \text{if} \quad \xi = 1 \quad (3.60)$$

and continue with the homogeneous analysis including the accompanying check of rank-one convexity outlined in Section 3.2. After the loss of rank-one convexity two micro-phases arise which bifurcate and continuously change their orientation and volume frac-



tions. Finally, it may happen that only one phase remains indicating a recovery of the stable homogeneous state.

**Finite Element Formulation of the Relaxed Problem.** An approximative numerical solution of the minimization problem (3.45) for the relaxed dissipative solid with the first-order rank-one-convexified stress potential (3.54) can be obtained by a finite element method. To this end, we discretize the macroscopic deformation map and its gradient by

$$\varphi_{n+1}^h(\mathbf{X}) = \mathbf{N}_e(\mathbf{X})\mathbf{d}_{n+1}^e \quad \text{and} \quad \nabla\varphi_{n+1}^h(\mathbf{X}) = \mathbf{B}_e(\mathbf{X})\mathbf{d}_{n+1}^e \quad \text{in } \mathcal{B}^e \quad (3.61)$$

in terms of  $n_e$  finite elements  $\mathcal{B}^e \subset \mathcal{B}$ . Then  $\mathbf{d}_{n+1} = \mathbf{A}_{e=1}^{n_e} \mathbf{d}_{n+1}^e \in \mathcal{R}^m$  is the finite-dimensional vector of nodal positions associated with the finite element mesh of the macro-structure. Insertion of approximations (3.61) into (3.45) defines the function

$$I_{R_1}^h(\mathbf{d}_{n+1}) = \mathbf{A}_{e=1}^{n_e} \int_{\mathcal{B}^e} W_{R_1}(\mathbf{B}_e \mathbf{d}_{n+1}^e) dV - [\Pi_{ext}^h(\mathbf{d}_{n+1}) - \Pi_{ext}^h(\mathbf{d}_n)] . \quad (3.62)$$

The first and second derivatives of this function define all finite element arrays

$$\left. \begin{aligned} I_{R_1, \mathbf{d}}^h &= \mathbf{A}_{e=1}^{n_e} \int_{\mathcal{B}^e} \mathbf{B}_e^T \partial_{\mathbf{F}} W_{R_1} dV - \mathbf{f}_{n+1}^{ext} \\ I_{R_1, \mathbf{d}\mathbf{d}}^h &= \mathbf{A}_{e=1}^{n_e} \int_{\mathcal{B}^e} \mathbf{B}_e^T \partial_{\mathbf{F}\mathbf{F}}^2 W_{R_1} \mathbf{B}_e dV \end{aligned} \right\} \quad (3.63)$$

needed below. Here, the first and second derivatives of the convexified stress potential  $W_{R_1}$  are the relaxed stresses  $\bar{\mathbf{P}}_{n+1}$  and moduli  $\bar{\mathbb{C}}_{n+1}$  defined in (3.56) and (3.58), respectively.

$$\mathbf{f}_{n+1}^{ext} = \mathbf{A}_{e=1}^{n_e} \left\{ \int_{\mathcal{B}^e} \mathbf{N}_e^T (\gamma_{n+1} - \gamma_n) dV + \int_{\partial\mathcal{B}_i^e} \mathbf{N}_e^T (\mathbf{t}_{n+1} - \mathbf{t}_n) dA \right\} \quad (3.64)$$

is the deformation-independent vector of incremental external nodal forces.  $\partial_{\mathbf{d}} I_{R_1}^h$  is the so-called residual vector, i.e. the difference between internal and external nodal forces.  $\partial_{\mathbf{d}\mathbf{d}}^2 I_{R_1}^h$  is the tangential stiffness matrix of the finite element mesh. The finite-dimensional discretized form of the variational principle (3.39) then reads

$$I_{R_1}^h(\mathbf{d}_{n+1}^*) = \inf_{\mathbf{d}_{n+1} \in \mathcal{R}^m} \{ I_{R_1}^h(\mathbf{d}_{n+1}) \} . \quad (3.65)$$

The necessary condition of this discrete minimum problem  $\partial_{\mathbf{d}} I_{R_1}^h = \mathbf{0}$  provides a non-linear algebraic system for the determination of the vector  $\mathbf{d}_{n+1}$  of nodal positions of the macro-structure. It can be solved by a Newton-Raphson iteration, yielding the update equations

$$\mathbf{d}_{n+1} \Leftarrow \mathbf{d}_{n+1} - [\partial_{\mathbf{d}\mathbf{d}}^2 I_{R_1}^h]^{-1} [\partial_{\mathbf{d}} I_{R_1}^h] \quad \text{for} \quad \|\partial_{\mathbf{d}} I_{R_1}^h\| > tol , \quad (3.66)$$

performed by some solver of linear equations. The iteration is terminated when  $\mathbf{d}_{n+1}^*$  is considered to be the solution of (3.65).



## 4. Application of Relaxation Theory to Phase Transformations

In the sequel, some aspects of the *martensitic phase transformation*, which is one of the most successful application areas of the relaxation theory, are studied. The main focus is put on equilibrium microstructures that are obtained by the relaxation of non-convex energy storage functions of multi-phase solids. The investigation of microstructures in phase transformations using the mathematical relaxation theory as the underlying principle is traced back to BALL & JAMES [14, 15]. The recent books by BHATTACHARYA [22] and DOLZMANN [60], the monograph by MÜLLER [163] and the review article by JAMES & HANE [107] provide comprehensive treatments of equilibrium microstructures in connection with the mathematical relaxation theory.

### 4.1. The Model Problem: Martensitic Phase Transformations

There are certain crystalline materials which can exist in more than a single solid phase where each phase is characterized by a specific crystal structure. Normally, under certain conditions, e.g. stress or temperature, one phase is favored whereas another is preferred under different conditions. Furthermore, these materials may transform abruptly from one phase to another due to a change of the stress or temperature. If the transition occurs without diffusion then it is called as a *displacive transformation*. Some examples of such materials are the shape memory alloy NiTi and the ferroelectric alloy BaTiO<sub>3</sub>.

A martensitic phase transformation is a diffusionless, solid to solid phase transformation from an austenite which is stable at high temperatures to a martensite which is stable at low temperatures. The atomic structure of the high temperature austenite phase has greater crystallographic symmetry than the low temperature martensite. This leads to the multiple symmetry-related variants of martensite. The variants of martensite have identical crystalline structure but they are oriented differently with respect to the austenite lattice, see Figure 4.1a. The number of variants is determined by the change of symmetry during the transformation. For example, a cubic to tetragonal transformation shown in Figure 4.1a gives rise to three martensite variants. In general, a crystalline solid does not transform from the austenite phase to a single variant of the martensite. However, the variants can arrange themselves by making a mixture of different variants and produce complex fine scale microstructures. The ability of martensitic materials to generate such microstructures together with the ability to change them lead to very unusual and unique properties such as the shape memory effect.

**4.1.1. Transformation Matrices and Energy Storage.** The lattice of austenite and martensite phases are characterized by the vectors  $\{e_1^A, e_2^A, e_3^A\}$  and  $\{e_1^{M_i}, e_2^{M_i}, e_3^{M_i}\}$  defining the corresponding unit cells, respectively. The transformation from the austenite lattice to martensite lattice can be described as a deformation since the process is diffusionless, i.e. there is no rearrangement of atoms. Therefore, one can introduce a second-order tensor  $U_i$  such that

$$e_j^{M_i} = U_i e_j^A \quad \text{for } j = 1 \dots 3 \quad \text{and } i = 1 \dots N \quad (4.1)$$

where  $N$  is the number of martensitic variants. The tensor  $U_i$  maps the austenite lattice to that of the  $i^{\text{th}}$  martensite variant and is called as the *transformation* or *Bain matrix*. The number of Bain matrices in a phase transformation is the same as the number of variants of martensite. In other words, each transformation matrix represents the one

variant of martensite. For instance, there are three transformation matrices in a cubic to tetragonal transformation with  $\xi > 1 > \eta$

$$\mathbf{U}_1 = \begin{bmatrix} \xi & 0 & 0 \\ 0 & \eta & 0 \\ 0 & 0 & \eta \end{bmatrix}, \quad \mathbf{U}_2 = \begin{bmatrix} \eta & 0 & 0 \\ 0 & \xi & 0 \\ 0 & 0 & \eta \end{bmatrix} \quad \text{and} \quad \mathbf{U}_3 = \begin{bmatrix} \eta & 0 & 0 \\ 0 & \eta & 0 \\ 0 & 0 & \xi \end{bmatrix} \quad (4.2)$$

corresponding to three variants of the martensite. Note that the values of  $\xi$  and  $\eta$  depend on the lattice parameters of the material and can be measured experimentally. Cubic to orthorhombic and cubic to monoclinic transformations are some other most commonly observed transformations having six and twelve martensitic variants, respectively.

The energy storage function of crystalline materials can be assumed to depend on the lattice vectors and the temperature. The austenite lattice vectors minimize the free energy at high temperatures whereas the martensite lattice vectors minimize at low temperatures. Consequently, there is a temperature called as the *critical* or *transformation temperature*  $\theta_c$  at which both phases have equal energy. A continuum energy storage is obtained from the energy function depending on the lattice vectors by employing the *Cauchy-Born hypothesis*, i.e. the lattice vectors deform according to the deformation gradient. In other words, the lattice vectors are assumed to behave like infinitesimal line elements in a solid continuum. We choose our reference configuration as the undeformed austenite lattice at the critical temperature  $\theta_c$ . Then it is possible to identify the identity tensor  $\mathbf{U}_0 = \mathbf{1}$  as

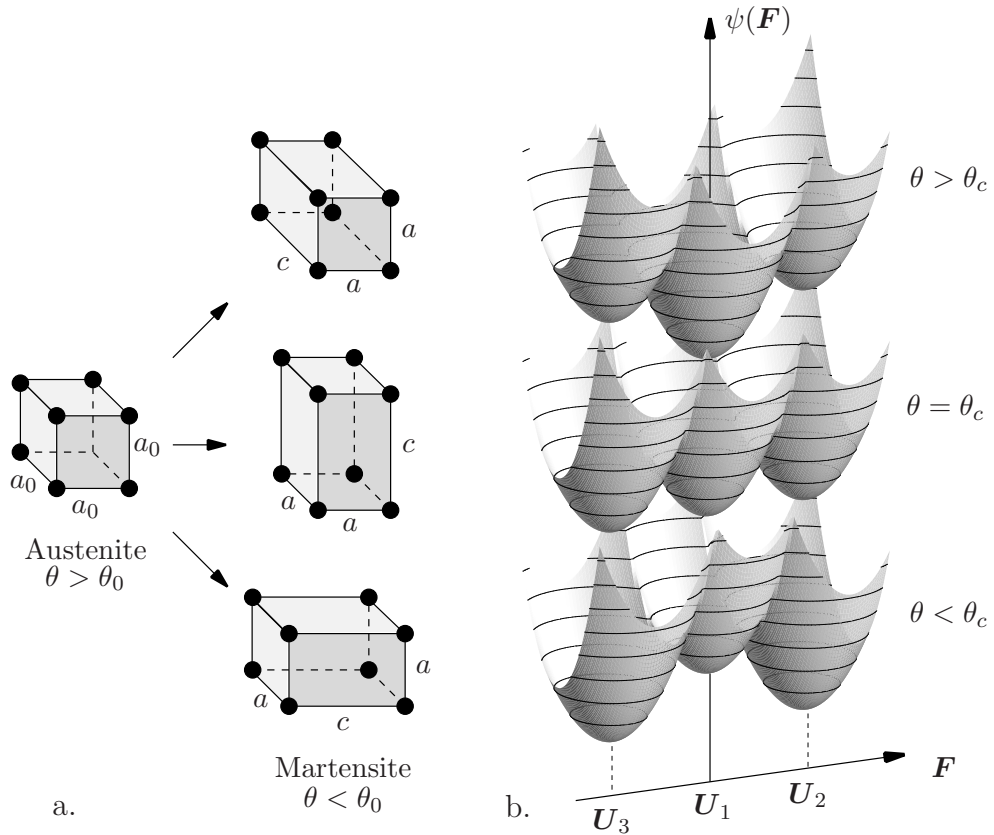


**Figure 4.1:** a.) Austenite and three variants of martensite in a cubic to tetragonal transformation. b.) Schematic representation of the evolution of the energy density with temperature for materials showing martensitic phase transformations.

the corresponding deformation gradient to the austenite phase. In an analogous way a deformation gradient equal to transformation matrix  $\mathbf{U}_i$  with  $i = 1 \dots N$  corresponds to the undeformed  $i^{\text{th}}$  martensite variant. Therefore, the continuum energy storage function fulfills, as shown in Figure 4.1b, the following conditions

$$\begin{aligned} \psi(\mathbf{1}, \theta) &\leq \psi(\mathbf{F}, \theta) && \text{if } \theta > \theta_c \\ \psi(\mathbf{1}, \theta) &= \psi(\mathbf{U}_i, \theta) \leq \psi(\mathbf{F}, \theta) && \text{if } \theta = \theta_c \\ \psi(\mathbf{U}_i, \theta) &\leq \psi(\mathbf{F}, \theta) && \text{if } \theta < \theta_c \end{aligned} \quad (4.3)$$

for  $i = 1 \dots N$  and  $\mathbf{F} \in \mathcal{R}_+^{3 \times 3}$ .

**4.1.2. Energy Wells.** The austenite lattice has greater symmetry than the martensite lattice in most of the martensitic transformations. This leads to the fact that the point group, i.e. the set of rotations that map a lattice back to itself, of the austenite  $\mathcal{P}_A$  includes completely the point group of the martensite  $\mathcal{P}_M$ . Indeed, the number of variants  $N$  are determined by the ratio of number of rotations in  $\mathcal{P}_A$  to that of  $\mathcal{P}_M$ . Since the variants of martensite are symmetry-related, the transformation matrices  $\mathbf{U}_i$  can be obtained from each other by

$$\mathbf{U}_i = \mathbf{R} \mathbf{U}_j \mathbf{R}^T \quad \text{for } \mathbf{R} \in \mathcal{P}_A \subset \mathcal{SO}(3) \quad \text{and } i, j = 1 \dots N \quad (4.4)$$

and all martensite variants have the same energy

$$\psi(\mathbf{U}_i, \theta) = \psi(\mathbf{U}_j, \theta) \quad \text{for } i, j = 1 \dots N. \quad (4.5)$$

Note that the energetic state of the crystal does not change if it is subjected to a rigid rotation, e.g. the austenite lattice stays as the austenite if it undergoes a rotation. Hence, (4.5) can be further generalized as

$$\psi(\mathbf{Q}_i \mathbf{U}_i, \theta) = \psi(\mathbf{Q}_j \mathbf{U}_j, \theta) \quad \text{for } \mathbf{Q}_i, \mathbf{Q}_j \in \mathcal{SO}(3) \quad \text{and } i, j = 1 \dots N. \quad (4.6)$$

In the following, we focus on processes around a close neighborhood of the critical temperature  $\theta_c$  and consequently suppress the temperature dependence from the notation. Without losing generality by adding appropriate constant to  $\psi(\mathbf{F})$  we may assume that the energy density satisfies

$$\psi(\mathbf{F}) = \begin{cases} = 0 & \text{if } \mathbf{F} \in \mathcal{K} \quad \text{or} \quad \mathbf{F} = \mathbf{Q} \mathbf{U}_0 = \mathbf{Q} \mathbf{1} = \mathbf{Q} \\ > 0 & \text{otherwise} \end{cases} \quad (4.7)$$

where the set  $\mathcal{K}$  denotes the energy wells of the martensite and is defined as

$$\mathcal{K} = \bigcup_{i=1}^N \mathcal{SO}(3) \mathbf{U}_i = \mathcal{SO}(3) \mathbf{U}_1 \cup \mathcal{SO}(3) \mathbf{U}_2 \cup \dots \cup \mathcal{SO}(3) \mathbf{U}_N. \quad (4.8)$$

A schematic visualization of martensitic energy wells  $\mathcal{K}$  together with the austenite well is given in Figure 4.2. In what follows we consider piecewise twice differentiable energy storage functions of the form

$$\psi(\mathbf{F}) = \min_{i=0 \dots N} \{\psi_i(\mathbf{F})\} \quad \text{with} \quad \psi_i(\mathbf{F}) = \begin{cases} = 0 & \text{if } \mathbf{F} = \mathbf{Q} \mathbf{U}_i \\ > 0 & \text{otherwise} \end{cases} \quad (4.9)$$

which fulfills the condition (4.7). In (4.9)  $\psi_i$  denotes the energy storage functions corresponding to the  $i^{\text{th}}$  variant of martensite for  $i = 1 \dots N$  and to the austenite for  $i = 0$ . An energy storage function that satisfies (4.9) is clearly not convex. Notice that the energy wells are disjoint, in other words, there exist no rotation such that  $QU_i = U_j$  for  $i, j = 1 \dots N$  and  $i \neq j$ . Furthermore, if there exist a rotation  $Q \in \mathcal{SO}(3)$  and Eulerian and Lagrangian vectors  $\mathbf{m}, \mathbf{N} \in \mathcal{R}^3$  such that

$$QU_i - U_j = \mathbf{m} \otimes \mathbf{N} \iff \text{rank}[QU_i - U_j] = 1 \quad (4.10)$$

then the energy wells  $U_i$  and  $U_j$  are said to be *rank-one connected* or *compatible*. There exist planar interfaces with the Lagrangian normal vector  $\mathbf{N}$  between two variants  $U_i$  and  $U_j$  provided that (4.10) holds. This equality is also known as the *Hadamard's jump condition*. The compatibility of wells has important consequences for the relaxation analysis. In the case of incompatible wells the computation of relaxed potential is generally more cumbersome. Furthermore, the variants with compatible transformation matrices can form different kind of twin microstructures. For a given two variants of martensite having transformation matrices  $U_i$  and  $U_j$  it is possible to determine whether they are compatible or not in the sense of (4.10). The solution procedure is due to BALL & JAMES [14] and also can be found in BHATTACHARYA [22] p.69. For example, it is possible to show that in cubic to tetragonal transformations governed by the transformation matrices (4.2) martensite variants can form twins among them. On the other hand, the austenite phase is incompatible with any of the martensite variants however, it can form a compatible interface with fine layered mixtures of the martensitic phases. The results of this procedure with regard to the prediction of possible microstructure formations coincide very well with the experimental observations, see CHU & JAMES [44] and BHATTACHARYA [22] for further details.

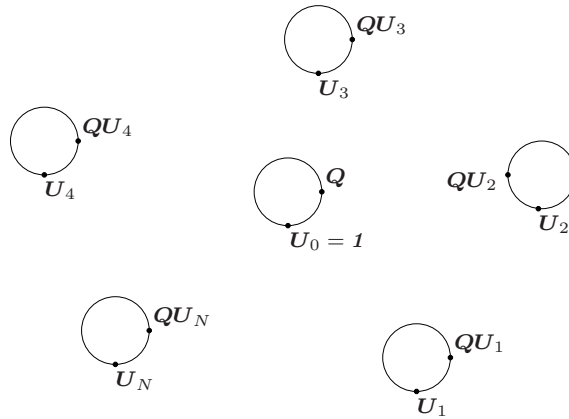


**Figure 4.2:** A schematic visualization of energy wells. In the space of all second order tensors characterized by the plane of the paper energy wells are represented by circles.

**4.1.3. The Geometrically Linear Theory.** The subsequent treatments in this chapter will be based on the geometrically linear theory. Therefore, here the decisive ingredients of the theory that is described so far are modified to the linearized kinematics. In the geometrically linear theory, the positions  $\mathbf{x} \in \mathcal{B}$  of material points are referred to as the current material coordinates. The small-strain deformation at time  $t \in \mathcal{R}_+$  is

governed by the displacement field on  $\mathcal{B}$

$$\mathbf{u}_t : \begin{cases} \mathcal{B} \rightarrow \mathcal{R}^3 \\ \mathbf{x} \mapsto \mathbf{u}_t(\mathbf{x}) \end{cases} . \quad (4.11)$$

We introduce the *displacement gradient*

$$\mathbf{h} = \nabla \mathbf{u}_t(\mathbf{x}) \quad (4.12)$$

where its norm is assumed to be bounded  $\|\mathbf{h}\| < \epsilon$  by a small number  $\epsilon$ . The displacement gradient can be decomposed additively into symmetric (infinitesimal) strain and skew-symmetric rotation tensors

$$\mathbf{h} = \boldsymbol{\varepsilon} + \boldsymbol{\omega} \quad \text{with} \quad \boldsymbol{\varepsilon} = \frac{1}{2}(\mathbf{h} + \mathbf{h}^T) \quad \text{and} \quad \boldsymbol{\omega} = \frac{1}{2}(\mathbf{h} - \mathbf{h}^T) \quad (4.13)$$

which is an approximation of the polar decomposition of the deformation gradient  $\mathbf{F}$  in the geometrically linear theory. The frame indifference with respect to infinitesimal rotations, i.e.  $\psi(\mathbf{h}) = \psi(\mathbf{h} + \boldsymbol{\omega})$  for all skew matrices, induce that the energy storage depends only on the symmetric part  $\boldsymbol{\varepsilon}$  of the displacement gradient  $\mathbf{h}$ . In what follows, we assume that the energy in the neighborhood of the energy wells can be assumed to be quadratic. Therefore, the energy storage is described by a piecewise quadratic function

$$\psi(\boldsymbol{\varepsilon}) = \min_{i=0\dots N} \left\{ \frac{1}{2}(\boldsymbol{\varepsilon} - \boldsymbol{\varepsilon}_i) : \mathbb{C}_i : (\boldsymbol{\varepsilon} - \boldsymbol{\varepsilon}_i) + \eta_i \right\} \quad (4.14)$$

where  $\eta_i$  describes the minimum energy value of the well  $i$  and is often referred to as the chemical energy.  $\mathbb{C}_i$  and  $\boldsymbol{\varepsilon}_i$  stand for the elastic moduli and the transformation strain of the variant  $i$ , respectively. Transformation strains in the geometrically linear theory are related those of large strain theory by  $\boldsymbol{\varepsilon}_i = \mathbf{U}_i - \mathbf{1}$  provided that  $\mathbf{U}_i$  is symmetric.

The compatibility condition for energy wells given in (4.10) reads in the geometrically linear theory as

$$\mathbf{h}_i - \mathbf{h}_j = \mathbf{m} \otimes \mathbf{n} \quad (4.15)$$

in terms of the displacement gradients  $\mathbf{h}_i$  and  $\mathbf{h}_j$  corresponding to the variants  $i$  and  $j$ . Contrary to the finite strain case (4.10), here we do not make any differentiation for the vectors  $\mathbf{m}, \mathbf{n} \in \mathcal{R}^3$  with respect to the configuration they belong to. The compatibility condition (4.15) can be written also in terms of the linearized strain tensors

$$\boldsymbol{\varepsilon}_i - \boldsymbol{\varepsilon}_j = \frac{1}{2}(\mathbf{m} \otimes \mathbf{n} + \mathbf{n} \otimes \mathbf{m}) . \quad (4.16)$$

We consider in the following discussions (4.16) as the necessary condition for energy wells to be compatible.

**4.1.4. Relaxation of Two-Well Potentials.** In the sequel, the relaxation of an energy storage function with two energy wells is discussed. A closed form expression of the quasiconvex envelope (relaxed energy) for the double-well energy is available and derived independently by KOHN [116] based on the Fourier analysis, and by PIPKIN [184] based on the so called translation method. The energy storage function has the piecewise quadratic form

$$\psi(\boldsymbol{\varepsilon}) = \min_{i=1\dots 2} \left\{ \frac{1}{2}(\boldsymbol{\varepsilon} - \boldsymbol{\varepsilon}_i) : \mathbb{C} : (\boldsymbol{\varepsilon} - \boldsymbol{\varepsilon}_i) + \eta_i \right\} \quad (4.17)$$

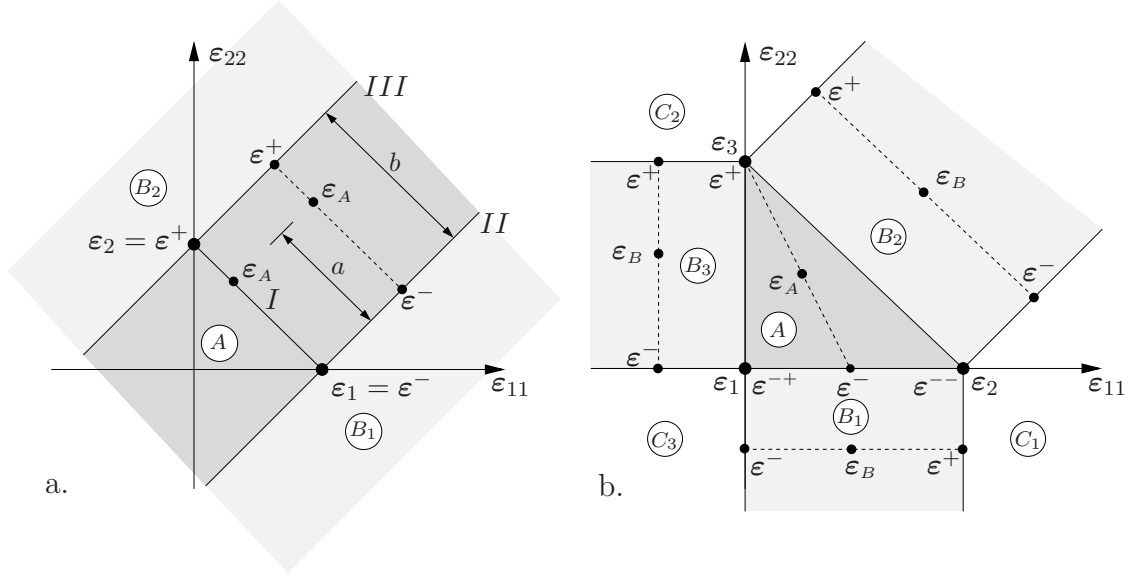


**Figure 4.3:** Schematic representation of energy wells the in  $\varepsilon_{11}$ - $\varepsilon_{22}$  plane and the decomposition of two homogeneous strains  $\varepsilon_A$  and  $\varepsilon_B$  into phases for a.) the double-well and b.) the three-well energies.

which is a simplification of (4.14) by assuming identical moduli ( $\mathbb{C}_1 = \mathbb{C}_2$ ) for both variants. The contour plot of the energy storage in  $\varepsilon_{11} - \varepsilon_{22}$  plane is given in Figure 4.4. The quasiconvex envelope of (4.17) for arbitrary wells, not necessarily compatible, reads

$$\psi_Q(\varepsilon) = \begin{cases} \psi_1(\varepsilon) & \text{if } \psi_2(\varepsilon) - \psi_1(\varepsilon) \geq \gamma/2 \\ \psi_2(\varepsilon) - \frac{[\psi_2(\varepsilon) - \psi_1(\varepsilon) + \gamma/2]^2}{2\gamma} & \text{if } |\psi_2(\varepsilon) - \psi_1(\varepsilon)| < \gamma/2 \\ \psi_2(\varepsilon) & \text{if } \psi_1(\varepsilon) - \psi_2(\varepsilon) \geq \gamma/2 \end{cases} \quad (4.18)$$

where  $\gamma$  is defined as

$$\gamma = \max_{|\mathbf{a}|=|\mathbf{b}|=1} \frac{[(\mathbf{a} \otimes \mathbf{b} + \mathbf{b} \otimes \mathbf{a}) : \mathbb{C} : (\varepsilon_1 - \varepsilon_2)]^2}{(\mathbf{a} \otimes \mathbf{b} + \mathbf{b} \otimes \mathbf{a}) : \mathbb{C} : (\mathbf{a} \otimes \mathbf{b} + \mathbf{b} \otimes \mathbf{a})}. \quad (4.19)$$

In the case of compatible wells satisfying (4.16),  $\gamma$  is simplified to

$$\gamma = (\varepsilon_1 - \varepsilon_2) : \mathbb{C} : (\varepsilon_1 - \varepsilon_2). \quad (4.20)$$

As already mentioned before, the compatibility of the wells has important consequences. In the case of rank-one connected wells, the relaxed energy is convex and the line joining the wells is flat. On the other hand, incompatible wells lead to a non-convex relaxed energy that exhibits a hump between  $\varepsilon_1$  and  $\varepsilon_2$  size of which depends on the amount of incompatibility, see BHATTACHARYA [22] p.219.

In the examples below we consider the following rank-one connected energy wells

$$\varepsilon_1 = \begin{bmatrix} \alpha & 0 & 0 \\ 0 & 0 & 0 \\ 0 & 0 & 0 \end{bmatrix} \quad \text{and} \quad \varepsilon_2 = \begin{bmatrix} 0 & 0 & 0 \\ 0 & \alpha & 0 \\ 0 & 0 & 0 \end{bmatrix} \quad (4.21)$$

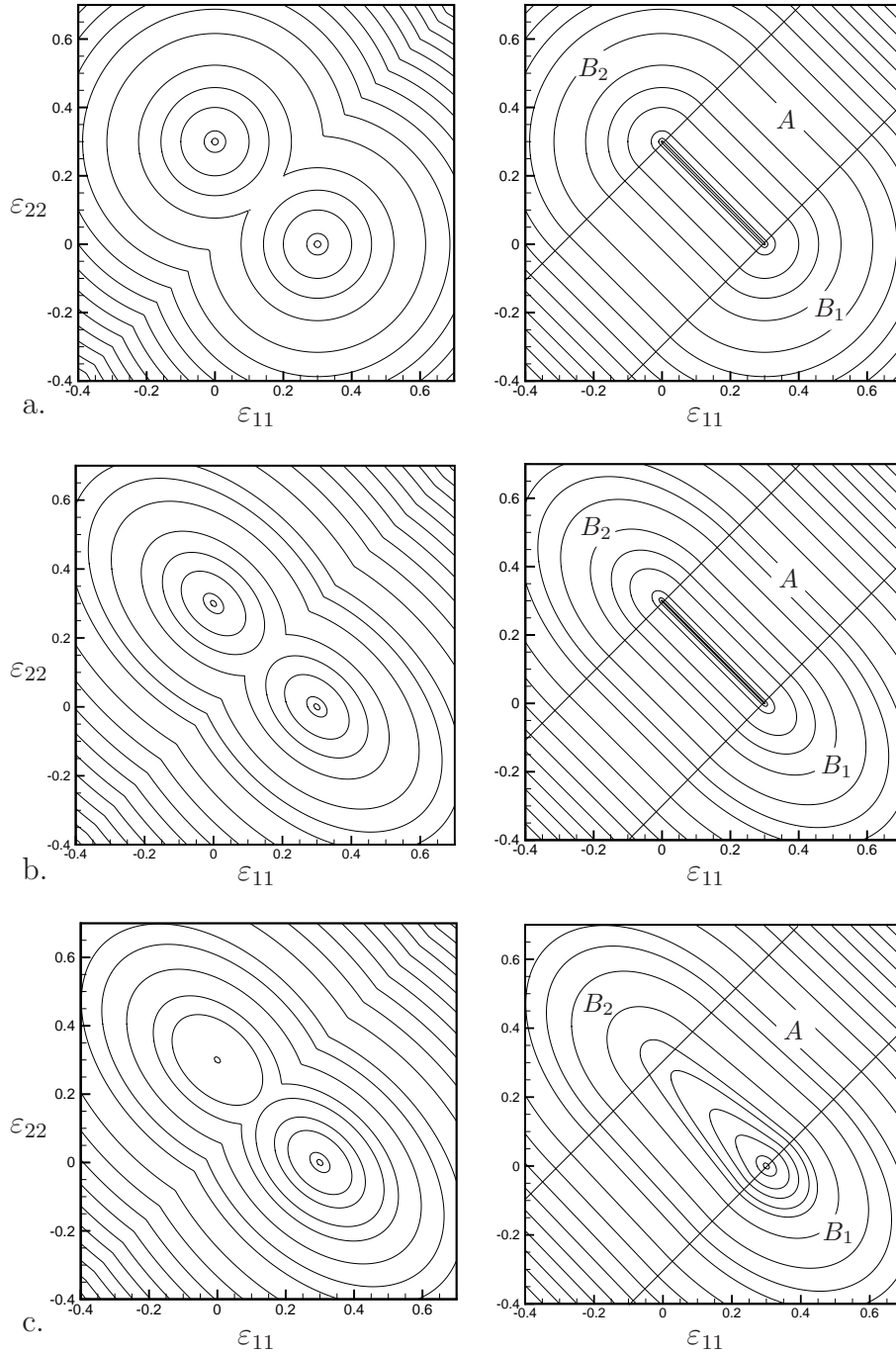


**Figure 4.4:** Double-well potential and its relaxation for various cases. Contours describe the energy levels. Two columns denote the unrelaxed and relaxed energies for a.) the moduli  $\mathbb{C} = \mathbb{I}$  and  $\eta_1 = \eta_2 = 0$ , b.) the moduli  $\mathbb{C} = \kappa \mathbf{1} \otimes \mathbf{1} + 2\mu \mathbb{P}$  and  $\eta_1 = \eta_2 = 0$ , c.) the moduli  $\mathbb{C} = \kappa \mathbf{1} \otimes \mathbf{1} + 2\mu \mathbb{P}$  and  $\eta_1 = 0$ ,  $\eta_2 > 0$ .

and study the effects of the moduli  $\mathbb{C}$  and the minimum energy values  $\eta_i$  on the relaxation of the energy (4.17), see Figure 4.4a for an illustration with  $\alpha = 0.3$  in the  $\varepsilon_{11} - \varepsilon_{22}$  plane. The minimization problem

$$\psi_R(\varepsilon) = \min_{\xi, \varepsilon^+, \varepsilon^-} \{ \xi \psi(\varepsilon^+) + (1 - \xi) \psi(\varepsilon^-) \} \text{ with } \begin{cases} \varepsilon^+ - \varepsilon^- = \frac{1}{2}(\mathbf{m} \otimes \mathbf{n} + \mathbf{n} \otimes \mathbf{m}) \\ \varepsilon = \xi \varepsilon^+ + (1 - \xi) \varepsilon^- \end{cases} \quad (4.22)$$



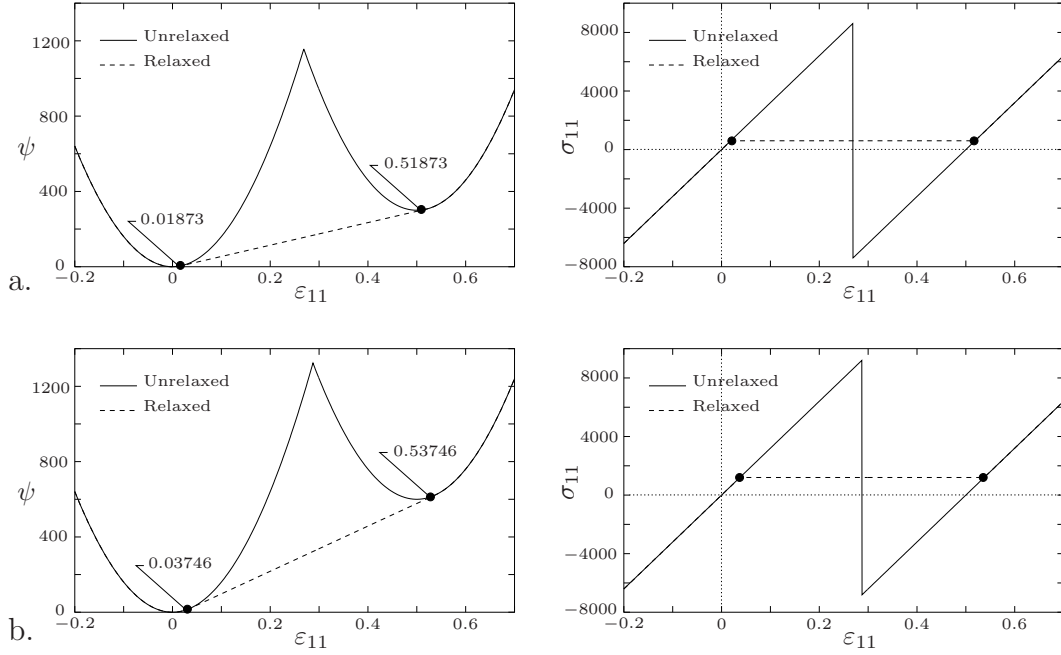


**Figure 4.5:** Unrelaxed and relaxed potential and stress for  $\boldsymbol{\varepsilon}_1 = \text{diag}[0.5 \ 0 \ 0]$  and  $\boldsymbol{\varepsilon}_2 = \mathbf{0}$  with a.)  $\eta_1 = 0$  and  $\eta_2 = 300$  MPa and b.)  $\eta_1 = 0$  and  $\eta_2 = 600$  MPa. Note that for both cases  $\varepsilon_{11}^+ - \varepsilon_{11}^-$  remains the same and the differences  $\boldsymbol{\varepsilon}^+ - \boldsymbol{\varepsilon}_2$  and  $\boldsymbol{\varepsilon}^- - \boldsymbol{\varepsilon}_1$  are proportional to  $\eta_2 - \eta_1$ .

for  $\xi \in [0, 1]$  and  $\boldsymbol{m}, \boldsymbol{n} \in \mathcal{R}^3$  yields the rank-one convexification of  $\psi(\boldsymbol{\varepsilon})$  defined in (4.17). Here,  $\boldsymbol{\varepsilon}^+$  and  $\boldsymbol{\varepsilon}^-$  denote the strain states in the phases (+) and (-), and  $\xi$  is the volume fraction of the phase (+). Owing to the specific choice of the wells (4.21), the minimization problem becomes two-dimensional. In this simplified two-dimensional double-well energy the rank-one convex envelope (4.22) can be computed numerically. As a result of the experience acquired by conducting numerical studies, the rank-one convexified potential is constructed as follows.

In the first case we assume that the elastic moduli are the fourth order identity tensors, i.e.  $\mathbb{C} = \mathbb{I}$  and  $(\boldsymbol{\varepsilon} - \boldsymbol{\varepsilon}_i) : \mathbb{C} : (\boldsymbol{\varepsilon} - \boldsymbol{\varepsilon}_i) = \|\boldsymbol{\varepsilon} - \boldsymbol{\varepsilon}_i\|^2$  for both variants, and  $\eta_1 = \eta_2 = 0$  in (4.17). Note that in the following discussions only  $\varepsilon_{11}$  and  $\varepsilon_{22}$  components of the strain are taken into account since the other components have no influence on the relaxation algorithm. In other words, the decomposition of homogeneous deformation takes place exclusively for those two components without effecting the rest of the strain tensor. The wells  $\boldsymbol{\varepsilon}_1$  and  $\boldsymbol{\varepsilon}_2$  are connected in the  $\varepsilon_{11} - \varepsilon_{22}$  plane by a line denoted as  $I$ , see Figure 4.3a. Two lines  $II$  and  $III$  which are perpendicular to  $I$  and pass through  $\boldsymbol{\varepsilon}_1$  and  $\boldsymbol{\varepsilon}_2$  are drawn. The lines  $II$  and  $III$  divide the  $\varepsilon_{11} - \varepsilon_{22}$  plane into three unbounded regions  $A, B_1$  and  $B_2$  as shown in Figure 4.3a. If a given strain tensor  $\boldsymbol{\varepsilon}_A$  (more precisely the point defined by 11 and 22 components of  $\boldsymbol{\varepsilon}_A$ ) lies on the line  $I$  then  $\boldsymbol{\varepsilon}^-$  and  $\boldsymbol{\varepsilon}^+$  defined in (4.22) coincide with the wells  $\boldsymbol{\varepsilon}_1$  and  $\boldsymbol{\varepsilon}_2$ . Then the phase fraction  $\xi$  is computed by the ratio of corresponding distances from the wells, i.e.

$$\xi = \frac{|\boldsymbol{\varepsilon}_A - \boldsymbol{\varepsilon}^-|}{|\boldsymbol{\varepsilon}^+ - \boldsymbol{\varepsilon}^-|},$$

see Figure 4.3a. Any other strain state  $\boldsymbol{\varepsilon}_A$  in the region  $A$  (not on the line  $I$ ) splits in a similar way, however  $\boldsymbol{\varepsilon}^+$  and  $\boldsymbol{\varepsilon}^-$  are not equal to  $\boldsymbol{\varepsilon}_1$  and  $\boldsymbol{\varepsilon}_2$  anymore. The line joining  $\boldsymbol{\varepsilon}^+$



**Table 4.1:** The  $\varepsilon_{11}$  component of the phases for different material parameters

$\eta_2$ [MPa]	$\varepsilon_{11}^+$	$\varepsilon_{11}^-$	$\varepsilon_{11}^+ - \varepsilon_{11}^-$
300	0.01873	0.518726	0.5
600	0.03746	0.537453	0.5

and  $\varepsilon^-$  is parallel to  $I$  and furthermore  $\varepsilon^+$  and  $\varepsilon^-$  lie on  $II$  and  $III$ , respectively. In the regions  $B_1$  and  $B_2$  the relaxed potential is equal to the original one and the homogeneous strain  $\varepsilon$  does not decompose into the phases. More precisely, in  $B_1$  and  $B_2$  the material is in the phase governed by  $\varepsilon_1$  and  $\varepsilon_2$ , respectively. The contour plots of the original and the relaxed energies are given in Figure 4.4a. Since the transformation strains are compatible the relaxed energy is convex and zero along the line  $I$  that connects the wells.

The second case corresponds to the isotropic linear elastic moduli  $\mathbb{C} = \kappa \mathbf{1} \otimes \mathbf{1} + 2\mu \mathbb{P}$  and  $\eta_1 = \eta_2 = 0$  with the material parameters bulk modulus  $\kappa = 17800$ MPa and the shear modulus  $\mu = 10680$ MPa. The main difference to the previous case is that the contours of the unrelaxed energy become elliptical instead of being circular. Figure 4.4b shows the the original and relaxed energy plots where the relaxed energy is still zero along the line connecting the wells.

In the last case, in addition to the isotropic linear elastic moduli, we modified the minimum value of one of the wells, i.e.  $\eta_1 = 0$  and  $\eta_2 > 0$ . The major difference to the former examples is the change of the lines  $II$  and  $III$ . These lines do not pass through the wells  $\varepsilon_1$  and  $\varepsilon_2$  anymore. In other words,  $\varepsilon^-$  and  $\varepsilon^+$  do not coincide with  $\varepsilon_1$  and  $\varepsilon_2$  even for a strain state on the line  $I$ . Indeed the lines  $II$  and  $III$  move same amount towards the well with higher energy. In Figure 4.5 the potential and the stress are plotted along  $\varepsilon_{11}$ -axis for  $\varepsilon_{22} = 0$  where the wells are chosen as  $\varepsilon_1 = \text{diag}[0.5 \ 0 \ 0]$  and  $\varepsilon_2 = \mathbf{0}$ . The values of  $\varepsilon^+$  and  $\varepsilon^-$  obtained from the minimization problem (4.22) are provided in Table 4.1. Note that the amount of the movement from the wells is proportional to the difference between  $\eta_1$  and  $\eta_2$ , but it is the same for both phases, i.e.  $\varepsilon_{11}^+ - \varepsilon_{11}^-$  is constant.

**4.1.5. Relaxation of Three-Well Potentials.** The energy storage function has the piecewise quadratic form

$$\psi(\varepsilon) = \min_{i=0..2} \left\{ \frac{1}{2} (\varepsilon - \varepsilon_i) : \mathbb{C} : (\varepsilon - \varepsilon_i) + \eta_i \right\} \quad (4.25)$$

where  $\varepsilon_0$ ,  $\varepsilon_1$  and  $\varepsilon_2$  are assumed to be the undeformed austenite and two stress free martensite variants. We consider the following transformation strains

$$\varepsilon_0 = \begin{bmatrix} 0 & 0 & 0 \\ 0 & 0 & 0 \\ 0 & 0 & 0 \end{bmatrix}, \quad \varepsilon_1 = \begin{bmatrix} \alpha & 0 & 0 \\ 0 & 0 & 0 \\ 0 & 0 & 0 \end{bmatrix} \quad \text{and} \quad \varepsilon_2 = \begin{bmatrix} 0 & 0 & 0 \\ 0 & \alpha & 0 \\ 0 & 0 & 0 \end{bmatrix} \quad (4.26)$$

and study, similar to double-well problem, the effects of  $\mathbb{C}$  and  $\eta_i$  on the relaxation of the energy (4.25), see Figure 4.6a for a particular illustration with  $\alpha = 0.3$  in the  $\varepsilon_{11} - \varepsilon_{22}$  plane. Note that the wells (4.26) are pair-wise compatible.

For the three-well problem considered (with compatible wells), the rank-one convex

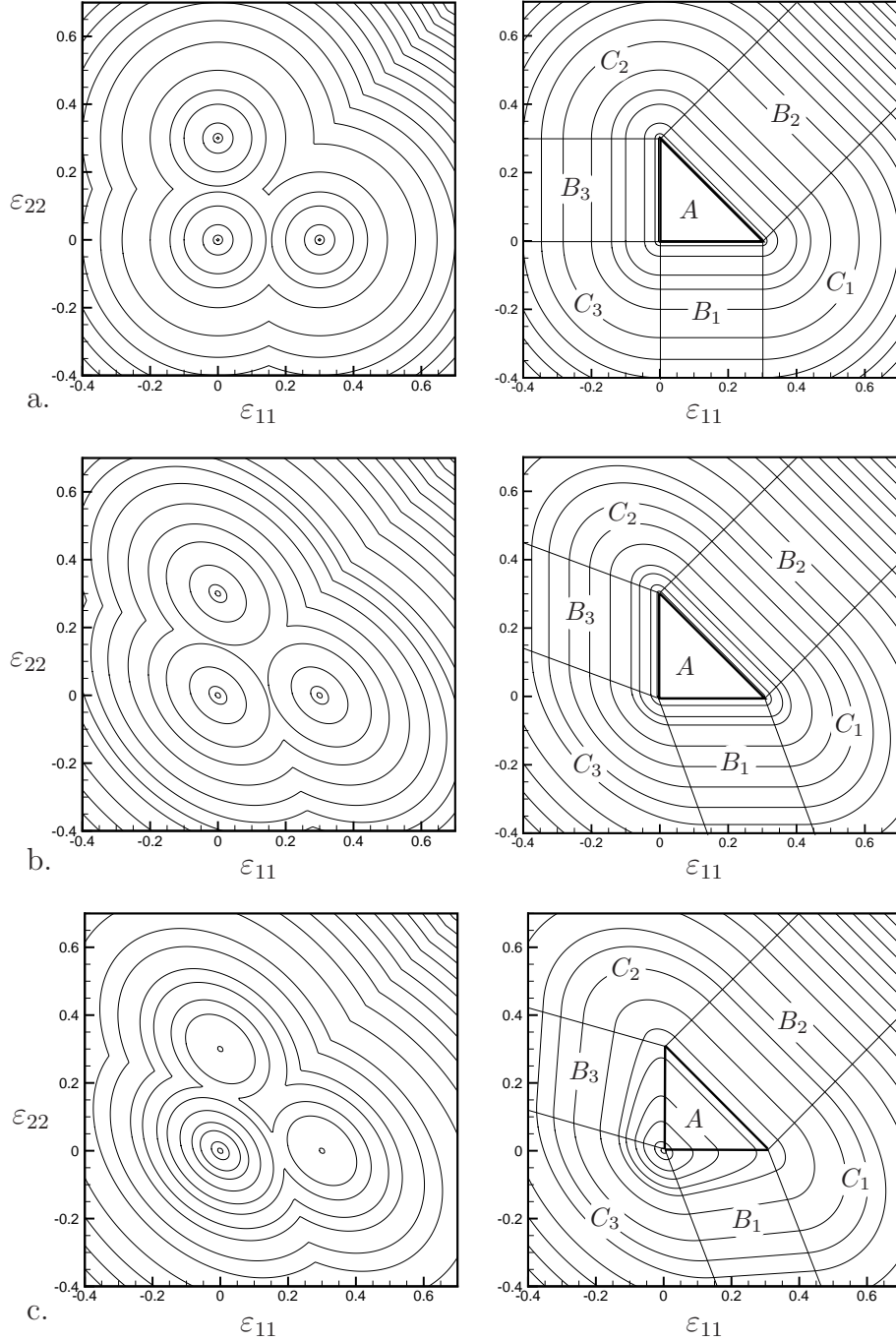


**Figure 4.6:** Three-well potential and its relaxation for various cases. Contours describe the energy levels. Two columns denote the unrelaxed and relaxed energies for a.) the moduli  $\mathbb{C} = \mathbb{I}$  and  $\eta_1 = \eta_2 = \eta_3 = 0$ , b.) the moduli  $\mathbb{C} = \kappa \mathbf{1} \otimes \mathbf{1} + 2\mu \mathbb{P}$  and  $\eta_1 = \eta_2 = \eta_3 = 0$ , c.) the moduli  $\mathbb{C} = \kappa \mathbf{1} \otimes \mathbf{1} + 2\mu \mathbb{P}$  and  $\eta_1 = 0$ ,  $\eta_2 = \eta_3 > 0$ .

envelope  $\psi_R$  is computed based on a second-order lamination, i.e.

$$\psi_R(\boldsymbol{\varepsilon}) = \min_{\xi, \lambda, \boldsymbol{\varepsilon}^+, \boldsymbol{\varepsilon}^{--}, \boldsymbol{\varepsilon}^{+-}} \left\{ \xi \psi(\boldsymbol{\varepsilon}^+) + (1 - \xi) [\lambda \psi(\boldsymbol{\varepsilon}^{--}) + (1 - \lambda) \psi(\boldsymbol{\varepsilon}^{+-})] \right\}$$

$$\text{with } \begin{cases} \boldsymbol{\varepsilon} = \xi \boldsymbol{\varepsilon}^+ + (1 - \xi) \boldsymbol{\varepsilon}^- & \text{and } \boldsymbol{\varepsilon}^+ - \boldsymbol{\varepsilon}^- = \frac{1}{2} (\mathbf{m}_1 \otimes \mathbf{n}_1 + \mathbf{n}_1 \otimes \mathbf{m}_1) \\ \boldsymbol{\varepsilon}^- = \lambda \boldsymbol{\varepsilon}^{--} + (1 - \lambda) \boldsymbol{\varepsilon}^{+-} & \text{and } \boldsymbol{\varepsilon}^{+-} - \boldsymbol{\varepsilon}^{--} = \frac{1}{2} (\mathbf{m}_2 \otimes \mathbf{n}_2 + \mathbf{n}_2 \otimes \mathbf{m}_2) \end{cases} \quad (4.27)$$

for  $\xi, \lambda \in [0, 1]$  and  $\mathbf{m}_1, \mathbf{n}_1, \mathbf{m}_2, \mathbf{n}_2 \in \mathcal{R}^3$ . The choices of the wells (4.26) lead to a minimization problem that is essentially two-dimensional and can be represented in the  $\varepsilon_{11}$ - $\varepsilon_{22}$  plane. In this simplified case the rank-one convex envelope (4.27) can be computed numerically.

Note that in the following, similar to the previous double-well study, only  $\varepsilon_{11}$  and  $\varepsilon_{22}$  components of the strain are taken into consideration as the other components have no influence on the relaxation algorithm. We connect the three wells and construct a triangle, see Figure 4.3b. In addition, two parallel lines are plotted from each pair of wells similar to *I* and *II* in Figure 4.3a. Consequently, we obtain the bounded region *A* and unbounded regions  $B_i$  and  $C_i$  for  $i = 1 \dots 3$ . A given strain state  $\boldsymbol{\varepsilon}_A$  (more precisely the point defined by 11 and 22 components of  $\boldsymbol{\varepsilon}_A$ ) located in *A* leads to the second-order laminates during energy minimization.  $\boldsymbol{\varepsilon}_A$  splits first into  $\boldsymbol{\varepsilon}^-$  and  $\boldsymbol{\varepsilon}^+$ , and  $\boldsymbol{\varepsilon}^-$  decomposes further into  $\boldsymbol{\varepsilon}^{--}$  and  $\boldsymbol{\varepsilon}^{-+}$ , i.e.

$$\boldsymbol{\varepsilon}_A = \xi \boldsymbol{\varepsilon}^+ + (1 - \xi) \boldsymbol{\varepsilon}^- \quad \text{with} \quad \boldsymbol{\varepsilon}^- = \lambda \boldsymbol{\varepsilon}^{-+} + (1 - \lambda) \boldsymbol{\varepsilon}^{--} \quad (4.28)$$

see Figure 4.3b. Considering only  $\varepsilon_{11}$  and  $\varepsilon_{22}$  components of the strain tensor, the volume fractions  $\xi$  and  $\lambda$  are computed by

$$\xi = \frac{|\boldsymbol{\varepsilon}_A - \boldsymbol{\varepsilon}^-|}{|\boldsymbol{\varepsilon}^+ - \boldsymbol{\varepsilon}^-|} \quad \text{and} \quad \lambda = \frac{|\boldsymbol{\varepsilon}^{--} - \boldsymbol{\varepsilon}^-|}{|\boldsymbol{\varepsilon}^{--} - \boldsymbol{\varepsilon}^{-+}|}. \quad (4.29)$$

The regions  $B_1$ ,  $B_2$  and  $B_3$  correspond to double-well problems with wells  $\boldsymbol{\varepsilon}_1$ - $\boldsymbol{\varepsilon}_2$ ,  $\boldsymbol{\varepsilon}_2$ - $\boldsymbol{\varepsilon}_3$  and  $\boldsymbol{\varepsilon}_1$ - $\boldsymbol{\varepsilon}_3$ , respectively. The relaxation in these cases is performed analogous to Section 4.1.4. In the regions  $C_i$  the relaxed potential is equal to the original one and the homogeneous strain does not decompose into phases.

In Figure 4.6a the contour plots of the original and the relaxed potentials are plotted for  $\eta_1 = \eta_2 = \eta_3 = 0$  and  $\mathbb{C} = \mathbb{I}$ . Inside the triangle formed by  $\boldsymbol{\varepsilon}_1$ ,  $\boldsymbol{\varepsilon}_2$  and  $\boldsymbol{\varepsilon}_3$  the energy is relaxed to zero and the phases  $\boldsymbol{\varepsilon}^+$ ,  $\boldsymbol{\varepsilon}^{--}$  and  $\boldsymbol{\varepsilon}^{-+}$  coincide with the transformation strains  $\boldsymbol{\varepsilon}_1$ ,  $\boldsymbol{\varepsilon}_2$  and  $\boldsymbol{\varepsilon}_3$ . The results for  $\eta_1 = \eta_2 = \eta_3 = 0$  and  $\mathbb{C} = \kappa \mathbf{1} \otimes \mathbf{1} + 2\mu \mathbb{P}$  are shown in Figure 4.6b. There is no difference to the previous case with respect to the second-order lamination inside the triangular zone. However, double-well relaxation zones  $B_1$  and  $B_3$  are not the same as the former ones, i.e. the lines bounding them have different slopes which can be computed numerically. The last case shown in Figure 4.6c is  $\eta_1 = 0$ ,  $\eta_2 = \eta_3 > 0$  and  $\mathbb{C} = \kappa \mathbf{1} \otimes \mathbf{1} + 2\mu \mathbb{P}$ . The increase in minimum values  $\eta_2$  and  $\eta_3$  causes a rigid movement of the triangle both in the  $+\varepsilon_{11}$  and  $+\varepsilon_{22}$  directions. The amount of the movement is proportional to the differences  $\eta_2 - \eta_1$  and  $\eta_3 - \eta_1$  similar to the double-well problem. Although there are second-order laminates in the region *A* the relaxed energy is no more zero, see Figure 4.6c.

## 4.2. Numerical Examples of Relaxation in Phase Transformations

**4.2.1. Simple Tension Test.** We consider the double-well problem (4.17) for the case  $\mathbb{C} = \mathbb{I}$  and  $\eta_1 = \eta_2 = 0$ . Therein, the potential energy is simplified as follows

$$\psi(\boldsymbol{\varepsilon}) = \frac{1}{2} \|(\boldsymbol{\varepsilon} - \boldsymbol{\varepsilon}_i)\|^2 \quad \text{for} \quad i = 1, 2 \quad (4.30)$$

where the wells are selected such as

$$\boldsymbol{\varepsilon}_1 = \begin{bmatrix} 0.3 & 0 & 0 \\ 0 & 0.1 & 0 \\ 0 & 0 & 0 \end{bmatrix} \quad \text{and} \quad \boldsymbol{\varepsilon}_2 = \begin{bmatrix} 0 & 0 & 0 \\ 0 & 0.4 & 0 \\ 0 & 0 & 0 \end{bmatrix}. \quad (4.31)$$

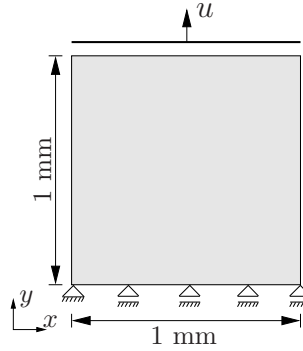


**Figure 4.7:** Simple tension test. Geometry, loading and boundary conditions.

A square specimen of length 1mm is chosen for the simulations. The specimen is subjected to a displacement controlled tensile loading with constant increments  $\Delta u = 0.025\text{mm}$  in  $y$  direction, see Figure 4.7 for the geometry and loading conditions. At the first time step, the structure stretches suddenly to the right such that  $\varepsilon_{11} = 0.3$  while the left-lower node is fixed in  $x$  direction. This holds for both the relaxed and unrelaxed formulations. The unrelaxed model, after an initial horizontal stretching, continues to elongate in  $y$  direction while the strain  $\varepsilon_{11}$  remains constant. It lasts until the prescribed displacement reaches  $u = 0.4\text{mm}$ . After this displacement level, the second well starts to govern the response. Consequently, the strain component  $\varepsilon_{11}$  in the specimen tries to vanish immediately. This leads to distortions depending on the mesh size as seen in Figure 4.8a. Employment of finer meshes causes more frequent fine scale distortions. However, when the relaxed energy is utilized the strain component  $\varepsilon_{11}$  decreases smoothly at every time increment.

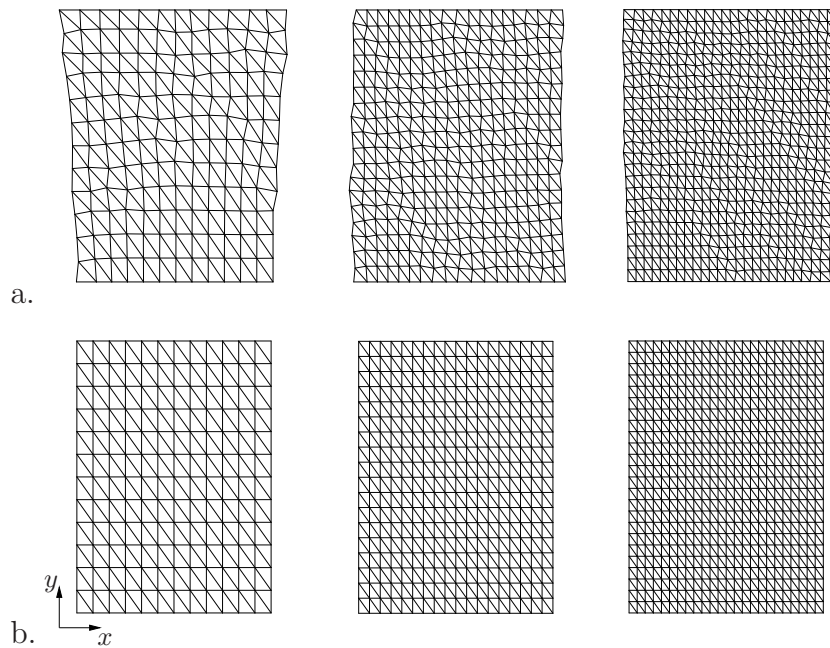


**Figure 4.8:** Simple tension test. Three deformed meshes, 12x12, 18x18 and 24x24, during transformation obtained by a.) the unrelaxed and b.) the relaxed formulation. All the meshes correspond to the prescribed displacement  $u = 0.5\text{mm}$ .

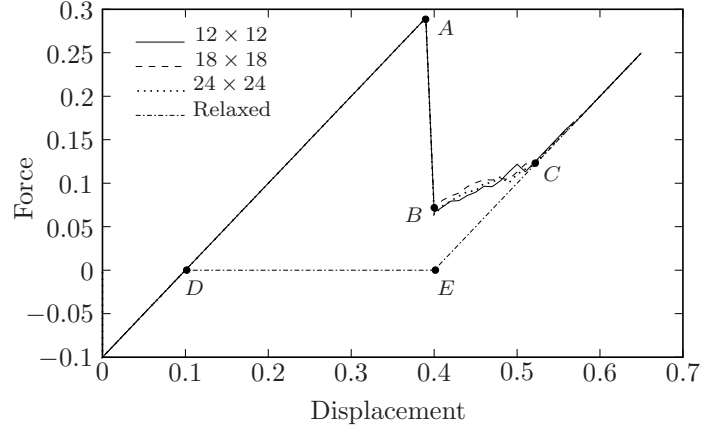


**Figure 4.9:** The load displacement curves computed by the unrelaxed and relaxed formulations. Three different meshes  $12 \times 12$ ,  $18 \times 18$  and  $24 \times 24$  are used for computations. Note that relaxed curves are identical for all the meshes.

Thus, the phase transformation occurs in a smooth manner without distortions in finite elements, see Figure 4.8b. In Figure 4.9, the load deflection curves of unrelaxed and relaxed material response are visualized for various mesh densities. The sudden change in the strain causes also a sudden decrease in the load from the point  $A$  to  $B$  in the load displacement curves. Note that the curves exhibit different oscillations for three meshes between the points  $B$  and  $C$  in Figure 4.9. On the other hand, the load deflection curves are identical for the relaxed formulation.

**4.2.2. Microstructure Development in a Homogeneous Test.** In this example the main aim is to visualize the development of microstructures for a strain driven loading parameterized as

$$\boldsymbol{\varepsilon}(t) = \begin{bmatrix} \alpha(t) & \gamma(t) & 0 \\ \gamma(t) & \beta(t) & 0 \\ 0 & 0 & 0 \end{bmatrix}. \quad (4.32)$$

Three different load paths are considered, (i)  $\alpha(t) = \beta(t) = \gamma(t) = t$ , (ii)  $\alpha(t) = 2\beta(t) = \gamma(t) = t$  and (iii)  $2\alpha(t) = \beta(t) = \gamma(t) = t$ . Note that the component  $\varepsilon_{12} = \gamma(t)$  has no influence on the relaxation algorithm. We assume that the energy storage is governed by the three-well energy function (4.25) with following transformation strains

$$\boldsymbol{\varepsilon}_0 = \begin{bmatrix} 0 & 0 & 0 \\ 0 & 0 & 0 \\ 0 & 0 & 0 \end{bmatrix}, \quad \boldsymbol{\varepsilon}_1 = \begin{bmatrix} 0 & 0 & 0 \\ 0 & 0.05 & 0 \\ 0 & 0 & 0 \end{bmatrix} \quad \text{and} \quad \boldsymbol{\varepsilon}_2 = \begin{bmatrix} 0.05 & 0 & 0 \\ 0 & 0 & 0 \\ 0 & 0 & 0 \end{bmatrix} \quad (4.33)$$

where  $\boldsymbol{\varepsilon}_0$  denotes the undeformed austenite phase and  $\boldsymbol{\varepsilon}_1$  and  $\boldsymbol{\varepsilon}_2$  are the stress free martensite variants. The material parameters are  $\eta_0 = 0$  and  $\eta_1 = \eta_2 = 7\text{MPa}$ . The linear isotropic elastic modulus is used with  $\kappa = 17800\text{MPa}$  and  $\mu = 10680\text{MPa}$ . In the current problem,  $\boldsymbol{\varepsilon}_0$  is compatible  $\boldsymbol{\varepsilon}_1$  and  $\boldsymbol{\varepsilon}_2$  whereas  $\boldsymbol{\varepsilon}_1$  and  $\boldsymbol{\varepsilon}_2$  are not compatible with each other. However, a mixture of  $\boldsymbol{\varepsilon}_0$  and  $\boldsymbol{\varepsilon}_1$  is rank-one connected with  $\boldsymbol{\varepsilon}_2$ .

The microstructure evolution is shown in Figure 4.10 where the initial state consists of only the phase  $\boldsymbol{\varepsilon}_0$ . In these illustrations the interfaces between different phases which are governed by the laminate normal vectors  $\mathbf{n}_1$  and  $\mathbf{n}_2$  are plotted. Each phase is denoted by a color (white, blue and yellow) and the volume fractions are characterized by the

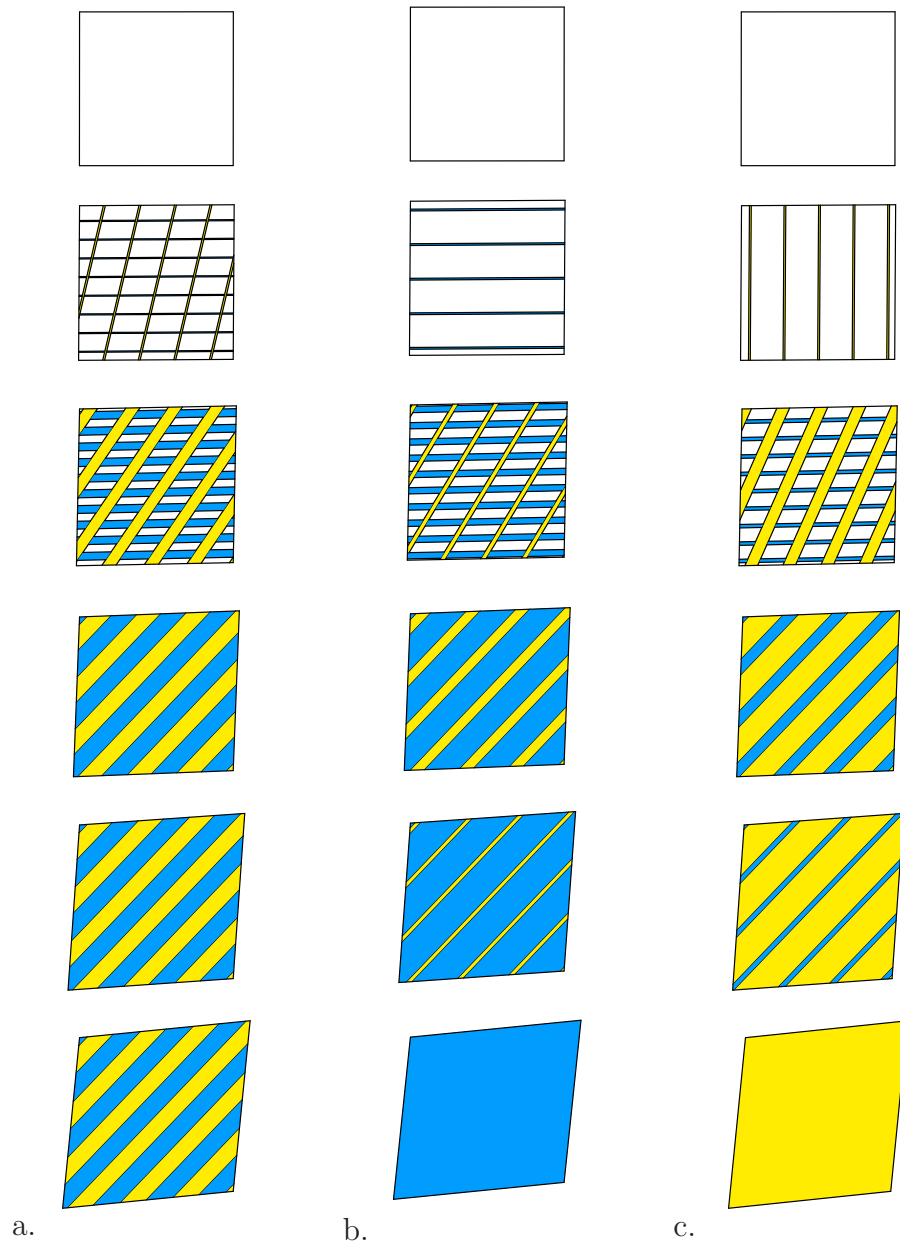


**Figure 4.10:** Microstructure evolution for different loading paths. White yellow and blue colors denote the phases  $\varepsilon_0$ ,  $\varepsilon_1$  and  $\varepsilon_2$ , respectively. Loading levels are  $t = 0.001, 0.006, 0.02, 0.04, 0.075, 0.11$  for loading paths a.)  $\varepsilon_{11} = \varepsilon_{22}$  b.)  $\varepsilon_{11} = 2\varepsilon_{22}$  and c.)  $2\varepsilon_{11} = \varepsilon_{22}$ .

associated thicknesses. Having computed the phases, the laminate vectors are determined from (4.27) which normally yields a pair of solution. We randomly choose one of these solutions for the visualization purposes.

Following the first loading path, the material transforms from the homogeneous state of  $\varepsilon_0$  into the second-order laminate mixture of  $\varepsilon_0$ ,  $\varepsilon_1$  and  $\varepsilon_2$ , contrary to the microstructures of the other two loading paths begin which first exhibit first-order laminates. This is due to fact that the loading case  $\varepsilon_{11} = \varepsilon_{22}$  enters directly the three-well triangle not through a two-well relaxation zone, see Figure 4.3b. On the other hand, other loading paths pass

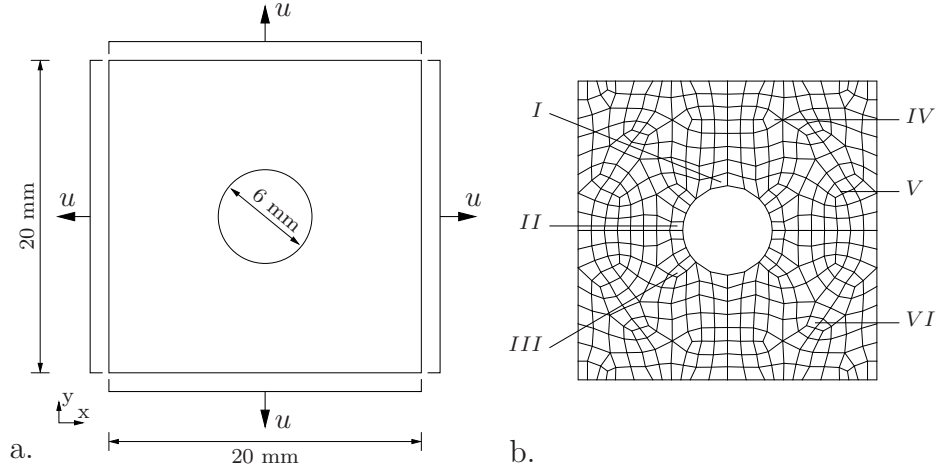


**Figure 4.11:** Biaxial tension of a perforated plate. a.) Geometry, loading and boundary conditions. b.) The meshed used and the selected elements for microstructure visualization. Although the complete specimen is shown, due to symmetry of the problem only one quarter is discretized only.

first from one of the double-well regions  $B_1$  or  $B_3$ . Later on, all three loading cases show second-order laminates. The final states of  $\varepsilon_{11} = 2\varepsilon_{22}$  and  $2\varepsilon_{11} = \varepsilon_{22}$  are governed by the homogeneous  $\varepsilon_1$  and  $\varepsilon_2$  phases, respectively. The loading  $\varepsilon_{11} = \varepsilon_{22}$  remains always in the double-well region  $B_2$  and shows a mixture of  $\varepsilon_1$  and  $\varepsilon_2$  with 50% volume fraction each.

**4.2.3. Biaxial Tension Test of a Perforated Plate.** In this example we consider the biaxial tension test of a square plate with a circular hole. The geometry, loading and boundary conditions are shown in Figure 4.11a. Owing to the symmetry, only one quarter of the specimen is discretized. All the computations are performed with constant increments  $\Delta u = 0.005\text{mm}$  up to the maximum load  $u_{max} = 0.75\text{mm}$ . We assume that the energy storage is governed by the three-well energy function (4.25) and the transformation strains are given by (4.33). The elastic moduli tensor is chosen as  $\mathbb{C} = \kappa \mathbf{1} \otimes \mathbf{1} + 2\mu \mathbb{P}$  with the same material parameters for  $\kappa$ ,  $\mu$  and  $\eta_i$  as in Section 4.2.2.

In Figure 4.12, the phase fractions of  $\varepsilon_0$ ,  $\varepsilon_1$  and  $\varepsilon_2$  are shown. Four different deformed states are considered in order to visualize the evolution of the phase fractions. Initially, the whole structure is in the phase  $\varepsilon_0$ . Then, the variants  $\varepsilon_1$  and  $\varepsilon_2$  start to develop around the hole. For  $u = 0.075\text{mm}$ , the phase  $\varepsilon_1$  starts to form from the left part and the other variant  $\varepsilon_2$  forms from the lower part of the quarter plate. Following a monotonous increase in the loading,  $\varepsilon_0$  disappears smoothly. At the load level  $u = 0.75\text{mm}$ , the phase  $\varepsilon_0$  is disappeared and each half of the specimen is occupied by  $\varepsilon_1$  and  $\varepsilon_2$ .

In Figure 4.13, the microstructure evolution is visualized for three different loading levels. The finite elements which are defined with letters  $I$ - $VI$  in Figure 4.11b are used here to show the microstructure development.  $\varepsilon_0$ ,  $\varepsilon_1$  and  $\varepsilon_2$  are denoted by the colors white, yellow and blue, respectively. Figure 4.13a corresponds to the load level  $u = 0.2\text{mm}$ . The microstructures in the elements  $I$  and  $II$  are completely in the phases  $\varepsilon_1$  and  $\varepsilon_2$ , respectively. In the elements  $III$ ,  $IV$  and  $V$  microstructures with second-order laminates exist. The element  $VI$  is still in the initial phase  $\varepsilon_0$ . The microstructures for the loading level  $u = 0.25\text{mm}$  are given in Figure 4.13b. Following further deformation, see Figure 4.13c for  $u = 0.3\text{mm}$ , the second-order laminates start to disappear and either



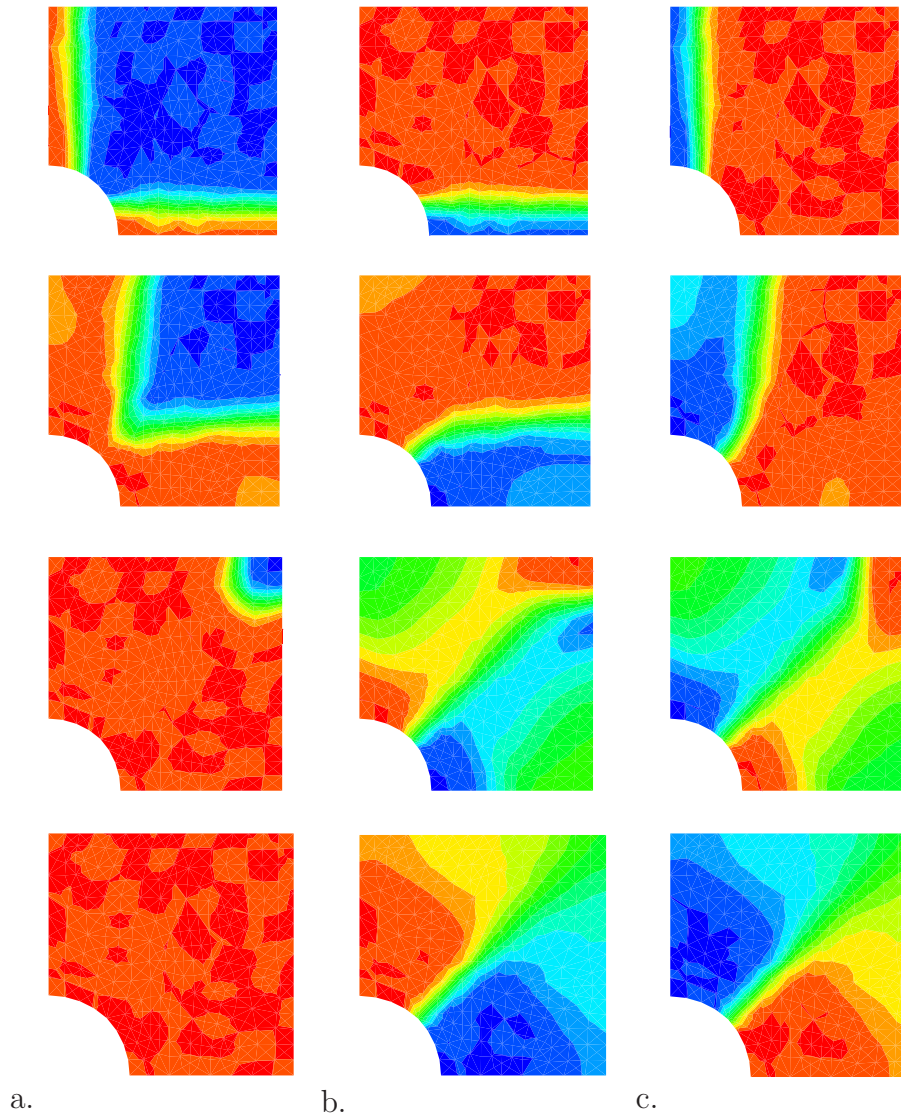


**Figure 4.12:** Evolution of the phase fractions obtained by the relaxation algorithm proposed. The volume fractions are a.)  $(1 - \xi)\lambda$  for the phase  $\varepsilon_0$ , b.)  $\xi$  for the first variant  $\varepsilon_1$  and c.)  $(1 - \xi)(1 - \lambda)$  for the second variant  $\varepsilon_2$ . Blue and red colors denote 100% and 0% of volume fractions, respectively. Each row corresponds to a different load level ( $u = 0.075, 0.2, 0.31$  and  $0.75$  mm).

homogeneous microstructures of  $\varepsilon_1$  or  $\varepsilon_2$ , or first-order laminate mixtures of  $\varepsilon_1$  and  $\varepsilon_2$  remain.

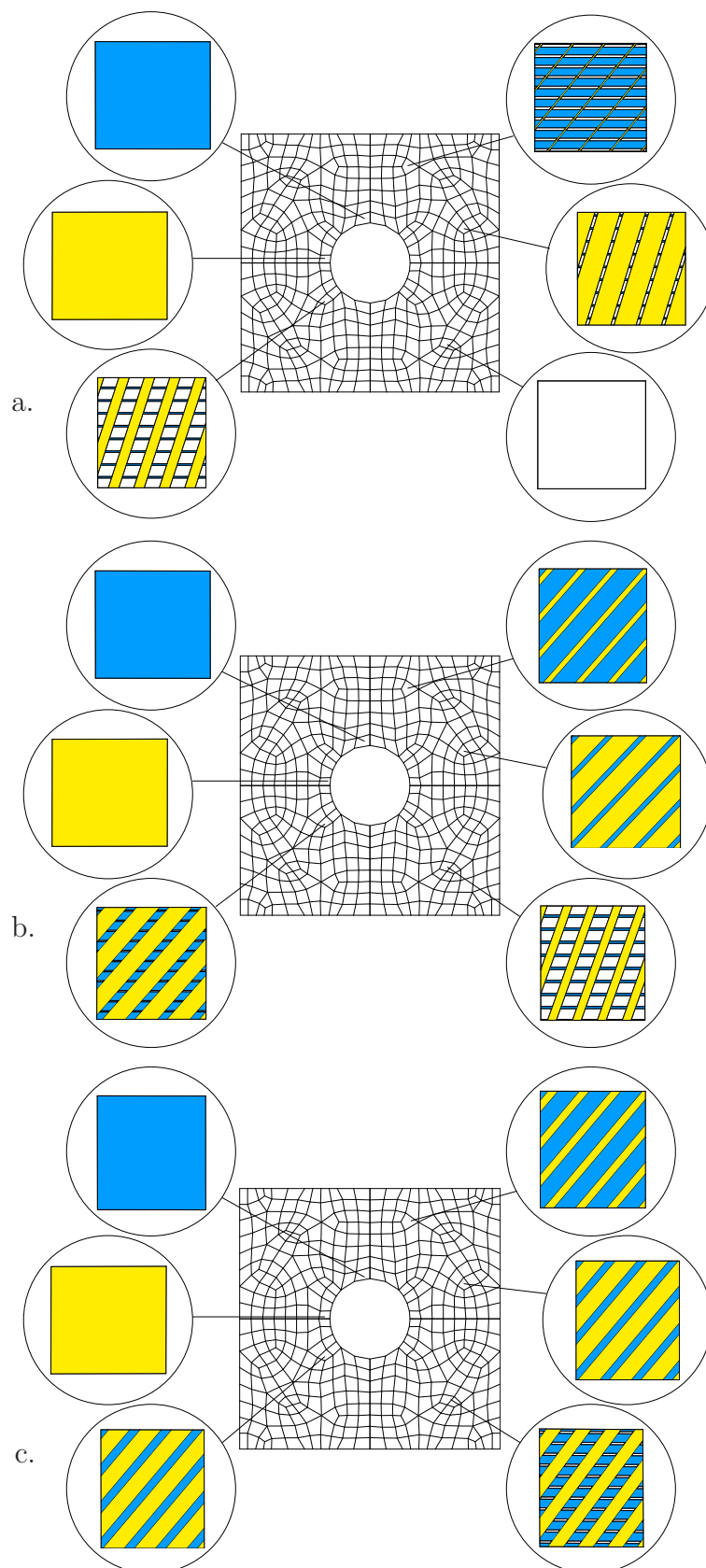


**Figure 4.13:** Microstructure evolution in six different finite elements obtained by the relaxation algorithm proposed. b.) White, yellow and blue colors denote the phases  $\varepsilon_0$ ,  $\varepsilon_1$  and  $\varepsilon_2$ , respectively. Loading levels are a.)  $u = 0.2$  mm, b.)  $u = 0.25$  mm and c.)  $u = 0.3$  mm.



## 5. Application of Relaxation Theory to Single-Slip Plasticity

We illustrate in this section algorithmic implementations of the variational formulation outlined in Section 3.1 for the case of *single-slip multiplicative plasticity* and propose a particular numerical relaxation algorithm. Finally, some numerical examples are presented to demonstrate the performance of the relaxation algorithm proposed. The single-slip plasticity provides a canonically simple model problem for the subsequently outlined convexification analyses, exhibiting characteristic features also observed in more complex models. This model problem has attracted in recent years many researchers' attention, see for example HACKL & HOPPE [91], CARSTENSEN, HACKL & MIELKE [40], BARTELS ET AL. [19], MIELKE [152], MIEHE, LAMBRECHT & GÜRSES [148], CONTI & ORTIZ [48] and CONTI & THEIL [49], due to its simplicity with regard to the application of the relaxation theory. Physically, single-slip models might be considered as multiple slip crystal plasticity models exhibiting infinite latent hardening.

### 5.1. The Canonical Model-Problem: Multiplicative Single-Slip Plasticity

**5.1.1. Energy Storage Function and Stress Response.** In multiplicative plasticity as proposed by LEE [126], the current deformation  $\mathbf{F}$  of the material is decomposed into a plastic and elastic part. In crystal plasticity, the plastic part is assumed to be an isochoric map

$$\mathbf{F}^p \in SL(3) := \{\mathbf{A} \in \mathcal{R}^{3 \times 3} \mid \det \mathbf{A} = 1\} \quad (5.1)$$

solely determined by the plastic slip on the crystallographic planes which leaves the crystal structure unchanged, see for example RICE [190], HAVNER [94] or ASARO [9]. Then the elastic part

$$\boxed{\mathbf{F}^e := \mathbf{F} \mathbf{F}^{p-1}} \quad (5.2)$$

contains lattice distortions and rigid body motions.  $\mathbf{F}^p$  is considered as the key internal variable of multiplicative plasticity. Hence, we identify internal variable vector  $\mathcal{I}$  for the model problem as

$$\mathcal{I} = \{\mathbf{F}^p \in SL(3)\} . \quad (5.3)$$

Note that it is possible to construct transformed internal forces  $\mathfrak{F}$  and fluxes  $\dot{\mathfrak{J}}$  from the original definitions  $\mathcal{F}$  and  $\dot{\mathcal{I}}$  in (3.7). The dependence of the dissipation function  $\phi$  on the current state  $\mathcal{I}$  can be included by a linear state-dependent operator  $\mathbf{T}(\mathcal{I})$  such that it defines transformed forces and fluxes via

$$\mathcal{D} = \mathfrak{F} \cdot \dot{\mathfrak{J}} \geq 0 \quad \text{with} \quad \mathfrak{F} := \mathbf{T}^{-T} \mathcal{F} \quad \text{and} \quad \dot{\mathfrak{J}} := \mathbf{T} \dot{\mathcal{I}} . \quad (5.4)$$

A convenient definition of the linear transformation  $\mathbf{T}$  often allows a representation of the dissipation functions  $\phi(\dot{\mathfrak{J}})$  and  $\phi^*(\mathfrak{F})$  exclusively in terms of the transformed forces and fluxes, respectively. Then the Legendre-Fenchel transformation (3.6) reads

$$\phi^*(\mathfrak{F}) = \sup_{\dot{\mathfrak{J}}} \{ \mathfrak{F} \cdot \dot{\mathfrak{J}} - \phi(\dot{\mathfrak{J}}) \} \quad (5.5)$$

and the Biot-type constitutive expressions (3.7) are replaced by

$$\mathfrak{F} \in \partial_{\dot{\mathfrak{J}}} \phi(\dot{\mathfrak{J}}) \quad \text{and} \quad \dot{\mathfrak{J}} \in \partial_{\mathfrak{F}} \phi^*(\mathfrak{F}) . \quad (5.6)$$

Note that the linear transformation (5.4) preserves the assumed convexity and homogeneity properties of the dissipation functions. From these results transformed flux vector  $\dot{\mathfrak{J}}$  introduced in (5.4) takes the following form for the multiplicative plasticity model under consideration

$$\dot{\mathfrak{J}} = \{ \mathbf{L}^p := \dot{\mathbf{F}}^p \mathbf{F}^{p-1} \in SL(3) \} . \quad (5.7)$$

The plastic evolution parameter  $\mathbf{L}^p$  is obtained from the flux  $\dot{\mathbf{F}}^p$  through the contraction with the state-dependent tensor  $\mathbf{F}^{p-1}$ . A central constitutive assumption of the multiplicative plasticity of crystals is to assume the invariance of the energy storage function with respect to previous plastic deformations

$$\psi(\mathbf{F} \mathbf{F}_0^p, \mathbf{F}^p \mathbf{F}_0^p) = \psi(\mathbf{F}, \mathbf{F}^p) \quad \text{for all } \mathbf{F}_0^p \in SL(3) . \quad (5.8)$$

This is a priori satisfied by making the energy storage dependent on the elastic map  $\mathbf{F}^e$  defined in (5.2), i.e.  $\psi(\mathbf{F}, \mathbf{F}^p) = \psi(\mathbf{F}^e)$ . In what follows, we focus on an elastically isotropic material with the property

$$\psi(\mathbf{F}^e \mathbf{Q}) = \psi(\mathbf{F}^e) \quad \text{for all } \mathbf{Q} \in \mathcal{SO}(3) . \quad (5.9)$$

As a concrete form, we employ a compressible Neo-Hookean material

$$\boxed{\psi(\mathbf{F}^e) = \frac{\mu}{2} [\|\mathbf{F}^e\|^2 - 3] + \frac{\kappa}{4} [J^2 - 2(1 + 2\frac{\mu}{\kappa}) \ln J - 1]} \quad (5.10)$$

with  $\mathbf{F}^e$  defined in (5.2) and  $J := \det \mathbf{F}^e = \det \mathbf{F}$ .  $\kappa > 0$  and  $\mu > 0$  denote the bulk and shear moduli, respectively. It can be shown that (5.10) is a *polyconvex function* of the argument  $\mathbf{F}^e$  in the sense of BALL [12]. Note that the linear transformation (5.2) preserves this convexity property also for the argument  $\mathbf{F}$ . With the stored energy function at hand, one obtains the nominal stresses  $\mathbf{P}$  from (3.2) and the internal forces dual to (5.7) in the form

$$\mathcal{F} = \{ \mathbf{P}^p := -\partial_{\mathbf{F}^p} \psi \} \quad \text{and} \quad \mathfrak{F} := \{ \boldsymbol{\Sigma} := \mathbf{P}^p \mathbf{F}^{pT} \} . \quad (5.11)$$

The modified forces  $\boldsymbol{\Sigma}$  consistent with definition (5.4), which is obtained from  $\mathbf{P}^p$  through the state-dependent contraction with  $\mathbf{F}^{pT}$ , are in finite plasticity theory often denoted as the *Mandel stress*.

**5.1.2. Dissipation Function and Evolution of Internal Variables.** We base our subsequent treatment on the modified internal forces  $\boldsymbol{\Sigma}$  and the flux  $\mathbf{L}^p$  defined in (5.11) and (5.7), respectively. Consequently, the elastic domain can alternatively be formulated in terms of the transformed driving force  $\mathfrak{F}$  defined in (5.4)

$$\mathbb{E} := \{ \mathfrak{F} \mid f(\mathfrak{F}) \leq c(\mathcal{I}) \} , \quad (5.12)$$

where  $f$  is convex and positively homogeneous of the degree one. The associated dissipation function is then defined by the maximum principle

$$\phi(\dot{\mathfrak{J}}) = \sup_{\mathfrak{F} \in \mathbb{E}} \{ \mathfrak{F} \cdot \dot{\mathfrak{J}} \} \quad (5.13)$$

in terms of the transformed flux  $\dot{\mathfrak{J}}$  defined in (5.4). The solution by a Lagrange method yields the alternative evolution system together with the loading-unloading condition

$$\dot{\mathfrak{J}} = \dot{\gamma} \partial_{\mathfrak{F}} f(\mathfrak{F}) \quad \wedge \quad \dot{\gamma} \geq 0 \quad \wedge \quad f \leq c \quad \wedge \quad \dot{\gamma}(f - c) = 0 . \quad (5.14)$$

We consider the level set function

$$f(\boldsymbol{\Sigma}) = |\tau| \quad \text{with} \quad \tau := \boldsymbol{\Sigma} : (\mathbf{S} \otimes \mathbf{T}), \quad (5.15)$$

where  $\tau$  is the so-called Schmid stress associated with the slip system of single-slip plasticity, governed by the slip direction  $\mathbf{S}$  and the slip normal  $\mathbf{T}$  with  $\mathbf{S} \cdot \mathbf{T} = 0$ . Furthermore, we assume the state-dependent threshold function

$$c(\gamma) = \tau_0 + h\gamma \quad \text{with} \quad \gamma := \int_0^t \dot{\gamma} dt \quad (5.16)$$

depending on the equivalent plastic strain  $\gamma$  defined by its rate  $\dot{\gamma}$  introduced below. The material parameters  $\tau_0 > 0$  and  $h \geq 0$  define the critical resolved shear stress and a linear hardening modulus, respectively. Then the flow rule for the transformed flux defined in (5.13) along with the loading-unloading conditions take the form

$$\mathbf{L}^p = \dot{\gamma} \frac{\tau}{|\tau|} \mathbf{S} \otimes \mathbf{T} \quad \wedge \quad \dot{\gamma} \geq 0 \quad \wedge \quad f \leq c \quad \wedge \quad \dot{\gamma}(f - c) = 0. \quad (5.17)$$

With this result in hand, from (3.22) we obtain the image of the dissipation function

$$\phi = (\tau_0 + h\gamma)\dot{\gamma}. \quad (5.18)$$

Now observe that an expression for the plastic parameter  $\dot{\gamma}$  in terms of the plastic flux  $\mathbf{L}^p$  can be obtained from (5.17)<sub>1</sub>, yielding the identifications

$$\dot{\gamma} = |\dot{s}| \quad \text{and} \quad \gamma = \int_0^t |\dot{s}| dt \quad \text{with} \quad \dot{s} := \mathbf{L}^p : (\mathbf{S} \otimes \mathbf{T}), \quad (5.19)$$

where  $\dot{s}$  is the slip in the two possible directions of the single-slip system. Insertion of these results into (5.18) finally identifies the dissipation function

$$\boxed{\phi(\mathbf{L}^p) = [\tau_0 + h\gamma] |\mathbf{L}^p : (\mathbf{S} \otimes \mathbf{T})|} \quad (5.20)$$

for the linear hardening model of single-slip plasticity in terms of the evolution operator  $\mathbf{L}^p$ . Clearly,  $\phi$  is a positively homogeneous function of the degree one. The exploitation of the Biot-type equation (5.6)<sub>1</sub> yields the equation for the internal forces

$$\boldsymbol{\Sigma} \in \begin{cases} (\tau_0 + h\gamma) \frac{\dot{s}}{|\dot{s}|} \mathbf{S} \otimes \mathbf{T} & \text{for } \mathbf{L}^p \neq \mathbf{0} \\ \text{int}\mathbb{E} & \text{otherwise} \end{cases} \quad (5.21)$$

alternative to the inverse evolution form (5.17).

**5.1.3. Algorithmic Approximation of the Incremental Work Function.** The key point of the incremental variational formulation at finite steps is the definition of the incremental work function

$$\mathcal{W}(\mathbf{F}_{n+1}, \mathbf{F}_{n+1}^p) = \psi(\mathbf{F}_{n+1}, \mathbf{F}_{n+1}^p) - \psi_n + \int_{t_n}^{t_{n+1}} \phi(\dot{\mathbf{F}}^p, \mathbf{F}^p) dt \quad (5.22)$$

that is minimized in (3.10) with respect to the internal variable  $\mathbf{F}_{n+1}^p$  in order to get the incremental potential  $W(\mathbf{F}_{n+1})$  for the current stresses  $\mathbf{P}_{n+1}$ . Here and all in that follows, the subscript  $n + 1$  is dropped and all variables without subscript are assumed to be evaluated at the current time  $t_{n+1}$ . Observe that the integral in the above expression is the dissipated work in the interval  $[t_n, t_{n+1}]$  under consideration. The value of this integral can exactly be computed by using the representation (5.18) of the dissipation function, yielding

$$\int_{t_n}^{t_{n+1}} \phi dt = \int_{\gamma_n}^{\gamma_{n+1}} (\tau_0 + h\gamma) d\gamma = \tau_0(\gamma - \gamma_n) + \frac{1}{2} h(\gamma^2 - \gamma_n^2) . \quad (5.23)$$

This expression determines the internal plastic work in terms of the increment  $\gamma - \gamma_n$  of the equivalent plastic strain. In order to relate this dissipated work to the current plastic deformation  $\mathbf{F}^p$ , we consider a conventional *update algorithm for the internal variable* that integrates the flow rule (5.17)<sub>1</sub> in the time increment under consideration. To this end, we express the current plastic deformation

$$\boxed{\mathbf{F}^p = \mathbf{f}^p \mathbf{F}_n^p} \quad (5.24)$$

in terms of the incremental plastic deformation  $\mathbf{f}^p \in SL(3)$ . An algorithmic counterpart to the flow rule (5.17)<sub>1</sub> that preserves the unimodular structure of  $\mathbf{f}^p$  reads

$$\mathbf{f}^p = \exp \left[ (\gamma - \gamma_n) \frac{\tau^*}{|\tau^*|} \mathbf{S} \otimes \mathbf{T} \right] , \quad (5.25)$$

see for example WEBER & ANAND [210] and MIEHE [141]. Here,  $\tau^*$  is the Schmid stress associated with the trial elastic deformation map

$$\mathbf{F}^{e*} := \mathbf{F} \mathbf{F}_n^{p-1} . \quad (5.26)$$

Hence, in the algorithmic setting, the incremental plastic deformation is considered to depend only on the increment  $\gamma - \gamma_n$  of equivalent plastic strain. Similar to (5.19), we then may resolve (5.25) for the increment

$$\gamma - \gamma_n = |s - s_n| \quad \text{with} \quad s - s_n := \ln \mathbf{f}^p : (\mathbf{S} \otimes \mathbf{T}) . \quad (5.27)$$

The insertion into (5.23) then gives a one-step algorithmic expression of the incremental plastic work

$$\int_{t_n}^{t_{n+1}} \phi dt = \tau_0 |\ln \mathbf{f}^p : (\mathbf{S} \otimes \mathbf{T})| + \frac{1}{2} h |\ln \mathbf{f}^p : (\mathbf{S} \otimes \mathbf{T})|^2 \quad (5.28)$$

in terms of the incremental plastic deformation  $\mathbf{f}^p$  which can be rewritten from (5.25) as the series representation of the exponential map

$$\mathbf{f}^p = \mathbf{1} + \sum_{k=1}^{\infty} \frac{1}{k!} \left\{ (\gamma - \gamma_n) \frac{\tau^*}{|\tau^*|} \mathbf{S} \otimes \mathbf{T} \right\}^k . \quad (5.29)$$

For the simple single-slip model with the orthogonal vectors  $\mathbf{S} \cdot \mathbf{T} = 0$  all higher terms with  $k > 1$  vanish and we get a closed form of (5.29)

$$\boxed{\mathbf{f}^p = \mathbf{1} + (\gamma - \gamma_n) \frac{\tau^*}{|\tau^*|} \mathbf{S} \otimes \mathbf{T} .} \quad (5.30)$$



As a consequence, the incremental plastic work (5.28) appears in the simple form

$$\int_{t_n}^{t_{n+1}} \phi dt = \tau_0 |(\mathbf{f}^p - \mathbf{1}) : (\mathbf{S} \otimes \mathbf{T})| + \frac{h}{2} |(\mathbf{f}^p - \mathbf{1}) : (\mathbf{S} \otimes \mathbf{T})|^2. \quad (5.31)$$

**5.1.4. Algorithmic Setting of the Constitutive Minimization Problem.** With the above two formulations (5.23) and (5.31) for the incremental plastic work at hand, we may define *two alternative algorithmic settings* of the constitutive minimization problem (3.10) for the definition of the incremental stress potential  $W(\mathbf{F})$ . The first representation minimizes the incremental work function

$$\hat{W}^h(\mathbf{F}, \mathbf{f}^p) = \psi(\mathbf{F}, \mathbf{f}^p \mathbf{F}_n^p) - \psi_n + \tau_0 |(\mathbf{f}^p - \mathbf{1}) : (\mathbf{S} \otimes \mathbf{T})| + \frac{h}{2} |(\mathbf{f}^p - \mathbf{1}) : (\mathbf{S} \otimes \mathbf{T})|^2 \quad (5.32)$$

obtained from (5.22) and (5.31) with respect to incremental plastic deformation  $\mathbf{f}^p$ , yielding

$$W(\mathbf{F}) = \inf_{\mathbf{f}^p \in SL(3)} \{ \hat{W}^h(\mathbf{F}, \mathbf{f}^p) \}. \quad (5.33)$$

The necessary condition of this minimization yields the algorithmic counterpart of the Biot-type equation (5.21)

$$\Sigma^h \in \begin{cases} (\tau_0 + h\gamma) \frac{s - s_n}{|s - s_n|} \mathbf{S} \otimes \mathbf{T} & \text{for } \mathbf{f}^p \neq \mathbf{1} \\ \text{int}\mathbb{E} & \text{otherwise} \end{cases} \quad (5.34)$$

for the driving force

$$\Sigma^h := -\partial_{\mathbf{f}^p} \psi(\mathbf{F}, \mathbf{f}^p \mathbf{F}_n^p) = \Sigma \mathbf{f}^{p-T} \quad (5.35)$$

consistent with the incremental update algorithm (5.30). Observe the simple relationship  $(s - s_n)/|s - s_n| = \tau^*/|\tau^*|$  of the slip direction to the sign of the trial Schmid stress.

The second representation exploits the simple structure (5.30) of the update algorithm that depends only on the increment  $\gamma - \gamma_n$  of the equivalent plastic strain. Inserting this algorithm into the free energy function, we minimize the incremental work function

$$\tilde{W}^h(\mathbf{F}, \gamma - \gamma_n) = \psi(\mathbf{F}, [\mathbf{1} + (\gamma - \gamma_n) \frac{\tau^*}{|\tau^*|} \mathbf{S} \otimes \mathbf{T}] \mathbf{F}_n^p) - \psi_n + \tau_0 (\gamma - \gamma_n) + \frac{h}{2} (\gamma - \gamma_n)^2 \quad (5.36)$$

obtained from (5.22), (5.30) and (5.23) with respect to incremental plastic strain

$$W(\mathbf{F}) = \inf_{\gamma - \gamma_n \geq 0} \{ \tilde{W}^h(\mathbf{F}, \gamma - \gamma_n) \}. \quad (5.37)$$

The necessary equations of this constrained minimization problem may be obtained by a Lagrange method, yielding the algorithmic counterpart

$$\mathbf{f}^p = \mathbf{1} + (\gamma - \gamma_n) \frac{\tau^*}{|\tau^*|} \mathbf{S} \otimes \mathbf{T} \quad \wedge \quad \gamma \geq \gamma_n \quad \wedge \quad f^h \leq c \quad \wedge \quad (\gamma - \gamma_n)(f^h - c) = 0 \quad (5.38)$$

to equations (5.17) in terms of the level set function

$$f^h := \partial_{(\gamma - \gamma_n)} \psi(\mathbf{F}, [\mathbf{1} + (\gamma - \gamma_n) \frac{\tau^*}{|\tau^*|} \mathbf{S} \otimes \mathbf{T}] \mathbf{F}_n^p) = \Sigma \mathbf{f}^{p-T} : \left( \frac{\tau^*}{|\tau^*|} \mathbf{S} \otimes \mathbf{T} \right) \quad (5.39)$$

consistent with the incremental update algorithm (5.30). For the model problem of single-slip plasticity, both minimization problems (5.33) and (5.37) yield identical results. Observe carefully that both *variational formulations are consistent with algorithmically modified yield functions*, governed by the stress  $\Sigma^h$  and the level set function  $f^h$  defined in (5.35) and (5.39), respectively. However, in single-slip plasticity the relationship  $f^h = f$  holds due to  $\mathbf{f}^{p-T} : (\mathbf{S} \otimes \mathbf{T}) = \mathbf{S} \otimes \mathbf{T}$ . Thus, in single-slip plasticity the algorithmic form of the flow criterion coincides with the continuous definition.

**5.1.5. Stress Update and Elastic-Plastic Moduli for Plastic Loading.** We base our following considerations on the form (5.37) of the constitutive minimization problem which is consistent with treatments suggested in MIEHE [142] and MIEHE, SCHOTTE & LAMBRECHT [149]. For *plastic loading*  $\gamma > \gamma_n$ , the updates are governed by the first and second derivatives of the incremental work function (5.36)

$$\left. \begin{aligned} \tilde{W}_{,\gamma}^h &= -\mu \mathbf{F}^{e*} \mathbf{S}^* \cdot \mathbf{F}^{e*} \mathbf{T} + \tau_0 + h\gamma_n + (\mu \mathbf{F}^{e*} \mathbf{S}^* \cdot \mathbf{F}^{e*} \mathbf{S}^* + h)(\gamma - \gamma_n) \\ \tilde{W}_{,\mathbf{F}}^h &= \mu \mathbf{F} \mathbf{F}^{p-1} \mathbf{F}^{p-T} + \frac{1}{2} (\kappa J^2 - \kappa - 2\mu) \mathbf{F}^{-T} \\ \tilde{W}_{,\mathbf{F}\mathbf{F}}^h &= \mu [\mathbf{F}^{p-1} \mathbf{F}^{p-T}]_{BD} \delta_{ac} + \kappa J^2 F_{Ba}^{-1} F_{Dc}^{-1} - \frac{1}{2} (\kappa J^2 - \kappa - 2\mu) F_{Ac}^{-1} F_{Da}^{-1} \\ \tilde{W}_{,\mathbf{F}\gamma}^h &= \mu \mathbf{F} (2(\gamma - \gamma_n) \mathbf{S}^* \otimes \mathbf{S}^* - \mathbf{F}_n^{p-1} \mathbf{T} \otimes \mathbf{S}^* - \mathbf{S}^* \otimes \mathbf{F}_n^{p-1} \mathbf{T}) \\ \tilde{W}_{,\gamma\gamma}^h &= \mu \mathbf{F}^{e*} \mathbf{S}^* \cdot \mathbf{F}^{e*} \mathbf{S}^* + h \end{aligned} \right\}, \quad (5.40)$$

where we introduced the abbreviation  $\mathbf{S}^* := \frac{\tau^*}{|\tau^*|} \mathbf{S}$ . From the necessary condition  $\tilde{W}_{,\gamma}^h = 0$  of the constitutive minimization problem (5.37) we obtain the closed form result

$$\boxed{\gamma - \gamma_n = \frac{\mu \mathbf{F}^{e*} \mathbf{S}^* \cdot \mathbf{F}^{e*} \mathbf{T} - \tau_0 - h\gamma_n}{\mu \mathbf{F}^{e*} \mathbf{S}^* \cdot \mathbf{F}^{e*} \mathbf{S}^* + h} > 0} \quad (5.41)$$

for the equivalent plastic strain. With this solution of the constitutive minimization problem (5.37) at hand, we compute the stresses based on a straightforward exploitation of the definitions (3.9). Taking the derivative of the function (5.36) with respect to the deformation gradient  $\mathbf{F}$  at the solution point (5.41), we get

$$\partial_{\mathbf{F}} W = \tilde{W}_{,\mathbf{F}}^h + [\tilde{W}_{,\gamma}^h][\gamma, \mathbf{F}]. \quad (5.42)$$

Here, the last term drops out due to the necessary condition of (5.37). Thus we identify the stresses as

$$\mathbf{P} = \tilde{W}_{,\mathbf{F}}^h \quad (5.43)$$

via (5.40)<sub>2</sub>, i.e. simply as the derivative of the storage function  $\psi$  with respect to the current deformation  $\mathbf{F}$ . The sensitivity of the stresses with respect to  $\mathbf{F}$  is governed by the algorithmic tangent moduli

$$\mathbb{C} := \partial_{\mathbf{F}\mathbf{F}}^2 W(\mathbf{F}) \quad (5.44)$$

of the material at time  $t_{n+1}$ . Taking the second derivative of the function (5.36) with respect to the strains  $\mathbf{F}$  at the solution point (5.41), we get

$$\partial_{\mathbf{F}\mathbf{F}}^2 W = \tilde{W}_{,\mathbf{F}\mathbf{F}}^h + [\tilde{W}_{,\mathbf{F}\gamma}^h][\gamma, \mathbf{F}]. \quad (5.45)$$

The sensitivity of the incremental plastic parameter with respect to the strains is obtained by taking the linearization of the necessary condition  $\tilde{W}_{,\gamma}^h = 0$ , yielding  $\gamma, \mathbf{F} =$

$-\tilde{\mathcal{W}}_{,\gamma\gamma}^h]^{-1}[\tilde{\mathcal{W}}_{,\gamma\mathbf{F}}^h]$ . Insertion into (5.45) finally specifies the definition (5.44) of the moduli as

$$\mathbb{C} = \tilde{\mathcal{W}}_{,\mathbf{F}\mathbf{F}}^h - [\tilde{\mathcal{W}}_{,\mathbf{F}\gamma}^h][\tilde{\mathcal{W}}_{,\gamma\gamma}^h]^{-1}[\tilde{\mathcal{W}}_{,\gamma\mathbf{F}}^h] \quad (5.46)$$

in terms of the matrices introduced in (5.40)<sub>3,4,5</sub>. The moduli consist of an elastic contribution and a softening part. The latter is the consequence of the internal degrees of the material represented by a change of plastic deformation within the time step under consideration.

**5.1.6. Relaxation of Non-Convex Multiplicative Single-Slip Plasticity.** We now point out details of the first-order rank-one convexification analysis for the model problem of single slip plasticity introduced in the beginning of Section 5.1. Here, a key contribution is the derivation of a *semi-analytical solution* that reduces for two-dimensional problems the independent micro-variables from four in  $\mathbf{q}$ , see (3.30), to just one variable. Recall the necessary conditions (3.35) of the minimization problem of relaxation

$$\left. \begin{aligned} \bar{W}_{,\xi}^h &= W^+ - W^- - d [\xi \mathbf{P}^+ + (1 - \xi) \mathbf{P}^-] : (\mathbf{F}\mathbf{M} \otimes \mathbf{N}) &= 0 \\ \bar{W}_{,d}^h &= \xi(1 - \xi) [\mathbf{P}^+ - \mathbf{P}^-] : (\mathbf{F}\mathbf{M} \otimes \mathbf{N}) &= 0 \\ \bar{W}_{,\varphi}^h &= \xi(1 - \xi) d [\mathbf{P}^+ - \mathbf{P}^-] : (\mathbf{F}\mathbf{M}_{,\varphi} \otimes \mathbf{N}) &= 0 \\ \bar{W}_{,\chi}^h &= \xi(1 - \xi) d [\mathbf{P}^+ - \mathbf{P}^-] : (\mathbf{F}\mathbf{M} \otimes \mathbf{N}_{,\chi}) &= 0 \end{aligned} \right\} \quad (5.47)$$

in terms of the four micro-variables  $\mathbf{q} := [\xi, d, \varphi, \chi]^T$ . In what follows we will evaluate these conditions and derive a semi-analytical solution for the minimizing laminate  $\mathbf{F}^\pm$ . The plastic deformation  $\mathbf{F}^{p\pm}$  and the hardening variable in the phases ( $\pm$ ) are denoted

$$\boxed{\mathbf{F}^{p\pm} = \mathbf{F}^{p*}(\mathbf{1} \pm \Delta\gamma^\pm \mathbf{S} \otimes \mathbf{T}) \quad \text{and} \quad \gamma^\pm = \gamma^* + \Delta\gamma^\pm,} \quad (5.48)$$

where  $\Delta\gamma^\pm = (\gamma - \gamma_n)^\pm$  are the incremental plastic arc lengths.  $\mathbf{F}^{p*}$  and  $\gamma^*$  are the plastic deformation and the hardening variable of the last stable homogeneous state, respectively. Equation (5.48) points out the cause of the phase decay for the model problem of single-slip plasticity that results from the *bifurcation of the plastic deformation* starting from  $\mathbf{F}^{p*}$  with  $\Delta\gamma^\pm$ . The equilibrium of the Schmidt stresses  $\tau^+ = \tau^-$  yields the identity

$$\Delta\gamma^+ = \Delta\gamma^- = \Delta\gamma \quad (5.49)$$

of the incremental slips. If one postulates the preservation of the volumetric deformation  $\det[\mathbf{F}^+] = \det[\mathbf{F}^-] = \det[\mathbf{F}]$  it turns out that the Lagrangian laminate vectors are orthogonal

$$\mathbf{N} \cdot \mathbf{M} = 0. \quad (5.50)$$

This result allows for the parameterization of these vectors in terms of the vectors of the slip system  $\mathbf{N} = \cos\theta \mathbf{S} - \sin\theta \mathbf{T}$  and  $\mathbf{M} = \sin\theta \mathbf{S} + \cos\theta \mathbf{T}$  where  $\theta$  is an in-plane orientation angle. The necessary conditions (5.47)<sub>2,3</sub> can be interpreted as the postulation of equilibrium of the traction vectors

$$\mathbf{t}^+ = \mathbf{t}^- \quad \text{with} \quad \mathbf{t}^\pm = \mathbf{P}^\pm \mathbf{N} \quad (5.51)$$

of the laminate phases. Exploitation of the equilibrium condition (5.51) together with the results (5.49), (5.50) and the definition (5.48) leads to the identification of the inclination

angle and a formula for the micro-intensity

$$\boxed{\tan \theta = -\mathbf{F}^{p*} : \mathbf{S} \otimes \mathbf{T} \quad \text{and} \quad d = \frac{2\Delta\gamma}{\cos^2 \theta (1 + \Delta\gamma^2)}} \quad (5.52)$$

Insertion of the above obtained results in the necessary conditions (5.47)<sub>1,4</sub> yields an expression for the volume fraction

$$\boxed{\xi = \frac{1}{2} + d^{-1} \left[ \frac{c_{NM}}{c_{MM}} + \tan \theta \right]}, \quad (5.53)$$

where we have introduced the abbreviation  $c_{XY} = \mathbf{X} \cdot \mathbf{C} \cdot \mathbf{Y}$ . The incremental plastic multiplier  $\Delta\gamma$  can be determined by an analogous application of (5.41) for the phase (+). Algebraic manipulations yield the formula

$$\boxed{\Delta\gamma = \frac{2d + E}{\cos^2 \theta d^2 + F}} \quad (5.54)$$

in terms of the coefficients

$$E = -4(h\gamma^* + c)/(\mu c_{MM}) \quad \text{and} \quad F = [4h/\mu + 4 \cos^2 \theta (c_{NN} - c_{NM}^2/c_{MM})]/c_{MM}. \quad (5.55)$$

Note that the incremental slip is only a function of the micro-intensity  $d$ . As a consequence, insertion of (5.54) into (5.52)<sub>2</sub> leads to a polynomial of degree five that *only depends on the micro-intensity*

$$p(d) = a_5 d^5 + a_3 d^3 + a_2 d^2 + a_1 d + a_0 = 0 \quad (5.56)$$

with the coefficients  $a_5 = \cos^6 \theta$ ,  $a_3 = 2F \cos^4 \theta$ ,  $a_2 = 2E \cos^2 \theta$ ,  $a_1 = (E^2 + F^2) \cos^2 \theta - 4F$ ,  $a_0 = -2EF$ . The equations (5.52)<sub>2</sub> and (5.53) bound the admissible range of the micro-intensity in the sense  $d \in [2 |c_{NM}/c_{MM} + \tan \theta|, \cos^{-2} \theta]$ . The solutions of the polynomial  $p(d)$  describe in relation with the equations (5.52) and (5.53) possible phases  $\mathbf{F}^\pm$  for which the necessary conditions (5.47) are satisfied. The relevant micro-intensity  $d^*$  minimizes the volume average of the stress-potentials in the two micro-phases

$$d^* = \arg \left\{ \inf_{d \in \mathcal{D}} [\bar{W}^h] \right\} \quad \text{with} \quad \mathcal{D} := \{d \mid p(d) = 0\}. \quad (5.57)$$

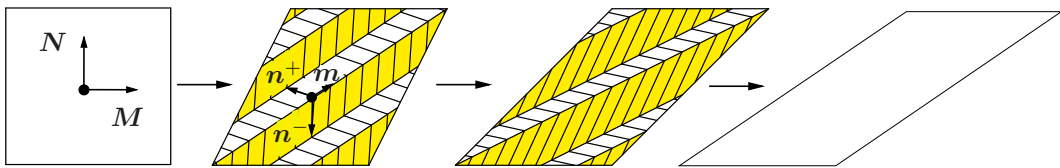


**Figure 5.1:** Microstructure development in the first-order relaxation analysis for a simple-shear test. After loss of rank-one convexity two bifurcated deformation phases arise which continuously change their orientation and volume fractions. Finally, only one phase remains indicating a recovery of the stable homogeneous state.

**Table 5.1:** Material Parameters of Single-Slip Plasticity.

<i>bulk modulus</i>	$\kappa$	15000	MPa
<i>shear modulus</i>	$\mu$	10000	MPa
<i>linear hardening</i>	$h$	1000/2000	MPa
<i>yield stress</i>	$\tau_0$	10	MPa

The relaxed stresses  $\bar{\mathbf{P}}$  and tangent moduli  $\bar{\mathbf{C}}$  can be determined by the formulas (3.56) and (3.58). Note that in cases where no or small plastic deformations have occurred before the loss of material stability, i.e.  $\mathbf{F}^{p*} = \mathbf{1}$ , the orientation vectors of the laminate denote

$$\boxed{\mathbf{M} = \mathbf{T} \quad \text{and} \quad \mathbf{N} = \mathbf{S} .} \quad (5.58)$$

The formulas (5.52)<sub>2</sub>, (5.53), (5.54) then simplify considerably because of the geometric relations  $\cos \theta = 1$  and  $\tan \theta = 0$ , i.e.

$$d = \frac{2\Delta\gamma}{1 + \Delta\gamma^2}, \quad \xi = \frac{1}{2} + d^{-1} \frac{c_{NM}}{c_{MM}} \quad \text{and} \quad \Delta\gamma = \frac{2d + E}{d^2 + F} \quad (5.59)$$

in terms of the coefficients  $E$  as given in (5.55) and  $F = [4h/\mu + 4(c_{NN} - c_{NM}^2/c_{MM})]/c_{MM}$ . In the following numerical examples we assume the condition (5.58) holds.

## 5.2. Numerical Examples of Relaxations in Single-Slip Plasticity

In what follows we demonstrate the performance of the above outlined relaxation technique by means of some representative numerical examples. The main goals of the numerical investigations are the analysis of the *developing microstructures* and the demonstration of the *mesh-invariance* of the relaxation technique proposed. In the first two examples we investigate a strain-driven tension and a simple shear test for three different orientations of the slip system.

Here, the development of the first-order laminates and the course of the stress-loading curves are documented. The next two numerical examples are concerned with the deformation of an elastoplastic strip that is loaded in shear and tension. We report on the

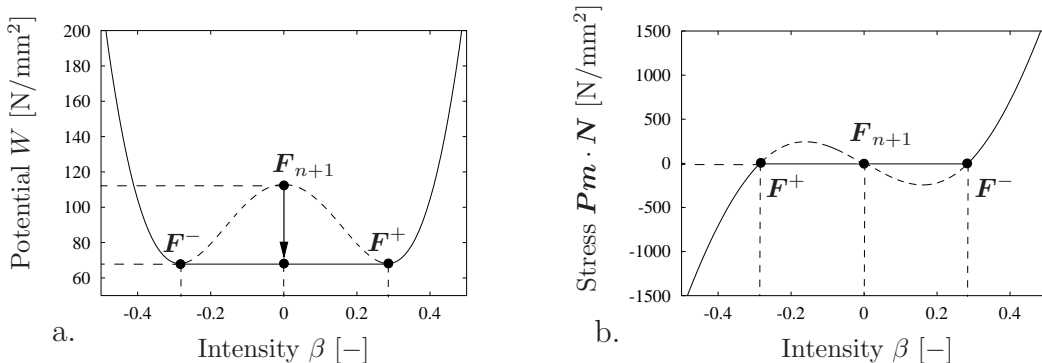


**Figure 5.2:** Plane strain tension test. Details of the rank-one convexification for the orientation angle  $\alpha = 90^\circ$  of the slip-system at  $\Lambda_{n+1} = 0.075$ .  $\beta$  parametrizes the intensity of the laminate  $\mathbf{F}^\pm = \mathbf{F}_{n+1} + \beta^\pm \mathbf{m} \otimes \mathbf{N}$ . a.) At  $\mathbf{F}_{n+1}$  the potential is not rank-one convex (dashed line).  $\mathbf{F}_{n+1}$  decomposes into micro-phases  $\mathbf{F}^\pm$  (solid line). b.) The relaxed stress-strain relation characterizes a snap-through Maxwell-line behavior between the micro-phases  $\mathbf{F}^\pm$ .

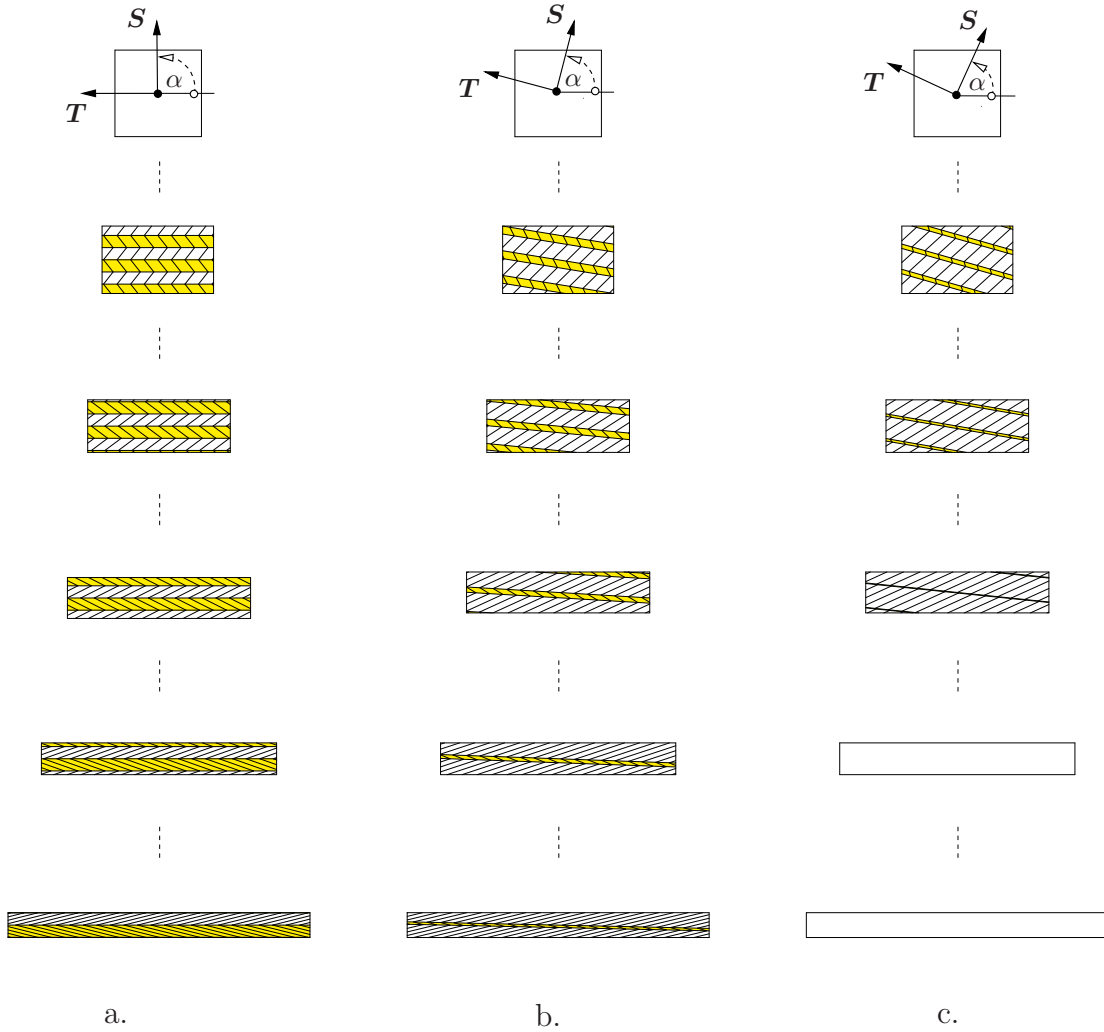


**Figure 5.3:** Plane strain tension test. Comparison of the evolution of the microstructures for the plane strain tension test with three different slip systems a.)  $\alpha = 90^\circ$ , b.)  $\alpha = 75^\circ$ , c.)  $\alpha = 65^\circ$ . After loss of material stability microstructures develop which are modeled as first-order rank-one laminates.

arising microstructures which are resolved by the proposed rank-one convexification of the non-convex incremental stress potential. The comparison of the relaxed and the non-relaxed load-displacement curves in typical finite element discretizations indicate a well-posedness of the first-level rank-one relaxed problem. The material parameters governing the energy storage and dissipation functions (5.10) and (5.20) are identical to those used in CARSTENSEN, HACKL & MIELKE [40] and HACKL & HOPPE [91]. They are summarized in Table 5.1. Only for the last example in Section 5.2.4 the hardening modulus is changed to  $h = 2000\text{MPa}$ . The vectors of the slip system are parameterized by  $\mathbf{S} = [\cos \alpha, \sin \alpha]^T$  and  $\mathbf{T} = [-\sin \alpha, \cos \alpha]^T$ , respectively.  $\alpha$  is the counterclockwise angle between the basis vector  $\mathbf{e}_1$  and the slip vector  $\mathbf{S}$ . In the case of the two strain-driven examples the rank-one convex envelope has been determined by solving the minimization problem (3.54) with respect to (i) four variables  $\mathbf{q} = [\xi, d, \varphi, \chi]^T$ , (ii) two variables  $\mathbf{q} = [\xi, d]^T$  for given laminate orientations given in (5.52) and (iii) by applying the semi-analytical solution outlined in Section 5.1.6. All solution procedures lead to the same relaxed stress response and

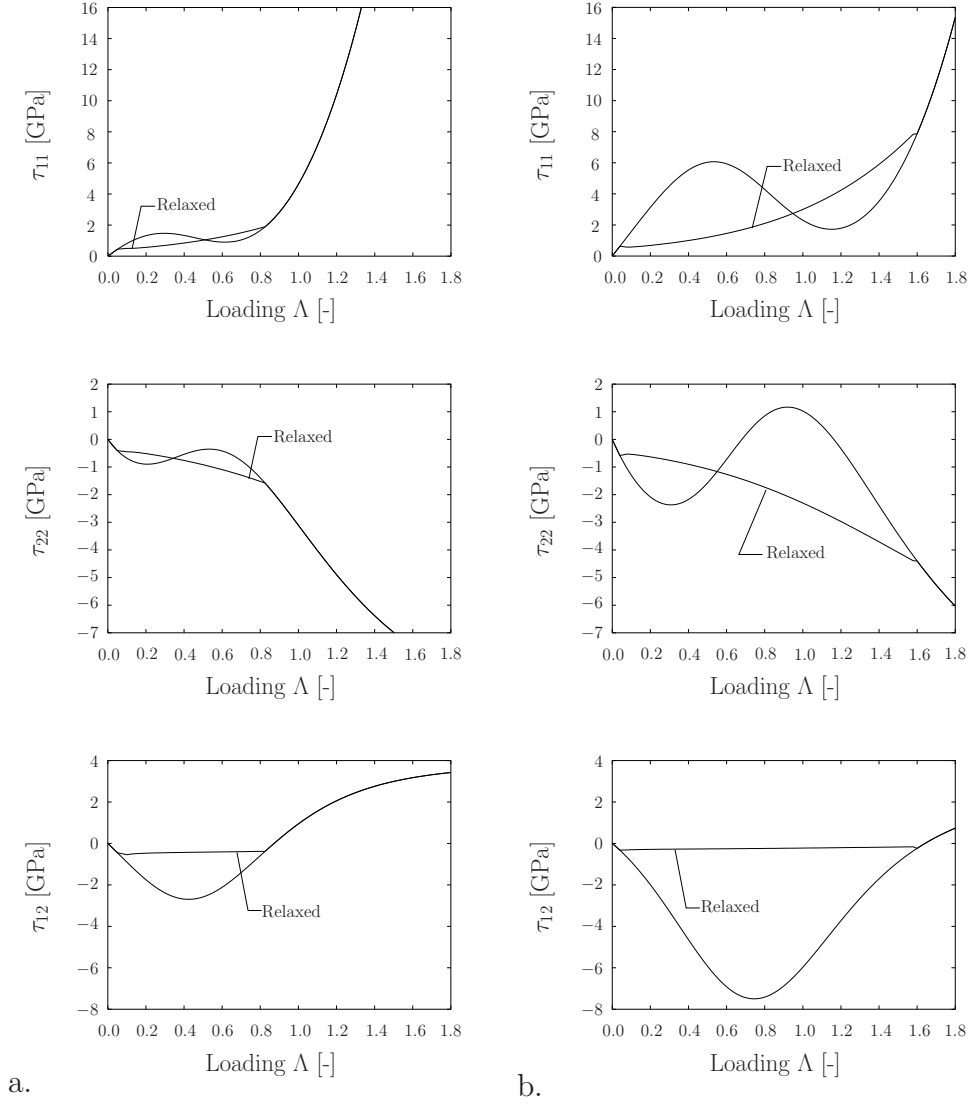


**Figure 5.4:** Plane strain tension test. Comparison of relaxed and unrelaxed Kirchhoff stress components for plane strain tension test and two different slip systems. a.)  $\alpha = 65^\circ$ , b.)  $\alpha = 75^\circ$ . The shape of the governing stress coordinates  $\tau_{11}$  and  $\tau_{22}$  represents a non-linear snap-through behavior within the non-convex range. After the recovery of the stable homogeneous state the relaxed and the unrelaxed stress responses coincide again.

therefore prove the semi-analytical results derived in Section 5.1.6. As a consequence, the boundary value problems are solved by using the semi-analytical method that is much less time consuming and more efficient. We use the four-node enhanced incompatible-mode finite element developed by SIMÓ & ARMERO [201]. The visualization of the emerging microstructures uses the mapping  $\mathbf{m} = \mathbf{F}^\pm \mathbf{M}$  and  $\mathbf{n}^\pm = \mathbf{F}^\pm \mathbf{N}$  of the laminate orientations  $\mathbf{M}$  and  $\mathbf{N}$ . These mappings hold because of the orthogonality condition (5.50). Figure 5.1 shows schematically the development of a first-order laminate after loss of material stability. The interface between the micro-phases is modeled by  $\mathbf{m}$ , whereas the intensity of the micro-bifurcation is represented by  $\mathbf{n}^\pm$ . The volumes of the micro-phases ( $\pm$ ) are filled yellow and white, respectively. Their thicknesses represent the associated volume fractions, respectively.



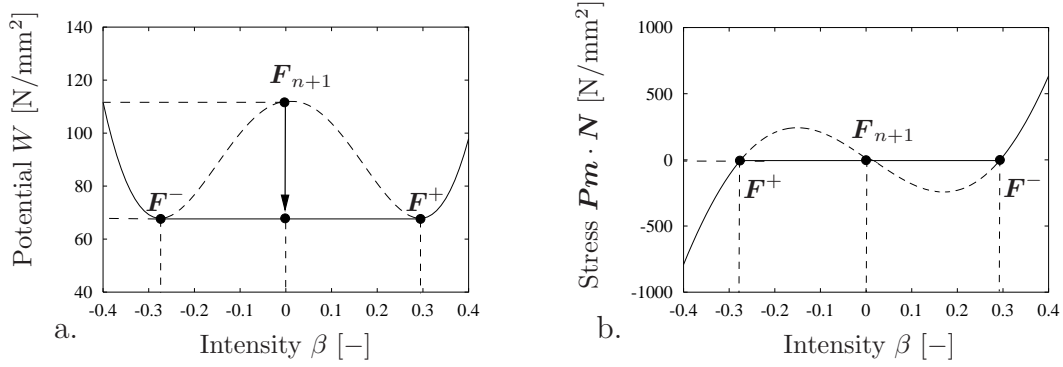


**Figure 5.5:** Simple shear test. Details of the rank-one convexification for the orientation angle  $\alpha = 135^\circ$  of the slip system at  $\Lambda_{n+1} = 0.15$ . a.) At  $\mathbf{F}_{n+1}$  the potential is not rank-one convex (dashed line).  $\mathbf{F}_{n+1}$  decomposes into micro-phases  $\mathbf{F}^\pm$  (solid line). b.) The relaxed stress-strain relation characterizes a snap-through Maxwell-line behavior.

**5.2.1. Microstructure Development in a Homogeneous Tension Test.** The first example is concerned with a volume preserving plane strain tension test described by the macroscopic deformation gradient

$$\mathbf{F} = \begin{bmatrix} \exp[\Lambda] & 0 & 0 \\ 0 & \exp[-\Lambda] & 0 \\ 0 & 0 & 1 \end{bmatrix}. \quad (5.60)$$

The loading parameter  $\Lambda$  is increased in increments  $\Delta\Lambda = 0.025$  up to the final value  $\Lambda_{max} = 1.8$ . We consider three different slip systems parameterized by the inclination angles  $\alpha = 65^\circ/75^\circ/90^\circ$ . Note that the orientations of the slip systems are not aligned to the loading mode. Consequence is a bifurcation of the plastic deformation into negative and positive slip directions, indicated by the loss of rank-one convexity of the incremental stress potential.

Figure 5.2a shows the shape of a non-convex incremental stress potential for an orientation of the slip-system  $\alpha = 90^\circ$  and loading  $\Lambda = 0.075$ . The variable  $\beta$  parameterizes the intensity of the rank-one perturbation  $\mathbf{F}^\pm = \mathbf{F}_{n+1} + \beta^\pm \mathbf{m} \otimes \mathbf{N}$ . Obviously, the incremental stress potential  $W(\mathbf{F}_{n+1})$  is greater than the interpolation of the potentials  $W(\mathbf{F}^+)$  and  $W(\mathbf{F}^-)$  corresponding to the micro-phases (+) and (-). As a consequence, the homogeneous deformation state is not stable and decomposes into the micro-deformations  $\mathbf{F}^\pm$  which minimize the function  $\bar{W}^h$  with respect to the variables  $\mathbf{q}$ . The relaxed stress-deformation relation plotted in Figure 5.2b characterizes a snap-through behavior (Maxwell line) between the two micro-phases  $\mathbf{F}^\pm$  due to the constant slope of the rank-one convex envelope. The arising microstructures are resolved by the rank-one convexification of the non-convex potential outlined in Section 5.1.6. In Figure 5.3 the evolution of the microstructures is documented for the three slip systems considered at  $\Lambda = 0/0.25/0.5/0.75/1.0/1.25$ . In the cases of  $\alpha = 65^\circ/75^\circ$  a recovery of a stable homogeneous state is observed. This is due to the rotating slip system that finally aligns to the principal tension mode. As a consequence, the homogeneous deformation becomes stable and the incremental stress potential convex. For  $\alpha = 90^\circ$  the homogeneous deformation bifurcates with the constant volume fraction  $\xi = 0.5$  as the orientation of the slip system does not change.

The in-plane Kirchhoff stress components of the relaxed and the unrelaxed response

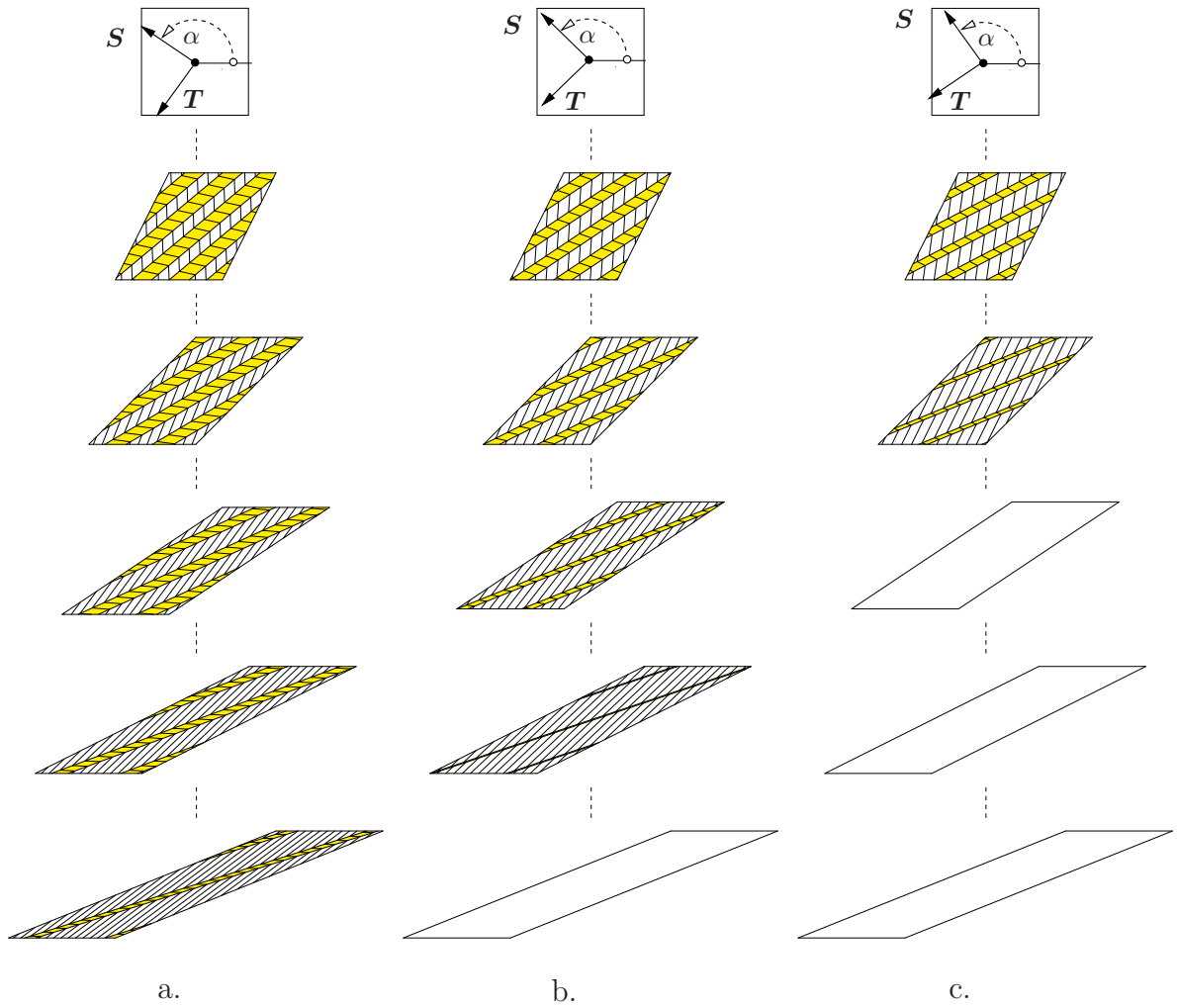


**Figure 5.6:** Simple shear test. Comparison of evolution of microstructures for simple shear test with three different slip systems a.)  $\alpha = 145^\circ$ , b.)  $\alpha = 135^\circ$ , c.)  $\alpha = 125^\circ$ . After loss of material stability first-order rank-one laminate-type microstructures develop.

for  $\alpha = 65^\circ/75^\circ$  are given in Figure 5.4 in dependence of the loading parameter  $\Lambda$ . The convexified stress-loading curves for  $\tau_{11}$  and  $\tau_{22}$  show a non-linear snap-through behavior within the non-convex range. After the recovery of the stable homogeneous state the relaxed and the unrelaxed stress responses coincide again.

**5.2.2. Microstructure Development in a Homogeneous Shear Test.** In the second example we investigate the stress response for a strain-driven simple shear test parameterized by the macroscopic deformation gradient

$$\mathbf{F} = \begin{bmatrix} 1 & \Lambda & 0 \\ 0 & 1 & 0 \\ 0 & 0 & 1 \end{bmatrix}. \quad (5.61)$$

All computations were performed with constant increments  $\Lambda = 0.05$  up to the maximum loading  $\Lambda_{max} = 3.5$ . Because of the non-aligned orientation of the slip systems  $\alpha = 125^\circ, 135^\circ, 145^\circ$  the material stability of the homogeneous deformation is lost and microstructures arise.

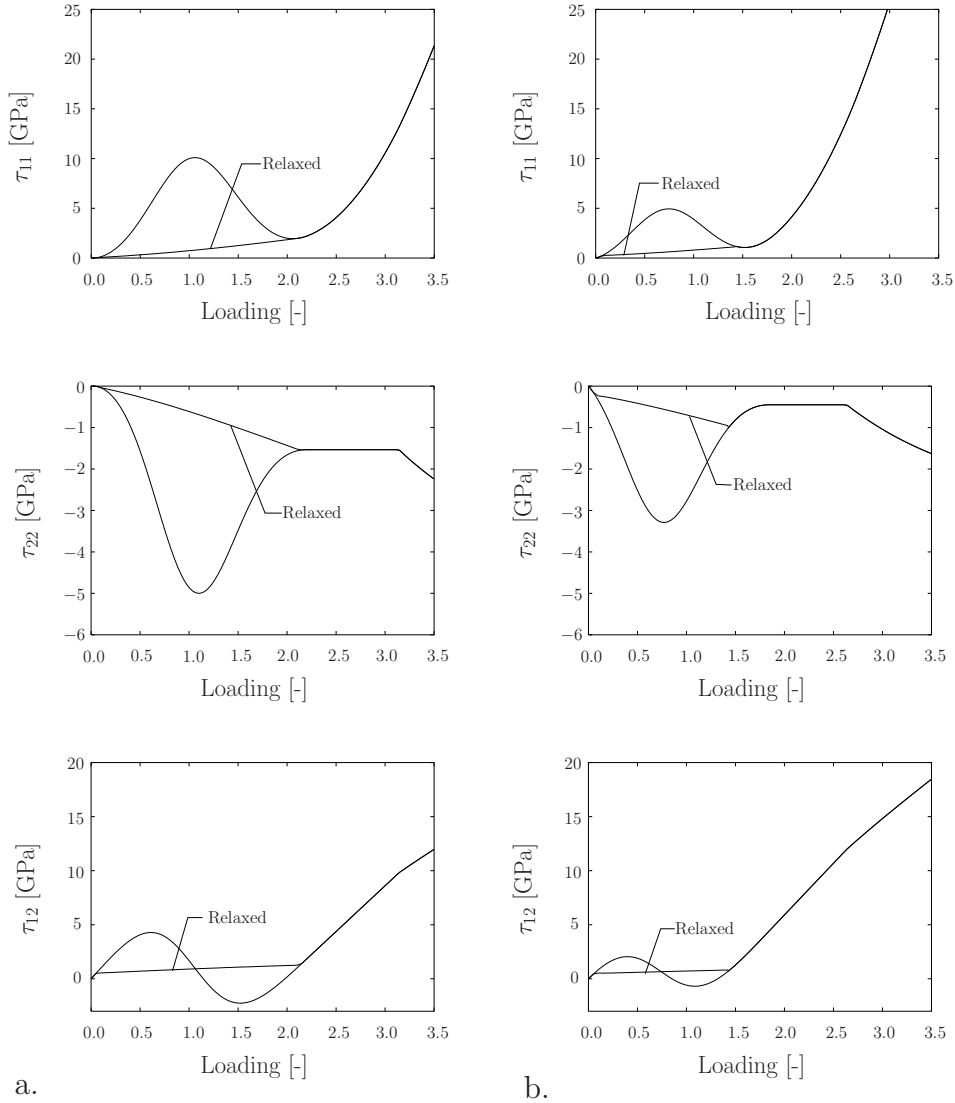


**Figure 5.7:** Simple shear test. Comparison of relaxed and unrelaxed Kirchhoff stress components for plane strain tension test and two different slip systems. a.)  $\alpha = 135^\circ$ , b.)  $\alpha = 125^\circ$ . The shape of the governing stress coordinate  $\tau_{12}$  represents a snap-through behavior within the non-convex range. After recovery of the stable homogeneous state the relaxed and the unrelaxed stress responses coincide again.

In Figure 5.5a the shape of a non-convex incremental stress potential for an orientation of the slip system  $\alpha = 135^\circ$  and loading  $\Lambda = 0.15$  is plotted. Because of the loss of rank-one convexity the homogeneous deformation state is not stable and decomposes into the micro-deformations  $\mathbf{F}^\pm$  which minimize the function  $\bar{W}^h$  with respect to the variables  $\mathbf{q}$ . The characteristic Maxwell line between the two micro-phases  $\mathbf{F}^\pm$  is visible in Figure 5.5b. The development of the first-order rank-one laminate is plotted in Figure 5.6 for  $\Lambda = 0/0.5/1.0/1.5/2.0/2.5$ . As already pointed out above the plastic slip systems start to rotate and align to the principal loading mode. The stronger the blocking of the principal deformation the longer the non-convex range. The in-plane Kirchhoff stress coordinates for the relaxed and the non-relaxed solutions are plotted in Figure 5.7 for  $\alpha = 125^\circ/135^\circ$ . The  $\tau_{12}$ - $\Lambda$ -curve mirrors the well-known straight Maxwell-line within the non-convex range.

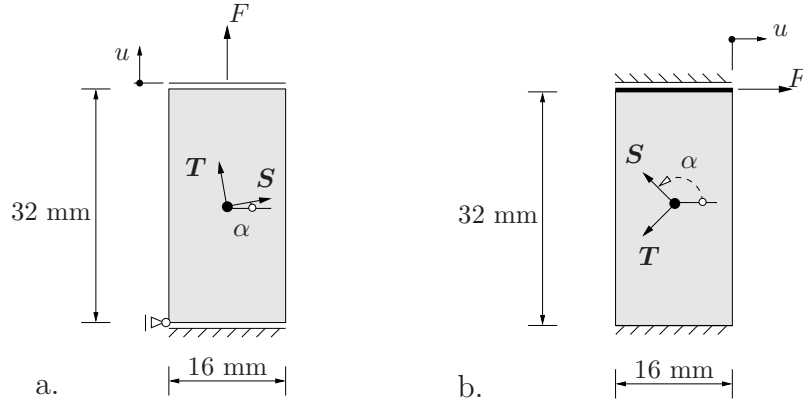


**Figure 5.8:** Rectangular specimen in a.) tension and b.) shear. Geometry, loading and boundary conditions.

**5.2.3. Relaxation of an Inhomogeneous Elastoplastic Strip in Tension.** The next example analyzes the deformation of a rectangular strip in tension under plane strain conditions. The dimensions of the strip are  $b = 16\text{mm}$  (width) and  $l = 32\text{mm}$  (length), respectively. Geometry, loading and boundary conditions are plotted in Figure 5.8a. The boundary conditions are such that the strip is able to perform unconstrained displacements perpendicular to the cross section. The strip is discretized with  $6 \times 12$ ,  $8 \times 16$ ,  $12 \times 24$ ,  $16 \times 32$  and  $20 \times 40$  finite elements. We treat the problem in a deformation-driven analysis with increments  $\Delta u = 0.05\text{mm}$ . For the finest mesh the increments are reduced to  $\Delta u = 0.025\text{mm}$ . In order to provoke a loss of material stability and a phase-decay of the homogeneous deformation into first-order laminates  $\mathbf{F}^\pm$ , we choose an orientation  $\alpha = 10^\circ$  of the slip system.

In Figure 5.9a the deformed meshes of the non-relaxed analysis are plotted for the five mesh discretizations considered. The blocking of the slip system leads to a stiffer response of the non-convex formulation, documented by partially strong distortions of the finite element meshes. In particular, the flexibility of the deformation depends on the mesh discretization applied. Figure 5.9b reports on the deformed meshes and the orientation of the directions of the laminate interfaces which result from the relaxation analysis. The development of the first-order laminates smoothes out the stress response and leads to more flexible and less distorted finite element meshes. In analogy to the strain-driven tension test discussed in Section 5.2.1 the interface orientation is parallel to the main loading direction. The unstable regions where the first-order laminates develop are given in Figures 5.9c. Note that for all mesh discretizations considered the figures coincide very well. This indicates the well-posedness of the first-order rank-one convexified problem. The mesh-dependent response of the unrelaxed formulation is evident by considering the load-displacement curves plotted in Figure 5.10.

In contrast to the unrelaxed formulation, application of the proposed relaxation technique yields a mesh-invariant response. The load-deflection curves do not depend on the mesh size, but are identical for all different mesh densities, see Figure 5.10b. It turns out that the resolution of the microstructure as a first-order laminate is sufficient with regard to an objective stress response. Note that the objectivity of the material behavior is obtained without the introduction of an internal length scale parameter. In Figure 5.11 the microstructures at the central integration points of the red-marked elements are

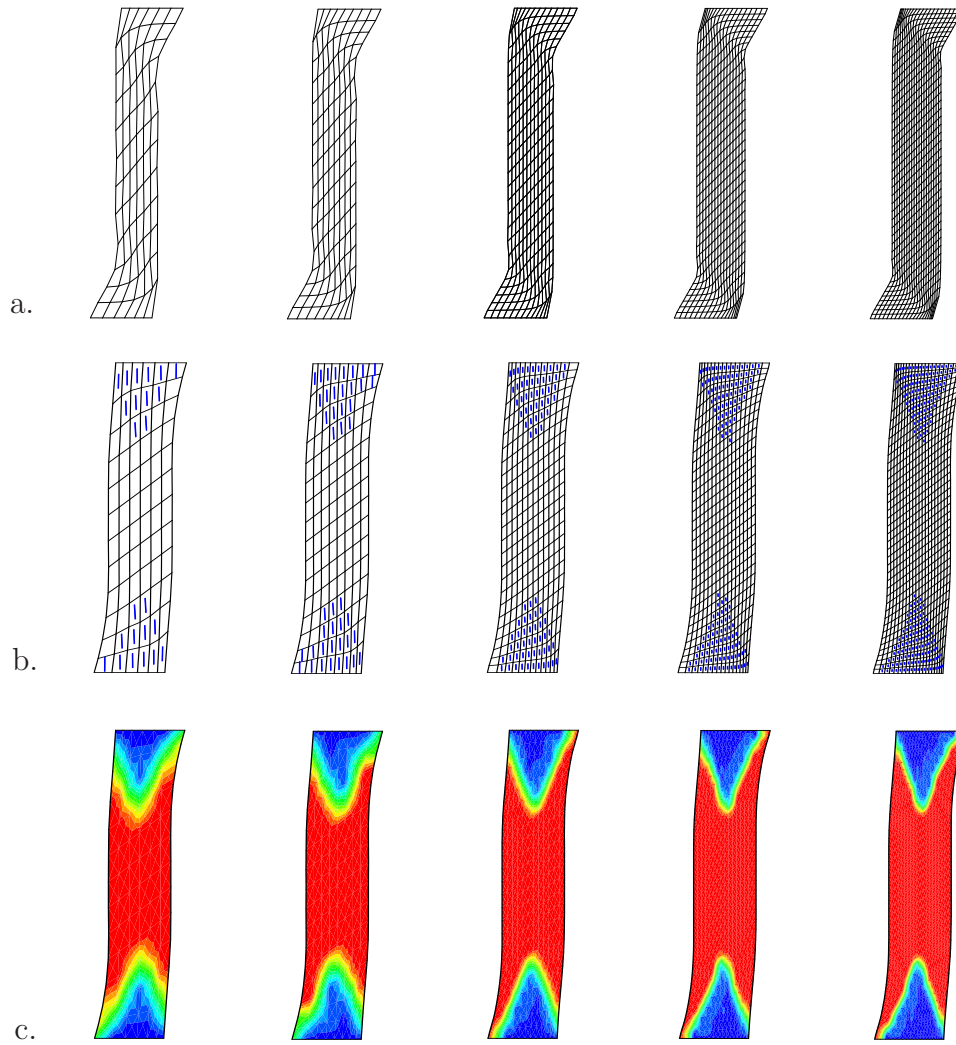


**Figure 5.9:** Rectangular specimen in tension. Comparison of different finite element meshes for relaxed and unrelaxed analyses at  $u = 30$  mm. a.) deformed meshes for unrelaxed analysis, b.) deformed meshes with interface-directions  $\mathbf{m}$ , c.) distribution of unstable regions where microstructures arise.

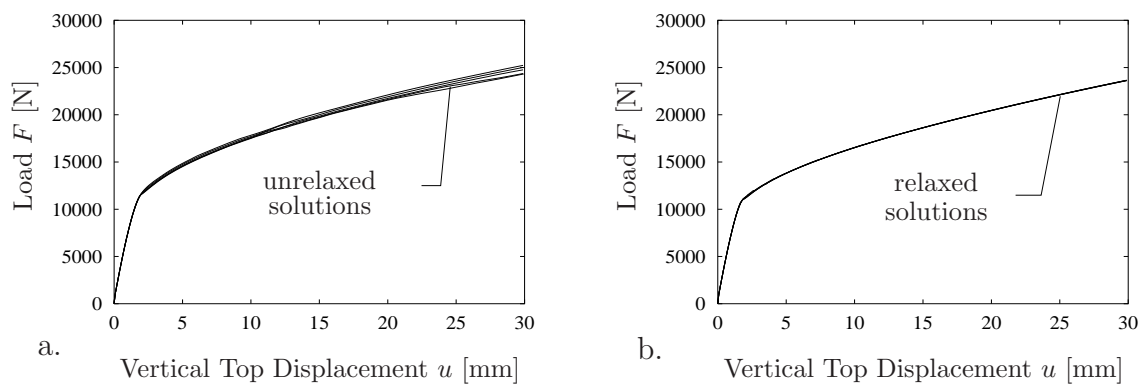


**Figure 5.10:** Rectangular specimen in tension. Load-displacement curves for five different finite element meshes in terms of a.) the unrelaxed (non-objective) formulation (the finer the mesh the softer the response) b.) the proposed relaxation technique.

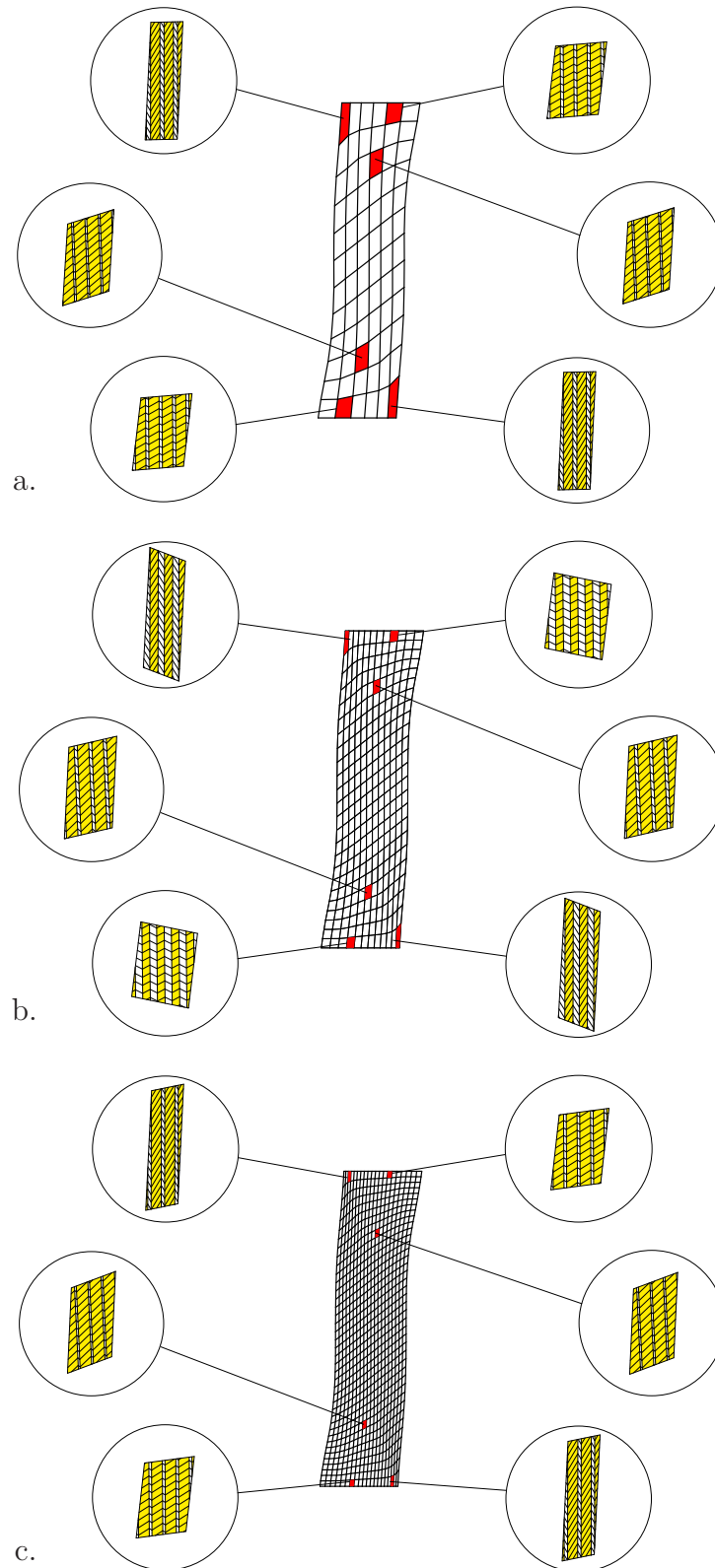


**Figure 5.11:** Rectangular specimen in tension. Visualization of microstructures at selected integration points a.) for 6x12, b.) for 12x24 and c.) for 20x40 mesh discretizations at  $u = 16$  mm. Note that for all three mesh densities the arising microstructures are very similar.

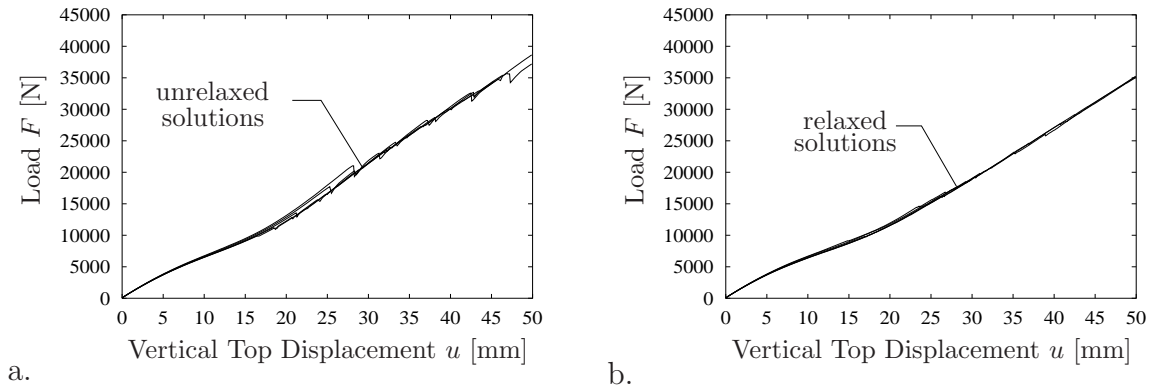


**Figure 5.12:** Rectangular specimen in shear. Load-displacement curves for five different finite element meshes in terms of a.) unrelaxed (non-objective) formulation (the finer the mesh the softer the response) b.) proposed relaxation technique.

magnified for the  $6 \times 12$ ,  $12 \times 24$  and  $20 \times 40$  finite element meshes at  $u = 16\text{mm}$ . For all three mesh densities the arising microstructures are very similar. This confirms the accuracy of the first-order rank-one convexification of the non-convex stress potential.

**5.2.4. Relaxation of an Inhomogeneous Elastoplastic Strip in Shear.** The last example discusses the unrelaxed and the relaxed stress responses of a rectangular strip in shear under plane strain conditions, see Figure 5.8b. Geometry and discretizations coincide with those used in Section 5.2.3. The upper and lower bounds of the strip are fixed in both horizontal and vertical directions. The upper edge is then moved horizontally in constant increments  $\Delta u = 0.05\text{mm}$  to its final displacement  $u = 30\text{mm}$ . The plastic slip system is oriented with  $\alpha = 135^\circ$ . In order to point out the mesh-objectivity of the relaxed formulation we compare the associated load-deflection curves plotted in Figure 5.12 for the five different mesh sizes considered. The zig-zagging of the unrelaxed solution results in Figure 5.12a from the abrupt activation of the slip systems that strongly depends on the coarseness of the mesh discretizations. As a consequence, the incremental boundary value problem is ill-posed and the non-convexified stress response not objective. In contrast to the non-convexified solution, the first-order rank-one convexification that incorporates the determination of the first-order laminate  $\mathbf{F}^\pm$  yields an objective and smoother load-displacement behavior documented in Figure 5.12b, indicating the well-posedness of the relaxed formulation.

In Figure 5.13 the evolution of the microstructures is documented for the  $8 \times 16$ -element mesh and three different displacements  $u = 20\text{mm}$ ,  $u = 25\text{mm}$  and  $u = 30\text{mm}$ . The magnified microstructures correspond to the center Gauss point of the red marked finite elements. With increasing deformation the bifurcation of the homogeneous deformation intensifies and the volume fraction  $1 - \xi$  of the micro-phase (–) augments. Figure 5.14 reports on the evolution of the non-convex zones for the discretizations with  $6 \times 12$ ,  $8 \times 16$ ,  $12 \times 24$  finite elements. After loss of rank-one convexity the microstructures are resolved as first-order laminates. The zones where microstructures arise change during the deformation process. In analogy to the strain-driven shear test investigated in Section 5.2.2, we observe a recovery of a stable homogeneous state. Note that the distribution of the non-convex regions coincides for the three discretizations considered.



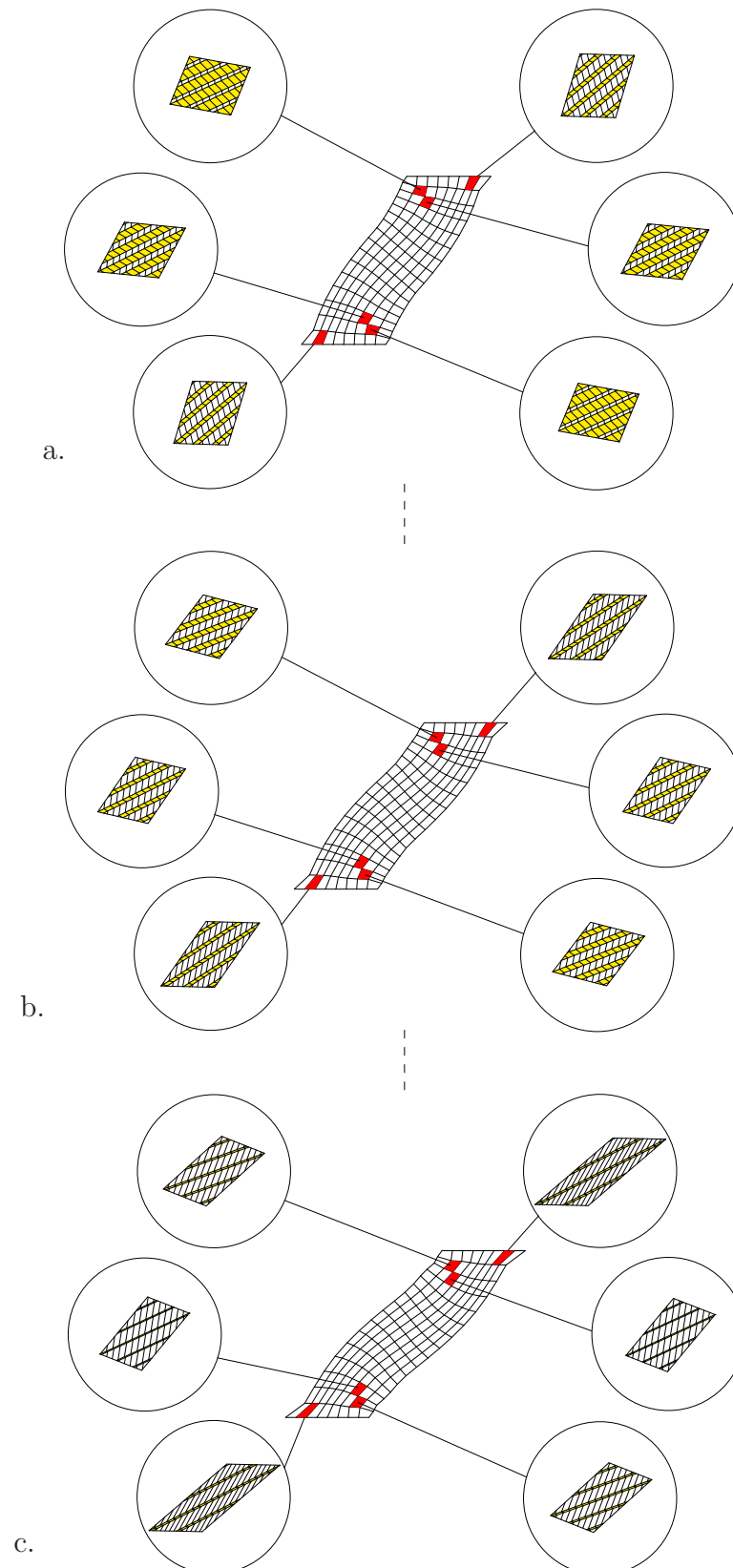


**Figure 5.13:** Rectangular specimen in shear. Visualization of microstructure developments at selected Gauss points for the discretization with  $8 \times 16$  elements at load levels a.)  $u = 20$  mm b.)  $u = 25$  mm and c.)  $u = 30$  mm.

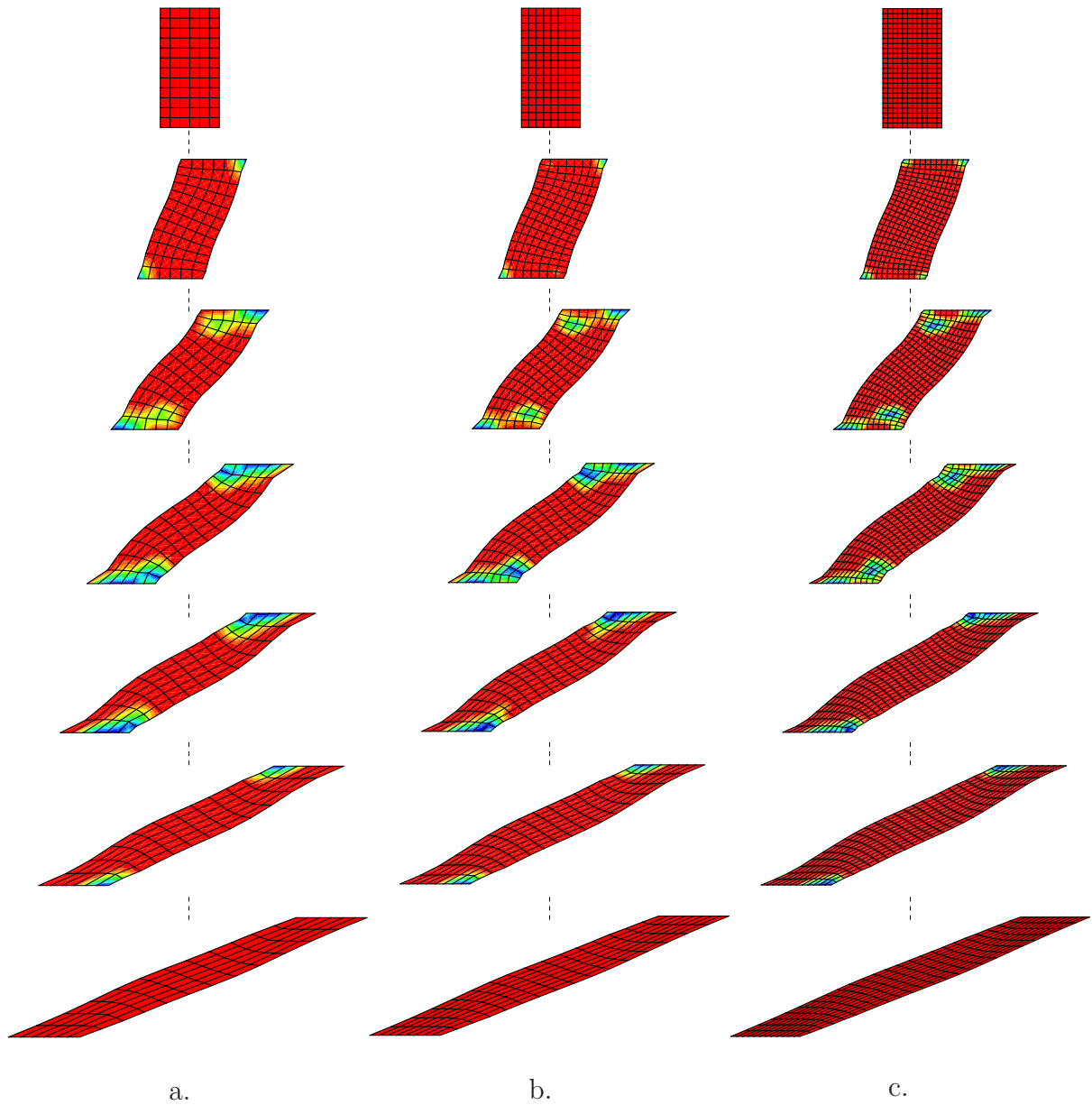


**Figure 5.14:** Rectangular specimen in shear. Development of the unstable regions for three different mesh discretizations  $6 \times 12$ ,  $8 \times 16$  and  $12 \times 24$

## 6. Application of Relaxation Theory to Damage Mechanics

This section is concerned with an application of the variational formulation presented in Section 3.1 to a simple  $1 - d$  damage model in small strains and the development of an associated numerical relaxation algorithm. We start with the consideration of a one-dimensional scalar damage model to discuss the important results of the convexification analysis which will be used later in the multi-dimensional framework. Afterwards a relaxation method based on an assumption of *a priori isotropic microstructures* is developed and applied to a two-dimensional isochoric damage model. It is shown that in two dimensions the relaxation based on *isotropic microstructures* coincides with the *first-order rank-one convexification*. The algorithm is then extended to general three-dimensional framework. Contrary to single slip models, there is hardly any study on the application of relaxation methods to damage mechanics. To our knowledge FRANCFORT & MARIGO [71], SCHMIDT-BALDASSARI & HACKL [196] and GÜRSES & MIEHE [86] are the only investigations. Finally, the performance of the relaxation algorithm is demonstrated by means of some numerical examples.

### 6.1. The Model Problem: Isotropic Damage Mechanics

**6.1.1. One-Dimensional Damage Model.** For the damage model-problem under consideration the scalar internal variable and the dual thermodynamical force are identified as

$$\mathcal{I} := \alpha \quad \text{and} \quad \mathcal{F} := \beta \quad (6.1)$$

with  $\alpha, \beta \in \mathcal{R}_+$ . The model problem is completed by the definition of the fundamental constitutive functions  $\psi$  and  $f$  for the energy storage and the level set of the elastic domain, respectively. The elastic response is governed by the energy storage

$$\psi(\varepsilon, \alpha) = [1 - d(\alpha)] \psi_0(\varepsilon) \quad \text{with} \quad \psi_0(\varepsilon) = \frac{1}{2} E \varepsilon^2 \quad (6.2)$$

as a function of the linearized scalar strain  $\varepsilon \in \mathcal{R}$  and the internal variable  $\alpha \in \mathcal{R}_+$ . In equation (6.2)  $\psi_0$  represents the effective elastic storage mechanism,  $d(\alpha)$  is the damage function and  $E \in \mathcal{R}_+$  denotes the elasticity modulus. The damage function is parameterized in terms of the scalar internal variable  $\alpha \in \mathcal{R}_+$  and allowed to take values between 0 and 1, i.e.  $d : \mathcal{R}_+ \rightarrow [0, 1]$ . The damage law as illustrated in Figure 6.1a is a monotonously increasing function of  $\alpha$  and assumed to have the particular form

$$d(\alpha) = d_\infty \left[ 1 - \exp\left(-\frac{\alpha}{\eta}\right) \right] \quad (6.3)$$

with  $\eta \in \mathcal{R}^+$ ,  $d_\infty \in [0, 1]$  specifying the saturation intensity and the maximum damage, respectively. Similar to usual damage models,  $d = 0$  stands for no damage whereas  $d = 1$  means a complete deterioration of the solid. The material parameters used in computations are  $E = 1 \text{ MPa}$ ,  $d_\infty = 0.99 [-]$  and  $\eta = 2.5 [-]$ . Here we require proper modifications of (3.2) and (3.3)<sub>2</sub> for the small strain context under consideration, i.e.

$$\boldsymbol{\sigma} = \partial_\varepsilon \psi(\boldsymbol{\varepsilon}, \mathcal{I}) \quad \text{and} \quad \mathcal{F} = -\partial_{\mathcal{I}} \psi(\boldsymbol{\varepsilon}, \mathcal{I}) . \quad (6.4)$$

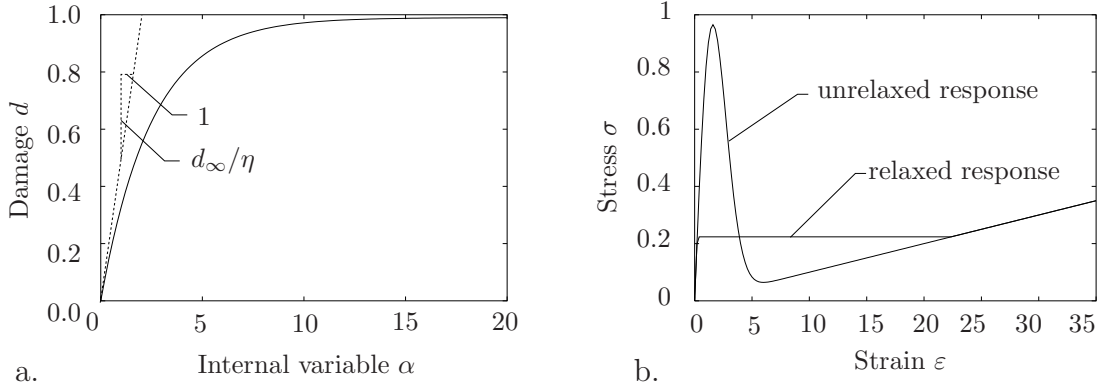


**Figure 6.1:** a.) Saturation type damage evolution law b.) Visualization of the non-convex and convexified constitutive stress response.

For further details of the incremental variational formulation of inelasticity in the geometrically linear theory see MIEHE [142]. Then exploitation of (6.4) yields the stress and the internal force

$$\sigma = (1 - d) \sigma_0 \quad \text{with} \quad \sigma_0 = \frac{\partial \psi_0(\varepsilon)}{\partial \varepsilon} \quad \text{and} \quad \beta = \psi_0 \frac{\partial d(\alpha)}{\partial \alpha} \quad (6.5)$$

With regard to the level set and the threshold we consider the functions

$$f(\beta) = \beta \quad \text{and} \quad c(\alpha) = \alpha \frac{\partial d(\alpha)}{\partial \alpha}. \quad (6.6)$$

Note that as a result of the above defined functions one identifies the internal variable with the effective strain energy, i.e.  $\alpha = \psi_0$ . Furthermore, the inelastic multiplier  $\dot{\gamma}$  in (3.19) coincides with the evolution of the internal variable  $\dot{\gamma} = \dot{\alpha}$ . Insertion of these results and (6.6) into the definition of the dissipation function yields

$$\boxed{\phi = \dot{\alpha} \alpha \frac{\partial d(\alpha)}{\partial \alpha}}. \quad (6.7)$$

Integration of the dissipation function within the time increment  $[t_n, t_{n+1}]$  gives

$$\Phi_{n,n+1} = \int_{t_n}^{t_{n+1}} \phi dt = d(\alpha_{n+1})[\alpha_{n+1} - \eta] - d(\alpha_n)[\alpha_n - \eta] + d_\infty(\alpha_{n+1} - \alpha_n). \quad (6.8)$$

In what follows we evaluate the discrete variational formulation of inelasticity, which is outlined in the large strain framework in Section 3.1, for the geometrically linear setting. For the model problem the integration of (3.19)<sub>1</sub> with a backward Euler algorithm yields the update  $\alpha_{n+1} = \alpha_n + \gamma$  of the internal variable with  $\gamma = \dot{\gamma}(t_{n+1} - t_n)$ . The incremental stress potential  $W$  defined in (3.10) has the following simplified representation

$$W(\varepsilon_{n+1}) = \min_{\gamma} \left\{ \frac{1}{2} [1 - d_{n+1}(\gamma)] E \varepsilon_{n+1}^2 - \frac{1}{2} [1 - d_n] E \varepsilon_n^2 + \Phi_{n,n+1}(\gamma) \right\} \quad (6.9)$$

where  $d_{n+1}(\gamma) = d(\alpha_{n+1}) = d(\alpha_n + \gamma)$  and  $d_n = d(\alpha_n)$ . For the case of inelastic loading the incremental multiplier  $\gamma$  is obtained by the simple formula

$$\gamma = \frac{1}{2} E \varepsilon_{n+1}^2 - \alpha_n \quad (6.10)$$

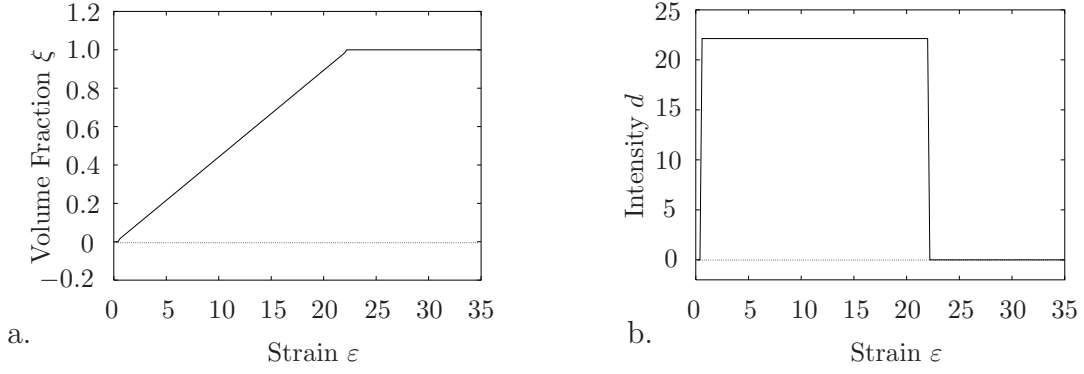


**Figure 6.2:** Development of the volume fraction and the intensity of micro-bifurcation. a.) The volume fraction increases linearly from  $\xi = 0$  to the final value  $\xi = 1$ . b.) The constant intensity of micro-bifurcation  $d = 22.1354$  determines the distance between the two phases (+) and (-).

identifying the current internal variable  $\alpha_{n+1}$  with the effective strain energy  $\psi_0$ , i.e.  $\alpha_{n+1} = \frac{1}{2} E \varepsilon_{n+1}^2$ . On the other hand, an elastic unloading leads to  $\alpha_{n+1} = \alpha_n$ . Exploitation of (3.9) and (3.14) together with above results yields the stress and tangent modulus

$$\sigma_{n+1} = (1 - d_{n+1}) E \varepsilon_{n+1} \quad \text{and} \quad \mathbb{C}_{n+1} = (1 - d_{n+1}) E - \frac{\partial d(\alpha_{n+1})}{\partial \alpha} E^2 \varepsilon_{n+1}^2. \quad (6.11)$$

Note that these formulas only hold as long as the incremental stress potential  $W(\varepsilon_{n+1})$  is convex. In order to detect whether  $W$  is convex for a given strain  $\varepsilon_{n+1}$  we consider the actual strain  $\varepsilon_{n+1}$  to be described by an interpolation between two strains  $\varepsilon^+$  and  $\varepsilon^-$ , i.e.  $\varepsilon_{n+1} := \xi \varepsilon^+ + (1 - \xi) \varepsilon^-$ . For the one-dimensional problem under consideration we employ the ansatz proposed in LAMBRECHT, MIEHE & DETTMAR [122]

$$\varepsilon^- := \varepsilon_{n+1} - \xi d \quad \text{and} \quad \varepsilon^+ := \varepsilon_{n+1} + (1 - \xi) d \quad (6.12)$$

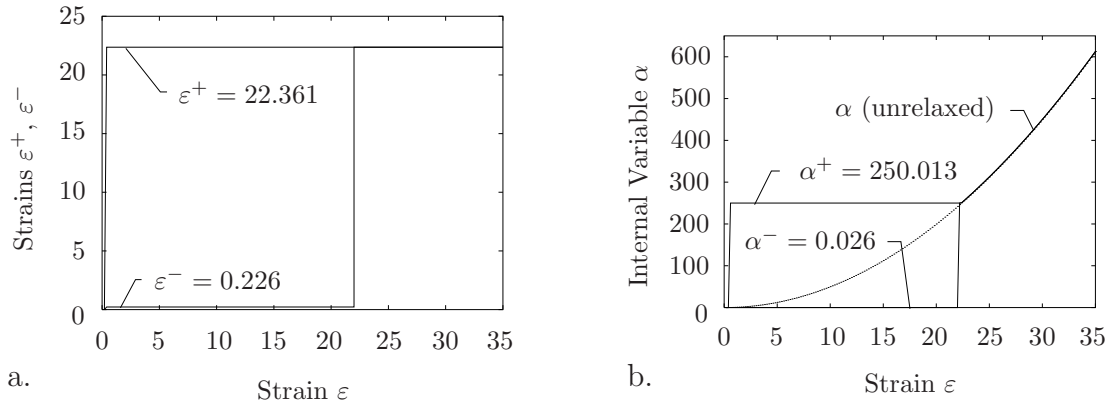


**Figure 6.3:** Development of the total strains and the internal damage variables in the micro-phases. a.) The strains in the phases  $\varepsilon^+$ ,  $\varepsilon^-$  do not change during the convexification analysis. b.) The internal damage variables  $\alpha^+$ ,  $\alpha^-$  in the phases remain constant as well in the non-convex span.

**Box 6.1:** One-Dimensional Two-Phase Relaxation Algorithm.

1. Determine a priori constant phases  $\varepsilon^+$ ,  $\varepsilon^-$  and micro bifurcation  $d = \varepsilon^+ - \varepsilon^-$  numerically
2. Given  $\varepsilon_{n+1}$  and  $\xi_n$  determine  $\xi_{n+1}$  by a case distinction scheme
  - A. Initial stable homogeneous state  $\xi_n = 0$ 
    - a.)  $\varepsilon_{n+1} \leq \varepsilon^-$ :  $\xi_{n+1} = 0$ ,
    - b.)  $\varepsilon^+ > \varepsilon_{n+1} > \varepsilon^-$ :  $\xi_{n+1} = (\varepsilon_{n+1} - \varepsilon^-) / (\varepsilon^+ - \varepsilon^-)$ ,
  - B. Phase decay of homogeneous state  $0 < \xi_n < 1$ 
    - a.)  $\varepsilon_{n+1} \leq \xi_n \varepsilon^+ + (1 - \xi_n) \varepsilon^-$ :  $\xi_{n+1} = \xi_n$
    - b.)  $\xi_n \varepsilon^+ + (1 - \xi_n) \varepsilon^- < \varepsilon_{n+1} < \varepsilon^+$ :  $\xi_{n+1} = (\varepsilon_{n+1} - \varepsilon^-) / (\varepsilon^+ - \varepsilon^-)$ ,
    - c.)  $\varepsilon_{n+1} \geq \varepsilon^+$ :  $\xi_{n+1} = 1$ ,
  - C. Recovery of stable homogeneous state  $\xi_n = 1$ :  $\xi_{n+1} = 1$
3. Compute the relaxed stress and tangent modulus

$$\bar{\sigma}_{n+1} = \partial_\varepsilon W_C(\varepsilon_{n+1}) \quad \text{and} \quad \bar{C}_{n+1} = \partial_{\varepsilon\varepsilon}^2 W_C(\varepsilon_{n+1})$$

that parameterizes  $\varepsilon^+$  and  $\varepsilon^-$  in terms of the variables  $\xi$  and  $d$ . The variable  $d = \varepsilon^+ - \varepsilon^-$  is denoted as the intensity of the micro-bifurcation and  $\xi$  as the volume fraction. Then convexity of  $W$  is guaranteed if

$$W(\xi\varepsilon^+ + (1 - \xi)\varepsilon^-) \leq \inf_{\xi, d} \{ \xi W(\varepsilon^+) + (1 - \xi)W(\varepsilon^-) \} \quad (6.13)$$

holds for all  $\xi \in [0, 1]$  and  $d \in \mathcal{R}_+$ . If the condition (6.13) is not fulfilled then a convexification procedure needs to be performed. The convexification requires at each time step for each Gauss point the solution of a non-convex optimization problem to determine the micro-variables  $\xi$ ,  $d$  and the convexified incremental potential  $W_C$ , i.e.

$$W_C(\varepsilon_{n+1}) = \inf_{\xi, d} \{ \xi W(\varepsilon^+) + (1 - \xi)W(\varepsilon^-) \}. \quad (6.14)$$

Recall that this minimization problem in a more general setting of rank-one convexity of two-dimensional problems has already been discussed in Section 3.2.1. The relaxed stress response that is obtained from the non-convex optimization problem is plotted together with the original (unrelaxed) response in the Figure 6.1b. As a result of the numerical convexification, it is found that the micro-variable  $d$  remains *constant* for the whole non-convex range of the incremental potential. The evolutions of  $\xi$  and  $d$  are plotted in Figure 6.2 which are computed by a numerical convexification algorithm with respect to both variables. From Figure 6.2b it is clear that micro-variable  $d$  remains constant. Consequently, it is not necessary to solve the minimization problem for two variables  $[\xi, d]$  at each time step. In fact one needs to determine micro-variable  $d$  once numerically and then it is possible to compute  $\xi$  directly. The two-phase relaxation analysis can be

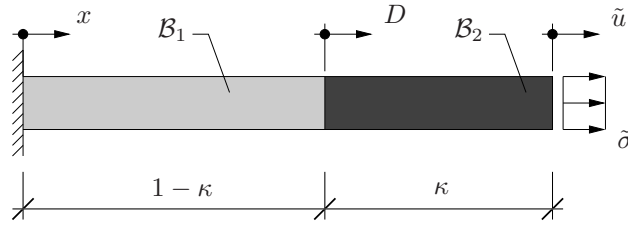


**Figure 6.4:** Localization of a bar in tension. The test specimen under consideration consists of two parts:  $\mathcal{B}_2$  with length  $\kappa$  and  $\mathcal{B}_1$  with length  $1 - \kappa$ . In  $\mathcal{B}_1$  the maximum damage  $d_\infty$  is decreased by 0.0001 % in order to trigger the localization.

summarized in two steps: We (i) *a priori* determine the *constant* micro-phases  $\varepsilon^\pm$  and the micro-intensity  $d$  *numerically* and (ii) set up a *case distinction scheme* depending on the volume fraction  $\xi_n$  of the previous time step and the current strain  $\varepsilon_{n+1}$ . The algorithm is summarized in Box 6.1. Such an algorithm obviously does not need any numerical solution of non-convex minimization problem at *each time step* and consequently is very robust and computationally efficient.

We close the one-dimensional section by consideration of an example from localization in strain softening materials. Main goal is the demonstration of the mesh invariance of the proposed relaxation technique. We consider the bar depicted in Figure 6.4 of length and cross section area 1, subject to a tensile stress  $\bar{\sigma}$ . The bar is fixed at its left boundary. This example in the context of strain softening elastoplasticity was previously investigated in LAMBRECHT, MIEHE & DETTMAR [122]. In order to point out the mesh dependence of the unrelaxed formulation we discretize the bar with two elements  $\mathcal{B}_1$  and  $\mathcal{B}_2$  for five different lengths  $\kappa = 0.2/0.4/0.6/0.8/1.0$ . A localization of the homogeneous boundary value problem is triggered by decreasing the maximum damage  $d_\infty$  in the element  $\mathcal{B}_1$  by 0.0001 %. Figure 6.5a depicts the load-displacement curves for the different discretizations mentioned above. We start at the origin of the diagram and proceed on the loading branch. At the peak of the curves in Figure 6.5a we observe a loss of global structural stability documented by a change of sign of the tangent. After the peak the element

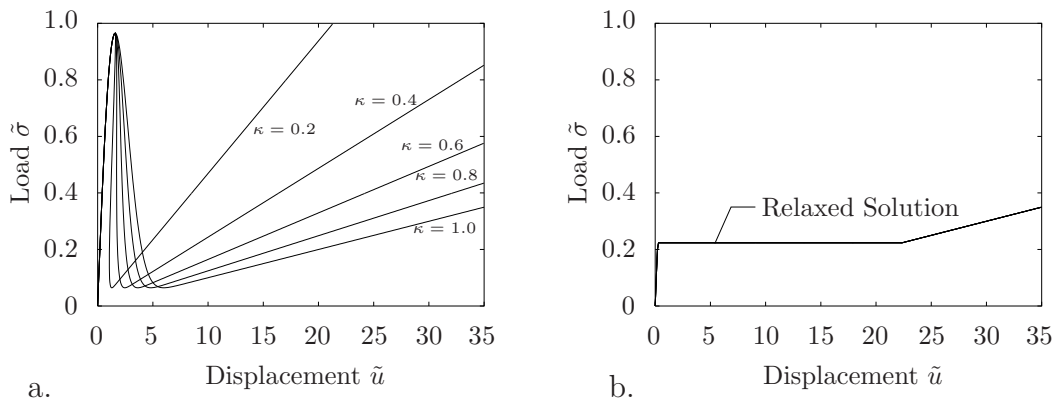


**Figure 6.5:** Global load-displacement curves of imperfect test specimen. a.) Visualization of the length dependent response for different choices  $\kappa$  within the standard formulation. b.) Invariant (relaxed) solution due to the convexification analysis.



$\mathcal{B}_1$  switches to a post-critical path while the element  $\mathcal{B}_2$  switches back to the elastic unloading path. The non-convex analysis yields the spectrum of equilibrium paths in Figure 6.5a. They document the well-known strong mesh dependence of the non-objective post-critical analysis. These post-critical results are physically meaningless. The crucial mesh dependence was pointed out for example by DE BORST [54] and BELYTSCHKO, FISH & ENGELMANN [21]. The ill-posed boundary value problem can be transformed into a well-posed one by means of the relaxation method proposed. The relaxed analysis yields an identical result for all mesh densities. The mesh invariant post-critical equilibrium path is documented in Figure 6.5b.

**6.1.2. Two-Dimensional Isochoric Damage Model.** In this section we consider a two-dimensional isochoric damage model which is described by the fundamental constitutive functions  $\psi$  and  $f$  for the energy storage and the level set of the elastic domain, respectively. The elastic response is governed by the strain energy

$$\psi(\boldsymbol{\varepsilon}, \alpha) = \frac{1}{2} \kappa \operatorname{tr}^2[\boldsymbol{\varepsilon}] + [1 - d(\alpha)] \psi_0^{iso}(\boldsymbol{\varepsilon}) \quad \text{with} \quad \psi_0^{iso}(\boldsymbol{\varepsilon}) = \mu \|\operatorname{dev}[\boldsymbol{\varepsilon}]\|^2. \quad (6.15)$$

Here,  $\kappa \in \mathcal{R}_+$  denotes the bulk modulus and  $\mu \in \mathcal{R}_+$  is the shear modulus. Note that in two-dimensional setting, i.e.  $\boldsymbol{\varepsilon} \in \mathcal{R}^{2 \times 2}$ , the isochoric-volumetric split is given as

$$\boldsymbol{\varepsilon} = \operatorname{dev}[\boldsymbol{\varepsilon}] + \frac{1}{2} \operatorname{tr}[\boldsymbol{\varepsilon}] \mathbf{1}. \quad (6.16)$$

Analogous to the one-dimensional case, the internal variable and the dual internal force are identified as  $\boldsymbol{\mathcal{I}} := \alpha$  and  $\boldsymbol{\mathcal{F}} := \beta$ . Note that the damage function  $d(\alpha)$  affects only the isochoric contribution of  $\psi$  and assumed to have the particular form

$$d(\alpha) = d_\infty [1 - (1 + \vartheta \alpha)^{-\nu}] \quad (6.17)$$

in terms of the material parameters  $d_\infty \in [0, 1]$ ,  $\vartheta \in \mathcal{R}_+$  and  $\nu \in \mathcal{R}_+ \setminus \{1\}$ . In principle, the damage law (6.17) has a saturation type behavior similar to the one shown in Figure 6.1. Evaluation of (6.4) leads to the expressions for the stresses  $\boldsymbol{\sigma}$  and thermodynamical forces  $\beta$

$$\boldsymbol{\sigma} = \kappa \operatorname{tr}[\boldsymbol{\varepsilon}] \mathbf{1} + [1 - d(\alpha)] 2\mu \operatorname{dev}[\boldsymbol{\varepsilon}] \quad \text{and} \quad \beta = \psi_0^{iso} \frac{\partial d(\alpha)}{\partial \alpha}. \quad (6.18)$$

With regard to the level set and the threshold we consider the same form as (6.6), i.e.

$$f(\beta) = \beta \quad \text{and} \quad c(\alpha) = \alpha \frac{\partial d(\alpha)}{\partial \alpha}. \quad (6.19)$$

Notice that in the case of an inelastic loading, (6.19) identifies the internal variable with the effective strain energy  $\alpha = \psi_0^{iso}$  since during the evolution of damage  $f(\beta) = c(\alpha)$  holds. As a consequence of definition (6.19), the normal direction has the simple representation  $\partial_\beta f = 1$ . The inelastic multiplier then coincides with the evolution of the internal variable  $\dot{\gamma} = \dot{\alpha}$ . Following the same steps as in Section 6.1.1 we get the dissipation function  $\phi = \dot{\alpha} \alpha \frac{\partial d(\alpha)}{\partial \alpha}$  in the same form of (6.7). Integration of the dissipation function  $\phi$  within the time increment  $\Delta t = [t_n, t_{n+1}]$  yields

$$\begin{aligned} \Phi_{n,n+1} &= d(\alpha_{n+1})\alpha_{n+1} - d(\alpha_n)\alpha_n \\ &\quad - d_\infty [\alpha_{n+1} - \alpha_n - \vartheta^{-1}(1 - \nu)[(1 + \vartheta\alpha_{n+1})^{1-\nu} - (1 + \vartheta\alpha_n)^{1-\nu}]] \end{aligned} \quad (6.20)$$

where the current internal variable is computed from the update  $\alpha_{n+1} = \alpha_n + \gamma$  with  $\gamma := \dot{\gamma}\Delta t$ . The incremental potential  $W$  in (3.10) can be written as a sum of a volumetric and an isochoric contributions  $W = W^{vol} + W^{iso}$

$$\left. \begin{aligned} W^{vol}(e_{n+1}) &= \frac{1}{2}\kappa(e_{n+1}^2 - e_n^2) \\ W^{iso}(q_{n+1}) &= \inf_{\gamma} \{ 2\mu [1 - d_{n+1}(\gamma)] q_{n+1}^2 - 2\mu [1 - d_n] q_n^2 + \Phi_{n,n+1}(\gamma) \} \end{aligned} \right\} \quad (6.21)$$

with the definitions  $e := \text{tr}[\boldsymbol{\varepsilon}]$ ,  $q := \|\text{dev}[\boldsymbol{\varepsilon}]\|$ ,  $d_{n+1}(\gamma) = d(\alpha_{n+1}) = d(\alpha_n + \gamma)$  and  $d_n = d(\alpha_n)$ . Then the update of the internal variable reads

$$\alpha_{n+1} = \begin{cases} \psi_0^{iso} = \mu q_{n+1}^2 & \text{if } 2\mu q_{n+1}^2 > \alpha_n \\ \alpha_n & \text{else .} \end{cases} \quad (6.22)$$

Exploitation of (6.4)<sub>1</sub> yields the stresses and moduli for the case of damage evolution  $d(\alpha_{n+1}) > d(\alpha_n)$

$$\begin{aligned} \boldsymbol{\sigma}_{n+1} &= \kappa \text{tr}[\boldsymbol{\varepsilon}_{n+1}] \mathbf{1} + [1 - d(\alpha_{n+1})] 2\mu \text{dev}[\boldsymbol{\varepsilon}_{n+1}] \\ \mathbb{C}_{n+1} &= \kappa \mathbf{1} \otimes \mathbf{1} + [1 - d(\alpha_{n+1})] 2\mu \mathbb{P} - \frac{\partial d(\alpha_{n+1})}{\partial \alpha} 4\mu^2 \text{dev}[\boldsymbol{\varepsilon}_{n+1}] \otimes \text{dev}[\boldsymbol{\varepsilon}_{n+1}] \end{aligned} \quad (6.23)$$

where  $\mathbb{P} = \mathbb{I} - \mathbf{1} \otimes \mathbf{1}/3$  is the fourth-order deviatoric projection tensor. In the case of an elastic unloading, i.e.  $d(\alpha_{n+1}) = d(\alpha_n)$ , the stresses are given by the same formula (6.23)<sub>1</sub> and the moduli expression becomes

$$\mathbb{C}_{n+1} = \kappa \mathbf{1} \otimes \mathbf{1} + [1 - d(\alpha_{n+1})] 2\mu \mathbb{P} . \quad (6.24)$$

Note that the formula (6.23) holds, provided that the incremental stress potential  $W(\boldsymbol{\varepsilon}_{n+1})$  satisfies the rank-one convexity condition (3.34). Otherwise the convexification procedure needs to be performed. For geometrically linear theory under consideration we introduce the appropriate ansatz in a similar way to (3.28)

$$\boxed{\begin{aligned} \boldsymbol{\varepsilon}^+ &:= \boldsymbol{\varepsilon}_{n+1} + (1 - \xi) d(\mathbf{m} \otimes \mathbf{n} + \mathbf{n} \otimes \mathbf{m}) \\ \boldsymbol{\varepsilon}^- &:= \boldsymbol{\varepsilon}_{n+1} - \xi d(\mathbf{m} \otimes \mathbf{n} + \mathbf{n} \otimes \mathbf{m}) \end{aligned}} \quad (6.25)$$

which fulfills the symmetry condition on  $\boldsymbol{\varepsilon}^+$  and  $\boldsymbol{\varepsilon}^-$ . Notice carefully that  $\boldsymbol{\varepsilon}^+$  and  $\boldsymbol{\varepsilon}^-$  are not rank-one connected. However, rank-one connectivity condition applies on the displacement gradients in small strain setting, i.e.  $\text{rank}[\nabla \mathbf{u}^+ - \nabla \mathbf{u}^-] \leq 1$ . In what follows we modify (6.25) and consider as a *specific choice* the parameterization given below

$$\boxed{\begin{aligned} \boldsymbol{\varepsilon}^- &:= \boldsymbol{\varepsilon}_{n+1} - \xi d \boldsymbol{\varepsilon}_{n+1} / \|\boldsymbol{\varepsilon}_{n+1}\| \\ \boldsymbol{\varepsilon}^+ &:= \boldsymbol{\varepsilon}_{n+1} + (1 - \xi) d \boldsymbol{\varepsilon}_{n+1} / \|\boldsymbol{\varepsilon}_{n+1}\| . \end{aligned}} \quad (6.26)$$

The motivation and the reason for this choice of parameterization will be more clear later. Since the damage affects only the isochoric part of the energy storage, see (6.15), the volumetric part  $W^{vol}(e_{n+1})$  of the incremental potential remains convex. Consequently, application of the relaxation procedure is required for the isochoric part  $W^{iso}(q_{n+1})$  of the

potential only. The relaxed potential then can be written as a sum of a volumetric part and a convexified isochoric part,

$$W_C(\boldsymbol{\varepsilon}_{n+1}) = W^{vol}(e_{n+1}) + W_C^{iso}(q_{n+1}) . \quad (6.27)$$

where  $e_{n+1} := \text{tr}[\boldsymbol{\varepsilon}_{n+1}]$  and  $q := \|\text{dev}[\boldsymbol{\varepsilon}_{n+1}]\|$ . The convexified incremental isochoric potential  $W_C^{iso}$  is defined by the minimization problem similar to (6.14)

$$W_C^{iso}(q_{n+1}) = \inf_{\xi, d} \{ \bar{W}^h(q_{n+1}, \xi, d) \} \quad \text{with} \quad \bar{W}^h = \xi W^{iso}(q^+) + (1 - \xi) W^{iso}(q^-) \quad (6.28)$$

in terms of the isochoric shear intensities of the phases

$$q^+ = q_{n+1} + (1 - \xi) d \quad \text{and} \quad q^- = q_{n+1} - \xi d \quad (6.29)$$

which can be obtained with some algebraic manipulations of the specific parameterization of the phases (6.26) written solely for deviatoric strains, i.e.

$$\begin{aligned} \text{dev}[\boldsymbol{\varepsilon}^-] &:= \text{dev}[\boldsymbol{\varepsilon}_{n+1}] - \xi d \text{dev}[\boldsymbol{\varepsilon}_{n+1}] / \|\text{dev}[\boldsymbol{\varepsilon}_{n+1}]\| \\ \text{dev}[\boldsymbol{\varepsilon}^+] &:= \text{dev}[\boldsymbol{\varepsilon}_{n+1}] + (1 - \xi) d \text{dev}[\boldsymbol{\varepsilon}_{n+1}] / \|\text{dev}[\boldsymbol{\varepsilon}_{n+1}]\| . \end{aligned} \quad (6.30)$$

Equation (6.29) can be written equivalently as follows

$$\begin{aligned} \|\text{dev}[\boldsymbol{\varepsilon}^+]\| &= \|\text{dev}[\boldsymbol{\varepsilon}]\| + (1 - \xi) d \\ \|\text{dev}[\boldsymbol{\varepsilon}^-]\| &= \|\text{dev}[\boldsymbol{\varepsilon}]\| - \xi d . \end{aligned} \quad (6.31)$$

The parameterization (6.31) can be interpreted as a decomposition of the norm of homogeneous isochoric strains into two phases. Due to the structure in (6.29) the *two-dimensional problem* becomes similar to the *one-dimensional damage model* discussed in Section 6.1.1. In other words, the micro-variable  $d$  and the isochoric micro-intensities  $q^+$  and  $q^-$ , which denote the start and end points of the rank-one convex hull, remain constant for any deformation process. These facts allow the derivation of a *semi-analytical solution* of the two-phase relaxation analysis in two steps: We (i) a priori determine the micro-intensities  $q^\pm$  numerically and (ii) set up a case distinction scheme depending on the volume fraction  $\xi_n$  of the previous time step and the current micro-intensity  $q_{n+1}$ . The algorithm is summarized in Box 6.2. Notice carefully that such an algorithm obviously does not need any numerical solution of non-convex minimization problem at each time step and consequently is very robust and computationally efficient.

**Remark:** Computation of the first-order rank-one convex hull normally requires determination of the laminate orientation vectors in addition to  $\xi$  and  $d$ . In the two-dimensional setting the first order necessary conditions (3.35) of rank-one convexification for the laminate vectors  $\mathbf{m} = [\cos \varphi \ \sin \varphi]$  and  $\mathbf{n} = [\cos \chi \ \sin \chi]$

$$\bar{W}_{,\varphi}^h = 0 \quad \text{and} \quad \bar{W}_{,\chi}^h = 0 \quad (6.32)$$

lead to a priori identification of the laminate orientations with the principal shear directions. Consequently, one obtains the following relation between the deviatoric strains and the dyadic product of the laminate vectors

$$(\mathbf{m} \otimes \mathbf{n} + \mathbf{n} \otimes \mathbf{m}) = \zeta \text{dev}[\boldsymbol{\varepsilon}] \quad (6.33)$$

**Box 6.2:** Two-Dimensional Two-Phase Relaxation Algorithm.

1. Determine a priori constant phases  $q^-$ ,  $q^+$  and micro-bifurcation  $d = q^+ - q^-$  numerically,
2. Given  $\boldsymbol{\varepsilon}_{n+1} = \text{dev}[\boldsymbol{\varepsilon}_{n+1}] + \frac{1}{2} \text{tr}[\boldsymbol{\varepsilon}_{n+1}] \mathbf{1}$  and  $\xi_n$ . Compute  $q_{n+1} = \|\text{dev}[\boldsymbol{\varepsilon}_{n+1}]\|$  and determine  $\xi_{n+1}$  by a case distinction scheme:
  - A. Initial stable homogeneous state  $\xi_n = 0$ 
    - a.)  $q_{n+1} \leq q^-$ :  $\xi_{n+1} = 0$ ,
    - b.)  $q^+ > q_{n+1} > q^-$ :  $\xi_{n+1} = (q_{n+1} - q^-) / (q^+ - q^-)$ ,
  - B. Phase decay of homogeneous state  $0 < \xi_n < 1$ 
    - a.)  $q_{n+1} \leq \xi_n q^+ + (1 - \xi_n) q^-$ :  $\xi_{n+1} = \xi_n$ ,
    - b.)  $\xi_n q^+ + (1 - \xi_n) q^- < q_{n+1} < q^+$ :  $\xi_{n+1} = (q_{n+1} - q^-) / (q^+ - q^-)$ ,
    - c.)  $q_{n+1} \geq q^+$ :  $\xi_{n+1} = 1$ ,
  - C. Recovery of stable homogeneous state  $\xi_n = 1$ :  $\xi_{n+1} = 1$  .
3. Compute the relaxed stresses and tangent moduli

$$\bar{\boldsymbol{\sigma}}_{n+1} = \partial_{\boldsymbol{\varepsilon}} W_C(\boldsymbol{\varepsilon}_{n+1}) \quad \text{and} \quad \bar{\mathbb{C}}_{n+1} = \partial_{\boldsymbol{\varepsilon}\boldsymbol{\varepsilon}}^2 W_C(\boldsymbol{\varepsilon}_{n+1})$$

with an arbitrary constant  $\zeta \in \mathcal{R}$ . Then the assumed form of the deviatoric strains in the phases (6.25) coincides with (6.26). In other words, the following two decompositions of the deviatoric strains are identical

$$\begin{aligned} \text{dev}[\boldsymbol{\varepsilon}^+] &= \text{dev}[\boldsymbol{\varepsilon}] + (1 - \xi) d \mathbf{A} & \iff & \text{dev}[\boldsymbol{\varepsilon}^+] = \text{dev}[\boldsymbol{\varepsilon}] + (1 - \xi) d (\mathbf{m} \otimes \mathbf{n})^{sym} \\ \text{dev}[\boldsymbol{\varepsilon}^-] &= \text{dev}[\boldsymbol{\varepsilon}] - \xi d \mathbf{A} & & \text{dev}[\boldsymbol{\varepsilon}^-] = \text{dev}[\boldsymbol{\varepsilon}] - \xi d (\mathbf{m} \otimes \mathbf{n})^{sym} \end{aligned}$$

(6.34)

with  $\mathbf{A} = \text{dev}[\boldsymbol{\varepsilon}] / \|\text{dev}[\boldsymbol{\varepsilon}]\|$  and  $(\mathbf{m} \otimes \mathbf{n})^{sym} = (\mathbf{m} \otimes \mathbf{n} + \mathbf{n} \otimes \mathbf{m})$ . Therefore, for two-dimensional isochoric damage model, a relaxation based on first order rank-one laminates (6.25) is equivalent to a relaxation based on isotropic phase decomposition (6.30).

**6.1.3. Extension of Relaxation Algorithm to Three-Dimensional Analysis.**

In this section we employ the ansatz of the phases given in (6.30) for the application of our relaxation algorithm to the three-dimensional framework. The main difference to the two-dimensional case is that in the three-dimensional consideration two parameterizations given in (6.34) do not coincide anymore. However, we consider a relaxation based on the parameterization (6.30) as a reasonable approximation of the rank-one convexification. The elastic response of the three-dimensional model is governed by the free energy given in (6.15) and the damage law is the particular saturation type given in (6.3). Similar to the two-dimensional case it is possible to apply an analytical solution of the two-phase relaxation analysis in two steps: We (i) a priori determine the micro-intensities  $q^\pm$  numerically and (ii) set up a case distinction scheme depending on the volume fraction  $\xi_n$  of the previous time step and the current micro-intensity  $q_{n+1}$ . The algorithm has a

**Table 6.1:** Set of material parameters for 2-D examples.

<i>bulk modulus</i>	–	$\kappa$	=	150.000	$\text{Nmm}^{-2}$
<i>shear modulus</i>	–	$\mu$	=	60.000	$\text{Nmm}^{-2}$
<i>maximum damage</i>	–	$d_\infty$	=	0.999 / 0.975	–
<i>saturation intensity</i>	–	$\vartheta$	=	0.100 / 0.390	–
<i>exponent</i>	–	$\nu$	=	2.000 / 0.950	–

small difference to one specified in Box 6.2 which is the definition of the deviatoric strain tensor. For the three-dimensional algorithm the multiplier in front of  $\text{tr}[\boldsymbol{\varepsilon}_{n+1}]$  has to be changed from  $\frac{1}{2}$  to  $\frac{1}{3}$ . The required derivatives for the computation of relaxed stresses and moduli are given in Appendix B.

**6.1.4. Visualization and Interpretation of Isotropic Microstructures.** We simply assume that the microstructures develop such that the norm of the strain decomposes into phases. A visualization of an evolving deformation microstructure is given in Figure 6.6. The outer circle in Figure 6.6 represents the intensity of the strain while the inner circle denotes the highly damaged (+) phase with volume fraction  $\xi$ . During loading both circles expand but the inner one faster, which corresponds to an increase in the damage of the material. On the other hand, during unloading both circle starts to shrink. However, relative to the outer circle the inner one either grows or stays constant for all loading conditions. This microstructure evolution is consistent with the irreversibility of the damage process which induces a natural restriction on the volume fraction

$$\dot{\xi} \geq 0 \quad \Leftrightarrow \quad \xi_{n+1} \geq \xi_n . \quad (6.35)$$

In other words, the damage is never recovered and having fulfilled (6.35) then the thermodynamical consistency is guaranteed. Note that for any process damage levels  $d^+$  and  $d^-$  of the phases stay constant but the volume fraction  $\xi$  of the highly damaged phase (+) is an increasing function satisfying the physical requirement, namely the increase in the damage variable in a volume averaged sense.

## 6.2. Numerical Examples of Relaxations in Damage Mechanics

We demonstrate the performance of the above outlined relaxation technique by means of representative numerical examples. The main goals of the numerical investigations are

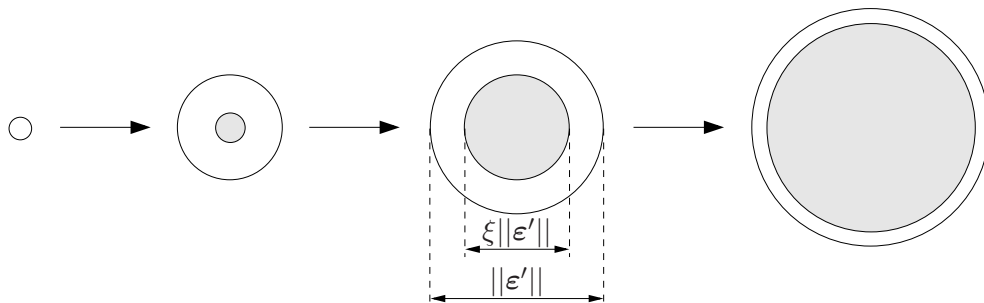


**Figure 6.6:** Visualization of an isotropic deformation microstructure during a loading process. Size of the outer circle is controlled by the norm of the deviatoric strain  $\|\boldsymbol{\varepsilon}'\|$ . The ratio of diameters of inner and outer circles determines the volume fraction  $\xi$ .

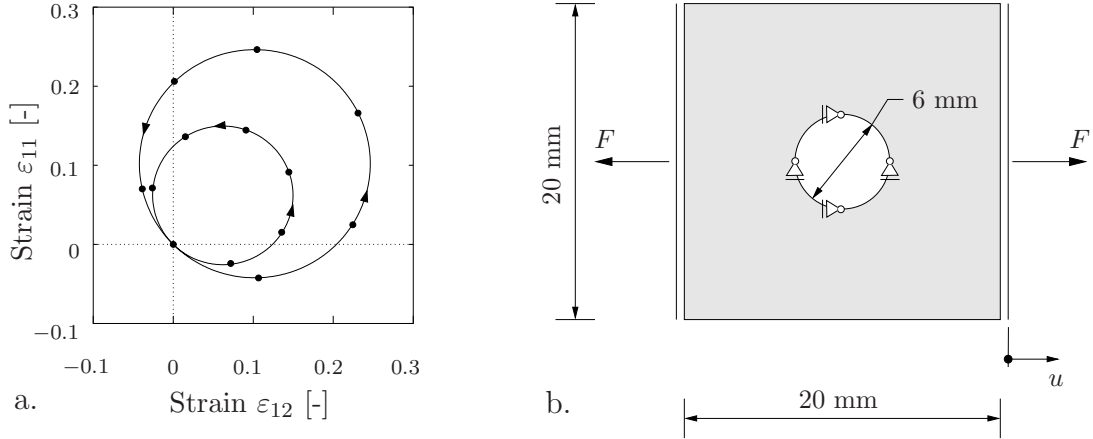


**Figure 6.7:** a.) Cyclic loading test. Isochoric loading path in the  $\varepsilon_{11}$ - $\varepsilon_{12}$  plane. b.) Perforated plate in tension. Geometry, loading and boundary conditions.

the analysis of the *developing microstructures* and the demonstration of the *objectivity of the relaxation technique* proposed. In the first example we investigate a strain-driven cyclic local loading test and document the development of microstructures. The second numerical example is concerned with the tension test of a perforated plate in the two-dimensional and three-dimensional plane strain frameworks. We report on the arising microstructures which are resolved by a convexification of the non-convex incremental stress potential. Comparison of the relaxed and the unrelaxed load-displacement curves underlines the objectivity of the relaxed stress response. The material parameters governing the energy storage function and the level set function for two-dimensional and three-dimensional damage models are summarized in Table 6.1 and Table 6.2, respectively.

**6.2.1. Volume Preserving Cyclic Loading Test.** The first example is concerned with a volume preserving cyclic loading test described by the macroscopic strain tensor

$$\varepsilon = a_i \begin{bmatrix} 1 - \sqrt{2} \cos[\Lambda] & 1 + \sqrt{2} \sin[\Lambda] \\ 1 + \sqrt{2} \sin[\Lambda] & -1 + \sqrt{2} \cos[\Lambda] \end{bmatrix} \quad (6.36)$$

with  $a_1 = 0.062$  for  $0 \leq \Lambda \leq 2\pi$  and  $a_2 = 0.102$  for  $2\pi < \Lambda \leq 4\pi$ . The loading parameter  $\Lambda$  is increased with increments  $\Delta\Lambda = 0.01$  up to the final value  $\Lambda_{max} = 4\pi$ . Figure 6.7a visualizes the isochoric loading path of the test in the  $\varepsilon_{11}$ - $\varepsilon_{12}$ -plane. In Figure 6.8 the development of the microstructures is documented at the points marked in Figure 6.7a. The first eight microstructures correspond to the first cycle ( $a_1 = 0.062$ ) and the following seven to the second cycle ( $a_2 = 0.102$ ). After the loss of material stability two micro-phases  $\varepsilon^\pm$  emerge. The fraction  $\xi$  increases if the intensity  $q = (\varepsilon_{11}^2 + \varepsilon_{12}^2)^{1/2}$  increases as well. Note that in the case of a decrease in intensity  $q$  the fraction  $\xi$  remains constant

**Table 6.2:** Set of material parameters for 3-D examples.

<i>bulk modulus</i>	–	$\kappa$	=	150.000	N mm <sup>-2</sup>
<i>shear modulus</i>	–	$\mu$	=	60.000	N mm <sup>-2</sup>
<i>maximum damage</i>	–	$d_\infty$	=	0.78	–
<i>saturation intensity</i>	–	$\eta$	=	500	–

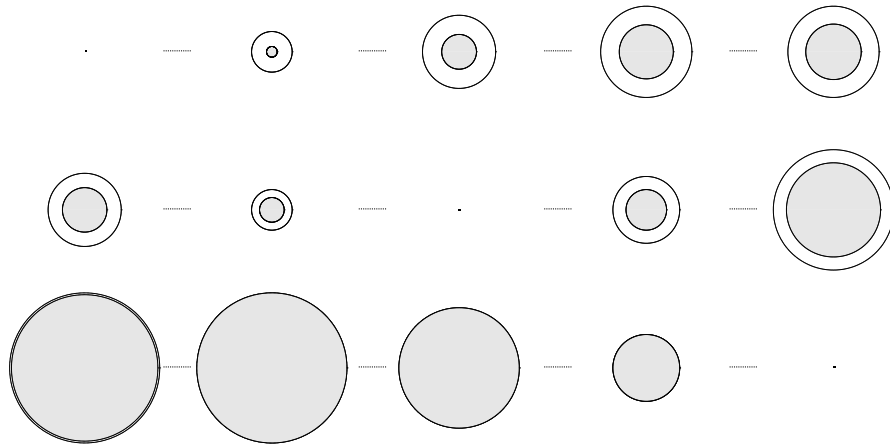


**Figure 6.8:** Cyclic loading test. Development of the microstructures After the loss of material stability microstructures emerge which are resolved as first-order rank-one laminates. The first eight microstructures correspond to the inner cycle, the following seven to the outer one in Figure 6.7a.

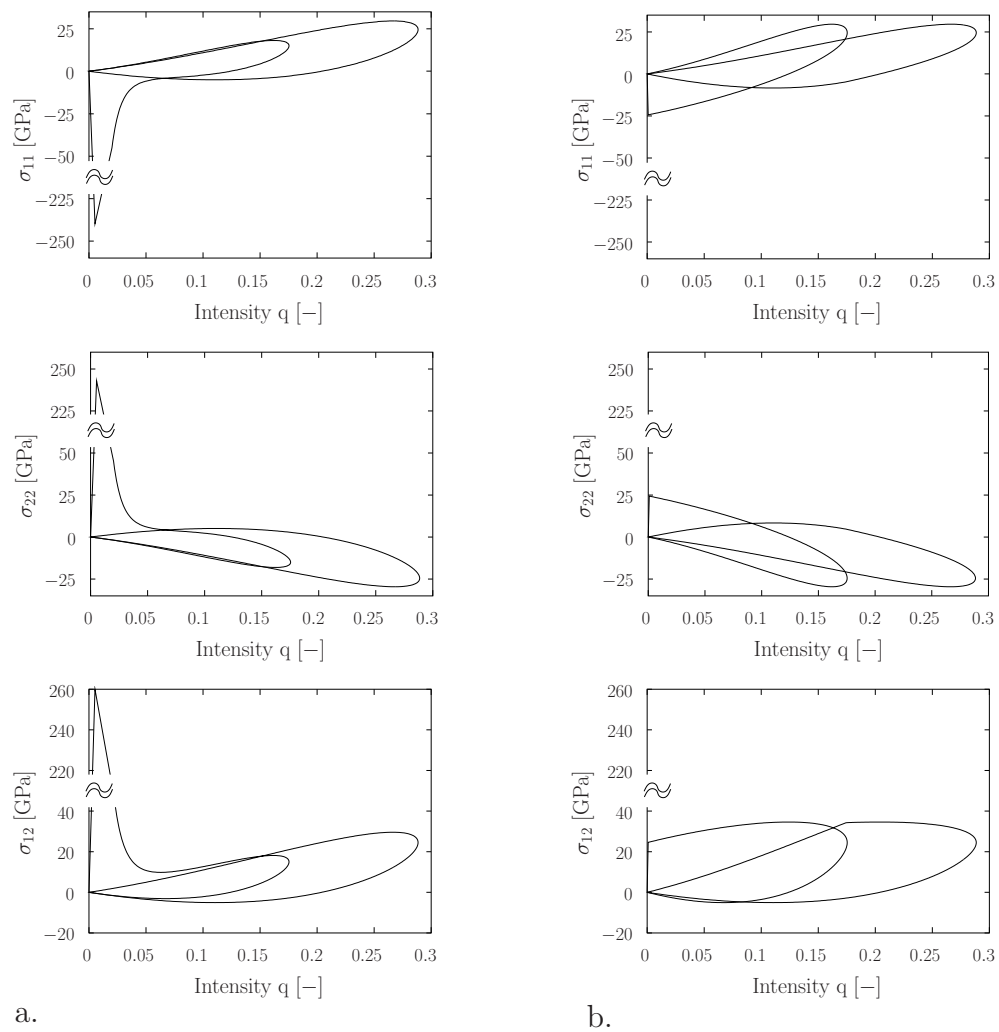


**Figure 6.9:** Comparison of stress components for cyclic loading test obtained by a.) the unrelaxed formulation and b.) the proposed relaxation technique.



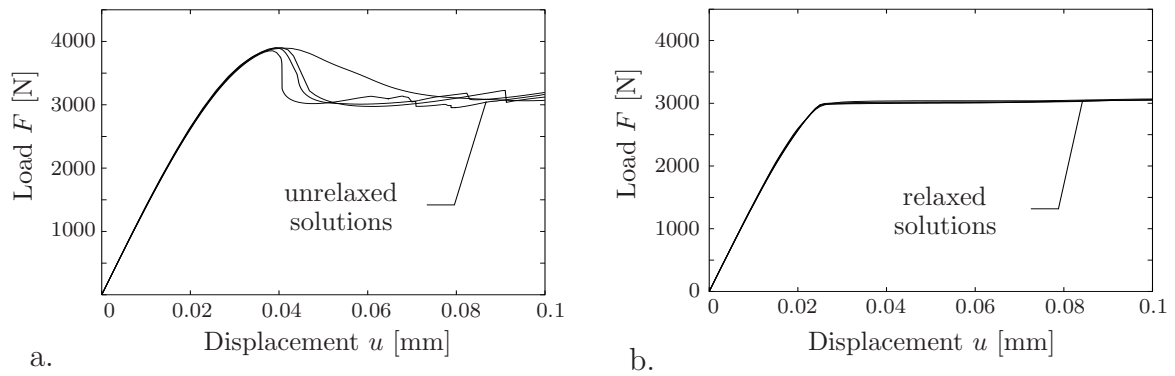


**Figure 6.10:** Perforated plate in tension (Two-dimensional framework). Load-displacement curves for four different *structured* finite element meshes based on a.) the unrelaxed (non-objective) formulation (the finer the mesh the softer the response) and on b.) the proposed relaxation technique. The global response of the relaxed formulation shows no mesh dependency.

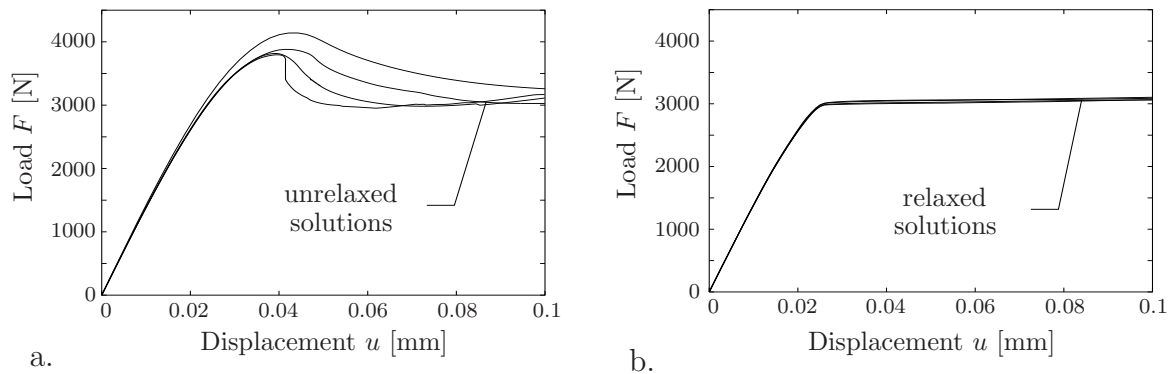


**Figure 6.11:** Perforated plate in tension (Two-dimensional framework). Load-displacement curves for four different *unstructured* finite element meshes based on a.) the unrelaxed (non-objective) formulation (the finer the mesh the softer the response) and on b.) the proposed relaxation technique. The global response of the relaxed formulation shows no mesh dependency.

as pointed out before. During the second cycle a recovery of a single-phase deformation occurs which is highly damaged. The stress components of the unrelaxed and relaxed computations are plotted in Figure 6.9. Note that after the recovery of single-phase state the stress components of both formulations coincide.

### 6.2.2. Tension Test of a Perforated Plate in Two-Dimensional Framework.

The second example analyzes the deformation of a perforated plate in tension. The geometry, loading and boundary conditions are described in Figure 6.7b. Owing to the symmetry, one fourth of the specimen is discretized with 16, 36, 64 and 100 structured finite elements. We also investigate four unstructured meshes with 24, 83, 109 and 204 finite elements. For the simulations the four node enhanced incompatible mode Q1E4 finite element formulation developed by SIMÓ & ARMERO [201] are used. The problem is treated

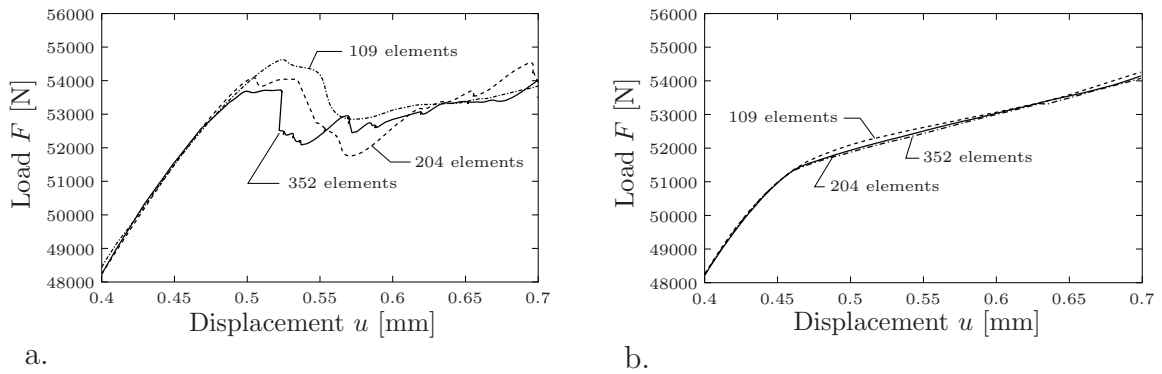


**Figure 6.12:** Perforated plate in tension (Three-dimensional plane strain framework). Zoomed in load-displacement curves for three different finite element meshes based on a.) the unrelaxed (non-objective) formulation (the finer the mesh the softer the response) and on b.) the proposed relaxation technique. The global response of the relaxed formulation shows no mesh dependency.

in a deformation-driven analysis with increments  $\Delta u = 0.001\text{mm}$  up to a maximum displacement of  $u = 0.1\text{mm}$ . The mesh-dependent response of the unrelaxed formulation is evident by considering the load-displacement curves plotted in Figures 6.10a and 6.11a for structured and unstructured meshes, respectively. In contrast to the unrelaxed formulation, application of the proposed relaxation technique yields a mesh-invariant response. The load-deflection curves do not depend on the mesh size and are identical for different mesh densities, see Figures 6.10b and 6.11b. Note that the objectivity of the material behavior is obtained without the introduction of an internal length scale parameter.

### 6.2.3. Tension Test of a Perforated Plate in Three-Dimensional Framework.

In the last example the previous boundary value problem with the geometry specified in Figure 6.7b is investigated in three-dimensional plane strain framework. Owing to the symmetry, one fourth of the specimen is discretized with 109, 204 and 352 unstructured finite elements. The single-phase unrelaxed computations are performed with an arc length method whereas the relaxed simulations are done with a displacement-controlled loading. They are both conducted up to a maximum displacement of  $u = 0.7\text{mm}$ . The mesh-dependent response of the unrelaxed formulation is evident by considering the overall load-displacement curves plotted in Figures 6.12a for three different mesh densities (109, 204 and 352 elements). In contrast to the unrelaxed formulation, the application of the proposed relaxation technique yields a mesh-invariant response, see 6.12b for overall load-displacement diagrams. The localization zones and corresponding unstable regions are given in Figure 6.13 for three different meshes. In Figure 6.14 the evolution of unstable regions are visualized together with the microstructures at the selected elements of the mesh having 204 finite elements for load levels  $u = 0.4, 0.5$  and  $0.6\text{mm}$ .

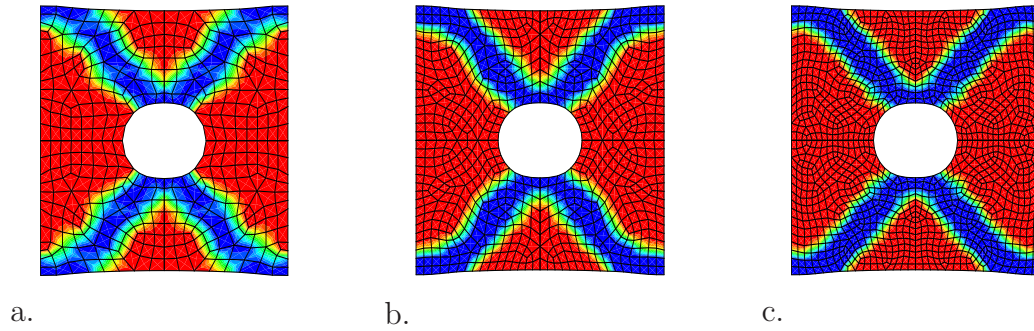


**Figure 6.13:** Perforated plate in tension (Three-dimensional plane strain framework). Comparison of relaxed simulations for three different mesh densities. Distributions of unstable regions at  $u = 0.7$  mm for a) 109, b) 204 and c) 352 finite elements.

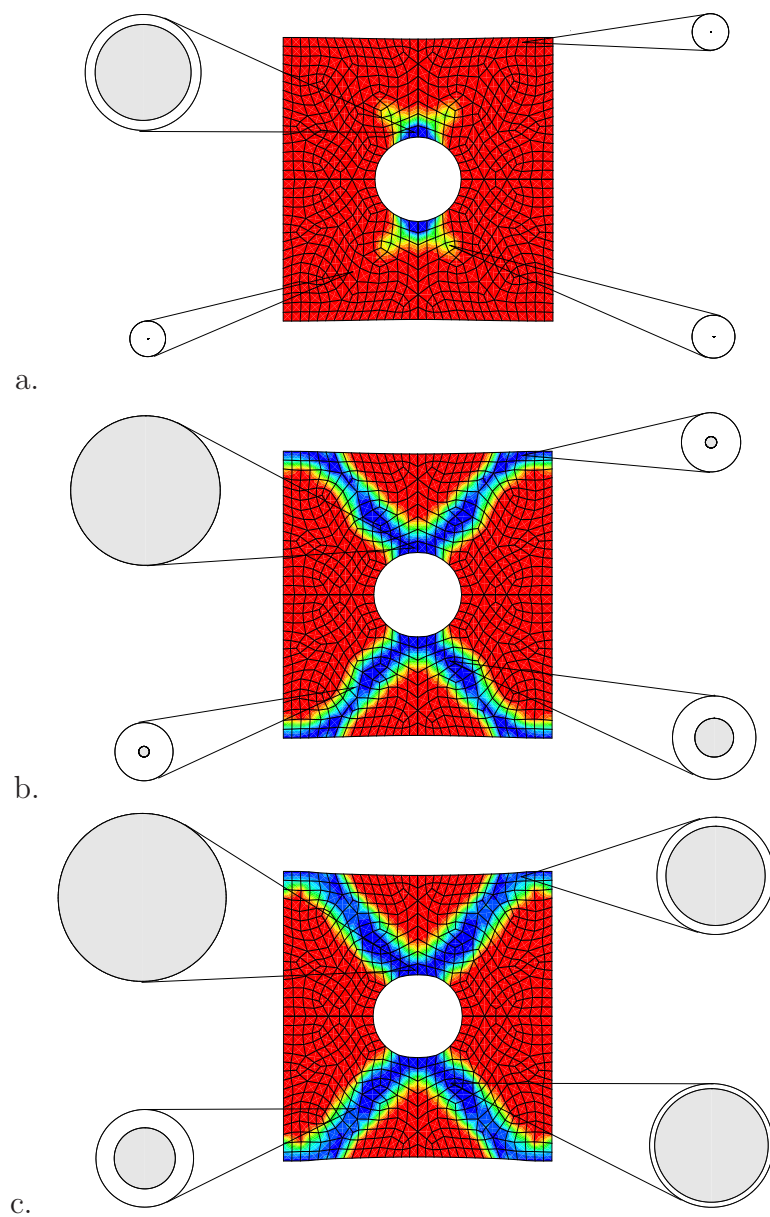


**Figure 6.14:** Perforated plate in tension (Three-dimensional plane strain framework). Evolution of the unstable regions and microstructures at the selected elements of the mesh having 204 finite elements for load levels a.)  $u = 0.4$  mm b.)  $u = 0.5$  mm and c.)  $u = 0.6$  mm.



## 7. Theories of Brittle Fracture

The goal of this section is to give a compact introduction to the fracture mechanics, in particular to the brittle fracture. It starts with the stress concentrations that occur inevitably in solids due to the presence of macroscopic cracks, flaws, defects or microcracks. A quantitative analysis of the stress concentrations in linear elastic bodies with simple geometries are presented as well. Further details of technical nature are provided in Appendices D and E. In addition, different approaches to brittle fracture are briefly pointed out. We refer to the books by KNOTT [114], KANNINEN & POPELAR [111], MEGUID [138], GDOUTOS [77], LAWN [125] and ANDERSON [6] for comprehensive treatments of the topic and the recent works of ERDOGAN [64] and COTTERELL [50] for historical overviews.

### 7.1. Stress Concentrations in Solids

In the sequel, the local stress concentrations in solid bodies with sharp geometrical changes are discussed. Before providing a rigorous prove of the stress concentrations within the theory of linear elasticity, a plausible description is given in terms of *stress trajectories* or *lines of force*.

**7.1.1. Stress Trajectories.** We consider two plates, one homogeneous and the other containing a central elliptical hole, subjected to a uniform tensile stress as depicted in Figure 7.1. An applied stress is transmitted from one end of the plate to the other through the use of lines of forces. In the first plate which is homogenous, the stress trajectories are all over evenly spaced. On the other hand, in the second plate, the lines of forces are spaced uniformly only away from the elliptical hole. As a consequence of the hole, the lines do not remain equally spaced especially in the close neighborhood of the hole. They concentrate near the ends of the hole yielding a decrease in the local spacing between the trajectories. Therefore, more lines of force are flowing through the same area indicating a local increase in the stress field.

**7.1.2. Infinite Plate with Circular Hole under Tension.** After having discussed conceptually the local increase in the stress field due to a sudden change in the geometry, next stress concentrations will be analyzed quantitatively. An infinite plate containing a small circular hole of radius  $a$  is subjected to the remote tensile stress  $\sigma_0$  as indicated in Figure 7.2. The solution of the problem can be obtained from the *Airy stress function* which provides a general framework for two-dimensional elasticity problems. First recall

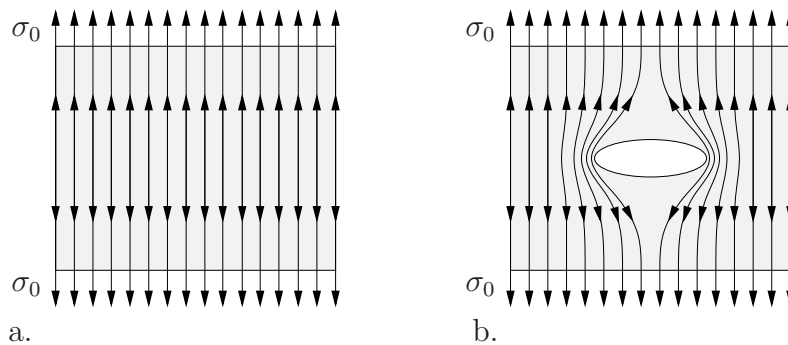


**Figure 7.1:** Stress concentrations in solids due to sharp geometrical changes. a.) Uniformly spaced stress trajectories in a homogeneous plate. b.) Perturbation of stress trajectories due to presence of an elliptical hole.

the strain displacement relations,

$$\varepsilon_{ij} = \frac{1}{2}(u_{i,j} + u_{j,i}) . \quad (7.1)$$

Differentiations of  $\varepsilon_{11}$  twice by  $x_2$ ,  $\varepsilon_{22}$  twice by  $x_1$  and  $\varepsilon_{12}$  by  $x_1$  and  $x_2$  give directly the compatibility equation

$$\frac{\partial^2 \varepsilon_{11}}{\partial x_2^2} + \frac{\partial^2 \varepsilon_{22}}{\partial x_1^2} = 2 \frac{\partial^2 \varepsilon_{12}}{\partial x_1 \partial x_2} \quad (7.2)$$

which guarantees the continuity of a two-dimensional body. The compatibility equation (7.2) can also be expressed in terms of stresses. In order to do so, the following representation of linear isotropic elasticity

$$\varepsilon_{ij} = \frac{1}{E} [(1 + \nu)\sigma_{ij} - \nu\sigma_{kk}\delta_{ij}] \quad (7.3)$$

given in terms of the Young's modulus  $E$  and the Poisson's ratio  $\nu$  will be utilized. Insertion of (7.3) into (7.2) and setting all out-of-plane stress components to zero, i.e.  $\sigma_{3i} = 0$ , yield

$$\frac{\partial^2}{\partial x_2^2}(\sigma_{11} - \nu\sigma_{22}) + \frac{\partial^2}{\partial x_1^2}(\sigma_{22} - \nu\sigma_{11}) + 2(1 + \nu) \frac{\partial^2 \sigma_{12}}{\partial x_1 \partial x_2} = 0 . \quad (7.4)$$

It is nothing but the compatibility equation (7.2) represented in terms of stresses for a two-dimensional isotropic linear elastic body. The stresses must satisfy additionally the static equilibrium equations, which in two dimensions and in the absence of body forces are written as

$$\frac{\partial \sigma_{11}}{\partial x_1} + \frac{\partial \sigma_{12}}{\partial x_2} = 0 \quad \text{and} \quad \frac{\partial \sigma_{12}}{\partial x_1} + \frac{\partial \sigma_{22}}{\partial x_2} = 0 . \quad (7.5)$$

The equations of equilibrium are identically satisfied by the stress function  $\Phi(x_1, x_2)$  introduced by G.B. Airy (1801-1892). It is related to the stresses as follows

$$\sigma_{11} = \frac{\partial^2 \Phi}{\partial x_2^2} , \quad \sigma_{22} = \frac{\partial^2 \Phi}{\partial x_1^2} \quad \text{and} \quad \sigma_{12} = -\frac{\partial^2 \Phi}{\partial x_1 \partial x_2} . \quad (7.6)$$

Direct substitution of above results into the compatibility condition (7.4) yields

$$\nabla^4 \Phi = \frac{\partial^4 \Phi}{\partial x_1^4} + 2 \frac{\partial^4 \Phi}{\partial x_1^2 \partial x_2^2} + \frac{\partial^4 \Phi}{\partial x_2^4} = 0 . \quad (7.7)$$

Therefore, any function  $\Phi(x_1, x_2)$  that is the solution of a biharmonic equation given in (7.7) satisfies the governing relations for equilibrium and geometric compatibility. At this stage it is important to note that the solution of (7.7) is not unique, indeed many functions could be written that satisfy the compatibility equation; for instance, setting  $\Phi = 0$  would always work. However, to find the correct solution for a particular problem the boundary conditions on the stress and displacement must be fulfilled as well. This is usually much more difficult to assure, and no general solution that works for all cases exists. It can be shown, however, that a solution satisfying both the compatibility equation and the boundary conditions is unique, i.e. that it is the only correct solution. Since it is more convenient for the infinite plate problem with circular hole under consideration to work in polar coordinates, in what follows a brief overview of the equilibrium equations,

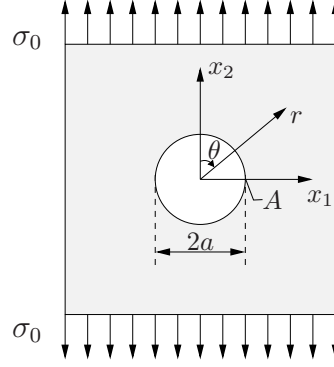


**Figure 7.2:** Infinite plate of unit thickness with a circular hole of diameter  $2a$  under remote tensile stress  $\sigma_0$ .

kinematic relations and compatibility conditions in polar coordinates will be given. First, the two-dimensional static equilibrium equations are given by

$$\begin{aligned} \frac{\partial \sigma_{rr}}{\partial r} + \frac{1}{r} \frac{\partial \sigma_{r\theta}}{\partial \theta} + \frac{\sigma_{rr} - \sigma_{\theta\theta}}{r} &= 0 \\ \frac{1}{r} \frac{\partial \sigma_{\theta\theta}}{\partial \theta} + \frac{\partial \sigma_{r\theta}}{\partial r} + 2 \frac{\sigma_{r\theta}}{r} &= 0 \end{aligned} \quad (7.8)$$

assuming that there are no body forces. The indices  $r$  and  $\theta$  represent the radial and circumferential components of the stress, respectively. The strain field which is defined by the following kinematic relations

$$\begin{aligned} \varepsilon_{rr} &= \frac{\partial u_r}{\partial r} \\ \varepsilon_{\theta\theta} &= \frac{1}{r} \frac{\partial u_\theta}{\partial \theta} + \frac{\partial u_r}{\partial r} \\ \varepsilon_{r\theta} &= \frac{1}{2} \left( \frac{\partial u_\theta}{\partial r} + \frac{1}{r} \frac{\partial u_r}{\partial \theta} - \frac{u_\theta}{r} \right) \end{aligned} \quad (7.9)$$

has to satisfy the compatibility equation

$$\frac{\partial^2 \varepsilon_{\theta\theta}}{r^2} + \frac{1}{r^2} \frac{\partial^2 \varepsilon_{rr}}{\partial \theta^2} + \frac{2}{r} \frac{\partial \varepsilon_{\theta\theta}}{\partial r} - \frac{1}{r} \frac{\partial \varepsilon_{rr}}{\partial r} = \frac{2}{r} \frac{\partial^2 \varepsilon_{r\theta}}{\partial r \partial \theta} + \frac{2}{r^2} \frac{\partial \varepsilon_{r\theta}}{\partial \theta}. \quad (7.10)$$

The equilibrium equations in (7.8) are satisfied by a stress function  $\Phi(r, \theta)$  for which the polar stress components are computed as

$$\begin{aligned} \sigma_{rr} &= \frac{1}{r} \frac{\partial \Phi}{\partial r} + \frac{1}{r^2} \frac{\partial^2 \Phi}{\partial \theta^2} \\ \sigma_{\theta\theta} &= \frac{\partial^2 \Phi}{\partial r^2} \\ \sigma_{r\theta} &= \frac{1}{r^2} \frac{\partial \Phi}{\partial \theta} - \frac{1}{r} \frac{\partial^2 \Phi}{\partial r \partial \theta}. \end{aligned} \quad (7.11)$$

The biharmonic equation (7.7) provided in Cartesian coordinates then becomes

$$\nabla^4 \Phi = \left( \frac{\partial^2}{\partial r^2} + \frac{1}{r} \frac{\partial}{\partial r} + \frac{1}{r^2} \frac{\partial^2}{\partial \theta^2} \right) \left( \frac{\partial^2 \Phi}{\partial r^2} + \frac{1}{r} \frac{\partial \Phi}{\partial r} + \frac{1}{r^2} \frac{\partial^2 \Phi}{\partial \theta^2} \right) = 0 \quad (7.12)$$



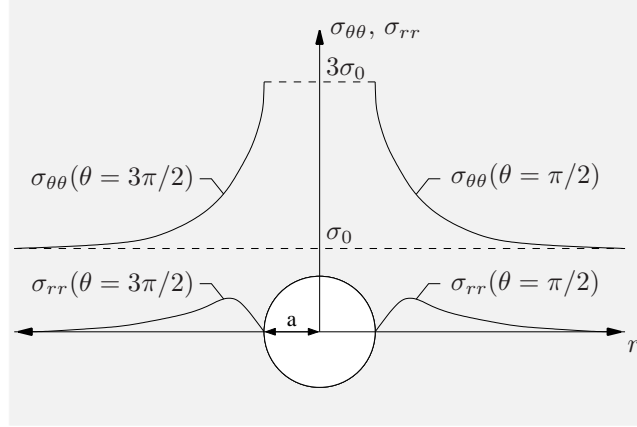


**Figure 7.3:** The stress field in a linear elastic infinite plate with a circular hole of radius  $a$  under remote tensile stress  $\sigma_0$ .

in polar coordinates. The problem can be solved now by finding a stress function which satisfies the compatibility condition (7.12) and the boundary conditions at the circumference of the hole

$$\sigma_{rr} = \sigma_{r\theta} = 0 \quad \text{at} \quad r = a \quad (7.13)$$

and also at the outer boundary

$$\sigma_{rr} = \frac{1}{2}\sigma_0(1 + \cos 2\theta), \quad \sigma_{\theta\theta} = \frac{1}{2}\sigma_0(1 - \cos 2\theta), \quad \sigma_{r\theta} = -\frac{1}{2}\sigma_0 \sin 2\theta \quad \text{for} \quad r \rightarrow \infty. \quad (7.14)$$

For this case, the following stress function is assumed

$$\Phi(r, \theta) = f_1(r) + f_2(r) \cos 2\theta \quad (7.15)$$

where  $f_1(r)$  and  $f_2(r)$  are yet to be determined. Substitution of (7.15) into the biharmonic equation (7.12) gives the following forms of the functions  $f_1$  and  $f_2$

$$f_1(r) = c_1 r^2 \ln r + c_2 r^2 + c_3 \ln r + c_4 \quad \text{and} \quad f_2(r) = c_5 r^2 + c_6 r^4 + c_7 r^2 + c_8 \quad (7.16)$$

with the integration constants  $c_i$  to be found from the boundary conditions. Imposition of the boundary conditions (7.13) and (7.14) yields

$$c_1 = 0, \quad c_2 = \frac{\sigma_0}{4}, \quad c_3 = -\frac{a^2 \sigma_0}{2}, \quad c_4 = \frac{\sigma_0}{4}, \quad c_5 = \frac{\sigma_0}{4}, \quad c_6 = 0, \quad c_7 = -\frac{a^4 \sigma_0}{4} \quad \text{and} \quad c_8 = \frac{a^2 \sigma_0}{2} \quad (7.17)$$

where  $c_4$  is undetermined but for the stress field it has no importance. After having determined the constants of integration, the stress field in an infinite plate containing a circular hole is accomplished by substituting the final form of (7.15) into (7.11), i.e.

$$\begin{aligned} \sigma_{rr} &= \frac{1}{2}\sigma_0 \left[ \left(1 - \frac{a^2}{r^2}\right) + \left(1 + \frac{3a^4}{r^4} - \frac{4a^2}{r^2}\right) \cos 2\theta \right] \\ \sigma_{\theta\theta} &= \frac{1}{2}\sigma_0 \left[ \left(1 + \frac{a^2}{r^2}\right) - \left(1 + \frac{3a^4}{r^4}\right) \cos 2\theta \right] \\ \sigma_{r\theta} &= -\frac{1}{2}\sigma_0 \left(1 - \frac{3a^4}{r^4} + \frac{2a^2}{r^2}\right) \sin 2\theta. \end{aligned} \quad (7.18)$$

The maximum value of the circumferential stress  $\sigma_{\theta\theta}$  is obtained for  $\theta = \pi/2$  or  $3\pi/2$  and  $r = a$ . The distribution of  $\sigma_{\theta\theta}$  and  $\sigma_{rr}$  for  $\theta = \pi/2$  and  $\theta = 3\pi/2$  are given by

$$\sigma_{\theta\theta} = \sigma_0 \left( 1 + \frac{a^2}{2r^2} + \frac{3a^4}{2r^4} \right) \quad \text{and} \quad \sigma_{rr} = \frac{3\sigma_0}{2} \left( \frac{a^2}{r^2} - \frac{a^4}{r^4} \right). \quad (7.19)$$

From the above results one concludes that if  $r \rightarrow \infty$  then the hoop stress becomes the uniform applied tensile stress, i.e.  $\sigma_{\theta\theta} \rightarrow \sigma_0$ , and if  $r = a$  and  $\theta = \pi/2$  then

$$\sigma_{\theta\theta}(r = a, \theta = \pi/2) = \sigma_{22}(x_1 = a, x_2 = 0) = 3\sigma_0. \quad (7.20)$$

In other words, the presence of the circular hole causes an increase in the tangential stress component which is three times of the applied stress  $\sigma_0$ . Note that also the radial stress  $\sigma_{rr}$  is non-zero due to the circular cavity, yielding a two-dimensional stress state despite of the uniaxial loading mode. The radial stress has the maximum value of  $(3/8)\sigma_0$  when  $r = \sqrt{2}a$  and vanishes, according to the necessary boundary conditions, at the free surface of the hole,  $r = a$ , and at the outer surface,  $r \rightarrow \infty$ . The distributions of  $\sigma_{\theta\theta}$  and  $\sigma_{rr}$  for  $\theta = \pi/2$  and  $\theta = 3\pi/2$  are plotted in Figure 7.3.

**7.1.3. Infinite Plate with Elliptical Hole under Tension.** In the following an infinite plate with an elliptical hole under the remote tensile stress  $\sigma_0$  is considered. The hole is assumed to have the major axis  $2a$  and the minor axis  $2b$ . Furthermore, the major axis is normal to the uniform tensile stress, as shown in Figure 7.4. This problem was first treated by INGLIS [102] where a specific curvilinear coordinate system and complex potentials were utilized, see also KNOTT [114] pp.46-53. Here the solution procedure is outlined. First, a complex variable  $p = \alpha + i\beta$  is defined where  $\alpha$  and  $\beta$  are coordinates in a particular curvilinear coordinate system, see Appendix A for the basics of complex numbers and functions. The variable  $p$  is related to  $z = x_1 + ix_2$  defined in the Cartesian coordinate system by

$$z := c \cosh p \quad (7.21)$$

where  $c$  is a constant. By separation of real and imaginary parts of  $z$  and  $p$  one obtains

$$x_1 = c \cosh \alpha \cos \beta \quad \text{and} \quad x_2 = c \sinh \alpha \sin \beta. \quad (7.22)$$

Elimination of  $\beta$  in (7.22) yields

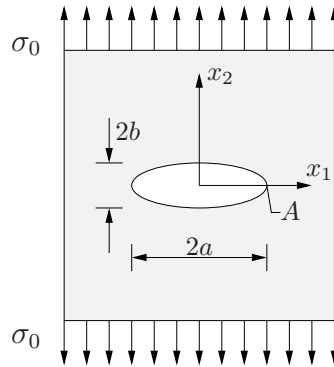


**Figure 7.4:** Infinite plate of unit thickness with an elliptical hole of major axis  $2a$  and minor axis  $2b$  under remote tensile stress  $\sigma_0$ .

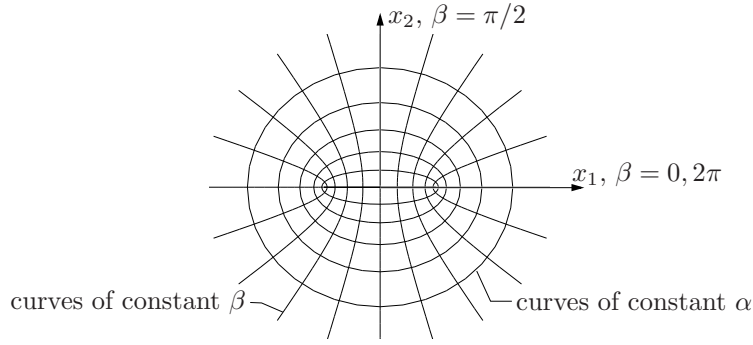


**Figure 7.5:** Visualization of an elliptical coordinate system. Elliptical coordinates  $\alpha$  and  $\beta$  are related to Cartesian coordinates  $x_1$  and  $x_2$  by  $x_1 = c \cosh \alpha \cos \beta$  and  $x_2 = c \sinh \alpha \sin \beta$ .

$$\frac{x_1^2}{\cosh^2 \alpha} + \frac{x_2^2}{\sinh^2 \alpha} = c^2 \quad (7.23)$$

which represents for a constant value of  $\alpha$  an ellipse in the Cartesian coordinate system. The curves of constant  $\beta$  generate in an analogous way a series of confocal hyperbolae intersecting the ellipses at right angles, see Figure 7.5 for the illustration of the coordinate system. The axes of the ellipse can be expressed now as follows

$$2a = 2c \cosh \alpha_0 \quad \text{and} \quad 2b = 2c \sinh \alpha_0 \quad (7.24)$$

and therefore one obtains by using (7.23)

$$\frac{x_1^2}{a^2} + \frac{x_2^2}{b^2} = 1 \quad (7.25)$$

which is nothing but the equation of an ellipse. Note that in the limit case  $\alpha_0 \rightarrow \infty$  the ellipse becomes a sharp crack of length  $2a$  whereas  $a = b$  results in a circle. In this coordinate system each value of  $\alpha$  describes an ellipse and a point on a given ellipse is parameterized by  $\beta$  which varies from 0 to  $2\pi$  as depicted in Figure 7.5. The main advantage of this coordinate system is that, suitable choices of the constant  $c$  in (7.21) yield very narrow slit like ellipses which can represent internal cracks. Similarly, a pair of hyperbolae may be adjusted in the form of external notches. A stress component  $\sigma_{\alpha\beta}$  is defined as acting on a face which is tangent to a curve of constant  $\alpha$ , in the direction of the normal to a curve of constant  $\beta$ . Relations of stress components in Cartesian and curvilinear coordinates are given by

$$\begin{aligned} \sigma_{\alpha\alpha} &= \sigma_{11} \cos^2 \theta + \sigma_{22} \sin^2 \theta + 2\sigma_{12} \sin \theta \cos \theta \\ \sigma_{\beta\beta} &= \sigma_{11} \sin^2 \theta + \sigma_{22} \cos^2 \theta - 2\sigma_{12} \sin \theta \cos \theta \\ \sigma_{\alpha\beta} &= (\sigma_{22} - \sigma_{11}) \sin \theta \cos \theta + \sigma_{12}(\cos^2 \theta - \sin^2 \theta) . \end{aligned} \quad (7.26)$$

Equation (7.26) is in fact the two-dimensional transformation of a stress tensor when referred to a new pair of orthogonal axes which are rotated with an angle  $\theta$  from  $x_1$  axis. From the above results it is possible to write

$$\begin{aligned} \sigma_{\alpha\alpha} + \sigma_{\beta\beta} &= \sigma_{11} + \sigma_{22} \\ \sigma_{\beta\beta} - \sigma_{\alpha\alpha} + 2i\sigma_{\alpha\beta} &= (\sigma_{22} - \sigma_{11} + 2i\sigma_{12})e^{2i\theta} . \end{aligned} \quad (7.27)$$

Similar to complex potentials utilized in (D.34) and (D.39) we can now write from (7.27)

$$\begin{aligned}\sigma_{\alpha\alpha} + \sigma_{\beta\beta} &= 2[\Omega'(z) + \bar{\Omega}'(\bar{z})] \\ \sigma_{\beta\beta} - \sigma_{\alpha\alpha} + 2i\sigma_{\alpha\beta} &= 2e^{2i\theta}[\bar{z}\Omega''(z) + \omega''(z)].\end{aligned}\quad (7.28)$$

Next step is the determination of complex potentials  $\Omega(z)$  and  $\omega(z)$  which satisfy the boundary conditions at infinity

$$\sigma_{22} = \sigma_0 \quad \text{and} \quad \sigma_{11} = \sigma_{12} = 0 \quad \text{for} \quad x_1 \rightarrow \infty \quad \text{or} \quad x_2 \rightarrow \infty \quad (7.29)$$

and which are periodic in  $\beta$  with a period of  $2\pi$ . INGLIS [102] proposed the following potentials

$$\begin{aligned}\Omega(z) &= \frac{\sigma_0 c}{4}[(1 + e^{2\alpha_0})\sinh p - e^{2\alpha_0}\cosh p] \\ \omega(z) &= -\frac{\sigma_0 c^2}{4}[(\cosh 2\alpha_0 - \cosh \pi)p + \frac{1}{2}e^{2\alpha_0} - \cosh 2(p - \alpha_0 - i\frac{\pi}{2})].\end{aligned}\quad (7.30)$$

Substitution of (7.30)<sub>1</sub> into (7.28)<sub>1</sub> delivers

$$\sigma_{\alpha\alpha} + \sigma_{\beta\beta} = \frac{\sigma_0}{2} \left[ (1 + e^{2\alpha_0}) \left( \frac{\cosh p}{\sinh p} + \frac{\cosh \bar{p}}{\sinh \bar{p}} \right) - 2e^{2\alpha_0} \right] \quad (7.31)$$

where  $\bar{p} = \alpha - i\beta$  is the complex conjugate of  $p$ . After some manipulations, the stress component  $\sigma_{\beta\beta}$  at the surface of ellipse, where  $\sigma_{\alpha\alpha} = 0$ , is determined as

$$\sigma_{\beta\beta}(\alpha = \alpha_0) = \sigma_0 \frac{\sinh 2\alpha_0 - 1 + e^{2\alpha_0} \cos 2\beta}{\cosh 2\alpha_0 - \cos 2\beta}. \quad (7.32)$$

The maximum value of (7.32) is attained at  $\beta = 0$  and  $\beta = \pi$  where  $\sigma_{\beta\beta}$  is equal to  $\sigma_{22}$

$$\sigma_{\beta\beta}(\alpha = \alpha_0, \beta = 0) = \sigma_{22}(x_1 = a, x_2 = 0) = \sigma_0 \frac{\sinh 2\alpha_0 - 1 + e^{2\alpha_0}}{\cosh 2\alpha_0 - 1}. \quad (7.33)$$

Having recalled the relations,  $c^2 = a^2 - b^2$ ,  $\sinh 2\alpha_0 = 2ab/c^2$ ,  $e^{2\alpha_0} = \cosh 2\alpha_0 + \sinh 2\alpha_0$  and  $\cosh 2\alpha_0 = (a^2 + b^2)/c^2$ , the stress at the tip of elliptical hole is found as

$$\sigma_{22}(x_1 = a, x_2 = 0) = \sigma_0 \left( 1 + 2\frac{a}{b} \right) \quad (7.34)$$

Note that the formula given in (7.34) recovers the stress concentration solution of circular hole where  $a = b$ , i.e.  $\sigma_{22} = 3\sigma_0$ . The most important consequence of (7.34) is the fact that if the ellipse becomes longer in the direction normal to the loading and shorter in the direction parallel to the applied traction, i.e.  $a/b \rightarrow \infty$ , then the stress at the tip point  $A$  of ellipse turns out to be unbounded,  $\sigma \rightarrow \infty$ . An alternative representation of (7.34) can also be given in terms of the radius of curvature  $\rho$  at the tip of ellipse, the point  $A$  in Figure 7.4. The curvature  $\rho$  of a parametrically defined curve, i.e.  $x_1 = x_1(t)$  and  $x_2 = x_2(t)$ , is given by

$$\rho = (x_1'^2 + x_2'^2)^{3/2} / |x_1'x_2'' - x_2'x_1''|. \quad (7.35)$$

Making use of the parametric definition of the ellipse, i.e.  $x_1(t) = a \cos t$  and  $x_2(t) = b \sin t$ , and evaluation of  $\rho$  at the point  $A$  where  $t = 0$  yields

$$\sigma_{22}(x_1 = a, x_2 = 0) = \sigma_0(1 + 2\sqrt{a/\rho}). \quad (7.36)$$

Above formulae (7.34) and (7.36) can be approximated for very slender ellipses  $a/b \gg 1$ , which can be regarded indeed as sharp cracks, by

$$\sigma_{22} \approx 2\sigma_0 a/b \approx 2\sigma_0 \sqrt{a/\rho}. \quad (7.37)$$

It is important to note that according to these results the stress concentrations in an infinite body depend on the shape (aspect ratio or tip curvature) of the elliptical cavity rather than the size of it.

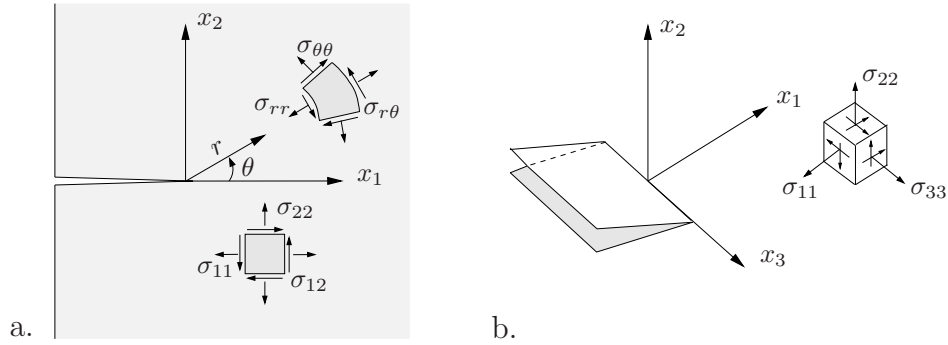


**Figure 7.6:** Crack tip coordinates and the stress field a.) for two-dimensional problems with rectangular  $x_1 - x_2$  and polar  $r - \theta$  stress components and b.) three-dimensional problems with rectangular  $x_1 - x_2 - x_3$  stress components.

## 7.2. Stress Intensity Factors Approach to Fracture

After the work of INGLIS [102] on stress concentrations in infinite bodies with elliptical holes, stress fields in isotropic linear elastic solids with particular crack configurations have been investigated by WESTERGAARD [213], SNEDDON [203] and WILLIAMS [214]. However, IRWIN [104, 105] was the first who recognized the general applicability of the singular stress field in the presence of cracks. Consequently, he introduced the concept of *stress intensity factor* as a measure of the strength of singularity. Based on the works of Irwin, it has been shown that the stress field in a linear elastic cracked solid can be expressed as

$$\sigma_{ij} = \left(\frac{k}{\sqrt{r}}\right)f_{ij}(\theta) + \sum_{n=0}^{\infty} A_n r^{n/2} g_{ij}^n(\theta) \quad (7.38)$$

in the polar coordinate system  $r - \theta$  shown in Figure 7.6. In (7.38)  $k$  is a constant and  $f_{ij}$  is a dimensionless function of  $\theta$ . The second term on the right hand side of (7.38) represents the higher order contributions to the solution which depend on the geometry of the problem. Note that the solution given above contains for any particular configuration a leading term depending on  $1/\sqrt{r}$  which approaches to infinity as  $r \rightarrow 0$ , while the other term vanishes.

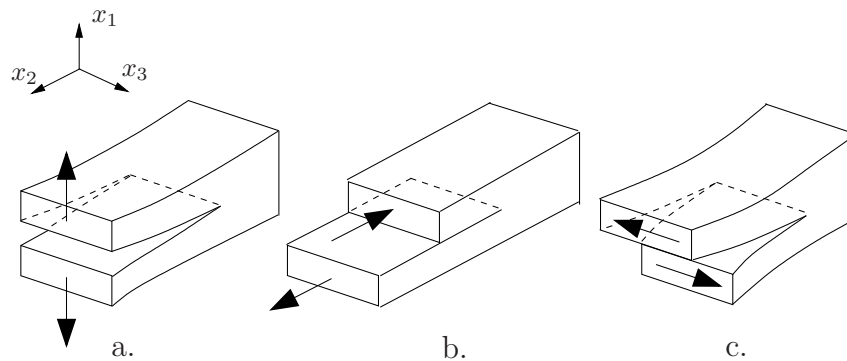


**Figure 7.7:** Visualization of the three basic modes of fracture. a.) Mode I (opening), b.) Mode II (sliding / in-plane shear) and c.) Mode III (tearing / out-of-plane shear).

Three basic modes of crack propagation were first pointed out by IRWIN [105]. They are based on the movements of two crack surfaces with respect to each other. A flat crack in  $x_2 - x_3$  plane extending through the thickness ( $x_3$  direction) of a plate is considered, see Figure 7.7. The three modes are summarized below.

- (i) Mode I (opening): The load is applied normal to the crack plane and crack surfaces separate such that  $\llbracket u_1 \rrbracket \neq 0$ ,  $\llbracket u_2 \rrbracket = 0$  and  $\llbracket u_3 \rrbracket = 0$ .
- (ii) Mode II (sliding / in-plane shear): The load is applied parallel to the crack plane corresponding to an in-plane shear loading and the crack surfaces separate such that  $\llbracket u_1 \rrbracket = 0$ ,  $\llbracket u_2 \rrbracket \neq 0$  and  $\llbracket u_3 \rrbracket = 0$ .
- (iii) Mode III (tearing / out-of-plane shear): The load is applied parallel to the crack plane corresponding to an out-of-plane shear loading and the crack surfaces separate such that  $\llbracket u_1 \rrbracket = 0$ ,  $\llbracket u_2 \rrbracket = 0$  and  $\llbracket u_3 \rrbracket \neq 0$ .

The jump bracket  $\llbracket u_i \rrbracket$  has been employed above to denote the difference of the displacement component  $u_i$  evaluated at both faces of the crack. That is,  $\llbracket u_i \rrbracket = u_i^+ - u_i^-$  with the displacement values at the upper and lower crack faces  $u_i^+$  and  $u_i^-$ , respectively. Above mentioned three basic modes of the crack extension are visualized in Figure 7.7. In general a cracked body may experience a combination of the three modes. All loading modes yield  $1/\sqrt{r}$  singularity given in (7.38) at the crack tip, but the constants  $k$  and  $f_{ij}$  are dependent on the crack extension mode. It is a common practice in the literature to denote the stress intensity factors with a subscript denoting the mode of loading, i.e.  $K_I$ ,  $K_{II}$  and  $K_{III}$ . Thus, the stress field around the neighborhood of the crack tip can be expressed for different modes as follows

$$\sigma_{ij}^I = \frac{K_I}{\sqrt{2\pi r}} f_{ij}^I(\theta), \quad \sigma_{ij}^{II} = \frac{K_{II}}{\sqrt{2\pi r}} f_{ij}^{II}(\theta) \quad \text{and} \quad \sigma_{ij}^{III} = \frac{K_{III}}{\sqrt{2\pi r}} f_{ij}^{III}(\theta) \quad (7.39)$$

with the polar coordinate system  $r - \theta$  depicted in Figure 7.6a. The key property of the compact representation (7.39) is that the cardinal elements of the stress field appear as separable factors. The intensity factors  $K_i$  with  $i = I, II, III$  depend on the outer boundary conditions, namely the applied load and the specimen geometry. As a consequence, they determine the intensity of the local field. On the other hand, the remaining factors depend only on the spatial coordinates, and determine the distribution of the field. In a general case of a loading, where all three modes are activated, the stress field can be computed as a summation of the three contributions,

$$\sigma_{ij} = \sigma_{ij}^I + \sigma_{ij}^{II} + \sigma_{ij}^{III} \quad (7.40)$$

which is due to the linear superposition principle of linear elasticity. The details of the computation of stress fields for different loading modes are discussed in Appendix D and the closed form solutions of stress intensity factors for some simple geometries are addressed in Appendix E. For example, the stress intensity factor  $K_I$  of an infinite plate with a sharp crack of length  $2a$  subjected to remote tensile stress  $\sigma_0$  is given as

$$K_I = \sigma_0 \sqrt{\pi a} . \quad (7.41)$$

Detailed tables and approximate expressions for the stress intensity factors can be found for example in ROOKE & CARTWRIGHT [194].

The concept of stress intensity factors permits a single parameter characterization of the singularity around the crack tip. Provided that the material is linear elastic, the stresses near the crack tip vary with  $1/\sqrt{r}$  and the stress intensity factor determines the amplitude of the singularity. If the stress intensity factor is known, then the displacement, strain and stress fields can be computed in the singularity dominated zone. Assuming that the local material failure is due to excessive stresses (or strains), there must be a critical value of  $K_I$  at which an extension of the crack occurs. This value is often denoted as  $K_{Ic}$  and is a measure of the fracture toughness. Therefore, the condition for a crack to propagate can be written as

$$K_I = K_{Ic} . \quad (7.42)$$

The fracture toughness is normally considered as a material parameter that is to some extent independent of the size and geometry of the body for a given mode. In fact, experiments point out that  $K_{Ic}$  varies with the thickness of the specimen, especially if the variation results in a change from a plane stress to a plane strain condition. See KNOTT [114] pp.114-130 and KANNINEN & POPELAR [111] pp.176-182 for further details. In the case of different loading modes, the critical stress intensity factors are in general different, i.e.  $K_{Ic} \neq K_{IIc} \neq K_{IIIc}$ . Since the majority of materials fail by normal tensile stresses rather than shear,  $K_{Ic}$  is generally the parameter that controls the failure. In other words,  $K_{IIc}$  and  $K_{IIIc}$  are usually greater than  $K_{Ic}$ .

### 7.3. Energetic Approach to Fracture

In the previous sections the main focus was put on the stress concentrations and the determination of singular stress fields in linear elastic solids in the presence of sharp geometrical changes. In the sequel, a conceptually different energy based approach is described. The energetic approach is traced back to the seminal works of GRIFFITH [84, 85] which led to the development of fracture mechanics as an engineering discipline. It requires an extension of the first law of thermodynamics in order to incorporate the energetic contribution due to a fracture process.

In fact, Griffith's motivation was apparently different, that is simple estimates for the strength of a crystalline solid based on its lattice parameters. However, this results in

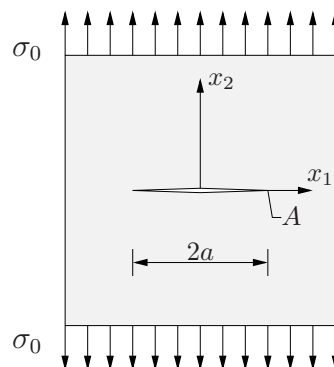


**Figure 7.8:** Infinite plate of unit thickness with a sharp crack of length  $2a$  under remote tensile stress  $\sigma_0$ .



theoretical strength values which are not attained by real materials. Main focus of his work was primarily on resolving this discrepancy. He figured out that, this difference is a result of the inevitable occurrence of flaws in a solid body. It is a point of interest to note that, a similar discrepancy exists between the theoretical shear strength of a crystalline solid and the observed values due to the existence of dislocations.

**7.3.1. Griffith Theory.** GRIFFITH [84] was the first who realized the importance of the variation of energy during a crack growth in brittle solids. Griffith proposed that *solids have a surface energy which must be compensated for a given crack to propagate*. Then the critical load level for a given crack is found by the principle of minimum potential energy of elasticity with an extension that takes into account the surface energy of the solid. In other words, the configuration that minimizes the total energy has to be sought in order to find an equilibrium state of the crack. The total energy  $\Pi$  has the following contributions, the strain energy  $\mathcal{E}$  stored in the elastic medium and the potential energy  $\mathcal{U}$  of the outer loading system under quasistatic conditions case without consideration of cracks. In order to include possible crack extensions, Griffith introduced an additional term  $\Gamma$  which corresponds to the energy expended in creating new crack surfaces. Consequently, the total energy  $\Pi$  reads

$$\Pi = \mathcal{E} + \mathcal{U} + \Gamma . \quad (7.43)$$

The sum of the strain energy  $\mathcal{E}$  and the potential energy of the outer loading  $\mathcal{U}$  is referred to as the total potential energy  $\Omega$  of the system, i.e.  $\Omega = \mathcal{E} + \mathcal{U}$ . If we concentrate on a system with a single crack, then the equilibrium is attained by a vanishing total energy over a virtual crack extension. Energetic terms in (7.43) can be parameterized in terms of the crack length  $a$ . Therefore, the Griffith energy balance is formally stated for a plate of unit thickness as

$$\boxed{\frac{d\Pi(a)}{da} = \frac{d\mathcal{E}(a)}{da} + \frac{d\mathcal{U}(a)}{da} + \frac{d\Gamma(a)}{da} = 0 .} \quad (7.44)$$

After addressing the main idea of the Griffith energy balance concept, we consider as a particular crack configuration an infinite plate of unit thickness having a sharp crack of length  $2a$  as shown in Figure 7.8. The outer loading is the remote tension  $\sigma_0$  and no body forces are considered. Based on the work of INGLIS [102] on stress concentrations around elliptical holes, GRIFFITH [84] computed the change in the strain energy in a linear elastic medium due to an elliptical cavity. He also evaluated the energy change for a sharp crack by considering an infinitely narrow elliptical cavity ( $2b \rightarrow 0$  in Figure 7.4). However, at the end of the same work he added a footnote to mention that the energy expression he computed was erroneous. In a later work, GRIFFITH [85], he provided a new corrected energy expression without showing any details about its derivation. Later SPENCER [204] and SIH & LIEBOWITZ [199] gave detailed solutions of the same problem, see also KANNINEN & POPELAR [111] p.35 for a simple solution based on the results of WESTERGAARD [213]. Under remote tensile loading conditions, the change in the strain energy of an infinite linear elastic medium due to a sharp crack of length  $2a$  is found to be

$$\Delta\mathcal{E}(a) = \frac{\pi a^2 \sigma_0^2}{E'} \quad (7.45)$$

with  $E' = E$  for plane stress and  $E' = E/(1 - \nu^2)$  for plane strain conditions.  $E$  and  $\nu$  denote the Young's modulus and the Poisson's ratio, respectively. The total elastic strain

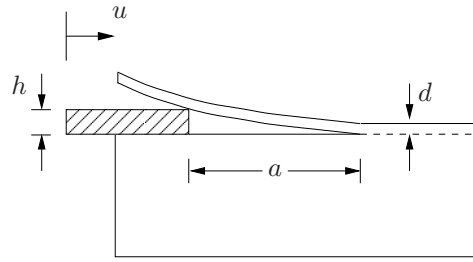


**Figure 7.9:** The setup of the experiment performed by OBRIMOFF [168] on mica. A wedge of thickness  $h$  is inserted to peel off cleavage flake of thickness  $d$ . The equilibrium configuration of the crack is stable if the position of the wedge is controlled.

energy of the system is

$$\mathcal{E}(a) = \mathcal{E}_0 + \Delta\mathcal{E}(a) \quad (7.46)$$

where  $\mathcal{E}_0$  is the initial strain energy of the uncracked specimen. Hence,  $\mathcal{E}_0$  does not depend on the crack length  $a$  and has no influence in the application of the Griffith energy balance principle (7.44). Owing to the Clapeyron's theorem (KANNINEN & POPELAR [111] p.112), it is possible for linear elastic materials to express the work done by the outer loading (negative of the potential energy  $\mathcal{U}$  of outer loading) as twice of the strain energy, i.e.

$$\mathcal{U}(a) = -2\mathcal{E}(a) . \quad (7.47)$$

The last contribution  $\Gamma$  in (7.43) is the surface energy of the cracked body and is a linear function of the total crack length  $2a$ ,

$$\Gamma(a) = 4\gamma a . \quad (7.48)$$

$\gamma$  is the surface energy per unit area and assumed to be a constant material parameter. The additional factor 2 in (7.48) comes from the fact that an extension of a crack creates two surfaces. Hence, the total energy of the system reads

$$\Pi(a) = -\mathcal{E}_0 - \frac{\pi a^2 \sigma_0^2}{E'} + 4\gamma a . \quad (7.49)$$

Substitution of (7.49) into (7.44) gives the critical value of the remote tensile stress

$$\sigma_{0f} = \sqrt{\frac{2E'\gamma}{\pi a}} \quad (7.50)$$

that is required to extend the initial crack of length  $2a$  in an infinite elastic body. In Figure 7.10a the variations of energy contributions are plotted with respect to the crack length. This result has a cardinal importance. It solves the paradox that the stresses at the tip of a sharp crack in an elastic body are infinite no matter how small is the applied stress. This fact led to a new argument that rupture does not occur when the stress at a point exceeds some critical value, but only when the energy supplied to the body by external agencies exceeds a critical value. Note that from (7.49) it is also possible to determine the critical half flaw size  $a_c$  (the critical crack has a total length of  $2a_c$ ) for a given remote stress  $\sigma_0$  as

$$a_c = \frac{2E'\gamma}{\pi\sigma_0^2} . \quad (7.51)$$

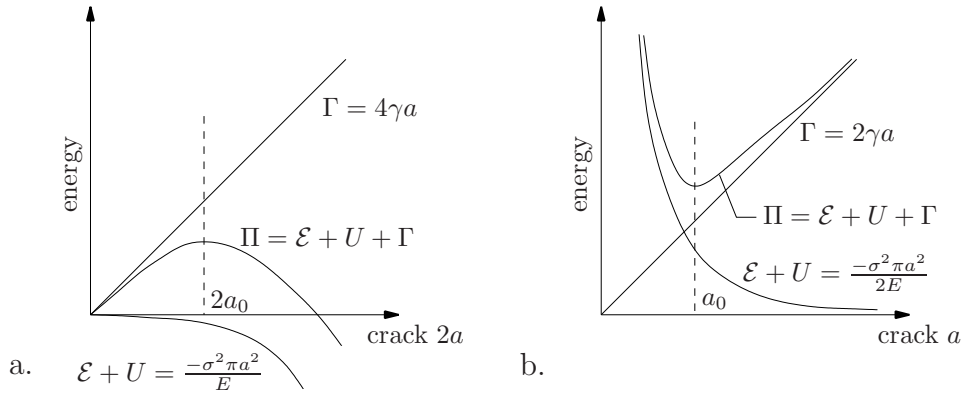


**Figure 7.10:** Energetics of unstable and stable crack growths. a.) The unstable crack growth in a load controlled uniform tension test from GRIFFITH [84]. b.) The stable crack growth in a displacement controlled bending test from OBREIMOFF [168].

Equation (7.51) states that for a given stress  $\sigma_0$  the crack in elastic medium remains stationary if  $a < a_c$  and otherwise it starts to extend. As we see from Figure 7.10a,  $d^2\Pi(a)/da^2$  is negative at the equilibrium. Therefore, the total energy attains a maximum at the equilibrium and the configuration is unstable. That means, for  $\sigma_0 < \sigma_{0f}$  the crack stays stationary at its initial size, and for  $\sigma_0 > \sigma_{0f}$  it propagates continuously without reaching a new equilibrium state.

The energy balance concept of Griffith (7.44) is not only restricted to the crack configuration in Figure 7.8. In order to emphasize its generality another application is considered where the crack extension is stable. The configuration is shown in Figure 7.10 and investigated experimentally by OBREIMOFF [168] for cleavage in mica. A wedge of thickness  $h$  is inserted beneath a thin layer of mica. Provided that the position of the wedge is controlled a stable configuration of the crack is always obtained. The energy of the system is determined by treating the cleavage flake as a cantilever beam of thickness  $d$ . The cantilever beam has a length of  $a$  and the prescribed displacement at its free end is  $h$ . Since the position of the wedge is controlled, the outer loading system performs no work, i.e.  $\mathcal{U} = 0$ . The elastic strain energy  $\mathcal{E}(a)$  and the surface energy  $\Gamma(a)$  are expressed as

$$\mathcal{E}(a) = \frac{Ed^3h^2}{8a^3} \quad \text{and} \quad \Gamma(a) = 2\gamma a, \quad (7.52)$$

where  $\mathcal{E}$  reads from the simple beam theory. Substitution of (7.52) into (7.44) leads to the equilibrium crack length  $a_c$  for a particular wedging condition

$$a_c = \left( \frac{3Ed^3h^2}{16\gamma} \right)^{1/4}. \quad (7.53)$$

The energy contributions  $\mathcal{E}$  and  $\Gamma$  in (7.52) are plotted in Figure 7.10b with respect to the crack length  $a$ . It is clear that the total energy attains a minimum at the equilibrium. Therefore, the crack configuration specified by (7.53) is stable, see also GDOUTOS [77] p.142 and LAWN [125] p.10. The stability condition for a brittle crack can be expressed as

$$\boxed{\frac{d^2\Pi(a)}{da^2} \begin{cases} < 0 : \text{unstable crack} \\ > 0 : \text{stable crack} \\ = 0 : \text{neutral crack} \end{cases}} \quad (7.54)$$

in terms of the total energy  $\Pi$  of the system. A crack configuration similar to the one investigated by OBRIMOFF [168] has been addressed in FREUND [73]. It has been shown that, the control of the displacement or load at the tip of cantilever arm yields the stable or unstable crack growth, respectively. The displacement controlled crack extension leads to energy contributions similar to Figure 7.10b whereas the force control is similar to Figure 7.10a, see FREUND [73] pp.5-8. On the other hand, the values of the critical stress  $\sigma_{0f}$  and the critical crack length  $a_c$  do not depend on whether the external load is applied under fixed grip (displacement controlled) or dead load (force controlled) conditions. Under fixed grip conditions, external agencies perform no work ( $\mathcal{U} = 0$ ) and therefore a crack extension results in a reduction in the stored elastic strain energy  $\mathcal{E}$ , see MEGUID [138] pp.159-162 and KNOTT [114], pp.98-103 for further discussions. In general, a stable crack growth is obtained more easily for displacement controlled experiments than load controlled ones.

**7.3.2. Energy Release Rate.** Irwin reformulated the energetic approach of Griffith into a form that is more suitable for engineering applications. We start with rewriting (7.44) such that it is considered as a crack extension criterion, i.e.

$$\underbrace{-\frac{1}{2}\left(\frac{d\mathcal{E}}{da} + \frac{d\mathcal{U}}{da}\right)}_{=:G} = \underbrace{\frac{1}{2}\frac{d\Gamma}{da}}_{=:G_c} \quad (7.55)$$

for a plate of unit thickness having a crack of length  $2a$ . The left hand side of (7.55) is the elastic energy per unit crack surface which is available for crack extension and called as the *energy release rate*  $G$ . IRWIN [104] introduced the concept of energy release rate and denoted it by  $G$  in honor of Griffith, see COTTERELL [50]. Since the energy release rate is derived from a potential function in a similar manner that of a conservative force, it is often referred to as the crack driving force, see for example MAUGIN [133] and FREUND [73]. The term on the right  $G_c$  is the energy required for an incremental crack extension and it is a material constant that measures the crack resistance. The factor  $1/2$  in the above equation is due to the particular crack configuration shown in Figure 7.8 where the crack extension takes place symmetrically at both ends of the crack. The condition (7.55) represents a crack growth criterion

$$\boxed{G = G_c} \quad (7.56)$$

which is similar to the condition (7.42) given in terms of the stress intensity factor. The energy release rate  $G$  reads from (7.45) and (7.47) as

$$\boxed{G = \frac{\pi\sigma_0^2 a}{E'}} \quad (7.57)$$

for a cracked linear elastic body illustrated in Figure 7.8. Similar to the determination of the critical crack length  $a_c$  and the critical stress  $\sigma_{0f}$ , the value of  $G$  is also independent of the external loading conditions (fixed grip or dead load) for linear elastic solids. The graphical representation of this statement is rather well-known and can be found in any fracture mechanics book, e.g. ANDERSON [6] and KNOTT [114]. Contrarily, in the case

of nonlinear elasticity it is different and for fixed grip conditions,  $G$  is often called as the elastic strain energy release rate, see GDOUTOS [77], p.117.

The energetic approach discussed so far is valid for elastic brittle fracture mechanics. It is mainly applicable for brittle materials like glass or ceramics. Later the Griffith theory has been extended independently by IRWIN [103] and OROWAN [173] to account for limited plastic behavior encountered around the crack tip. They proposed that the resistance to crack extension in ductile materials is the sum of the elastic surface energy  $\gamma$  and the plastic dissipation  $\gamma_p$  per unit area of surface created. Therefore, this extension involves in principal no new mathematical developments and the failure stress (7.50) is modified as

$$\sigma_{0f} = \sqrt{\frac{2E'(\gamma + \gamma_p)}{\pi a}} . \quad (7.58)$$

For typical ductile materials such as metals,  $\gamma_p$  is much larger than  $\gamma$  and the resistance to a crack extension is mainly governed by the plastic dissipation, e.g. Orowan estimated that  $\gamma_p$  is three orders of magnitude greater than  $\gamma$  in metals. Contrary to ideally brittle materials, where a crack is formed due to the breaking of atomic bonds, in metals when a crack propagates dislocation motions occur in the vicinity of the crack tip yielding an additional energy dissipation. Hence, the term  $\gamma_p$  in (7.58) has a sound micromechanical motivation for ductile crystalline solids.

The crack growth resistance curves (R-curves) is an alternative method which can be closely related to the extended version the Griffith theory. The concept was proposed by IRWIN & KIES [106] to study slow stable crack growth possibly accompanied by some inelastic deformations. In principal, the crack growth condition looks the same as (7.56). The only difference is  $G_c$  is replaced with  $R$  which denotes the rate of energy dissipation during a stable crack growth, i.e.

$$G = R . \quad (7.59)$$

$R$  consists of two parts. Namely, the energy consumed during the generation of new crack surfaces and the energy dissipated as a consequence of inelastic deformations.

**7.3.3. Equivalence of Energy Release Rate and Stress Intensity Factor.** Two fundamental parameters, the stress intensity factor  $K$  and the energy release rate  $G$ , which can be employed to describe the behavior of cracks, have been discussed in previous sections. The factor  $K$  describes the intensity of stress, strain and displacement fields near the crack tip. On the other hand, the parameter  $G$  specifies the net change in the potential energy associated with an increment of crack extension. Therefore, it is possible to say that, the stress intensity factor is a local parameter while the energy release rate describes the global behavior. In the following, the relation between the strain energy release rate and the stress intensity factor is derived for a linear elastic solid. Thus, we show that the energetic and stress intensity approaches to fracture mechanics are essentially equivalent provided that the material under consideration is linear elastic.

The parameters  $G$  and  $K_I$  for a crack of length  $2a$  in an infinite plate subjected to a remote tensile stress are provided in (7.57) and (7.41), respectively. Combination of (7.57) and (7.41) yields the following representation

$$\boxed{G = \frac{K_I^2}{E'} ,} \quad (7.60)$$

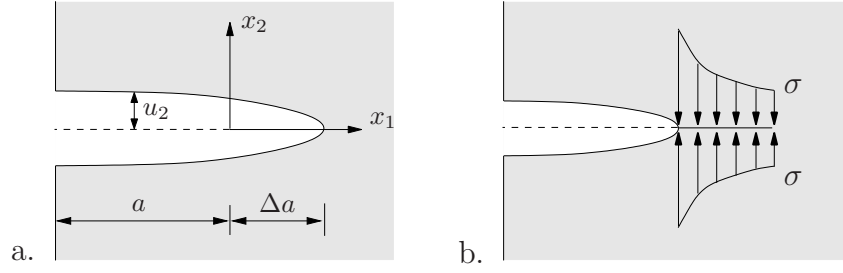


**Figure 7.11:** Crack closure procedure. a) The original crack. b) Closure of the original crack with an amount of  $\Delta a$  by the application of the stress  $\sigma$ .

where  $E' = E$  for plane stress and  $E' = E/(1 - \nu^2)$  for plane strain problems. Although the relation (7.60) is obtained for a particular crack geometry, it is a general relationship that applies also to other configurations. It can be proven based on an crack closure analysis following the work of IRWIN [104]. In Mode I loading a crack of initial length  $a + \Delta a$  is considered, as shown in Figure 7.11a. In the given configuration tractions are applied to crack surfaces from  $x_1 = 0$  to  $x_1 = \Delta a$  such that the crack is closed in that region, see Figure 7.11b. Then the work of crack closure is computed as

$$\Delta W = \int_0^{\Delta a} \sigma_{22} u_2 dx_1, \quad (7.61)$$

where the displacement  $u_2$  in  $x_1$  axis is obtained from (D.57) by setting  $\theta = \pi$ ,

$$u_2 = \frac{(\kappa + 1)K_I(a + \Delta a)}{\mu} \sqrt{\frac{\Delta a - x_1}{2\pi}} \quad (7.62)$$

with  $K_I(a + \Delta a)$  representing the stress intensity factor of the original crack tip with crack length  $a + \Delta a$ . The stress necessary to close the crack is determined from the solution of the problem with the crack length  $a$ , i.e.

$$\sigma_{22} = \frac{K_I(a)}{\sqrt{2\pi x_1}}. \quad (7.63)$$

Furthermore, the work of closure  $\Delta W$  given in (7.61) is related to the energy release rate

$$G = \lim_{\Delta a \rightarrow 0} \left( \frac{\Delta W}{\Delta a} \right) \quad (7.64)$$

under frozen loading conditions. Using the above results, (7.61)-(7.64), the following relationship is obtained

$$G = \lim_{\Delta a \rightarrow 0} \frac{(\kappa + 1)K_I(a + \Delta a)K_I(a)}{4\pi\mu\Delta a} \int_0^{\Delta a} \sqrt{\frac{\Delta a - x_1}{x_1}} dx_1. \quad (7.65)$$

Evaluation of the limit in (7.65) yields the final expression

$$G = \frac{(\kappa + 1)K_I^2}{8\mu} = \frac{K_I^2}{E'}. \quad (7.66)$$

If all the three modes of crack extension are present, then the relation between the energy release rate and the intensity factors is given by

$$G = \frac{K_I^2}{E'} + \frac{K_{II}^2}{E'} + \frac{K_{III}^2}{2\mu}. \quad (7.67)$$

As a result of above discussions, it is possible to conclude that, the stress intensity factor and the energy release rate based approaches are equivalent for linear elastic bodies. Notice carefully that the mixed mode energy release rate given in equation (7.67) is valid only for self similar crack growth. However, in reality Mode II cracks do not propagate their own plane and they follow a path which is not known a priori. Hence, an analytical computation of  $G$  for Mode II is not possible as explained here for Mode I, see e.g. GDOUTOS [77] p.128 and ANDERSON [6] p.72.

**7.3.4.  $J$ -Integral.** The concepts of the energy release rate and the stress intensity factors discussed in previous sections are restricted to the linear elastic material behavior. A generalization to the nonlinear elastic behavior and the deformation theory of plasticity can be achieved by the *path-independent  $J$ -integral*. Although the concept of  $J$ -integral has been developed first by ESHELBY [66, 67], its application to two-dimensional notch problems has been performed by RICE [188, 189]. Eshelby concerned with the characterization of generalized forces on dislocations and defects in elastic solids using the energy momentum tensor. Two earlier works by CHEREPANOV [42] and SANDERS [195] are also closely related to the  $J$ -integral of Rice and worth to mention. The concept of  $J$ -integral and path-independent integrals are indeed directly connected to the *configurational mechanics* which is also referred to as the mechanics in material space or the Eshelbian mechanics, see for example comprehensive treatments by MAUGIN [133], GURTIN [88] and KIENZLER & HERMANN [113]. A discussion of invariant integrals in a broader setting, especially in connection with the configurational mechanics, will be discussed in Section 8.3.

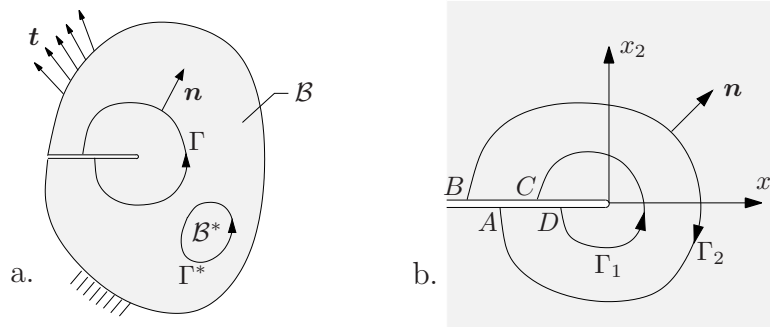


**Figure 7.12:** a.) A body with flat parallel crack surfaces. b.) Magnified view of the crack surfaces. Paths  $\Gamma_1$  and  $\Gamma_2$  around the crack tip running counterclockwise and clockwise, respectively.  $\mathbf{n}$  is the outward unit normal vector.

In the sequel, the  $J$ -integral is introduced in the form proposed by RICE [188, 189]. We consider a two-dimensional homogeneous linear or nonlinear elastic solid free of body forces. The body contains a flat crack where the crack surfaces are parallel to each other as shown in Figure 7.12a. There is no traction applied to the cracks surfaces. The tip of the notch is an arc where a sharp crack is treated as the limiting case. The strain energy density of the elastic medium is

$$W(\boldsymbol{\varepsilon}) := \int_0^{\boldsymbol{\varepsilon}} \boldsymbol{\sigma} : d\boldsymbol{\varepsilon} . \quad (7.68)$$



The vectorial  $J$ -integral is defined by

$$\mathbf{J} := \int_{\Gamma} [ W \mathbf{n} - \mathbf{t} \cdot \nabla \mathbf{u} ] ds , \quad (7.69)$$

where  $\Gamma$  is an arbitrary curve that surrounds the crack tip running counterclockwise from the lower flat notch surface to the upper one, see Figure 7.12a. The vectors  $\mathbf{n}$  and  $\mathbf{t} = \boldsymbol{\sigma} \cdot \mathbf{n}$  denote the unit outward normal to the curve  $\Gamma$  and the traction vector on  $\Gamma$ , respectively. Note that the original definition of  $J$ -integral by RICE [188, 189] is a scalar quantity,

$$J_1 = \int_{\Gamma} [ W n_1 - \mathbf{t} \cdot \frac{\partial \mathbf{u}}{\partial x_1} ] ds \quad (7.70)$$

obtained by a scalar multiplication of (7.69) with the unit vector in  $x_1$  direction. Equation (7.69) can also be written as

$$\mathbf{J} = \int_{\Gamma} [ W \mathbf{1} - \nabla^T \mathbf{u} \cdot \boldsymbol{\sigma} ] \cdot \mathbf{n} ds . \quad (7.71)$$

The line integral (7.71) can be recast into a volume integral by the application of divergence theorem

$$\mathbf{J} = \int_{\mathcal{B}^*} \text{div} [ W \mathbf{1} - \nabla^T \mathbf{u} \cdot \boldsymbol{\sigma} ] dV \quad (7.72)$$

if it is computed for a closed curve  $\Gamma^*$  that surrounds the domain  $\mathcal{B}^*$ , see Figure 7.12a. The integrand of (7.72) reads in indicial notation

$$\begin{aligned} [ W \delta_{ij} - u_{k,i} \sigma_{kj} ]_{,j} &= W_{,i} - u_{k,ij} \sigma_{kj} - u_{k,i} \sigma_{kj,j} \\ &= \sigma_{mn} \varepsilon_{mn,i} - u_{k,ij} \sigma_{kj} \\ &= \sigma_{mn} u_{m,ni} - \sigma_{mn} u_{m,ni} \\ &= 0 . \end{aligned} \quad (7.73)$$

In (7.73) we make use of the identity  $\sigma_{mn} = \partial W / \partial \varepsilon_{mn}$ , the divergence free stress ( $\sigma_{kj,j} = 0$ ) in the absence of body forces and also the symmetry of the stress tensor ( $\sigma_{mn} \varepsilon_{mn,i} = \sigma_{mn} u_{m,ni}$ ). Since the integrand (7.73) vanishes identically, the vectorial  $J$ -integral defined in (7.69) is equal to zero for a path enclosing elastic medium free of any defects or singularities. It is self evident that the original definition of the  $J$ -integral (7.70) vanishes for such a closed path as well.

As a next step the path independency of the  $J$ -integral is proved. We consider the closed contour  $\Gamma_1 C B \Gamma_2 A D$  as shown in Figure 7.12b. Since the area enclosed by this path is free of singularities, the corresponding  $J$ -integral has to vanish

$$J_1 = \underbrace{\int_{\Gamma_1} [ W n_1 - t_i u_{i,1} ] ds}_{=: J_{\Gamma_1}} + \underbrace{\int_{\Gamma_2} [\dots] ds}_{=: -J_{\Gamma_2}} + \underbrace{\int_{CB} [\dots] ds}_{=: J_{CB}} + \underbrace{\int_{AD} [\dots] ds}_{=: J_{AD}} = 0 , \quad (7.74)$$

where  $[\dots]$  denotes the same integrand in the first term of (7.74). The second integral over  $\Gamma_2$  given above is defined with a minus sign in front, because the contour  $\Gamma_2$  is clockwise.

The integrals  $J_{AD}$  and  $J_{CB}$  are zero while the normal vectors has no component in  $x_1$  direction along  $AB$  and  $CD$  ( $n_1 = 0$ ) and the crack surfaces are traction free ( $t_i = 0$ ). As a consequence, (7.74) boils down to

$$J_{\Gamma_1} = J_{\Gamma_2} . \quad (7.75)$$

Equation (7.75) demonstrates the path independence of the  $J$ -integral defined in (7.70). Note that the independency is valid for elastic materials, possibly also nonlinear and anisotropic, under quasistatic loading conditions and in the absence of body forces. The notch in the elastic solid must have flat and parallel traction free crack surfaces.

**7.3.5. Relationship Between  $J$ -Integral and Energy Release Rate.** In the sequel, the physical interpretation of the  $J$ -integral is discussed and its relation to the energy release rate  $G$  is presented for self similar crack growth conditions. A two-dimensional elastic body shown in Figure 7.13 is considered. The potential energy of the body with an initial crack of length  $a$  is

$$\Omega(a) = \mathcal{E}(a) + \mathcal{U}(a) = \int_{\mathcal{B}} W dV - \int_{\partial\mathcal{B}_t} \mathbf{t} \cdot \mathbf{u} ds \quad (7.76)$$

under quasistatic loading and in the absence of body forces.  $\partial\mathcal{B}_t$  denotes the part of the boundary on which the tractions are prescribed. It is assumed that the external tractions  $\mathbf{t}$  are independent of the crack length  $a$  and the crack surfaces are traction free. Differentiation of (7.76) with respect to the crack length  $a$  yields

$$\frac{d\Omega}{da} = \int_{\mathcal{B}} \frac{dW}{da} dV - \int_{\partial\mathcal{B}} \mathbf{t} \cdot \frac{d\mathbf{u}}{da} ds , \quad (7.77)$$

where the integration domain  $\partial\mathcal{B}_t$  of the second integral is replaced with  $\partial\mathcal{B}$  while the displacements are independent of the crack length for the rest of the boundary, i.e.  $d\mathbf{u}/da = \mathbf{0}$  on  $\partial\mathcal{B}_u$  where  $\partial\mathcal{B} = \partial\mathcal{B}_t \cup \partial\mathcal{B}_u$ . It is possible to choose the contour of the  $J$ -integral as the outer boundary of the body in the counterclockwise direction from the lower crack face to the upper one. Because the tractions  $\mathbf{t}$  are zero on the crack surfaces  $\partial\mathcal{B} \setminus \Gamma$ , the integration domain  $\partial\mathcal{B}$  of the second term in (7.77) can be changed to the contour  $\Gamma$  of the  $J$ -integral. A new coordinate system  $\tilde{x}_1 - \tilde{x}_2$  attached to the crack tip is introduced, i.e.  $\tilde{x}_i = x_i - a\delta_{i1}$ . As a consequence, one obtains

$$\frac{d}{da} = \frac{\partial}{\partial a} + \frac{\partial}{\partial x_1} \frac{\partial x_1}{\partial a} = \frac{\partial}{\partial a} - \frac{\partial}{\partial x_1} = \frac{\partial}{\partial a} - \frac{\partial}{\partial \tilde{x}_1} \quad (7.78)$$

since  $\partial x_1 / \partial a = -1$  and  $\partial / \partial x_1 = \partial / \partial \tilde{x}_1$ . Substitution of (7.78) into (7.77) gives

$$\frac{d\Omega}{da} = \int_{\mathcal{B}} \left[ \boldsymbol{\sigma} : \nabla \left( \frac{\partial \mathbf{u}}{\partial a} \right) + \frac{\partial W}{\partial x_1} \right] dV - \int_{\Gamma} \mathbf{t} \cdot \left[ \frac{\partial \mathbf{u}}{\partial a} - \frac{\partial \mathbf{u}}{\partial x_1} \right] ds \quad (7.79)$$

where the symmetry of the stress tensor and the constitutive relation  $\boldsymbol{\sigma} = \partial W / \partial \boldsymbol{\varepsilon}$  have been utilized during the derivation. Considering  $\partial \mathbf{u} / \partial a$  as a kinematically admissible displacement field, it is possible to write the principle of virtual work in the following form

$$\int_{\mathcal{B}} \left[ \boldsymbol{\sigma} : \nabla \left( \frac{\partial \mathbf{u}}{\partial a} \right) \right] dV = \int_{\Gamma} \mathbf{t} \cdot \frac{\partial \mathbf{u}}{\partial a} ds . \quad (7.80)$$

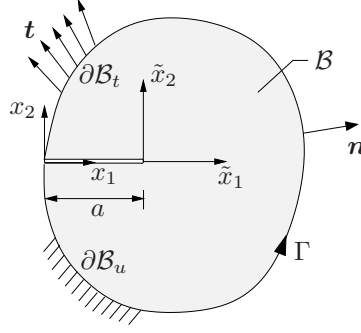


**Figure 7.13:** A body with a flat crack of length  $a$ . The coordinate system  $\tilde{x}_1 - \tilde{x}_2$  is attached to the crack tip and related to the fixed coordinate system  $x_1 - x_2$  by  $\tilde{x}_i = x_i - a\delta_{i1}$ . The contour  $\Gamma$  traces the outer boundary of the body.

Equation (7.79) along with (7.80) yields

$$-\frac{d\Omega}{da} = \int_{\mathcal{B}} \frac{\partial W}{\partial x_1} dV - \int_{\Gamma} \mathbf{t} \cdot \frac{\partial \mathbf{u}}{\partial x_1} ds . \quad (7.81)$$

Finally, the application of divergence theorem to (7.81) renders

$$-\frac{d\Omega}{da} = \int_{\Gamma} \left[ W n_1 - \mathbf{t} \cdot \frac{\partial \mathbf{u}}{\partial x_1} \right] ds . \quad (7.82)$$

The right hand side of the above equation is nothing but the  $J$ -integral, see (7.70). The quantity on the left is the rate of decrease of the potential energy. Thus,  $J_1$  is indeed equivalent to the rate of decrease of the potential energy with respect to the crack length  $a$  both for the linear and nonlinear elastic response. In fact, if the material is linear elastic, then  $J_1$  reduces to the energy release rate  $G$  defined in (7.55), which is in turn related to the stress intensity factor  $K_I$  as discussed in Section 7.3.3, i.e.

$$\boxed{J_1 = G = \frac{K_I^2}{E'} .} \quad (7.83)$$

The  $J$ -integral has been employed later also for elastoplastic materials in the context of the deformation theory of plasticity. The deformation theory of plasticity (also known as the Hencky's type plasticity) relates total strains to stresses. Hence, it can be considered as non-linear elastic response provided that the body is subjected to monotonically increasing loads only. HUTCHINSON [101] and RICE & ROSENGREN [192] showed that the  $J$ -integral characterizes the crack tip stresses and strains in hardening materials. If the strain hardening is characterized by a power law, then the singularity in the solution is often referred to as HRR singularity due to the investigations of Hutchinson, Rice and Rosengren.

Analogous to the fracture criteria governed by the intensity factors (7.42) and the energy release rate (7.56), it is possible to introduce an alternative condition based on the  $J$ -integral. This criterion of crack propagation reads

$$\boxed{J = J_c ,} \quad (7.84)$$

where  $J_c$  is a material parameter that denotes the critical value of the  $J$ -integral.

### 7.4. Atomistic Approach to Fracture

In the preceding sections, the crack propagation is discussed in a continuum framework. On the other hand, when sufficient stress is applied fracture occurs on an atomic level by a breakage of bonds holding atoms together. Consequently, the tensile strength of an ideal crystalline body is found as the stress that is required to break these bonds. On the atomic level, solids may be represented as assembly of point masses connected by non-linear springs. The point masses and springs stand for atoms and atomic bonds, respectively. Although the mass-spring representation is over-simplistic, it can lead to a deeper understanding of brittle fracture. A cubic lattice of spacing  $r_0$  is subjected to a tensile stress  $\sigma_0$ , see Figure 7.14. The lattice spacing corresponds to the equilibrium position of atoms where the potential energy is at a minimum. A pair of atoms,  $A_1$ - $A_2$ , from the cubic lattice is considered. In Figures 7.15a and 7.15b schematic plots of the potential energy and force versus the separation distance are depicted for the pair  $A_1$ - $A_2$ . Although the details of such curves differ depending on the type of bonding associated with a specific material, in general their forms for metals are similar. In order to increase the separation distance from the equilibrium position, a tensile force is required which has to exceed a particular cohesive force to separate the bond completely. The total amount of energy  $U_B$  that must be supplied to sever the two atoms completely is called as the bond energy and given by the following integral

$$U_B = \int_{r_0}^{\infty} F dr , \quad (7.85)$$

where  $F$  is the applied force. Note that the bond energy is equal to twice the surface tension  $\gamma$ . Thus, the bond energy  $U_B$  can be estimated by an extrapolation of experiments conducted to measure surface tensions of liquid droplets.

The force  $F$  is zero at the equilibrium spacing  $r_0$  and reaches its maximum value at the point of inflection of the potential curve. The slope of the force-spacing curve is the stiffness of the spring connecting the atoms and related to the Young's modulus of the material. In order to estimate the strength of the material at the atomic level, the force-atomic spacing curve given in Figure 7.15b is approximated by a half sine curve in the attractive region. Hence, the force-atomic spacing relation is obtained as

$$F = F_c \sin\left(\frac{\pi x}{\lambda}\right) \quad \text{with} \quad x := r - r_0 \quad \text{for} \quad x \geq 0 . \quad (7.86)$$

For small displacements, the relationship given in (7.86) can be further approximated as

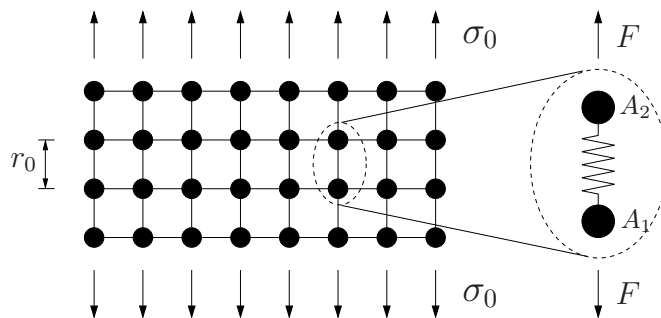
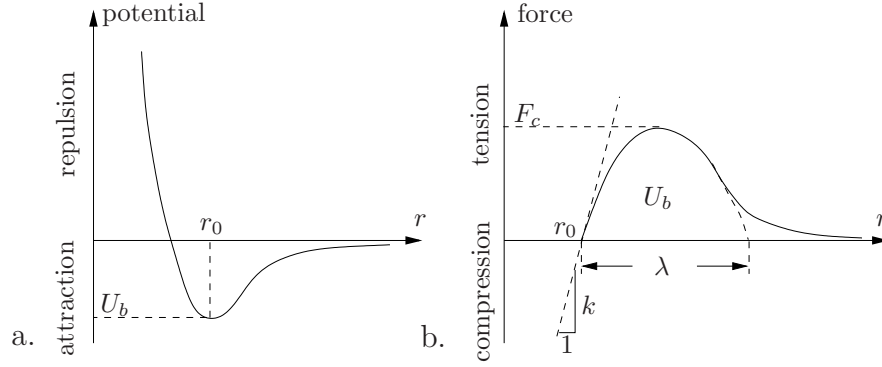


Figure 7.14: Atomistic approach to fracture.



**Figure 7.15:** Atomistic approach to fracture. a.) Interatomic potential. b.) Interatomic force-separation relation.

linear, i.e.  $\sin x \approx x$ ,

$$F = F_c \frac{\pi x}{\lambda} \quad (7.87)$$

and consequently, the stiffness of the bond is given by

$$k = F_c \frac{\pi}{\lambda}. \quad (7.88)$$

The cohesive stress  $\sigma_c$  is then estimated from (7.88) in terms of the Young's modulus  $E$ , the equilibrium spacing  $r_0$  and the half of the period of the sine function  $\lambda$ ,

$$\sigma_c = \frac{E\lambda}{\pi r_0}. \quad (7.89)$$

The estimate (7.89) is obtained by a multiplication of both sides of (7.88) by the number of bonds per unit area  $N$  and the equilibrium spacing  $r_0$  resulting in following identifications,  $\sigma_c = FN$  and  $E = kNr_0$ . Equation (7.89) is further simplified, if  $\lambda$  is assumed roughly to be equal to  $r_0$ ,

$$\sigma_c \approx \frac{E}{\pi}. \quad (7.90)$$

The area under the sine curve represents the work supplied when the bond is broken. Hence, the surface energy  $\gamma \approx U_b N/2$  is estimated from (7.86) by a multiplication with  $N$  and an integration as follows

$$\gamma = \frac{1}{2} \int_0^\lambda \sigma_c \sin\left(\frac{\pi x}{\lambda}\right) dx = \sigma_c \frac{\lambda}{\pi}. \quad (7.91)$$

Notice that the surface energy  $\gamma$  is equal to one half the fracture energy while two surfaces are created when a fracture occurs. Insertion of (7.91) into (7.89) gives the following estimate for the ideal fracture strength

$$\sigma_c = \sqrt{\frac{E\gamma}{r_0}}. \quad (7.92)$$

All the previous expressions derived in this section are considering the interaction energies only between pairs of atoms across the fracture surface. It is possible to improve these approximations by considering not only the pairs but also further neighboring atoms. Substitution of  $\rho = r_0$  in (7.37) sets the radius of the crack tip on the order of atomic

spacing and it gives an appraisal of the local stress concentration at the tip of an atomic crack

$$\sigma_{22}(A) = 2\sigma_0 \sqrt{\frac{a}{r_0}}, \quad (7.93)$$

where  $\sigma_{22}(A)$  refers to the stress computed at the point  $A$  in Figure 7.4. By equating (7.93) to cohesive stress in (7.92), the remote stress at failure is computed as

$$\sigma_{0f} = \sqrt{\frac{E\gamma}{4a}}. \quad (7.94)$$

A point worthy of note is that, (7.94) is a rough calculation of the stress at failure while the result in (7.37) is based on continuum assumptions and it is not valid at the atomic level. Nevertheless, the prediction of failure stress  $\sigma_{0f}$  in (7.94) obtained from the atomistic considerations together with a stress analysis shows a clear similarity in the form to that given in (7.50) and they differ by less than 40%. Thus, both approaches are consistent with each other for sharp cracks in ideally elastic brittle media.

### 7.5. Crack Tip Plasticity and Cohesive Fracture Theories

In Section 7.2 the stress field in the vicinity of a sharp crack is evaluated by the use of stress intensity factors for linear elastic materials. The solutions showed that there exist stress singularities at the crack tip, i.e if  $r \rightarrow 0$  then  $\sigma \rightarrow \infty$ . It is clear that, an occurrence of infinite stress is not to be expected in real materials. In fact, some inelastic processes like plasticity (yielding) or damage (void nucleation) put a bound on the level of stress and prevents it from being infinite. In the following, it is assumed that the size of the inelastic zone  $\rho_{in}$  in the neighborhood of the crack tip is small compared to the sizes of both the crack  $a$  and the  $K$ -dominant region  $\rho_K$  in which the stress intensity factor solution is valid. The fracture under above mentioned conditions is referred to as small scale yielding situation (RICE [188]), see Figure 7.16. In the sequel, we will discuss small scale yielding problems and give possible estimates of the size of the inelastic zone  $\rho_{in}$ . Note that the crack propagation under small scale yielding conditions can still be treated as brittle fracture while the material is assumed to be elastic except at a very small region around the crack tip.

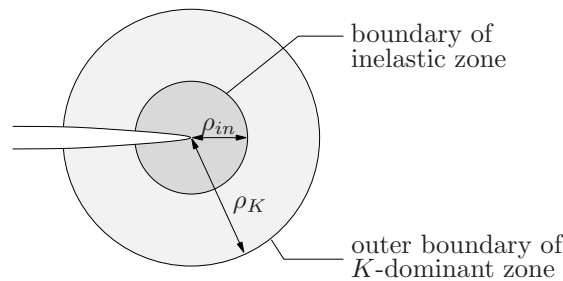


**Figure 7.16:** Basis of the small scale yielding hypothesis. The size of the inelastic region  $\rho_{in}$  is small compared to the size of  $K$ -dominant region  $\rho_K$  and any other geometrical dimension of the body.

A first estimate of the size of a plastic region is obtained as follows. We consider a mode-I loading where the stress field along the horizontal axis ( $y = 0$  or  $\theta = 0$ ) can be

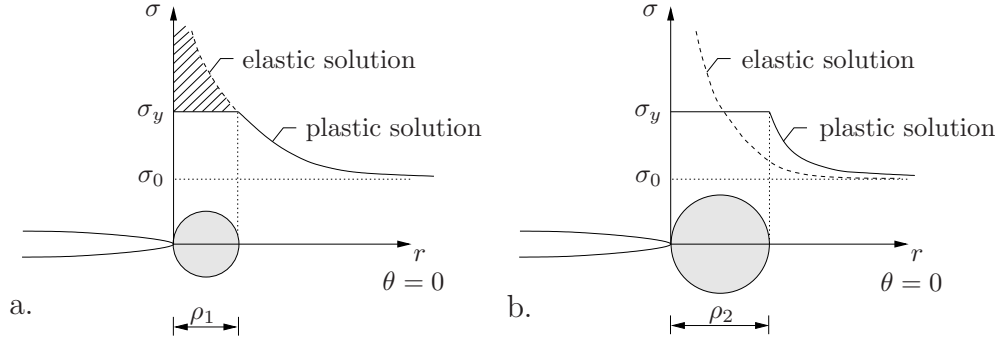


**Figure 7.17:** Estimates of the size of plastic zone at the crack tip. a.) The first-order and b.) the second-order estimates by IRWIN [105].

computed from (D.55) or (D.58) as

$$\sigma_{22} = \sigma_{\theta\theta} = \frac{\sigma_0 \sqrt{\pi a}}{\sqrt{2\pi r}} = \frac{K_I}{\sqrt{2\pi r}} . \quad (7.95)$$

The variation of the stress field in the vicinity of the crack is plotted in Figure 7.17. If an ideal elastoplastic material with the yield limit  $\sigma_y$  is considered, then an estimate of the plastic zone size  $\rho_1$  is determined as

$$\rho_1 = \frac{1}{2\pi} \left( \frac{K_I}{\sigma_y} \right)^2 \quad (7.96)$$

by simply equating  $\sigma_y$  to (7.95) and then solving it for  $r$ . The result  $\rho_1$  is a rough prediction which underestimates the plastic zone size, see for example ANDERSON [6] and MEGUID [138]. The corresponding tensile stress distribution is plotted in Figure 7.17a. Indeed, this simple analysis is not strictly correct, while it is based on the elastic crack tip solution. On the other hand, as a result of yielding, a stress redistribution must take place to satisfy the equilibrium. IRWIN [105] proposed a modified approach for the same crack problem based on the following equilibrium condition

$$\int_0^{\rho_1} \frac{K_I}{\sqrt{2\pi r}} dr = 2\rho_2 \sigma_y . \quad (7.97)$$

The integral in (7.97) computes the hatched area in Figure 7.17a that is responsible for further yielding. This contribution was not considered in the first estimate. Integration of (7.97) and then the solution of the resultant equation for  $\rho_2$  yields

$$\rho_2 = \frac{1}{\pi} \left( \frac{K_I}{\sigma_y} \right)^2 \quad (7.98)$$

which is the twice of the one obtained by the first estimate. The corresponding stress distribution is visualized in Figure 7.17b. Contrary to the first estimate, in Irwin's approach the equilibrium is maintained inside the body.

Another model, which is known as the *strip yield model*, for the description of the plastic zone around the crack tip has been proposed by DUGDALE [61]. We consider a crack of length  $2a$  in an infinite plate subjected to the uniform tensile stress  $\sigma_0$ . The model is based on two hypotheses. First, all plastic deformations are assumed to concentrate in a



line in front of the crack. Second, a concept of effective crack is introduced which is longer than the physical crack by the length of the inelastic zone considered, i.e.  $a_{eff} = a + \rho_3$ . The size of the plastic zone  $\rho_3$  is determined such that the stress at the tip of the effective crack should be bounded and equal to the yield stress  $\sigma_y$ . In fact, the model approximates the elastoplastic behavior by considering a superposition of two elastic solutions. Namely, a crack under a remote tension and the same crack with the yield stress applied to the plastic zone at the crack tip. The solution of this problem can be obtained by employing the stress function of WESTERGAARD [213]. It can be found in GDOUTOS [77] pp.96-98 which reads for small values of  $\sigma_0/\sigma_y$  as

$$\rho_3 = \frac{\pi}{8} \left( \frac{K_I}{\sigma_y} \right)^2. \quad (7.99)$$

A comparison of (7.98) and (7.99) indicates that, there is about 20% difference between Irwin's and Dugdale's predictions with respect to the size of the plastic zone.

Alternative to the strip yield model of DUGDALE [61], an apparently similar model has been proposed by BARENBLATT [16]. The theoretical account developed by Barenblatt is often referred to as the *cohesive theory of fracture*. He postulated that, the cohesive forces act over a small interval at the ends of a given crack, see Figure 7.19. In this model, underlying atomic nature of the fracture process is recognized by specifying the resistance at the crack tip in terms of a non-linear cohesive force function. The presence of the cohesion zone results in the removal of the singularity at the crack tip in an analogous manner to the strip yield model of DUGDALE [61]. In spite of the apparent similarities between the two models, it is important to realize the fundamental difference in their physical motivations. The former one represents the macroscopic plasticity in the vicinity of a crack tip while the other constitutes the interatomic forces in the cohesive zone.

The cohesive crack problem of BARENBLATT [16] can be treated as a superposition of two linear elastic problems similar to the solution of the strip yield model. The remote loading and the cohesive forces are applied separately to a linear elastic infinite medium containing a crack of length  $2a + 2\rho_{cz}$ , see Figure 7.19. The stress intensity factors of both problems can be superposed yielding a net stress intensity factor. Then the removal of the stress singularity requires that the net stress intensity factor has to vanish. Clearly, the solution of this problem depends on the choice of the cohesive stress function  $t(x)$  and a

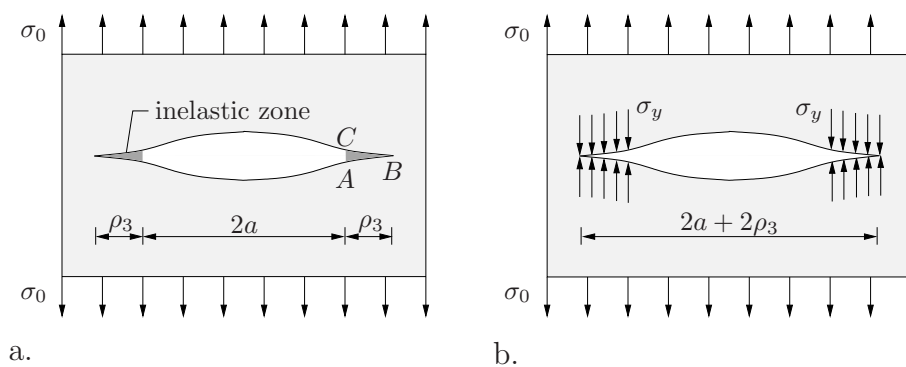


**Figure 7.18:** The strip yield model by DUGDALE [61]. a.) The concept of the effective crack  $a_{eff} = a + \rho_3$  which is longer than the physical crack  $a$  by the length of the plastic zone  $\rho_3$  ahead the crack tip. b.) Plastic zone is realized by the application of a stress equal to the yield stress  $\sigma_y$  of the material.

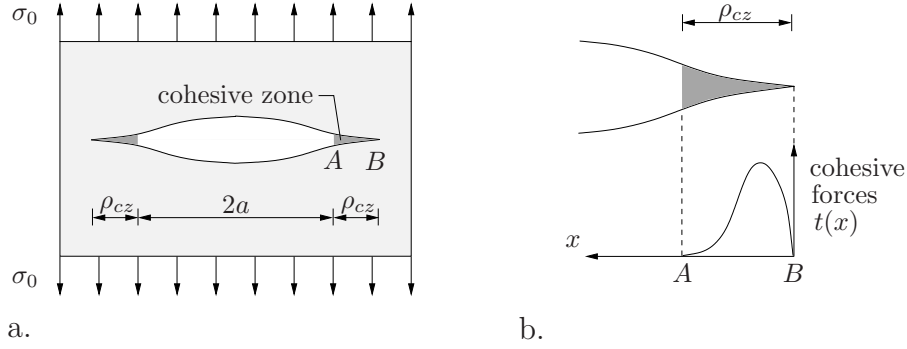


**Figure 7.19:** The cohesive zone model by BARENBLATT [16]. a.) The concept of the cohesive zone  $\rho_{cz}$  ahead the crack tip. b.) Magnified view of the crack tip. The variation of cohesive forces in the cohesive zone ahead the crack tip.

general analytical solution is not available. However, for some special cases approximate solutions can be obtained, see LAWN [125]. A point of interest is the comparison of the crack profile of the cohesive crack with the linear elastic crack surface. Under mode-I loading conditions, according to the solution (D.57), traction free crack surfaces take the shape of a parabola, i.e.  $u_2 \propto x_1^{1/2}$ , see Figure 7.20a. On the other hand, the cohesive forces acting at the crack tip closes the contour into the form of a cusp, i.e.  $u_2 \propto x_1^{3/2}$ , as depicted in Figure 7.20b. Thus, the displacement gradient for a cohesive crack approaches smoothly to zero in the crack tip region,  $\partial u_2 / \partial x_1 \rightarrow 0$  as  $x_1 \rightarrow 0$  whereas in the case of parabola it diverges.

The application of  $J$ -integral (7.70) to the strip yield model leads to important results. We consider the contour  $ABC$  which is shrunk to the boundary of the yield zone as shown in Figure 7.18a. Along the path  $ABC$ ,  $n_1 = t_1 = 0$ ,  $t_2 = \sigma_y$  and consequently  $J_1$  becomes

$$J_1 = - \int_0^{\rho_3} \sigma_y \left[ \frac{\partial u_2^+}{\partial x_1} - \frac{\partial u_2^-}{\partial x_1} \right] dx_1 \quad (7.100)$$

where  $u_2^+$  and  $u_2^-$  are  $x_2$  displacements of the upper and lower crack surfaces, respectively. Introducing the separation (displacement jump)  $\delta = u_2^+ - u_2^-$ , (7.100) can be written as

$$J_1 = - \int_0^{\rho_3} \sigma_y \frac{\partial \delta}{\partial x_1} dx_1 = \int_0^{\delta(A)} \sigma_y d\delta = \sigma_y \delta(A) \quad (7.101)$$

in terms of the yield stress  $\sigma_y$  and the displacement jump  $\delta(A)$  at the tip of the physical crack  $A$ . The separation  $\delta(A)$  is referred to as the *crack tip opening displacement* (CTOD) and is an important fracture parameter. The concept of CTOD has been introduced by

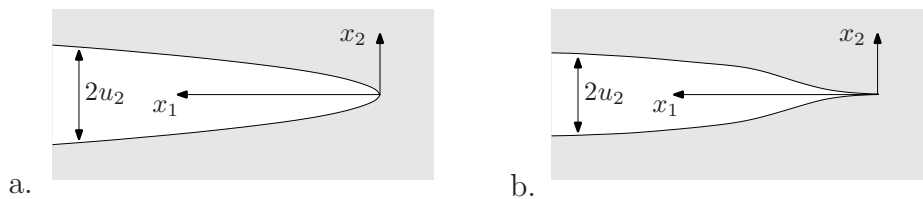


**Figure 7.20:** Crack profiles in the vicinity of the crack tip. a.) Linear elastic solution with traction free crack surfaces yields a parabolic profile  $u_2 \propto x_1^{1/2}$ . b.) Cohesive crack solution leads to a profile characterized by  $u_2 \propto x_1^{3/2}$ .

WELLS [211] and employed especially in elastoplastic fracture mechanics. Note that the  $J$ -integral, the energy release rate, the stress intensity factor, and the crack tip opening displacement are equivalent fracture parameters for linear elastic materials under the assumption of small scale yielding,

$$J_1 = G = \frac{K_I^2}{E'} = \sigma_y \delta(A) . \quad (7.102)$$

Therefore, the same fracture criterion can be expressed in terms of any of the four parameters.

In a similar way  $J$ -integral can be applied to cohesive cracks, that is

$$J_1 = - \int_0^{\rho_{cz}} t(x_1) \left[ \frac{\partial u_2^+}{\partial x_1} - \frac{\partial u_2^-}{\partial x_1} \right] dx_1 = \int_0^{\delta(A)} t(\delta) d\delta . \quad (7.103)$$

The last integral in (7.103) is the work done by the cohesive forces on the separation, i.e. the intrinsic work of cohesion, see LAWN [125] pp.70-72. In his cohesive fracture theory BARENBLATT [16] introduced the *modulus of cohesion*  $K_{coh}$

$$K_{coh} = \int_0^{\rho_{cz}} \frac{t(x)}{x_1} dx_1 \quad (7.104)$$

as a new material constant. This quantity characterizes the resistance of a material against a crack extension caused by the action of cohesive forces and is related to the surface energy  $\gamma$  by

$$K_{coh} = \sqrt{\pi E' \gamma} . \quad (7.105)$$

We refer to WILLIS [215] for a detailed investigation of the relation between the modulus of cohesion and the surface energy.



## 8. Configurational Forces in Brittle Fracture Mechanics

This section outlines briefly the concept of *configurational forces* and addresses different viewpoints to them. Starting with the Eshelby's thought experiment alternative derivations of the energy momentum tensor are outlined. These cover approaches based on a Lagrangian density, a projection of balance laws onto material manifold, the Noether's theorem and particular invariance requirements. The topic presented here is far from being complete and we refer to books by MAUGIN [133], GURTIN [88] and KIENZLER & HERMANN [113] for comprehensive treatments. Furthermore, a thermodynamically consistent variational formulation of brittle crack propagation based on configurational forces is proposed. It is shown that both the elastic equilibrium response as well as the local crack evolution follow in a natural format by exploitation of a global Clausius-Planck inequality in the sense of Coleman's method. Consequently, the crack propagation direction is identified by the material configurational force which maximizes the local dissipation at the crack front.

### 8.1. Concept of Configurational Forces

The concept of physical forces, which engineers often deal with, is traced back to Newton and Galilei. The physical forces are generated by a change of the actual placement of a material particle in a physical space. On the other hand, the *configurational forces* (they are also known as the *material* or *non-Newtonian forces*) are related to changes of the positions of material points in the reference configuration. ESHELBY [66] was the first who introduced them as forces acting on imperfections in crystals, i.e. dislocations, foreign atoms, vacancies or grain boundaries. Eshelby considered the total energy of a system as a function of a set of parameters required to specify the configurations of imperfections. Then, for a constant external loading state, he defined the configurational force as the negative gradient of the total energy with respect to the position of an imperfection. In fact, the term *configurational force* was not used by ESHELBY [66, 67], he rather called it as the force on a singularity, defect or an imperfection. This force is computed in two dimensions by an integral over a contour that encloses the defect or singularity. The integrand is the contraction of the *energy momentum tensor* with the outward unit normal of the contour. In the three-dimensional case, the contour integral is replaced by a surface integral.

### 8.2. Alternative Derivations of Energy Momentum Tensor

The subsequent discussions are devoted to alternative derivations of the *energy momentum tensor*, which is interchangeably referred to as the *Eshelby stress* tensor. It outlines first briefly the works of ESHELBY [66, 68]. Furthermore, different viewpoints by MAUGIN [133], GURTIN [87, 88] and KIENZLER & HERMANN [113] are presented, see also PODIO-GUIDUGLI [185].

**8.2.1. Eshelby's Thought Experiment.** Following the works of ESHELBY [66, 67], the energy momentum tensor can be derived in a geometrically linear setting from the computation of the force on a defect in an elastic medium. Here, only a short description of the idea is presented, for further details see ESHELBY [66, 67, 68, 69] or MAUGIN [133]. An externally loaded linear elastic body containing a defect enclosed by the surface  $\mathcal{S}$  is considered. Then  $\mathcal{S}$  is moved by an infinitesimal displacement  $-\delta\xi$  in the undeformed

state and the surface  $\mathcal{S}'$  is obtained. Eshelby investigated the energy change associated with this displacement by considering some imaginary operations. Finally, he computed the energy change as

$$\delta E = -\delta \boldsymbol{\xi} \cdot \int_{\mathcal{S}} [\psi \mathbf{1} - (\nabla^T \mathbf{u}) \boldsymbol{\sigma}] \cdot \mathbf{n} dA \quad (8.1)$$

where  $\mathbf{n}$  is the outward unit normal to  $\mathcal{S}$  and  $\psi$  is the energy storage function of the solid. If we consider the energy change  $\delta E$  a priori as a scalar product of a conjugate force  $\mathcal{F}$  with the infinitesimal displacement  $-\delta \boldsymbol{\xi}$ , then (8.1) can be rewritten as

$$\delta E = -\delta \boldsymbol{\xi} \cdot \mathcal{F} . \quad (8.2)$$

A comparison of the last two equations leads to the following identification of the force  $\mathcal{F}$  as an integral taken over the closed surface  $\mathcal{S}$

$$\mathcal{F} := \int_{\mathcal{S}} \boldsymbol{\Sigma} \cdot \mathbf{N} dA . \quad (8.3)$$

$\boldsymbol{\Sigma}$  in (8.3) denotes the *energy momentum tensor*

$$\boxed{\boldsymbol{\Sigma} := \psi \mathbf{1} - (\nabla^T \mathbf{u}) \boldsymbol{\sigma}} \quad (8.4)$$

which is introduced by ESHELBY [66] in the framework of small strain elasticity. Indeed, he called  $\boldsymbol{\Sigma}$  as the *Maxwell tensor of elasticity* for the case of elastostatics and later in ESHELBY [69], he used the expression *energy momentum tensor*. As ESHELBY [69] pointed out, the energy momentum tensor can be related to the Maxwell tensor in electrostatics. In an analogous manner to the force on a singularity in (8.3), the integral of the Maxwell tensor contracted with the outer normal taken over a closed surface  $\mathcal{S}$  gives the total force on all the electric charges inside the surface  $\mathcal{S}$ .

Note that if the integration path  $\mathcal{S}$  in (8.3) encloses the tip of a two-dimensional crack, the component of the force  $\mathcal{F}$  parallel to the crack turns out to be the well-known path independent *J*-integral of fracture mechanics originally proposed by RICE [188, 189]. The *J*-integral is often interpreted as the crack driving force analogously to the force  $\mathcal{F}$  acting on a defect.

**8.2.2. Formal Derivation from a Lagrangian Density.** Next, the *energy momentum tensor* is presented in a geometrically non-linear framework as a natural outcome of a Lagrangian density  $\mathcal{L}$  in a similar way proposed by ESHELBY [68, 69]. We consider a Lagrangian density

$$\mathcal{L} = \mathcal{L}(\mathbf{x}, \nabla_{\mathbf{X}} \mathbf{x}, \mathbf{X}) \quad (8.5)$$

as a function of the current position  $\mathbf{x}$ , the deformation gradient  $\nabla_{\mathbf{X}} \mathbf{x} =: \mathbf{F}$  and the reference coordinates  $\mathbf{X}$ . Indeed, the original derivation of ESHELBY [68, 69] defines the Lagrangian as a function of the displacement field  $\mathbf{u}$  and the displacement gradient  $\nabla_{\mathbf{X}} \mathbf{u}$  instead of  $\mathbf{x}$  and  $\nabla_{\mathbf{X}} \mathbf{x}$ , i.e.

$$\mathcal{L} = \mathcal{L}(\mathbf{u}, \nabla_{\mathbf{X}} \mathbf{u}, \mathbf{X}) . \quad (8.6)$$

The requirement of the Lagrangian density  $\mathcal{L}$  in (8.5) to be extremum when it is integrated over a solid body results in the local condition

$$\frac{\partial \mathcal{L}}{\partial \mathbf{x}} - \frac{\partial}{\partial \mathbf{X}} \frac{\partial \mathcal{L}}{\partial \mathbf{F}} = \mathbf{0} \quad (8.7)$$

which is referred to as the Euler-Lagrange equations of the extremum problem. The gradient of the Lagrangian density  $\mathcal{L}$  reads

$$\frac{\partial \mathcal{L}}{\partial \mathbf{X}} = \frac{\partial \mathcal{L}}{\partial \mathbf{x}} \frac{\partial \mathbf{x}}{\partial \mathbf{X}} + \frac{\partial \mathcal{L}}{\partial \mathbf{F}} \frac{\partial \mathbf{F}}{\partial \mathbf{X}} + \left( \frac{\partial \mathcal{L}}{\partial \mathbf{X}} \right)_{exp} \quad (8.8)$$

with the following notation of explicit partial derivative from ESHELBY [68, 69]

$$\left( \frac{\partial \mathcal{L}}{\partial \mathbf{X}} \right)_{exp} = \frac{\partial \mathcal{L}}{\partial \mathbf{X}} \Bigg|_{\mathbf{x}, \nabla \mathbf{x} \text{ const.}} . \quad (8.9)$$

Employing the indicial notation, (8.8) can be reformulated as

$$\frac{\partial \mathcal{L}}{\partial X_i} = \left( \frac{\partial \mathcal{L}}{\partial x_j} - \frac{\partial}{\partial X_k} \frac{\partial \mathcal{L}}{\partial F_{jk}} \right) F_{ji} + \frac{\partial}{\partial X_k} \left( \frac{\partial \mathcal{L}}{\partial F_{jk}} F_{ji} \right) + \left( \frac{\partial \mathcal{L}}{\partial X_i} \right)_{exp} . \quad (8.10)$$

The first term on the right hand side of (8.10) is the Euler-Lagrange equation (8.7) and vanishes. Hence, one can write from (8.10) the following equation

$$\text{Div} \boldsymbol{\Sigma} = - \left( \frac{\partial \mathcal{L}}{\partial \mathbf{X}} \right)_{exp} \quad (8.11)$$

in terms of the *energy momentum* or the *Eshelby stress*

$$\boldsymbol{\Sigma} = -\mathcal{L} \mathbf{1} + \mathbf{F}^T \frac{\partial \mathcal{L}}{\partial \mathbf{F}} . \quad (8.12)$$

If the Lagrangian density  $\mathcal{L}$  is chosen as the negative of the energy storage function  $\psi$ , then (8.12) renders the Eshelby stress of elastostatics

$$\boldsymbol{\Sigma} = \psi \mathbf{1} - \mathbf{F}^T \mathbf{P} , \quad (8.13)$$

where  $\mathbf{P}$  denotes the first Piola-Kirchhoff stress tensor and is computed from the energy storage by the well-known formula  $\mathbf{P} = \partial_{\mathbf{F}} \psi$ . Note that if we start with the Lagrangian (8.6) defined as a function of  $\mathbf{u}$  instead of  $\mathbf{x}$ , then the energy momentum tensor takes the form as stated originally in ESHELBY [69]

$$\bar{\boldsymbol{\Sigma}} = \psi \mathbf{1} - (\nabla^T \mathbf{u}) \mathbf{P} . \quad (8.14)$$

It is worth to make some comments on  $\boldsymbol{\Sigma}$  and  $\bar{\boldsymbol{\Sigma}}$ . The energy momentum tensor  $\boldsymbol{\Sigma}$  given in (8.13) is *symmetric* if the material is *isotropic*. Insertion of the relation  $\mathbf{P} = \mathbf{F} \mathbf{S}$  into (8.13) gives

$$\boldsymbol{\Sigma} = \psi \mathbf{1} - \mathbf{C} \mathbf{S} , \quad (8.15)$$

where  $\mathbf{S}$  and  $\mathbf{C}$  denote the second Piola-Kirchhoff stress and the right Cauchy-Green tensors, respectively. Isotropy induces the coaxiality of the conjugate stress-strain variables  $\mathbf{S}$  and  $\mathbf{C}$ , i.e.  $\mathbf{S} \mathbf{C} = \mathbf{C} \mathbf{S}$  and this proves the symmetry of  $\boldsymbol{\Sigma}$  in (8.15). On the other hand, the isotropy condition does not lead to the symmetry of  $\bar{\boldsymbol{\Sigma}}$ . Similarly, the energy momentum tensor defined in (8.4) for the case of small strain elastostatics is also asymmetric even for the isotropic material response. Further discussions on the symmetry and alternative definitions of energy momentum tensors can be found in CHADWICK [41] and ESHELBY [68, 69].



The extension to elastodynamics is possible if the Lagrangian density  $\mathcal{L}$  is defined in terms of the energy storage  $\psi$  and the kinetic energy  $\mathcal{K}$  as

$$\mathcal{L} := \mathcal{K} - \psi \quad \text{with} \quad \mathcal{K} := \frac{1}{2} \rho_0 |\mathbf{v}|^2 \quad (8.16)$$

where  $\rho_0$  and  $\mathbf{v}$  are the density and velocity fields, respectively. Consequently, the energy momentum tensor reads

$$\Sigma = (\psi - \mathcal{K}) \mathbf{1} - \mathbf{F}^T \mathbf{P} . \quad (8.17)$$

Note that from (8.11) one can conclude that, if the Lagrangian  $\mathcal{L}$  does not depend explicitly on the reference coordinates  $\mathbf{X}$ , then the energy momentum tensor is divergence free

$$\text{Div} \Sigma = \mathbf{0} . \quad (8.18)$$

This, in the case of elastodynamics, corresponds to a homogeneous continuum where the free energy and the density are not function of  $\mathbf{X}$  explicitly. Furthermore, it provides an additional balance equation similar to  $\text{Div} \mathbf{P} = \mathbf{0}$  which is the linear momentum balance under quasistatic conditions in the absence of body forces.

**8.2.3. Projection of Balance Laws onto Material Manifold.** As an alternative derivation of the *energy momentum tensor* we consider next the approach proposed by MAUGIN [133, 134]. The main idea is the projection of the local momentum balance equation onto the material manifold. Recall the balance of linear momentum

$$\rho \dot{\mathbf{v}} = \text{div} \boldsymbol{\sigma} + \rho \mathbf{b} \quad (8.19)$$

which is formulated with respect to the current configuration.  $\boldsymbol{\sigma}$  and  $\mathbf{b}$  denote the Cauchy stress and the body forces per unit mass, respectively. The divergence operator refers to the current coordinates  $\mathbf{x}$  if it starts with a lowercase letter. Otherwise, it refers to the reference coordinates  $\mathbf{X}$ . The balance of linear momentum can also be written in terms of the first Piola-Kirchhoff stress  $\mathbf{P}$  and the reference density  $\rho_0$

$$\rho_0 \dot{\mathbf{v}} = \text{Div} \mathbf{P} + \rho_0 \mathbf{b} . \quad (8.20)$$

Equation (8.20) is obtained from (8.19) by making use of the relations  $\mathbf{P} = J \boldsymbol{\sigma} \mathbf{F}^{-T}$ ,  $\text{div} \boldsymbol{\sigma} = (\text{Grad} \boldsymbol{\sigma}) : \mathbf{F}^{-T}$ ,  $\text{div}(J^{-1} \mathbf{F}^T) = \mathbf{0}$  and  $\rho_0 = J \rho$  with  $J := \det \mathbf{F}$ . In the case of quasistatics, i.e.  $\dot{\mathbf{v}} = \mathbf{0}$ , without any body forces, i.e.  $\mathbf{b} = \mathbf{0}$ , (8.20) reduces to

$$\text{Div} \mathbf{P} = \mathbf{0} . \quad (8.21)$$

Multiplication of (8.21) with  $\mathbf{F}^T$  yields in indicial notation

$$\begin{aligned} 0 &= F_{aB} P_{aA,A} \\ &= (F_{aB} P_{aA})_{,A} - F_{aB,A} P_{aA} \\ &= (F_{aB} P_{aA})_{,A} - F_{aA,B} P_{aA} , \end{aligned} \quad (8.22)$$

where we made use of the property  $\partial^2 x_a / \partial X_B \partial X_A = \partial^2 x_a / \partial X_A \partial X_B$ . Next, the following identity is employed

$$\begin{aligned} \frac{\partial(\psi \delta_{BC})}{\partial X_C} &= \frac{\partial \psi}{\partial F_{aA}} \frac{\partial F_{aA}}{\partial X_C} \delta_{BC} + \left( \frac{\partial \psi}{\partial X_C} \right)_{exp} \delta_{BC} \\ &= P_{aA} F_{aA,B} + \left( \frac{\partial \psi}{\partial X_B} \right)_{exp} . \end{aligned} \quad (8.23)$$

Substitution of this result into the second term of (8.22) results in

$$\text{Div}[\psi \mathbf{1} - \mathbf{F}^T \mathbf{P}] = \left( \frac{\partial \psi}{\partial \mathbf{X}} \right)_{exp} . \quad (8.24)$$

The identification of the Eshelby stress given in (8.13) leads to

$$\text{Div} \Sigma = \left( \frac{\partial \psi}{\partial \mathbf{X}} \right)_{exp} . \quad (8.25)$$

In the case of homogeneous materials where the free energy does not depend explicitly on  $\mathbf{X}$ , above equation simplifies to (8.18). On the other hand, for dynamic problems with the presence of body forces and inhomogeneities (8.25) reads

$$\boxed{\frac{\partial \mathcal{P}}{\partial t} = \text{Div} \Sigma + \rho_0 \mathbf{b}_{inh} .} \quad (8.26)$$

Note that in the previous equation the energy momentum tensor is defined by (8.17) where the contribution of the kinetic energy is also included.  $\mathcal{P}$  in (8.26) is referred to as the *pseudomomentum* and defined by

$$\mathcal{P} := -\rho_0 \mathbf{F}^T \mathbf{v} . \quad (8.27)$$

The material inhomogeneity force  $\mathbf{b}_{inh}$  per unit mass is identified as

$$\rho_0 \mathbf{b}_{inh} := \frac{1}{2} |\mathbf{v}|^2 \text{Grad} \rho_0 - \left( \frac{\partial \psi}{\partial \mathbf{X}} \right)_{exp} - \rho_0 \mathbf{F}^T \mathbf{b} . \quad (8.28)$$

The gradient operator above refers to the reference coordinates  $\mathbf{X}$  since it starts with an uppercase letter. Observe that the configurational volume forces  $\rho_0 \mathbf{b}_{inh}$  appear if the density  $\rho_0$  or the energy storage function  $\psi$  is not homogeneous, or there exist physical body forces  $\mathbf{b}$ . For further details see MAUGIN [133, 134].

**8.2.4. Derivation from the Noether's Theorem.** The conservation laws for elastic materials can be derived following the *Noether's theorem* that is applicable for systems having a Lagrangian density  $\mathcal{L}$ . The usual variations of the integral of  $\mathcal{L}$  over the body lead to the Euler-Lagrange equations, i.e. the equations of motion. On the other hand, by simultaneous variations of both the dependent and independent variables of the Lagrangian one obtains the *material conservation laws*. The material conservation laws for homogeneous materials in the case of linear elastostatics read

$$\boxed{\begin{aligned} J_i &= \int_{\partial \mathcal{B}} \Sigma_{ji} n_i dA = 0 \\ L_i &= \int_{\partial \mathcal{B}} e_{ijk} (x_j \Sigma_{lk} + u_j \sigma_{lk}) n_l dA = 0 \\ M &= \int_{\partial \mathcal{B}} (x_j \Sigma_{ij} - \frac{1}{2} u_j \sigma_{ij}) n_i dA = 0 , \end{aligned}} \quad (8.29)$$

where  $e_{ijk}$  is the permutation symbol. The first equation is the well-known  $J$ -integral and corresponds to the divergence free Eshelby stress. The other two equations are

known as  $L$ - and  $M$ -integrals. The second balance law (8.29)<sub>2</sub> ( $L$ -integral) is restricted to isotropic materials. The  $J$ -,  $L$ - and  $M$ -integrals govern the balance equations in the material (configurational) space related with a translation, rotation and scaling of a defect, respectively. The extension of these conservation laws to finite kinematics can be found in KNOWLES & STERNBERG [115]. For further details we refer to the works by BUDIANSKY & RICE [35], EISCHEN & HERRMANN [62], STEINMANN [205], a recent book by KIENZLER & HERMANN [113] and references therein.

**8.2.5. Derivation from Invariance Requirements.** A conceptually different approach to derive the *energy momentum tensor* is based on the *invariance arguments of the energy* as proposed by GURTIN [87, 88]. It is well-known that the linear and the angular momentum balances can be obtained from the energy equation by using the invariance condition under superposed rigid body motions, see e.g. GREEN & RIVLIN [83]. Alternatively, following GURTIN [87, 88], the same balance equations can be deduced by the invariance requirement of the work done on a referential control volume under changes in a spatial observer. Furthermore, it is possible in a similar manner to obtain the configurational force balance from the invariance condition under changes in the material observer.

**Derivation of Standard Balance Equations.** We consider the global energy balance equation under purely isothermal conditions

$$\frac{d}{dt} \int_{\mathcal{B}_0} \rho_0 \left( e + \frac{1}{2} \mathbf{v} \cdot \mathbf{v} \right) dV = \int_{\mathcal{B}_0} \rho_0 \mathbf{b} \cdot \mathbf{v} dV + \int_{\partial \mathcal{B}_0} \mathbf{P} \mathbf{N} \cdot \mathbf{v} dA, \quad (8.30)$$

where  $\mathbf{v}$  is the velocity,  $e$  is the internal energy and  $\mathbf{b}$  is the body force. Note that  $e$  and  $\mathbf{b}$  are defined per unit mass. Following GREEN & RIVLIN [83], we require the energy balance equation (8.30) to hold also for  $\tilde{\mathbf{v}} := \mathbf{v} + \mathbf{w}$  where  $\mathbf{w}$  is a translational rigid body velocity. Rewriting (8.30) for  $\tilde{\mathbf{v}}$ , one gets

$$\int_{\mathcal{B}_0} \rho_0 \dot{\mathbf{v}} dV \cdot \mathbf{w} = \left( \int_{\mathcal{B}_0} \rho_0 \mathbf{b} dV + \int_{\partial \mathcal{B}_0} \mathbf{P} \mathbf{N} dA \right) \cdot \mathbf{w}. \quad (8.31)$$

Equation (8.31) must hold for any arbitrary translational rigid body velocity  $\mathbf{w}$  which yields the global form of the linear momentum balance

$$\int_{\mathcal{B}_0} \rho_0 \dot{\mathbf{v}} dV = \int_{\mathcal{B}_0} \rho_0 \mathbf{b} dV + \int_{\partial \mathcal{B}_0} \mathbf{P} \mathbf{N} dA. \quad (8.32)$$

The global balance (8.32) induces the standard local form

$$\rho_0 \dot{\mathbf{v}} = \rho_0 \mathbf{b} + \text{Div} \mathbf{P}. \quad (8.33)$$

Furthermore, it is possible to obtain the angular momentum balance, i.e. the symmetry condition on the stress. By employing (8.33), equation (8.30) can be rewritten as

$$\int_{\mathcal{B}_0} \rho_0 \dot{e} dV = \int_{\mathcal{B}_0} (\mathbf{P} \mathbf{F}^T) : \text{grad}[\mathbf{v}] dV. \quad (8.34)$$

Next, the invariance condition with respect to a rotational rigid body velocity is imposed. Equation (8.34) can be reformulated by replacing  $\text{grad}[\mathbf{v}]$  with  $\text{grad}[\tilde{\mathbf{v}}] := \text{grad}[\mathbf{v}] + \mathbf{\Omega}$  as

$$\int_{\mathcal{B}_0} (\mathbf{P} \mathbf{F}^T) : \mathbf{\Omega} dV = 0, \quad (8.35)$$

where  $\boldsymbol{\Omega}$  is a skew symmetric tensor denoting a constant rigid body angular velocity. In order (8.35) to hold for arbitrary  $\boldsymbol{\Omega}$  the integrand  $(\mathbf{P}\mathbf{F}^T) : \boldsymbol{\Omega}$  has to vanish. Since  $\boldsymbol{\Omega}$  is an arbitrary skew symmetric tensor,  $\mathbf{P}\mathbf{F}^T$  needs to be symmetric, i.e.

$$\mathbf{P}\mathbf{F}^T = \mathbf{F}\mathbf{P}^T \quad (8.36)$$

which is indeed the same result of the balance of angular momentum.

Instead of starting from the balance of energy, the same results can be recovered following GURTIN [88] from the invariance of the work under changes in the spatial observer. The work done on a steady control volume  $\mathcal{P}$  in a pure mechanical quasistatic theory is defined by

$$W(\mathcal{P}) = \int_{\partial\mathcal{P}} \mathbf{P}\mathbf{N} \cdot \mathbf{v} dA + \int_{\mathcal{P}} \rho_0 \mathbf{b} \cdot \mathbf{v} dV . \quad (8.37)$$

As a physical constraint, the work defined in (8.37) must be invariant under changes in the spatial observer. Consider the following change in the spatial observer

$$\tilde{\mathbf{v}} = \mathbf{v} + \mathbf{w} + \boldsymbol{\omega} \times \mathbf{x} \quad (8.38)$$

for which the work  $W(\mathcal{P})$  has to remain the same. This invariance condition results in two conditions

$$\begin{aligned} \int_{\partial\mathcal{P}} \mathbf{P}\mathbf{N} dA + \int_{\mathcal{P}} \rho_0 \mathbf{b} dV &= \mathbf{0} \\ \int_{\partial\mathcal{P}} \mathbf{x} \times \mathbf{P}\mathbf{N} dA + \int_{\mathcal{P}} \mathbf{x} \times \rho_0 \mathbf{b} dV &= \mathbf{0} . \end{aligned} \quad (8.39)$$

The first equation is the global form of the balance of linear momentum written for the control volume  $\mathcal{P}$  under quasistatic conditions. It induces the local form

$$\text{Div}\mathbf{P} + \rho_0 \mathbf{b} = \mathbf{0} \quad (8.40)$$

by using the divergence theorem. In order to satisfy (8.39)<sub>2</sub> the following tensor

$$\int_{\partial\mathcal{P}} \mathbf{x} \otimes \mathbf{P}\mathbf{N} dA + \int_{\mathcal{P}} \mathbf{x} \otimes \rho_0 \mathbf{b} dV \quad (8.41)$$

has to be symmetric. By making use of the divergence theorem and (8.40) it can be shown the following equality

$$\int_{\partial\mathcal{P}} \mathbf{x} \otimes \mathbf{P}\mathbf{N} dA + \int_{\mathcal{P}} \mathbf{x} \otimes \rho_0 \mathbf{b} dV = \int_{\mathcal{P}} \mathbf{F}\mathbf{P}^T dV \quad (8.42)$$

has to hold for any control volume. Owing to the symmetry of (8.41), the right hand side of (8.42) is required to be symmetric. Therefore, it results in the symmetry condition (8.36) of the stress, see GURTIN [88] for further details. In order to incorporate the work performed by the configurational forces, an extension of steady control volumes to unsteady ones, i.e. migrating through the reference configuration  $\mathcal{B}_0$ , is required. The subsequent treatment is devoted to the concept of migrating control volumes.

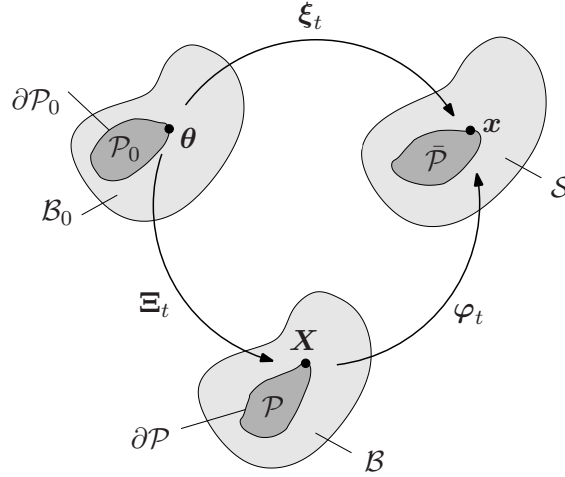


**Figure 8.1:** Migrating control volumes. Both the reference and the spatial configurations are independently parameterized by the material and the spatial maps  $\Xi_t$  and  $\xi_t$ , respectively. The change of  $\Xi_t$  in time describes the movement of the control volume. The deformation map is the composition  $\varphi_t = \xi_t \circ \Xi_t^{-1}$ .

**Migrating Control Volume and Change in Reference Configuration.** A migrating control volume  $\mathcal{P}_0$ , which is originally introduced by GURTIN [88], is a subregion of the reference body  $\mathcal{B}_0$  that moves through  $\mathcal{B}$ . Configurational forces perform work on these volumes by the transfer of material. In the treatment of migrating control volumes together with standard deformations, consideration of three different velocity fields is required. Consider a one-to-one piecewise differentiable transformation  $\Xi_t : \mathcal{B}_0 \rightarrow \mathcal{B}$  of the reference configuration onto itself. It reflects a time-dependent change of the initial Lagrangian coordinates  $\theta \in \mathcal{B}_0$  to the current Lagrangian coordinates  $\mathbf{X} \in \mathcal{B}$  in the sense of a movement of the control volume  $\mathcal{P}_0$ . The material coordinate map  $\Xi_t$  reads

$$\Xi_t : \begin{cases} \mathcal{B}_0 \rightarrow \mathcal{B} \\ (\theta, t) \mapsto \mathbf{X} = \Xi(\theta, t) \end{cases} \quad (8.43)$$

at time  $t \in \mathcal{R}_+$ . With this viewpoint at hand, we introduce also the spatial coordinate map  $\xi_t : \mathcal{B}_0 \rightarrow \mathcal{S}$  as a time-dependent change of the initial Lagrangian coordinates  $\theta \in \mathcal{B}_0$  to Eulerian ones  $\mathbf{x} \in \mathcal{S}$

$$\xi_t : \begin{cases} \mathcal{B}_0 \rightarrow \mathcal{S} \\ (\theta, t) \mapsto \mathbf{x} = \xi(\theta, t) \end{cases} \quad (8.44)$$

at time  $t \in \mathcal{R}_+$ . The material and spatial coordinate maps (8.43) and (8.44) yield the deformation map by the composition

$$\varphi_t(\mathbf{X}) = \xi_t(\theta) \circ \Xi_t^{-1}(\mathbf{X}) \quad (8.45)$$

as visualized in Figure 8.1. Note that the subscript  $t$  next to a mapping is used to show that the mapping is time dependent, e.g.  $\varphi_t(\mathbf{X}) = \varphi(\mathbf{X}, t)$ . Based on the three point maps defined above the following velocity fields are introduced

$$\mathbf{V} := \frac{\partial \Xi(\theta, t)}{\partial t}, \quad \mathbf{v} := \frac{\partial \xi(\mathbf{x}, t)}{\partial t} \quad \text{and} \quad \dot{\varphi} := \frac{\partial \varphi(\mathbf{X}, t)}{\partial t}. \quad (8.46)$$

The material vector field  $\mathbf{V}$  is assigned to the boundary  $\partial\mathcal{P}_0$  of  $\mathcal{P}_0$  and characterizes the velocity at which material is transferred through  $\partial\mathcal{P}_0$ . The velocity fields defined in (8.46) are related to each other by

$$\boxed{\mathbf{v} = \dot{\boldsymbol{\varphi}} + \mathbf{F}\mathbf{V} .} \quad (8.47)$$

The above relation is obtained by considering the time derivative of the decomposition  $\boldsymbol{\xi}_t(\boldsymbol{\theta}) = \boldsymbol{\varphi}_t(\mathbf{X}) \circ \boldsymbol{\Xi}_t(\boldsymbol{\theta})$ , i.e.

$$\frac{\partial \boldsymbol{\xi}_t}{\partial t} = \frac{\partial \boldsymbol{\varphi}_t}{\partial t} + \frac{\partial \boldsymbol{\varphi}_t}{\partial \mathbf{X}} \frac{\partial \boldsymbol{\Xi}_t}{\partial t} . \quad (8.48)$$

Insertion of the definitions in (8.46) and  $\mathbf{F} := \partial\boldsymbol{\varphi}/\partial\mathbf{X}$  into (8.48) yields the result (8.47). Having defined the velocity fields, the work performed on the migrating control volume  $\mathcal{P}$  can be written as

$$\boxed{W(\mathcal{P}) := \int_{\partial\mathcal{P}} \boldsymbol{\Sigma}\mathbf{N} \cdot \mathbf{V}dA + \int_{\partial\mathcal{P}} \mathbf{P}\mathbf{N} \cdot \mathbf{v}dA + \int_{\mathcal{P}} \rho_0\mathbf{b} \cdot \dot{\boldsymbol{\varphi}}dV} \quad (8.49)$$

which involves the sum of three parts. The first two terms in (8.49) represent the working of the standard and the configurational stresses and the last one is the working of the external body forces. Note that for the case of a static control volume, i.e.  $\mathbf{V} = \mathbf{0}$  and  $\mathbf{v} = \dot{\boldsymbol{\varphi}}$ , the work expression becomes identical to (8.37).

**Invariance under Changes in Velocity Field and Material Observer.** The working (8.49) may be reformulated with the help of (8.47) as

$$W(\mathcal{P}) = \int_{\partial\mathcal{P}} (\mathbf{F}^T \mathbf{P}\mathbf{N} + \boldsymbol{\Sigma}\mathbf{N}) \cdot \mathbf{V}dA + \int_{\partial\mathcal{P}} \mathbf{P}\mathbf{N} \cdot \dot{\boldsymbol{\varphi}}dA + \int_{\mathcal{P}} \rho_0\mathbf{b} \cdot \dot{\boldsymbol{\varphi}}dV . \quad (8.50)$$

Following GURTIN [88], we require the work  $W(\mathcal{P})$  to be independent of the tangential component (tangent to  $\partial\mathcal{P}$ ) of the velocity  $\mathbf{V}$  of the control volume. This condition induces

$$\int_{\partial\mathcal{P}} \mathbf{T} \cdot (\mathbf{F}^T \mathbf{P} + \boldsymbol{\Sigma})\mathbf{N}dA = 0 , \quad (8.51)$$

where  $\mathbf{T}$  is an arbitrary vector tangent to  $\mathcal{P}$ . In order to satisfy (8.51) for any pair  $\mathbf{T}$  and  $\mathbf{N}$ , the tensor  $\boldsymbol{\Sigma} + \mathbf{F}^T \mathbf{P}$  has to be a scalar multiple of the identity tensor. As a consequence, the configurational stress  $\boldsymbol{\Sigma}$  can be expressed as

$$\boldsymbol{\Sigma} = \Pi \mathbf{1} - \mathbf{F}^T \mathbf{P} , \quad (8.52)$$

where  $\Pi$  is a scalar field not yet identified. Substitution of (8.52) into (8.50) results in

$$W(\mathcal{P}) = \int_{\partial\mathcal{P}} \mathbf{P}\mathbf{N} \cdot \dot{\boldsymbol{\varphi}}dA + \int_{\mathcal{P}} \rho_0\mathbf{b} \cdot \dot{\boldsymbol{\varphi}}dV + \int_{\partial\mathcal{P}} \Pi\mathbf{V} \cdot \mathbf{N}dA . \quad (8.53)$$

Next, in order to identify the scalar field  $\Pi$  we employ the second law of the thermodynamics for the migrating control volume  $\mathcal{P}$ . It requires that the rate at which work is performed on  $\mathcal{P}$  has to be greater than the rate of energy stored in  $\mathcal{P}$ , i.e.

$$\boxed{\frac{d}{dt} \left[ \int_{\mathcal{P}} \psi dV \right] \leq W(\mathcal{P}) .} \quad (8.54)$$

Owing to a standard transport theorem, the first term in (8.54) may be rewritten as

$$\frac{d}{dt} \left[ \int_{\mathcal{P}} \psi dV \right] = \int_{\mathcal{P}} \dot{\psi} dV + \int_{\partial\mathcal{P}} \psi \mathbf{V} \cdot \mathbf{N} dA . \quad (8.55)$$

Insertion of the results (8.53) and (8.55) into (8.54) yields

$$\int_{\mathcal{P}} \dot{\psi} dV \leq \int_{\partial\mathcal{P}} \mathbf{P} \mathbf{N} \cdot \dot{\boldsymbol{\varphi}} dV + \int_{\mathcal{P}} \rho_0 \mathbf{b} \cdot \dot{\boldsymbol{\varphi}} dV + \int_{\partial\mathcal{P}} (\Pi - \psi) \mathbf{V} \cdot \mathbf{N} dA . \quad (8.56)$$

This inequality has to be satisfied for any arbitrary migrating control volume. It is possible to find another control volume  $\tilde{\mathcal{P}}$  which coincides with  $\mathcal{P}$  at a given time but has a different normal velocity  $\tilde{\mathbf{V}} \cdot \mathbf{N} \neq \mathbf{V} \cdot \mathbf{N}$ . As a consequence, to guarantee the inequality (8.56), it necessitates that  $\Pi = \psi$  holds. It yields together with (8.52) the *Eshelby stress*

$$\boxed{\boldsymbol{\Sigma} = \psi \mathbf{1} - \mathbf{F}^T \mathbf{P} .} \quad (8.57)$$

Having obtained the previous result, the final step is to derive the configurational force balance from the invariance restriction under changes in material observer. GURTIN [88] indeed starts with a priori introduction of three non-standard fields additional to the usual ones, i.e. the configurational stress  $\boldsymbol{\Sigma}$ , the configurational internal force  $\mathbf{g}$  and the configurational external body forces  $\mathbf{e}$ . Both forces  $\mathbf{g}$  and  $\mathbf{e}$  are defined per unit mass. Observe that both the external and the internal configurational forces have no contribution to the working (8.49). On the contrary, they perform work for a material observer who views the material in a motion with constant velocity. Invariance of the working (8.49) under changes in such material observers leads to the balance equation

$$\text{Div} \boldsymbol{\Sigma} + \rho_0 \mathbf{g} + \rho_0 \mathbf{e} = \mathbf{0} , \quad (8.58)$$

where the configurational external and internal body forces are identified as

$$\rho_0 \mathbf{e} := -\rho_0 \mathbf{F}^T \mathbf{b} \quad \text{and} \quad \rho_0 \mathbf{g} := -\frac{\partial \psi}{\partial \mathbf{X}} + \mathbf{P} : \frac{\partial \mathbf{F}}{\partial \mathbf{X}} . \quad (8.59)$$

For further details of the derivation see GURTIN [88], pp.34-43. Note that with the identification  $\mathbf{b}_{inh} = \mathbf{g} + \mathbf{e}$  the final results (8.58) and (8.59) have a similar structure to the equations (8.26)-(8.28) under quasistatic conditions. The fundamental difference is due to the second term  $\mathbf{P} : \text{Grad} \mathbf{F}$  in the configurational internal force  $\mathbf{g}$ .

### 8.3. Configurational-Force-Driven Brittle Crack Propagation

In the sequel, configurational forces are presented particularly as the driving forces of brittle crack propagation in elastic solids. A variational formulation of crack propagation is addressed which is originally proposed in MIEHE & GÜRSSES [143]. It is first developed in the *geometrically non-linear theory*. Then, following MIEHE, GÜRSSES & BIRKLE [145], the formulation is discussed with slight modifications in *linearized kinematics*. The presented approach is based on configurational forces and conceptually in line with STUMPF & LE [207] and MAUGIN & TRIMARCO [135]. It exploits the principle of maximum dissipation locally at the crack front and results in a crack propagation law governed by material forces. See also related theoretical treatments of configurational forces in brittle fracture by GURTIN & PODIO-GUIDUGLI [89, 90], ADDA-BEDIA ET AL. [2], OLEAGA [169, 170] and AGIASOFITOU & KALPAKIDES [3].



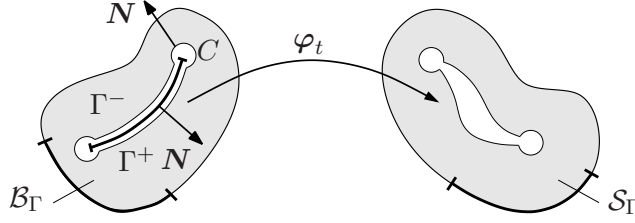


**Figure 8.2:** Deformation of a solid with a crack. The crack surface  $\Gamma$  with crack tip  $\partial\Gamma$  is obtained by the limits  $\Gamma^- \rightarrow \Gamma$ ,  $\Gamma^+ \rightarrow \Gamma$  and  $|C| \rightarrow 0$  of material points of the solid bulk  $\mathbf{X} \in \mathcal{B}_\Gamma := \mathcal{B} \setminus \{\Gamma \cup \partial\Gamma\}$  with the surface  $\partial\mathcal{B}_\Gamma := \partial\mathcal{B} \cup \Gamma^- \cup \Gamma^+ \cup C$ . The point deformation map  $\varphi_t : \mathbf{X} \mapsto \mathbf{x}$  is defined on the solid bulk  $\mathcal{B}_\Gamma$ .

### 8.3.1. Basic Geometry of a Solid with a Crack.

**Definition of a Body with a Crack.** Consider a fixed reference configuration  $\mathcal{B} \subset \mathcal{R}^3$  of a body which contains a generic crack as visualized in Figure 8.2. The crack is defined by a family of time-dependent non-self-intersecting surfaces  $\Gamma(t) \subset \mathcal{B}$  such that

$$\Gamma(t_1) \subset \Gamma(t_2) \quad \text{for } t_1 \leq t_2 \quad (8.60)$$

with a smooth boundary  $\partial\Gamma(t)$ . We denote this boundary as the crack tip or front. In two-dimensional problems a crack surface is a curve and a crack tip is a point. As a result of (8.60) the crack propagation is allowed only through the motion of the front  $\partial\Gamma$ . A local coordinate system is attached to the points  $\mathbf{X} \in \partial\Gamma$  at the crack front such that  $\mathbf{e}_2$  is tangent to  $\partial\Gamma$ , see Figure 8.3b. The current crack surface  $\Gamma(t)$  is the set

$$\Gamma(t) = \Gamma(0) \cup \{ \partial\Gamma(\tilde{t}) \mid 0 < \tilde{t} \leq t \} \quad (8.61)$$

where  $\Gamma(0)$  is the initial crack surface. In the current scenario, material points occupy the region

$$\mathcal{B}_\Gamma(t) := \mathcal{B} \setminus \{ \Gamma(t) \cup \partial\Gamma(t) \} \subset \mathcal{R}^3 \quad (8.62)$$

of the Euclidean space  $\mathcal{R}^3$ , having the exterior boundary  $\partial\mathcal{B}$  and the interior boundary formed by the crack. In particular, this boundary is considered to be of the form

$$\partial\mathcal{B}_\Gamma := \partial\mathcal{B} \cup \Gamma^- \cup \Gamma^+ \cup C \subset \mathcal{R}^3, \quad (8.63)$$

where  $\Gamma^-$  and  $\Gamma^+$  are the two faces of the crack and  $C$  a torus-like tube surface that surrounds the crack tip  $\partial\Gamma$ . Here,  $C$  is a surface that encircles the crack front  $\partial\Gamma$ , see Figure 8.3a. The subsequent investigations consider the limits

$$\Gamma^- \rightarrow \Gamma, \quad \Gamma^+ \rightarrow \Gamma, \quad |C| \rightarrow 0. \quad (8.64)$$

Furthermore, in a standard manner the exterior surface  $\partial\mathcal{B}$  of the solid is decomposed via

$$\partial\mathcal{B} = \partial\mathcal{B}_\varphi \cup \partial\mathcal{B}_t \quad (8.65)$$

into a part  $\partial\mathcal{B}_\varphi$  where the deformation is prescribed by Dirichlet-type boundary conditions and a part  $\partial\mathcal{B}_t$  where tractions are prescribed by Neumann-type conditions. Clearly, we have  $\partial\mathcal{B}_\varphi \cap \partial\mathcal{B}_t = \emptyset$ .

**Deformation of a Cracked Body.** The coordinates  $\mathbf{X} \in \mathcal{B}_\Gamma$  of the solid in its reference configuration  $\mathcal{B}_\Gamma$  are referred to as the material or Lagrangian coordinates. In a deformed configuration at the time  $t \in \mathcal{R}_+$ , these coordinates are mapped by the deformation map

$$\varphi_t : \begin{cases} \mathcal{B}_\Gamma \rightarrow \mathcal{S}_\Gamma \\ \mathbf{X} \mapsto \mathbf{x} = \varphi_t(\mathbf{X}) \end{cases} \quad (8.66)$$

onto the spatial or Eulerian coordinates  $\mathbf{x} \in \mathcal{S}_\Gamma$ , where  $\mathcal{S}_\Gamma \subset \mathcal{R}^3$  denotes the current configuration of the solid. This deformation is assumed to be prescribed on the part  $\partial\mathcal{B}_\varphi \subset \partial\mathcal{B}$  of the exterior surface by the Dirichlet condition

$$\varphi_t(\mathbf{X}) = \mathbf{X} + t\bar{\mathbf{v}}(\mathbf{X}) \quad \text{at } \mathbf{X} \in \partial\mathcal{B}_\varphi \quad (8.67)$$

in a monotonous format with given velocity function  $\bar{\mathbf{v}}$ . In the interior domain  $\mathcal{B}_\Gamma$ , the deformation map is constrained by the condition

$$\det \mathbf{F} > 0 \quad \text{at } \mathbf{X} \in \partial\mathcal{B}_\Gamma \quad \text{with } \mathbf{F} := \nabla\varphi_t(\mathbf{X}), \quad (8.68)$$

where  $\mathbf{F}$  denotes the deformation gradient of the solid at  $\mathbf{X} \in \partial\mathcal{B}_\Gamma$  and time  $t \in \mathcal{R}_+$ . Observe carefully that the deformation map  $\varphi_t$  is *not defined* at points  $\mathbf{X} \in \{\Gamma \cup \partial\Gamma\}$  of the crack. Typically, the deformation map jumps across the surfaces of the crack

$$[[\varphi_t]] := \varphi_t(\mathbf{X}^+) - \varphi_t(\mathbf{X}^-) \neq \mathbf{0} \quad (8.69)$$

with  $\mathbf{X}^+ \in \Gamma^+$  and  $\mathbf{X}^- \in \Gamma^-$ .

**Material and Spatial Configurational Changes.** We introduce next material and spatial coordinate maps in an analogous way to the discussion of migrating control volumes in Section 8.2.5. Consider a one-to-one piecewise differentiable transformation  $\Xi_t : \mathcal{B}_{\Gamma_0} \rightarrow \mathcal{B}_\Gamma$  of the reference configuration onto itself. This mapping is considered as the time-dependent *parameterization of the medium* that accounts for *material structural changes in the form of a crack propagation*. It reflects indeed a time-dependent change of the initial Lagrangian coordinates  $\boldsymbol{\theta} \in \mathcal{B}_{\Gamma_0}$  to the current Lagrangian coordinates  $\mathbf{X} \in \mathcal{B}_\Gamma$  in a sense of a change of material structure. With this viewpoint at hand, we introduce the material and spatial coordinate maps

$$\Xi_t : \begin{cases} \mathcal{B}_{\Gamma_0} \rightarrow \mathcal{B}_\Gamma \\ \boldsymbol{\theta} \mapsto \mathbf{X} = \Xi_t(\boldsymbol{\theta}) \end{cases} \quad \text{and} \quad \xi_t : \begin{cases} \mathcal{B}_{\Gamma_0} \rightarrow \mathcal{S}_\Gamma \\ \boldsymbol{\theta} \mapsto \mathbf{x} = \xi_t(\boldsymbol{\theta}) \end{cases} \quad (8.70)$$

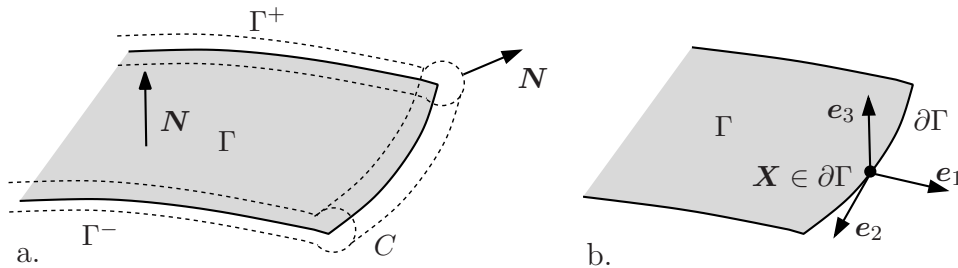


**Figure 8.3:** a.) The three-dimensional crack surface  $\Gamma$  with crack front  $\partial\Gamma$  in the reference configuration is obtained by the limits  $\Gamma^- \rightarrow \Gamma$ ,  $\Gamma^+ \rightarrow \Gamma$  and  $|C| \rightarrow 0$  of material points of the solid bulk  $\mathbf{X} \in \mathcal{B}_\Gamma := \mathcal{B} \setminus \{\Gamma \cup \partial\Gamma\}$  with the surface  $\partial\mathcal{B}_\Gamma := \partial\mathcal{B} \cup \Gamma^- \cup \Gamma^+ \cup C$ . b.) A local coordinate system is attached to points  $\mathbf{X} \in \partial\Gamma$  such that  $\mathbf{e}_2$  is parallel to the crack front  $\partial\Gamma$ .

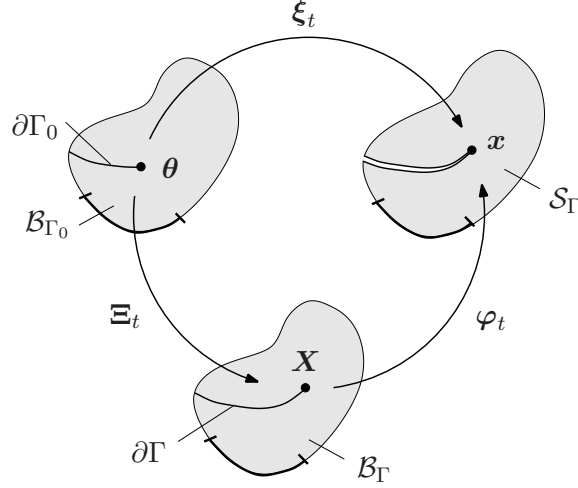


**Figure 8.4:** Structural changes and deformation. Both the reference and the spatial configurations are independently parameterized by the material and the spatial maps  $\Xi_t$  and  $\xi_t$ . The change of  $\Xi_t$  in time describes material structural changes, particularly in the context of fracture the rate  $\dot{\mathbf{a}}$  of crack propagation at the crack tip  $\partial\Gamma$ . The deformation map is the composition  $\varphi_t = \xi_t \circ \Xi_t^{-1}$ .

at time  $t \in \mathcal{R}_+$  and express the deformation map defined in (8.66) by the composition

$$\varphi_t(\mathbf{X}) = \xi_t(\boldsymbol{\theta}) \circ \Xi_t^{-1}(\mathbf{X}) \quad (8.71)$$

as visualized in Figure 8.4. Note that the parameterization of the reference and current configurations leads to a structure very similar to one discussed in Section 8.2.5 in connection with the concept of migrating control volumes. As a consequence of (8.71), the deformation gradient defined in (8.68) appears as the composition

$$\mathbf{F} = \mathbf{j} \cdot \mathbf{J}^{-1} \quad \text{with} \quad \mathbf{j} = \nabla_{\boldsymbol{\theta}} \xi_t \quad \text{and} \quad \mathbf{J} = \nabla_{\boldsymbol{\theta}} \Xi_t \quad (8.72)$$

of the gradients of the material and spatial coordinate maps introduced in (8.70). Furthermore, the volume elements of the Lagrangian configurations  $dV_0$  and  $dV$  are connected by the determinant of gradient of the material coordinate map  $\Xi$ , i.e.

$$dV = \det \mathbf{J} dV_0. \quad (8.73)$$

With these definitions at hand, we obtain the total time derivative of the above kinematic objects by

$$\dot{\boldsymbol{\varphi}} = \mathbf{v} - \mathbf{F} \cdot \mathbf{V}, \quad \dot{\mathbf{F}} = \nabla \mathbf{v} - \mathbf{F} \cdot \nabla \mathbf{V} \quad \text{and} \quad \dot{\overline{dV}} = (\mathbf{1} : \nabla \mathbf{V}) dV \quad (8.74)$$

in terms of the spatial and material velocity fields

$$\mathbf{v} := \left[ \frac{\partial}{\partial t} \xi_t(\boldsymbol{\theta}) \right] \circ \Xi_t^{-1}(\mathbf{X}) \quad \text{and} \quad \mathbf{V} := \left[ \frac{\partial}{\partial t} \Xi_t(\boldsymbol{\theta}) \right] \circ \Xi_t^{-1}(\mathbf{X}), \quad (8.75)$$

respectively. The above objects (8.74) and (8.75) provide the kinematic basis for the subsequent rate formulation of the cracked body. They are parameterized by the Lagrangian coordinates  $\mathbf{X} \in \mathcal{B}_\Gamma$  and the time  $t \in \mathcal{R}_+$ . Hence, the operators in (8.74)

$$[\dot{\cdot}] := \frac{\partial}{\partial t} [\cdot](\mathbf{X}, t) \quad \text{and} \quad \nabla[\cdot] := \frac{\partial}{\partial \mathbf{X}} [\cdot](\mathbf{X}, t) \quad (8.76)$$

denote the material time derivative at frozen Lagrangian coordinates  $\mathbf{X} \in \mathcal{B}_\Gamma$  and the gradient with respect to  $\mathbf{X} \in \mathcal{B}_\Gamma$ , respectively.

The fields (8.75) govern possible variations of both the Lagrangian as well as the Eulerian coordinates  $\mathbf{X} \in \mathcal{B}_\Gamma$  and  $\mathbf{x} \in \mathcal{S}_\Gamma$ . Clearly, these fields are restricted by some typical boundary conditions in the material and physical space, respectively. We have for the monotonous loading process (8.67) the admissible spatial velocity field

$$\mathbf{v} \in \mathcal{W}_v := \{ \mathbf{v} \mid \mathbf{v} = \bar{\mathbf{v}} \text{ on } \partial\mathcal{B}_\varphi \} . \quad (8.77)$$

Furthermore, we do not allow material configurational changes perpendicular to the external surface of the solid but allow arbitrary configurational changes of the homogeneous bulk. Thus the admissible material velocity field is

$$\mathbf{V} \in \mathcal{W}_V := \{ \mathbf{V} \mid \mathbf{V} \cdot \mathbf{N} = 0 \text{ on } \partial\mathcal{B} \cup \Gamma \text{ and } \mathbf{V} = \dot{\mathbf{a}} \text{ on } \partial\Gamma \} . \quad (8.78)$$

Here,  $\dot{\mathbf{a}}$  is the rate of extension of the crack surface  $\Gamma$  at the crack tip  $\partial\Gamma$  and satisfies the physical constraint  $\dot{\mathbf{a}} \cdot \mathbf{e}_2 = 0$ , see Figure 8.3b. This global rate of crack extension is determined by the constitutive formulation outlined below.

### 8.3.2. Global Elastic Response of a Solid with Cracks.

**Global Dissipation Inequality.** We focus on an elastic response of the solid with evolving cracks. In order to set up the global constitutive equations for the crack evolution in the elastic solid, we consider a global dissipation analysis in the sense of Coleman's method. This includes a comparison of the global power applied to the solid by external tractions on its boundary with the global energy storage of the solid. The global power of the external stresses acting on the surface  $\partial\mathcal{B}$  is given by the expression

$$\mathcal{P} := \int_{\partial\mathcal{B}} \mathbf{t} \cdot \dot{\boldsymbol{\varphi}} dA , \quad (8.79)$$

where  $\mathbf{t}$  is the traction vector on  $\partial\mathcal{B}$ . The total stress power done to the solid is balanced with the total bulk energy storage of the solid

$$\Psi := \int_{\mathcal{B}_\Gamma} \psi(\mathbf{F}) dV , \quad (8.80)$$

where  $\psi$  denotes the energy storage function with respect to unit volume of the reference configuration  $\mathcal{B}_\Gamma$ . This function is assumed to satisfy the standard restrictions of objectivity and polyconvexity. Thus  $\psi(\mathbf{Q}\mathbf{F}) = \psi(\mathbf{F})$  is valid for all  $\mathbf{Q} \in \mathcal{SO}(3)$  and  $\psi = \tilde{\psi}(\det \mathbf{F}, \mathbf{F}, \text{cof } \mathbf{F})$ , where  $\tilde{\psi}$  is a convex function, see Section 2.5.2 for further details. Note that we focus on a homogeneous bulk response of the solid where the energy storage is not explicitly dependent on the position  $\mathbf{X} \in \mathcal{B}_\Gamma$ . The global dissipation of the fracturing elastic solid follows from the comparison of the stress power with the evolution of the energy storage. We have the global postulate

$$\boxed{\mathcal{D} := \mathcal{P} - \frac{d}{dt} \Psi \geq 0 .} \quad (8.81)$$

This statement is the demand of the second axiom of thermodynamics in the pure mechanical context. It is the global counterpart to the classical Clausius-Duhem inequality of continuum thermodynamics.

**Global Elastic Response.** Insertion of the total bulk energy storage (8.80) into the global postulate (8.81) yields

$$\mathcal{D} = \mathcal{P} - \frac{d}{dt} \int_{\mathcal{B}_\Gamma} \psi(\mathbf{F}) dV . \quad (8.82)$$

Observe carefully that the time derivative is applied to both the energy storage  $\psi(\mathbf{F})$  and the infinitesimal volume element  $dV$ , i.e.

$$\mathcal{D} = \mathcal{P} - \int_{\mathcal{B}_\Gamma} \frac{\partial \psi}{\partial \mathbf{F}} : \dot{\mathbf{F}} dV - \int_{\mathcal{B}_\Gamma} \psi(\mathbf{F}) \overline{dV} . \quad (8.83)$$

Substitution of the kinematic relationships (8.74) into (8.83) results in the representation

$$\mathcal{D} = \mathcal{P} - \int_{\mathcal{B}_\Gamma} \{ \mathbf{P} : \nabla \mathbf{v} + \boldsymbol{\Sigma} : \nabla \mathbf{V} \} dV \geq 0 \quad (8.84)$$

in terms of the constitutive expressions

$$\boxed{\mathbf{P} := \partial_{\mathbf{F}} \psi(\mathbf{F}) \quad \text{and} \quad \boldsymbol{\Sigma} := \psi(\mathbf{F}) \mathbf{1} - \mathbf{F}^T \partial_{\mathbf{F}} \psi(\mathbf{F})} \quad (8.85)$$

for the first Piola-Kirchhoff stress tensor  $\mathbf{P}$  and the Eshelby stress tensor  $\boldsymbol{\Sigma}$ , respectively. A reformulation with application of the Gauss theorem which is generalized appropriately, see e.g. MAUGIN & TRIMARCO [135],

$$\int_{\mathcal{B}_\Gamma} \text{Div}(\bullet) dV = \int_{\partial \mathcal{B}} (\bullet) \cdot \mathbf{N} dA - \int_{\Gamma} [(\bullet)] \cdot \mathbf{N} dA - \int_{\partial \Gamma} \left\{ \lim_{|C| \rightarrow 0} \int_C (\bullet) \cdot \mathbf{N} dS \right\} dS \quad (8.86)$$

for the cracked solid visualized in Figure 8.2 results with (8.79) in the global expression for the dissipation

$$\begin{aligned} \mathcal{D} &= \int_{\mathcal{B}_\Gamma} \{ \text{Div} \mathbf{P} \cdot \mathbf{v} + \text{Div} \boldsymbol{\Sigma} \cdot \mathbf{V} \} dV + \int_{\partial \mathcal{B}} \{ [\mathbf{t} - \mathbf{P} \cdot \mathbf{N}] \cdot \mathbf{v} - [\mathbf{F}^T \cdot \mathbf{t} + \boldsymbol{\Sigma} \cdot \mathbf{N}] \cdot \mathbf{V} \} dA \\ &+ \int_{\Gamma} \{ [(\mathbf{v} \cdot \mathbf{P})] \cdot \mathbf{N} + [(\mathbf{V} \cdot \boldsymbol{\Sigma})] \cdot \mathbf{N} \} dA + \int_{\partial \Gamma} \{ \mathbf{p} \cdot \mathbf{v} + \mathbf{g} \cdot \mathbf{V} \} dS \geq 0 . \end{aligned} \quad (8.87)$$

Here, we introduced the limits

$$\boxed{\mathbf{p} := \lim_{|C| \rightarrow 0} \int_C \mathbf{P} \cdot \mathbf{N} dS \quad \text{and} \quad \mathbf{g} := \lim_{|C| \rightarrow 0} \int_C \boldsymbol{\Sigma} \cdot \mathbf{N} dS} \quad (8.88)$$

at the crack tip  $\partial \Gamma$  where  $\mathbf{N}$  is the inward normal to the curve  $C$  which surrounds the crack tip, see Figure 8.2. This dissipation inequality has to be satisfied for all admissible spatial and material velocity fields  $\mathbf{v}$  and  $\mathbf{V}$  defined in (8.77) and (8.78), respectively. Admissible arbitrary spatial velocity fields (8.77) induce the the local equations

$$\boxed{\text{Div} \mathbf{P} = \mathbf{0} \text{ in } \mathcal{B}_\Gamma , \quad \mathbf{P} \cdot \mathbf{N} = \mathbf{t} \text{ on } \partial \mathcal{B} , \quad \mathbf{P} \cdot \mathbf{N} = \mathbf{0} \text{ on } \Gamma , \quad \mathbf{p} = \mathbf{0} \text{ on } \partial \Gamma .} \quad (8.89)$$

The first two equations cover the equilibrium condition for the elastic bulk material  $\mathcal{B}_\Gamma$  and the traction boundary condition on the external surface  $\partial \mathcal{B}$ . The third equation

characterizes traction free crack lips  $\Gamma^-$  and  $\Gamma^+$  and the last statement enforces the integral (8.88)<sub>1</sub> to be zero at the crack tip  $\partial\Gamma$ . Admissible arbitrary material velocity fields (8.78) induce the local equation

$$\boxed{\text{Div}\boldsymbol{\Sigma} = \mathbf{0} \text{ in } \mathcal{B}_\Gamma} \quad (8.90)$$

for the Eshelby stress field in the bulk  $\mathcal{B}_\Gamma$  of the homogeneous elastic solid. Note that we obtained here the condition (8.90), which has already been discussed in Section 8.2, from a global dissipation analysis.

**8.3.3. Crack Evolution Obtained by Maximum Dissipation.** Taking into account the conditions (8.89), we obtain from (8.87) the *reduced global dissipation inequality*

$$\mathcal{D} = \int_{\partial\Gamma} \delta dS \geq 0 \quad \text{with} \quad \delta := \mathbf{g} \cdot \dot{\mathbf{a}} \geq 0. \quad (8.91)$$

Here,  $\delta$  is the dissipation per unit length of the crack tip  $\partial\Gamma$ . It is an inner product of the driving force  $\mathbf{g}$  defined in (8.88)<sub>2</sub> and the crack propagation rate  $\dot{\mathbf{a}}$  at  $\mathbf{X} \in \partial\Gamma$ , see Figure 8.4. The crack propagation  $\dot{\mathbf{a}}$  rate needs to be specified by a constitutive assumption. To this end, consider the classical isotropic Griffith-type crack criterion function

$$\boxed{\phi(\mathbf{g}) = |\mathbf{g}| - g_c \leq 0,} \quad (8.92)$$

where  $g_c$  is a material parameter specifying the critical energy release per unit length of the crack. With this notion at hand, an associated evolution equation for the crack propagation may be constructed by a local principle of maximum dissipation. Introducing an *elastic domain* for the material forces at the crack tip

$$\boxed{\mathcal{E} := \{\mathbf{g} \in \mathcal{R}^3 \mid \phi(\mathbf{g}) \leq 0\}} \quad (8.93)$$

in terms of the above crack criterion function, the principle of maximum dissipation at the point  $\mathbf{X} \in \partial\Gamma$  of the crack tip reads

$$\mathbf{g} \cdot \dot{\mathbf{a}} \geq \mathbf{g}^* \cdot \dot{\mathbf{a}} \quad \text{for all} \quad \mathbf{g}^* \in \mathcal{E}. \quad (8.94)$$

Then the real driving force maximizes the dissipation for all admissible forces. Introducing the Lagrangian function

$$\mathcal{L}(\mathbf{g}, \dot{\mathbf{a}}) := -\mathbf{g} \cdot \dot{\mathbf{a}} + \dot{\mathbf{a}} \phi(\mathbf{g}) \rightarrow \text{Stationary!}, \quad (8.95)$$

we derive the evolution equation for the local crack propagation in an isotropic solid

$$\boxed{\dot{\mathbf{a}} = \dot{\mathbf{a}} \partial_{\mathbf{g}} \phi(\mathbf{g}) = \dot{\mathbf{a}} \frac{\mathbf{g}}{|\mathbf{g}|}} \quad (8.96)$$

along with the crack loading-unloading conditions in Karush-Kuhn-Tucker form

$$\dot{\mathbf{a}} \geq 0, \quad \phi(\mathbf{g}) \leq 0 \quad \text{and} \quad \dot{\mathbf{a}} \phi(\mathbf{g}) = 0. \quad (8.97)$$

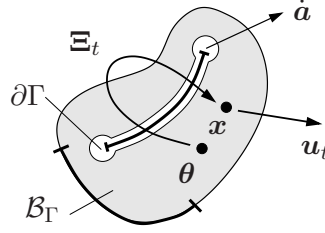


**Figure 8.5:** The displacement field  $\mathbf{u}_t = \mathbf{U}_t \circ \Xi_t^{-1}$  is defined on the solid bulk  $\mathcal{B}_\Gamma$  by composition of a displacement field  $\mathbf{U}_t$  with the structural parameter map  $\Xi_t$ . The latter describes material structural changes in time, particularly in the context of fracture the rate  $\dot{\mathbf{a}}$  of crack propagation at the crack tip  $\partial\Gamma$ .

Thus  $\dot{\mathbf{a}}$  decomposes into the rate  $\dot{\gamma}$  of the amount of crack propagation and its direction  $\partial_g\phi$ , which is collinear to the driving configurational force (8.88)<sub>2</sub>. Observe that the above constitutive equations determine the direction of the local crack propagation at  $\mathbf{X} \in \partial\Gamma$  and its discontinuous evolution but do not specify the value of  $\dot{\gamma}$ . The insertion of the evolution equation (8.96) into (8.91) gives the thermodynamic constraint

$$\mathcal{D} = \int_{\partial\Gamma} g_c \dot{\gamma} dS \geq 0 \quad (8.98)$$

that is satisfied for  $g_c > 0$  due to (8.97)<sub>1</sub>. Owing to the relation  $d\Gamma = d\gamma dS$ , the above expression for the dissipation contains the change of the crack surface. Thus we may write

$$\mathcal{D} = \frac{d}{dt} E_s \geq 0 \quad \text{with} \quad E_s := \int_\Gamma g_c d\Gamma, \quad (8.99)$$

where  $E_s$  is often denoted as the *surface energy* associated with the crack surface  $\Gamma$ .

#### 8.4. Restriction to Geometrically Linear Theory

In the following, the variational framework of brittle fracture, which is already discussed in Section 8.3 in the geometrically nonlinear setting, is presented in the small strain framework. The positions  $\mathbf{x} \in \mathcal{B}_\Gamma$  of material points are referred to as the current material coordinates. The small strain deformation at time  $t \in \mathcal{R}_+$  is described by the displacement field on  $\mathcal{B}_\Gamma$

$$\mathbf{u}_t : \begin{cases} \mathcal{B}_\Gamma \rightarrow \mathcal{R}^3 \\ \mathbf{x} \mapsto \mathbf{u}_t(\mathbf{x}) \end{cases} \quad (8.100)$$

as indicated in Figure 8.5. The deformation is assumed to be prescribed on the part  $\partial\mathcal{B}_u \subset \partial\mathcal{B}$  of the exterior surface by the Dirichlet condition  $\mathbf{u}_t(\mathbf{x}) = t\bar{\mathbf{v}}(\mathbf{x})$  at  $\mathbf{x} \in \partial\mathcal{B}_u$  in a monotonous format with given velocity function  $\bar{\mathbf{v}}$ . In the interior domain  $\mathcal{B}_\Gamma$ , the strains are assumed to be small. Thus, the norm of the displacement gradient

$$\|\mathbf{h}\| < \epsilon \quad \text{with} \quad \mathbf{h} := \nabla \mathbf{u}_t(\mathbf{x}) \quad (8.101)$$

is bounded by a small number  $\epsilon$ . Observe carefully that the displacement field  $\mathbf{u}_t$  is *not defined* at points  $\mathbf{x} \in \{\Gamma \cup \partial\Gamma\}$  of the crack. Furthermore, the displacement field jumps across the crack similar to the deformation map in (8.69), i.e.  $\llbracket \mathbf{u}_t \rrbracket := \mathbf{u}_t(\mathbf{x}^+) - \mathbf{u}_t(\mathbf{x}^-) \neq \mathbf{0}$  with  $\mathbf{x}^+ \in \Gamma^+$  and  $\mathbf{x}^- \in \Gamma^-$ .



Now consider a one-to-one piecewise differentiable transformation  $\Xi_t : \mathcal{B}_{\Gamma_0} \rightarrow \mathcal{B}_\Gamma$  of the body onto itself. This mapping is the time-dependent parameterization of the medium that accounts for the crack propagation. It indicates a time-dependent change of the coordinates  $\boldsymbol{\theta} \in \mathcal{B}_{\Gamma_0}$  to  $\boldsymbol{x} \in \mathcal{B}_\Gamma$  in a sense of a change of material structure. Therefore we can express the displacement field defined in (8.100) by the composition

$$\boldsymbol{u}_t(\boldsymbol{x}) = \boldsymbol{U}_t(\boldsymbol{\theta}) \circ \Xi_t^{-1}(\boldsymbol{x}) \quad (8.102)$$

in a similar structure to (8.71). As a consequence, the displacement gradient defined in (8.101) appears as the composition

$$\boldsymbol{h} = \boldsymbol{j} \cdot \boldsymbol{J}^{-1} \quad \text{with} \quad \boldsymbol{j} = \nabla_{\boldsymbol{\theta}} \boldsymbol{U}_t \quad \text{and} \quad \boldsymbol{J} = \nabla_{\boldsymbol{\theta}} \Xi_t \quad (8.103)$$

in terms of the gradient of the material coordinate map  $\Xi_t$ . Furthermore, the current volume element of the solid is now defined in terms of the material coordinate map  $dV = \det \boldsymbol{J} dV_0$ . With these definitions at hand, we obtain the total time derivative of the above kinematic objects by

$$\dot{\boldsymbol{u}} = \boldsymbol{v} - \boldsymbol{h} \cdot \boldsymbol{V}, \quad \dot{\boldsymbol{h}} = \nabla \boldsymbol{v} - \boldsymbol{h} \cdot \nabla \boldsymbol{V} \quad \text{and} \quad \dot{dV} = (\boldsymbol{1} : \nabla \boldsymbol{V}) dV \quad (8.104)$$

in terms of the spatial and material velocity fields  $\boldsymbol{v}$  and  $\boldsymbol{V}$ , respectively. The spatial and material velocity fields  $\boldsymbol{v}$  and  $\boldsymbol{V}$  govern possible variations of both the physical displacement  $\boldsymbol{u}$  as well as the material structural coordinates  $\boldsymbol{x} \in \mathcal{B}_\Gamma$ . Clearly, these fields are restricted by some typical boundary conditions in the material and physical space, respectively. The admissible spatial and material velocity fields have the same structure as (8.77) and (8.78).

Analogous to Section 8.3.2 we consider a global dissipation analysis in the sense of Coleman's method for elastic solids with evolving cracks. The global power  $\mathcal{P}$  of the external traction  $\boldsymbol{t}$  acting on the surface  $\partial\mathcal{B}$  and the total bulk energy storage  $\Psi$  of the solid are given by

$$\mathcal{P} := \int_{\partial\mathcal{B}} \boldsymbol{t} \cdot \dot{\boldsymbol{u}} dA \quad \text{and} \quad \Psi := \int_{\mathcal{B}_\Gamma} \psi(\boldsymbol{\varepsilon}) dV \quad \text{with} \quad \boldsymbol{\varepsilon} := \frac{1}{2} [\boldsymbol{h} + \boldsymbol{h}^T]. \quad (8.105)$$

Note that we focus on a homogeneous bulk response of the solid where the elastic stored energy only depends on the small strain tensor field  $\boldsymbol{\varepsilon}$ . We have the global postulate (8.81) which is the demand of the second axiom of thermodynamics in the pure mechanical context. The insertion of the bulk energy in (8.105)<sub>2</sub> along with (8.104) results in the representation

$$\mathcal{D} = \mathcal{P} - \int_{\mathcal{B}_\Gamma} \{ \boldsymbol{\sigma} : \nabla \boldsymbol{v} + \boldsymbol{\Sigma} : \nabla \boldsymbol{V} \} dV \geq 0 \quad (8.106)$$

in terms of the constitutive expressions

$$\boldsymbol{\sigma} := \partial_{\boldsymbol{\varepsilon}} \psi(\boldsymbol{\varepsilon}) \quad \text{and} \quad \boldsymbol{\Sigma} := \psi(\boldsymbol{\varepsilon}) \boldsymbol{1} - \boldsymbol{h}^T \partial_{\boldsymbol{\varepsilon}} \psi(\boldsymbol{\varepsilon}) \quad (8.107)$$

for the symmetric linearized stress tensor  $\boldsymbol{\sigma}$  and the non-symmetric Eshelby stress tensor  $\boldsymbol{\Sigma}$ , respectively. A reformulation analogous to steps in (8.86) and (8.87) leads to

$$\text{Div} \boldsymbol{\sigma} = \boldsymbol{0} \text{ in } \mathcal{B}_\Gamma, \quad \boldsymbol{\sigma} \cdot \boldsymbol{n} = \boldsymbol{t} \text{ on } \partial\mathcal{B}, \quad \boldsymbol{\sigma} \cdot \boldsymbol{n} = \boldsymbol{0} \text{ on } \Gamma, \quad \text{Div} \boldsymbol{\Sigma} = \boldsymbol{0} \text{ in } \mathcal{B}_\Gamma \quad (8.108)$$

for arbitrary spatial (8.77) and material (8.78) velocity fields. Note that, (8.108) corresponds to the results (8.89) and (8.90) in the geometrically linear setting under consideration. Taking into account the conditions (8.108), we obtain the *reduced global dissipation*

$$\mathcal{D} = \int_{\partial\Gamma} \delta dS \geq 0 \quad \text{with} \quad \delta := \mathbf{g} \cdot \dot{\mathbf{a}} \geq 0 \quad \text{and} \quad \mathbf{g} := \lim_{|C| \rightarrow 0} \int_C \boldsymbol{\Sigma} \cdot \mathbf{n} dS. \quad (8.109)$$

Here,  $\delta$  is the dissipation per unit length of the crack tip  $\partial\Gamma$ . It is an inner product of the driving force  $\mathbf{g}$  and the crack propagation rate  $\dot{\mathbf{a}}$  at  $\mathbf{x} \in \partial\Gamma$ . The crack propagation rate  $\dot{\mathbf{a}}$  needs to be specified by a constitutive assumption. To this end, we consider the classical isotropic Griffith-type crack criterion function (8.92). Having introduced the crack criterion function, an associated evolution equation for the crack evolution is constructed by a local principle of maximum dissipation, see Section 8.3.3. Then the real driving force maximizes the dissipation for all admissible forces and yields the crack propagation law in an isotropic solid

$$\boxed{\dot{\mathbf{a}} = \dot{\gamma} \frac{\mathbf{g}}{|\mathbf{g}|}} \quad (8.110)$$

along with the crack loading-unloading conditions in Karush-Kuhn-Tucker form (8.99). Note that except some differences in the definition of point maps, the variational formulations presented are very similar for geometrically non-linear and linear cases.



## 9. Staggered Algorithm for Brittle Crack Propagation

The subsequent discussions are devoted to a finite element implementation of the brittle fracture theory outlined in the previous section. It starts with a two-dimensional formulation which is based on MIEHE & GÜRSSES [143]. A treatment of geometrically linear theory and an extension to three-dimensional fracture problems are also presented, see also MIEHE, GÜRSSES & BIRKLE [145] and MIEHE & GÜRSSES [144]. This includes a straightforward implementation in terms of a displacement type finite element method. The crack evolution is realized by a staggered scheme of stress computation at frozen mesh accompanied by a successive crack release based on node doubling. Thus, the continuous formulation outlined before is transferred in a consistent manner to discrete nodal points. The fracture occurs in the discretized setting pointwise at the nodes and generates a node breaking accompanied by a discrete crack propagation. This crack propagation takes place in discrete steps of the order of the current finite element discretization.

### 9.1. Spatial Discretization of the Solid with a Crack

The spatial discretization of the configurational maps  $\Xi_t$  and  $\xi_t$  in (8.70) is performed by isoparametric finite elements in the element domain  $\mathcal{B}_{\Gamma_0}^e$  as shown in Figure 9.1. We have

$$\xi_t^h(\boldsymbol{\theta}) = \tilde{\mathbf{N}}(\boldsymbol{\theta})\mathbf{d}_t \quad \text{and} \quad \Xi_t^h(\boldsymbol{\theta}) = \tilde{\mathbf{N}}(\boldsymbol{\theta})\mathbf{D}_t, \quad (9.1)$$

in terms of the matrix of shape functions  $\tilde{\mathbf{N}}$  that depends on the position  $\boldsymbol{\theta} \in \mathcal{B}_{\Gamma_0}^e$  of the element domain  $\mathcal{B}_{\Gamma_0}^e$ . Here,  $\mathbf{d}_t \in \mathcal{R}^{N_t \cdot n_{dim}}$  and  $\mathbf{D}_t \in \mathcal{R}^{N_t \cdot n_{dim}}$  are the vectors of spatial and material nodal positions, where  $N_t$  denotes the *current number* of nodes at time  $t$  and  $n_{dim}$  is the dimension of the problem. For given positions, the discrete gradients of (9.1)

$$\mathbf{j}^h := \tilde{\mathbf{B}}(\boldsymbol{\theta})\mathbf{d}_t \quad \text{and} \quad \mathbf{J}^h := \tilde{\mathbf{B}}(\boldsymbol{\theta})\mathbf{D}_t \quad (9.2)$$

allow the computation of the current deformation gradient (8.72) in the form

$$\mathbf{F}^h = \mathbf{j}^h \cdot \mathbf{J}^{h-1} =: \mathbf{B}(\mathbf{X}^h)\mathbf{d}_t \quad \text{in } \mathcal{B}_{\Gamma_t}^e. \quad (9.3)$$

in terms of the interpolation matrix  $\mathbf{B}(\mathbf{X}^h)$  which represents derivatives with respect to the Lagrangian coordinates  $\mathbf{X}^h \in \mathcal{B}_{\Gamma_t}^e$ . Owing to this basic kinematic variable, the first Piola-Kirchhoff stress  $\mathbf{P}^h$  and the Eshelby stress  $\boldsymbol{\Sigma}^h$  are computed from (8.85), i.e.

$$\mathbf{P}^h = \partial_{\mathbf{F}}\psi(\mathbf{F}^h) \quad \text{and} \quad \boldsymbol{\Sigma}^h = \psi(\mathbf{F}^h)\mathbf{1} - \mathbf{F}^{hT}\partial_{\mathbf{F}}\psi(\mathbf{F}^h) \quad (9.4)$$

in a standard manner at typical integration points of the finite element mesh.

### 9.2. Global Response of the Spatially Discretized Solid

With the above discretization at hand, the material gradients of the spatial and material velocities in (8.75) take the discrete form

$$\nabla \mathbf{v}^h = \mathbf{B}\dot{\mathbf{d}}_t \quad \text{and} \quad \nabla \mathbf{V}^h = \mathbf{B}\dot{\mathbf{D}}_t \quad (9.5)$$

in terms of the time derivatives

$$\dot{\mathbf{d}}_t := \frac{d}{dt}\mathbf{d}_t \in \mathcal{R}^{N_t \cdot n_{dim}} \quad \text{and} \quad \dot{\mathbf{D}}_t := \frac{d}{dt}\mathbf{D}_t \in \mathcal{R}^{N_t \cdot n_{dim}} \quad (9.6)$$

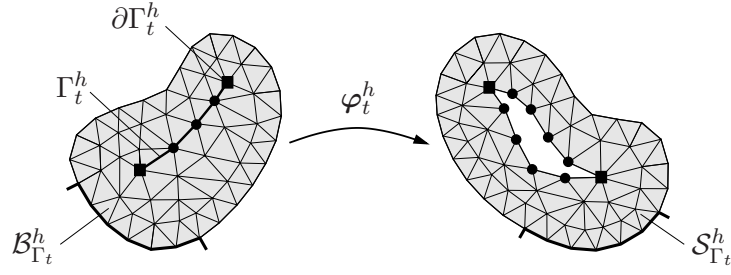


**Figure 9.1:** Two-dimensional finite element discretization of a cracked solid based on nodal doubling. The crack lips  $\Gamma_t^{h-}$  and  $\Gamma_t^{h+}$  at time  $t$  appear as external surfaces of a standard finite element mesh with double nodes at  $\mathbf{X} \in \Gamma_t^h$ . The crack tips  $\partial\Gamma_t^h$  are represented by single nodes.

of the discrete nodal position vectors introduced in (9.1). As a result of (9.6), the rate formulation of the global dissipation (8.84) appears as a sum

$$\mathcal{D}^h := \mathcal{P}^h - \frac{d}{dt} \Psi^h = \sum_{I=1}^{N_t} \left\{ [\mathbf{p}_I + \mathbf{f}_I] \cdot \dot{\mathbf{d}}_I + \mathbf{g}_I \cdot \dot{\mathbf{D}}_I \right\} \geq 0 \quad (9.7)$$

over the discrete number  $N_t$  of current nodes of the mesh. Here,

$$\mathbf{p}_I := \mathbf{A} \int_{\partial\mathcal{B}_{\Gamma_t}^e} \mathbf{N}_I^T \mathbf{t}^h dA \quad (9.8)$$

is the discrete external force caused by tractions  $\mathbf{t}^h$  acting on the nodes  $I \in \partial\mathcal{B}_{\Gamma_t}^e$  of the external element surface  $\mathcal{B}_{\Gamma_t}^e$ .

$$\mathbf{f}_I := - \mathbf{A} \int_{\mathcal{B}_{\Gamma_t}^e} \mathbf{B}_I^T \mathbf{P}^h dV \quad \text{and} \quad \mathbf{g}_I := - \mathbf{A} \int_{\mathcal{B}_{\Gamma_t}^e} \mathbf{B}_I^T \boldsymbol{\Sigma}^h dV \quad (9.9)$$

are the spatial and material discrete nodal forces acting on the discrete node  $I \in \mathcal{B}_{\Gamma_t}^e$  of the element domain  $\mathcal{B}_{\Gamma_t}^e$ . In the above equations,  $\mathbf{A}_{e=1}^E$  denotes the standard finite element assembling operator for a mesh with  $E$  elements.  $\mathbf{N}_I$  and  $\mathbf{B}_I$  are the shape function and the strain interpolation matrices, referred to the node  $I \in \mathcal{B}_{\Gamma_t}^e$ , respectively. The computation of configurational forces in the finite element context is proposed originally by BRAUN [33], see also STEINMANN, ACKERMANN & BARTH [206] and DENZER, BARTH & STEINMANN [56].

The above formulation (9.7) is the starting point for the exploitation of the global dissipation postulate in the spatially discretized setting. The exploitation in the sense of a global Coleman method is based on the admissible discrete spatial velocities

$$\mathbf{v}_I \in \mathcal{W}_{\mathbf{v}}^h := \left\{ \mathbf{v}_I \mid \mathbf{v}_I = \bar{\mathbf{v}}_I \text{ on } \partial\mathcal{B}_{\varphi}^h \right\} \quad (9.10)$$

and the admissible material velocities

$$\mathbf{V}_I \in \mathcal{W}_{\mathbf{V}}^h := \left\{ \mathbf{V}_I \mid \mathbf{V}_I \cdot \mathbf{N} = 0 \text{ on } \partial\mathcal{B}_{\Gamma_t}^h \cup \Gamma_t^h \text{ and } \mathbf{V}_I = \dot{\mathbf{a}}_I \text{ on } \partial\Gamma_t^h \right\} \quad (9.11)$$

as the discrete counterparts to (8.77) and (8.78). The above discrete dissipation postulate has to be satisfied for all admissible spatial and material velocity fields. As a consequence of the physical admissible fields, we get the conditions of the physical equilibrium

$$\boxed{\mathbf{f}_I = \mathbf{0} \text{ in } \mathcal{B}_{\Gamma_t}^h, \quad \mathbf{f}_I + \mathbf{p}_I = \mathbf{0} \text{ on } \partial\mathcal{B}_{\Gamma_t}^h \quad \text{and} \quad \mathbf{f}_I = \mathbf{0} \text{ on } \Gamma_t^h.} \quad (9.12)$$

Thus, the equilibrium is characterized in the discretized setting by vanishing discrete internal nodal forces  $\mathbf{f}_I$  in the domain  $\mathcal{B}_{\Gamma_t}^h$  and on the crack lips  $\Gamma_t^h$ . On the external boundary  $\partial\mathcal{B}_{\Gamma_t}^h$ , the internal nodal forces  $\mathbf{f}_I$  are in equilibrium with the external nodal forces  $\mathbf{p}_I$ . Furthermore, the discrete dissipation postulate has to be satisfied for all material velocities in the domain of the solid. As a consequence, we have the discrete condition

$$\boxed{\mathbf{g}_I = \mathbf{0} \text{ in } \mathcal{B}_{\Gamma_t}^h} \quad (9.13)$$

for the material nodal forces. This condition may be employed for the development of mesh optimization algorithms in terms of r- or h-adaptive methods. It is considered to be satisfied for an optimal mesh that resolves the homogeneous structure, see e.g. MUELLER, GROSS & MAUGIN [160], ASKES, KUHL & STEINMANN [10], HEINTZ ET AL. [96], THOUTIREDDY & ORTIZ [208] and MOSLER & ORTIZ [159]. Notice that an arbitrary inhomogeneous mesh causes an artificial heterogeneity that would violate the condition (9.13).

### 9.3. Time Discretization of the Crack Evolution Problem

Taking the above conditions (9.12) and (9.13) into account, we end up with a reduced dissipation inequality

$$\boxed{\mathcal{D}^h = \sum_{I \in \partial\Gamma_t^h} \mathbf{g}_I \cdot \dot{\mathbf{a}}_I \geq 0} \quad (9.14)$$

in the discretized setting. It represents an inner product of the material forces  $\mathbf{g}_I$  acting on nodes at the crack tip  $I \in \partial\Gamma_t^h$  and the associated material velocity  $\dot{\mathbf{a}}_I$  of the node in the material structural configuration.

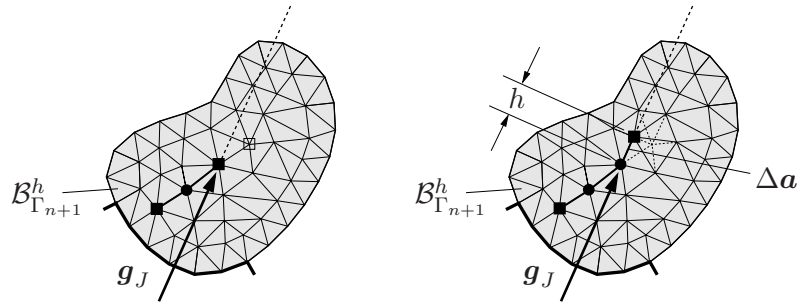


**Figure 9.2:** Discretization of the crack evolution. Two successive crack releases  $\Delta \mathbf{a} = h\mathbf{g}_J/|\mathbf{g}_J|$  for  $|\bar{\mathbf{g}}_J| > g_c$  in a typical load increment  $[t_n, t_{n+1}]$  of critical nodes  $J := \arg \{ \max_{I=1 \dots N_{n+1}} (|\bar{\mathbf{g}}_I|) \}$  accompanied by a node doubling and the alignment of critical segments in the direction of the configurational force  $\mathbf{g}_J$ .

Next step is to set up a constitutive characterization of the velocity  $\dot{\mathbf{a}}_I$ . Following MIEHE & GÜRSES [143] we adopt the pointwise setting of the continuous formulation outlined in (8.96). Thus, we consider the evolution equation

$$\boxed{\dot{\mathbf{a}}_I = \dot{\gamma}_t \frac{\mathbf{g}_I}{|\mathbf{g}_I|} \quad \text{locally at nodes } I \in \partial\Gamma_t^h .} \quad (9.15)$$

It describes the movement of the nodes  $I$  at the crack tip along with the loading-unloading conditions

$$\dot{\gamma}_I \geq 0, \quad [|\bar{\mathbf{g}}_I| - g_c] \leq 0, \quad \dot{\gamma}_I [|\bar{\mathbf{g}}_I| - g_c] = 0, \quad (9.16)$$

in the Karush-Kuhn-Tucker form. Note that in the above equation a new quantity  $\bar{\mathbf{g}}_I$  is introduced to preserve the dimensional consistency with  $g_c$ . In two-dimensional problems  $\mathbf{g}_I = \bar{\mathbf{g}}_I$  while they are not the same in three dimensions. They are related by an effective length which will be discussed in Section 9.4. This formulation summarizes the discrete setting in the spatially discretized formulation. Observe the analogy between plasticity formulations and above outlined framework. However, recall that the parameters  $\dot{\gamma}_I$  at the nodes  $I \in \partial\Gamma_t^h$  of the crack tip are *global*. They represent the amount of the rate of extension of the crack surface.

Notice carefully that the formulation and the algorithmic treatment presented so far are independent of the dimension of the problem, i.e. it has formally the same structure for both the two- and three-dimensional crack propagation. On the other hand, after the time integration of the above evolution equation some technical differences arise depending on the dimension of the problem. To this end, we consider a time discretization of the dissipation in a typical time interval  $[t_n, t_{n+1}]$

$$\Delta\mathcal{D}_{n+1}^h := \int_{t_n}^{t_{n+1}} \mathcal{D}^h dt \approx \sum_{I \in \partial\Gamma_{n+1}^h} \mathbf{g}_I \cdot \Delta\mathbf{a}_I \geq 0,$$

where  $\Delta\mathbf{a}_I$  is a line segment and coincides with the increment of the crack in *two-dimensional* problems, see Figure 9.2. However, an increment in a crack  $\Delta\Gamma^h$  is a two-dimensional surface for *three dimensional* fracture. It is apparent that  $\Delta\mathbf{a}_I$  which is a line segment cannot coincide with  $\Delta\Gamma^h$  which is an area element. Therefore, we interpret in three-dimensional problems  $\Delta\mathbf{a}_I$  as a line segment parallel to  $\mathbf{g}_I$  that lies in the new increment  $\Delta\Gamma^h$  of the crack surface. Furthermore, in two-dimensional problems the crack increment  $\Delta\mathbf{a}_I$  is uniquely determined solely through  $\mathbf{g}_I$ . On the contrary, the crack increment  $\Delta\Gamma^h$  in three-dimensional problems cannot be uniquely determined exclusively through  $\mathbf{g}_I$  and it requires additional information. This issue will be addressed in Section 9.7.2.

The amount of this increment  $\Delta\mathbf{a}_I$  is assumed to be related to step-wise crack segment releases related to the space discretization. As a consequence, the associated discretization reads

$$\Delta\mathbf{a}_I = \Delta\gamma_I \frac{\mathbf{g}_I}{|\mathbf{g}_I|} \quad \text{locally at nodes } I \in \partial\Gamma_{n+1}^h \quad (9.19)$$

with *constant* increments of the amount of crack extension

$$\Delta\gamma_I = \begin{cases} h & \text{for } |\bar{\mathbf{g}}_I| > g_c \\ 0 & \text{otherwise .} \end{cases} \quad (9.20)$$



Here,  $h$  is the relevant size of the mesh, e.g. triangle or tetrahedron depending on the dimension of the problem. More precisely,  $h$  is the length of a segment that emanates from the critical node in the direction of  $\mathbf{g}_I$  and lies inside the crack front triangle or tetrahedron. Observe carefully that the discrete crack extension can occur within one loading step several times in a successive manner. It is a consequence of the staggered algorithm outlined in Section 9.4, see also Figure 9.2.

#### 9.4. Staggered Algorithm for Incremental Energy Minimization

In order to obtain a stable setting for this incremental scenario, we apply a staggered scheme of energy minimization at frozen crack pattern and a successive crack release by single nodal doubling. In a typical time interval  $[t_n, t_{n+1}]$ , this procedure works as follows. After increasing the incremental load, we perform an elastic energy minimization at frozen crack  $\Gamma_{n+1}^h$ , i.e.

$$\Psi_{n+1}^h = \int_{\mathcal{B}_{\Gamma_{n+1}^h}} \psi(\mathbf{F}_{n+1}) dV \rightarrow \text{Minimum!} \quad (9.21)$$

which is equivalent to the discrete equilibrium conditions (9.12) for the physical internal nodal forces  $\mathbf{f}_I$ . In a second step, we identify the maximum loaded node  $\mathcal{N}_c$  which is the potential candidate for a possible point of crack propagation. For this purpose we introduce a *quasi-distributed configurational force*

$$\boxed{\bar{\mathbf{g}}_I = \mathbf{g}_I / L_I,} \quad (9.22)$$

where  $L_I$  is the length of the part of crack front  $\partial\Gamma_{n+1}^h$  that is driven by the material force  $\mathbf{g}_I$ , i.e. for three-dimensional problems the half of the sum of length of two crack front segments that emanate from the node  $I$ . Note that  $L_I = 1$  for two-dimensional fracture but it still possesses a unit of length. Therefore,  $\bar{\mathbf{g}}_I$  and  $\mathbf{g}$  become dimensionally consistent and we identify the critical node  $\mathcal{N}_c$

$$\boxed{\mathcal{N}_c := \arg \left\{ \max_{I \in \partial\Gamma_{n+1}^h} (|\bar{\mathbf{g}}_I|) \right\}} \quad (9.23)$$

by controlling the norm of the discrete quasi-distributed nodal configurational force vectors. For the maximum loaded node  $\mathcal{N}_c$ , the discrete crack condition of the form is checked

$$\boxed{\phi_{\mathcal{N}_c} := |\bar{\mathbf{g}}_{\mathcal{N}_c}| - g_c.} \quad (9.24)$$

For  $\phi_{\mathcal{N}_c} < 0$  in (9.24), the current time interval at the given loading has a stationary crack state. In this frozen crack state, we proceed with the next load increment. For the case  $\phi_{\mathcal{N}_c} \geq 0$ , the most loaded node  $\mathcal{N}_c$  is critical and has to be released. We then perform in two-dimensional cases the *segment alignment procedure* illustrated in Figures 9.2 and 9.5 by releasing the crack via doubling of the critical node  $\mathcal{N}_c$ , see Section 9.6.2. This is in the line with an incremental crack release

$$\Delta \mathbf{a}_{\mathcal{N}_c} = h \frac{\mathbf{g}_{\mathcal{N}_c}}{|\mathbf{g}_{\mathcal{N}_c}|} \quad (9.25)$$

associated with a fixed segment length  $h$  given by the spatial discretization. In three-dimensional problems the release of critical node is followed by the *facet reorientation* procedure which will be discussed in Section 9.7.2, see also Figure 9.9. The crack increment  $\Delta\Gamma^h$  is then obtained by the union of a set of critical facets that are already reoriented, see (9.34). Having performed the nodal release and the reorientation, we then proceed with a new energy minimization step (9.21) for the new relaxed system that is not yet in equilibrium. The typical sequences of the staggered energy relaxation algorithm are provided in Box 9.1 and Box 9.2 for two- and three-dimensional cases, respectively.

### 9.5. Discretization in Geometrically Linear Theory

In this section we briefly command on a finite element implementation for the above outlined scenario of crack propagation in the *geometrically linear setting*. This includes a straightforward implementation in terms of a displacement type finite element method in an analogous manner to the geometrically non-linear case. The algorithm consists of a staggered scheme of stress computation at frozen mesh accompanied by a crack propagation realized by successive nodal releases. We have the spatial discretizations of the displacement field and the structural configurational map

$$\mathbf{U}_t^h(\boldsymbol{\theta}) = \tilde{\mathbf{N}}(\boldsymbol{\theta})\mathbf{d}_t \quad \text{and} \quad \boldsymbol{\Xi}_t^h(\boldsymbol{\theta}) = \tilde{\mathbf{N}}(\boldsymbol{\theta})\mathbf{D}_t, \quad (9.26)$$

in terms of the matrix of shape functions  $\tilde{\mathbf{N}}$ , *nodal displacements*  $\mathbf{d}_t \in \mathcal{R}^{N_t \cdot n_{dim}}$  and *nodal positions*  $\mathbf{D}_t \in \mathcal{R}^{N_t \cdot n_{dim}}$  where  $N_t$  denotes the current number of nodes at time  $t$  and  $n_{dim}$  is the dimension of the problem. For given positions, the discrete gradients of (9.26), i.e.  $\mathbf{j}^h := \tilde{\mathbf{B}}(\boldsymbol{\theta})\mathbf{d}_t$  and  $\mathbf{J}^h := \tilde{\mathbf{B}}(\boldsymbol{\theta})\mathbf{D}_t$ , allow the computation of the current displacement gradient (8.103) in the form

$$\mathbf{h}^h = \mathbf{j}^h \cdot \mathbf{J}^{h-1} =: \mathbf{B}(\mathbf{x}^h)\mathbf{d}_t \quad \text{in } \mathcal{B}_{\Gamma_t}^e \quad (9.27)$$

in terms of the interpolation matrix  $\mathbf{B}(\mathbf{x}^h)$  which represents derivatives with respect to the coordinates  $\mathbf{x}^h \in \mathcal{B}_{\Gamma_t}^e$ . With this formulation at hand, the discrete rate formulation of the global dissipation (8.106) appears in the form identical to (9.7), i.e.

$$\mathcal{D}^h := \mathcal{P}^h - \frac{d}{dt}\Psi^h = \sum_{I=1}^{N_t} \left\{ [\mathbf{p}_I + \mathbf{f}_I] \cdot \dot{\mathbf{d}}_I + \mathbf{g}_I \cdot \dot{\mathbf{D}}_I \right\} \geq 0 \quad (9.28)$$

as a sum over the discrete number  $N_t$  of current nodes of the mesh. In (9.28),  $\mathbf{p}_I$  is the discrete external nodal forces caused by tractions, see (9.8).  $\mathbf{f}_I$  and  $\mathbf{g}_I$  are the spatial and material discrete nodal forces acting on the node  $I$  of the element  $\mathcal{B}_{\Gamma_t}^e$

$$\mathbf{f}_I := - \mathbf{A} \int_{\mathcal{B}_{\Gamma_t}^e} \mathbf{B}_I^T \boldsymbol{\sigma}^h dV \quad \text{and} \quad \mathbf{g}_I := - \mathbf{A} \int_{\mathcal{B}_{\Gamma_t}^e} \mathbf{B}_I^T \boldsymbol{\Sigma}^h dV \quad (9.29)$$

in terms of the symmetric linearized stress field

$$\boldsymbol{\sigma}^h = \partial_{\boldsymbol{\varepsilon}} \psi(\text{sym}[\mathbf{B}\mathbf{d}_{n+1}]) \quad (9.30)$$

and in terms of the energy momentum tensor

$$\boldsymbol{\Sigma}^h = \psi(\text{sym}[\mathbf{B}\mathbf{d}_{n+1}])\mathbf{1} - [\mathbf{B}\mathbf{d}_{n+1}]^T \partial_{\boldsymbol{\varepsilon}} \psi(\text{sym}[\mathbf{B}\mathbf{d}_{n+1}]) . \quad (9.31)$$

Exploitation of (9.28) for admissible discrete spatial and material velocities of the form (9.10) and (9.11) yields the discrete counterpart of equations given in (8.108).

**Box 9.1:** Two-Dimensional Staggered Scheme for Crack Propagation.

1. *Initialization.* Update external load at  $t_{n+1}$  and set the initial crack front  $\partial\Gamma_{n+1}^h$ .
2. *Elastic Energy Minimization.* At frozen crack geometry associated with the discrete mesh  $\mathcal{B}_\Gamma^e$ , solve the nonlinear elastic energy minimization problem

$$\mathbf{f}_I := - \mathbf{A} \int_{\mathcal{B}_\Gamma^e} \mathbf{B}_I^T \mathbf{P}^h dV = \mathbf{0} \quad \text{for } I = 1 \dots N_{n+1}$$

in terms of the first Piola-Kirchhoff stress field

$$\mathbf{P}^h = \partial_{\mathbf{F}} \psi(\mathbf{B} \mathbf{d}_{n+1})$$

for the current spatial nodal positions  $\mathbf{d}_{n+1}$  by a global Newton iteration.

3. *Configurational Forces.* For the obtained equilibrium state at frozen crack compute the configurational nodal forces

$$\mathbf{g}_I := - \mathbf{A} \int_{\mathcal{B}_\Gamma^e} \mathbf{B}_I^T \boldsymbol{\Sigma}^h dV \quad \text{for } I = 1 \dots N_{n+1}$$

in terms of the Eshelby energy momentum tensor

$$\boldsymbol{\Sigma}^h = \psi(\mathbf{B} \mathbf{d}_{n+1}) \mathbf{1} - [\mathbf{B} \mathbf{d}_{n+1}]^T \partial_{\mathbf{F}} \psi(\mathbf{B} \mathbf{d}_{n+1})$$

4. *Check of Fracture Criterion.* At frozen deformation, find the maximum loaded node and check the Griffith criterion

$$\mathcal{N}_c := \arg \left\{ \max_{I \in \partial\Gamma_{n+1}^h} (|\bar{\mathbf{g}}_I|) \right\} : \quad \text{If } |\bar{\mathbf{g}}_{\mathcal{N}_c}| < g_c \text{ Exit.}$$

5. *Critical Crack Segment.* Define unit vectors  $\mathbf{m}_S$  in the direction of the element edges  $\mathcal{S} = 1 \dots n_{seg}$  emanating from  $\mathcal{N}_c$ . Get the critical crack segment

$$\mathcal{S}_c = \arg \left\{ \max_{\mathcal{S}=1 \dots n_{seg}} (\mathbf{g}_{\mathcal{N}_c} \cdot \mathbf{m}_S) \right\}$$

6. *Crack Segment Alignment.* Reorient the critical segment  $\mathcal{S}_c$  by moving the other node of  $\mathcal{S}_c$  (other than  $\mathcal{N}_c$ ) such that for the segment direction the following holds

$$\mathbf{g}_{\mathcal{N}_c} \times \mathbf{m}_{\mathcal{S}_c} = \mathbf{0}$$

7. *Discrete Crack Release.* Release the segment  $\mathcal{S}_c$  by doubling the critical node  $\mathcal{N}_c$  and perform necessary updates of the data structure described in Boxes 9.4 and 9.5. Go to step 2.

## 9.6. Algorithmic Treatment of Two-Dimensional Crack Propagation

**9.6.1. Data Structures for Crack Release with Node Doubling.** The data structures required for incremental crack segment releases with node doubling follows conceptually the three-dimensional formulation outlined by PANDOLFI & ORTIZ [178].

**Box 9.2:** Three-Dimensional Staggered Scheme for Crack Propagation.

1. *Initialization.* Update external load at  $t_{n+1}$  and set the initial crack front  $\partial\Gamma_{n+1}^h$ .
2. *Elastic Energy Minimization.* At frozen crack geometry associated with the discrete mesh  $\mathcal{B}_\Gamma^e$ , solve the nonlinear elastic energy minimization problem

$$\mathbf{f}_I := - \mathbf{A} \int_{\mathcal{B}_\Gamma^e} \mathbf{B}_I^T \mathbf{P}^h dV = \mathbf{0} \quad \text{for } I = 1 \dots N_{n+1}$$

in terms of the first Piola-Kirchhoff stress field

$$\mathbf{P}^h = \partial_{\mathbf{F}} \psi(\mathbf{B}\mathbf{d}_{n+1})$$

for the current spatial nodal positions  $\mathbf{d}_{n+1}$  by a global Newton iteration.

3. *Configurational Forces.* For the obtained equilibrium state at frozen crack compute the configurational nodal forces

$$\mathbf{g}_I := - \mathbf{A} \int_{\mathcal{B}_\Gamma^e} \mathbf{B}_I^T \boldsymbol{\Sigma}^h dV \quad \text{for } I = 1 \dots N_{n+1}$$

in terms of the Eshelby energy momentum tensor

$$\boldsymbol{\Sigma}^h = \psi(\mathbf{B}\mathbf{d}_{n+1}) \mathbf{1} - [\mathbf{B}\mathbf{d}_{n+1}]^T \partial_{\mathbf{F}} \psi(\mathbf{B}\mathbf{d}_{n+1})$$

4. *Check of Fracture Criterion.* At frozen deformation, find the maximum loaded node and check the Griffith criterion

$$\mathcal{N}_c := \arg \left\{ \max_{I \in \partial\Gamma_{n+1}^h} (|\bar{\mathbf{g}}_I|) \right\} : \quad \text{If } |\bar{\mathbf{g}}_{\mathcal{N}_c}| < g_c \text{ Exit.}$$

5. *Critical Crack Facets.* Determine the critical facets  $\mathcal{F}_{c_i}$  and approximate the crack increment  $\Delta\Gamma$

$$\Delta\Gamma \approx \Delta\Gamma^h = \mathcal{F}_{c_1} \cup \mathcal{F}_{c_1} \cup \dots \mathcal{F}_{c_n}$$

6. *Reorientation of Critical Facets.* Reorient  $\mathcal{F}_{c_i}$  in the desired crack propagation direction based on the configurational force and the crack front constraints
7. *Discrete Crack Release.* Release the facets  $\mathcal{F}_{c_i}$  by doubling of the critical node  $\mathcal{N}_c$  and perform updates of the data structure in Box 9.7 and Box 9.8. Update the crack front  $\partial\Gamma^h$

$$\partial\Gamma^h \Leftarrow \partial\Gamma^h \cup \mathcal{N}_1 \cup \dots \cup \mathcal{N}_{n-1} - \mathcal{N}_c \quad \text{and go to step 2.}$$

Here, we first focus on *two-dimensional data structures* where triangular finite elements are considered as a composition of three set of *objects*: (i) *triangles*  $\mathcal{T}$ , (ii) *segments*  $\mathcal{S}$  and (iii) *nodes*  $\mathcal{N}$  as visualized in Figure 9.3 and described in Box 9.3. A *triangle*  $\mathcal{T}$  is composed of three nodes  $\{\mathcal{N}_1, \mathcal{N}_2, \mathcal{N}_3\}$  and three segments  $\{\mathcal{S}_1, \mathcal{S}_2, \mathcal{S}_3\}$ . Additional to the node and the segment information, the neighboring triangles  $\{\mathcal{T}_1, \mathcal{T}_2, \mathcal{T}_3\}$  of the triangle  $\mathcal{T}$  need to be stored. If a triangle  $\mathcal{T}$  has only one or two neighbors then the corresponding set

**Box 9.3:** Additional Topology Information for Crack Propagation.

1. <i>Data structure of the triangle <math>\mathcal{T}</math></i>		
1.1	nodes belonging to the triangle $\mathcal{T}$	$\{\mathcal{N}_1, \mathcal{N}_2, \mathcal{N}_3\}$
1.2	segments belonging to the triangle $\mathcal{T}$	$\{\mathcal{S}_1, \mathcal{S}_2, \mathcal{S}_3\}$
1.3	neighboring triangles to the triangle $\mathcal{T}$	$\{\mathcal{T}_1, \mathcal{T}_2, \mathcal{T}_3\}$
2. <i>Data structure of the segment <math>\mathcal{S}</math></i>		
2.1	neighboring triangles to the segment $\mathcal{S}$	$\{\mathcal{T}_1, \mathcal{T}_2\}$
2.2	connectivity of the segment $\mathcal{S}$	$\{\mathcal{N}_1, \mathcal{N}_2\}$
3. <i>Data structure of the node <math>\mathcal{N}</math></i>		
3.1	number of segments having the node $\mathcal{N}$	$numseg(\mathcal{N})$
3.2	number of triangles having the node $\mathcal{N}$	$numtri(\mathcal{N})$
3.3	segments having the node $\mathcal{N}$	$\{\mathcal{S}_i \mid i = 1 \dots numseg(\mathcal{N})\}$
3.4	triangles having the node $\mathcal{N}$	$\{\mathcal{T}_i \mid i = 1 \dots numtri(\mathcal{N})\}$
3.5	inner/outer flag of the node $\mathcal{N}$	$1 \rightarrow \text{inner}$ and $0 \rightarrow \text{outer}$

will be  $\{\mathcal{T}_1, 0, 0\}$  or  $\{\mathcal{T}_1, \mathcal{T}_2, 0\}$ , respectively. A *segment*  $\mathcal{S}_1$  consists of two nodes  $\{\mathcal{N}_1, \mathcal{N}_2\}$  and has at most two neighboring triangles  $\{\mathcal{T}_1, \mathcal{T}_2\}$ . Note that for boundary segments there is only one neighboring triangle  $\mathcal{T}_1$ . The third class of objects is a typical *node*  $\mathcal{N}_1$  of the mesh. Here, first the number of segments  $numseg(\mathcal{N}_1)$  and triangles  $numtri(\mathcal{N}_1)$  having the node  $\mathcal{N}_1$  are stored. Also lists of all segments  $\{\mathcal{S}_i \mid i = 1 \dots numseg(\mathcal{N}_1)\}$  and triangles  $\{\mathcal{T}_i \mid i = 1 \dots numtri(\mathcal{N}_1)\}$  having the node  $\mathcal{N}_1$  is required. Finally a flag to specify  $\mathcal{N}_1$  as an outer or inner node is needed. The flag is set to 1 for inner nodes and to 0 for outer ones. The data structures summarized in Box 9.3 are generated at the beginning of a loading process from a given standard displacement type finite element topology. It remains unchanged unless a crack progress occurs. An advance in the crack requires two steps. First, a *change in the standard connectivity information* of the finite elements is necessary. Second, a *new data structure generation* from the modified topology needs to be performed. In the subsequent section we discuss these necessary updates in the data structure.

**9.6.2. Data Update due to Segment Release and Node Doubling.** The algorithm for the data update as a consequence of a crack progress can be divided into three

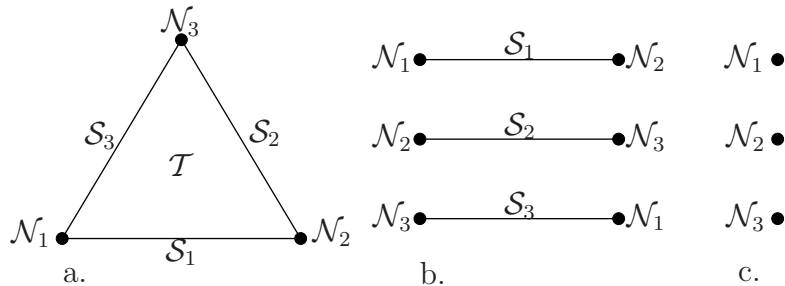


**Figure 9.3:** Necessary objects for the description of three-noded triangular finite element. a.) The triangle  $\mathcal{T}$  is defined by three nodes  $\{\mathcal{N}_1, \mathcal{N}_2, \mathcal{N}_3\}$  and three segments  $\{\mathcal{S}_1, \mathcal{S}_2, \mathcal{S}_3\}$ . b.) Segments  $\mathcal{S}_1, \mathcal{S}_2$  and  $\mathcal{S}_3$  of the triangle  $\mathcal{T}$  are defined by nodes  $\{\mathcal{N}_1, \mathcal{N}_2\}, \{\mathcal{N}_2, \mathcal{N}_3\}$  and  $\{\mathcal{N}_1, \mathcal{N}_3\}$ , respectively. c.) Nodes  $\mathcal{N}_1, \mathcal{N}_2, \mathcal{N}_3$ .

**Box 9.4:** Necessary Topology Update due to a Segment Doubling.

- |     |   |   |
|-----|---|---|
| 1.  | segments to be doubled and generated                | $\mathcal{S}_c, \mathcal{S}_n$  |
| 2.  | set the connectivity of $\mathcal{S}_n$             | $\mathcal{N}_c, \mathcal{N}_1$  |
| 3.  | set the neighboring triangles of $\mathcal{S}_n$    | $\mathcal{T}_2, 0$  |
| 4.  | change the neighboring triangles of $\mathcal{S}_c$ | $\mathcal{T}_1, 0$  |
| 5.  | change the segments of $\mathcal{T}_2$              | $\mathcal{S}_n, \mathcal{S}_3, \mathcal{S}_4$   |
| 6.  | change the neighboring triangles of $\mathcal{T}_1$ | $\mathcal{T}_4, \mathcal{T}_5$  |
| 7.  | change the neighboring triangles of $\mathcal{T}_2$ | $\mathcal{T}_7, \mathcal{T}_8$  |
| 8.  | change the neighboring segments of $\mathcal{N}_c$  | $\mathcal{S}_c, \mathcal{S}_1, \mathcal{S}_4, \mathcal{S}_5, \mathcal{S}_8, \mathcal{S}_9, \mathcal{S}_{10}, \mathcal{S}_n$ |
| 9.  | change the neighboring segments of $\mathcal{N}_1$  | $\mathcal{S}_c, \mathcal{S}_2, \mathcal{S}_3, \mathcal{S}_6, \mathcal{S}_7, \mathcal{S}_n$                                  |
| 10. | change the number of segments for $\mathcal{N}_c$   | $numseg(\mathcal{N}_c) = numseg(\mathcal{N}_c) + 1$   |
| 11. | change the number of segments for $\mathcal{N}_1$   | $numseg(\mathcal{N}_1) = numseg(\mathcal{N}_1) + 1$   |

parts: (i) Find the critical node  $\mathcal{N}_c$  and the critical segment  $\mathcal{S}_c$ , (ii) double the critical segment including the update of the data structure and finally (iii) double the critical node including the update of the data structure.

**Determination of Critical Tip Node and Critical Segment.** The algorithmic check of the crack criterion at the nodal points follows the treatment of Section 9.4 and is summarized in Box 9.1. The critical step is the computation of the configurational force vectors  $\mathbf{g}_{\mathcal{N}}$  at all nodal points of the finite element mesh. Next, the critical node  $\mathcal{N}_c$  is determined by constructing a loop over all crack front nodes of the finite element mesh, i.e.  $\mathcal{N} \in \partial\Gamma_{n+1}^h$ , to find the one having the maximum configurational force vector  $\mathbf{g}_{\mathcal{N}_c}$ . Then  $\mathcal{N}_c$  describes the crack tip where a possible advance of a crack may take place. After having found  $\mathcal{N}_c$ , the critical segment  $\mathcal{S}_c$  has to be determined. This is accomplished by another loop over all segments having the critical node  $\mathcal{N}_c$ , i.e.  $\{\mathcal{S}_i \mid i = 1 \dots numseg(\mathcal{N}_c)\}$ . Then,  $\mathcal{S}_c$  is the segment which emanates from  $\mathcal{N}_c$  and makes an angle with the configurational

**Box 9.5:** Necessary Topology Update due to Node Doubling.

- |     |   |
|-----|---|
| 1.  | <i>Generation of the new node <math>\mathcal{N}_n</math> and the new segment <math>\mathcal{S}_n</math></i> |
| 1.1 | Find the critical segment $\mathcal{S}_c$ (Box 9.1) and duplicate it : $\mathcal{S}_n$                      |
| 1.2 | Find the critical node $\mathcal{N}_c$ (Box 9.1) and duplicate it : $\mathcal{N}_n$                         |
| 1.3 | Perform the data structure update described in Box 9.4  |
| 2.  | <i>Assignment of the new node <math>\mathcal{N}_n</math> to associated finite elements</i>                  |
| 2.1 | find the triangle $\mathcal{T}_1$ having both the critical segment $\mathcal{S}_c$ and node $\mathcal{N}_c$ |
| 2.2 | find the next triangle $\mathcal{T}_4$ neighbor to $\mathcal{T}_1$ and having the node $\mathcal{N}_c$      |
| 2.3 | find the set of triangles $\{\mathcal{T}_1, \mathcal{T}_4, \mathcal{T}_3\}$ in a similar manner             |
| 2.  | <i>Generation of the new data structure</i>   |
| 3.1 | assign the new node $\mathcal{N}_n$ to triangles $\{\mathcal{T}_2, \mathcal{T}_8, \mathcal{T}_9\}$          |
| 3.2 | keep the old node $\mathcal{N}_c$ for triangles $\{\mathcal{T}_1, \mathcal{T}_4, \mathcal{T}_3\}$           |
| 3.3 | increase the total number of nodal points   |
| 3.4 | generate the new data structure described in Box 9.3  |

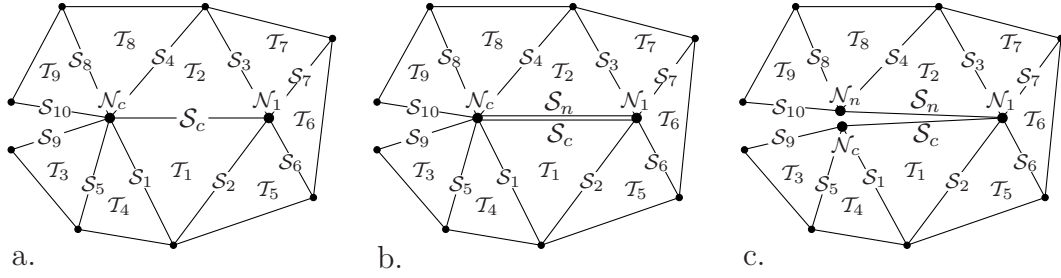


**Figure 9.4:** Necessary topology update for segment doubling. a.) Segment  $S_c$  with connectivity  $N_c, N_1$  and with neighboring triangles  $T_1, T_2$  is to be doubled. b.) Segment  $S_n$  with connectivity  $N_c, N_1$  and with single neighboring triangle  $T_2$  is generated. Neighboring triangle of segment  $S_c$  is changed to only  $T_1$ . c.) New node  $N_n$  is generated.

force vector  $\mathbf{g}_{N_c}$  that is closer to zero than those of other segments. The final and very crucial step is the adaptive reorientation of the critical segment at the crack tip. As already mentioned, the configurational force vector  $\mathbf{g}_{N_c}$  shows the direction that the crack should advance. In most of the cases this direction does not coincide with one of the current segments at the crack tip. Thus, having determined  $N_c$  and  $S_c$ , we reorient the critical segment  $S_c$  such that it becomes parallel to the configurational force vector  $\mathbf{g}_{N_c}$ . This alignment is performed such that the second node of  $S_c$  that is different from  $N_c$  is moved along the edge that is opposite to the node  $N_c$ . This movement of a single node along the edge provides a reorientation procedure without severe distortions of the triangular elements at the crack tip. The algorithmic steps are summarized in Box 9.1 and visualized for a simple mesh in Figure 9.5.

**Doubling of Critical Segments.** After having found the critical node  $N_c$  and the critical segment  $S_c$ , the next step is the doubling of  $S_c$  and the accompanying update of the data structure. These steps are outlined in Box 9.4 for the simple mesh given in Figure 9.4. First, a new segment  $S_n$  is generated and its connectivity information is assigned as  $\{N_c, N_1\}$ , which is identical to the one of  $S_c$ . Then the neighboring triangles of  $S_c$  and  $S_n$  are set to  $\{T_1, 0\}$  and  $\{T_2, 0\}$ , respectively. The segments of the triangle  $T_2$  become  $\{S_n, S_3, S_4\}$ . Note that the segments of  $T_1$  remain unchanged. After the generation of the new segment  $S_n$ , the triangles  $T_1$  and  $T_2$  are no more neighbor of each other. Their neighboring triangle information has to be changed to  $\{T_4, T_5, 0\}$  for  $T_1$  and to  $\{T_7, T_8, 0\}$  for  $T_2$ . Finally, the set and the number of neighboring segments for the nodes  $N_c$  and  $N_1$  has to be updated. In the example considered the sets for  $N_c$  and  $N_1$

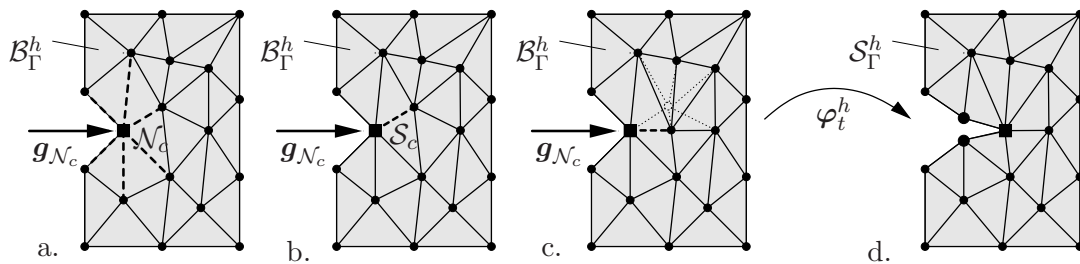


**Figure 9.5:** Adaptive segment alignment and node doubling procedure. a.) Identification of maximal loaded node  $N_c$  with configurational force  $\mathbf{g}_{N_c}$  and its corresponding segments. b.) Identification of the critical segment  $S_c$ . c.) Alignment of critical segment  $S_c$  in direction of the driving force  $\mathbf{g}_{N_c}$  and node doubling. d.) Current deformation state with new mesh data.



become  $\{\mathcal{S}_c, \mathcal{S}_1, \mathcal{S}_4, \mathcal{S}_5, \mathcal{S}_8, \mathcal{S}_9, \mathcal{S}_{10}, \mathcal{S}_n\}$  and  $\{\mathcal{S}_c, \mathcal{S}_2, \mathcal{S}_3, \mathcal{S}_6, \mathcal{S}_7, \mathcal{S}_n\}$ , respectively.

**Doubling of Critical Node.** The generation of a new node  $\mathcal{N}_n$  is the next step to be performed. The crucial point here is to determine which triangles take the new node  $\mathcal{N}_n$  and which ones retain  $\mathcal{N}_c$ . For this purpose, first the triangle  $\mathcal{T}_1$  having both the critical segment  $\mathcal{S}_c$  and node  $\mathcal{N}_c$  has to be found, see Figure 9.4. Then the triangle  $\mathcal{T}_4$  as being a neighbor of  $\mathcal{T}_1$  and having the node  $\mathcal{N}_c$  is identified. In a similar way  $\mathcal{T}_3$  is found as a neighbor of  $\mathcal{T}_4$  and having the node  $\mathcal{N}_c$ . Following this procedure, the set of triangles  $\{\mathcal{T}_1, \mathcal{T}_4, \mathcal{T}_3\}$  which keep the old node  $\mathcal{N}_c$  are uniquely determined. The topologies of all other triangles which have  $\mathcal{N}_c$  in their connectivity, i.e.  $\{\mathcal{T}_2, \mathcal{T}_8, \mathcal{T}_9\}$ , have to be changed. In the connectivity information of  $\{\mathcal{T}_2, \mathcal{T}_8, \mathcal{T}_9\}$  the node  $\mathcal{N}_c$  is replaced with  $\mathcal{N}_n$ . As a result of a new node generation, the total number of nodes is increased and the coordinates of  $\mathcal{N}_n$  is assigned to be the same as  $\mathcal{N}_c$ . Finally, the complete data structure that is discussed in Box 9.5 has to be created for the new topology.

## 9.7. Algorithmic Treatment of Three-Dimensional Crack Propagation

**9.7.1. Data Structures for 3-D Crack Release with Node Doubling.** In this section we extend the *two-dimensional data structures* discussed previously to the *three-dimensional* ones which are necessary for the description of the crack propagation. In this context, linear tetrahedral finite elements are considered as a composition of four set of

### Box 9.6: Topology Information for Three-Dimensional Crack Propagation.

1. <i>Data structure of the tetrahedron <math>\mathcal{T}</math></i>	
1.1 nodes belonging to $\mathcal{T}$	$\{\mathcal{N}_1, \dots, \mathcal{N}_4\}$
1.2 segments belonging to $\mathcal{T}$	$\{\mathcal{S}_1, \dots, \mathcal{S}_6\}$
1.3 facets belonging to the $\mathcal{T}$	$\{\mathcal{F}_1, \dots, \mathcal{F}_4\}$
1.4 neighboring tetrahedra to $\mathcal{T}$	$\{\mathcal{T}_1, \dots, \mathcal{T}_4\}$
2. <i>Data structure of the facet <math>\mathcal{F}</math></i>	
2.1 nodes belonging to $\mathcal{F}$	$\{\mathcal{N}_1, \dots, \mathcal{N}_3\}$
2.2 segments belonging to $\mathcal{F}$	$\{\mathcal{S}_1, \dots, \mathcal{S}_3\}$
2.3 neighboring tetrahedra to $\mathcal{F}$	$\{\mathcal{T}_1, \mathcal{T}_2\}$
2.4 inner/outer flag of $\mathcal{F}$	$1 \rightarrow \text{inner} \quad \text{and} \quad 0 \rightarrow \text{outer}$
3. <i>Data structure of the segment <math>\mathcal{S}</math></i>	
3.1 connectivity of $\mathcal{S}$	$\{\mathcal{N}_1, \mathcal{N}_2\}$
3.2 number of facets having $\mathcal{S}$	$numfac(\mathcal{S})$
3.3 number of tetrahedra having $\mathcal{S}$	$numtet(\mathcal{S})$
3.4 facets having $\mathcal{S}$	$\{\mathcal{F}_i \mid i = 1 \dots numfac(\mathcal{S})\}$
3.5 tetrahedra having $\mathcal{S}$	$\{\mathcal{T}_i \mid i = 1 \dots numtet(\mathcal{S})\}$
4. <i>Data structure of the node <math>\mathcal{N}</math></i>	
4.1 number of segments having $\mathcal{N}$	$numseg(\mathcal{N})$
4.2 number of tetrahedra having $\mathcal{N}$	$numtet(\mathcal{N})$
4.3 segments having $\mathcal{N}$	$\{\mathcal{S}_i \mid i = 1 \dots numseg(\mathcal{N})\}$
4.4 tetrahedrons having $\mathcal{N}$	$\{\mathcal{T}_i \mid i = 1 \dots numtet(\mathcal{N})\}$
4.5 inner/outer flag of $\mathcal{N}$	$1 \rightarrow \text{inner} \quad \text{and} \quad 0 \rightarrow \text{outer}$

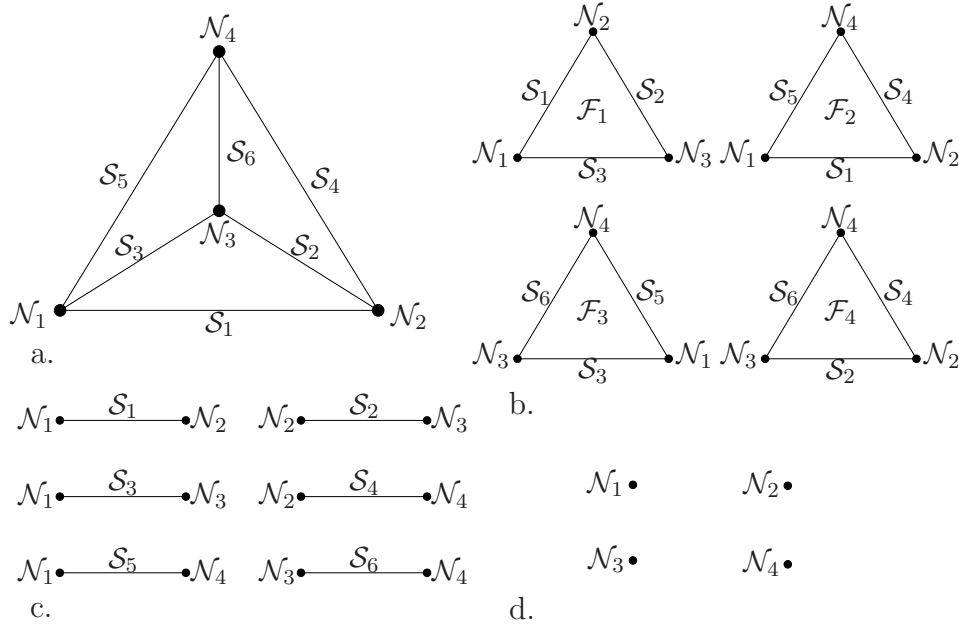


**Figure 9.6:** Necessary objects for the description of a four-noded tetrahedral finite element mesh. a.) The tetrahedron  $\mathcal{T}$  is defined by four nodes  $\{\mathcal{N}_1, \mathcal{N}_2, \mathcal{N}_3, \mathcal{N}_4\}$ , six segments  $\{\mathcal{S}_1, \mathcal{S}_2, \mathcal{S}_3, \mathcal{S}_4, \mathcal{S}_5, \mathcal{S}_6\}$  and four facets  $\{\mathcal{F}_1, \mathcal{F}_2, \mathcal{F}_3, \mathcal{F}_4\}$ . b.) Facets  $\mathcal{F}_1, \mathcal{F}_2, \mathcal{F}_3$  and  $\mathcal{F}_4$  are defined by segments  $\{\mathcal{S}_3, \mathcal{S}_2, \mathcal{S}_1\}, \{\mathcal{S}_1, \mathcal{S}_4, \mathcal{S}_5\}, \{\mathcal{S}_3, \mathcal{S}_5, \mathcal{S}_6\}, \{\mathcal{S}_2, \mathcal{S}_4, \mathcal{S}_6\}$  and nodes  $\{\mathcal{N}_1, \mathcal{N}_3, \mathcal{N}_2\}, \{\mathcal{N}_1, \mathcal{N}_2, \mathcal{N}_4\}, \{\mathcal{N}_3, \mathcal{N}_1, \mathcal{N}_4\}, \{\mathcal{N}_3, \mathcal{N}_2, \mathcal{N}_4\}$ , respectively. c.) Segments  $\mathcal{S}_1, \mathcal{S}_2, \mathcal{S}_3, \mathcal{S}_4, \mathcal{S}_5$  and  $\mathcal{S}_6$  are defined by nodes  $\{\mathcal{N}_1, \mathcal{N}_2\}, \{\mathcal{N}_2, \mathcal{N}_3\}, \{\mathcal{N}_1, \mathcal{N}_3\}, \{\mathcal{N}_2, \mathcal{N}_4\}, \{\mathcal{N}_1, \mathcal{N}_4\}$  and  $\{\mathcal{N}_3, \mathcal{N}_4\}$ , respectively. d.) Nodes  $\mathcal{N}_1, \mathcal{N}_2, \mathcal{N}_3$  and  $\mathcal{N}_4$ .

objects: (i) tetrahedra  $\mathcal{T}$ , (ii) facets  $\mathcal{F}$ , (iii) segments  $\mathcal{S}$  and (iv) nodes  $\mathcal{N}$  as visualized in Figure 9.6 and described in Box 9.6. A tetrahedron  $\mathcal{T}$  is composed of four nodes  $\{\mathcal{N}_1 \dots \mathcal{N}_4\}$ , six segments  $\{\mathcal{S}_1 \dots \mathcal{S}_6\}$  and four facets  $\{\mathcal{F}_1 \dots \mathcal{F}_4\}$ . Additional to the node, segment and facet information, the neighboring tetrahedra  $\{\mathcal{T}_1 \dots \mathcal{T}_4\}$  of the tetrahedron  $\mathcal{T}$  need to be stored. A tetrahedron  $\mathcal{T}$  may have maximum four neighbors and if it has less than four then the corresponding entries are set to 0. A facet  $\mathcal{F}_1$  consists of three nodes  $\{\mathcal{N}_1 \dots \mathcal{N}_3\}$ , three segments  $\{\mathcal{S}_1 \dots \mathcal{S}_3\}$  and has at most two neighboring tetrahedra  $\{\mathcal{T}_1, \mathcal{T}_2\}$ . Note that boundary facets have only one neighboring tetrahedron and they are set as outer. A segment  $\mathcal{S}_1$ , similar to a line element, consists of two nodes  $\{\mathcal{N}_1, \mathcal{N}_2\}$ . The number of facets  $numfac(\mathcal{S}_1)$  and tetrahedra  $numtet(\mathcal{S}_1)$  having the segment  $\mathcal{S}_1$  are also stored. Moreover, lists of all facets  $\{\mathcal{F}_i \mid i = 1 \dots numfac(\mathcal{S}_1)\}$  and tetrahedra  $\{\mathcal{T}_i \mid i = 1 \dots numtet(\mathcal{S}_1)\}$  having the segment  $\mathcal{S}_1$  are generated. The last class of objects is a typical node  $\mathcal{N}_1$  of the mesh. Here, first the number of segments  $numseg(\mathcal{N}_1)$  and tetrahedra  $numtet(\mathcal{N}_1)$  having the node  $\mathcal{N}_1$  are stored. Also the information about all segments  $\{\mathcal{S}_i \mid i = 1 \dots numseg(\mathcal{N}_1)\}$  and tetrahedra  $\{\mathcal{T}_i \mid i = 1 \dots numtet(\mathcal{N}_1)\}$  having the node  $\mathcal{N}_1$  is required. Finally, a flag to specify  $\mathcal{N}_1$  as an outer or inner node is needed. The flag is set to 1 for inner nodes and to 0 for outer ones.

The data structures summarized in Box 9.6 are generated at the beginning of a loading process from a given standard displacement type finite element topology. It remains unchanged unless a crack propagation occurs. An advance in the crack requires two steps: First, a *change in the standard connectivity information* of the finite elements and second, a *new data structure generation* from the modified topology. In the subsequent section we discuss these necessary updates in the data structure.

**Box 9.7:** Necessary Topology Update due to Doubling of Facets  $\mathcal{F}_{c_1}$  and  $\mathcal{F}_{c_2}$ .

1. facets to be doubled and generated	$\{\mathcal{F}_{c_1}, \mathcal{F}_{c_2}\}$ and $\{\mathcal{F}_{n_1}, \mathcal{F}_{n_2}\}$
2. set the connectivity of $\mathcal{F}_{n_1}$ and $\mathcal{F}_{n_2}$	$\{\mathcal{N}_c, \mathcal{N}_2, \mathcal{N}_1\}$ and $\{\mathcal{N}_c, \mathcal{N}_3, \mathcal{N}_2\}$
3. set neigh. tetrahedra of $\mathcal{F}_{n_1}$ and $\mathcal{F}_{n_2}$	$\{\mathcal{T}_1, 0\}$ and $\{\mathcal{T}_3, 0\}$
4. change neigh. tetrahedra of $\mathcal{F}_{c_1}$ and $\mathcal{F}_{c_2}$	$\{\mathcal{T}_4, 0\}$ and $\{\mathcal{T}_6, 0\}$
5. change neigh. tetrahedra of $\mathcal{T}_1$ and $\mathcal{T}_3$	$\{\mathcal{T}_2, 0, 0, 0\}$
6. change neigh. tetrahedra of $\mathcal{T}_4$ and $\mathcal{T}_6$	$\{\mathcal{T}_5, 0, 0, 0\}$

**9.7.2. Data Update due to Facet Release and Node Doubling.** The algorithm for the data update as a consequence of a crack propagation is divided into four parts: (i) Find the critical node  $\mathcal{N}_c$ , the neighboring segments  $\mathcal{S}_1, \mathcal{S}_2$  at the crack front and compute the normal vector to new crack surface. (ii) Find all critical facets  $\mathcal{F}_c$  by tracing relevant facets starting from  $\mathcal{S}_1$  to  $\mathcal{S}_2$  and reorient them. (iii) Double all the critical facets including the necessary update of the data structure. (iv) Double the critical node  $\mathcal{N}_c$  including the update of the data structure.

**Determination of Critical Node and Crack Surface Normal.** The algorithmic check of the crack criterion at the nodal points follows the treatment of Section 9.4 and is summarized in Box 9.2. Note that when a solid body is considered in the continuous setting before a finite element discretization, then a smooth crack front turns out to be a three-dimensional curve. Furthermore, the configurational forces constitute vectorial objects acting per unit length of the crack front. As a consequence of the finite element discretization the distributed material forces become discrete nodal vectors acting on the nodes of the mesh those are located at the crack front. In Figures 9.7a and b the distributed and discrete nodal configurational forces acting on a crack front are illustrated.

The first step is the computation of the configurational force vectors  $\mathbf{g}_{\mathcal{N}}$  at all nodal points of the finite element mesh. Next, the critical node  $\mathcal{N}_c$  is determined by constructing a loop over all crack front nodes  $\mathcal{N}_i \in \partial\Gamma^h$  of the finite element mesh to find the one having the maximum *quasi-distributed configurational force vector*  $\bar{\mathbf{g}}_{\mathcal{N}_c}$ , see Figure 9.7. Then,  $\mathcal{N}_c$  describes the crack tip where a possible advance of the crack may take place. Recall that  $\mathbf{g}_{\mathcal{N}_c}$  itself cannot be used directly in the crack criterion due to dimensional inconsistency as already explained in Section 9.4, see equation (9.22). On the other hand, for the determination of the crack surface normal it is not necessary to modify the definition of  $\mathbf{g}_{\mathcal{N}_c}$ . In order to identify uniquely an advance of the crack front, it is necessary to determine the normal vector  $\mathbf{N}$  of the incremental crack surface  $\Delta\Gamma_{n+1}^h$ . Observe that by using only the configurational force vector  $\mathbf{g}_{\mathcal{N}_c}$  at the critical node one cannot identify the normal  $\mathbf{N}$  uniquely, i.e. a rotational indeterminacy of the surface  $\Delta\Gamma_{n+1}^h$  remains around the axis given by the configurational force  $\mathbf{g}_{\mathcal{N}_c}$  as visualized in Figure 9.7c. A remedy of this problem could be to take into account additional information from the neighborhood of the critical node  $\mathcal{N}_c$  at the current crack front  $\partial\Gamma_{n+1}^h$ . One possibility is to employ the configurational forces acting on nodes  $\mathcal{N}_1$  and  $\mathcal{N}_2$  next to the critical one  $\mathcal{N}_c$ , see Figure 9.8c. Another solution is to consider the crack front segments  $\mathcal{S}_1$  and  $\mathcal{S}_2$  that emanate from  $\mathcal{N}_c$  as shown in Figure 9.8c and 9.9a. The segments  $\mathcal{S}_1$  and  $\mathcal{S}_2$  put indeed a constraint on the formation of a new surface and this constraint provides a smooth propagation of

**Box 9.8:** Necessary Topology Update due to Node Doubling in 3-D.

1. *Generation of the new node  $\mathcal{N}_n$  and the new facets  $\mathcal{F}_{n_i}$* 
  - 1.1 Find the critical facets  $\mathcal{F}_{c_i}$  (Box 9.1) and duplicate it :  $\mathcal{F}_{n_i}$
  - 1.2 Find the critical node  $\mathcal{N}_c$  (Box 9.1) and duplicate it :  $\mathcal{N}_n$
  - 1.3 Perform the data structure update described in Box 9.7
2. *Assignment of the new node  $\mathcal{N}_n$  to associated finite elements*
  - 2.1 find the tetrahedron  $\mathcal{T}_1$  having both the critical facet  $\mathcal{F}_{c_1}$  and node  $\mathcal{N}_c$
  - 2.2 find the next tetrahedron  $\mathcal{T}_2$  neighbor to  $\mathcal{T}_1$  and having the node  $\mathcal{N}_c$
  - 2.3 find the set of tetrahedra  $\{\mathcal{T}_1, \mathcal{T}_2, \mathcal{T}_3\}$  in a similar manner
2. *Generation of new data structure*
  - 3.1 assign the new node  $\mathcal{N}_n$  to tetrahedra  $\{\mathcal{T}_4, \mathcal{T}_5, \mathcal{T}_6\}$
  - 3.2 keep the old node  $\mathcal{N}_c$  for tetrahedra  $\{\mathcal{T}_1, \mathcal{T}_2, \mathcal{T}_3\}$
  - 3.3 increase the total number of nodal points
  - 3.4 generate the new data structure described in Box 9.6

the crack. Here, we follow the second approach and define an average crack front vector that describes the crack front in the neighborhood of the critical node  $\mathcal{N}_c$ . The average crack front vector  $\tilde{\mathbf{s}}$  is defined by

$$\tilde{\mathbf{s}} = \frac{\mathbf{s}_1 + \mathbf{s}_2}{|\mathbf{s}_1 + \mathbf{s}_2|}, \quad (9.32)$$

where  $\mathbf{s}_1$  and  $\mathbf{s}_2$ , as shown in Figure 9.9a, are the unit vectors along the segments  $\mathcal{S}_1$  and  $\mathcal{S}_2$ , respectively. Then the unit normal vector  $\mathbf{N}$  to the new crack surface increment  $\Delta\Gamma_{n+1}^h$  is determined by

$$\mathbf{N} = \frac{\mathbf{g}_{\mathcal{N}_c} \times \tilde{\mathbf{s}}}{|\mathbf{g}_{\mathcal{N}_c} \times \tilde{\mathbf{s}}|}. \quad (9.33)$$

If the critical node  $\mathcal{N}_c$  is either the first or the last node of the crack front  $\partial\Gamma_{n+1}^h$  then there exists only one neighboring segment of  $\mathcal{N}_c$ . In this case, the average front vector  $\tilde{\mathbf{s}}$  is equal to the relevant crack front vector  $\mathbf{s}_i$  of the segment  $\mathcal{S}_i$ . Note that the illustrations of the crack front in Figure 9.9 represent a special case where the three vectors  $\mathbf{s}_1$ ,  $\mathbf{s}_2$  and  $\mathbf{g}_{\mathcal{N}_c}$  are coplanar. Normally, for a general case it is not possible to define a surface with constant unit normal such that  $\mathbf{s}_1$ ,  $\mathbf{s}_2$  and  $\mathbf{g}_{\mathcal{N}_c}$  lie in a plane.

**Determination of Critical Facets and Reorientation.** After having found  $\mathcal{N}_c$  and  $\mathcal{S}_1$ , the critical facets  $\mathcal{F}_{c_i}$  have to be determined. This is accomplished by a loop over all facets having the segment  $\mathcal{S}_1$ , i.e.  $\{\mathcal{F}_i \mid i = 1 \dots \text{numfac}(\mathcal{S}_1)\}$ . Then,  $\mathcal{F}_{c_1}$  is the facet having the following three properties: (i) One of the segments of  $\mathcal{F}_{c_1}$  should be  $\mathcal{S}_1$ . (ii)  $\mathcal{F}_{c_1}$  should be an inner facet, i.e. the inner/outer flag has to be 1. (iii) The absolute value of the scalar product between the unit normal  $\mathbf{n}_1$  of  $\mathcal{F}_{c_1}$  and  $\mathbf{N}$  has to be maximum. Having determined the first critical facet  $\mathcal{F}_{c_1}$ , we project the node  $\mathcal{N}_1$  perpendicularly onto the desired increment of the crack surface  $\Delta\Gamma_{n+1}^h$ . As a consequence of the projection, the normal vector  $\mathbf{n}_1$  of the critical facet  $\mathcal{F}_{c_1}$  is aligned to the required normal  $\mathbf{N}$ , see Figure

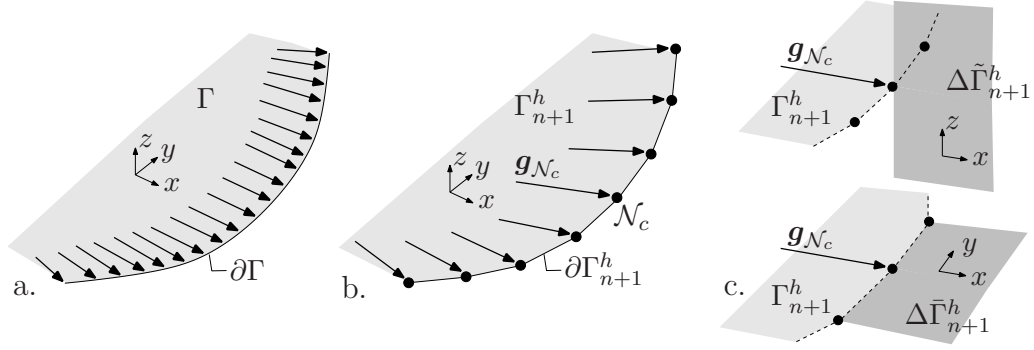


**Figure 9.7:** a.) Distributed configurational forces acting on the front  $\partial\Gamma$  of the crack surface  $\Gamma$  which lies entirely in the  $x-y$  plane. b.) Discrete configurational forces acting on crack front nodes  $\mathcal{N} \in \partial\Gamma_{n+1}^h$  as a consequence of the finite element discretization. c.) The configurational force  $\mathbf{g}_{\mathcal{N}_c}$  (which also lies in the  $x-y$  plane) acting on the critical node  $\mathcal{N}_c$  and two possible crack surface increments that are parallel to  $\mathbf{g}_{\mathcal{N}_c}$ . Two possible crack surface increments  $\Delta\tilde{\Gamma}_{n+1}^h$  and  $\Delta\bar{\Gamma}_{n+1}^h$  are in the  $x-z$  and  $x-y$  planes, respectively. Consequently, new increment of the crack surface  $\Delta\Gamma_{n+1}^h$  cannot be determined uniquely by  $\mathbf{g}_{\mathcal{N}_c}$  alone.

9.9. Note that in some cases a complete reorientation of the facet  $\mathcal{F}_{c_1}$  by moving the node  $\mathcal{N}_1$  cannot be performed due to undesired mesh distortions. It is even possible to obtain some tetrahedra with negative Jacobians. In order to overcome this problem we compute the Jacobians of all tetrahedra having the node  $\mathcal{N}_1$ , i.e.  $\{\mathcal{T}_i \mid i = 1 \dots \text{numtet}(\mathcal{N}_1)\}$ , both before and after the reorientation. We prevent undesired distortions of the finite element mesh by controlling the ratio of the final Jacobian value to the initial one. If this ratio exceeds some given limit then instead of a complete alignment a partial reorientation is performed and the possibility of severe distortions are precluded. After the alignment procedure, next segment of the facet  $\mathcal{F}_{c_1}$  that emanates from  $\mathcal{N}_c$  is considered. In a similar manner discussed above the next critical facet  $\mathcal{F}_{c_2}$  is determined and also reoriented. This procedure is kept going until it reaches to the second neighboring crack front segment  $\mathcal{S}_2$ . Note that in this procedure the number of critical facets is not known a priori. After the determination and reorientation of the critical facets, the crack surface increment  $\Delta\Gamma$  is approximated as the union of  $\mathcal{F}_{c_i}$ . The new crack surface increment reads as

$$\Delta\Gamma \approx \Delta\Gamma_{n+1}^h = \mathcal{F}_{c_1} \cup \mathcal{F}_{c_2} \cup \dots \cup \mathcal{F}_{c_n} \quad (9.34)$$

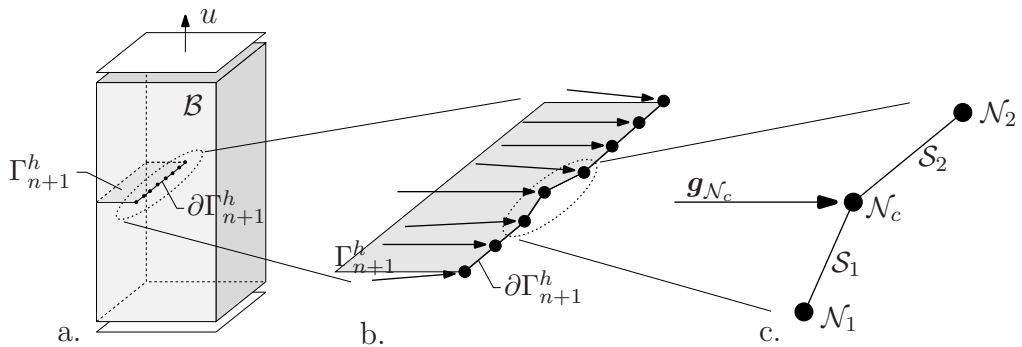


**Figure 9.8:** a.) A three-dimensional body  $\mathcal{B}$  with crack surface  $\Gamma_{n+1}^h$  and crack front  $\partial\Gamma_{n+1}^h$ . b.) Configurational forces  $\mathbf{g}_I$  at the crack front  $\partial\Gamma_{n+1}^h$ . c.) Critical node  $\mathcal{N}_c$ , corresponding configurational force  $\mathbf{g}_{\mathcal{N}_c}$  and the neighboring segments  $\mathcal{S}_1$  and  $\mathcal{S}_2$  at the crack front, which define the *quasi-distributed critical force*  $\mathbf{g}_{\mathcal{N}_c}/L_{\mathcal{N}_c}$  with  $L_{\mathcal{N}_c} := (|\mathcal{S}_1| + |\mathcal{S}_2|)/2$ .

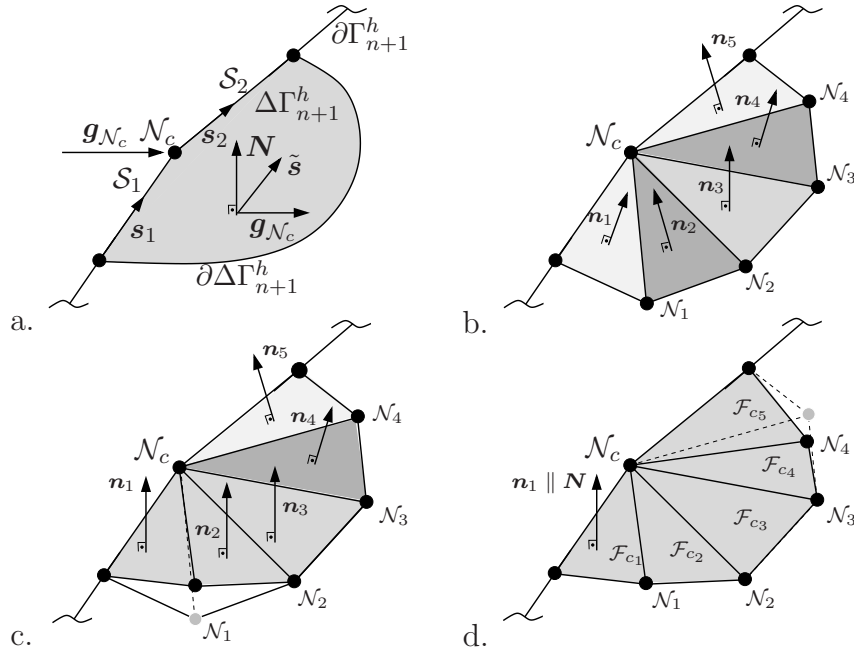


**Figure 9.9:** Adaptive facet alignment algorithm. a.) Critical node  $\mathcal{N}_c$  and two neighboring crack front segments  $\mathcal{S}_1, \mathcal{S}_2$  are identified. An average unit vector  $\tilde{\mathbf{s}}$  is defined based on crack front vectors  $\mathbf{s}_1$  and  $\mathbf{s}_2$ . The vector product of  $\tilde{\mathbf{s}}$  and the configurational force  $\mathbf{g}_{\mathcal{N}_c}$  gives the normal vector  $\mathbf{N}$  to the new developed incremental crack surface. b.) Critical facets  $\mathcal{F}_{c_i}$  with unit normal  $\mathbf{n}_i$  are found such that the scalar product  $\mathbf{N} \cdot \mathbf{n}_i$  is maximum. c.) - d.) The facets are aligned such that the nodes  $\mathcal{N}_1, \mathcal{N}_2, \mathcal{N}_3, \mathcal{N}_4$  are projected onto the plane with normal  $\mathbf{N}$ , i.e. the new facet normals  $\mathbf{n}_i$  satisfy  $\mathbf{N} \times \mathbf{n}_i = \mathbf{0}$ .

in the undeformed reference configuration.

**Doubling of Critical Facets.** Having accomplished the alignment procedure, new copies ( $\mathcal{F}_{n_i}$ ) of the facets  $\mathcal{F}_{c_i}$  with the same nodal connectivity of the original ones are created. Next, the critical  $\mathcal{F}_{c_i}$  and the new generated facets  $\mathcal{F}_{n_i}$  are set as outer. In addition, the neighboring information of the tetrahedra that are originally in contact with each other through the facets  $\mathcal{F}_{c_i}$  needs to be changed. In Figure 9.10a this doubling procedure is visualized where the number of critical facets is two. After the generation of new facets, the tetrahedra  $\mathcal{T}_1$  and  $\mathcal{T}_3$  are no more neighbors of  $\mathcal{T}_4$  and  $\mathcal{T}_6$ , respectively.

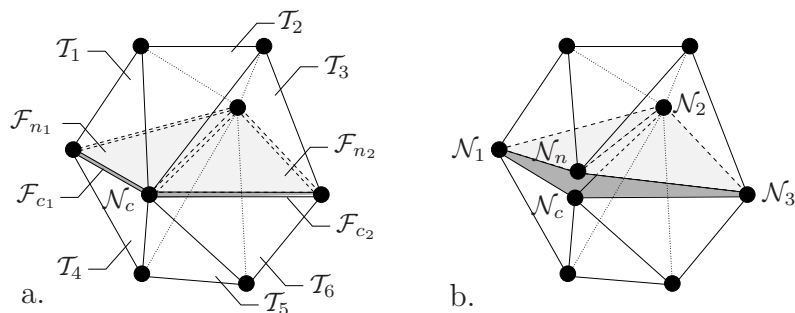


**Figure 9.10:** Doubling of the critical facets  $\mathcal{F}_{c_i}$  and the critical node  $\mathcal{N}_c$ . a.) New facets  $\mathcal{F}_{n_1}$  and  $\mathcal{F}_{n_2}$  are generated from the critical facets  $\mathcal{F}_{c_1}$  and  $\mathcal{F}_{c_2}$ . New facets have the same nodal connectivity as original ones.  $\mathcal{F}_{c_1}, \mathcal{F}_{c_2}, \mathcal{F}_{n_1}$  and  $\mathcal{F}_{n_2}$  are set as outer. The neighborhood information of tetrahedra  $\mathcal{T}_1, \mathcal{T}_3, \mathcal{T}_4$  and  $\mathcal{T}_6$  is changed. Tetrahedra  $\mathcal{T}_1$  and  $\mathcal{T}_3$  are no more neighbors of  $\mathcal{T}_4$  and  $\mathcal{T}_6$ , respectively. b.) Finally, the new node  $\mathcal{N}_n$  is generated from the critical node  $\mathcal{N}_c$ .

This information is crucial in the determination of the new connectivity of the tetrahedra after the doubling of the critical node  $\mathcal{N}_c$ .

**Doubling of Critical Node.** The subsequent step that is necessary for the description of the crack propagation is the doubling of the critical node  $\mathcal{N}_c$ . The decisive point after the generation of a copy of  $\mathcal{N}_c$  is the distribution of the new node  $\mathcal{N}_n$  and the old one  $\mathcal{N}_c$  among the tetrahedra. We start with considering the tetrahedron  $\mathcal{T}_1$  as the only neighbor of the facet  $\mathcal{F}_{n_1}$  (it is the copy of the first critical facet  $\mathcal{F}_{c_1}$ ), see Figure 9.10a. Then we check all neighbors of  $\mathcal{T}_1$  and find the tetrahedra those have  $\mathcal{N}_c$  in their nodal connectivity. For the case visualized in Figure 9.10a it corresponds to  $\mathcal{T}_2$ . Note that there can be also two tetrahedra which are neighbor to  $\mathcal{T}_1$  and contain  $\mathcal{N}_c$  in their connectivity. In a similar manner one continues with  $\mathcal{T}_2$  and reaches to  $\mathcal{T}_3$ . From  $\mathcal{T}_3$  it is not possible to find any tetrahedron (except  $\mathcal{T}_2$  which is already traced) neighbor to  $\mathcal{T}_3$  and contains  $\mathcal{N}_c$ . Consequently, the algorithm determines  $\mathcal{T}_1$ ,  $\mathcal{T}_2$  and  $\mathcal{T}_3$  get the new node  $\mathcal{N}_n$  while  $\mathcal{T}_4$ ,  $\mathcal{T}_5$  and  $\mathcal{T}_6$  retain the old one  $\mathcal{N}_c$ . The final step is the update of the crack front nodes. As an example it reads for the crack topology shown in Figure 9.9d

$$\partial\Gamma_{n+1}^h \Leftarrow \partial\Gamma_{n+1}^h \cup \{\mathcal{N}_1, \mathcal{N}_2, \mathcal{N}_3, \mathcal{N}_4\} - \mathcal{N}_c . \quad (9.35)$$

Observe that upon a crack propagation the critical node  $\mathcal{N}_c$  has to be removed from the crack front for all possible topologies. On the other hand, the number of nodes that will be added to the new front is not always constant and depends on the crack geometry. Although the generation of the new node  $\mathcal{N}_n$  intrinsically induces doubling of some segments, it is not discussed explicitly while there is no direct influence of the segments on the algorithm.



## 10. Representative Numerical Examples

### 10.1. Two-Dimensional Crack Propagation Examples

In this section several crack propagation problems are considered and the predictive capabilities of the proposed formulation are shown by comparing the computational results with the experimental observations. The bulk material response is governed by the quadratic energy storage function

$$\psi(\boldsymbol{\varepsilon}) = \frac{\kappa}{2} \text{tr}^2[\boldsymbol{\varepsilon}] + \mu \|\text{dev}[\boldsymbol{\varepsilon}]\|^2 \quad (10.1)$$

in terms of the bulk modulus  $\kappa$  and the shear modulus  $\mu$ . First, the accuracy of the configurational nodal force computation is checked and its application both as a crack propagation criterion and a crack direction predictor is evaluated for a tensile test of a *single edge notched* (SEN) specimen. Here, we compare the numerical results with analytical values of the  $J$ -integral available in the literature. Furthermore, the numerically obtained direction of crack propagation is validated by comparison with the expected crack direction. For these investigations, results obtained by the configurational force vector at the singularity are compared with those obtained by a resultant configurational force vector of a finite domain around the singularity. Then, another SEN specimen in tension is considered in order to show the importance of the reorientation of the critical segment at the crack tip to capture right crack trajectories. A *symmetric three point bending test* with a pure mode-I crack propagation and an *asymmetric three point bending specimen with holes* are considered next. Furthermore, the fracture of a cylindrical specimen under compression, the so-called *Brazilian test*, and a *double notched tensile specimen with two holes* are investigated. Finally a mode-II problem is studied, i.e. a *square notched specimen under simple shear*. For this example, we compare also the results with alternative crack propagation criteria available in the literature.

**10.1.1. Single Edge Notched Tensile Test I.** In order to estimate the accuracy of the configurational nodal force computation, a notched plane strain benchmark is considered which is studied in LARSSON & FAGERSTRÖM [124], see Figure 10.1a. The

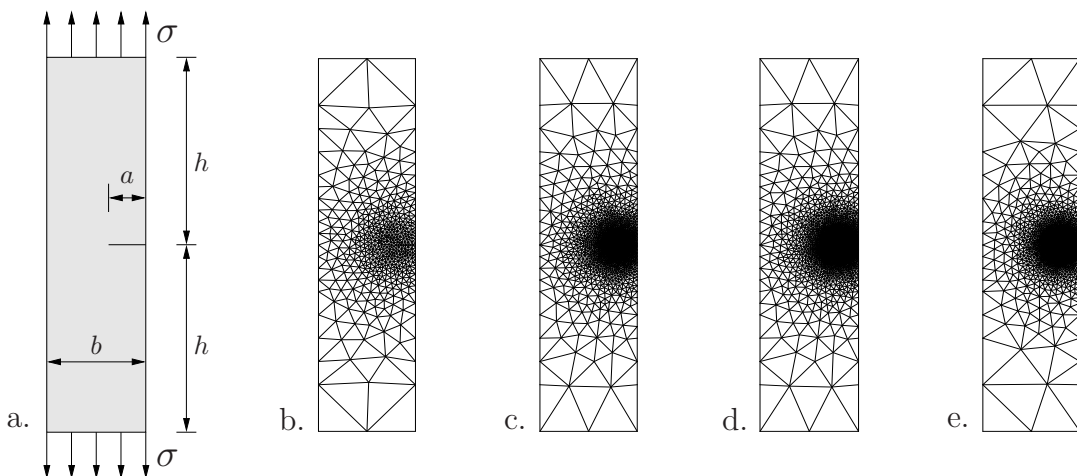


**Figure 10.1:** Tensile test of a single edge notched specimen. a.) Geometry, loading and different discretizations with b.) 925, c.) 4239, d.) 7258 and e.) 17230 constant strain triangles.

dimensions are  $a = 0.1\text{m}$ ,  $b = 0.5\text{m}$ ,  $h = 1\text{m}$  and the applied tensile stress is  $\sigma = 10\text{MPa}$ . Referring to the results of the linear theory of elasticity, the stress intensity factor  $K_I$  for this geometry can be estimated by the polynomial approximation

$$K_I/K_0 = 1.12 - 0.23 a/b + 10.6 (a/b)^2 - 21.7 (a/b)^3 + 30.4 (a/b)^4 \quad (10.2)$$

outlined by ROOKE & CARTWRIGHT [194] as a function of the ratio  $a/b$ .  $K_0$  in (10.2) is the well-known stress intensity factor

$$K_0 = \sigma\sqrt{\pi a} \quad (10.3)$$

for a crack of length  $2a$  in an infinite sheet subjected to a remote tensile stress  $\sigma$ . The  $J$ -integral and the energy release rate  $G$  for plane strain conditions can be expressed in terms of  $K_I$ , the shear modulus  $\mu$  and the Poisson's ratio  $\nu$

$$G = J = \frac{K_I^2 (1 - \nu)}{2\mu}, \quad (10.4)$$

see equation (7.83). The material parameters are given as  $\mu = 80\text{GPa}$  and  $\nu = 0.3$ . The computation of the configurational force vector is performed by nine different discretizations with 925, 1997, 4239, 7258, 8502, 11096, 13078, 15814 and 17230 constant strain triangles, where four of the meshes are shown in Figure 10.1b-10.1e. First, we consider a frozen crack without any propagation. Figure 10.2a shows the norm of the configurational force vector at the tip for the different discretizations and the analytical result obtained from (10.2) and (10.4). The values determined from the *discrete force at the crack tip* show no uniform convergence behavior and are oscillating for different discretizations. The relative error is between 2 and 15%. Figure 10.2b compares the computed angle between the configurational force vector and the  $\mathbf{e}_1$ -direction with the theoretically expected value of  $0^\circ$ . Again, the results obtained from the crack tip evaluation are oscillating for different discretizations, varying from  $0.1^\circ$  to  $2.5^\circ$ .

An improvement can be obtained by considering a *resultant configurational force vector* of an *influence domain* that surrounds the crack tip, as suggested by DENZER, BARTH & STEINMANN [56]. To this end, we define a domain with radius  $r = 0.05\text{m}$  around the crack tip. The results are depicted in Figures 10.2a and 10.2b for the nine different discretizations. The values obtained from this *domain evaluation* yield a better convergence behavior than those obtained by the above *crack tip evaluation*. The relative error for the

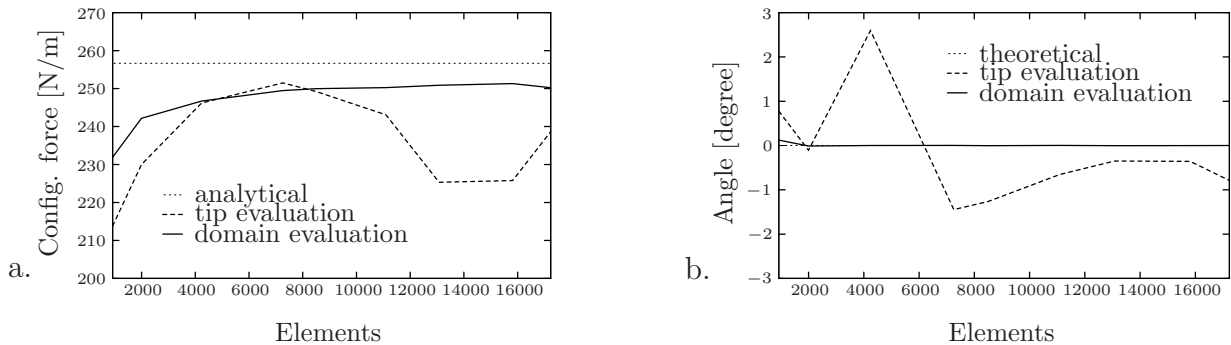


**Figure 10.2:** Tensile test of single edge notched specimen. a.) Norm of the configurational force vector and b.) the crack propagation angle evaluated by three methods for different meshes.

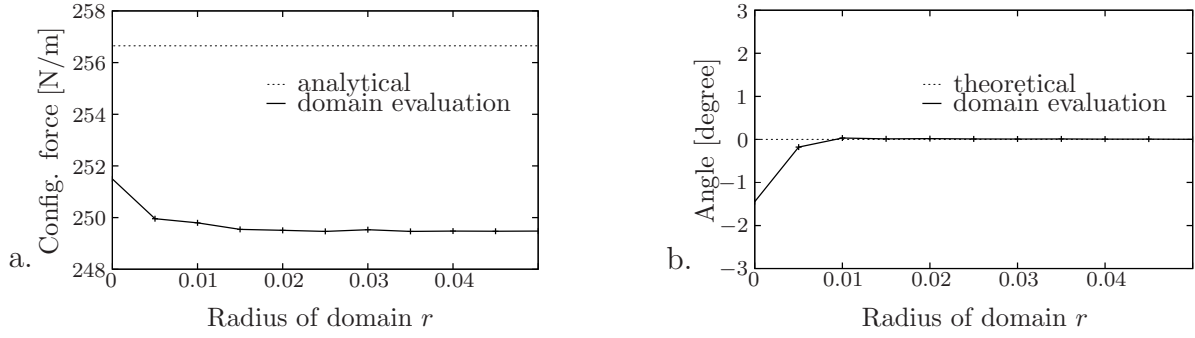


**Figure 10.3:** Tensile test of single edge notched specimen. Dependence on radius  $r$  for the domain evaluation. a.) Norm of the configurational force vector and b.) the crack propagation angle for a mesh with 7258 elements.

energy release rate is between 2 and 8%, and the observed crack propagation angles fall between  $0.0004^\circ$  and  $0.2^\circ$ . The discrepancy between the analytical and the computational results must be traced back to the poor discretization with constant strain triangles. It is well-known that these elements do not capture the  $r^{-1/2}$  singularity of the stresses at the crack tip. In order to capture this singularity, specific crack tip elements could be used as discussed for example in BARSOU [17, 18], HENSHELL & SHAW [97], LI, SHIH & NEEDLEMAN [127] and STEINMANN, ACKERMANN & BARTH [206]. We consider different radii of the domain for the mesh with 7258 elements to show the *effect of the domain size* on the evaluation of the resultant configurational force vector. The results for the norm of the configurational force vector and the crack propagation angle are depicted in Figures 10.3a and 10.3b, respectively. After a critical value of the domain radius, the domain size does not have an influence and yields similar results.

We now admit crack propagation. To this end, we consider the same meshes as depicted in Figure 10.1a but move in a displacement controlled tensile test the upper boundary. Figure 10.4a depicts the discrete crack propagation angles obtained during the deformation process for the mesh with 7258 elements up to the complete separation of the specimen into two pieces. Each crack propagation step in Figure 10.4a is associated with a critical segment release at the crack tip. Again, we compare the expected results with computed values from the *crack tip evaluation* and the *domain evaluation* with the radius  $r = 0.05\text{m}$ . The results determined at the crack tip oscillate around the expected value of  $0^\circ$  in a range between  $-4.0^\circ$  and  $+8.0^\circ$ . For the domain method, we observe

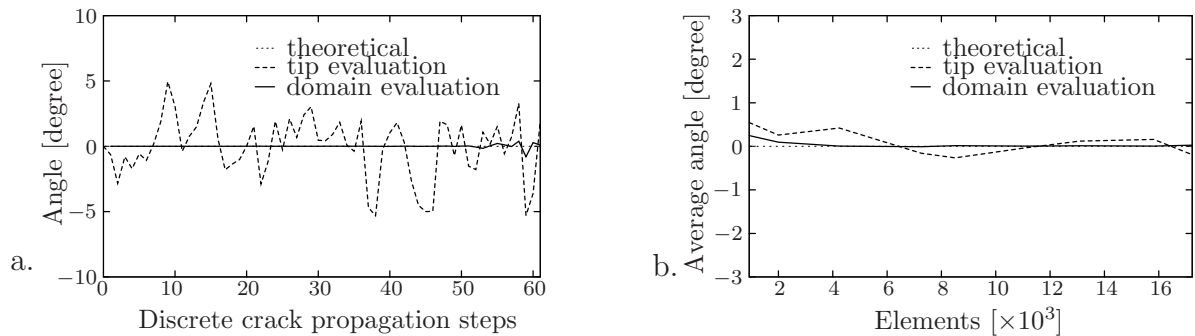


**Figure 10.4:** Tensile test of single edge notched specimen. a.) Discrete crack propagation angles versus complete fracturing process for a mesh with 7258 elements and b.) averaged crack propagation angle of complete fracturing process versus number of elements, evaluated by three methods.

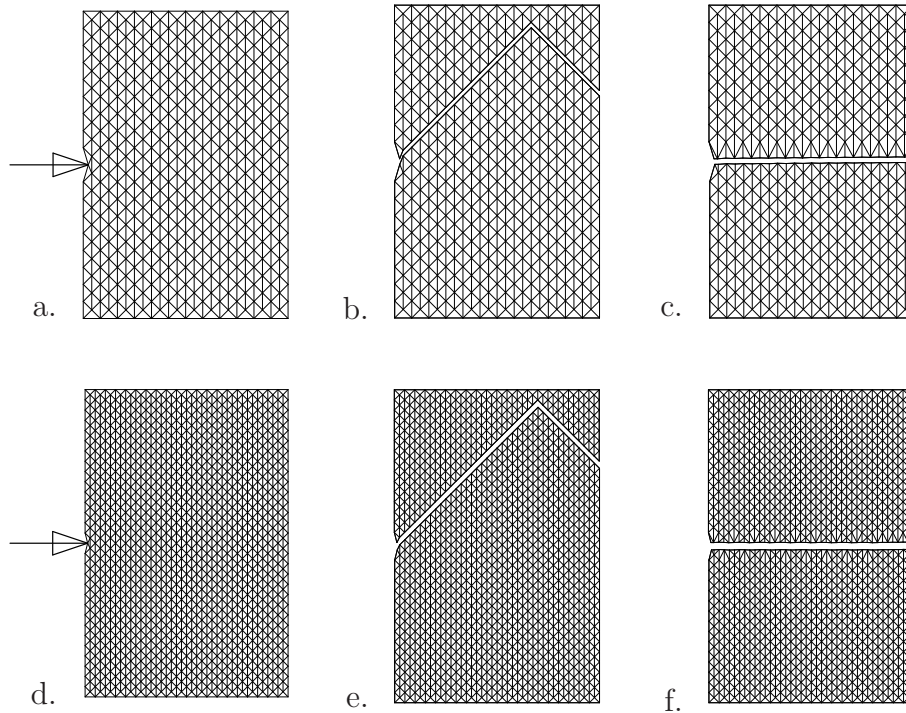


**Figure 10.5:** Single edge notched specimen. Effect of the adaptive movements of FE-nodes on the crack trajectory. a.) The initial mesh with 864 elements and the configurational force vector at the crack tip. The crack trajectories b.) with the fixed nodal positions and c.) with the adaptive movement of the nodes based on the configurational force vector at the crack tip. d.) The initial mesh with 2400 elements and the configurational force vector at the crack tip. The crack trajectories e.) with the fixed nodal positions and f.) with the possible movement of the nodes based on the configurational force vector at the crack tip.

strongly reduced oscillations between  $-0.4^\circ$  and  $+0.2^\circ$ , see Figure 10.4a. However, with regard to an average of the angles for the full crack length, the results become close to the expected value of  $0^\circ$  even for the investigations based on the crack tip evaluation. This is demonstrated in Figure 10.4b. As a result, the crack trajectories obtained by the crack tip evaluation can be considered to be acceptable. This is further underlined by the subsequent examples which demonstrate the predictive capabilities of the formulation to capture experimentally observed complex crack trajectories.

**10.1.2. Single Edge Notched Tensile Test II.** Another single edge notched specimen in tension is analyzed in order to show how the adaptive reorientation of the critical

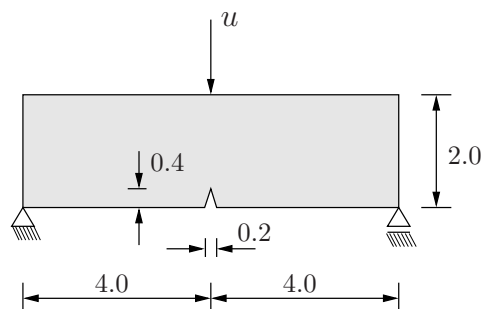


**Figure 10.6:** Geometry, loading and boundary conditions of the symmetric three point bending specimen.

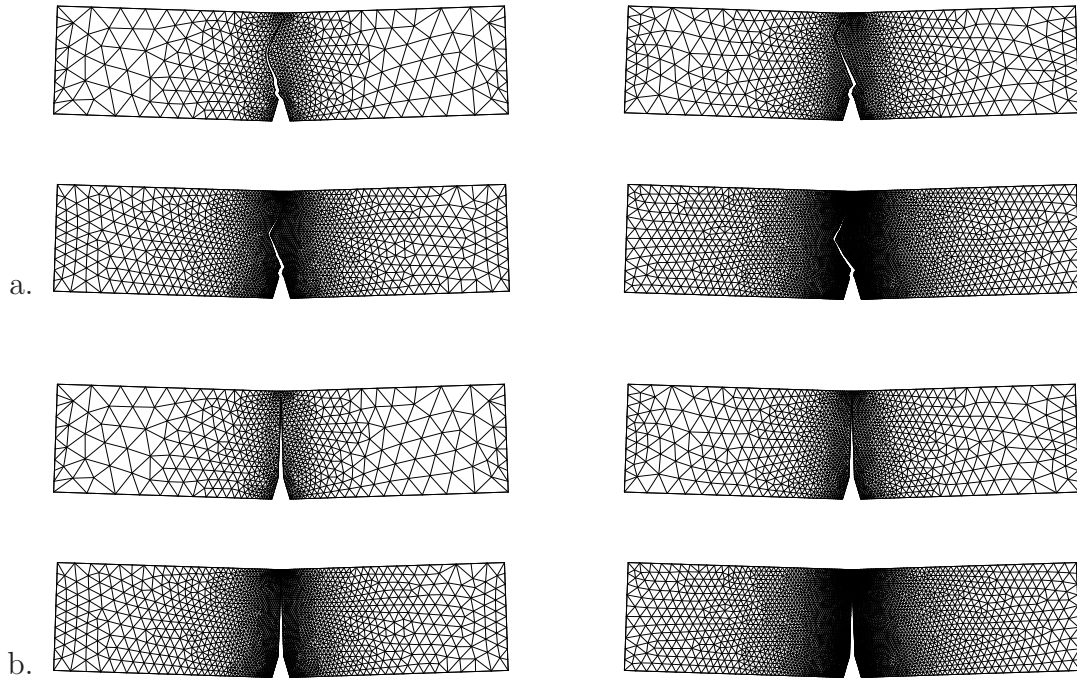


**Figure 10.7:** Three point bending test of a notched beam. Different discretizations with 1424, 2582, 4874 and 10360 elements. Crack trajectories a.) with the fixed nodal positions and b.) with the possible movement of the nodes based on the configurational force vector at the crack tip.

segments effects the crack propagation. The critical segment reorientation algorithm is discussed in Box 9.1. Two different meshes with 864 and 2400 elements are considered as shown in Figures 10.5a and 10.5d together with the configurational force vectors at the notches. Both meshes are generated intentionally such that there are no internal segments parallel to the configurational force direction. The construction of a mesh with all segments far away from being parallel to the configurational force vector at the crack tip results in a completely unphysical crack trajectory in the case of fixed nodal positions, see Figures 10.5b and 10.5e. In the figures it is shown that a finer mesh with the same topological structure does not improve the quality of the predicted crack pattern. On the other hand, the adaptive reorientation of the segments at the crack tip yields the theoretical crack trajectories for both mesh densities, see Figures 10.5c and 10.5f. This emphasizes the importance of the r-adaptive reorientation procedure to capture theoretic-

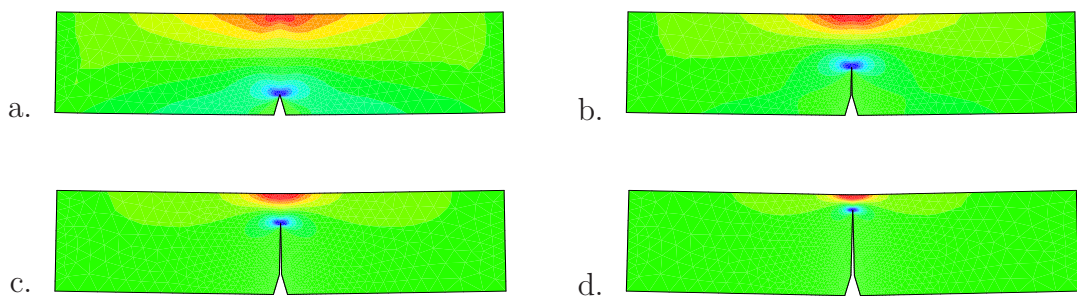


**Figure 10.8:** Three point bending test of a notched beam. Normal stress  $\sigma_{11}$  during the crack evolution a.) - d.) for the mesh with 4874 elements. Blue and red colors correspond to the maximum tensile and compressive stresses, respectively.



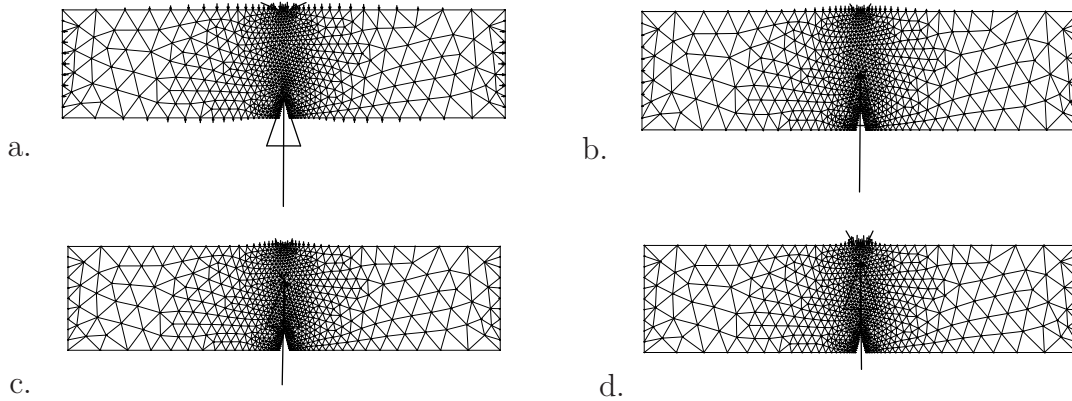


**Figure 10.9:** The three point bending test of a notched beam. The nodal configurational forces a.) before the propagation of the crack and b.) - d.) during the crack propagation for the mesh with 1424 elements.

cal crack trajectories.

**10.1.3. Symmetric Three Point Bending Test.** A three point bending test of a simply supported notched beam, which is one of the most investigated examples in the literature, is considered next. The geometry and the loading of the problem are given in Figure 10.6. The material parameters are specified in terms of the shear modulus  $\mu = 8.0\text{GPa}$ , the Poisson's ratio  $\nu = 0.3$  and the critical energy release rate  $g_c = 5 \times 10^{-4}\text{N/m}$ . Figure 10.7a shows four different meshes with 1424, 2582, 4874 and 10360 elements which are used in simulations. The influence of the segment alignment procedure is investigated first. The crack trajectories are displayed in Figures 10.7a and 10.7b for fixed nodes and a possible reorientation of the critical crack tip segment, respectively. A crack starting from the notch and propagating straight to the load is expected theoretically. In the case of simulations with fixed nodes, the obtained crack profiles represent the theoretical patterns poorly and moreover for different mesh densities they differ from each other. On the other hand, the computations with an alignment of the critical segment capture the theoretical crack patterns very well for all mesh densities. The normal stress  $\sigma_{11}$  during the crack evolution is visualized in Figure 10.8. Blue and red colors correspond to the maximum tensile and compressive stresses, respectively. In Figure 10.9, the nodal configurational force vectors in the undeformed configuration are plotted for the mesh with 1424 elements

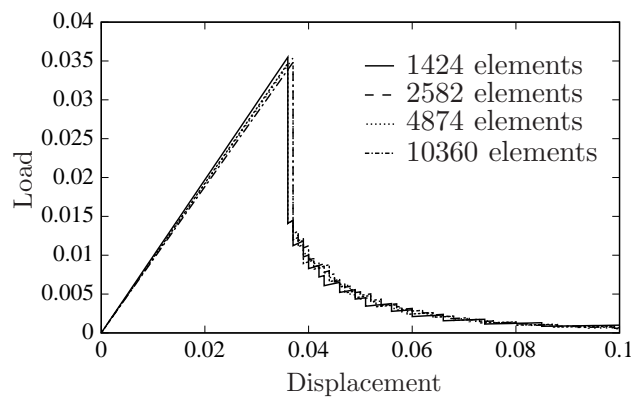


**Figure 10.10:** Three point bending test of a notched beam. Comparison of load–deflection curves for discretizations with 1424, 2582, 4874 and 10360 elements.

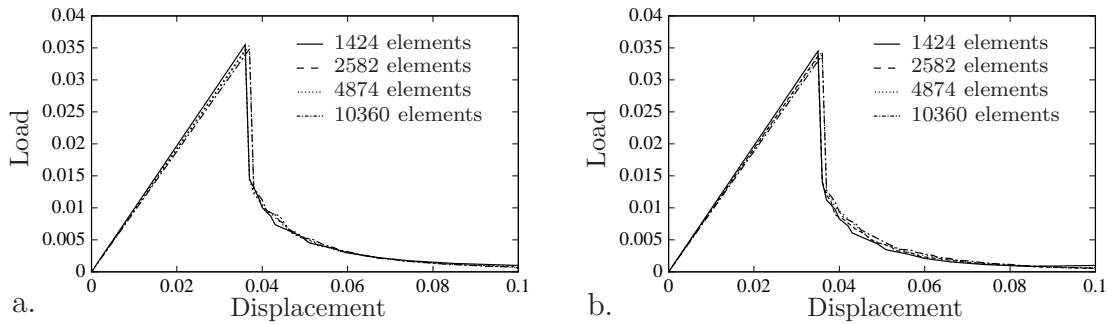


**Figure 10.11:** Three point bending test of a notched beam. Comparison of a.) upper envelopes and b.) lower envelopes of the load–deflection curves for discretizations with 1424, 2582, 4874 and 10360 elements.

at four different levels of the loading. The nodal configurational force vector at the crack tip is nearly vertical for all four cases showing the theoretical crack propagation direction. Note that there are also some configurational forces at the places close to the load and supports due to the associated singularities.

The mesh-independency of the load-deflection curves is shown next. The load-deflection curves are plotted in Figure 10.10 for all four meshes together. The staggered scheme outlined in Box 9.1 yields the zigzag-shaped load deflection curves due to the fact that at each time increment an elastic computation is done with a possible crack progress afterwards. In the curves a vertical drop is due to an advance in the crack while the parts of the curve with a positive slope correspond to elastic steps with a frozen crack. It can be observed that with finer meshes the frequency of zigzags increases and load-deflection curves become smoother. From the load-displacement curves in Figure 10.10 one can construct upper and lower envelopes for each discretization separately. The upper and lower envelopes are plotted in Figure 10.11a and 10.11b, respectively. In all three figures the load-deflection curves are in a good agreement for four different mesh densities showing that there is no mesh-dependency of the proposed algorithm.

Finally, the effect of time discretization on the global response is analyzed. The upper envelopes of the load-displacement curves are plotted for the mesh with 1424 elements in Figure 10.12 for three different algorithmic time steps,  $\Delta t = 1 \times 10^{-3}$ ,  $5 \times 10^{-4}$ ,  $1 \times 10^{-4}$ .

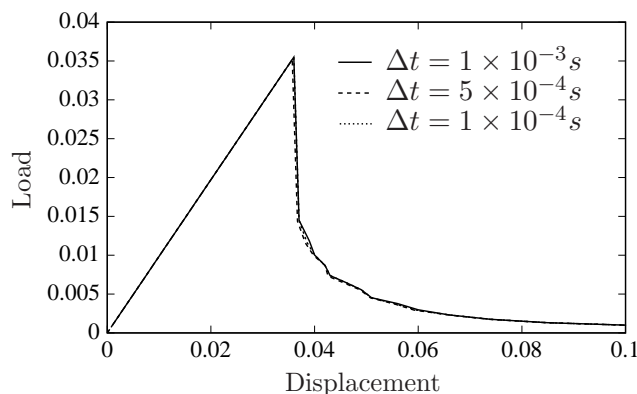


**Figure 10.12:** Three point bending test of a notched beam. Upper envelopes of the load deflection curves computed with different time steps for the mesh with 1424 elements.



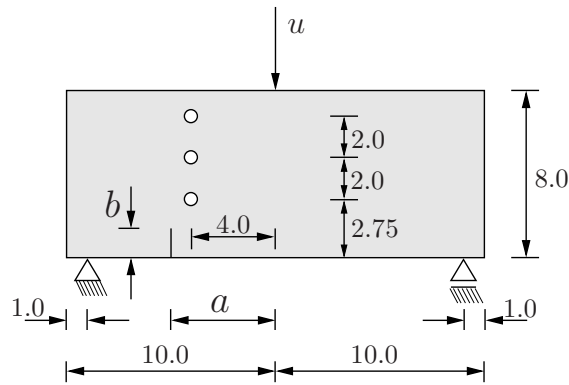


**Figure 10.13:** Geometry, loading and boundary conditions of the two type of notched beams with three holes. All holes have a diameter of 1.0 unit. Notches are parameterized in terms of the distance of notches to the middle of the beam  $a$  and the notch size  $b$ . Notch geometry I:  $a = 5.0$  and  $b = 1.5$ . Notch geometry II:  $a = 6.0$  and  $b = 1.0$ .

They are on top of each other exhibiting no dependency on the time step chosen.

**10.1.4. Asymmetric Three Point Bending Test.** Next, we apply our methodology to a problem in which more complex curvilinear crack trajectories are observed experimentally. The crack propagation of this problem was investigated first experimentally and numerically in BITTENCOURT ET AL. [25] by using numerically computed stress intensity factors and adaptive remeshing techniques around crack tip. They also compared different methods for the computation of stress intensity factors in the finite element context. The same example was simulated later by PHONGTHANAPANICH & DECHAUMPHAI [183] using stress intensity factors as a fracture criterion combined with an object-oriented

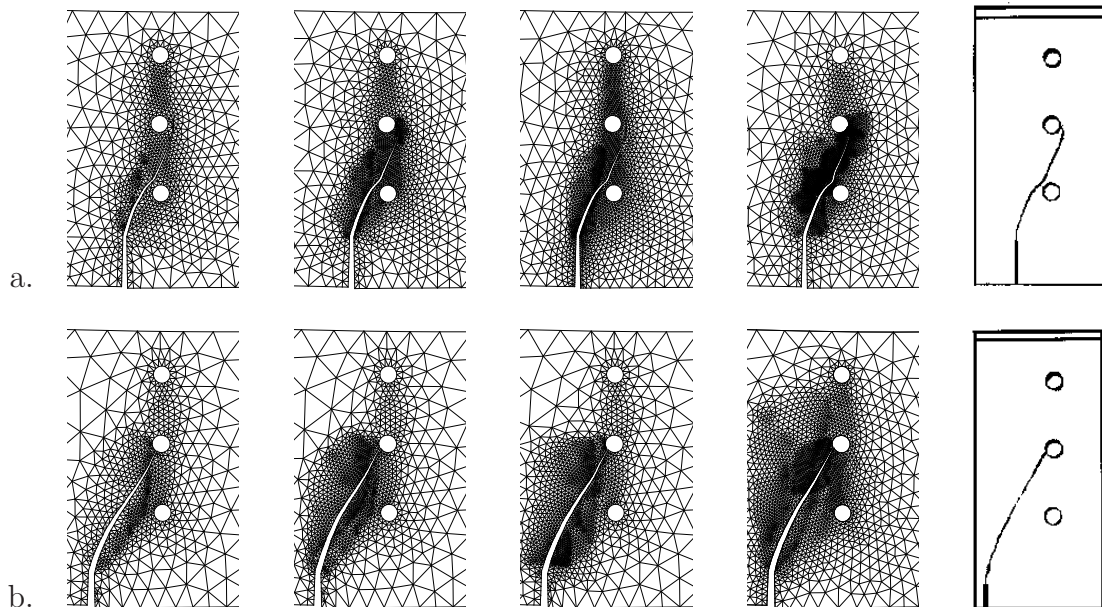


**Figure 10.14:** Notched beams with three holes a.) Crack patterns of notch I for different discretizations with 2021, 3205, 4042, 4912 elements and the experimentally observed trajectory. b.) Crack patterns of notch II for different discretizations with 1664, 2652, 3080, 4642 elements and the experimentally observed trajectory. The experimental crack trajectories are taken from BITTENCOURT ET AL. [25]

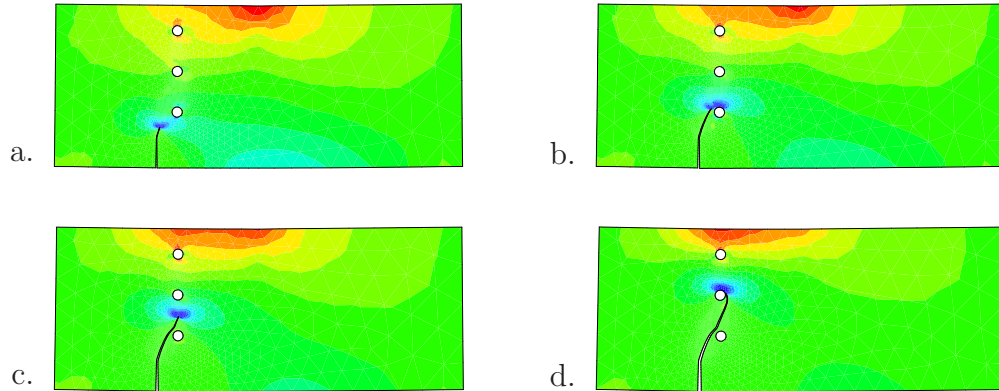


**Figure 10.15:** The notched beam with three holes. The normal stress  $\sigma_{11}$  during the crack evolution a.) - d.) for the notch geometry I with 3205 elements. Blue and red colors correspond to the maximum tensile and compressive stresses, respectively.

adaptive remeshing algorithm. HEINTZ [95] also investigated this example by employing configurational forces in the context of discontinuous Galerkin method introduced by HANSBO & HANSBO [93].

The geometry of the problem is described in Figure 10.13. The material parameters are specified as the shear modulus  $\mu = 8.0\text{GPa}$ , the Poisson's ratio  $\nu = 0.3$  and the critical energy release rate  $g_c = 1 \times 10^{-3}\text{N/m}$ . As a consequence of the holes and the initial notch the stress and the strain fields are perturbed yielding curved crack patterns which are highly sensitive to the position and the depth of the initial notch. Two different geometries are chosen as described in BITTENCOURT ET AL. [25], where the differences are only in the position and the depth of the initial notch.

The experimental and the computed crack trajectories of the first notch geometry are compared in Figure 10.14a for four different discretizations. The computational results for all discretizations ranging from 2021 to 4912 elements show a very good agreement with the experimental crack trajectory. The same comparison is done also for the second notch geometry as depicted in Figure 10.14b showing that the algorithm presented can capture complex curved crack patterns very well. In Figures 10.15 and 10.16 the normal stresses  $\sigma_{11}$  during the crack evolution are depicted for the notch geometry I with 3205

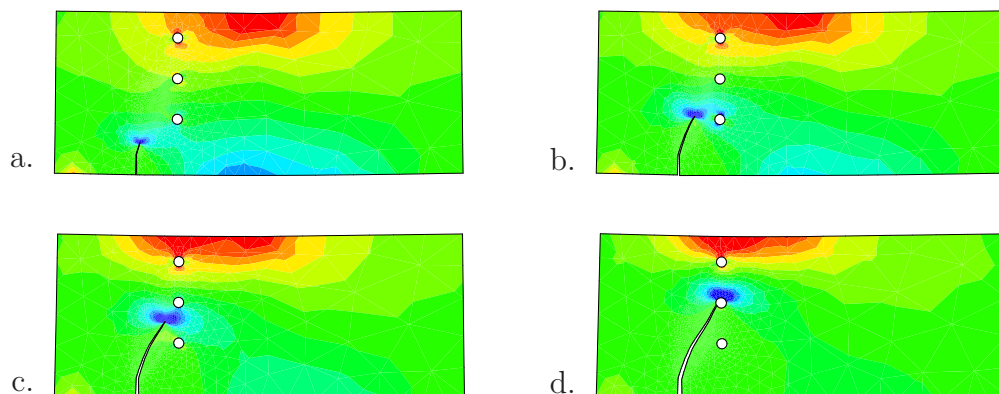


**Figure 10.16:** The notched beams with three holes. The normal stress  $\sigma_{11}$  during the crack evolution a.) - d.) for the notch geometry II with 2652 elements. Blue and red colors correspond to the maximum tensile and compressive stresses, respectively.

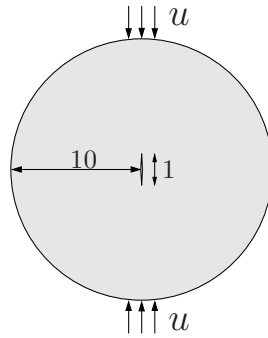


**Figure 10.17:** Geometry and loading of the Brazilian splitting test with an internal notch.

elements and II with 2652 elements, respectively. Blue and red colors in both figures correspond to the maximum tensile and compressive stresses, respectively.

**10.1.5. Brazilian Splitting Test.** The Brazilian splitting test, investigated for example by BOUCHARD ET AL. [27], is often used to predict the tensile strength of brittle or quasi-brittle materials like concrete. The setup of the problem is given in Figure 10.17. The material parameters are the shear modulus  $\mu = 8.0\text{GPa}$ , the Poisson's ratio  $\nu = 0.3$  and the critical energy release rate  $g_c = 1 \times 10^{-3}\text{N/m}$ . The displacements at the upper and lower parts are specified, no contact algorithm is considered. An initial crack parallel to the loading axis is placed at the center of the specimen. Two unstructured meshes with 2920 and 4294 elements are considered. The crack patterns corresponding to both meshes, given in Figures 10.18a and 10.18b, show very similar behavior. Observe their straight form obtained by the r-adaptive procedure summarized in Box 9.1. These results are in a good qualitative agreement with experimental observations. Figure 10.19 depicts the normal stresses  $\sigma_{11}$  during the crack evolution. Blue and red colors correspond to the maximum tensile and compressive stresses, respectively.

**10.1.6. Tensile Test with Two Notches and Holes.** This problem was analyzed in BOUCHARD, BAY & CHASTEL [26]. It is a tension test of a double edge notched specimen with two holes. The authors made a comparison of different crack propagation criteria combined with an adaptive remeshing of finite elements. Here, the maximum circumferential stress, the minimum strain energy density and the maximum strain energy release rate criteria were compared. They found that the maximum circumferential stress and maximum strain energy release rate criteria give quite equivalent results. The geometry and the loading are described in Figure 10.20. We choose the shear modulus  $\mu =$

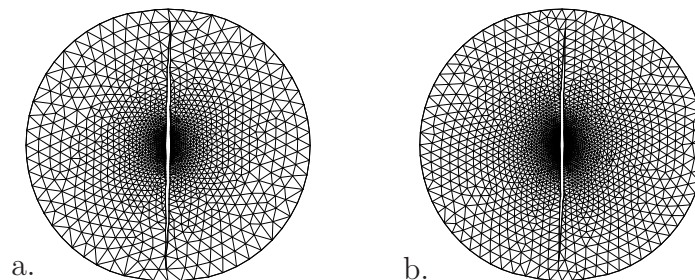


**Figure 10.18:** Brazilian cylinder splitting test. Final crack trajectories for meshes with a.) 2920 elements and b.) 4294 elements.

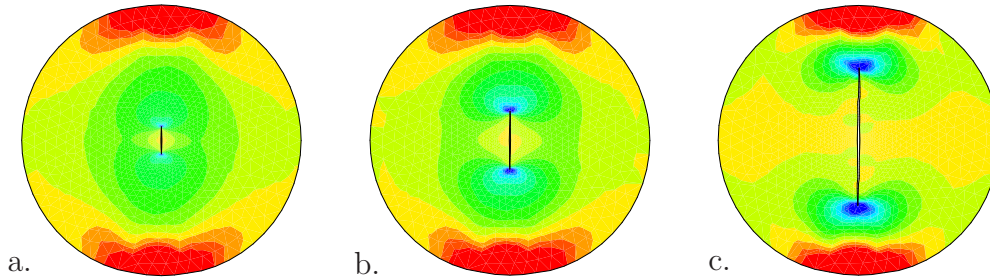


**Figure 10.19:** Brazilian cylinder splitting test. Normal stress  $\sigma_{11}$  during the crack evolution a.) - c.) for the mesh with 2920 elements. Blue and red correspond to the maximum tensile and compressive stresses, respectively.

8.0GPa, the Poisson's ratio  $\nu = 0.3$  and the critical energy release rate  $g_c = 1 \times 10^{-3}$ N/m. Different from the previous examples, the propagation of two separate cracks has to be considered. The cracks are forced to advance one after the other such that successive progress of the same crack is prevented. The resulting crack profiles are shown for two different meshes with 2394 and 4170 elements in Figures 10.21a and 10.21b, respectively. Both cracks first show a tendency to propagate towards the holes and once the holes are passed they reorient themselves horizontally. The crack trajectories predicted by the proposed algorithm are in a good agreement with results reported in BOUCHARD, BAY & CHASTEL [26] and BOUCHARD ET AL. [27]. Figure 10.22 shows the normal stresses  $\sigma_{22}$  during the crack evolution for the mesh with 2394 elements. Blue and red colors correspond to the maximum and minimum tensile stresses, respectively.

**10.1.7. Square Notched Specimen under Simple Shear.** Next, we apply the proposed methodology to a square plate with a horizontal notch that is placed at the middle height and running from the left outer surface to the center of the specimen. The geometric setup of the problem is given in Figure 10.23. We choose the shear modulus  $\mu = 8.0$ GPa, the Poisson's ratio  $\nu = 0.3$  and the critical energy release rate  $g_c = 1 \times 10^{-3}$ N/m. For simple shear, we prescribe in a deformation-driven context the horizontal displacements of the vertical boundaries varying linearly from 0 to  $u$ . In addition, the upper boundary is driven horizontally by an amount of  $u$ . According to the experimental data of ERDOGAN & SIH [65], the subsequent crack pattern measures an angle of approximately  $70^\circ$  to the initial notch. Figures 10.24a and 10.24b show two different meshes having 2048 elements. The first mesh depicted in Figure 10.24a is completely regular and homogeneous, whereas the second mesh in Figure 10.24b has a geometric imperfection by slightly disturbed elements around the initial crack tip. In these pictures,

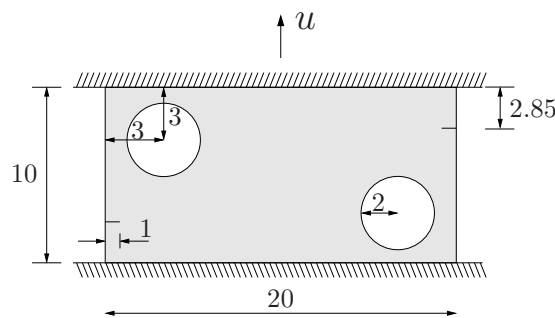


**Figure 10.20:** Geometry, loading and boundary conditions of a tensile test of notched specimen with two holes.



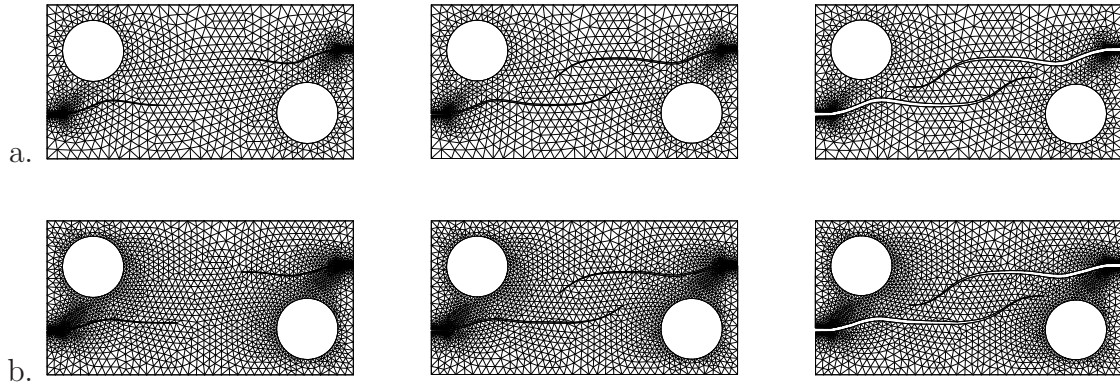


**Figure 10.21:** Tensile test of a notched specimen with two holes. Crack trajectories with a.) 2394 elements and b.) 4170 elements.

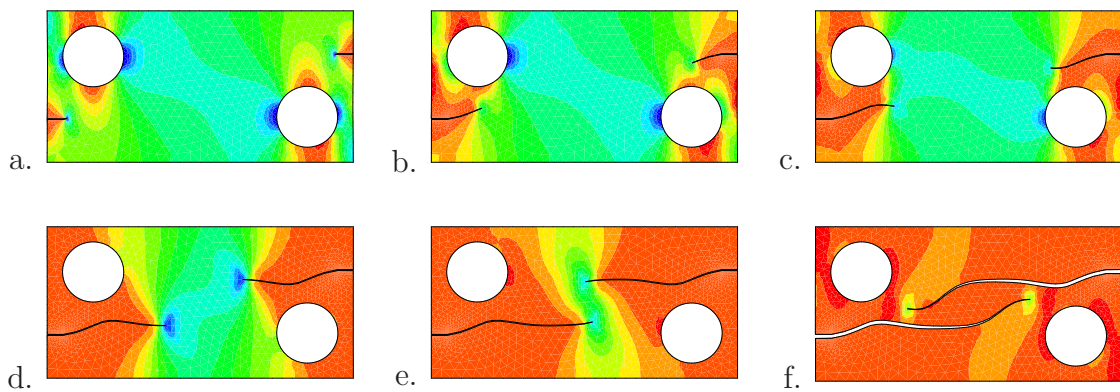


**Figure 10.22:** Tensile test of a notched specimen with two holes. Normal stress  $\sigma_{22}$  during the crack evolution a.) - f.) for the mesh with 2394 elements. Blue and red colors correspond to the maximum and the minimum tensile stresses, respectively.

the configurational force at the crack tip is depicted for the beginning and a subsequent state of the crack propagation. For the first mesh without imperfection, the configurational force vector points in a horizontal direction during the whole deformation process, yielding a horizontal crack pattern. This is *not* in agreement with experimental results. The response for the perturbed mesh is shown in Figure 10.24b. Here, as a consequence of the imperfection, the configurational force vector at the onset of crack propagation slightly differs from the horizontal direction. In the subsequent stages, it *smoothly changes* up to

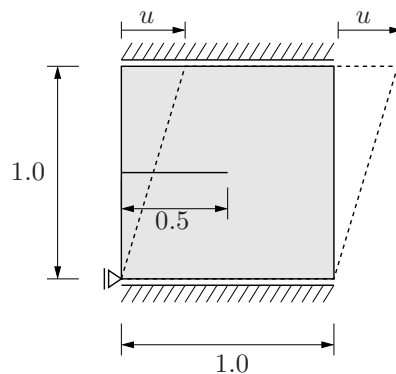


**Figure 10.23:** Geometry, loading and boundary conditions of simple shearing of a squared notched plate. Horizontal displacements are prescribed on the upper boundary and on the vertical boundaries as well.

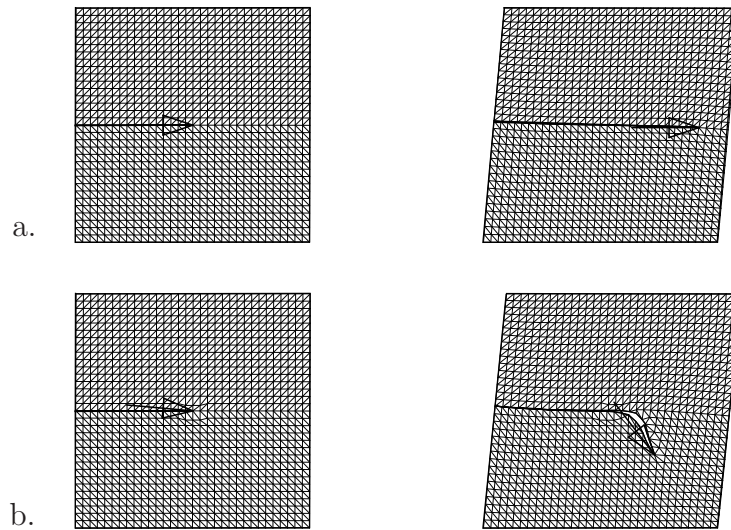


**Figure 10.24:** Simple shearing of a notched plate. Different discretizations with 2048 elements. The configurational force at the crack tip for the beginning and at a later state of the deformation process for a.) a homogeneous mesh and b.) a mesh with a geometric imperfection around the crack tip.

an angle between  $70^\circ$  and  $75^\circ$ , as observed experimentally and theoretically in ERDOGAN & SIH [65]. This observation shows the *inability of simulation of non-smooth crack kinking* by the proposed configurational force method. Furthermore, it reveals an *instability phenomena*, where only the introduction of a slight imperfection in the form of a mesh distortion yields the experimentally observed trajectory. Next, the same problem is computed by two different unstructured discretizations with 2000 elements as shown in Figure 10.25. Here, crack trajectories are displayed for a.) a homogeneous discretization and b.) a mesh with a refined discretization around the crack tip. The results show that crack propagation starts with an angle smaller than  $70^\circ$  but changes smoothly to approximately  $70^\circ$  in subsequent propagation steps. Again, the crack path is smooth. However, for the mesh in Figure 10.25b with refined discretization at the notch tip, the curvature of the crack localizes at the beginning of the propagation. Hence, in combination with a high mesh density around the notch tip, the method is able to resolve a crack kinking as experimentally expected. The shear stresses  $\sigma_{12}$  during crack evolution for the refined

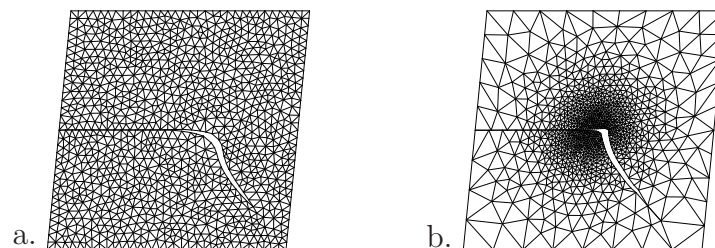


**Figure 10.25:** Simple shearing of a notched plate. Different unstructured discretizations with 2000 elements. The crack trajectories for a.) an irregular homogeneous mesh and b.) a refined mesh around the crack tip.

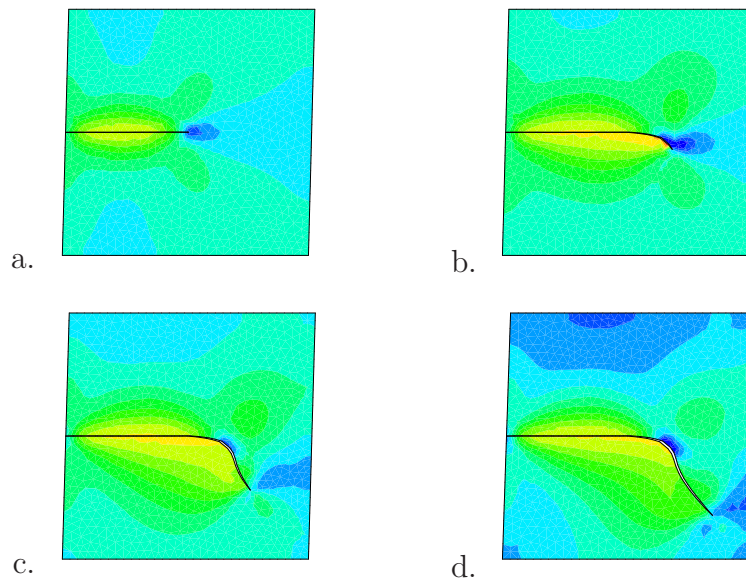


**Figure 10.26:** Simple shearing of a notched plate. Shear stresses  $\sigma_{12}$  during the crack evolution at four different loading levels a.) - d.) for a discretization of 2000 elements with refined mesh around the crack tip. Blue and yellow corresponds to the maximum and minimum shear stresses, respectively.

discretization are visualized at four different levels of loading in Figure 10.26. Blue and yellow colors correspond to the maximum and minimum levels, respectively. At the beginning of the loading process, a high concentration of  $\sigma_{12}$  stresses is observed at the crack tip. Therefore, the crack propagation represent a pure mode II fracture mode. Later, the crack reorientates towards  $70^\circ$  accompanied by decreasing shear stresses at the tip. Then, a mode I dominated fracture propagation is observed.

**10.1.8. Comparison of Different Crack Criteria.** We now compare results obtained from the configurational-force-driven propagation algorithm summarized in Box 9.1 with alternative criteria available in the literature, such as pointed out in the recent article by BOUCHARD, BAY & CHASTEL [26]. To this end, we investigate four crack propagation criteria: (i) the proposed configurational force criterion (*CFC*) of Box 9.1, (ii) a maximum circumferential stress (hoop stress) criterion (*MCSC*) introduced in ERDOGAN

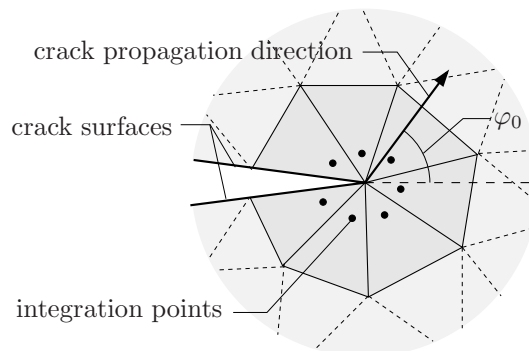


**Figure 10.27:** Maximum principal stress criterion. The direction of crack propagation at the crack tip is obtained from the stress state at the integration points.



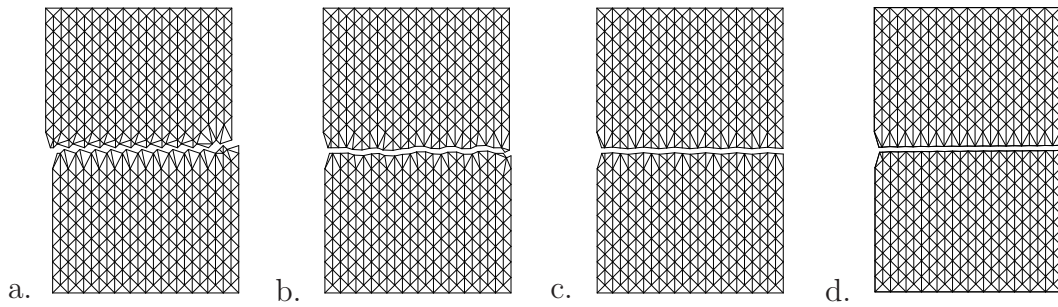


**Figure 10.28:** Single edge notched specimen under tension discretized by 864 elements. Effect of different criteria on the crack propagation direction. a.) The maximum circumferential stress criterion, b.) the averaged maximum circumferential stress criterion, c.) the maximum principal stress criterion and d.) the maximum configurational force criterion.

& SIH [65], (iii) an averaged maximum circumferential stress criterion (*AMCSC*) and (iv) a maximum principal stress criterion (*MPSC*). The latter was first proposed in MAITI & SMITH [129] and modified by BOUCHARD, BAY & CHASTEL [26]. The *MCSC* assumes a crack propagation in the plane which is perpendicular to the highest circumferential stress (hoop stress), provided that the value of this stress becomes critical. In the discretized setting, the crack extends in the direction towards the integration point close to the crack tip which maximizes the circumferential stress. A slight modification has been introduced for the *AMCSC*. Here, the direction of the crack is determined by a weighted average of each direction with respect to the value of the circumferential stresses. For the *MPSC*, the crack propagates in the direction corresponding to the plane perpendicular to the maximum principal stress. In the numerical setting, an eigenvalue analysis at each integration point around the crack tip is performed, which yields the local direction of the

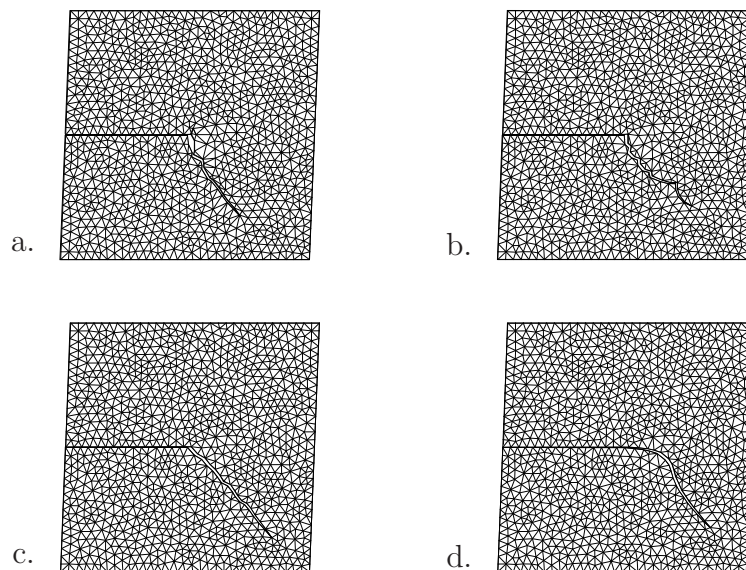


**Figure 10.29:** Simple shearing of a notched plate discretized with 2048 elements. Effect of different criteria on the crack propagation direction. a.) the maximum circumferential stress criterion, b.) the averaged maximum circumferential stress criterion, c.) the maximum principal stress criterion and d.) the maximum configurational force criterion.

**Table 10.1:** Comparison of crack propagation angles for different criteria.

Criterion	<i>MCSC</i>	<i>AMCSC</i>	<i>MPSC</i>	<i>CFC</i>
Initial angle	84.42°	86.25°	47.91°	5.07°
Angle after five steps	66.88°	46.01°	53.29°	11.90°
Angle after ten steps	56.49°	22.45°	48.30°	72.20°

principal stresses. Finally, the direction of crack propagation is determined by a weighted average of each principal direction with respect to the distance between the integration point and the crack tip, see Figure 10.27.

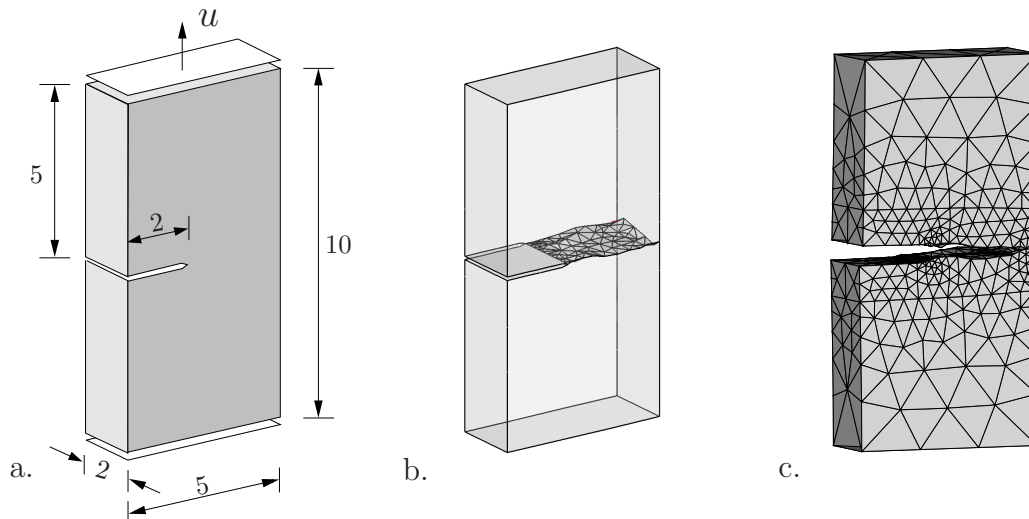
In order to show the effects of these different criteria, the single edge notched specimen in tension is analyzed as depicted in Figure 10.1a. A coarse mesh with 864 elements is considered. Figures 10.28a-10.28d demonstrate the deformation state where the specimen is completely fractured for a.) *MCSC*, b.) *AMCSC*, c.) *MPSC* and d.) the proposed configurational force crack criterion *CFC*. For the *MCSC*, the crack propagation is oscillating depending on the current positions of the integration points around the crack tip, see Figure 10.28a. Thus, the direction of crack propagation depends critically on the mesh around the crack tip. For the *AMCSC* and *MPSC*, the crack pattern is much smoother as shown in Figures 10.28b and 10.28c, respectively. Figure 10.28d presents the crack pattern for the proposed configurational force criterion *CFC*. Clearly, it yields the best agreement with the expected crack trajectory.

Next, we apply the above described criteria to the square plate with a horizontal notch as depicted in Figure 10.23. According to the experiments reported in ERDOGAN & SIH [65], the crack pattern proceeds by an angle of approximately 70° to the initial notch. Figures 10.29a-10.29d demonstrate the crack patterns corresponding to the different crack propagation criteria. For all four criteria, we observe rather similar patterns. For the *MCSC* and the *AMCSC* depicted in Figures 10.29a and 10.29b, we observe for the first step steep angles of about 85°. The subsequent propagation angles vary in a wide range. As in the previous investigation, we observe smoother cracks for the *MPSC* and in particular the *CFC* as shown in Figures 10.29c and 10.29d, respectively. The crack propagation is approximately 50° for the *MPSC*, whereas for the proposed criterion the crack angle starts with 5° and increases within the first steps up to an angle of approximately 70°. Table 10.1 reports the angles for the crack propagation for the first, the fifth and the tenth crack propagation steps for the different crack propagation criteria. It again emphasizes the inability of simulation of non-smooth crack kinking by the proposed configurational force method if only the first crack propagation step is considered.

## 10.2. Three-Dimensional Crack Propagation Examples

In this section the performance of the proposed three-dimensional configurational forced driven brittle fracture algorithm is investigated. A variety of examples is provided. These include *the simple tension*, *different type of the bending* and also *torsion tests*.

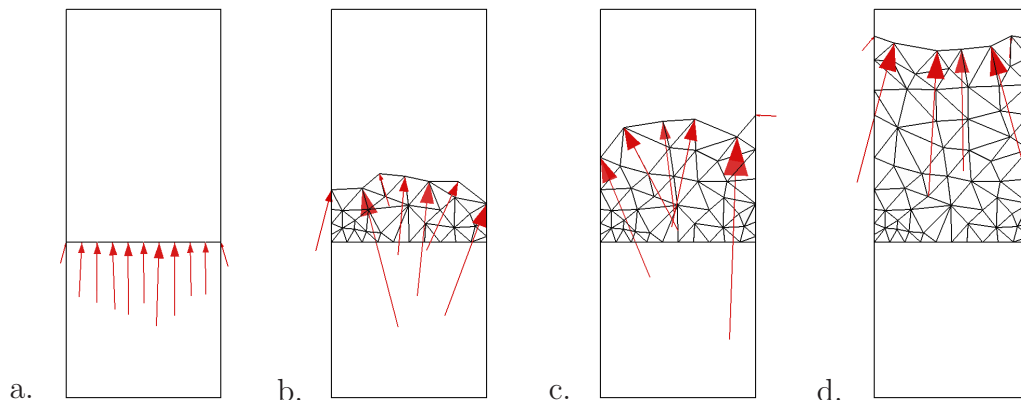
**10.2.1. Simple Tension Test.** The first example is concerned with a simple tension test of a thin notched prismatic specimen. The geometry and the loading is given in



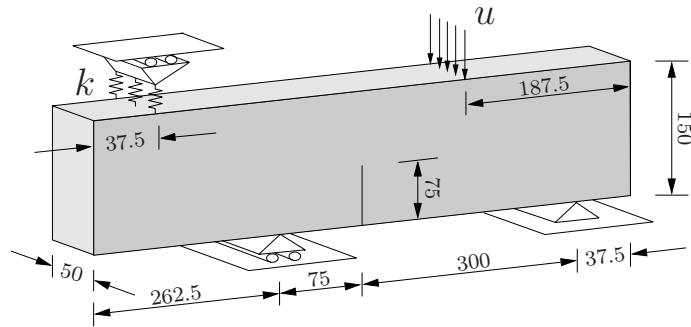
**Figure 10.30:** Tensile test of a notched specimen. a.) Geometry, loading and boundary conditions. All dimensions are given in mm. b.) The final crack surface in the undeformed configuration and c.) the final deformed mesh (ten times magnified). The specimen is discretized with 3738 elements.

Figure 10.30a. The problem is solved with the displacement controlled loading and a mesh that consists of 3738 linear tetrahedra. In Figure 10.30b the crack is visualized in the undeformed configuration as a single surface. Note that the final crack shows some roughness but still is close to be a planar surface. Close to the free end of the specimen the roughness of the surface increases. The final deformed shape together with the mesh is plotted in Figure 10.30c where the displacements are scaled by a factor of two.

The plane view of the crack propagation and the configurational forces at the crack front are provided in Figure 10.31a-10.31d. During the propagation the inner nodes of the crack front run faster than the outer ones as observed in experiments, see also MUELLER & MAUGIN [162] for the distribution of material forces in a CT-specimen before the movement of the crack front. Note that contrary to Figure 10.31a, the distribution of the material forces for inner nodes at the crack front in MUELLER & MAUGIN [162] is uniform. The variation of the configurational forces among the inner nodes in Figure 10.31a is due to the unstructured mesh considered.



**Figure 10.31:** Tensile test of a notched specimen. The plane view of the crack surface. a.) Configurational forces at the crack front just before the propagation. b.) - d.) Evolution of the crack front and the configurational forces.



**Figure 10.32:** Geometry, loading and boundary conditions of the notched specimen subjected to asymmetric bending. Two limiting cases with spring constant  $k = 0$  and  $k = \infty$  are investigated. All dimensions are given in mm.

**10.2.2. Asymmetric Bending of Notched Specimens.** In this example asymmetric bending tests of notched beams are investigated. The experimental setup has been proposed by GÁLVEZ ET AL. [74] to study the mixed mode (Mode I/II) crack propagation in concrete. In the experimental work mentioned, results on three different specimen sizes and different boundary conditions were reported. We consider here only the intermediate size beams and the two extreme cases of the boundary conditions. The description of the test is provided in Figure 10.32. The first boundary condition corresponds to the case where the spring constant  $k = 0$  and the other is  $k = \infty$ . GÁLVEZ ET AL. [74] also provided a comparison of the crack paths with two-dimensional numerical predictions obtained by the maximum tangential stress criterion of ERDOGAN & SIH [65]. Three-dimensional analysis of the same problem for the first boundary condition ( $k = 0$ ) has been done in a recent work by AREIAS & BELYTSCHKO [8] using the cohesive fracture theory and the extended finite element method (XFEM).

In Figure 10.33 the final deformed shapes for the both boundary conditions are visualized. The crack propagates in the first case ( $k = 0$ ) approximately with an angle of

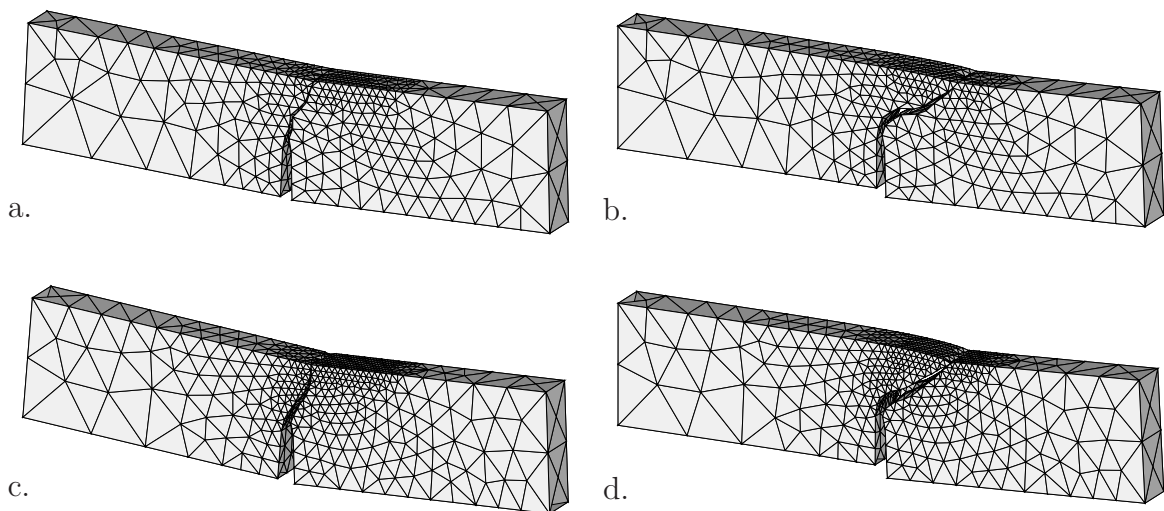


**Figure 10.33:** The final crack trajectories for different discretizations and different boundary conditions. a.) Discretization with 3448 elements and  $k = 0$ . b.) Discretization with 3448 elements and  $k = \infty$ . c.) Discretization with 5811 elements and  $k = 0$ . d.) Discretization with 5811 elements and  $k = \infty$ .

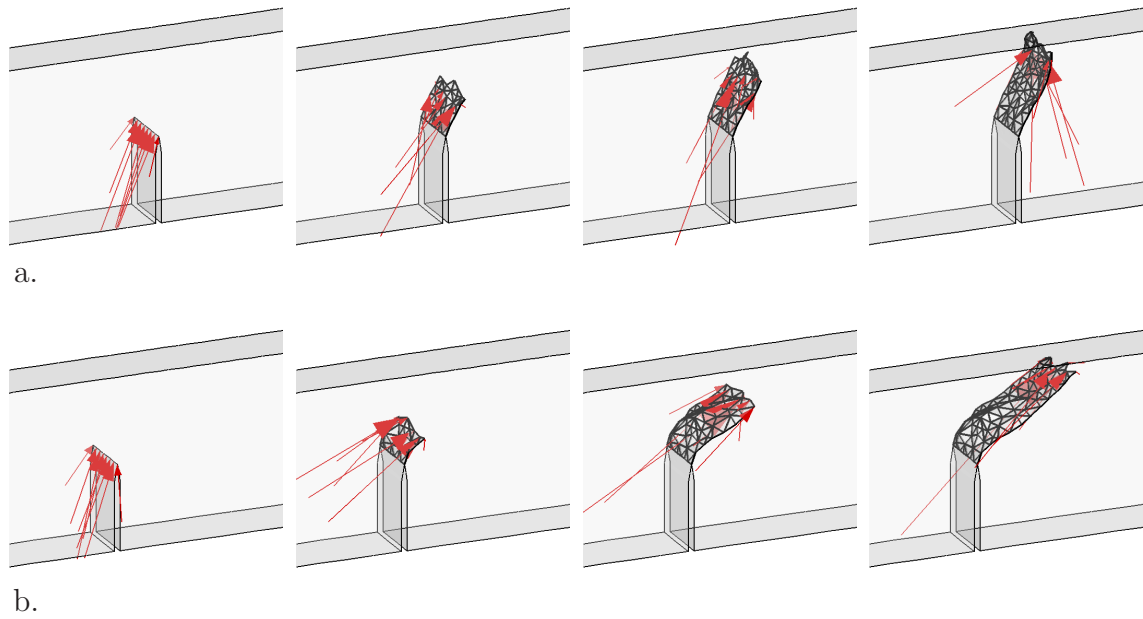


**Figure 10.34:** Visualization of the crack propagation and the configurational forces for different boundary conditions with a discretization having 5811 elements. a.)  $k = 0$ . b.)  $k = \infty$ . Note that configurational forces are scaled for each picture independently and the crack surfaces are plotted in the undeformed reference configuration.

30° to the initial notch and reaches to the upper free surface. On the other hand, in the second case ( $k = \infty$ ) the crack is more inclined and propagates over a longer distance

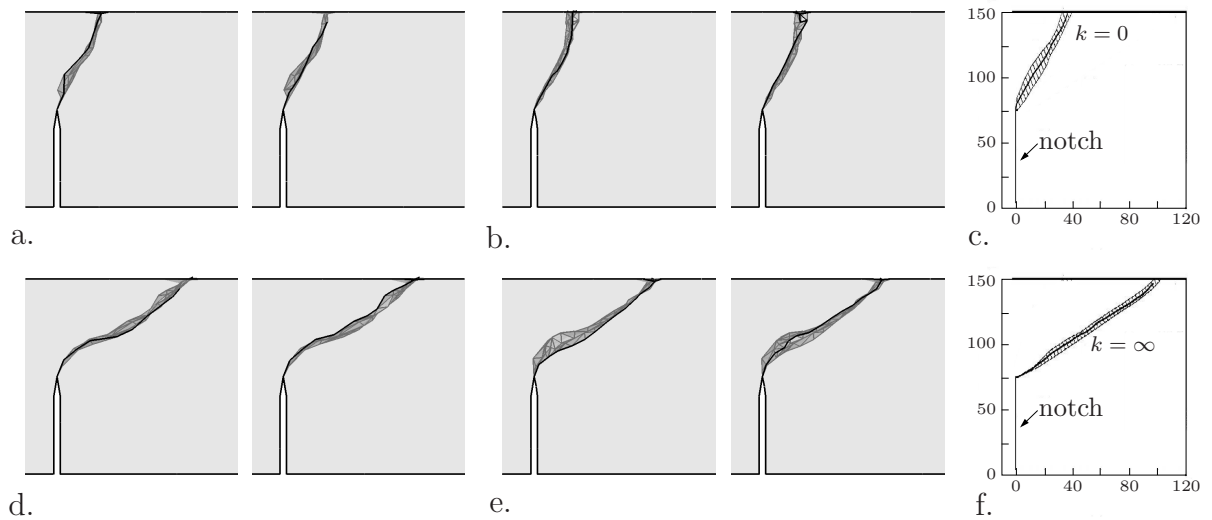


**Figure 10.35:** Visualization of the final crack surfaces for different boundary conditions and discretizations. Both the front and rear views of the specimen are shown. a.)  $k = 0$  and 3448 elements. b.)  $k = 0$  and 5811 elements. c.) Experimental trajectory for  $k = 0$ . d.)  $k = \infty$  and 3448 elements. e.)  $k = \infty$  and 5811 elements. f.) Experimental trajectory for  $k = \infty$ . Note that configurational forces are scaled for each picture independently and the crack surfaces are plotted in the undeformed reference configuration.

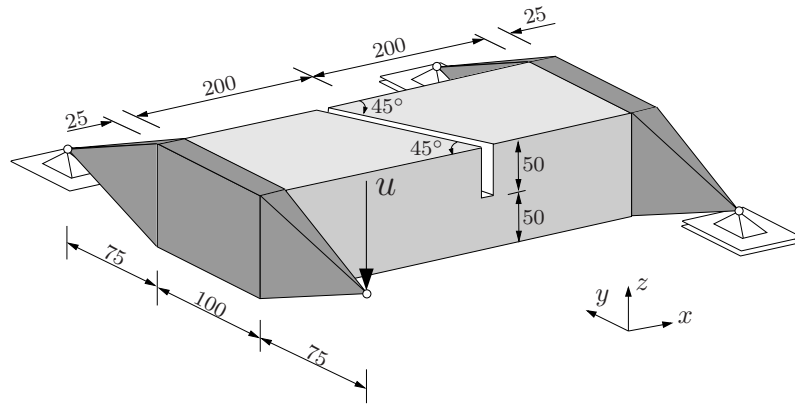


**Figure 10.36:** Geometry, loading and boundary conditions of the notched prismatic beam subjected to torsion. All dimensions are given in mm.

than the first one. In order to see the effect of the discretization, two different meshes are considered, one with 3448 and the other with 5811 elements. The final crack surfaces for both discretizations are in a very good agreement. The propagation of the crack and the evolution of configurational forces are plotted in Figure 10.34 in the undeformed configuration for both boundary conditions.

A comparison with experimental crack trajectories from GÁLVEZ ET AL. [74] is provided in Figure 10.35. Front and rear surface views are plotted for two different mesh densities. The specimen is visualized partially transparent in order to see the roughness of the crack surface in the inner part of the body. Although concrete is a quasi-brittle material and the fracture behavior is non-linear, the crack path still can be captured with a reasonable accuracy by the proposed configurational-force-driven brittle fracture theory. Note that the discretizations considered are relatively coarse (3448 and 5811 elements) compared to the ones in AREIAS & BELYTSCHKO [8] (11506 and 46380 elements).

**10.2.3. Torsion Test of Notched Prismatic Beam.** This example is taken from an experimental study BROKENSHIRE [34] which is concerned with different torsion tests on concrete specimens. The detailed description of the experimental procedure together with

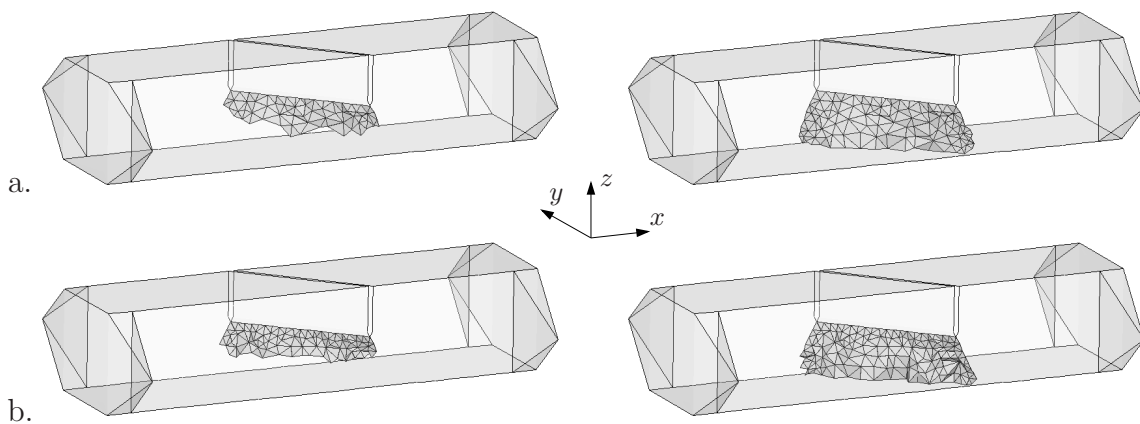


**Figure 10.37:** Visualization of the crack propagation for discretizations with a.) 4510 elements and b.) 4943 elements. Note that the crack surfaces are plotted in the undeformed reference configuration.



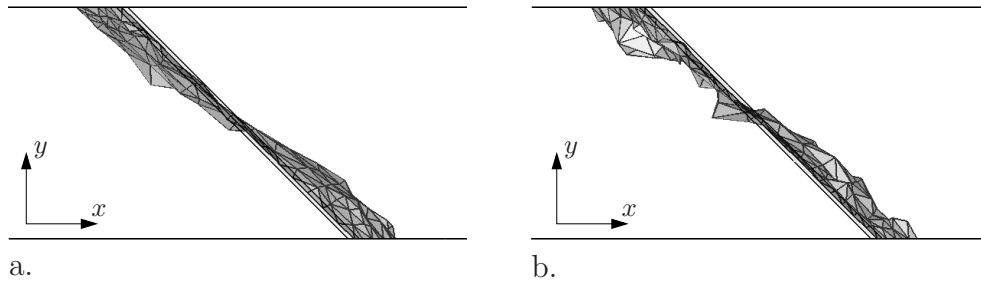


**Figure 10.38:** Top view of the final crack surface for discretizations with a.) 4510 elements and b.) 4943 elements. Note that the crack surfaces are plotted in the undeformed reference configuration.

the numerical modeling can be found in JEFFERSON ET AL. [108]. We refer to GASSER & HOLZAPFEL [76] for another simulation of this problem based on the partition of unity finite element method and the cohesive crack approach. In Figure 10.36 the geometry and boundary conditions are specified. Different from all previous examples, this test cannot be simplified to a two-dimensional model and requires a fully three-dimensional analysis.

Two different meshes with 4510 and 4943 elements are considered in the analysis. Although the number of elements in both discretizations are close to each other, the second one has a finer resolution of the crack front. The evolution of the discontinuity surfaces in the reference configuration are illustrated in Figure 10.37. The planar views of two discretizations are given in Figure 10.38. The final crack trajectories of both meshes are in good agreement. Note that the surfaces have also a curvature through the beam thickness ( $y$ -direction) which requires a complete three-dimensional solution of the problem. In Figure 10.39a and 10.39b two different views of the deformed body are plotted where the displacements are scaled by a factor of ten. The final crack surfaces obtained by the proposed algorithm capture the experimental results provided in JEFFERSON ET AL. [108]. Note that our predictions have been obtained by relatively coarse meshes (4510 and 4943 elements) compared to the ones in GASSER & HOLZAPFEL [76] (40610 elements).

The configurational forces at the crack front just before the propagation are drawn in Figure 10.40. The first picture is the top and other two are the side views. The planar view in Figure 10.40a clearly shows the tendency of the crack to propagate with a curvature in the  $y$ -direction.

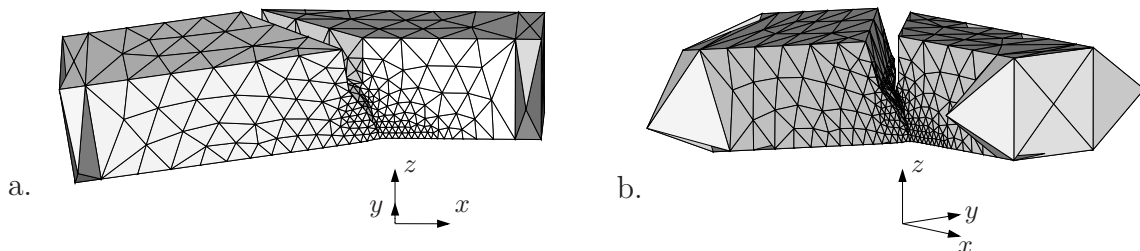


**Figure 10.39:** Visualization of the deformed mesh from two different viewpoints a.) and b.) for a discretizations with 4510 elements. Note that the deformation is 40 times magnified.



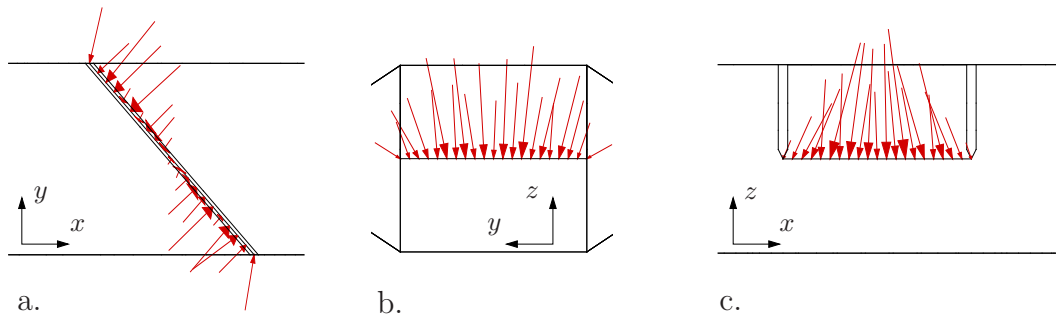


**Figure 10.40:** Three different plane views a.) - c.) of the configurational forces at the crack front just before the crack propagation.

**10.2.4. Bending of Notched Beams with Holes.** The final example is concerned with bending tests on notched prismatic beams with holes. The setup of the experiments were proposed by BITTENCOURT ET AL. [25] and the problem was already analyzed in the two-dimensional setting in Section 10.1.4. The tests were performed on polymethylmethacrylate (PMMA) beams. This problem in two-dimensional setting analyzed previously by PHONGTHANAPANICH & DECHAUMPHAI [183], HEINTZ [95] and MIEHE & GÜRSSES [143]. PHONGTHANAPANICH & DECHAUMPHAI [183] solved this problem with finite elements based on an adaptive Delaunay triangulation. The stress intensity factors were employed as the crack criterion. HEINTZ [95] used discontinuous finite elements originally proposed by HANSBO & HANSBO [93] and utilized the configurational forces as the crack propagation criterion.

The geometry and boundary conditions are specified in Figure 10.41 where two different notch geometries are considered. The crack trajectories are found to be very sensitive to the position and the length of the initial notch, see BITTENCOURT ET AL. [25]. In our numerical investigations, we show the influence of the notch geometry on the crack propagation. In our simulations, two different discretizations are considered. The first beam with a longer notch is analyzed with a mesh consist of 5842 elements while the second one is discretized with 5871 elements. In Figures 10.42a and 10.42b the final cracked state of the deformed bodies are shown for the notch geometries I and II, respectively.

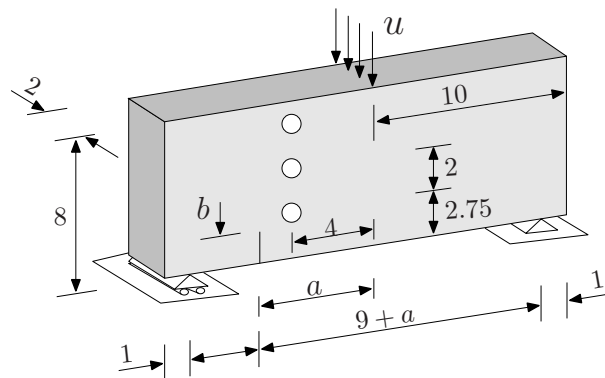


**Figure 10.41:** Geometry, loading and boundary conditions of the notched beam with three holes subjected to bending. Two different notch geometries are considered. Notch geometry I:  $a = 5.0$  and  $b = 1.5$ . Notch geometry II:  $a = 6$  and  $b = 1.0$ . All dimensions are given in mm and holes have a diameter of 1.0.

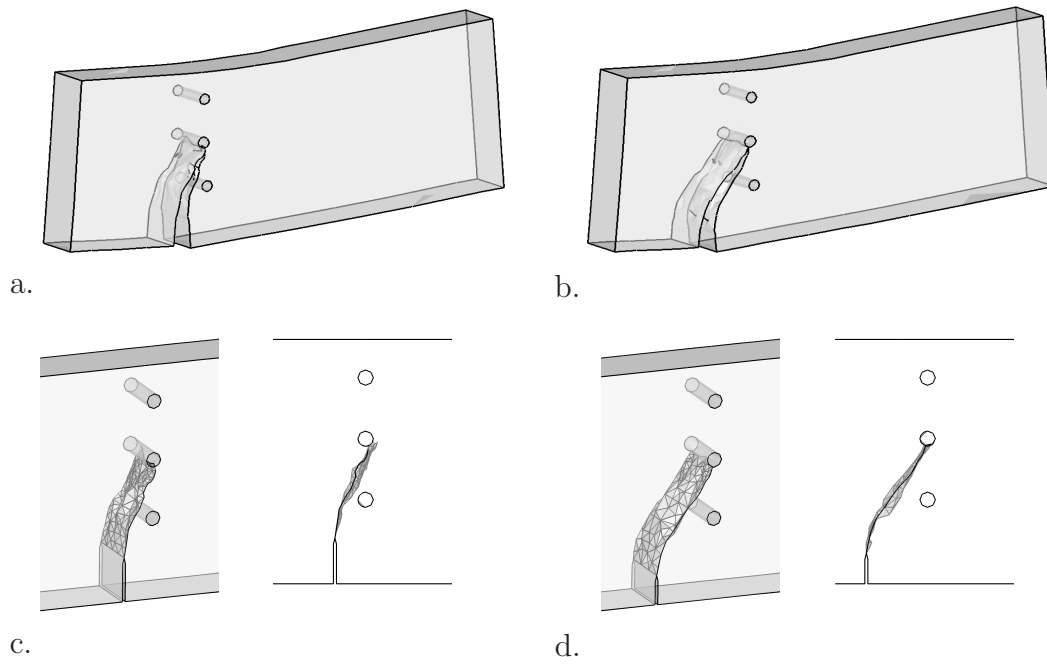


**Figure 10.42:** Visualization of the final crack surfaces. a.) Deformed specimen for the notch geometry I discretized with 5842 elements. b.) Deformed specimen for the notch geometry II discretized with 5871 elements. Note that the deformation is five times magnified. c.) Crack surface in the undeformed reference configuration for notch I. d.) Crack surface in the undeformed reference configuration for notch II.

Figures 10.42c and 10.42d visualize two different views of the final crack surfaces in the undeformed reference configuration. The final trajectories of the simulations capture the experimental results presented in BITTENCOURT ET AL. [25].



## 11. Summary and Outlook

The main objective of this work was to employ *energy minimization principles* for the description of particular problems in theoretical and computational solid mechanics. We concentrated especially on two aspects: (i) *Description of inelastic deformation microstructures and their evolution in non-convex unstable solids* and (ii) *development of a variational framework for configurational-force-driven brittle fracture*.

### 11.1. Description of Microstructures based on Energy Relaxation

In the first part of the thesis the main focus was the theoretical description and the computational treatment of microstructures and their evolution in elastic and inelastic solids. In this work microstructures were considered to have complex patterns with length-scales much smaller than macroscopic dimensions and arise in an attempt to achieve the minimum energy. More precisely, the reason for the formation of microstructures is that no exact minimum exists and infimizing sequences develop finer and finer oscillations. We showed that it is possible to describe these microstructures mathematically by *non-convex variational problems* or equivalently by the minimization of energy functionals

$$I(\boldsymbol{\varphi}) = \int_{\mathcal{B}} \psi(\nabla \boldsymbol{\varphi}) dV + \Pi(\boldsymbol{\varphi}) \longrightarrow \text{Minimum} \quad (11.1)$$

that lack of *sequential weak lower semicontinuity*. The problems governed by functionals that are not sequentially weakly lower semicontinuous often do not have minimizers in the classical sense and instead lead to *fine scale oscillatory infimizing sequences* which we interpret as *microstructures*. To this end, the weak limit of the infimizing sequences are regarded as the macroscopic or homogeneous deformation. In the case of vector valued calculus of variations the weak lower semicontinuity of the energy functional  $I$  is (under suitable growth assumptions on  $\psi$ ) equivalent to the quasiconvexity the function  $\psi$  to be integrated. The *relaxation* theory is a possible approach to overcome the problem with lack of minimizers. It is based on the determination of the largest lower semicontinuous functional  $I_Q$  below the given one  $I$ . This is achieved by the replacement of  $\psi$  in the energy functional  $I$  by the quasiconvex envelope  $\psi_Q$ , i.e. the largest quasiconvex function less than or equal to  $\psi$ . It is important to note that the minimum of the relaxed functional is exactly equal to the infimum of original problem, i.e.  $\min I_Q = \inf I$ . The relaxed density  $\psi_Q$  describes the macroscopic or effective energy of the system which is the smallest energy per unit volume that is needed to deform an infinitesimal volume with given affine boundary conditions. Here, through the relaxation the material is allowed to form microstructures that minimize the energy.

We considered three different type of constitutive material response where non-convex (non-quasiconvex in vectorial problems) potentials arise. These are the *martensitic phase transformations* in elastic crystals, the *single-slip multiplicative plasticity* of single crystals and the *isotropic damage mechanics*. The non-convexity in the considered problems have distinct origins. Martensitic phase transformations are symmetry breaking transformations with multiple stress free configurations. Therefore, the materials that exhibit such transformations are governed by multi-well energy storage functions which are naturally non-convex. On the other hand, in the single-slip plasticity, which can be considered as the limiting case of infinite latent hardening in multi-slip single crystal plasticity, the source of non-convexity is of geometrical nature. The necessity of the crystal to deform

in single-slip at all material points introduces a strong constraint and renders non-convex variational problems for certain combinations of the loading and the slip system. The damage models, however, furnish non-convexity due to extensive accumulation of damage if it starts to stimulate softening in the constitutive material response.

Since the constitutive behavior of single-slip plasticity and damage models are inelastic we extended the results of nonlinear elasticity and presented the *incremental variational formulation of inelasticity*. It was shown that a sequence of quasi-hyperelastic energy densities may be constructed by incremental minimization of energetic expressions with respect to internal variables. Hence, the incremental quasi-hyperelastic potential plays a crucial role in the analysis analogous to the energy storage function of elasticity. The incremental character of the variational principle reflects the inelastic and irreversible nature of the single-slip and damage models. In this work, particular relaxation methods are designed based on approximations of quasiconvex envelopes by the rank-one convexification. In addition, specific assumptions are utilized on the type of developing microstructures and semi-analytical methods are developed. Moreover, several numerical studies on homogeneous macro-deformation modes as well as inhomogeneous macroscopic boundary-value problems have been performed. These studies confirm the well-posed behavior of the proposed computational relaxation methods by the independence of typical finite element solutions on the mesh-size.

Note that in all our investigations there is no *interface energy* or *length scale* involved and consequently the microstructures are infinitely fine. However, in reality the microstructures are of finite size that is determined by the atomic structure, i.e. there is a finite interatomic distance which prohibits finer microstructures. This constraint is often incorporated by the introduction of surface energies in the energy functionals.

## 11.2. Configurational Force Driven Brittle Fracture

In the second part of the thesis the main focus was put on the development of a thermodynamically consistent variational formulation of brittle crack propagation in elastic solids which is based on energy minimization principles. First of all, an overview about brittle fracture theories was provided with some of the well-known approaches from the literature. These cover the stress intensity factors of Irwin, the energetic approach and the energy release rate of Griffith and the  $J$ -integral of Rice. As a natural outcome of the energy based local variational formulation of brittle fracture the *configurational forces* arise as dual objects to the crack propagation. Indeed, they are generalization of the well known  $J$ -integral to the vectorial case and have a broader area of application than the  $J$ -integral.

An essential part was the discussion of the configurational forces with a particular focus on their application to fracture mechanics. Starting with the Eshelby's thought experiment the alternative derivations of the *energy momentum tensor* were outlined. These include approaches based on a Lagrangian density, a projection of balance laws onto material manifold, the Noether's theorem and particular invariance requirements. Furthermore, we developed a thermodynamically consistent variational framework for quasi-static crack propagation in elastic solids and showed that both the elastic equilibrium response as well as the local crack evolution follow in a natural format by the exploitation of a global Clausius-Planck inequality in the sense of Coleman's method. Consequently, we demonstrated that the *crack propagation direction* is identified by the

material configurational force which maximizes the local dissipation at the crack front.

The computational treatment of the variational formulation outlined is one of the novel contributions of the thesis. The variational formulation of fracture was realized numerically by a spatial discretization with standard three-noded constant strain triangles and four-noded linear tetrahedral finite elements in two and three dimensions, respectively. Therefore, the constitutive setting of crack propagation in the space-discretized finite element context was naturally related to discrete nodes of a typical finite element mesh. Consistent with this node-based setting, the discretization of the evolving crack discontinuity was performed by doubling of critical nodes and interface segments of the mesh. The crucial step for the success of this procedure was its embedding into an r-adaptive crack-segments and facets reorientation procedure based on configurational-force-based indicators in conjunction with crack front constraints. Here, successive crack releases appeared in discrete steps associated with the given space discretization. These were performed by a staggered loading-release algorithm of energy minimization at frozen crack state followed by the successive crack releases at frozen deformation. This constitutes a sequence of positive definite discrete subproblems with successively decreasing overall stiffness, providing a very robust algorithmic setting in the postcritical range.

Finally, we demonstrated the predictive capabilities of the proposed formulation of brittle crack propagation by means of representative numerical simulations and comparisons with experiments from the literature. These include a broad spectrum of examples both in two and three dimensions such as simple tension, symmetric and asymmetric bending, Brazilian splitting, shear and torsion tests. Moreover studies with respect to the accuracy of the numerical computation of configurational forces were performed and comparisons with other crack propagation criteria were presented.

Finally, we make some remarks about the limitations of the formulation developed. The framework presented here is restricted in its current state to quasi-static brittle fracture for elastic materials. However, it allows for geometrical and material nonlinearities. The cohesive fracture is not covered but certainly of interest for further research. The simulation of crack branching which is intrinsically related to dynamic fracture is also not possible with the formulation presented.





## A. Derivatives for Convexification of Single-Slip Plasticity

In order to obtain a compact representation of the higher-order derivatives we introduce the following abbreviations

$$\left. \begin{aligned} W^\pm &:= W(\mathbf{F}^\pm), & \mathbf{P}^\pm &:= \partial_{\mathbf{F}} W(\mathbf{F}^\pm), & \mathbb{C}^\pm &:= \partial_{\mathbf{F}\mathbf{F}}^2 W(\mathbf{F}^\pm), \\ \mathbf{M}' &:= \partial_\varphi \mathbf{M}, & \mathbf{N}' &:= \partial_\chi \mathbf{N} & \mathbf{m}' &:= \mathbf{F}\mathbf{M}', \end{aligned} \right\} \quad (\text{A.1})$$

where the vectors are parameterized by  $\mathbf{M}(\varphi) = [\cos \varphi \ \sin \varphi]^T$  and  $\mathbf{N}(\chi) = [\cos \chi \ \sin \chi]^T$ . The first derivatives of the function  $\bar{W}^h$  with respect to the micro-variables  $[\xi, d, \varphi, \chi]$  have the following representations

$$\left. \begin{aligned} \bar{W}_{,\xi}^h &= W^+ - W^- - d [\xi \mathbf{P}^+ + (1 - \xi) \mathbf{P}^-] : (\mathbf{m} \otimes \mathbf{N}), \\ \bar{W}_{,d}^h &= \xi(1 - \xi) [\mathbf{P}^+ - \mathbf{P}^-] : (\mathbf{m} \otimes \mathbf{N}), \\ \bar{W}_{,\varphi}^h &= \xi(1 - \xi) d [\mathbf{P}^+ - \mathbf{P}^-] : (\mathbf{m}' \otimes \mathbf{N}), \\ \bar{W}_{,\chi}^h &= \xi(1 - \xi) d [\mathbf{P}^+ - \mathbf{P}^-] : (\mathbf{m} \otimes \mathbf{N}'). \end{aligned} \right\} \quad (\text{A.2})$$

The second derivatives then read

$$\left. \begin{aligned} \bar{W}_{,\xi\xi}^h &= 2d [\mathbf{P}^- - \mathbf{P}^+] : (\mathbf{m} \otimes \mathbf{N}) \\ &+ d^2 (\mathbf{m} \otimes \mathbf{N}) : [\xi \mathbb{C}^+ + (1 - \xi) \mathbb{C}^-] : (\mathbf{m} \otimes \mathbf{N}), \\ \bar{W}_{,\xi d}^h &= (1 - 2\xi) [\mathbf{P}^+ - \mathbf{P}^-] : (\mathbf{m} \otimes \mathbf{N}) \\ &- d\xi(1 - \xi) (\mathbf{m} \otimes \mathbf{N}) : [\mathbb{C}^+ - \mathbb{C}^-] : (\mathbf{m} \otimes \mathbf{N}), \\ \bar{W}_{,\xi\varphi}^h &= (1 - 2\xi) d [\mathbf{P}^+ - \mathbf{P}^-] : (\mathbf{m}' \otimes \mathbf{N}) \\ &- d^2 \xi(1 - \xi) (\mathbf{m} \otimes \mathbf{N}) : [\mathbb{C}^+ - \mathbb{C}^-] : (\mathbf{m}' \otimes \mathbf{N}), \\ \bar{W}_{,\xi\chi}^h &= (1 - 2\xi) d [\mathbf{P}^+ - \mathbf{P}^-] : (\mathbf{m} \otimes \mathbf{N}') \\ &- d^2 \xi(1 - \xi) (\mathbf{m} \otimes \mathbf{N}) : [\mathbb{C}^+ - \mathbb{C}^-] : (\mathbf{m} \otimes \mathbf{N}'), \\ \bar{W}_{,dd}^h &= \xi(1 - \xi) (\mathbf{m} \otimes \mathbf{N}) : [(1 - \xi) \mathbb{C}^+ + \xi \mathbb{C}^-] : (\mathbf{m} \otimes \mathbf{N}), \\ \bar{W}_{,d\varphi}^h &= \xi(1 - \xi) [\mathbf{P}^+ - \mathbf{P}^-] : (\mathbf{m}' \otimes \mathbf{N}) \\ &+ d\xi(1 - \xi) (\mathbf{m} \otimes \mathbf{N}) : [(1 - \xi) \mathbb{C}^+ + \xi \mathbb{C}^-] : (\mathbf{m}' \otimes \mathbf{N}), \\ \bar{W}_{,d\chi}^h &= \xi(1 - \xi) [\mathbf{P}^+ - \mathbf{P}^-] : (\mathbf{m} \otimes \mathbf{N}') \\ &+ d\xi(1 - \xi) (\mathbf{m} \otimes \mathbf{N}) : [(1 - \xi) \mathbb{C}^+ + \xi \mathbb{C}^-] : (\mathbf{m} \otimes \mathbf{N}'), \\ \bar{W}_{,\varphi\varphi}^h &= \xi(1 - \xi) d [\mathbf{P}^- - \mathbf{P}^+] : (\mathbf{m} \otimes \mathbf{N}) \\ &+ \xi(1 - \xi) d^2 (\mathbf{m}' \otimes \mathbf{N}) : [(1 - \xi) \mathbb{C}^+ + \xi \mathbb{C}^-] : (\mathbf{m}' \otimes \mathbf{N}), \\ \bar{W}_{,\varphi\chi}^h &= \xi(1 - \xi) d [\mathbf{P}^+ - \mathbf{P}^-] : (\mathbf{m}' \otimes \mathbf{N}') \\ &+ \xi(1 - \xi) d^2 (\mathbf{m}' \otimes \mathbf{N}) : [(1 - \xi) \mathbb{C}^+ + \xi \mathbb{C}^-] : (\mathbf{m} \otimes \mathbf{N}'), \\ \bar{W}_{,\chi\chi}^h &= \xi(1 - \xi) d [\mathbf{P}^- - \mathbf{P}^+] : (\mathbf{m} \otimes \mathbf{N}) \\ &+ \xi(1 - \xi) d^2 (\mathbf{m} \otimes \mathbf{N}') : [(1 - \xi) \mathbb{C}^+ + \xi \mathbb{C}^-] : (\mathbf{m} \otimes \mathbf{N}'). \end{aligned} \right\} \quad (\text{A.3})$$

Note that the second order derivatives are symmetric, e.g.  $\bar{W}_{,\xi d}^h = \bar{W}_{,d\xi}^h$  and so forth.

The following derivatives are required for the computation of the relaxed stresses  $\bar{\mathbf{P}}$  and the relaxed moduli  $\bar{\mathbf{C}}$

$$\left. \begin{aligned}
\bar{W}_{,\mathbf{F}}^h &= \xi \mathbf{P}^+ \mathbf{L}^{+T} + (1 - \xi) \mathbf{P}^- \mathbf{L}^{-T}, \\
\bar{W}_{,\mathbf{F}\mathbf{F}}^h &= \xi \mathbf{L}^+ \mathbf{C}^+ \mathbf{L}^{+T} + (1 - \xi) \mathbf{L}^- \mathbf{C}^- \mathbf{L}^{-T}, \\
\bar{W}_{,\mathbf{F}\xi}^h &= \mathbf{P}^+ \mathbf{L}^{+T} - \mathbf{P}^- \mathbf{L}^{-T} \\
&\quad - d [\xi \mathbf{L}^+ \mathbf{C}^+ + (1 - \xi) \mathbf{L}^- \mathbf{C}^-] : (\mathbf{F}\mathbf{M} \otimes \mathbf{N}) \\
&\quad - d [\xi \mathbf{P}^+ + (1 - \xi) \mathbf{P}^-] (\mathbf{M} \otimes \mathbf{N})^T, \\
\bar{W}_{,\mathbf{F}d}^h &= \xi(1 - \xi) [\mathbf{L}^+ \mathbf{C}^+ - \mathbf{L}^- \mathbf{C}^-] : (\mathbf{F}\mathbf{M} \otimes \mathbf{N}) \\
&\quad + \xi(1 - \xi) [\mathbf{P}^+ - \mathbf{P}^-] (\mathbf{M} \otimes \mathbf{N})^T, \\
\bar{W}_{,\mathbf{F}\varphi}^h &= \xi(1 - \xi) d [(\mathbf{C}^+ : \mathbf{m}' \otimes \mathbf{N})(\mathbf{1} + (1 - \xi) d \mathbf{N} \otimes \mathbf{M}) + \mathbf{P}^+ \mathbf{N} \otimes \mathbf{M}'] \\
&\quad - \xi(1 - \xi) d [(\mathbf{C}^- : \mathbf{m}' \otimes \mathbf{N})(\mathbf{1} - \xi d \mathbf{N} \otimes \mathbf{M}) + \mathbf{P}^- \mathbf{N} \otimes \mathbf{M}'], \\
\bar{W}_{,\mathbf{F}\chi}^h &= \xi(1 - \xi) d [(\mathbf{C}^+ : \mathbf{m} \otimes \mathbf{N}')(\mathbf{1} + (1 - \xi) d \mathbf{N} \otimes \mathbf{M}) + \mathbf{P}^+ \mathbf{N}' \otimes \mathbf{M}] \\
&\quad - \xi(1 - \xi) d [(\mathbf{C}^- : \mathbf{m} \otimes \mathbf{N}')(\mathbf{1} - \xi d \mathbf{N} \otimes \mathbf{M}) + \mathbf{P}^- \mathbf{N}' \otimes \mathbf{M}],
\end{aligned} \right\} \quad (\text{A.4})$$

where  $\mathbf{L}^+$  and  $\mathbf{L}^-$  are defined as

$$\left. \begin{aligned}
\mathbf{L}^+ &= \mathbf{1} + (1 - \xi) d \mathbf{M} \otimes \mathbf{N} \\
\mathbf{L}^- &= \mathbf{1} - \xi d \mathbf{M} \otimes \mathbf{N}
\end{aligned} \right\} \quad (\text{A.5})$$

## B. Derivatives for Convexification in Damage Mechanics

In order to obtain a compact representation of the higher-order derivatives we introduce the following abbreviations. In what follows it is assumed that the linearized strain  $\boldsymbol{\varepsilon}$  is purely isochoric

$$\left. \begin{aligned}
W^\pm &:= W(\boldsymbol{\varepsilon}^\pm), \quad \boldsymbol{\sigma}^\pm := \partial_{\boldsymbol{\varepsilon}} W(\boldsymbol{\varepsilon}^\pm), \quad \mathbf{C}^\pm := \partial_{\boldsymbol{\varepsilon}\boldsymbol{\varepsilon}}^2 W(\boldsymbol{\varepsilon}^\pm), \\
\mathbb{E}^\pm &:= \partial_{\boldsymbol{\varepsilon}\boldsymbol{\varepsilon}}^2 \boldsymbol{\varepsilon}^\pm, \quad \mathbf{A} := \frac{\boldsymbol{\varepsilon}}{\|\boldsymbol{\varepsilon}\|}.
\end{aligned} \right\} \quad (\text{B.1})$$

The first and second derivatives of the function  $\bar{W}^h$  with respect to the micro-variables  $\xi$  and  $d$ , which are required for the convexification algorithm, have the following representations

$$\left. \begin{aligned}
\bar{W}_{,\xi}^h &= W^+ - W^- - d [\xi \boldsymbol{\sigma}^+ + (1 - \xi) \boldsymbol{\sigma}^-] : \mathbf{A}, \\
\bar{W}_{,d}^h &= \xi(1 - \xi) [\boldsymbol{\sigma}^+ - \boldsymbol{\sigma}^-] : \mathbf{A},
\end{aligned} \right\} \quad (\text{B.2})$$

$$\left. \begin{aligned}
\bar{W}_{,\xi\xi}^h &= 2d [\boldsymbol{\sigma}^- - \boldsymbol{\sigma}^+] : \mathbf{A} + d^2 \mathbf{A} : [\xi \mathbf{C}^+ + (1 - \xi) \mathbf{C}^-] : \mathbf{A}, \\
\bar{W}_{,\xi d}^h &= (1 - 2\xi) [\boldsymbol{\sigma}^+ - \boldsymbol{\sigma}^-] : \mathbf{A} - d \xi(1 - \xi) \mathbf{A} : [\mathbf{C}^+ - \mathbf{C}^-] : \mathbf{A}, \\
\bar{W}_{,dd}^h &= \xi(1 - \xi) \mathbf{A} : [(1 - \xi) \mathbf{C}^+ + \xi \mathbf{C}^-] : \mathbf{A}
\end{aligned} \right\} \quad (\text{B.3})$$

Note that the second order derivative is symmetric, i.e.  $\bar{W}_{,\xi d}^h = \bar{W}_{,d\xi}^h$ .

The following derivatives are required for the computation of the relaxed stresses  $\bar{\sigma}$  and the moduli  $\bar{\mathbb{C}}$

$$\begin{aligned}
\bar{W}_{,\varepsilon}^h &= \xi \boldsymbol{\sigma}^+ + (1 - \xi) \boldsymbol{\sigma}^- + \frac{\xi(1 - \xi)d}{\|\boldsymbol{\varepsilon}\|} [\boldsymbol{\sigma}^+ - \boldsymbol{\sigma}^-] : (\mathbb{I} - \mathbf{A} \otimes \mathbf{A}), \\
\bar{W}_{,\varepsilon\xi}^h &= \boldsymbol{\sigma}^+ - \boldsymbol{\sigma}^- - d[\xi \mathbb{C}^+ + (1 - \xi) \mathbb{C}^-] : \mathbf{A} \\
&\quad + \frac{(1 - 2\xi)d}{\|\boldsymbol{\varepsilon}\|} [\boldsymbol{\sigma}^+ - \boldsymbol{\sigma}^-] : [\mathbb{I} - \mathbf{A} \otimes \mathbf{A}] \\
&\quad - \frac{\xi(1 - \xi)d^2}{\|\boldsymbol{\varepsilon}\|} \left\{ (\mathbb{C}^+ - \mathbb{C}^-) : \mathbf{A} + [\mathbf{A} : (\mathbb{C}^+ - \mathbb{C}^-) : \mathbf{A}] \mathbf{A} \right\}, \\
\bar{W}_{,\varepsilon d}^h &= \xi(1 - \xi) [\mathbb{C}^+ - \mathbb{C}^-] : \mathbf{A} + \frac{\xi(1 - \xi)}{\|\boldsymbol{\varepsilon}\|} [\boldsymbol{\sigma}^+ - \boldsymbol{\sigma}^-] : (\mathbb{I} - \mathbf{A} \otimes \mathbf{A}) \\
&\quad + \frac{\xi(1 - \xi)d}{\|\boldsymbol{\varepsilon}\|} \left\{ [(1 - \xi) \mathbb{C}^+ + \xi \mathbb{C}^-] : \mathbf{A} - (\mathbf{A} : [(1 - \xi) \mathbb{C}^+ + \xi \mathbb{C}^-] : \mathbf{A}) \mathbf{A} \right\}, \\
\bar{W}_{,\varepsilon\varepsilon}^h &= \xi \mathbb{C}^+ : \mathbb{E}^+ + (1 - \xi) \mathbb{C}^- : \mathbb{E}^- + \frac{\xi(1 - \xi)d}{\|\boldsymbol{\varepsilon}\|} [\mathbb{C}^+ : \mathbb{E}^+ - \mathbb{C}^- : \mathbb{E}^-] \\
&\quad - \frac{\xi(1 - \xi)d}{\|\boldsymbol{\varepsilon}\|^2} [\boldsymbol{\sigma}^+ - \boldsymbol{\sigma}^-] \otimes \mathbf{A} - \frac{\xi(1 - \xi)d}{\|\boldsymbol{\varepsilon}\|} \mathbf{A} \otimes \mathbf{A} : [\mathbb{C}^+ : \mathbb{E}^+ - \mathbb{C}^- : \mathbb{E}^-] \\
&\quad - \frac{\xi(1 - \xi)d}{\|\boldsymbol{\varepsilon}\|^2} \mathbf{A} \otimes [\boldsymbol{\sigma}^+ - \boldsymbol{\sigma}^-] - \frac{\xi(1 - \xi)d}{\|\boldsymbol{\varepsilon}\|^2} [(\boldsymbol{\sigma}^+ - \boldsymbol{\sigma}^-) : \mathbf{A}] \mathbb{I} \\
&\quad - \frac{\xi(1 - \xi)d}{\|\boldsymbol{\varepsilon}\|^2} [3(\boldsymbol{\sigma}^+ - \boldsymbol{\sigma}^-) : \mathbf{A}] \mathbf{A} \otimes \mathbf{A}.
\end{aligned} \tag{B.4}$$

## C. Basics of Complex Functions

The aim of this chapter is to summarize some of the fundamental definitions and properties of complex numbers and functions of complex variables. They are frequently used in analytical solutions of two-dimensional elasticity problems. We refer to the monograph by ENGLAND [63] for a detailed treatment of the complex functions in the elasticity theory. A complex number  $z$  can be expressed in the Cartesian coordinates  $x_1$  and  $x_2$  as

$$z := x_1 + ix_2 \tag{C.1}$$

or alternatively, in the polar coordinates  $r$  and  $\theta$  as

$$z := r(\cos \theta + i \sin \theta) = re^{i\theta} \tag{C.2}$$

with  $i = \sqrt{-1}$  and real numbers  $x_1, x_2, r, \theta \in \mathcal{R}$ . Note that the Cartesian and the polar coordinates are related by  $r = \sqrt{x_1^2 + x_2^2}$  and  $\tan \theta = x_2/x_1$ . A power of a complex number is given by

$$z^n = r^n(\cos n\theta + i \sin n\theta) \tag{C.3}$$

which is obtained by using the representation (C.2) and is valid for integral values of  $n$ , both positive and negative. Having defined the integral powers, the general rational power of a complex number is determined by

$$z^{p/q} = r^{p/q} \left[ \cos \frac{p}{q}(\theta + 2k\pi) + i \sin \frac{p}{q}(\theta + 2k\pi) \right] \quad \text{with} \quad k = 0, 1, \dots \quad (\text{C.4})$$

Next, we introduce the complex conjugate  $\bar{z}$  of a complex number  $z$  as

$$\bar{z} := x_1 - ix_2 \quad (\text{C.5})$$

in the Cartesian coordinates or alternatively

$$\bar{z} = r(\cos \theta - i \sin \theta) = r e^{-i\theta} \quad (\text{C.6})$$

in the polar coordinates. From the definitions (C.1) and (C.5), the following relations are obtained

$$x_1 = \Re(z) = \frac{1}{2}(z + \bar{z}) \quad \text{and} \quad x_2 = \Im(z) = \frac{1}{2}(z - \bar{z}) \quad (\text{C.7})$$

where  $\Re(z)$  and  $\Im(z)$  stand for the real and imaginary parts of  $z$ , respectively. After a brief introduction to complex numbers, now fundamental properties of the functions of a complex variable will be discussed. Let  $S$  be an arbitrary set of points in the complex plane. If to each point  $z = x_1 + ix_2$  of the set  $S$  there corresponds a complex number  $u_1(x_1, x_2) + iu_2(x_1, x_2)$ , then a complex function  $f(z)$  is defined on  $S$ . The value of the function at the point  $z$  is

$$f(z) = u_1(x_1, x_2) + iu_2(x_1, x_2), \quad (\text{C.8})$$

where  $u_1$  and  $u_2$  are real functions of the variables  $x_1$  and  $x_2$ . The derivative of a function  $f$  of a complex variable  $z$  is

$$\frac{\partial f}{\partial z} = f'(z) = \lim_{\delta z \rightarrow 0} \frac{f(z + \delta z) - f(z)}{\delta z} \quad (\text{C.9})$$

which is formally identical with the derivative of a function of a real variable. From (C.1), partial derivatives of  $f$  with respect to  $x_1$  and  $x_2$  are computed as

$$\begin{aligned} \frac{\partial f}{\partial x_1} &= \frac{\partial f}{\partial z} \frac{\partial z}{\partial x_1} = f'(z) \\ \frac{\partial f}{\partial x_2} &= \frac{\partial f}{\partial z} \frac{\partial z}{\partial x_2} = if'(z) \end{aligned} \quad (\text{C.10})$$

by a simple application of the chain rule. Note that  $\delta z \rightarrow 0$  can be achieved in infinitely many ways in the complex plane, since  $\delta z = \delta x_1 + i\delta x_2$ . Consequently, the existence of the derivative  $f'(z)$  requires that the limit given in (C.9) has to be the same no matter how  $\delta z \rightarrow 0$ . Choosing two limiting case for  $\delta z$ , a pure real one  $\delta z = \delta x_1$  and a pure imaginary one  $\delta z = i\delta x_2$ , and equating both of them yield the so-called *the Cauchy-Riemann equations*

$$\frac{\partial u_1}{\partial x_1} = \frac{\partial u_2}{\partial x_2} \quad \text{and} \quad \frac{\partial u_1}{\partial x_2} = -\frac{\partial u_2}{\partial x_1}. \quad (\text{C.11})$$

If  $u_1$ ,  $u_2$ ,  $\partial u_1/\partial x$ ,  $\partial u_2/\partial y$ ,  $\partial u_1/\partial y$  and  $\partial u_2/\partial x$  are continuous at  $z$ , then the Cauchy-Riemann equations are the necessary and sufficient conditions for the existence of the derivative  $f'(z)$  at  $z$ . At this stage, two operators  $\partial/\partial\bar{z}$  and  $\partial/\partial z$  can be defined

$$\frac{\partial}{\partial\bar{z}} = \frac{1}{2}\left(\frac{\partial}{\partial x_1} + i\frac{\partial}{\partial x_2}\right) \quad \text{and} \quad \frac{\partial}{\partial z} = \frac{1}{2}\left(\frac{\partial}{\partial x_1} - i\frac{\partial}{\partial x_2}\right) \quad (\text{C.12})$$

which is obtained by using the chain rule and the definitions in (C.7). Following the latter result it is possible to write

$$4\frac{\partial^2}{\partial z\partial\bar{z}} = \frac{\partial^2}{\partial x_1^2} + \frac{\partial^2}{\partial x_2^2} = \nabla^2. \quad (\text{C.13})$$

A complex function  $f(z)$  is said to be *analytical* or *holomorphic* in a region  $S$  provided that it is single valued in  $S$  and its complex derivative  $f'(z)$  exists at each point of  $S$ . The sum of the derivatives of (C.11)<sub>1</sub> with respect to  $x_1$  and (C.11)<sub>2</sub> with respect to  $x_2$  yields

$$\nabla^2 u_1 = \frac{\partial^2 u_1}{\partial x_1^2} + \frac{\partial^2 u_1}{\partial x_2^2} = 0. \quad (\text{C.14})$$

Following the same procedure, but taking the derivatives in the opposite order renders

$$\nabla^2 u_2 = \frac{\partial^2 u_2}{\partial x_1^2} + \frac{\partial^2 u_2}{\partial x_2^2} = 0. \quad (\text{C.15})$$

The last two equations have important consequences. They indicate that the real and imaginary parts of any analytic function are solutions to the *Laplace equation*. This property motivates the application of complex variable methods to the theory of elasticity.

## D. The Linear Elastic Crack Tip Fields

The purpose of the subsequent discussions is to show the  $r^{-1/2}$  type stress singularities which arise in the linear elastic fracture mechanics. In the sequel, stress singularities in the Mode III (the anti-plane shear) and the Mode I crack problems will be studied, see KANNINEN & POPELAR [111] for further details.

### D.1. The Anti-Plane Shear Problem - Mode III Cracking

The anti-plane deformation state is defined by prescribing the displacement field  $\mathbf{u} = (u_1, u_2, u_3)$  as follows

$$u_1 = u_2 = 0 \quad \text{and} \quad u_3 = \hat{u}_3(x_1, x_2). \quad (\text{D.1})$$

Insertion of (D.1) into the usual definition of the linear strain tensor  $\varepsilon_{ij} = (u_{i,j} + u_{j,i})/2$  yields the anti-plane shears

$$\varepsilon_{3\alpha} = \varepsilon_{\alpha 3} = \frac{1}{2}u_{3,\alpha} \quad \text{for} \quad \alpha = 1, 2 \quad (\text{D.2})$$

as the only non-vanishing components of  $\boldsymbol{\varepsilon}$ . Recall the linear elastic stress-strain relation

$$\sigma_{ij} = \lambda \varepsilon_{kk} \delta_{ij} + 2\mu \varepsilon_{ij} \quad (\text{D.3})$$

which leads to the following non-zero stress components

$$\sigma_{3\alpha} = 2\mu \varepsilon_{3\alpha} \quad \text{for } \alpha = 1, 2 . \quad (\text{D.4})$$

Recall the equation of equilibrium ( $\sigma_{ij,j} = 0$  for  $i, j = 1, 2, 3$ ) for static problems in the absence of body forces which has the following simplified form

$$\sigma_{3\alpha,\alpha} = 0 \quad \text{for } \alpha = 1, 2 \quad (\text{D.5})$$

for the anti-plane shear problem under consideration. Insertion of (D.2) and (D.4) into (D.5) yields the so-called the *Laplace equation*

$$\boxed{u_{3\alpha,\alpha} = \nabla^2 u = 0 \quad \text{for } \alpha = 1, 2} \quad (\text{D.6})$$

which can be solved by complex variable methods. The real and the imaginary parts of any analytic function are solutions to Laplace equation, see Appendix C. Therefore, the solution of (D.6) can be written as

$$\boxed{u_3 = \frac{1}{\mu} [f(z) + \bar{f}(\bar{z})] ,} \quad (\text{D.7})$$

where  $f(z) = u(x_1, x_2) + iv(x_1, x_2)$  is an analytical function,  $\bar{f}(\bar{z}) = u(x_1, x_2) - iv(x_1, x_2)$  is its complex conjugate,  $u(x_1, x_2)$  and  $v(x_1, x_2)$  are two real functions and  $i = \sqrt{-1}$  is the complex number. Insertion of (D.7) into (D.2) yields

$$\varepsilon_{31} = \frac{1}{2\mu} [f'(z) + \bar{f}'(\bar{z})] \quad \text{and} \quad \varepsilon_{32} = \frac{i}{2\mu} [f'(z) - \bar{f}'(\bar{z})] , \quad (\text{D.8})$$

From (D.8) the stress components read

$$\sigma_{31} = [f'(z) + \bar{f}'(\bar{z})] \quad \text{and} \quad \varepsilon_{32} = i [f'(z) - \bar{f}'(\bar{z})] , \quad (\text{D.9})$$

and a straightforward manipulation of (D.9) gives

$$\boxed{\sigma_{31} - i\sigma_{32} = 2f'(z) .} \quad (\text{D.10})$$

We investigate the anti-plane shear problem depicted in Figure 7.7 with a coordinate system located at the crack tip. We consider the following analytical function

$$f(z) = Cz^{\lambda+1} \quad \text{with } C = A + iB , \quad (\text{D.11})$$

where  $A$ ,  $B$  and  $\lambda$  are undetermined real constants. Note that  $f(z)$  in (D.11) can also be written as  $f(z) = u(x_1, x_2) + iv(x_1, x_2)$ . In order to obtain finite displacements at the crack tip ( $|z| = r = 0$ ),  $\lambda$  has to be greater than  $-1$ . Insertion of (D.11) into (D.10) yields

$$\sigma_{31} - i\sigma_{32} = 2(\lambda + 1) Cz^\lambda . \quad (\text{D.12})$$

Some manipulations of (D.12) based on (C.3) leads to an alternative representation

$$\sigma_{31} - i\sigma_{32} = 2(\lambda + 1) r^\lambda (A + iB) (\cos \lambda\theta + i \sin \lambda\theta) . \quad (\text{D.13})$$

By equating separately the real and imaginary parts of (D.13), one gets

$$\begin{aligned}\sigma_{31} &= 2(\lambda + 1)r^\lambda (A \cos \lambda\theta - B \sin \lambda\theta) \\ \sigma_{32} &= -2(\lambda + 1)r^\lambda (A \sin \lambda\theta + B \cos \lambda\theta) \quad .\end{aligned}\quad (\text{D.14})$$

We consider a sharp crack with traction free crack lips which requires the following conditions on the cracks surfaces

$$\sigma_{32} = 0 \quad \text{for} \quad \theta = \mp\pi . \quad (\text{D.15})$$

Insertion of the condition (D.15) into (D.14)<sub>2</sub> gives two equations in terms of the unknown constants  $A$  and  $B$

$$\underbrace{\begin{bmatrix} \sin \lambda\pi & \cos \lambda\pi \\ \sin \lambda\pi & -\cos \lambda\pi \end{bmatrix}}_{=: \mathbf{K}} \begin{bmatrix} A \\ B \end{bmatrix} = \begin{bmatrix} 0 \\ 0 \end{bmatrix} . \quad (\text{D.16})$$

In order to avoid the trivial solution  $A = B = 0$ , the determinant of  $\mathbf{K}$  has to vanish which is satisfied if

$$\sin 2\pi\lambda = 0 . \quad (\text{D.17})$$

Considering the restriction on  $\lambda$  to have a bounded displacement field at the crack tip ( $\lambda > -1$ ), the roots of (D.17) are found to be

$$\lambda = -\frac{1}{2}, \frac{n}{2} \quad \text{for} \quad n = 0, 1, 2, \dots \quad (\text{D.18})$$

From the set of solutions for  $\lambda$  given in (D.18), the first one  $\lambda = -\frac{1}{2}$  provides, around a small neighborhood of the crack tip, the most significant contribution. If  $\lambda = -\frac{1}{2}$  is set, then the equations in (D.16) are satisfied for  $A = 0$ , but  $B$  still remains as an unknown. Now, from (D.14) it is possible to write

$$\boxed{\begin{bmatrix} \sigma_{31} \\ \sigma_{32} \end{bmatrix} = \frac{K_{III}}{(2\pi r)^{1/2}} \begin{bmatrix} -\sin(\theta/2) \\ \cos(\theta/2) \end{bmatrix}} , \quad (\text{D.19})$$

where  $B$  is chosen such that

$$K_{III} = \lim_{r \rightarrow 0} \left[ (2\pi r)^{1/2} \sigma_{32} \Big|_{\theta=0} \right] . \quad (\text{D.20})$$

Then, the displacement field is determined by insertion of (D.11) into (D.7) with  $\lambda = -\frac{1}{2}$ ,  $A = 0$  and the use of (C.4), i.e.

$$\boxed{u_3 = \frac{2K_{III}}{\mu} \left(\frac{r}{2\pi}\right)^{1/2} \sin \frac{\theta}{2}} . \quad (\text{D.21})$$

The quantity  $K_{III}$  is referred to as the Mode III stress intensity factor, which is established by the far field boundary conditions and is solely a function of the applied loading and the geometry of the cracked body. The stresses for  $\lambda \neq -\frac{1}{2}$  but satisfying (D.18) are finite at the crack tip. Away from the crack tip other terms with  $\lambda \neq -\frac{1}{2}$  start to play



an important role, and they cannot be neglected. Alternatively, the stress field can also be written in the polar coordinates

$$\boxed{\begin{bmatrix} \sigma_{rz} \\ \sigma_{\theta z} \end{bmatrix} = \frac{K_{III}}{(2\pi r)^{1/2}} \begin{bmatrix} \sin(\theta/2) \\ \cos(\theta/2) \end{bmatrix}} \quad (\text{D.22})$$

Both the Cartesian (D.19) and the polar representations (D.22) show that there is the well-known  $r^{-1/2}$  singularity of the stress field at the crack tip in the case of an anti-plane shear problem of linear elasticity.

## D.2. Mode I Cracking

The displacement field has the following parameterization

$$u_1 = \hat{u}_1(x_1, x_2), \quad u_2 = \hat{u}_2(x_1, x_2) \quad \text{and} \quad u_3 = 0 \quad (\text{D.23})$$

for a Mode I crack problem under consideration. As a consequence of (D.23),  $\varepsilon_{31} = \varepsilon_{32} = \varepsilon_{33} = 0$ , and the other components of the strain are

$$\varepsilon_{\alpha\beta} = \frac{1+\nu}{E} [\sigma_{\alpha\beta} - \nu\delta_{\alpha\beta}\sigma_{\gamma\gamma}] \quad \text{for} \quad \alpha, \beta, \gamma = 1, 2, \quad (\text{D.24})$$

where  $\delta_{\alpha\beta}$  is the Kronecker delta. As a consequence of (D.23) and (D.24), stresses fulfill the conditions given by

$$\sigma_{33} = \nu\sigma_{\gamma\gamma} \quad \text{and} \quad \sigma_{3\alpha} = 0 \quad \text{for} \quad \alpha = 1, 2. \quad (\text{D.25})$$

In the absence of body forces the static equilibrium is  $\sigma_{\alpha\beta,\beta} = 0$  where  $\alpha, \beta = 1, 2$  for the two-dimensional problem studied. In the case of plane problems six independent compatibility conditions boil down to

$$\varepsilon_{\alpha\beta,\alpha\beta} - \varepsilon_{\alpha\alpha,\beta\beta} = 0 \quad \text{or} \quad 2\varepsilon_{12,12} - \varepsilon_{12,12} - \varepsilon_{22,11} = 0. \quad (\text{D.26})$$

The static equilibrium condition  $\sigma_{\alpha\beta,\beta} = 0$  will be identically satisfied if stresses are expressed in the following form

$$\sigma_{\alpha\beta} = -\Psi_{,\alpha\beta} + \Psi_{,\gamma\gamma}\delta_{\alpha\beta}, \quad (\text{D.27})$$

where  $\Psi$  is the *Airy stress function*. Insertion of (D.27) into (D.24) gives the non-zero strain components in terms of the Airy stress function

$$\begin{aligned} \varepsilon_{11} &= \frac{1+\nu}{E} [-\Psi_{,11} + (1-\nu)(\Psi_{,11} + \Psi_{,22})], \\ \varepsilon_{22} &= \frac{1+\nu}{E} [-\Psi_{,22} + (1-\nu)(\Psi_{,11} + \Psi_{,22})], \\ \varepsilon_{12} &= \frac{1+\nu}{E} [-\Psi_{,12}]. \end{aligned} \quad (\text{D.28})$$

Then the compatibility condition (D.26) can be reformulated by using the representation of strains in (D.28) as follows

$$\nabla^2(\nabla^2\Psi) = \Psi_{,\alpha\alpha\beta\beta} = 0 \quad (\text{D.29})$$

which states that  $\nabla^2\Psi$  satisfies the Laplace equation. Consequently, one can write  $\nabla^2\Psi$  as the sum of an analytical function and its complex conjugate

$$\nabla^2\Psi = 4\frac{\partial^2\Psi}{\partial z\partial\bar{z}} = f(z) + \bar{f}(\bar{z}), \quad (\text{D.30})$$

where  $f(z)$  is an analytical function, see Appendix C for the definition of analytical functions. Integration of (D.30) results in a real function

$$\Psi = \frac{1}{2} [\bar{z}\Omega(z) + z\bar{\Omega}(\bar{z}) + \omega(z) + \bar{\omega}(\bar{z})]. \quad (\text{D.31})$$

Insertion of (D.31) into (D.30) yields  $f(z) = 2\partial\Omega(z)/\partial z$  and  $\bar{f}(\bar{z}) = 2\partial\bar{\Omega}(\bar{z})/\partial\bar{z}$  where  $\Omega(z)$  and  $\omega(z)$  are analytic functions. Note that from (D.27) and (D.30) it is possible to write

$$\sigma_{11} + \sigma_{22} = \Psi_{,11} + \Psi_{,22} = \nabla^2\Psi = 4\frac{\partial^2\Psi}{\partial z\partial\bar{z}}. \quad (\text{D.32})$$

Combination of (D.31) and (D.30) gives

$$4\frac{\partial^2\Psi}{\partial z\partial\bar{z}} = 2[\Omega'(z) + \bar{\Omega}'(\bar{z})], \quad (\text{D.33})$$

where  $\Omega'(z)$  and  $\bar{\Omega}'(\bar{z})$  represent the derivatives of  $\Omega$  and  $\bar{\Omega}$  with respect to  $z$  and  $\bar{z}$ , respectively. By comparison of (D.32) with (D.33) one obtains

$$\boxed{\sigma_{11} + \sigma_{22} = 2[\Omega'(z) + \bar{\Omega}'(\bar{z})]}. \quad (\text{D.34})$$

The second derivative of  $\Psi$  with respect to  $\bar{z}$  is computed from (D.31)

$$4\frac{\partial^2\Psi}{\partial\bar{z}\partial\bar{z}} = 2[z\bar{\Omega}''(\bar{z}) + \bar{\omega}''(\bar{z})]. \quad (\text{D.35})$$

The following sum of three components of the stress is constructed

$$\sigma_{22} - \sigma_{11} - 2i\sigma_{12} = \Psi_{,11} - \Psi_{,22} + 2i\Psi_{,12} \quad (\text{D.36})$$

by using the expression in (D.27). Twice application of the operator  $\partial/\partial\bar{z}$  defined in (C.12) to the function  $\Psi$  induces

$$4\frac{\partial^2\Psi}{\partial\bar{z}\partial\bar{z}} = \frac{\partial^2\Psi}{\partial x_1^2} - \frac{\partial^2\Psi}{\partial x_2^2} + 2i\frac{\partial^2\Psi}{\partial x_1\partial x_2} \quad (\text{D.37})$$

and a comparison of (D.35), (D.36) and (D.37) yields the representation

$$\boxed{\sigma_{22} - \sigma_{11} - 2i\sigma_{12} = 2[z\bar{\Omega}''(\bar{z}) + \bar{w}''(\bar{z})]}. \quad (\text{D.38})$$

Alternative to (D.38) the following relation is often accounted in the literature

$$\boxed{\sigma_{22} - \sigma_{11} + 2i\sigma_{12} = 2[\bar{z}\Omega''(z) + w''(z)]}. \quad (\text{D.39})$$

Using the representation of the stress in (D.27), one can write

$$\sigma_{22} - i\sigma_{12} = \Psi_{,11} + i\Psi_{,12} \quad (\text{D.40})$$

and insertion of the Airy function (D.31) into (D.40) yields

$$\sigma_{22} - i\sigma_{12} = \Omega'(z) + \bar{\Omega}'(\bar{z}) + z\bar{\Omega}''(\bar{z}) + \bar{w}''(\bar{z}) . \quad (\text{D.41})$$

In the sequel, the two-dimensional complex displacement field  $D$  and its complex conjugate  $\bar{D}$  in the following form

$$D = u_1 + iu_2 \quad \text{and} \quad \bar{D} = u_1 - iu_2 \quad (\text{D.42})$$

are considered. Application of the operators  $\partial/\partial\bar{z}$  and  $\partial/\partial z$  defined in (C.12) to the displacement  $D$  and its complex conjugate  $\bar{D}$  renders

$$2\frac{\partial D}{\partial z} = \varepsilon_{11} + \varepsilon_{22} + i(u_{2,1} - u_{1,2}) \quad \text{and} \quad 2\frac{\partial \bar{D}}{\partial \bar{z}} = \varepsilon_{11} + \varepsilon_{22} + i(u_{1,2} - u_{2,1}) \quad (\text{D.43})$$

and with the help of latter result one can write

$$\frac{\partial D}{\partial z} + \frac{\partial \bar{D}}{\partial \bar{z}} = \varepsilon_{11} + \varepsilon_{22} . \quad (\text{D.44})$$

Insertion of (D.24) into (D.43)<sub>2</sub> and then the obtained expression into (D.36) delivers

$$2\mu\frac{\partial D}{\partial \bar{z}} = -[z\bar{\Omega}''(\bar{z}) + \bar{w}''(\bar{z})] \quad \text{with} \quad \mu = E/2(1 + \nu) . \quad (\text{D.45})$$

Right hand side of (D.44) can be represented in terms of the stress components by using (D.24) and employing further (D.34), i.e.

$$\frac{2\mu}{1 - 2\nu} \left[ \frac{\partial D}{\partial \bar{z}} + \frac{\partial \bar{D}}{\partial \bar{z}} \right] = 2[\Omega'(z) + \bar{\Omega}'(\bar{z})] \quad (\text{D.46})$$

Integration of (D.45) and (D.46) gives the final representation of the displacement field in terms of the complex functions

$$\begin{aligned} 2\mu D &= \kappa\Omega(z) - z\bar{\Omega}'(\bar{z}) - \bar{w}'(\bar{z}) \\ 2\mu\bar{D} &= \kappa\bar{\Omega}(\bar{z}) - \bar{z}\Omega'(z) - \omega'(z) \end{aligned} , \quad (\text{D.47})$$

where  $\kappa = 3 - 4\nu$  for plane strain and  $\kappa = (3 - \nu)/(1 + \nu)$  for plane stress problems. Next, a coordinate system positioned at the crack tip is considered. Taking into account the symmetry of the problem with respect to the crack plane, a solution of the form

$$\Omega(z) = Az^{\lambda+1} \quad \text{and} \quad \omega'(z) = Bz^{\lambda+1} \quad (\text{D.48})$$

is assumed where  $A$ ,  $B$  and  $\lambda$  are real constants. The boundedness of the displacement field at the crack tip requires  $\lambda > -1$ . Substitution of (D.48) into (D.41) after some manipulations yields

$$\begin{aligned} \sigma_{22} - i\sigma_{12} &= (\lambda + 1)r^\lambda \left[ A[2\cos\lambda\alpha + \lambda\cos(\lambda - 2)\alpha] + B\cos\lambda\theta \right] \\ &- i \left[ A\lambda\sin(\lambda - 2)\theta + B\sin\lambda\theta \right] . \end{aligned} \quad (\text{D.49})$$

The condition of traction free crack lips requires for  $\theta = \pm\pi$  the stress components  $\sigma_{22} = \sigma_{12} = 0$ . By putting  $\theta = \pi$  in (D.49) and setting the real and imaginary parts separately to zero one gets

$$\underbrace{\begin{bmatrix} (\lambda + 2) \cos \lambda\pi & \cos \lambda\pi \\ \lambda \sin \lambda\pi & \sin \lambda\pi \end{bmatrix}}_{=:K} \begin{bmatrix} A \\ B \end{bmatrix} = \begin{bmatrix} 0 \\ 0 \end{bmatrix}, \quad (\text{D.50})$$

where the properties  $\cos(\lambda - 2)\pi = \cos \lambda\pi$  and  $\sin(\lambda - 2)\pi = \sin \lambda\pi$  of trigonometric functions are employed. A non-trivial solution of (D.50) demands that the determinant of  $K$  has to vanish. The equation  $\det K = 0$  is fulfilled for

$$\sin 2\lambda\pi = 0 \quad (\text{D.51})$$

which gives, excluding  $\lambda < -1$  due to unphysical displacement singularity, the following set of solutions

$$\lambda = -\frac{1}{2}, \frac{n}{2} \quad \text{for } n = 0, 1, 2, \dots \quad (\text{D.52})$$

It is clear that the most dominant contribution to the crack tip stress and displacement fields comes from  $\lambda = -1/2$  and from (D.47) for  $\lambda = -1/2$  one obtains  $A = 2B$ . Insertion of these results into (D.49) gives for the real and imaginary parts separately

$$\begin{aligned} \sigma_{22} &= \frac{A}{r^{1/2}} \cos \frac{\theta}{2} \left(1 + \sin \frac{\theta}{2} \sin \frac{3\theta}{2}\right) \\ \sigma_{12} &= \frac{A}{r^{1/2}} \cos \frac{\theta}{2} \sin \frac{\theta}{2} \cos \frac{3\theta}{2}. \end{aligned} \quad (\text{D.53})$$

The last component of the stress  $\sigma_{11}$  can be recovered by substitution of (D.34)<sub>1</sub> into (D.34) which reads

$$\sigma_{11} = \frac{A}{r^{1/2}} \cos \frac{\theta}{2} \left(1 - \sin \frac{\theta}{2} \sin \frac{3\theta}{2}\right). \quad (\text{D.54})$$

Finally, by choosing  $A$  such that  $A = K_I/\sqrt{2\pi}$  in terms of the Mode I stress intensity factor  $K_I$ , the stress field is obtained as

$$\boxed{\begin{bmatrix} \sigma_{11} \\ \sigma_{22} \\ \sigma_{12} \end{bmatrix} = \frac{K_I}{(2\pi r)^{1/2}} \begin{bmatrix} \cos(\theta/2) [1 - \sin(\theta/2) \sin(3\theta/2)] \\ \cos(\theta/2) [1 + \sin(\theta/2) \sin(3\theta/2)] \\ \cos(\theta/2) \sin(\theta/2) \cos(3\theta/2) \end{bmatrix}}. \quad (\text{D.55})$$

The Mode I stress intensity factor is defined as the following limit

$$K_I = \lim_{r \rightarrow 0} \left[ (2\pi r)^{1/2} \sigma_{22} \Big|_{\theta=0} \right]. \quad (\text{D.56})$$

The associated displacement field is computed by substitution of above results into (D.47) and considering the real and imaginary parts separately

$$\boxed{\begin{bmatrix} u_1 \\ u_2 \end{bmatrix} = \frac{K_I}{2\mu} \left(\frac{r}{2\pi}\right)^{1/2} \begin{bmatrix} \cos(\theta/2) [\kappa - 1 + 2 \sin^2(\theta/2)] \\ \sin(\theta/2) [\kappa + 1 - 2 \cos^2(\theta/2)] \end{bmatrix}}. \quad (\text{D.57})$$

Alternative to Cartesian coordinate system representation, the polar stress components can also be computed

$$\boxed{\begin{bmatrix} \sigma_{rr} \\ \sigma_{\theta\theta} \\ \sigma_{r\theta} \end{bmatrix} = \frac{K_I}{(2\pi r)^{1/2}} \begin{bmatrix} \cos(\theta/2) [1 + \sin^2(\theta/2)] \\ \cos^3(\theta/2) \\ \sin(\theta/2) \cos^2(\theta/2) \end{bmatrix}}, \quad (\text{D.58})$$

and the associated displacements are

$$\boxed{\begin{bmatrix} u_r \\ u_\theta \end{bmatrix} = \frac{K_I}{2\mu} \left(\frac{r}{2\pi}\right)^{1/2} \begin{bmatrix} \cos(\theta/2) [\kappa - 1 + 2 \sin^2(\theta/2)] \\ \sin(\theta/2) [-\kappa + 1 + 2 \cos^2(\theta/2)] \end{bmatrix}}. \quad (\text{D.59})$$

### D.3. Mode II Cracking

Here, we provide without any derivation only the stress and displacement fields in the vicinity of a crack tip loaded under Mode II conditions. They read in the Cartesian coordinates

$$\boxed{\begin{bmatrix} \sigma_{11} \\ \sigma_{22} \\ \sigma_{12} \end{bmatrix} = \frac{K_{II}}{(2\pi r)^{1/2}} \begin{bmatrix} -\sin(\theta/2) [2 + \cos(\theta/2) \cos(3\theta/2)] \\ \cos(\theta/2) [1 - \sin(\theta/2) \sin(3\theta/2)] \\ \sin(\theta/2) \cos(\theta/2) \cos(3\theta/2) \end{bmatrix}}, \quad (\text{D.60})$$

$$\boxed{\begin{bmatrix} u_1 \\ u_2 \end{bmatrix} = \frac{K_{II}}{2\mu} \left(\frac{r}{2\pi}\right)^{1/2} \begin{bmatrix} \sin(\theta/2) [\kappa + 1 + 2 \cos^2(\theta/2)] \\ \cos(\theta/2) [-\kappa + 1 + 2 \sin^2(\theta/2)] \end{bmatrix}}, \quad (\text{D.61})$$

and in the polar coordinates

$$\boxed{\begin{bmatrix} \sigma_{rr} \\ \sigma_{\theta\theta} \\ \sigma_{r\theta} \end{bmatrix} = \frac{K_{II}}{(2\pi r)^{1/2}} \begin{bmatrix} \sin(\theta/2) [1 - 3 \sin^2(\theta/2)] \\ -3 \sin(\theta/2) \cos^2(\theta/2) \\ \cos(\theta/2) [1 - 3 \sin^2(\theta/2)] \end{bmatrix}}, \quad (\text{D.62})$$

$$\boxed{\begin{bmatrix} u_r \\ u_\theta \end{bmatrix} = \frac{K_{II}}{2\mu} \left(\frac{r}{2\pi}\right)^{1/2} \begin{bmatrix} \sin(\theta/2) [-\kappa + 1 + 6 \cos^2(\theta/2)] \\ \cos(\theta/2) [-\kappa + 1 - 6 \sin^2(\theta/2)] \end{bmatrix}}. \quad (\text{D.63})$$

## E. Closed Form Solutions of Stress Intensity Factors

In the sequel, closed form solutions of the stress intensity factors are addressed. Recalling the relation (D.34) and the stress fields around a sharp crack in the Mode I and Mode II given by equations (D.55) and (D.60), one can write

$$\sigma_{11} + \sigma_{22} = \frac{2}{(2\pi r)^{1/2}} \left[ K_I \cos \frac{\theta}{2} - K_{II} \sin \frac{\theta}{2} \right] = 2\Omega'(z) + 2\bar{\Omega}'(\bar{z}). \quad (\text{E.1})$$

The above equation can be reformulated as

$$\sigma_{11} + \sigma_{22} = \frac{K_I - iK_{II}}{(2\pi r)^{1/2}} \left[ \cos \frac{\theta}{2} - i \sin \frac{\theta}{2} \right] + \frac{K_I + iK_{II}}{(2\pi r)^{1/2}} \left[ \cos \frac{\theta}{2} + i \sin \frac{\theta}{2} \right]. \quad (\text{E.2})$$

Note that the second term of the right hand side of (E.2) is the complex conjugate of the first term. As a consequence, it is possible to identify that

$$2\Omega'(z) = \frac{K_I - iK_{II}}{(2\pi r)^{1/2}} \left[ \cos \frac{\theta}{2} - i \sin \frac{\theta}{2} \right]. \quad (\text{E.3})$$

Equation (E.3) further can be recast with the help of (C.3) into

$$2\Omega'(z) = \frac{K_I - iK_{II}}{(2\pi)^{1/2}} r^{-1/2} \left[ \cos\left(-\frac{\theta}{2}\right) + i \sin\left(-\frac{\theta}{2}\right) \right] = \frac{K_I - iK_{II}}{(2\pi)^{1/2}} z^{-1/2}. \quad (\text{E.4})$$

The above representation allows us to write the following relation

$$K_I - iK_{II} = \lim_{z \rightarrow 0} \left[ 2(2\pi z)^{1/2} \Omega'(z) \right] \quad (\text{E.5})$$

which reduces the task of determining the stress intensity factors to the establishment of  $\Omega'(z)$  and the computation of the limit in (E.5).

Next, we consider an infinite body with a prescribed far field loading and a crack lying along a segment  $L$  of the  $x_1$  axis, i.e.  $-a \leq x_1 \leq a$  and  $x_2 = 0$ . The original problem can be defined as a superposition of two subproblems, see Figure E.1. The subproblem 1 is the original problem without the crack. The subproblem 2 is the infinite body with the prescribed crack and with zero loading at infinity, but the resultant stress of the subproblem 1 is applied to the crack surfaces with a negative sign. Now only the subproblem 2 will be considered which has the same singularity of the original problem at the crack tip. Suppose that for the given loading of the subproblem 1 the stress field along the segment  $L = [-a, a]$  is

$$\sigma_{2i} = p_i(x_1) \quad \text{for } x_1 \in L. \quad (\text{E.6})$$

Then the subproblem 2 has a traction free remote boundary and the prescribed stress components on the crack surfaces are

$$\sigma_{2i} = -p_i(x_1) \quad \text{for } x_1 \in L. \quad (\text{E.7})$$

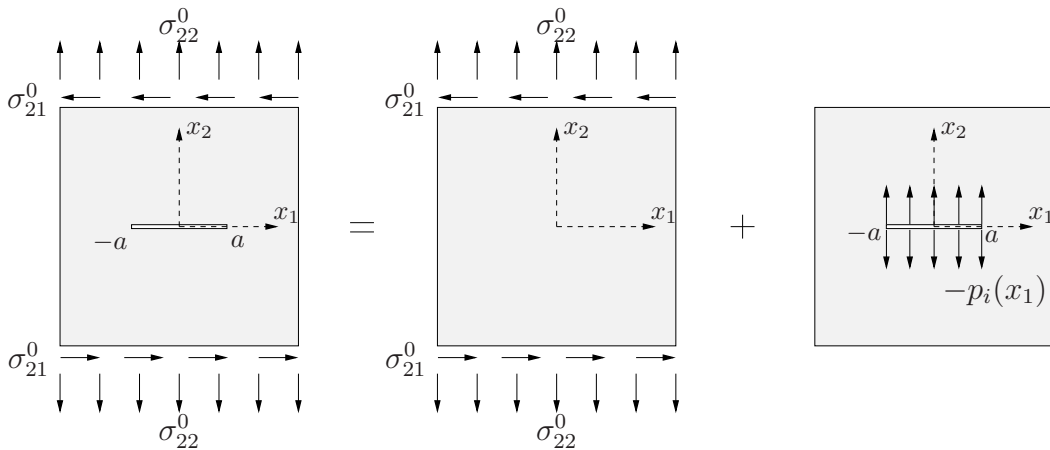


**Figure E.1:** Decomposition of the original problem as a superposition of two subproblems.

Along the  $x_1$  axis but outside of the crack surfaces, i.e.  $x_1 \notin L$  and  $x_2 = 0$ , the stress components and the displacements are continuous. The continuity of displacements requires

$$\lim_{x_2 \rightarrow 0^+} [\kappa\Omega(z) - z\bar{\Omega}'(\bar{z}) - \bar{\omega}'(\bar{z})] = \lim_{x_2 \rightarrow 0^-} [\kappa\Omega(z) - z\bar{\Omega}'(\bar{z}) - \bar{\omega}'(\bar{z})] \quad (\text{E.8})$$

when the representation (D.47)<sub>1</sub> of the displacement field in terms of complex functions are used. A rearrangement of the terms in (E.8) yields

$$\lim_{x_2 \rightarrow 0^+} [\kappa\Omega(z)] + \lim_{x_2 \rightarrow 0^-} [z\bar{\Omega}'(\bar{z}) + \bar{\omega}'(\bar{z})] = \lim_{x_2 \rightarrow 0^-} [\kappa\Omega(z)] + \lim_{x_2 \rightarrow 0^+} [z\bar{\Omega}'(\bar{z}) + \bar{\omega}'(\bar{z})]. \quad (\text{E.9})$$

Here we recall the definitions

$$\begin{aligned} \Omega(z) &= u_1(x_1, x_2) + iu_2(x_1, x_2) \\ \bar{\Omega}(\bar{z}) &= u_1(x_1, x_2) - iu_2(x_1, x_2) \\ \Omega(\bar{z}) &= u_1(x_1, -x_2) + iu_2(x_1, -x_2) \\ \overline{\Omega(\bar{z})} &= u_1(x_1, -x_2) - iu_2(x_1, -x_2) \end{aligned} \quad (\text{E.10})$$

which result in the following limit conditions

$$\begin{aligned} \lim_{x_2 \rightarrow 0^+} \Omega(z) &= \lim_{x_2 \rightarrow 0^-} \Omega(\bar{z}) \quad , \quad \lim_{x_2 \rightarrow 0^+} \bar{\Omega}(\bar{z}) = \lim_{x_2 \rightarrow 0^-} \overline{\Omega(\bar{z})} \\ \lim_{x_2 \rightarrow 0^-} \Omega(z) &= \lim_{x_2 \rightarrow 0^+} \Omega(\bar{z}) \quad , \quad \lim_{x_2 \rightarrow 0^-} \bar{\Omega}(\bar{z}) = \lim_{x_2 \rightarrow 0^+} \overline{\Omega(\bar{z})}. \end{aligned} \quad (\text{E.11})$$

Insertion of (E.11) into (E.9) yields

$$\lim_{x_2 \rightarrow 0^+} [\kappa\Omega(z) + z\overline{\Omega'(\bar{z})} + \overline{\omega'(z)}] = \lim_{x_2 \rightarrow 0^-} [\kappa\Omega(z) + z\overline{\Omega'(\bar{z})} + \overline{\omega'(z)}]. \quad (\text{E.12})$$

Consequently, the function

$$\Phi(z) = \kappa\Omega(z) + z\overline{\Omega'(\bar{z})} + \overline{\omega'(z)} \quad (\text{E.13})$$

is continuous outside the cracks on  $x_2 = 0$  and analytic (holomorphic) in the whole plane. Recalling (D.41), the requirement of stress continuity can be written as

$$\lim_{x_2 \rightarrow 0^+} [\Omega'(z) + \bar{\Omega}'(\bar{z}) + z\bar{\Omega}''(\bar{z}) + \bar{\omega}''(\bar{z})] = \lim_{x_2 \rightarrow 0^-} [\Omega'(z) + \bar{\Omega}'(\bar{z}) + z\bar{\Omega}''(\bar{z}) + \bar{\omega}''(\bar{z})] \quad (\text{E.14})$$

or alternatively

$$\lim_{x_2 \rightarrow 0^+} [\Omega'(z)] - \lim_{x_2 \rightarrow 0^-} [\bar{\Omega}'(\bar{z}) + z\bar{\Omega}''(\bar{z}) + \bar{\omega}''(\bar{z})] = \lim_{x_2 \rightarrow 0^-} [\Omega'(z)] - \lim_{x_2 \rightarrow 0^+} [\bar{\Omega}'(\bar{z}) + z\bar{\Omega}''(\bar{z}) + \bar{\omega}''(\bar{z})] \quad (\text{E.15})$$

which is recast by the use of (E.11) into

$$\lim_{x_2 \rightarrow 0^+} [\Omega'(z) - \overline{\Omega'(\bar{z})} - z\overline{\Omega''(\bar{z})} - \overline{\omega''(\bar{z})}] = \lim_{x_2 \rightarrow 0^-} [\Omega'(z) - \overline{\Omega'(\bar{z})} - z\overline{\Omega''(\bar{z})} - \overline{\omega''(\bar{z})}]. \quad (\text{E.16})$$

Therefore, the function  $\Psi'(z) = \Omega'(z) - \overline{\Omega'(\bar{z})} - z\overline{\Omega''(\bar{z})} - \overline{\omega''(\bar{z})}$  has to be continuous. The integration of  $\Psi'(z)$  is

$$\Psi(z) = \Omega(z) - z\overline{\Omega'(\bar{z})} - \overline{\omega'(z)} \quad (\text{E.17})$$

which must be also continuous outside of the cracks on  $x_2 = 0$  and analytic in the whole plane cut along  $L$ . The summation of  $\Phi(z)$  in (E.13) and  $\Psi(z)$  in (E.17) reads

$$\Psi(z) + \Phi(z) = (1 + \kappa)\Omega(z) \quad (\text{E.18})$$



inducing that the function  $\Omega(z)$  has to be analytic. From (E.17) one can write  $\overline{\omega'(\bar{z})} = \Omega(z) - z\Omega'(\bar{z}) - \Psi(z)$  or alternatively by replacing  $z \rightarrow \bar{z}$  and  $\bar{z} \rightarrow z$

$$\bar{\omega}'(\bar{z}) = \Omega(\bar{z}) - \bar{z}\bar{\Omega}'(\bar{z}) - \Psi(\bar{z}) . \quad (\text{E.19})$$

The derivative of (E.19) is

$$\bar{\omega}''(\bar{z}) = \Omega'(\bar{z}) - \bar{\Omega}'(\bar{z}) - \bar{z}\bar{\Omega}''(\bar{z}) - \Psi'(\bar{z}) . \quad (\text{E.20})$$

Substitution of (E.19) and (E.20) into (D.47)<sub>1</sub> and (D.41) gives

$$\begin{aligned} 2\mu D &= \kappa\Omega(z) - \Omega(\bar{z}) + (\bar{z} - z)\bar{\Omega}'(\bar{z}) + \Psi(\bar{z}) \\ \sigma_{22} - i\sigma_{12} &= \Omega'(z) + (z - \bar{z})\bar{\Omega}''(\bar{z}) + \Omega'(\bar{z}) - \Psi'(\bar{z}) . \end{aligned} \quad (\text{E.21})$$

Next, the boundary conditions on the both crack surfaces are expressed by the use of (E.21)<sub>2</sub> and (E.6)

$$\begin{aligned} -p_2(x_1) + ip_1(x_1) &= \Omega'^+(x_1) + \Omega'^-(x_1) - \Psi'^-(x_1) \quad \text{for } x_2 \rightarrow 0^+ \\ -p_2(x_1) + ip_1(x_1) &= \Omega'^-(x_1) + \Omega'^+(x_1) - \Psi'^+(x_1) \quad \text{for } x_2 \rightarrow 0^- , \end{aligned} \quad (\text{E.22})$$

where

$$\begin{aligned} \Omega'^+(x_1) &= \lim_{x_2 \rightarrow 0^+} \Omega'(z) = \lim_{x_2 \rightarrow 0^-} \Omega'(z) , & \Psi'^-(x_1) &= \lim_{x_2 \rightarrow 0^+} \Psi'(\bar{z}) \\ \Omega'^-(x_1) &= \lim_{x_2 \rightarrow 0^-} \Omega'(z) = \lim_{x_2 \rightarrow 0^+} \Omega'(z) , & \Psi'^+(x_1) &= \lim_{x_2 \rightarrow 0^-} \Psi'(\bar{z}) \end{aligned} \quad (\text{E.23})$$

and  $z - \bar{z} = 0$  for  $x_2 = 0$ . Addition and subtraction of (E.22)<sub>1</sub> and (E.22)<sub>2</sub> yield

$$\begin{aligned} 2\Omega'^+(x_1) - \Psi'^+(x_1) + 2\Omega'^-(x_1) - \Psi'^-(x_1) &= -2p_2(x_1) + 2ip_1(x_1) \\ \Psi'^+(x_1) - \Psi'^-(x_1) &= 0 \end{aligned} \quad (\text{E.24})$$

for  $x_1 \in [-a, a]$  and  $x_2 = 0$ . The two equations (E.24)<sub>1</sub> and (E.24)<sub>2</sub> are two *Hilbert problems* for the determination of  $\Psi'(z)$  and  $2\Omega'(z) - \Psi'(z)$ . Here, without discussing the details, the general solution of the Hilbert problem will be given.

$$\begin{aligned} \Psi'(z) &= \frac{1}{2\pi i} \int_L \frac{0}{t - z} dt + Q(z) \\ 2\Omega'(z) - \Psi'(z) &= \frac{X(z)}{2\pi i} \int_L \frac{p_2(t) - ip_1(t)}{X^+(t)(t - z)} dt + P(z)X(z) . \end{aligned} \quad (\text{E.25})$$

Further details of the Hilbert problems can be found in ENGLAND [63] and KANNINEN & POPELAR [111]. Since the stress components are zero at infinity, one concludes that  $\Omega'(z)$  and  $\omega'(z)$  are of  $O(z^{-1})$  and hence  $\Psi'(z) = O(z^{-1})$  as  $|z| \rightarrow \infty$ . In (E.25)<sub>1</sub> the zero is put purposely inside the integral due to the fact that the right hand side of (E.24)<sub>2</sub> is zero.  $Q(z)$  in (E.25)<sub>1</sub> is a polynomial in general and since  $\Psi'(z) = O(z^{-1})$  as  $|z| \rightarrow \infty$  it vanishes in our case, i.e.  $Q(z) = 0$  and as a consequence  $\Psi'(z) = 0$ . The preceding solution includes the so-called *Plemelj function*  $X(z)$  which is defined as

$$X(z) = (z^2 - a^2)^{-1/2} \quad (\text{E.26})$$

for a single crack segment of  $L = [-a, a]$ . General form of the *Plemelj function* for an array of cracks can be found in KANNINEN & POPELAR [111] pp.149. Note that due to the definition of  $X(z)$  in (E.26), it can be shown that  $zX(z) \rightarrow 1$  as  $|z| \rightarrow \infty$ . The undetermined function  $P(z)$  in (E.25)<sub>2</sub> is analytic in the whole plane. Because of vanishing stresses at infinity,  $P(z)$  is a polynomial of order  $n - 1$  if  $X(z)$  is of  $-n$  for large  $z$ . Since  $n = 1$  and the resultant force over the crack has to be zero in the current case,  $P(z)$  is a constant and in fact, the value of the constant is zero, i.e.  $P(z) = 0$ . As a result of above observations, (E.25)<sub>2</sub> is expressed as

$$\Omega'(z) = -\frac{(z^2 - a^2)^{-1/2}}{2\pi} \int_{-a}^a \frac{(a^2 - t^2)^{1/2} [p_2(t) - ip_1(t)]}{t - z} dt \quad (\text{E.27})$$

for a crack segment of  $L = [-a, a]$ . A change of variable,  $z = \xi + a$ , in (E.5) yields

$$K_I - iK_{II} = \lim_{\xi \rightarrow 0} [2(2\pi\xi)^{1/2}\Omega'(\xi)] \quad (\text{E.28})$$

and insertion of (E.28) into (E.27) gives after some algebraic manipulations

$$K_I - iK_{II} = \frac{1}{(\pi a)^{1/2}} \int_{-a}^a \left(\frac{a+t}{a-t}\right)^{1/2} [p_2(t) - ip_1(t)] dt . \quad (\text{E.29})$$

A similar analysis for the anti-plane shear problem yields

$$K_{III} = \frac{1}{(\pi a)^{1/2}} \int_{-a}^a \left(\frac{a+t}{a-t}\right)^{1/2} p_3(t) dt . \quad (\text{E.30})$$

If we consider an infinite body subjected to uniform remote tractions  $\sigma_{ij}^0$ , then  $p_i(t) = \sigma_{2i}^0$  in (E.29) and (E.30) and the intensity factors are determined as

$$\boxed{K_I = \sigma_{22}^0 \sqrt{\pi a} , \quad K_{II} = \sigma_{21}^0 \sqrt{\pi a} \quad \text{and} \quad K_{III} = \sigma_{23}^0 \sqrt{\pi a} .} \quad (\text{E.31})$$

## References

- [1] ACERBI, E.; FUSCO, N. [1984]: *Semicontinuity Problems in the Calculus of Variations*. Archive of Rational Mechanics and Analysis, 86: 125–145.
- [2] ADDA-BEDIA, M.; ARIAS, R.; BEN AMAR, M.; LUND, F. [1999]: *Generalized Griffith Criterion for Dynamic Fracture and the Stability of Crack Motion at High Velocities*. Physical Review E, 60: 2366–2376.
- [3] AGIASOFITOU, E. K.; KALPAKIDES, V. K. [2006]: *The Concept of a Balance Law for a Cracked Elastic Body and the Configurational Force and Moment at the Crack Tip*. International Journal of Engineering Science, 44: 127–139.
- [4] ALIBERT, J. J.; DACOROGNA, B. [1992]: *An Example of a Quasiconvex Function that is not Polyconvex in Two Dimensions*. Archive of Rational Mechanics and Analysis, 117: 155–166.
- [5] AMBROSIO, L.; FUSCO, N.; PALLARA, D. [2000]: *Functions of Bounded Variation and Free Discontinuity Problems*. Oxford University Press, New York.
- [6] ANDERSON, T. L. [1995]: *Fracture Mechanics: Fundamentals and Applications*. CRC Press, 2nd Edition.
- [7] ARANDA, E.; PEDREGAL, P. [2001]: *On the Computation of the Rank-One Convex Hull of a Function*. SIAM Journal on Scientific Computing, 22: 1772–1790.
- [8] AREIAS, P.; BELYTSCHKO, T. [2005]: *Analysis of Three-Dimensional Crack Initiation and Propagation using the Extended Finite Element Method*. International Journal for Numerical Methods in Engineering, 63: 760–788.
- [9] ASARO, R. [1983]: *Micromechanics of Crystals and Polycrystals*. Advances in Applied Mechanics, 23: 1–115.
- [10] ASKES, H.; KUHL, E.; STEINMANN, P. [2004]: *An ALE Formulation based on Spatial and Material Settings of Continuum Mechanics. Part 2: Classification and Applications*. Computer Methods in Applied Mechanics and Engineering, 193: 4223–4245.
- [11] AUBRY, S.; FAGO, M.; ORTIZ, M. [2003]: *A Constrained Sequential-Lamination Algorithm for the Simulation of Sub-Grid Microstructure in Martensitic Materials*. Computer Methods in Applied Mechanics and Engineering, 192: 2823–2843.
- [12] BALL, J. M. [1977]: *Convexity Conditions and Existence Theorems in Nonlinear Elasticity*. Archive of Rational Mechanics and Analysis, 63: 337–403.
- [13] BALL, J. M. [2002]: *Some Open Problems in Elasticity*. In NEWTON, P.; HOLMES, P.; WEINSTEIN, A. (Editors): *Geometry, Mechanics, and Dynamics*, pp. 3–59. Springer, New York.
- [14] BALL, J. M.; JAMES, R. D. [1987]: *Fine Phase Mixtures as Minimizers of Energy*. Archive of Rational Mechanics and Analysis, 100: 13–52.
- [15] BALL, J. M.; JAMES, R. D. [1992]: *Proposed Experimental Tests of a Theory of Fine Microstructure and the Two-Well Problem*. Philosophical Transactions: Physical Sciences and Engineering, 338: 389–450.
- [16] BARENBLATT, G. I. [1962]: *The Mathematical Theory of Equilibrium Cracks in Brittle Fracture*. Advances in Applied Mechanics, 7: 55–129.

- [17] BARSOU, R. S. [1976]: *On the use of Isoparametric Finite Elements in Linear Fracture Mechanics*. International Journal for Numerical Methods in Engineering, 10: 25–37.
- [18] BARSOU, R. S. [1977]: *Triangular Quarter-Point Elements as Elastic and Perfectly-Plastic Crack Tip Elements*. International Journal for Numerical Methods in Engineering, 11: 85–98.
- [19] BARTELS, S.; CARSTENSEN, C.; HACKL, K.; HOPPE, U. [2004]: *Effective Relaxation for Microstructure Simulations: Algorithms and Applications*. Computer Methods in Applied Mechanics and Engineering, 193: 5143–5175.
- [20] BELYTSCHKO, T.; BLACK, T. [1999]: *Elastic Crack Growth in Finite Elements with Minimal Remeshing*. International Journal for Numerical Methods in Engineering, 45: 601–620.
- [21] BELYTSCHKO, T.; FISH, J.; ENGELMANN, E. [1988]: *A Finite Element with Embedded Localization Zones*. Computer Methods in Applied Mechanics and Engineering, 70: 59–89.
- [22] BHATTACHARYA, K. [2003]: *Microstructure of Martensite: Why It Forms and How It Gives Rise to the Shape-Memory Effect*. Oxford University Press Inc., New York.
- [23] BHATTACHARYA, K.; DOLZMANN, G. [2000]: *Relaxed Constitutive Relations for Phase Transforming Materials*. Journal of the Mechanics and Physics of Solids, 48: 1493–1517.
- [24] BIOT, M. A. [1965]: *Mechanics of Incremental Deformations*. John Wiley & Sons Inc., New York.
- [25] BITTENCOURT, T. N.; WAWRZYNEK, P. A.; INGRAFFEA, A. R.; SOUSA, J. L. [1996]: *Quasi-Automatic Simulation of Crack Propagation for 2D LEFM Problems*. Engineering Fracture Mechanics, 55: 321–334.
- [26] BOUCHARD, P. O.; BAY, F.; CHASTEL, Y. [2003]: *Numerical Modelling of Crack Propagation: Automatic Remeshing and Comparison of Different Criteria*. Computer Methods in Applied Mechanics and Engineering, 192: 3887–3908.
- [27] BOUCHARD, P. O.; BAY, F.; CHASTEL, Y.; TOVENA, I. [2000]: *Crack Propagation Modelling Using an Advanced Remeshing Technique*. Computer Methods in Applied Mechanics and Engineering, 189: 723–742.
- [28] BOURDIN, B. [1999]: *Image Segmentation with a Finite Element Method*. Mathematical Modelling and Numerical Analysis, 33: 229–244.
- [29] BOURDIN, B.; CHAMBOLLE, A. [2000]: *Implementation of an Adaptive Finite Element Approximation of the Mumford-Shah Functional*. Numerische Mathematik, 85: 609–646.
- [30] BOURDIN, B.; FRANCFORT, G. A.; MARIGO, J. J. [2000]: *Numerical Experiments in Revisited Brittle Fracture*. Journal of the Mechanics and Physics of Solids, 48: 797–826.
- [31] BRAIDES, D. P. [1998]: *Approximation of Free Discontinuity Problems*. Springer Verlag, Berlin.
- [32] BRAIDES, D. P. [2002]:  *$\Gamma$ -Convergence for Beginners*. Oxford University Press, New York.

- [33] BRAUN, M. [1997]: *Configurational Forces Induced by Finite-Element Discretization*. Proceedings of the Estonian Academy of Sciences, Physics, Mathematics, 46: 24–31.
- [34] BROKENSHIRE, D. R. [1996]: *A Study of Torsion Fracture Tests*. Ph.D. Thesis, Cardiff University.
- [35] BUDIANSKY, B.; RICE, J. R. [1973]: *Conservation Laws and Energy Release Rates*. Journal of Applied Mechanics, 40: 201–203.
- [36] BULIGA, M. [1999]: *Energy Minimizing Brittle Crack Propagation*. Journal of Elasticity, 52: 201–238.
- [37] CAMACHO, G. T.; ORTIZ, M. [1996]: *Computational Modelling of Impact Damage in Brittle Materials*. International Journal of Solids and Structures, 33: 2899–2938.
- [38] CARSTENSEN, C. [2001]: *Numerical Analysis of Microstructure*. In BLOWEY, J. F.; COLEMAN, J. P.; CRAIG, A. W. (Editors): *Theory and Numerics of Differential Equations*, pp. 59–126. Springer Verlag, Berlin Heidelberg.
- [39] CARSTENSEN, C. [2003]: *Nonconvex Energy Minimization and Relaxation in Computational Material Science*. In MIEHE, C. (Editor): *Computational Mechanics of Solid Materials at Large Strains*, pp. 3–20. Kluwer Academic Publishers.
- [40] CARSTENSEN, C.; HACKL, K.; MIELKE, A. [2002]: *Non-Convex Potentials and Microstructures in Finite-Strain Plasticity*. Proceedings of the Royal Society London A, 458: 299–317.
- [41] CHADWICK, P. [1975]: *Applications of an Energy Momentum Tensor in Non-Linear Elastostatics*. Journal of Elasticity, 5: 249–258.
- [42] CHEREPANOV, G. P. [1967]: *Crack Propagation in Continuous Media*. Journal of Applied Mathematics and Mechanics (PMM), 31: 476–488.
- [43] CHERKAEV, A. [2000]: *Variational Methods for Structural Optimization*. Springer-Verlag, New York.
- [44] CHU, C.; JAMES, R. D. [1995]: *Analysis of Microstructures in Cu–14%Al–3.9%Ni by Energy Minimization*. Journal de Physique IV, 5: 143–149.
- [45] CIARLET, P. G. [1988]: *Mathematical Elasticity*. Elsevier Science Publishers B.V., Amsterdam.
- [46] COLEMAN, B.; NOLL, W. [1959]: *On the Thermo-statics of Continuous Media*. Archive of Rational Mechanics and Analysis, 4: 97–128.
- [47] CONTI, S.; DESIMONE, A.; DOLZMANN, G. [2002]: *Soft Elastic Response of Stretched Sheets of Nematic Elastomers: A Numerical Study*. Journal of the Mechanics and Physics of Solids, 50: 1431–1451.
- [48] CONTI, S.; ORTIZ, M. [2005]: *Dislocation Microstructures and the Effective Behavior of Single Crystals*. Archive of Rational Mechanics and Analysis, 176: 103–147.
- [49] CONTI, S.; THEIL, F. [2005]: *Single-Slip Elastoplastic Microstructures*. Archive of Rational Mechanics and Analysis, 178: 125–148.
- [50] COTTERELL, B. [2002]: *The Past, Present, and Future of Fracture Mechanics*. Engineering Fracture Mechanics, 69: 533–553.

- [51] DACOROGNA, B. [1989]: *Direct Methods in the Calculus of Variations*. Springer-Verlag, Berlin Heidelberg.
- [52] DACOROGNA, B. [2004]: *Introduction to the Calculus of Variations*. Imperial College Press, London.
- [53] DAL MASO, G. [1993]: *An Introduction to  $\Gamma$ -Convergence*. Birkhäuser, Boston.
- [54] DE BORST, R. [1987]: *Computation of Post-Bifurcation and Post-Failure Behavior of Strain-Softening Solids*. Computers and Structures, 25: 211–224.
- [55] DE BORST, R.; REMMERS, J. J. C.; NEEDLEMAN, A. [2006]: *Mesh-Independent Discrete Numerical Representations of Cohesive Zone Models*. Engineering Fracture Mechanics, 73: 160–177.
- [56] DENZER, R.; BARTH, F. J.; STEINMANN, P. [2003]: *Studies in Elastic Fracture Mechanics Based on the Material Force Method*. International Journal for Numerical Methods in Engineering, 58: 1817–1835.
- [57] DESIMONE, A.; DOLZMANN, G. [2000]: *Material Instabilities in Nematic Elastomers*. Physica D, 136: 175–191.
- [58] DESIMONE, A.; DOLZMANN, G. [2002]: *Macroscopic Response of Nematic Elastomers via Relaxation of a Class of  $SO(3)$ -Invariant Energies*. Archive of Rational Mechanics and Analysis, 161: 181–204.
- [59] DOLZMANN, G. [1999]: *Numerical Computation of Rank-One Convex Envelopes*. SIAM Journal on Numerical Analysis, 36: 1621–1635.
- [60] DOLZMANN, G. [2003]: *Variational Methods for Crystalline Microstructure – Analysis and Computation*. Springer-Verlag, Berlin Heidelberg.
- [61] DUGDALE, D. S. [1960]: *Yielding of Steel Sheets Containing Slits*. Journal of the Mechanics and Physics of Solids, 8: 100–104.
- [62] EISCHEN, J. W.; HERRMANN, G. [1987]: *Energy Release Rates and Related Balance Laws in Linear Elastic Defect Mechanics*. Journal of Applied Mechanics, 54: 388–392.
- [63] ENGLAND, A. H. [1971]: *Complex Variable Methods in Elasticity*. Wiley-Interscience.
- [64] ERDOGAN, F. [2000]: *Fracture Mechanics*. International Journal of Solids and Structures, 37: 171–183.
- [65] ERDOGAN, F.; SIH, G. C. [1963]: *On the Crack Extension in Plates under Plane Loading and Transverse Shear*. Journal of Basic Engineering, 85: 519–527.
- [66] ESHELBY, J. D. [1951]: *The Force on an Elastic Singularity*. Philosophical Transactions of the Royal Society London A, 244: 87–112.
- [67] ESHELBY, J. D. [1956]: *The Continuum Theory of Lattice Defects*. In SEITZ, F.; THURNBULL, D. (Editors): *Solid State Physics*, pp. 79–144.
- [68] ESHELBY, J. D. [1970]: *Energy Relations and the Energy-Momentum Tensor in Continuum Mechanics*. In KANNINEN, M. F. ET AL. (Editor): *Inelastic Behavior of Solids*, pp. 77–115.
- [69] ESHELBY, J. D. [1975]: *The Elastic Energy-Momentum Tensor*. Journal of Elasticity, 5: 321–335.



- [70] FAGERSTRÖM, M.; LARSSON, R. [2006]: *Theory and Numerics for Finite Deformation Fracture Modelling using Strong Discontinuities*. International Journal for Numerical Methods in Engineering, 66: 911–948.
- [71] FRANCFORT, G. A.; MARIGO, J. J. [1993]: *Stable Damage Evolution in a Brittle Continuous Medium*. European Journal of Mechanics, A/Solids, 12: 149–189.
- [72] FRANCFORT, G. A.; MARIGO, J. J. [1998]: *Revisiting Brittle Fracture as an Energy Minimization Problem*. Journal of the Mechanics and Physics of Solids, 46: 1319–1342.
- [73] FREUND, L. B. [1998]: *Dynamic Fracture Mechanics*. Cambridge University Press.
- [74] GÁLVEZ, J. C.; ELICES, M.; GUINEA, G. V.; PLANAS, J. [1998]: *Mixed-Mode Fracture of Concrete under Proportional and Nonproportional Loading*. International Journal of Fracture, 94: 267–284.
- [75] GASSER, T. C.; HOLZAPFEL, G. A. [2005]: *Modeling 3D Crack Propagation in Unreinforced Concrete using PUFEM*. Computer Methods in Applied Mechanics and Engineering, 194: 2859–2896.
- [76] GASSER, T. C.; HOLZAPFEL, G. A. [2006]: *3D Crack Propagation in Unreinforced Concrete. A Two-Step Algorithm for Tracking 3D Crack Paths*. Computer Methods in Applied Mechanics and Engineering, 195: 5198–5219.
- [77] GDOUTOS, E. E. [1990]: *Fracture Mechanics Criteria and Applications*. Kluwer Academic Publishers, Dordrecht.
- [78] GERMAIN, P. [1973]: *Cours de Mécanique des Milieux Continus*. Masson et Cie, Paris.
- [79] GOVINDJEE, S.; HACKL, K.; HEINEN, R. [2007]: *An Upper Bound to the Free Energy of Mixing by Twin-Compatible Lamination for  $n$ -Variant Martensitic Phase Transformations*. Continuum Mechanics and Thermodynamics, 18: 443–453.
- [80] GOVINDJEE, S.; MIEHE, C. [2001]: *A Multi-Variant Martensitic Phase Transformation Model: Formulation and Numerical Implementation*. Computer Methods in Applied Mechanics and Engineering, 191: 215–238.
- [81] GOVINDJEE, S.; MIELKE, A.; HALL, G. J. [2002]: *The Free Energy of Mixing for  $n$ -Variant Martensitic Phase Transformations using Quasi-Convex Analysis*. Journal of the Mechanics and Physics of Solids, 50: 1897–1922.
- [82] GRAVOUIL, A.; MOËS, N.; BELYTSCHKO, T. [2002]: *Non-Planar 3D Crack Growth by the Extended Finite Element and Level Sets - Part II: Level Set Update*. International Journal for Numerical Methods in Engineering, 53: 2569–2586.
- [83] GREEN, A. E.; RIVLIN, R. S. [1964]: *On Cauchy's Equations of Motion*. Zeitschrift für Angewandte Mathematik und Physik (ZAMP), 15: 290–292.
- [84] GRIFFITH, A. A. [1921]: *The Phenomena of Rupture and Flow in Solids*. Philosophical Transactions of the Royal Society of London A, 221: 163–198.
- [85] GRIFFITH, A. A. [1924]: *The theory of rupture*. In BIEZENO, C. B.; BURGERS, J. M. (Editors): *Proceedings of the First International Congress for Applied Mechanics, Delft*, pp. 55–63.



- [86] GÜRSES, E.; MIEHE, C. [2007]: *On Evolving Deformation Microstructures in Non-Convex Isotropic Damage Mechanics*. Submitted to International Journal of Solids and Structures.
- [87] GURTIN, M. E. [1995]: *The Nature of Configurational Forces*. Archive for Rational Mechanics and Analysis, 131: 67–100.
- [88] GURTIN, M. E. [2000]: *Configurational Forces as Basic Concepts of Continuum Physics*. Springer-Verlag, New York.
- [89] GURTIN, M. E.; PODIO-GUIDUGLI, P. [1996]: *Configurational Forces and the Basic Laws for Crack Propagation*. Journal of the Mechanics and Physics of Solids, 44: 905–927.
- [90] GURTIN, M. E.; PODIO-GUIDUGLI, P. [1998]: *Configurational Forces and a Constitutive Theory for Crack Propagation that Allows for Kinking and Curving*. Journal of the Mechanics and Physics of Solids, 46: 1343–1378.
- [91] HACKL, K.; HOPPE, U. [2003]: *On the Calculation of Microstructures for Inelastic Materials Using Relaxed Energies*. In MIEHE, C. (Editor): *Computational Mechanics of Solid Materials at Large Strains*, pp. 77–86. Kluwer Academic Publishers.
- [92] HALPHEN, B.; NGUYEN, Q. S. [1975]: *Sur les Matériaux Standards Généralisés*. Journal de Mécanique, 14: 39–63.
- [93] HANSBO, A.; HANSBO, P. [2004]: *A Finite Element Method for the Simulation of Strong and Weak Discontinuities in Solid Mechanics*. Computer Methods in Applied Mechanics and Engineering, 193: 3523–3540.
- [94] HAVNER, K. S. [1992]: *Finite Plastic Deformation of Crystalline Solids*. Cambridge University Press, Cambridge.
- [95] HEINTZ, P. [2006]: *On the Numerical Modelling of Quasi-Static Crack Growth in Linear Elastic Fracture Mechanics*. International Journal for Numerical Methods in Engineering, 65: 174–189.
- [96] HEINTZ, P.; LARSSON, F.; HANSBO, P.; RUNESSON, K. [2004]: *Adaptive Strategies and Error Control for Computing Material Forces in Fracture Mechanics*. International Journal for Numerical Methods in Engineering, 60: 1287–1299.
- [97] HENSHELL, R. D.; SHAW, K. G. [1975]: *Crack Tip Finite Elements are Unnecessary*. International Journal for Numerical Methods in Engineering, 9: 495–507.
- [98] HILLERBORG, A.; MODÉER, M.; PETERSSON, P. E. [1976]: *Analysis of Crack Formation and Crack Growth in Concrete by means of Fracture Mechanics and Finite Elements*. Cement and Concrete Research, 6: 773–782.
- [99] HILL, R. [1957]: *On Uniqueness and Stability in the Theory of Finite Elastic Strain*. Journal of the Mechanics and Physics of Solids, 5: 229–241.
- [100] HILL, R. [1962]: *Acceleration Waves in Solids*. Journal of the Mechanics and Physics of Solids, 10: 1–16.
- [101] HUTCHINSON, J. W. [1968]: *Singular Behavior at the End of a Tensile Crack Tip in a Hardening Material*. Journal of the Mechanics and Physics of Solids, 16: 13–31.
- [102] INGLIS, C. E. [1913]: *Stresses in a Plate Due to the Presence of Cracks and Sharp Corners*. Transactions of the Royal Institution of Naval Architects, 55: 219–230.

- [103] IRWIN, G. R. [1948]: *Fracture Dynamics*. In *Fracturing of Metals*, pp. 147–166.
- [104] IRWIN, G. R. [1957]: *Analysis of Stresses and Strains Near the End of a Crack Traversing a Plate*. *Journal of Applied Mechanics*, 24: 361–364.
- [105] IRWIN, G. R. [1958]: *Fracture*. In FLÜGGE, S. (Editor): *Encyclopedia of Physics*, Vol. 6, Elasticity and Plasticity, pp. 551–590. Springer.
- [106] IRWIN, G. R.; KIES, J. A. [1954]: *Critical Energy Rate Analysis of Fracture Strength*. *Welding Research Supplement*, 19: 193–198.
- [107] JAMES, R. D.; HANE, K. F. [2000]: *Martensitic Transformations and Shape Memory Materials*. *Acta Materialia*, 48: 197–222.
- [108] JEFFERSON, A. D.; BARR, B. I. G.; BENNETT, T.; HEE, S. C. [2004]: *Three Dimensional Finite Element Simulations of Fracture Tests using the Craft Concrete Model*. *Computer and Concrete*, 1: 261–284.
- [109] JIRÁSEK, M. [2000]: *Comparative Study on Finite Elements with Embedded Discontinuities*. *Computer Methods in Applied Mechanics and Engineering*, 188: 307–330.
- [110] JOST, J.; LI-JOST, X. [1998]: *Calculus of Variations*. Cambridge University Press, Cambridge.
- [111] KANNINEN, M. F.; POPELAR, C. H. [1985]: *Advanced Fracture Mechanics*. Oxford University Press, New York.
- [112] KARIHALOO, B. L.; XIAO, Q. Z. [2003]: *Modelling of Stationary and Growing Cracks in FE Framework without Remeshing: A State-of-the-Art Review*. *Computers and Structures*, 81: 119–129.
- [113] KIENZLER, R.; HERRMANN, G. [2000]: *Mechanics in Material Space: With Applications in Defect and Fracture Mechanics*. Springer-Verlag, Berlin, Heidelberg.
- [114] KNOTT, J. F. [1973]: *Fundamentals of Fracture Mechanics*. Butterworth, London.
- [115] KNOWLES, J. K.; STERNBERG, E. [1972]: *On a Class of Conservation Laws in Linearized and Finite Elastostatics*. *Archive for Rational Mechanics and Analysis*, 44: 187–211.
- [116] KOHN, R. V. [1991]: *The Relaxation of a Double-Well Energy*. *Continuum Mechanics and Thermodynamics*, 3: 193–236.
- [117] KOHN, R. V.; STRANG, G. [1986]: *Optimal Design and Relaxation of Variational Problems I, II, III*. *Communications on Pure and Applied Mathematics*, 39: 113–137, 139–182, 353–377.
- [118] KOLLING, S.; MUELLER, R. [2005]: *On Configurational Forces in Short-Time Dynamics and Their Computation with Explicit Solver*. *Computational Mechanics*, 35: 392–399.
- [119] KREYSZIG, E. [1978]: *Introductory Functional Analysis with Applications*. John Wiley & Sons.
- [120] KRUŽÍK, M.; MIELKE, A.; ROUBÍČEK, T. [2005]: *Modelling of Microstructure and its Evolution in Shape-Memory-Alloy Single-Crystals, in Particular in CuAlNi*. *Meccanica*, 40: 389–418.

- [121] LAMBRECHT, M. [2002]: *Theorie und Numerik von Materialinstabilitäten elasto-plastischer Festkörper auf der Grundlage inkrementeller Variationsformulierungen*. Ph.D. Thesis, Universität Stuttgart.
- [122] LAMBRECHT, M.; MIEHE, C.; DETTMAR, J. [2003]: *Energy Relaxation of Non-Convex Incremental Stress Potentials in a Strain-Softening Elastic-Plastic Bar*. International Journal of Solids and Structures, 40: 1369–1391.
- [123] LANCZOS, C. [1986]: *The Variational Principles of Mechanics*. Dover Publications, 4<sup>th</sup> Edition.
- [124] LARSSON, R.; FAGERSTRÖM, M. [2005]: *A Framework for Fracture Modelling based on the Material Forces Concept with XFEM Kinematics*. International Journal for Numerical Methods in Engineering, 62: 1763–1788.
- [125] LAWN, B. R. [1993]: *Fracture of Brittle Solids*. Cambridge University Press, 2nd Edition.
- [126] LEE, E. H. [1969]: *Elastic-Plastic Deformations at Finite Strains*. Journal of Applied Mechanics, 36: 1–6.
- [127] LI, F. Z.; SHIH, C. F.; NEEDLEMAN, A. [1985]: *A Comparison of Methods for Calculating Energy Release Rates*. Engineering Fracture Mechanics, 21: 405–421.
- [128] LUSKIN, M. [1996]: *On the Computation of Crystalline Microstructure*. Acta Numerica, 5: 191–258.
- [129] MAITI, S. K.; SMITH, R. [1983]: *Comparison of the Criteria for Mixed Mode Brittle Fracture based on the Preinstability Stress-Strain Field Part I: Slit and Elliptical Cracks under Uniaxial Tensile Loading*. International Journal of Fracture, 23: 281–295.
- [130] MARSDEN, J. E.; HUGHES, T. J. R. [1994]: *Mathematical Foundations of Elasticity*. Dover Publications Inc., New York.
- [131] MARTIN, J. B. [1975]: *Plasticity. Fundamentals and General Results*. MIT press, Cambridge, Massachusetts.
- [132] MAUGIN, G. A. [1992]: *The Thermomechanics of Plasticity and Fracture*. Cambridge University Press, Cambridge.
- [133] MAUGIN, G. A. [1993]: *Material Inhomogeneities in Elasticity*. Chapman & Hall, London.
- [134] MAUGIN, G. A. [1995]: *Material Forces: Concepts and Applications*. Applied Mechanics Reviews, 48: 213–245.
- [135] MAUGIN, G. A.; TRIMARCO, C. [1992]: *Pseudomomentum and Material Forces in Nonlinear Elasticity: Variational Formulations and Application to Brittle Fracture*. Acta Mechanica, 94: 1–28.
- [136] MEDIAVILLA, J.; PEERLINGS, R. H. J.; GEERS, M. G. D. [2006]: *An Integrated Continuous-Discontinuous Approach Towards Damage Engineering in Sheet Metal Forming Processes*. Engineering Fracture Mechanics, 73: 895–916.
- [137] MEDIAVILLA, J.; PEERLINGS, R. H. J.; GEERS, M. G. D. [2006]: *A Robust and Consistent Remeshing-Transfer Operator for Ductile Fracture Simulations*. Computers and Structures, 84: 604–623.

- [138] MEGUID, S. A. [1989]: *Engineering Fracture Mechanics*. Elsevier Science Publishers, England.
- [139] MELENK, J. M.; BABUŠKA, I. [1996]: *The Partition of Unity Finite Element Method: Basic Theory and Applications*. Computer Methods in Applied Mechanics and Engineering, 139: 289–314.
- [140] MERGHEIM, J.; KUHL, E.; STEINMANN, P. [2004]: *A Hybrid Discontinuous Galerkin/Interface Method for the Computational Modelling of Failure*. Communications in Numerical Methods in Engineering, 20: 511–519.
- [141] MIEHE, C. [1996]: *Exponential Map Algorithm for Stress Updates in Anisotropic Multiplicative Elastoplasticity for Single Crystals*. International Journal for Numerical Methods in Engineering, 39: 3367–3390.
- [142] MIEHE, C. [2002]: *Strain-Driven Homogenization of Inelastic Microstructures and Composites Based on an Incremental Variational Formulation*. International Journal for Numerical Methods in Engineering, 55: 1285–1322.
- [143] MIEHE, C.; GÜRSES, E. [2006]: *A Robust Algorithm for Configurational-Force-Driven Brittle Crack Propagation with R-Adaptive Mesh Alignment*. International Journal for Numerical Methods in Engineering, DOI: 10.1002/nme.1999.
- [144] MIEHE, C.; GÜRSES, E. [2007]: *A Computational Framework of Three-Dimensional Configurational-Force-Driven Brittle Crack Propagation*. Submitted to Computer Methods in Applied Mechanics and Engineering.
- [145] MIEHE, C.; GÜRSES, E.; BIRKLE, M. [2007]: *A Computational Framework of Configurational-Force-Driven Brittle Fracture Based on Incremental Energy Minimization*. International Journal of Fracture, DOI: 10.1007/s10704-007-9078-1.
- [146] MIEHE, C.; LAMBRECHT, M. [2003]: *Analysis of Microstructure Development in Shearbands by Energy Relaxation of Incremental Stress Potentials: Large-Strain Theory for Standard Dissipative Solids*. International Journal for Numerical Methods in Engineering, 58: 1–41.
- [147] MIEHE, C.; LAMBRECHT, M. [2003]: *A Two-Scale Finite Element Relaxation Analysis of Shear Bands in Non-Convex Inelastic Solids: Small-Strain Theory for Standard Dissipative Materials*. Computer Methods in Applied Mechanics and Engineering, 192: 473–508.
- [148] MIEHE, C.; LAMBRECHT, M.; GÜRSES, E. [2004]: *Analysis of Material Instabilities in Inelastic Solids by Incremental Energy Minimization and Relaxation Methods: Evolving Deformation Microstructures in Finite Plasticity*. Journal of the Mechanics and Physics of Solids, 52: 2725–2769.
- [149] MIEHE, C.; SCHOTTE, J.; LAMBRECHT, M. [2002]: *Homogenization of Inelastic Solid Materials at Finite Strains Based on Incremental Minimization Principles. Application to the Texture Analysis of Polycrystals*. Journal of the Mechanics and Physics of Solids, 50: 2123–2167.
- [150] MIELKE, A. [2002]: *Finite Elastoplasticity, Lie Groups and Geodesics on  $SL(d)$* . In NEWTON, P.; WEINSTEIN, A.; HOLMES, P. J. (Editors): *Geometry, Dynamics, and Mechanics*, pp. 61–90. Springer Verlag, Berlin Heidelberg.
- [151] MIELKE, A. [2003]: *Energetic Formulation of Multiplicative Elasto-Plasticity Using Dissipation Distances*. Continuum Mechanics and Thermodynamics, 15: 351–382.



- [152] MIELKE, A. [2004]: *Deriving New Evolution Equations for Microstructures via Relaxation of Variational Incremental Problems*. Computer Methods in Applied Mechanics and Engineering, 193: 5095–5127.
- [153] MOËS, N.; BELYTSCHKO, T. [2002]: *Extended Finite Element Method for Cohesive Crack Growth*. Engineering fracture Mechanics, 69: 813–833.
- [154] MOËS, N.; DOLBOW, J.; BELYTSCHKO, T. [1999]: *A Finite Element Method for Crack Growth without Remeshing*. International Journal for Numerical Methods in Engineering, 46: 131–150.
- [155] MOËS, N.; GRAVOUIL, A.; BELYTSCHKO, T. [2002]: *Non-Planar 3D Crack Growth by the Extended Finite Element and Level Sets - Part I: Mechanical Model*. International Journal for Numerical Methods in Engineering, 53: 2549–2568.
- [156] MOREAU, J. J. [1974]: *On Unilateral Constraints, Friction and Plasticity*. In CAPRIZ, G.; STAMPACCHIA, G. (Editors): *New Variational Techniques in Mathematical Physics, CISM Course*, pp. 175–322. Springer Verlag, Berlin Heidelberg.
- [157] MORREY, C. B. [1952]: *Quasi-Convexity and the Lower Semicontinuity of Multiple Integrals*. Pacific Journal of Mathematics, 2: 25–53.
- [158] MOSLER, J. [2004]: *On the Modeling of Highly Localized deformations Induced by Material Failure: The Strong Discontinuity Approach*. Archives of Computational Methods in Engineering, 11: 389–446.
- [159] MOSLER, J.; ORTIZ, M. [2006]: *On the Numerical Implementation of Variational Arbitrary Lagrangian-Eulerian (VALE) Formulations*. International Journal for Numerical Methods in Engineering, 67: 1272–1289.
- [160] MUELLER, R.; GROSS, D.; MAUGIN, G. A. [2004]: *Use of Material Forces in Adaptive Finite Element Methods*. Computational Mechanics, 33: 421–434.
- [161] MUELLER, R.; KOLLING, S.; GROSS, D. [2002]: *On Configurational Forces in the Context of the Finite Element Method*. International Journal for Numerical Methods in Engineering, 53: 1557–1574.
- [162] MUELLER, R.; MAUGIN, G. A. [2002]: *On Material Forces and Finite Element Discretizations*. Computational Mechanics, 29: 52–60.
- [163] MÜLLER, S. [1999]: *Variational Models for Microstructure and Phase Transitions*. In HILDERBRANDT, S.; STRUWE, M. (Editors): *Calculus of Variation and Geometric Evolution Problems, Lecture Notes in Mathematics 1713*, pp. 85–210. Springer Verlag, Berlin Heidelberg.
- [164] MÜLLER, S.; QI, T.; YAN, B. S. [1994]: *On a New Class of Elastic Deformations not Allowing for Cavitation*. Annales de l’Institut Henri Poincaré (C), Analyse non linéaire, 11: 217–243.
- [165] MUMFORD, D.; SHAH, J. [1989]: *Optimal Approximations by Piecewise Smooth Functions and Associated Variational Problems*. Communications on Pure and Applied Mathematics, 42: 577–685.
- [166] NEEDLEMAN, A. [1987]: *A Continuum model for Void Nucleation by Inclusion Debonding*. Journal of Applied Mechanics, 54: 525–531.
- [167] NGUYEN, Q. S. [2000]: *Stability and Nonlinear Solid Mechanics*. John Wiley & Sons, New York.

- [168] OBREIMOFF, J. W. [1930]: *The Splitting Strength of Mica*. Proceedings of the Royal Society of London A, 127: 290–297.
- [169] OLEAGA, G. E. [2001]: *Remarks on a Basic Law for Dynamic Crack Propagation*. Journal of the Mechanics and Physics of Solids, 49: 2273–2306.
- [170] OLEAGA, G. E. [2003]: *On the Dynamics of Cracks in Three Dimension*. Journal of the Mechanics and Physics of Solids, 51: 169–185.
- [171] OLIVER, J. [1996]: *Modelling Strong Discontinuities in Solid Mechanics via Strain Softening Constitutive Equations. Part1: Fundamentals and Part 2: Numerical Simulation*. International Journal for Numerical Methods in Engineering, 39: 3575–3600, 3601–3623.
- [172] OLIVER, J.; HUESPE, A. E.; SANCHEZ, P. J. [2006]: *A Comparative Study on Finite Elements for Capturing Strong Discontinuities: E-FEM vs. X-FEM*. Computer Methods in Applied Mechanics and Engineering, 195: 4732–4752.
- [173] OROWAN, E. [1955]: *Energy Criteria of Fracture*. Welding Journal Research Supplement, 34: 157–160.
- [174] ORTIZ, M.; PANDOLFI, A. [1999]: *Finite-Deformation Irreversible Cohesive Elements for Three-Dimensional Crack-Propagation Analysis*. International Journal for Numerical Methods in Engineering, 44: 1267–1282.
- [175] ORTIZ, M.; REPETTO, E. A. [1999]: *Nonconvex Energy Minimization and Dislocation Structures in Ductile Single Crystals*. Journal of the Mechanics and Physics of Solids, 47: 397–462.
- [176] ORTIZ, M.; REPETTO, E. A.; STAINIER, L. [2000]: *A Theory of Subgrain Dislocation Structures*. Journal of the Mechanics and Physics of Solids, 48: 2077–2114.
- [177] ORTIZ, M.; STAINIER, L. [1999]: *The Variational Formulation of Viscoplastic Constitutive Updates*. Computer Methods in Applied Mechanics and Engineering, 171: 419–444.
- [178] PANDOLFI, A.; ORTIZ, M. [2002]: *An Efficient Adaptive Procedure for Three-Dimensional Fragmentation Simulations*. Engineering with Computers, 18: 148–159.
- [179] PEDREGAL, P. [1993]: *Laminates and Microstructure*. European Journal of Applied Mathematics, 4: 121–149.
- [180] PEDREGAL, P. [2000]: *Variational Methods in Nonlinear Elasticity*. SIAM.
- [181] PETRYK, H. [1992]: *Material Instability and Strain-Rate Discontinuities in Incrementally Nonlinear Continua*. Journal of the Mechanics and Physics of Solids, 40: 1227–1250.
- [182] PETRYK, H. [2000]: *Theory of Material Instability in Incrementally Nonlinear Plasticity*. In PETRYK, H. (Editor): *Material Instabilities in Elastic and Plastic Solids, CISM Courses and Lectures No 414*, pp.
- [183] PHONGTHANAPANICH, S.; DECHAUMPHAI, P. [2004]: *Adaptive Delaunay Triangulation with Object-Oriented Programming for Crack Propagation Analysis*. Finite Elements in Analysis and Design, 40: 1753–1771.
- [184] PIPKIN, A. C. [1991]: *Elastic Materials with Two Preferred States*. The Quarterly Journal of Mechanics and Applied Mathematics, 44: 1–15.

- [185] PODIO-GUIDUGLI, P. [2001]: *Configurational Balances via Variational Arguments*. Interfaces and Free Boundaries, 3: 223–232.
- [186] REDDY, B. D. [1998]: *Introductory Functional Analysis with Applications to Boundary Value Problems and Finite Elements*. Springer-Verlag, New York.
- [187] REMMERS, J. J. C.; BORST, R. DE ; NEEDLEMAN, A. [2003]: *A Cohesive Segments Method for the Simulation of Crack Growth*. Computational Mechanics, 31: 69–77.
- [188] RICE, J. R. [1968]: *Mathematical Analysis in the Mechanics of Fracture*. In LIEBOWITZ, H. (Editor): *Fracture an Advanced Treatise*, Vol. 2, Chapter 3, pp. 191–311. Academic Press, New York.
- [189] RICE, J. R. [1968]: *A Path Independent Integral and the Approximate Analysis of Strain Concentration by Notches and Cracks*. Journal of Applied Mechanics, 35: 379–386.
- [190] RICE, J. R. [1971]: *Inelastic Constitutive Relations for Solids: An Internal-Variable Theory and its Application to Metal Plasticity*. Journal of the Mechanics and Physics of Solids, 19: 433–455.
- [191] RICE, J. R. [1976]: *The Localization of Plastic Deformation*. In KOITER, W. T. (Editor): *Theoretical and Applied Mechanics*, pp. 207–220. North-Holland, Amsterdam.
- [192] RICE, J. R.; ROSENGREN, G. F. [1968]: *Plane Strain Deformation near a Crack Tip in a Power Law Hardening Material*. Journal of the Mechanics and Physics of Solids, 16: 1–12.
- [193] ROCKAFELLAR, R. T. [1970]: *Convex Analysis*. Princeton University Press, Princeton.
- [194] ROOKE, D. P.; CARTWRIGHT, D. J. [1976]: *Compendium of Stress Intensity Factors*. Hillingdon Press, Uxbridge.
- [195] SANDERS, J. L. JR. [1960]: *On the Griffith-Irwin Fracture Theory*. Journal of Applied Mechanics, 27: 352–353.
- [196] SCHMIDT-BALDASSARI, M.; HACKL, K. [2003]: *Incremental Variational Principles in Damage Mechanics*. PAMM, 2: 216–217.
- [197] SCHRÖDER, J. [2000]: *Homogenisierungsmethoden der nichtlinearen Kontinuumsmechanik unter Beachtung von Stabilitätsproblemen*. Habilitationsschrift, Universität Stuttgart.
- [198] SCHRÖDER, J.; NEFF, P. [2003]: *Invariant Formulation of Hyperelastic Transverse Isotropy based on Polyconvex Free Energy Functions*. International Journal of Solids and Structures, 40: 401–445.
- [199] SIH, G. C.; LIEBOWITZ, H. [1967]: *On the Griffith Energy Criterion for Brittle Fracture*. International Journal of Solids and Structures, 3: 1–22.
- [200] ŠILHAVÝ, M. [1997]: *The Mechanics and Thermodynamics of Continuous Media*. Springer-Verlag, Berlin Heidelberg New York.
- [201] SIMÓ, J. C.; ARMERO, F. [1992]: *Geometrically Non-Linear Enhanced Strain Mixed Methods and the Method of Incompatible Modes*. International Journal for Numerical Methods in Engineering, 33: 1413–1449.



- [202] SIMO, J. C.; OLIVER, J.; ARMERO, F. [1993]: *An Analysis of Strong Discontinuities induced by Strain-Softening in Rate-Independent Inelastic Solids*. Computational Mechanics, 12: 277–296.
- [203] SNEDDON, I. N. [1946]: *The Distribution of Stress in the Neighbourhood of a Crack in an Elastic Solid*. Proceedings of the Royal Society of London A, 187: 229–260.
- [204] SPENCER, A. J. M. [1965]: *On the Energy of the Griffith Crack*. International Journal of Engineering Science, 3: 441–449.
- [205] STEINMANN, P. [2000]: *Application of Material Forces to Hyperelastostatic Fracture Mechanics. I. Continuum Mechanical Setting*. International Journal of Solids and Structures, 37: 7371–7391.
- [206] STEINMANN, P.; ACKERMANN, D.; BARTH, F. J. [2001]: *Application of Material Forces to Hyperelastostatic Fracture Mechanics. II. Computational Setting*. International Journal of Solids and Structures, 38: 5509–5526.
- [207] STUMPF, H.; LE, K. C. [1990]: *Variational Principles of Nonlinear Fracture Mechanics*. Acta Mechanica, 83: 25–37.
- [208] THOUTIREDDY, P.; ORTIZ, M. [2004]: *A Variational  $r$ -Adaptation and Shape Optimization Method for Finite-Deformation Elasticity*. International Journal for Numerical Methods in Engineering, 61: 1–21.
- [209] TRUESDELL, C.; NOLL, W. [1965]: *The Non-Linear Field Theories of Mechanics*. In FLÜGGE, S. (Editor): *Handbuch der Physik*, Chapter Bd. III/3. Springer-Verlag, Berlin.
- [210] WEBER, G.; ANAND, L. [1990]: *Finite Deformation Constitutive Equations and a Time Integration Procedure for Isotropic, Hyperelastic-Viscoplastic Solids*. Computer Methods in Applied Mechanics and Engineering, 79: 173–202.
- [211] WELLS, A. A. [1963]: *Application of Fracture Mechanics at and Beyond General Yielding*. British Welding Journal, 10: 563–570.
- [212] WELLS, G. N.; SLUYS, L. J. [2001]: *A New Method for Modelling Cohesive Cracks using Finite Elements*. International Journal for Numerical Methods in Engineering, 50: 2667–2682.
- [213] WESTERGAARD, H. M. [1939]: *Bearing Pressures and Cracks*. Journal of Applied Mechanics, 6: 49–53.
- [214] WILLIAMS, M. L. [1957]: *On the Stress Distribution at the Base of a Stationary Crack*. Journal of Applied Mechanics, 24: 109–114.
- [215] WILLIS, J. R. [1967]: *A Comparison of the Fracture Criteria of Griffith and Barenblatt*. Journal of the Mechanics and Physics of Solids, 15: 151–162.
- [216] XU, X. P.; NEEDLEMAN, A. [1994]: *Numerical Simulations of Fast Crack Growth in Brittle Solids*. Journal of the Mechanics and Physics of Solids, 42: 1397–1434.
- [217] YOUNG, L. C. [1969]: *Lectures on the Calculus of Variations and Optimal Control Theory*. Saunders, London.
- [218] ZIEGLER, H.; WEHRLI, C. [1987]: *The Derivation of Constitutive Relations from the Free Energy and the Dissipation Function*. In WU, TH. Y.; HUTCHINSON, J. W. (Editors): *Advances in Applied Mechanics, Vol. IV*. Academic Press Inc.



# Curriculum Vitae

## Personal Data

Name	Ercan Gürses
Date of Birth	May 9, 1978
Place of Birth	Ankara, Turkey
Parents	Dr. Deniz Gürses and Sülun Gürses
Siblings	Dr. Eren Gürses
Marital Status	Single
Nationality	Turkish

## School Education

1983-1985	Maltepe Primary School, Ankara
1985-1988	Sadettin Tezcan Primary School, İzmir
1988-1991	Ali Erentürk Secondary School, İzmir
1991-1994	Ankara Science High School, Ankara

## University Education

1994-1999	Undergraduate Studies of Civil Engineering Middle East Technical University, Ankara
1999-2000	Graduate Studies of Civil Engineering Middle East Technical University, Ankara
2000-2002	M.Sc. in Computational Mechanics of Materials and Structures (COMMAS), University of Stuttgart

## Professional Occupation

1999-2000	Teaching Assistant, Structural Mechanics Laboratory Middle East Technical University, Ankara
2002-2007	Research Associate, Institute of Applied Mechanics Civil Engineering, University of Stuttgart



**In dieser Schriftenreihe bisher erschienene Berichte:**

- I-1(1996) *Theoretische und algorithmische Konzepte zur phänomenologischen Beschreibung anisotropen Materialverhaltens*, J. Schröder, Dissertation, 1996.
- I-2(1996) *Zur Theorie und Numerik finiter elastoplastischer Deformationen von Schalentragwerken*, B. Seifert, Dissertation, 1996.
- I-3(1996) *Zur Modellierung des künstlichen Infrarot-Dichroismus in Polymerfolien bei großen Verformungen*, J. Buhler, Dissertation, 1996.
- I-4(1998) *Verfahren zur Ermittlung der Erdbebenlasten mit Berücksichtigung des stochastischen Charakters des Bebens*, S. Zhang, Dissertation, 1998.
- I-5(1998) *Zur Beschreibung finiter Deformationen von Polymeren: Experimente, Modellbildung, Parameteridentifikation und Finite-Elemente- Formulierung*, J. Keck, Dissertation, 1998.
- I-6(1999) *Berechnungsverfahren instationär erregter Systeme im Frequenzbereich*, A. Jaworek, Dissertation, 1999.
- I-7(2000) *Homogenisierungsmethoden der nichtlinearen Kontinuumsmechanik unter Beachtung von Stabilitätsproblemen*, J. Schröder, Habilitation, 2000.
- I-8(2002) *Theorie und Numerik von Materialinstabilitäten elastoplastischer Festkörper auf der Grundlage inkrementeller Variationsformulierungen*, M. Lambrecht, Dissertation, 2002.
- I-9(2002) *Mikromechanisch motivierte Modelle zur Beschreibung finiter Deformationen gummiartiger Polymere: physikalische Modellbildung und numerische Simulation*, F. Lulei, Dissertation, 2002.
- I-10(2003) *Adaptive Finite-Elemente-Berechnungen der nichtlinearen Festkörpermechanik bei kleinen und großen Verzerrungen*, A. Koch, Dissertation, 2003.
- I-11(2003) *Theorie und Numerik der Parameteridentifikation von Materialmodellen der finiten Elastizität und Inelastizität auf der Grundlage optischer Feldmeßmethoden*, G. Scheday, Dissertation, 2003.
- I-12(2004) *Approaches to the Description of Anisotropic Material Behaviour at Finite Elastic and Plastic Deformations, Theory and Numerics*, N. Apel, Dissertation, 2004.
- I-13(2004) *Temperaturabhängige Beschreibung visko-elasto-plastischer Deformationen kurzglasfaserverstärkter Thermoplaste: Modellbildung, Numerik und Experimente*, S. Rieger, Dissertation, 2004.
- I-14(2005) *Zur Parameteridentifikation komplexer Materialmodelle auf der Basis realer und virtueller Testdaten*, A. Rieger, Dissertation, 2005.
- I-15(2005) *Viskoelastisches Verhalten von Elastomeren bei finiten Verzerrungen: Experimente, Modellierung und Simulationen*, H. Zecha, Dissertation, 2005.

- I-16(2005) *Mehrskalenmodelle in der Festkörpermechanik und Kopplung von Mehrgittermethoden mit Homogenisierungsverfahren*, C.G. Bayreuther, Dissertation, 2005.
- I-17(2005) *Static and Dynamic Homogenization Analyses of Discrete Granular and Atomistic Structures on Different Time and Length Scales*, J. Dettmar, Dissertation, 2005.
- I-18(2006) *Incompatibility and Instability Based Size Effects in Crystals and Composites at Finite Elastoplastic Strains*, M. Becker, Dissertation, 2006.
- I-19(2007) *Aspects of Energy Minimization in Solid Mechanics: Evolution of Inelastic Microstructures and Crack Propagation*, E. Gürses, Dissertation, 2007.